2015

QCD
and
High Energy Interactions

Sponsored by

. CNRS (Centre National de la Recherche Scientifique)
. FNRS (Fond National de la Recherche Scientifique)
. BSP (Belgian Science Policy)

50th Rencontres de Moriond

La Thuile, Aosta Valley, Italy – March 21-28, 2015

2015 QCD and High Energy Interactions

ISBN : 978-2-9546400-7-5

web

Proceedings of the 50th RENCONTRES DE MORIOND

QCD and High Energy Interactions

La Thuile, Aosta Valley Italy *March 21-28, 2015*

2015

QCD and High Energy Interactions

edited by

Etienne Augé,
Jacques Dumarchez
and
Jean Trân Thanh Vân

The 50th Rencontres de Moriond

2015 QCD and High Energy Interactions

was organized by :

Etienne Augé (LAL, Orsay)
Jacques Dumarchez (LPNHE, Paris)

with the active collaboration of :

E. Berger (A.N.L. Argonne)
S. Bethke (M.P.I. Munich)
A. Capella (L.P.T. Orsay)
A. Czarnecki (U. Alberta)
D. Denegri (C.E.A. Saclay)
N. Glover (Durham)
B. Klima (Fermilab)
M. Krawczyk (University of Warsaw)
L. McLerran (Brookhaven Nat. Lab.)
B. Pietrzyk (L.A.P.P. Annecy)
L. Schoeffel (CEA - IRFU/SPP - Saclay)
Chung-I Tan (Brown University)
J. Trân Thanh Vân (L.P.T. Orsay)
U. Wiedemann (CERN)

2015 RENCONTRES DE MORIOND

The 50^{th} Rencontres de Moriond were held in La Thuile, Valle d'Aosta, Italy.

The first meeting took place at Moriond in the French Alps in 1966. There, experimental as well as theoretical physicists not only shared their scientific preoccupations, but also the household chores. The participants in the first meeting were mainly french physicists interested in electromagnetic interactions. In subsequent years, a session on high energy strong interactions was added.

The main purpose of these meetings is to discuss recent developments in contemporary physics and also to promote effective collaboration between experimentalists and theorists in the field of elementary particle physics. By bringing together a relatively small number of participants, the meeting helps develop better human relations as well as more thorough and detailed discussion of the contributions.

Our wish to develop and to experiment with new channels of communication and dialogue, which was the driving force behind the original Moriond meetings, led us to organize a parallel meeting of biologists on Cell Differentiation (1980) and to create the Moriond Astrophysics Meeting (1981). In the same spirit, we started a new series on Condensed Matter physics in January 1994. Meetings between biologists, astrophysicists, condensed matter physicists and high energy physicists are organized to study how the progress in one field can lead to new developments in the others. We trust that these conferences and lively discussions will lead to new analytical methods and new mathematical languages.

The 50^{th} Rencontres de Moriond in 2014 comprised three physics sessions:

- March 14 - 21: "Electroweak Interactions and Unified Theories"
- March 21 - 28: "QCD and High Energy Hadronic Interactions"
- March 21 - 28: "Gravitation: 100 years after GR"

We thank the organizers of the 50^{th} Rencontres de Moriond:

- A. Abada, E. Armengaud, J. Conrad, P. Fayet, J.-M. Frère, P. Hernandez, L. Iconomidou-Fayard, P. Janot, M. Knecht, J. P. Lees, S. Loucatos, F. Montanet, L. Okun, J. Orloff, A. Pich, S. Pokorski, V. Tisserand, D. Wood for the "Electroweak Interactions and Unified Theories" session,
- E. Augé, E. Berger, S. Bethke, A. Capella, A. Czarnecki, D. Denegri, N. Glover, B. Klima, M. Krawczyk, L. McLerran, B. Pietrzyk, L. Schoeffel, Chung-I Tan, J. Trân Thanh Vân, U. Wiedemann for the "QCD and High Energy Hadronic Interactions" session,
- P. Binétruy, M.-A. Bizouard, L. Blanchet, L. Cacciapuoti, F. Cavalier, M. Cruise, P. Delva, J. Dumarchez, J.-M. Le Goff, S. Léon-Hirtz, E. Rasel, S. Reynaud, F. Ricci, J.-Y. Vinet for the "Gravitation: 100 years after GR" session

and the conference secretariat and technical staff:

V. de Sá-Varanda and C. Bareille, I. Cossin, G. Dreneau, D. Fliegel, F. Legrand, G. Perrin, N. Ribet, S. Vydelingum.

We are also grateful to Giorgio Palmucci, Francesco Cante, Ida Liseno, Francesco Quinto and the Planibel Hotel staff who contributed through their hospitality and cooperation to the well-being of the participants, enabling them to work in a relaxed atmosphere.

The Rencontres were sponsored by the Centre National de la Recherche Scientifique, the Fonds de la Recherche Scientifique (FRS-FNRS) and the Belgium Science Policy. We would like to express our thanks for their encouraging support.

It is our sincere hope that a fruitful exchange and an efficient collaboration between the physicists and the astrophysicists will arise from these Rencontres as from previous ones.

The 50^{th} edition of these Rencontres offered us the possibility to celebrate with dedicated talks by some of the pillars of Moriond, giving their personnal recollections or panoramic views of the evolution of physics ideas along these 50 Rencontres. We would like to warmly thank D. Treille, G. Altarelli, E. Fischbach, M. Krawczyk, D. Goulianos, and B. Klima. Videos of these moments can be viewd on: `https://webcast.in2p3.fr/events-moriond_2015`*, thanks to the webcast services at CC-IN2P3 and LAL, and particularly to O. Drevon and G. Dreneau. The 50^{th} Rencontres were also the occasion of renewing some long-standing traditions of Moriond, like the slalom: tens of participants of all ages skied down the track in all times and styles to eventually win ... a glass of mulled wine! And delving into the archives we have produced a list of the nearly 10000 participants of these 50 Rencontres, which has been put up as wallpaper along the corridor leading to the bar, resulting in persistant traffic jams!*

E. Augé, J. Dumarchez and J. Trân Thanh Vân

Contents

1.
Higgs

Study of Higgs production in fermionic decay channels at the LHC

Aruna Kumar Nayak
Deutsches Elektronen-Synchrotron, Hamburg, Germany
(On behalf of the ATLAS and CMS collaborations)

The results of the searches for a Higgs boson decaying to down-type fermions are presented using the proton-proton collision data collected by the ATLAS and CMS experiments at the LHC, at a centre-of-mass energy of 7 & 8 TeV. The results obtained with the available data provides a strong evidence for a Higgs boson coupling to fermions. Results are also presented for a Higgs boson production in association with a pair of top quarks.

1 Introduction

A Higgs boson of mass around 125 GeV has recently been discovered by the ATLAS and CMS experiments at LHC [1,2]. The discovery was made in channels where the Higgs boson decays to a pair of gauge bosons. However, there was no direct observation in fermionic channels. Thereafter, the LHC added more data and the analysis strategies for the searches in fermionic final states have been greatly improved. In SM, the Higgs boson couples to fermions via Yukawa interactions, where the coupling strength is proportional to the fermion mass. Thus, $\mathrm{H} \to \tau\tau$ and $\mathrm{H} \to \mathrm{b\bar{b}}$ are two major fermionic channels to search for the Higgs boson at LHC.

Due to the nature of the Yukawa coupling in the SM, the Higgs boson is expected to have strong coupling to the top quark relative to the other fermions. The coupling to the top quark can be accessed indirectly through the measurements of gluon fusion production mechanism and Higgs boson decay to photons, which involves the fermion loop dominated by the top quark contribution. The current measurements of top quark Yukawa couplings are consistent with that of SM predictions within the experimental uncertainties [3,4]. However, the production of the Higgs boson in association with a top-quark pair ($t\bar{t}$H) allows for a direct probe of top-quark Yukawa coupling. A measurement of the $t\bar{t}$H production rate will provide a direct test of the Higgs boson's coupling to top quark.

This article summarizes the results of the searches for the SM Higgs boson in the channels $\mathrm{H} \to \mathrm{b\bar{b}}$, $\mathrm{H} \to \tau\tau$, $\mathrm{H} \to \mu\mu$, and $\mathrm{H} \to ee$ with the data collected by the ATLAS and CMS experiments at LHC at a centre-of-mass energy of 7 & 8 TeV, corresponding to an integrated luminosity of approximately 5 & 20 fb^{-1}, respectively. The results of a search for $t\bar{t}$H production in the above experiments are also described.

2 Searches for VH, H $\to$ b$\bar{\text{b}}$

Since the inclusive production of H $\to$ b$\bar{\text{b}}$ is overwhelmingly dominated by the QCD multi-jets background, the search is performed in the production mode where the Higgs boson is produced in association with a vector boson [5,6]. The following search channels are considered: W($\mu\nu$)H, W(eν)H, W($\tau\nu$)H, Z($\mu\mu$)H, Z(ee)H, and Z($\nu\nu$)H, where H decays to b$\bar{\text{b}}$. The major backgrounds arise from the production of W/Z+jets, $t\bar{t}$, dibosons and QCD multi-jet events. The analysis strategy is based on the reconstruction of the vector bosons in their leptonic decay modes and of the Higgs boson decay into two b-tagged jets. The events are further categorized based on the p_{T} of the vector bosons, and b-tagging discriminator values of the jets. The H $\to$ b$\bar{\text{b}}$ decay is reconstructed by selecting a pair of b-tagged jets, for which p_{T}(jj) is highest. Both the experiments have developed techniques to improve the b-jet energy calibration, thus improving the Higgs boson mass resolution. The sensitivity of the search is improved using a multivariate analysis (MVA) approach. Dedicated Boosted Decision Tree (BDT) discriminants are trained combining dijet mass with other variables sensitive to kinematic, topological and b-tagging properties of the selected events.

The CL$_s$ method [7] is used to obtain 95% confidence level (CL) upper limits on σ/σ_{SM}. For a Higgs boson of mass 125 GeV, the observed (expected) limits are 1.2 (0.8) and 1.89 (0.95), obtained by ATLAS and CMS experiments, respectively. The best fit values of the signal strength parameter, μ (σ/σ_{SM}), for $m_{\mathrm{H}} = 125$ GeV are found to be 0.51$\pm$0.31(stat.)$\pm$0.24(syst.) by the ATLAS, and 0.84$\pm$0.44 by the CMS experiment, respectively. The ATLAS measured an observed local significance of 1.4σ, to be compared to an expectation of 2.6σ, for a Higgs boson mass of 125 GeV, while the CMS found an observed (expected) significance of 2.0σ (2.6σ). Note that the values of μ and significance obtained by the CMS also includes the production process $t\bar{t}$H, H $\to$ b$\bar{\text{b}}$ and $gg \to$ ZH, H $\to$ b$\bar{\text{b}}$ [4], while the later production process is included in the ATLAS result. All these results are compatible with the presence of the SM Higgs boson of mass approximately 125 GeV.

3 Searches for H $\to \tau^+\tau^-$

Both the ATLAS and CMS experiments have searched for the SM Higgs boson decaying to a pair of τ leptons [8,9]. The search strategy for H $\to \tau\tau$ makes use of all leading production mechanisms at LHC: gluon-gluon fusion (ggF), vector boson fusion (VBF), and associated production with a W or Z boson. The analyses consider all possible decays of τ lepton, hadronically or leptonically, leading to six different final states: $\mu\tau_h$, eτ_h, $\tau_h\tau_h$, eμ, $\mu\mu$, and ee, where τ_h denotes the hadronic decay of τ lepton. The major backgrounds arise from the production of Z $\to \tau\tau$, W+jets, $t\bar{t}$+jets and QCD multi-jet events. Most of the background yields are estimated, and their distributions are modeled, using data.

To maximize the sensitivity of the analysis, the ATLAS experiment employs a MVA approach. The events are divided in to two broad categories: VBF and boost category. The VBF category targets events produced in the VBF production mechanism, while the boost category targets events with a boosted Higgs boson produced in ggF process. Separate BDTs are trained for each analysis channel and category, for a Higgs boson mass of 125 GeV, combining the variables sensitive to the kinematic properties of the leptons and jets, $E_{\mathrm{T}}^{\mathrm{miss}}$, and the reconstructed invariant mass of the τ-lepton pair ($m_{\tau\tau}$). In both the experiments, $m_{\tau\tau}$ is computed using likelihood based techniques from the four-momenta of the individual leptons and the $E_{\mathrm{T}}^{\mathrm{miss}}$ vector. The CMS experiment adopted a cut-based analysis approach to enhance the sensitivity of the analysis. The events are divided in to several categories using the variables such as number of jets, dijet mass (m_{jj}), η difference between the jets ($\Delta\eta_{jj}$), visible p_{T} of the τ leptons, and p_{T} of the reconstructed di-τ candidates. The distribution of the BDT discriminant and $m_{\tau\tau}$ are used as the final discriminator in ATLAS and CMS analyses, respectively.

An excess of events is observed with respect to the background-only hypothesis, which is

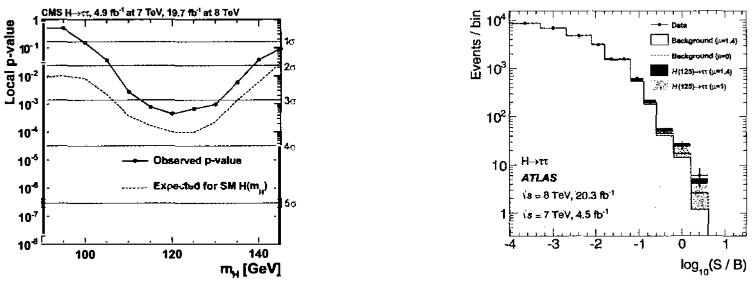

Figure 1 – Left: Local p-value and significance as function of SM Higgs boson mass hypothesis from CMS analysis. Right: Event yields as a function of $\log_{10}$(S/B), where S (signal yield) and B (background yield) are taken from BDT output, assuming $\mu = 1.4$.

compatible with the presence of the SM Higgs boson of mass 125 GeV. The excess is quantified by the local p-values, which is shown in Fig. 1(left) for CMS analysis. For $m_{\rm H} = 125$ GeV, the expected and observed p-values correspond to a significance of 3.7 and 3.2 standard deviations, respectively. The corresponding values from ATLAS analysis are 3.4σ (expected) and 4.5σ (observed) at $m_{\rm H} = 125.36$ GeV. The best fit values of μ are $1.43^{+0.43}_{-0.37}$ at $m_{\rm H} = 125.36$ GeV and 0.78 ± 0.27 at $m_{\rm H} = 125$ GeV from ATLAS and CMS analyses, respectively. The distribution of event yield, in bins of $\log_{10}$(S/B), for all signal region bins is shown in Fig. 1(right) for ATLAS analysis, which is calculated assuming $\mu = 1.4$. These observations provide a strong evidence for the coupling of the Higgs boson to τ leptons as expected from the SM.

The CMS experiment combined the results of the searches for a Higgs boson decaying to b quarks and τ leptons [10], which results in a strong evidence for the direct coupling of the observed 125 GeV Higgs boson to down-type fermions. The observed significance for a Higgs boson to down-type fermion coupling is 3.8σ, to be compared to an expectation of 4.4σ.

4 Searches for $\rm H \to \mu^+\mu^-$ & $\rm H \to e^+e^-$

The CMS experiment performed a search for a SM-like Higgs boson decaying to a pair of muons or a pair of electrons [11], while the ATLAS experiment searched for a Higgs boson decaying to a pair of muons [12]. No excess of events are observed, and a 95% CL upper limit is obtained on the production cross section times branching fraction using the CL$_s$ method. For a SM Higgs boson with a mass of 125 GeV (125.5 GeV for ATLAS), the upper limit obtained on branching fractions are $\mathcal{B}(\rm H \to \mu^+\mu^-) < 0.0016$ and $\mathcal{B}(\rm H \to e^+e^-) < 0.0019$ from CMS analysis, and $\mathcal{B}(\rm H \to \mu^+\mu^-) < 0.0015$ from ATLAS analysis, respectively. These results provide a confirmation for the fact that the Higgs boson coupling to leptons are not flavor universal, unlike vector bosons.

5 Searches for $t\bar{t}$H production

The search for a Higgs boson produced in association with a pair of top quarks at LHC is extremely challenging due to its small production cross section, approximately 130 fb at 8 TeV, and large background contribution from inclusive $t\bar{t}$+jets production process. The searches are performed in final states where W bosons from both the top quarks decay to leptons, or W boson from one top quark decays to lepton while the other decays to jets. The ATLAS experiment performed searches for $t\bar{t}$H production where the Higgs boson decays to $\rm b\bar{b}$ [13], and where the Higgs boson decays to leptons via the decay of WW*, $\tau\tau$, and ZZ* [14]. The CMS experiment performed searches for $t\bar{t}$H production where the following signatures of Higgs boson decay are considered: H $\to$ hadrons, H $\to$ photons, and H $\to$ leptons [15]. These decays proceed via the decay of Higgs boson to $\rm b\bar{b}$, $\tau\tau$, WW*, ZZ*, and $\gamma\gamma$.

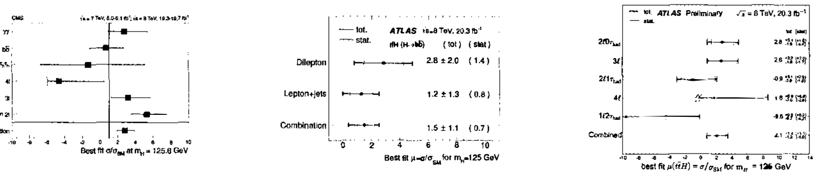

Figure 2 – The best fit value of the signal strength parameter $\mu = \sigma/\sigma_{SM}$ for each $t\bar{t}$H channel.

The general strategy is to select $t\bar{t}$-like events requiring at least one or more b-tagged jets. To enhance the signal over $t\bar{t}$ background, the events are divided in to several categories based on the number of jets and b-tagged jets. Both experiments use MVA approach to separate signal from backgrounds.

The combined CMS results obtained an observed (expected) upper limit of 4.5 (1.7) on σ/σ_{SM} at 95% CL. The upper limits obtained by ATLAS are compatible with the presence of a SM Higgs boson. Figure 2 shows measured values of signal strength μ in both the experiments. While the measured μ values in ATLAS are consistent with SM expectations within the uncertainty, the combined value of μ obtained in CMS have a roughly 2 standard deviation upward fluctuation. The CMS experiment also performed a separate analysis for the search of $t\bar{t}$H, H $\rightarrow$ b$\bar{\text{b}}$ using matrix-element method [16], which improves the sensitivity by approximately 15% compared to the standard $t\bar{t}$H, H $\rightarrow$ b$\bar{\text{b}}$ analysis. The ATLAS experiment has also utilized matrix-element discriminators in some of the high purity categories of the $t\bar{t}$H, H $\rightarrow$ b$\bar{\text{b}}$ analysis, which were used as input to the multivariate discriminant.

6 Conclusion

The results of the searches for the SM Higgs boson decaying to a pair of b quarks or a pair of τ leptons using the ATLAS and CMS detectors provide a strong evidence for the Higgs boson coupling to down-type fermions. The experiments have made strong progress in the direct measurement of Higgs boson coupling to top quark. The results obtained with the available data are consistent with the SM expectations. The LHC run at 13 TeV, expected to start from mid 2015, will provide definitive answers about the Higgs boson coupling to fermions.

References

1. ATLAS Collaboration, *Phys. Lett.* B **716**, 1 (2012).
2. CMS Collaboration, *Phys. Lett.* B **716**, 30 (2012).
3. ATLAS Collaboration, ATLAS-CONF-2015-007 (2015).
4. CMS Collaboration, arXiv:1412.8662 [hep-ex] (2014).
5. ATLAS Collaboration, *JHEP* **01**, 069 (2015).
6. CMS Collaboration, *Phys. Rev.* D **89**, 012003 (2014).
7. A. L. Read, *J. Phys. G* **28**, 2693 (2002).
8. ATLAS Collaboration, *JHEP* **04**, 117 (2015).
9. CMS Collaboration, *JHEP* **05**, 104 (2014).
10. CMS Collaboration, *Nature Physics* **10**, 557 (2014).
11. CMS Collaboration, *Phys. Lett.* B **744**, 184 (2015).
12. ATLAS Collaboration, *Phys. Lett.* B **738**, 68 (2014).
13. ATLAS Collaboration, arXiv:1503.05066 [hep-ex] (2015).
14. ATLAS Collaboration, ATLAS-CONF-2015-006 (2015).
15. CMS Collaboration, *JHEP* **09**, 087 (2014).
16. CMS Collaboration, arXiv:1502.02485 [hep-ex] (2015).

Combination of Higgs Boson Coupling Measurements from ATLAS and CMS

Roko Pleština
for the ATLAS and CMS collaborations
Institute of High Energy Physics, CAS, Beijing, China

Properties of the Higgs boson with mass near 125 GeV are measured in proton-proton collisions with integrated luminosities of up to 5.1 fb^{-1} at $\sqrt{s} = 7$ TeV and 20.3 fb^{-1} at $\sqrt{s} = 8$ TeV, recorded by the ATLAS and CMS detectors in 2011 and 2012. Combining all production modes and decay channels, the measured signal yield, normalized to the Standard Model expectation, is $1.18^{+0.15}_{-0.14}$ (ATLAS), and $1.00^{+0.14}_{-0.13}$ (CMS). The observed Higgs boson production and decay rates are interpreted in a leading order coupling framework, exploring a wide range of benchmark coupling models both with and without assumptions on the Higgs boson width and the SM particle content in loop processes. The observed data are found to be compatible with the SM expectations.

1 Introduction

I report selected results of the compatibility tests of the Higgs boson couplings to SM particles and of searches for deviations of the couplings from the SM predictions, using a tree-level motivated benchmark model from LHC Higgs XS WG [1]. For details on detector and analyses, the reader is kindly asked to consult the publications from ATLAS [2,?] and CMS [4,?].

These results are derived from a combination of all analyzed decays and production modes of the Higgs boson. To achieve the best sensitivity the analyses are categorized according to different signal over background and/or production mode and decay compositions. The categorization allows for extraction of Higgs couplings to different particles. The actual combinations are done with gluon-gluon fusion (ggF), vector boson fusion (VBF), Higgs strahlung (VH) and $t\bar{t}$ associated ($t\bar{t}H$) production categories and $\gamma\gamma$, ZZ, WW, $\tau\tau$, $b\bar{b}$, $Z\gamma$, $\mu\mu$ Higgs decay categories. As a figure of merit of complexity, a total of 207 categories are combined in CMS, using 2519 nuisance parameters corresponding to sources of uncertainty other than those arising from data statistical uncertainties. The invariant mass of the Higgs boson is considered to be a known parameter — 125.36 GeV (ATLAS) and 125.02 GeV (CMS).

2 Signal Strength

The signal strength parameter is a measure of potential deviations from the SM prediction under the assumption that the Higgs boson production and decay kinematics do not change appreciably from the SM expectations. In particular, the transverse momentum and rapidity distributions of the Higgs boson are assumed to be those predicted for the SM Higgs boson by state-of-the-art event generators and calculations of each production process.

Assuming a common multiplier to all signal yields, they can be combined to result in a global, more precise measurement of the signal strength parameter, providing the simplest consistency test with the SM expectation. Combining all measurements using the profile likelihood ratio $\Lambda(\mu)$ results in a global signal strength value of $\mu = 1.18 \pm 0.10(\text{stat.})^{+0.08}_{-0.07}(\text{theo.}) \pm 0.07(\text{syst.})$ observed in ATLAS data, and $\mu = 1.00 \pm 0.09(\text{stat.})^{+0.08}_{-0.07}(\text{theo.}) \pm 0.07(\text{syst.})$ in CMS data.

Figure 1a shows the signal strength measurements grouped by decay modes from ATLAS where same decay channels are combined together for all the ATLAS analyses.

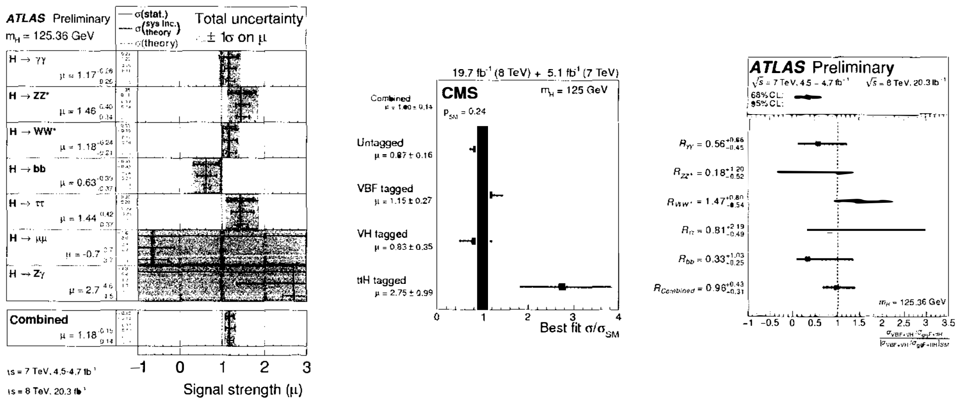

Figure 1 – Signal strengths grouped by decay modes (left) from ATLAS, by production modes (middle) from CMS, and the cross-section ratios between vector boson and fermion-mediated processes relative to their SM values (right) measured by ATLAS.

Figure 1b shows the signal strength measurements grouped by production modes from CMS where SM branching fractions are assumed in order to factor out the signal strengths from production modes. All results are found to be consistent with one and the largest deviations is a small excess at the level of two sigma observed in $t\bar{t}H$ channel in both experiments.

Compatibility of couplings to bosons and fermions with SM expectations can be examined by looking at signal strengths of different Higgs production mechanisms. The production mechanisms are grouped into two: $(ggF,\ t\bar{t}H)$ that scales mostly with fermionic, and $(VBF,\ VH)$ that scales mostly with bosonic Higgs couplings. The ATLAS measurements of the ratio $\mu_{VBF,VH}/\mu_{ggF,t\bar{t}H}$ in each decay mode, enabling the branching fractions to cancel out, are combined and shown on Fig. 1c.

3 Standard Framework for Couplings Measurements

In the previous section signal strengths for given Higgs boson production or decay modes are discussed. However, for a measurement of Higgs boson coupling strengths, production and decay modes cannot be treated independently, as each observed process involves at least two Higgs boson coupling strengths. Therefore, a standardized framework has been provided in Ref. [1].

Following the leading order tree level motivated framework and benchmark models, measurements of coupling strength multipliers κ_j are implemented for the combination of all analyses and channels. This is the simplest parametrization of Higgs couplings deviations from SM (denoted by $\kappa_j = 1$) which assumes kinematics compatible with SM, single and narrow CP-even resonance, and validity of zero-width approximation.

4 Couplings to Vector Bosons and Fermions

We compare the observation with the expectation for the SM Higgs boson by fitting two parameters, κ_V and κ_f. We assume no contribution from BSM particles ($\Gamma_{BSM} = 0$). At leading order, all partial widths, except for $\Gamma_{\gamma\gamma}$, scale either as κ_V^2 or κ_f^2. On the other hand, the partial width $\Gamma_{\gamma\gamma}$ is induced via loops of virtual W bosons or top quarks and scales as a function of κ_V and κ_f. For that reason, the $\gamma\gamma$ channel is the channel with the largest sensitivity to the relative sign of κ_V and κ_f. Figure 2a shows likelihood fits in $\kappa_V - \kappa_f$ plane for different Higgs boson decay modes measured by ATLAS. Individual channels converge in the SM quadrant and agree well with each other and the SM within the uncertainties.

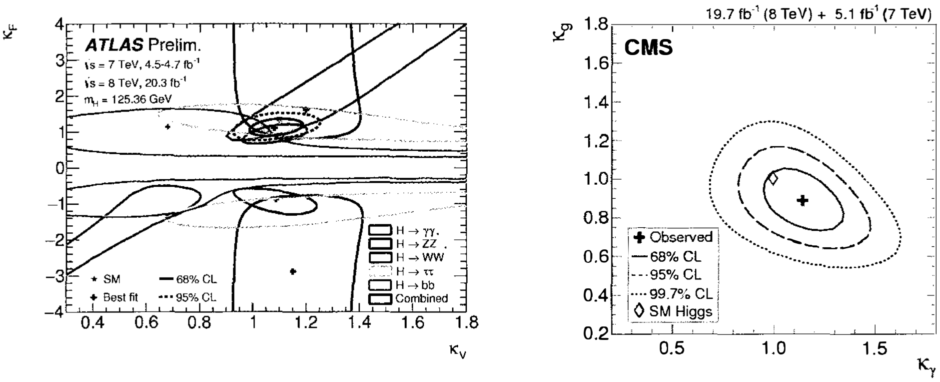

Figure 2 – The 68% C.L. contours for individual channels (colored swaths) and for the overall combination (thick curve) for the (κ_V,κ_f) parameters (left) from ATLAS. The C.L. contours fit for (κ_γ, κ_g) parameters assuming unaltered partial widths and decay modes (right) from CMS.

5 Searching for New Physics in Loops — κ_γ vs κ_g

The presence of BSM physics can considerably modify the Higgs boson phenomenology even if the underlying Higgs boson sector in the model remains unaltered. Processes induced by loop diagrams ($H \to \gamma\gamma$, $gg \to H$ and $H \to Z\gamma$) can be particularly susceptible to the presence of new particles. We combine and fit the data for the multipliers κ_γ and κ_g for these processes. The fit results where the partial widths associated with the tree-level production processes and decay modes are assumed to be unaltered are shown on Fig. 2b. Additional measurements allowing for the new particle contribution to the total width (Γ_{BSM}) are performed by profiling the κ_γ and κ_g parameters. This measurements set upper limits on branching fractions to new invisible and undetected particles to be 0.27 (ATLAS) and 0.32 (CMS) at 95% C.L.

6 Model with SM Particles in Loops and No Invisible Higgs Boson Decay Width

In the benchmark models that we previously presented, specific aspects of the Higgs sector are tested by combining under certain assumptions coupling strength scale factors into a minimum number of parameters, thereby maximizing the sensitivity to the scenarios under study. In the case of the generic models presented in this and the following section, the coupling strength scale factors κ_W, κ_Z, κ_t, κ_b, κ_τ, and κ_μ are treated independently. For the $gg \to H$ production, $H \to \gamma\gamma$ decay, $H \to Z\gamma$ decay and the total width Γ_H the SM particle content is assumed.

Without loss of generality the W coupling strength scale factor is assumed to be positive. Due to the interference terms, the fit is sensitive to the relative sign between the W and t couplings and the relative sign between the Z and t coupling, providing indirect sensitivity to the relative sign between the W and Z coupling. All measured coupling strengths are found to be compatible with the SM expectation within one standard deviation.

To confirm the scaling of the couplings to Higgs boson with the particle mass, the fit results from this generic model are shown on Fig. 3a (CMS) with reduced coupling strength scale factors. The scaling factor for vector bosons is $y_{V,i} = \sqrt{\kappa_{V,i}}\frac{m_V}{vev}$ and for fermions $y_{F,i} = \kappa_F\frac{m_F}{vev}$, where m_V, m_F are the masses of vector bosons and fermions, and the vev is vacuum expectation value. A Higgs boson mass of 125.02 GeV is used for the fit.

7 Model without Constrains on Loop Coupling Strengths and Total Width

In this generic model, the six absolute coupling strengths and three effective loop coupling strengths are used, and expressed as ratios of scale factor that can be measured independent of any assumptions on the Higgs boson total width. The free parameters (ratios) are: κ_{gZ}, λ_{WZ}, λ_{Zg}, λ_{bZ}, $\lambda_{\gamma Z}$,λ_{tZ}, and λ_{tg}. Additional parameters $\lambda_{\mu Z}$ and $\lambda_{(Z\gamma)Z}$ were used only by ATLAS. The results of the fits by ATLAS and CMS are shown on Fig. 3b and 3c.

These fits use only the basic assumptions as stated at the beginning of this section and hence represents the most model-independent determination of coupling strength scale factors that is currently possible.

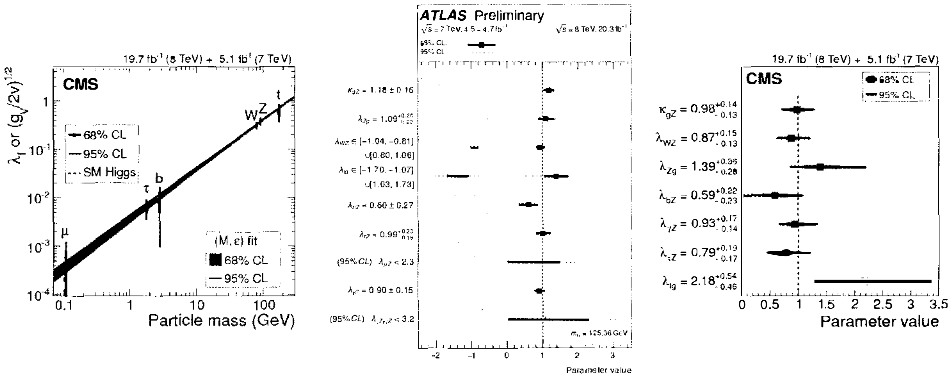

Figure 3 – The scaling of the reduced coupling strength to Higgs boson as a function of the particle mass from CMS (left). Results of fits for the generic model: allowing deviations in vertex loop coupling strengths and in the total width from ATLAS (center) and CMS (right).

8 Conclusions

This report shows a selection from a palette of measurements performed by ATLAS and CMS. Both experiments performed a search for deviations from Higgs couplings to SM particles using tree-level motivated benchmark models both with and without assumptions on the Higgs boson width and on the SM particle content of loop processes. Indirect measurements set moderate limits (27% at 95 C.L.) on Higgs boson coupling strength to invisible or undetectable particles and no significant deviations from the SM expectations in loop processes are observed.

The most generic benchmark model uses only the basic assumptions and hence represents the most model-independent determination of the coupling strength scale factors currently possible. In this model ratios of couplings are constrained with a precision at the below 40% level, depending on the ratio considered.

References

1. S. Heinemeyer *et al.*, arXiv:1307.1347 [hep-ph].
2. G. Aad *et al.* [ATLAS Collaboration], JINST **3** (2008) S08003.
3. G. Aad *et al.* [ATLAS Collaboration], ATLAS-CONF-2015-007.
4. S. Chatrchyan *et al.* [CMS Collaboration], JINST **3** (2008) S08004.
5. V. Khachatryan *et al.* [CMS Collaboration], Eur. Phys. J. C **75** (2015) 5, 212.

Measurement of other Higgs boson properties

Tatsuya Masubuchi
On behalf of the ATLAS and CMS Collaborations.
International Center for Elementary Particle Physics (ICEPP), the University of Tokyo, Tokyo 113-0033 Japan

Recent measurement of the Higgs boson properties: cross section, spin-CP and non-standard model couplings (Lepton flavor violation and flavor changing neutral current), by the ATLAS and CMS experiments are reported. The total cross section is $33.0 \pm 5.3(stat.) \pm 1.6(sys.)$pb at $\sqrt{s}$ = 8 TeV. The differential cross sections with respect to several variables show fair agreement with theory predictions. Various hypothesis tests for spin $1^{\pm}$ and $2^{\pm}$ scenarios have been performed. No indication favoring spin 1 or 2 models has been observed. CP-mixing scenarios for spin 0 have also been investigated. No significant deviation from the Standard Model 0^{+} hypothesis has been observed. Searches are also made for anomalous couplings, the lepton flavor violating decay in $H \to \mu\tau$ events and flavor changing neutral current in the $t \to qH$ events. No significant excess of events has been observed in the LHC Run-I data.

1 Introduction

The ATLAS [1] and CMS [2] experiments reported the discovery of a Higgs boson at the LHC using ZZ^*, $\gamma\gamma$ and WW^* decay modes in July 2012 [3]. Since then, both experiments have measured properties of the Higgs boson using the LHC Run-I data ($\sim$25fb^{-1}), taken at $\sqrt{s}$ = 7 TeV in 2011 and $\sqrt{s}$ = 8 TeV in 2012. ATLAS and CMS precisely measured the mass of the Higgs boson 125.09$\pm$0.24 GeV [4]. The couplings of the Higgs boson to vector bosons and fermions have been measured in detail [5]. Nevertheless properties of the Higgs boson are not fully understood yet. Precise measurement of the Higgs boson may reveal hints of beyond the Standard Model (BSM) through the Higgs sector. This proceedings reports recent measurement of the Higgs boson properties, in particular cross section, spin-CP, and search for anomalous couplings, using the Run-I data of ATLAS and CMS.

2 Cross Section Measurements

ATLAS measured total and differential cross sections for Higgs boson production using the $H \to \gamma\gamma$ and $H \to ZZ^* \to 4\ell$ events at $\sqrt{s}$ = 8 TeV [6]. Both channels provide a clear Higgs mass peak which makes identifying the Higgs boson easier. These channels are suitable for defining fiducial regions and measuring the cross section inclusively. The measured cross sections account for detector efficiency, fiducial acceptances and branching fractions. Figure 1 shows the total cross section for each channel and combined value. The measured total cross section is $33.0 \pm 5.3(stat.) \pm 1.6(sys.)$pb which is higher than NNLO and N^{3}LO calculations [7], but still consistent with the theory predictions. It is found that the cross section for the exclusive 1-jet bin shows the largest deviation from the theory predictions. Figure 2 shows the differential cross section as a function of the Higgs boson transverse momentum p_T^H and rapidity. The measured Higgs boson p_T distribution is harder than the theory prediction. The rapidity distribution agrees well.

In the $H \to \gamma\gamma$ channel leading jet p_T (sensitive to QCD modeling), m_{jj} and Δy_{jj} (sensitive to VBF topology) and $|\cos(\theta^*)|$ (sensitive to spin property) [6] are also measured. Overall, the event generator predictions are in fair agreement with the observed data within the current uncertainties.

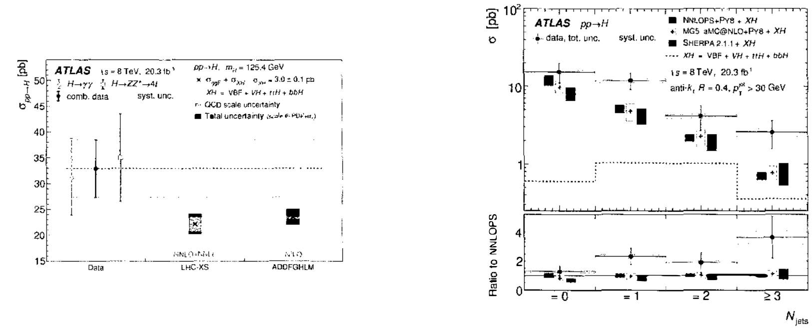

Figure 1 – Measured total cross section for Higgs boson production compared to two calculations of the gluon-fusion cross section [6] (left). The cross sections in exclusive jet binning for inclusive Higgs boson production at $\sqrt{s} = 8$TeV [6] (right).

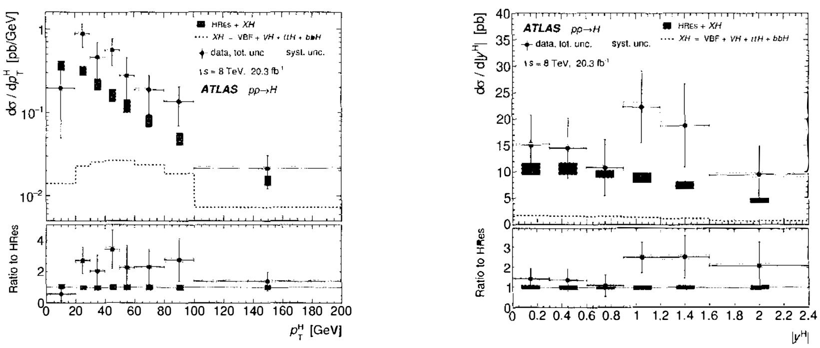

Figure 2 – Differential cross section for inclusive Higgs boson production with respect to the Higgs boson transverse momentum p_T^H [6] (left) and its rapidity $|y^H|$ [6] (right).

3 Spin/CP Measurements

The ATLAS and CMS collaborations have tested spin $1^{\pm}$ and $2^{\pm}$ hypotheses against the SM Higgs boson 0^+. CMS uses an anomalous coupling approach [9], while ATLAS uses an effective field theory (EFT) approach [8]. In non-universal coupling spin 2 models of EFT the high-p_T^H tail is enhanced, that is inconsistent with observations (e.g. differential cross section measurements). Therefore cut-offs on p_T^H ($p_T^H < 300$ GeV or 125 GeV) are applied to test spin 2 models in EFT.

Figure 3 shows results of the hypothesis tests for various spin $1^{\pm}$ and $2^{\pm}$ scenarios. All of the spin 1 and 2 models are excluded at more than 98%(96%) confidence level (C.L.) by the CMS(ATLAS) results. For spin 0 models, some CP-mixing scenarios in the Higgs sector have been considered using the $H \to WW^* \to \ell\nu\ell\nu$ and $H \to ZZ^* \to 4\ell$ events. Figure 4 shows likelihood scan as a function of BSM CP-odd and CP-even coupling parameters. The observed results are consistent with no BSM coupling, and no CP violation in the Higgs sector is observed within the current precision.

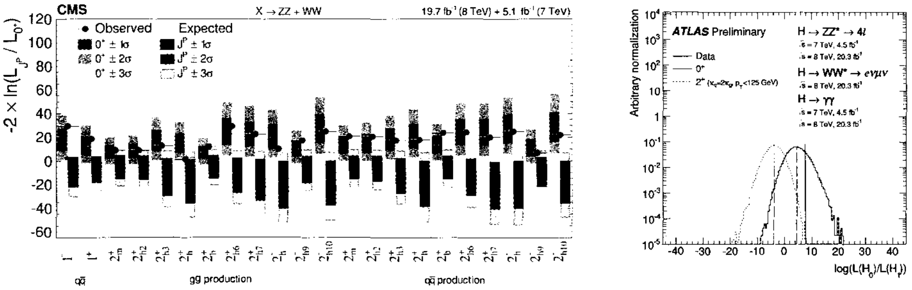

Figure 3 – A summary distribution of the test statistic $-2\ln(\mathcal{L}_{J^P}/\mathcal{L}_{0^+})$ for spin-one and spin-two J^P models tested against the SM Higgs boson hypothesis [9] (left). Test statistic distribution for spin-2 hypothesis in non universal couplings (p_T cut-off at 125 GeV) [8] (right).

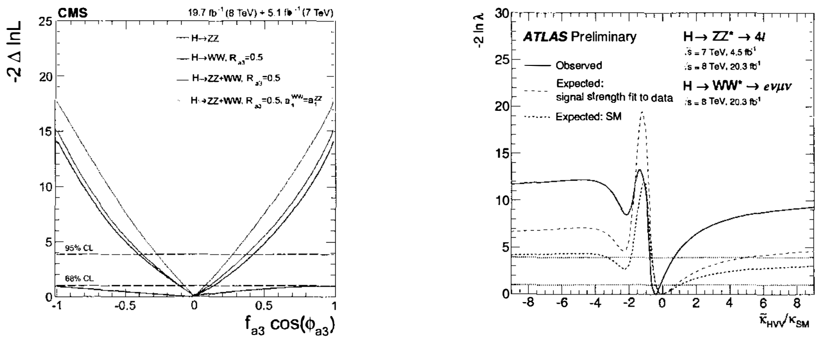

Figure 4 – Observed likelihood scan for effective fraction f_{a3} which is sensitive to the mixing of CP-odd Higgs boson in several scenarios [9] (left). Observed and expected likelihood scan as a function of BSM coupling ratios $\tilde{\kappa}_{\rm HVV}/\kappa_{\rm SM}$. The horizontal lines show the 68% and 95% C.L. exclusion regions [8] (right).

4 Lepton Flavor Violating Decay

Lepton flavor violation is not allowed in the SM, however it is expected to occur in many BSM models. CMS searches for lepton flavor violating decay in the $H \to \mu\tau_e$ and $\mu\tau_{\rm had}$ modes. In this process it is expected that the missing transverse momentum aligns to the τ direction. Therefore, $m_{\mu\tau}$ with collinear approximation is used as the final discriminant. The signal regions are categorized by number of jets to maximize search sensitivity. Figure 5 shows $m_{\mu\tau}$ distribution combined with each category weighted by S/(S+B). We observe an excess of events at the 2.4σ level around 125 GeV, which comes from several categories. The upper limit on $\mathcal{B}(H \to \mu\tau)$ is 1.51% at the 95% C.L.. The best fit gives the branching ratio of $0.84^{+0.39}_{-0.37}\%$ [10].

5 Flavor Changing Neutral Current

The ATLAS and CMS collaborations search for flavor changing neutral current (FCNC) in top decays ($t \to qH$). FCNC is not allowed at tree level in the SM. The existence of FCNC would give clear evidence of BSM. The $H \to \gamma\gamma$ is the most sensitive decay mode in this search. ATLAS searches for diphoton mass resonance in the $t\bar{t}$ topology. Figure 5 shows the $m_{\gamma\gamma}$ distribution. An upper limit of 0.79% is set on $\mathcal{B}(t \to qH)$ at the 95% C.L., corresponding to a limit on coupling $\sqrt{\lambda^2_{\mathrm{tcH}} + \lambda^2_{\mathrm{tuH}}} < 0.17$[11]. CMS searches for FCNC using various multilepton final state in addition to $H \to \gamma\gamma$. A 95% C.L. upper limit on $\mathcal{B}(t \to qH)$ is set at 0.56% [12].

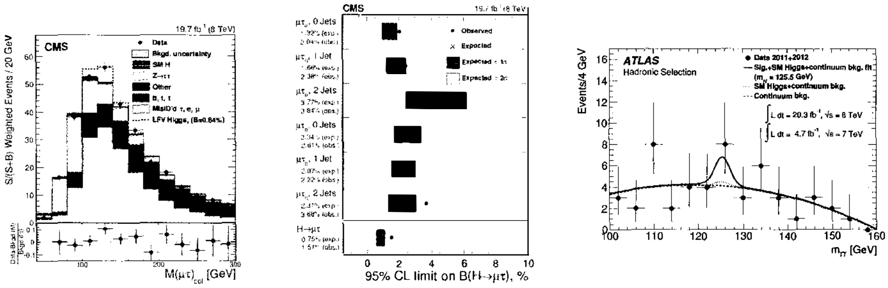

Figure 5 – Collinear mass $M(\mu\tau)_{\mathrm{col}}$ distribution for all categories combined with each category weighted by significance (S/(S+B)). The Monte-Carlo Higgs signal with $\mathcal{B}(H \to \mu\tau) = 0.84\%$ (best fit value) is shown [10] (left). The 95% C.L. upper limits by category for the LFV $H \to \mu\tau$ decays [10] (middle). The $m_{\gamma\gamma}$ distribution for the selected events in the top hadronic channel in the $t \to qH$ search [11] (right).

6 Conclusion

ATLAS and CMS have measured properties of the Higgs boson. No strong indication of BSM is observed in the Run-I data. However, results from most analyses are still limited by statistical uncertainty. We continue measurement of Higgs boson properties in Run-II in 2015. The precision will be improved significantly because of larger amount of data and higher beam energy, bringing sensitivity to smaller deviations, which might be observed in Run-II and beyond.

References

1. ATLAS Collaboration, JINST **3** (2008) S08003.
2. CMS Collaboration, JINST **3** (2008) S08004.
3. ATLAS Collaboration, *Phys. Lett.* B **716**, 1 (2012); CMS Collaboration, *Phys. Lett.* B **716**, 30 (2012).
4. ATLAS and CMS Collaborations, arXiv:1503.07589.
5. ATLAS Collaboration, ATLAS-CONF-2015-007; CMS Collaboration, arXiv:1412.8662.
6. ATLAS Collaboration, arXiv:1504.05833; ATLAS Collaboration, *Phys. Lett.* B **738**, 234-253 (2014); ATLAS Collaboration, *J. High Energy Physics.* **09**, 112 (2014).
7. LHC Higgs cross section working group, CERN-2011-002 (2011), arXiv:1101.0593; C. Anastasiou, *et al.*, arXiv:1503.06056
8. ATLAS Collaboration, arXiv:1503.03643; ATLAS Collaboration ATLAS-CONF-2015-008.
9. CMS Collaboration, arXiv:1411.3441.
10. CMS Collaboration, arXiv:1502.07400.
11. ATLAS Collaboration, *J. High Energy Physics.* **06**, 008 (2014).
12. CMS Collaboration, *Phys. Rev.* D **90**, 112013 (2014); CMS Collaboration, CMS-PAS-TOP-13-017.

Studies of Higgs Boson Properties in Future LHC Runs

Si Xie for the ATLAS and CMS Collaborations
California Institute of Technology, Pasadena, CA 91125, USA

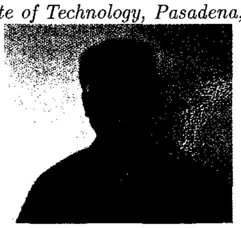

As the LHC begins its Run 2 period, it will quickly become the first and only Higgs factory in the world. The unique nature of the Higgs boson demands careful and precision studies of its properties. Future projections for precision measurements of its couplings are discussed, as well as prospects for observing and measuring rare decay modes. Future projections of studies of the Higgs potential through the Higgs pair production process at the LHC is also presented.

1 Introduction

The observation of the Higgs boson by the ATLAS and CMS experiments at the LHC [1,2] brought with it a new era in collider physics. For the first time in history, we can produce fundamental scalar particles in the laboratory. Due to its uniqueness, the Higgs boson is anticipated to be deeply involved in understanding many of the unresolved questions remaining in particle physics. Therefore, a careful, thorough, and systematic approach to determining as many of its properties as possible is demanded. The High Luminosity LHC (HL-LHC) project is explicitly geared towards this goal. This upgrade, to be implemented in Long Shutdown 3 around 2022, will increase the instantaneous luminosity of the LHC to about 5×10^{34} cm^{-2}s^{-1} allowing to reach an integrated luminosity of 3000 fb^{-1} after about ten years of operation. This dataset of unprecedented size will allow measurements of Higgs boson couplings to a high level of precision, as well as studies of extremely rare decay modes.

Since the early days of its discovery, a lot more is now known about the Higgs boson. Its decays to $\gamma\gamma$, ZZ, and WW, has been established beyond doubt, and its decay to tau leptons has also been observed with fairly large certainty [3,4]. The mass of the Higgs boson has been established to better than two parts in a thousand [5], and its main couplings have been established to the $\sim 20\%$ level. However, an even larger set of very important properties have yet to be established:

- Does the Higgs boson couple to b-quarks, and with what strength?
- Does the Higgs boson get produced in association with top quark pairs and at what rate?

- Does the Higgs boson couple to second generation fermions?
- Does the Higgs boson decay to a Z boson and a photon, and at what rate?
- Does the Higgs boson decay to particles that escape detection by the LHC experiments?
- Does the Higgs boson exhibit any anomalous couplings?
- What can we say about the Higgs self-coupling and the shape of the Higgs potential?

All of these questions require a significantly larger dataset to provide an answer. I will discuss measurement projections that attempt to answer many of these important questions.

2 Higgs Coupling Projections

With 3000 fb^{-1} of integrated luminosity, the decay channels to $\gamma\gamma$, ZZ, WW, and $\tau\tau$, that have been well studied already in Run 1 of the LHC, can be studied very thoroughly and with great precision. Their rates can be measured to $5-10\%$, depending on how well systematic and theoretical uncertainties can be improved, and they can also be measured separately in the sub-leading vector boson fusion, and WH and ZH associated production modes [6,12].

The decay mode to $b\bar{b}$ can be established to a large significance [9,12], well above five standard deviations, and the decay rates can be measured to better than 14%. The production mode where the Higgs boson is produced in association with a pair of top quarks can also be established to a significance well above 5σ, and can be measured separately in various decay modes [8,12]. These measurements allow a direct determination of the top Yukawa coupling to the Higgs boson to better than about 10%.

3 Rare Higgs Decays

In the Standard Model, the Higgs boson couples to particles according to their mass. Therefore, it can be very revealing to study Higgs boson decays to second generation fermions as their masses are typically much smaller than the third generation fermions, and a large enhancement in the coupling would indicate physics beyond the Standard Model. With 3000 fb^{-1} of integrated luminosity, the Higgs decay channel to $\mu\mu$ can be established with a significance well beyond 5σ [10,12], and the Higgs to muon coupling strength can be measured to about 8%.

The very rare Higgs decay mode to $Z\gamma$ can also be very revealing because the existence of yet unknown particles can significantly enhance the rate through enhancements in the loop diagrams which yields this decay. This decay channel can be observed to about 4σ per experiment, and the effective coupling can be measured to better than 14% [11,12]. Finally, searches for Higgs decaying to particles escaping detection in the ZH associated production channel can yield 95% confidence level upper limits on the branching ratio to such particles at the level of about 15% [10,12].

4 Higgs Self-Coupling

The shape of the Higgs potential and the nature of the electroweak phase transition is one of the most important questions in particle physics, with far-reaching implications. Studies of the Higgs self-coupling is a critical step to understanding this question. At the LHC, the only process that can be used to study the Higgs self-coupling is the Higgs pair production process. Two destructively interfering diagrams contribute to this process, making it particularly challenging to extract the self-coupling. Furthermore, the production cross section is very low, which requires an extremely large dataset to proceed with this study.

Of the decay channels studied so far, the most sensitive decay channel is the one where one Higgs boson decays to $b\bar{b}$ and the other Higgs boson decays to $\gamma\gamma$. The presence of two resonant decays allows to sufficiently reduce the background to extract the signal out of the large QCD background. In Figure 1, the distributions of the diphoton mass and the dijet mass are shown with signal and background processes stacked. With 3000 fb^{-1}, the cross section for the Higgs pair production process can be measured to the level of about $60 - 80\%$ per experiment, and to better than 50% when combined[13,7]. The projection for CMS is shown in Figure 2. The precision of this measurement depends critically on the detector performance under HL-LHC detector aging and pileup conditions. On the right of Figure 2, we see that a modest improvement in object selection efficiency can yield a significant improvement to the precision of the measurement.

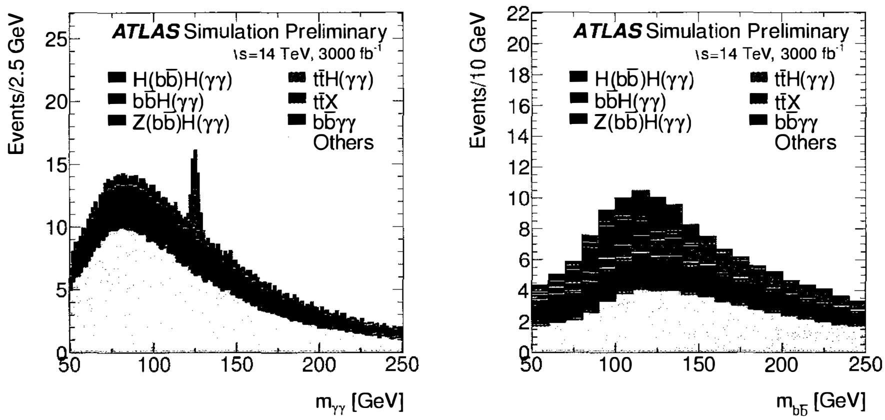

Figure 1 – Stacked histograms for the Higgs pair production signal and all of the background processes show the expected distributions for the diphoton mass (left) and the dijet mass (right) for 3000 fb^{-1} of integrated luminosity[7].

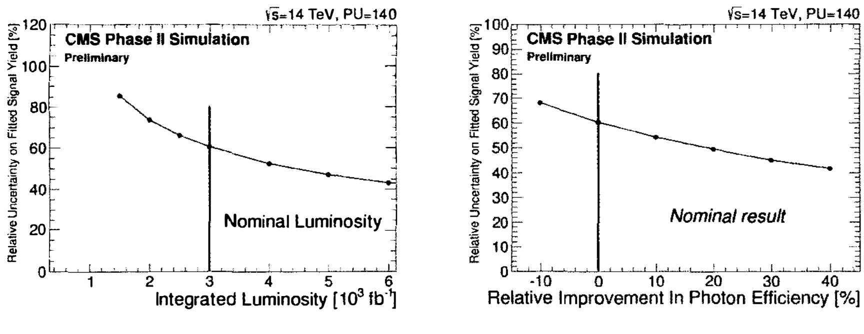

Figure 2 – The expected uncertainty on the Higgs pair production cross section measurement is shown as a function of the integrated luminosity (left) and the hypothetical improvement to the photon selection efficiency (right).

5 Summary of Projections

All of the HL-LHC projections for the Higgs boson measurements can be summarized through a leading-order coupling fit framework employed by both ATLAS and CMS collaborations. In Table 1, we summarize the precision to which the Higgs couplings can be determined using an integrated luminosity of 3000 fb^{-1} in this framework. The majority of the measurements are limited by the systematic uncertainty. As a guide for potential future improvements on theoretical systematic uncertainties, ATLAS has determined that in order for the theory uncertainties to contribute less than 10% to the total uncertainty, one has to reduce the PDF uncertainty and the uncertainty from missing higher order corrections for the gluon fusion Higgs production cross section to less than 1.3% and 1.1% respectively [6]. Furthermore, one can get an idea of the impact of systematic uncertainties from Table 2, where I show what the Higgs coupling uncertainties would be for the CMS experiment if the theory uncertainties are reduced by 50% and if the experimental systematic uncertainties are scaled down according to $1/\sqrt{\text{Luminosity}}$ [12].

Table 1: Projected Uncertainties for Higgs couplings measurements with 3000 fb^{-1}.

Experiment	κ_γ	κ_W	κ_Z	κ_g	κ_b	κ_t	κ_γ	$\kappa_{Z\gamma}$	κ_μ	BR_{invis}
ATLAS	5%	5%	4%	9%	12%	11%	10%	14%	8%	14%
CMS	5%	5%	4%	5%	7%	10%	5%	12%	8%	17%

Table 2: The projected Higgs coupling measurement uncertainties from the CMS experiment assuming current systematic uncertainties are compared against those obtained when the theoretical uncertainties are reduced by 50% and the experimental systematic uncertainties are scaled down according to $1/\sqrt{\text{Luminosity}}$.

Experiment	κ_γ	κ_W	κ_Z	κ_g	κ_b	κ_t	κ_γ	$\kappa_{Z\gamma}$	κ_μ	BR_{invis}
Current Systematics	5%	5%	4%	5%	7%	10%	5%	12%	8%	17%
Reduced Systematics	2%	2%	2%	3%	4%	7%	2%	10%	8%	6%

In summary, a comprehensive Higgs physics program lies ahead for the HL-LHC project. Precise and systematic measurements of all Higgs boson properties will be one of the keys to understanding the yet unresolved questions in particle physics.

References

1. ATLAS Collaboration, Phys. Lett. B **716**, 1 (2012).
2. CMS Collaboration, Phys. Lett. B **716**, 30 (2012).
3. CMS Collaboration, JHEP **05**, 104 (2014).
4. ATLAS Collaboration, JHEP **04**, 117 (2015).
5. ATLAS and CMS Collaborations, ATLAS-HIGG-2014-14, CMS-HIG-14-042, (2015).
6. ATLAS Collaboration, ATL-PHYS-PUB-2014-016 (2014).
7. ATLAS Collaboration, ATL-PHYS-PUB-2014-019 (2014).
8. ATLAS Collaboration, ATL-PHYS-PUB-2014-012 (2014).
9. ATLAS Collaboration, ATL-PHYS-PUB-2014-011 (2014).
10. ATLAS Collaboration, ATL-PHYS-PUB-2013-014 (2014).
11. ATLAS Collaboration, ATL-PHYS-PUB-2014-006 (2014).
12. CMS Collaboration, CMS-NOTE-2013-002 (2013).
13. A. Apyan for the ATLAS and CMS Collaborations, "Prospect on Higgs Physics at the HL-LHC", ECFA Workshop 2014 (2014).

2.
Top

RECENT TOP QUARK PRODUCTION RESULTS FROM THE TEVATRON

O. BRANDT on behalf of the CDF and D0 COLLABORATIONS
Kirchhoff-Institut für Physik, Im Neuenheimer Feld 227,
69120 Heidelberg, Germany

In this article, I review recent measurements of the production of the top quark in $p\bar{p}$ collisions at a centre-of-mass energy of $\sqrt{s}$ = 1.96 TeV in Run II of the Fermilab Tevatron Collider, recorded by the CDF and D0 Collaborations. I will present the Tevatron combination of measurements of the $t\bar{t}$ production cross section and its differential measurement, the first evidence for and observation of the production of single top quarks in the s-channel, as well the final Tevatron combination of the production of single top quarks the s- and t-channels. Furthermore, I will review the measurements of the forward-backward asymmetry in $t\bar{t}$ events, which can be experimentally uniquely accessed in the CP-invariant $p\bar{p}$ initial state at the Tevatron, and conclude with the measurements of this asymmetry in the $b\bar{b}$ system.

The pair-production of the top quark was discovered in 1995 by the CDF and D0 experiments[1] at the Fermilab Tevatron proton-antiproton collider. Observation of the electroweak production of single top quarks was presented only six years ago[2]. The large top quark mass[3] indicates that the top quark could play a crucial role in electroweak symmetry breaking. Precise measurements of the production of the top quark and of its properties provide a crucial test of the consistency of the SM and could hint at physics beyond the standard model (BSM). This article discusses recent precision measurements of the top production at the Tevatron, while recent measurements of the intrinsic properties of the top quark, including the world's most precise single measurement of the top quark mass m_t [6], are covered in Ref. [7]. All Tevatron results in the top sector can be found in Refs. [4,5]. The corresponding measurements by the LHC experiments are discussed in Refs. [8].

Top quarks are mostly produced in pairs via the strong interaction. At the Tevatron, the production process $q\bar{q} \to t\bar{t}$ dominates with a contribution of $\approx 85\%$ over the $gg \to t\bar{t}$ reaction, while at the LHC their respective fractions are approximately reversed. Another striking difference between the two colliders is that the $p\bar{p}$ initial state at the Tevatron is an eigenstate of the CP transformation. The relative contribution of the s-channel to the total production cross section of single top quarks σ_t is $\approx 30\%$ at the Tevatron, making it experimentally easier to access than at the LHC, where it contributes only $\approx 5\%$. In the SM, the top quark decays to a W boson and a b quark nearly 100% of the time. Thus, $t\bar{t}$ events decay to a $W^+W^-b\bar{b}$ final state, which is further classified according to the W boson decays into "dileptonic", "ℓ+jets", or "all–jets" channels. Accordingly, single top production in the s-channel proceeds dominantly through $q\bar{q} \to t\bar{b}$, while the $qg \to q't\bar{b}$ process dominates in the t-channel.

1 Production of $t\bar{t}$ pairs

The CDF and D0 Collaborations combined their most precise measurements of the $t\bar{t}$ production cross section $\sigma_{t\bar{t}}$ in Run II of the Tevatron [9], summarised in Fig. 1 (a). The combination is

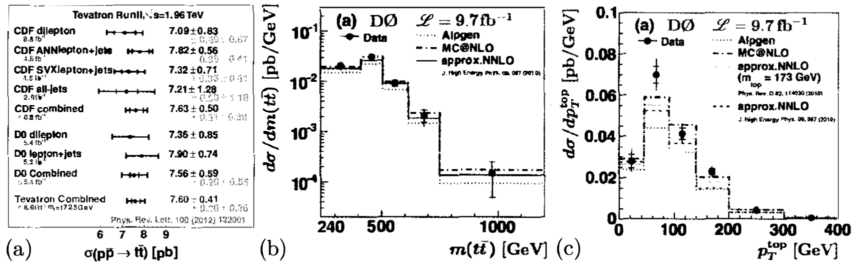

(a) (b) (c)

Figure 1 – **(a)** The combination of $\sigma_{t\bar{t}}$ from CDF and D0 in $p\bar{p}$ collisions at $\sqrt{s} = 1.96$ TeV compared to the SM prediction at NNLO+NNLL. **(b)** The distribution of $\mathrm{d}\sigma_{t\bar{t}}/\mathrm{d}m_{t\bar{t}}$ after background subtraction and regularised unfolding measured by D0 in the ℓ+jets channel using 9.7 fb^{-1} of data, compared with theory predictions. **(c)** Same as (b), but for $\mathrm{d}\sigma_{t\bar{t}}/\mathrm{d}p_T^{\mathrm{top}}$. Both t and $\bar{t}$ contribute in each event in (c).

performed using the best linear unbiased estimator (BLUE) technique, considering all sources of systematic uncertainties and their correlations. The combined value of $\sigma_{t\bar{t}} = 7.60 \pm 0.41$ pb is in good agreement with the SM prediction of $\sigma_{t\bar{t}} = 7.35^{+0.28}_{-0.33}$ pb [10], which is calculated at next-to-next-to-leading order (NNLO) with next-to-next-to-leading logarithmic (NNLL) corrections.

D0 recently measured $\sigma_{t\bar{t}}$ differentially in various kinematic distributions in the ℓ+jets chanel using 9.7 fb^{-1} of data [11]. After subtraction of backgrounds, the distributions are corrected for detector effects through a regularised matrix unfolding. A representative selection of results is shown in Fig. 1 (b) for $\mathrm{d}\sigma_{t\bar{t}}/\mathrm{d}m_{t\bar{t}}$ and in (c) for $\mathrm{d}\sigma_{t\bar{t}}/\mathrm{d}p_T^{\mathrm{top}}$. The SM MC simulations considered are able to describe the differential dependence up to an overall normalisation factor.

2 Production of single top quarks

The production of single top quarks in the s-channel is difficult to observe at the LHC given its small cross section of $\sigma_{s\text{-ch.}} = 5.5 \pm 0.2$ pb [12]. The experimental situation is less challenging at the Tevatron given that $\sigma_{s\text{-ch.}} = 1.05 \pm 0.06$ pb contributes about 1/3 of the total σ_t.

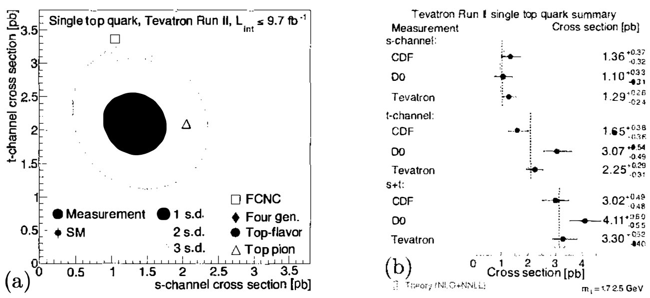

(a) (b)

Figure 2 – **(a)** The combination of measured cross sections for the production of single top quarks in the s- and t-channel compared to SM expectation and BSM predictions. **(b)** The overview of the measurements of single top quark production in the s- and t-channels.

The first evidence for single top production was provided by D0 [13] in the ℓ+jets channel using 9.7 fb^{-1} of data. The sensitivity of the analysis was enhanced by categorising events into signal-enriched and signal-depleted categories according to the jet and b-tag multiplicity.Two discriminants sensitive to the s- and t-channel were used to extract $\sigma_{s\text{-ch.}}$ and $\sigma_{t\text{-ch.}}$ simultaneously. Without any assumption on $\sigma_{t\text{-ch.}}$, D0 measures $\sigma_{s\text{-ch.}} = 1.10 \pm 0.33$ pb, which corresponds to a significance of 3.7 standard deviations (SD). Recently, CDF also reported an evidence for single top production in the s-channel at the level of 4.2 SDs [14] using 9.5 fb^{-1} of data. They combined the analyses in two channels, ℓ+jets[14] and $\not\!\!E_T$+jets (where the lepton is missed)[15], both using a discriminant optimised to the s-channel only. By combining these three measurements, CDF and D0 discovered single top production in the s-channel with an observed (expected) significance of 6.3 (5.1) SDs[16].

CDF and D0 performed the final combination of their best measurements in the s- and t channels by constructing a joint discriminant and considering all uncertainties and their correlations[17]. The simultaneously extracted $\sigma_{s\text{-ch.}} = 1.29 \pm 0.25$ pb and $\sigma_{t\text{-ch.}} = 2.25 \pm 0.30$ pb, shown in Fig. 2 (a), agree with the SM expectation and, combined, can exclude a number of BSM scenarios. The overview of single top measurements at the Tevatron is given in Fig. 2 (b).

3 Forward-backward asymmetry in $t\bar{t}$ events

In the SM, the pair production of top quarks in $p\bar{p}$ collisions exhibits a forward-backward asymmetry $A_{\rm FB}^{t\bar{t}} \equiv \frac{N^{\Delta y>0}-N^{\Delta y<0}}{N^{\Delta y>0}+N^{\Delta y>0}}$ of $\approx 10\%$ at NNLO with NNLL corrections in the $t\bar{t}$ rest frame[18], where $\Delta y \equiv y_t - y_{\bar{t}}$ and $y_t = \frac{1}{2}\ln\frac{E+p_{z,t}}{E_t-p_{z,t}}$ is the rapidity of the t quark.

D0 measured $A_{\rm FB}^{t\bar{t}} = 10.6 \pm 3.0\%$ in the ℓ+jets channel using events with at least one b-tagged jet in 9.7 fb^{-1} of data[19], as shown in Fig. 3 (a). The kinematic fitter used for the reconstruction was extended to cover events with only three jets. A similar measurement was performed by CDF in the ℓ+jets channel[20] using 9.4 fb^{-1} of data. Their result of $A_{\rm FB}^{t\bar{t}} = 16.4 \pm 4.7\%$ is ≈ 1.5 SD away from the SM expectation. Both Collaborations also investigated the dependence of $A_{\rm FB}^{t\bar{t}}$ on the invariant mass of the $t\bar{t}$ system $m_{t\bar{t}}$ which is compared to SM expectation[18] in Fig. 3 (b), and on $|\Delta y|$.

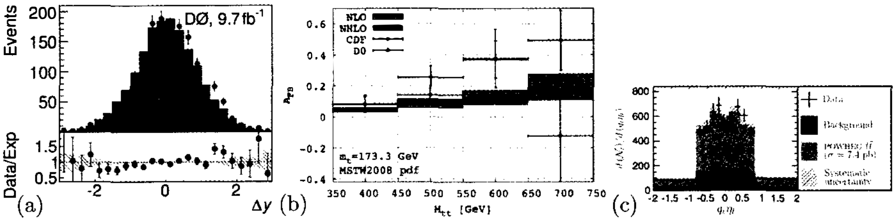

Figure 3 – **(a)** The distribution in Δy in data compared to simulations in the ℓ+jets channel using 9.7 fb^{-1} of D0 data. The data prefers a larger asymmetry than MC@NLO that is used to simulate $t\bar{t}$ events. **(b)** The distribution in $A_{\rm FB}^{t\bar{t}}$ in the $t\bar{t}$ rest frame versus $M_{t\bar{t}}$, after background subtraction and corrected for experimental effects from the CDF and D0 experiments, is compared to NNLO+NNLL calculations. **(c)** The distribution in $q\eta_\ell$ in data compared with sumulations in the dilepton channel using 9.1 fb^{-1} of CDF data.

The lepton-based asymmetry $A_{\rm FB}^{\ell} \equiv \frac{N^{q\eta>0}-N^{q\eta<0}}{N^{q\eta>0}+N^{q\eta>0}}$ is sensitive to $A_{\rm FB}^{t\bar{t}}$ through the charge-signed pseudorapidity $q\eta$ of charged leptons in $t \to \ell\nu b$ decays. CDF measured $A_{\rm FB}^{\ell} = 7.2\pm6.0\%$ in the dilepton channel using 9.1 fb^{-1} of data, as shown in Fig. 3 (c), while D0 found $A_{\rm FB}^{\ell} = 4.4\pm3.9\%$ using 9.7 fb^{-1}. Both results are consistent with SM expectation.

D0 applied the matrix element method, which calculates the probability of each event to come from $t\bar{t}$ production as a function of Δy, to reconstruct $A_{\rm FB}^{t\bar{t}}$ in kinematically underconstrained dilepton events[24], and found $A_{\rm FB}^{t\bar{t}} = 18.0 \pm 8.6\%$. The distribution in Δy is shown in Fig. 4 (a).

An overview of all measurements of the forward-backward asymmetry is given in Fig. 4 (b). Both Collaborations have investigated $A_{\rm FB}$ in the $b\bar{b}$ system at high $M_{b\bar{b}}$, where $q\bar{q} \to b\bar{b}$ dominates[25]. These results are discussed in detail in Ref.[26].

Acknowledgments

I would like to thank my collaborators from the CDF and D0 experiments for their help in preparing this article. I also thank the staffs at Fermilab and collaborating institutions, as well as the CDF and D0 funding agencies.

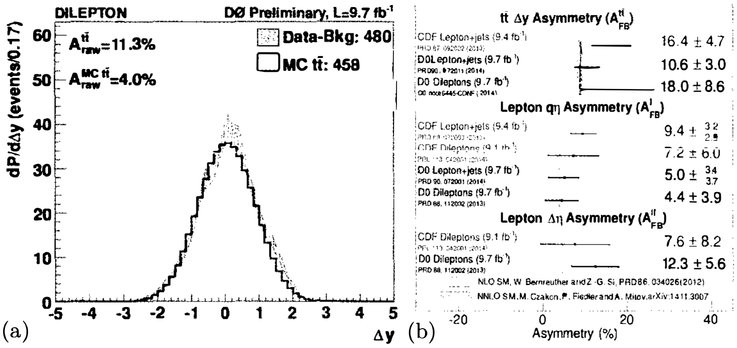

Figure 4 – **(a)** The distribution in Δy in data compared to simulations after reconstruction with the ME method and before calibration in the dilepton channel using 9.7 fb^{-1} of D0 data. **(b)** The overview of the measurements of $A_{\rm FB}^{t\bar{t}}$, $A_{\rm FB}^{\ell}$, and $A_{\rm FB}^{\ell\ell}$ (not discussed here) by CDF and D0, compared to theory predictions.

References

1. F. Abe *et al.* (CDF Coll.), Phys. Rev. Lett. **74**, 2626 (1995), S. Abachi *et al.* (D0 Coll.), Phys. Rev. Lett. **74**, 2632 (1995).
2. T. Aaltonen *et al.* (CDF Coll.), Phys. Rev. Lett. **103**, 092001 (2009), V. M. Abazov *et al.* (D0 Coll.), Phys. Rev. Lett. **103**, 092002 (2009).
3. T. Aaltonen *et al.* (CDF and D0 Coll.), arXiv:1407.2682 (2014).
4. http://www-cdf.fnal.gov/physics/new/top/public_mass.html
5. http://www-d0.fnal.gov/Run2Physics/WWW/results/top.htm.
6. V. M. Abazov *et al.* (D0 Coll.), Phys. Rev. Lett. **113**, 032002 (2014).
7. M. Cremonesi, these proceedings.
8. G. Benelli, F. Balli, Y. Chao, and C. Escobar, these proceedings.
9. T. Aaltonen *et al.* (CDF and D0 Coll.), Phys. Rev. D **89**, 072001 (2014).
10. P. Bärnreuther, M. Czakon, and A. Mitov, Phys. Rev. Lett. **109**, 132001 (2012).
11. V. M. Abazov *et al.* (D0 Coll.), Phys. Rev. D **90** 092006 (2014).
12. N. Kidonakis, Phys. Rev. D **81**, 054028 (2010), assuming $m_t = 172.5$ GeV.
13. V. M. Abazov *et al.* (D0 Coll.), Phys. Lett. B **726** 656 (2013).
14. T. Aaltonen *et al.* (CDF Coll.), Phys. Rev. Lett. **112**, 231804 (2014).
15. T. Aaltonen *et al.* (CDF Coll.), Phys. Rev. Lett. **112**, 231805 (2014).
16. T. Aaltonen *et al.* (CDF and D0 Coll.), Phys. Rev. Lett. **112**, 231803 (2014).
17. T. Aaltonen *et al.* (CDF and D0 Coll.), subm. to Phys. Rev. Lett., arXiv:1503.05027.
18. M. Czakon, F. Fiedler, and A. Mitov, arXiv:1411.3007 (2014).
19. V. M. Abazov *et al.* (D0 Coll.), Phys. Rev. D **90** 072011 (2014).
20. T. Aaltonen *et al.* (CDF Coll.), Phys. Rev. D **90**, 072011 (2014).
21. V. M. Abazov *et al.* (D0 Coll.), Phys. Rev. D **88** 112002 (2013).
22. T. Aaltonen *et al.* (CDF Coll.), Phys. Rev. Lett. **113**, 042001 (2014).
23. W. Bernreuther and Z.-G. Si, Phys. Rev. D **86**, 034026 (2012).
24. V. M. Abazov *et al.* (D0 Coll.), D0 CONF-Note 6445 (2014).
25. T. Aaltonen *et al.* (CDF Coll.), CDF Conf. Note 11092 (2014), CDF Conf. Note 11156 (2015); V. M. Abazov *et al.* (D0 Coll.), Phys. Rev. Lett. **114**, 051803 (2015).
26. D. Lucchesi, these proceedings.

Measurement of the top mass at the LHC

Fabrice Balli, on behalf of the ATLAS and CMS Collaborations
Manchester University, United Kingdom

The top quark is the most massive fundamental particle ever observed. As such, it plays a particular role in the theories of elementary constituents of matter. The motivation for a precise measurement of the top quark mass ensues from this role. The ATLAS and CMS experiments at the LHC have taken part in this effort and achieve precisions below one GeV, using data collected during the years 2011 and 2012, at a centre-of-mass energy $\sqrt{s}$ of 7 TeV and 8 TeV respectively. This document reviews the measurements performed by the two collaborations at the time of writing.

1 Introduction

Since the discovery of the top quark at Tevatron in 1995, physicists have developed an increasing number of methods in order to reduce uncertainties on the measurement of its mass, and have provided these in numerous topologies. These efforts are part of the LHC program, in particular for the ATLAS [1] and CMS [2] experiments. This document classifies the analysis techniques in three categories :

- direct kinematic measurements : these measurements make use of observables reconstructed from the decay products of the top or antitop quark in top-antitop ($t\bar{t}$) final state events to estimate its mass, m_{top}. Among all existing measurements, they can achieve the best precision on m_{top} ; the main disadvantage of these techniques is that the measured parameter is the m_{top} injected in the simulation, which is not unambiguously mapped to the top quark pole mass. The LHC results coming from these techniques are described in section 2.

- alternative measurements : these measurements also use observables reconstructed from the decay of the top quark, but in unusual topologies, or make use of specific techniques, sensitive to different effects than the standard ones. Although they reach a lower level of precision at the time this document is written, these techniques have usually orthogonal uncertainties to the direct kinematic measurements. The most recent measurements from the LHC are discussed in section 3.

- measurements from the cross-section, given in section 4 : these measurements, although usually limited by theoretical predictions accuracy, as well as experimental systematic uncertainties, offer the advantage of providing values of m_{top} with in a well-defined theoretical scheme.

Some conclusions on the existing measurements, as well as outlooks on future measurements at the LHC are given in section 5.

All CMS results from direct kinematic measurements and all ATLAS results made public by March 2015 are given in fig. 1.

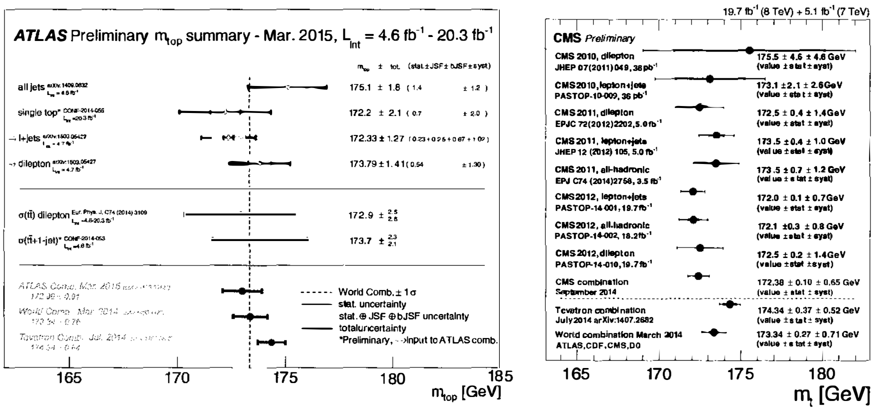

Figure 1 – Summary figure of recent m_{top} measurements from ATLAS [3] (left) and CMS [4] (right).

2 Direct kinematic measurements

The direct kinematic measurements make use of an observable sensitive to the top quark mass. In the fully hadronic channel and in the semi-leptonic (ℓ+jets) channel, it is possible to fully reconstruct at least onc top or antitop quark invariant mass ($m_{\rm top}^{\rm reco}$) from the hadronically decaying top(s) or antitop(s). In these two channels, the potentially dominant uncertainty arises from the knowledge of the jet energy scale (JES). It has become a widespreaded technique to use the reconstructed invariant mass(es) of the hadronically decaying W(s), $m_{\rm W}^{\rm reco}$, to constrain it. The dileptonic channel is kinematically underconstrained and cannot make use of a similar technique. CMS results are all referenced in the combination of the measurements [4]. ATLAS results are included in two papers [5,6].

2.1 *Fully hadronic channel*

The ATLAS measurement uses the $R_{3/2}$ observable, defined as the ratio of $m_{\rm top}^{\rm reco}$ to $m_{\rm W}^{\rm reco}$ in each event. Templates are built at various values of $m_{\rm top}$, and an binned likelihood fit to the data at 7 TeV is performed. This measurement should benefit from increased statistics; besides this, the dominant uncertainties come from JES, relative JES from b-jets (bJES) and hadronisation.

The CMS experiment uses an ideogram method to reconstruct the estimator for two measurements (7 and 8 TeV data). The reconstructed top quark mass, $m_{\rm top}^{\rm reco}$, is used to estimate $m_{\rm top}$, and $m_{\rm W}^{\rm reco}$ is used to constrain the JES. A simultaneous fit of the two observables (2D fit) to the data is performed. For both these measurements, the dominant uncertainties come from JES and statistical uncertainties.

2.2 *Dileptonic channel*

The ATLAS measurement uses a 1D template fit to the 7 TeV data, with the $m_{\ell b}^{\rm reco}$ observable as estimator. This observable is defined as the average invariant mass of the two lepton-jet pairs, choosing the permutation with lowest value for $m_{\ell b}^{\rm reco}$. This measurement should benefit from 8 TeV increased statistics.

The CMS experiment has performed several measurements of $m_{\rm top}$ in the dileptonic channel. Two of them (7 and 8 TeV) use the AMWT observable. This observable has values close to the top quark mass and is reconstructed using all the event kinematics. One preliminary result from CMS in this channel uses the $m_{\ell b}^{\rm reco}$ observable to measure $m_{\rm top}$ and builds a folding matrix with simulated events. This allows to fold any theoretical calculation for the $m_{\ell b}^{\rm reco}$ observable and thus measure $m_{\rm top}$ in a well-defined scheme. The obtained result is [7] : $m_{\rm top}$ ($\sqrt{s}$ = 8 TeV) =172.3 $\pm$ 1.3 GeV (preliminary result).

2.3 Semi-leptonic channel

In the CMS experiment, $m_{\rm top}^{\rm reco}$ and $m_{\rm W}^{\rm reco}$ are reconstructed with an ideogram method and a 2D template fit to the data is performed (in both 7 and 8 TeV measurements). The 8 TeV measurement is the most precise result for a single $m_{\rm top}$ measurement in the LHC. It is also in tension with the latest D0 measurement [8].

The ATLAS experiment uses a novel technique, which is a 3D template analysis, with 7 TeV data. In this improved method, an additional observable, $R_{\rm bq}^{\rm reco}$, is used to constrain the potentially highest systematic uncertainty, that is the one related to bJES. A simultaneous unbinned likelihood fit of the three observables is performed, and the bJES uncertainty is reduced to an insignificant value, at a cost of an increased statistical uncertainty. This should be reduced using a bigger amount of data, e.g. 8 TeV statistics.

2.4 Combinations of the direct measurements

The CMS experiment has performed a preliminary combination including most of the measurements described above [4]. The result is $m_{\rm top}$ =172.4 $\pm$ 0.1 (stat) $\pm$ 0.7 (syst) GeV (preliminary result). The ATLAS experiment combined the dileptonic and ℓ+jets channels [5]. The result is $m_{\rm top}$ =173.0 $\pm$ 0.5 (stat) $\pm$ 0.8 (syst) GeV. Both measurement reach precisions similar to the one of the preliminary world combination, as can be observed in fig. 1.

3 Alternative measurements

3.1 Measurement with single top events in the t-channel

The ATLAS experiment used single top events to measure $m_{\rm top}$ [9] with 8 TeV data. This channel is orthogonal to the other channels and as such, offers possibilities of improvement when combined. The final result, dominated by the JES uncertainty in the forward region of the detector, was obtained with a 1D template analysis using the $m_{\ell b}^{\rm reco}$ observable.

3.2 Kinematic end-points and B-hadron decay lifetime

The CMS experiment has performed two alternative measurements, that are also sensitive to different effects with respect to the standard measurements. The kinematic end-points analysis makes a minimal use of the simulation and relies mostly on analytical formulas. The result [10] is $m_{\rm top}$ ($\sqrt{s}$ = 7 TeV) =173.9 $\pm$ 0.9 (stat) $\pm$ 2.3 (syst) GeV. Though being dominated by the JES uncertainty, it has very small sensitivity to modeling effects.

The measurement based on the B-hadron decay lifetime($m_{\rm top}$ ($\sqrt{s}$ = 8 TeV) =173.5 $\pm$ 1.5 (stat) $\pm$ 2.9 (syst) GeV, preliminary [11]) uses only tracker variables, and is therefore also sensitive to different effects. It is dominated by top quark transverse momentum modeling.

4 Measurements of the pole mass from the cross-section

4.1 Measurement from the inclusive cross-section

Measurements of $m_{\rm top}$ from the $t\bar{t}$ cross-section were performed by both the ATLAS and CMS experiments in the dileptonic channel [12,13] . Both measurements use PDF4LHC prescriptions and full NNLO+NNLL predictions. The results are dominated by theoretical uncertainty for

ATLAS and by the systematic uncertainty for CMS. The results are the following :

$$\begin{aligned} m_{\text{top}}(\sqrt{s} = 7+8 \ \ \text{TeV}) = & \ \ 172.9^{+2.5}_{-2.6} \text{ GeV (ATLAS)}, \\ m_{\text{top}}(\sqrt{s} = 7 \ \ \text{TeV}) = & \ \ 176.7^{+3.0}_{-2.8} \text{ GeV (CMS)}. \end{aligned} \tag{1}$$

4.2 Measurement with $t\bar{t}$+1 jet events

The ATLAS experiment measured m_{top} with the differential $t\bar{t}$+1 jet cross section as a function of a quantity, ρ_s, proportional to the inverse of the invariant mass of the $t\bar{t}$+1 jet system [14]. Theoretical calculations of the differential distribution were made at the parton level (NLO+PS). Unfolding the data then allows to measure the top quark pole mass. This measurement, which uses 7 TeV data, should benefit from increased statistics at 8 TeV.

5 Summary and outlooks

It was shown that the LHC experiments reach high precision on the m_{top} measurement, with potential improvements since final results from Run1 are not public yet. It is also expected that combining techniques sensitive to different effects will provide more information on the value of m_{top}. Finally, efforts are required to have a better harmonization of the treatment of systematic uncertainties across the LHC experiments, in particular for the hadronisation uncertainty. This will be a key ingredient to final LHC and world combinations.

References

1. ATLAS Collaboration, 2008 JINST 3 S08003.
2. CMS Collaboration, 2008 JINST 3 S08004.
3. `http://atlas.web.cern.ch/Atlas/GROUPS/PHYSICS/CombinedSummaryPlots/TOP.`
4. CMS Collaboration, *Combination of the CMS top-quark mass measurements from Run 1 of the LHC*, CMS-PAS-TOP-14-015.
5. ATLAS Collaboration, *Measurement of the top quark mass in the $t\bar{t}$ →lepton+jets and $t\bar{t}$ →dilepton channels using $\sqrt{s}$ =7 TeV ATLAS data*, arXiv : 1503.05427.
6. ATLAS Collaboration, *Measurement of the top-quark mass in the fully hadronic decay channel from ATLAS data at $\sqrt{s}$ = 7 TeV*, Eur. Phys. J. C (2015) 75:158.
7. CMS Collaboration, *Determination of the top-quark mass from the m(lb) distribution in dileptonic ttbar events at $\sqrt{s}$ = 8 TeV*, CMS-PAS-TOP-14-014.
8. D0 Collaboration, *Precision Measurement of the Top Quark Mass in Lepton+Jets Final States*, Phys. Rev. Lett. 113, 032002 (2014).
9. ATLAS Collaboration, *Measurement of the top quark mass in topologies enhanced with single top quarks produced in the t-channel at $\sqrt{s}$ = 8 TeV using the ATLAS experiment*, ATLAS-CONF-2014-055.
10. CMS Collaboration, *Measurement of masses in the $t\bar{t}$ system by kinematic endpoints in pp collisions at $\sqrt{s}$ = 7 TeV*, Eur. Phys. J C (2013) 73:2494.
11. CMS Collaboration, *Measurement of the top quark mass using the B-hadron lifetime technique*, CMS-PAS-TOP-12-030.
12. ATLAS Collaboration, *Measurement of the $t\bar{t}$ production cross-section using eμ events with b-tagged jets in pp collisions at $\sqrt{s}$=7 and 8 TeV with the ATLAS detector*, Eur. Phys. J C (2014) 74:3109.
13. CMS Collaboration, *"Determination of the top-quark pole mass and strong coupling constant from the $t\bar{t}$ production cross section in pp collisions at $\sqrt{s}$ = 7 TeV"*, Phys. Lett. B 728 (2014) 496 (corrigendum: Phys. Lett. B 738 (2014) 526).
14. ATLAS Collaboration, *Determination of the top-quark pole mass using $t\bar{t}$+1-jet events collected with the ATLAS experiment in 7 TeV pp collisions*, ATLAS-CONF-2014-053.

MEASUREMENT OF TOP QUARK PROPERTIES AT THE LHC

Y. CHAO
Department of Physics, National Taiwan University, No. 1, Sec. 4, Roosevelt Rd., Taipei, Taiwan

We present the recent measurements of top-quark properties conducted by the LHC experiments. The data collected in proton-proton collisions at centre-of-mass energies of 7 and 8 TeV in the years 2011 and 2012 are used. The results include the measurements of the W-boson helicity in top-quark decays, the top-quark charge asymmetry, and the $t\bar{t}$ spin correlations and polarization. Furthermore several searches for flavor-changing neutral currents in decays and production of top quarks are performed. So far the results are found to agree with the predictions from the standard model within the corresponding uncertainties.

1 Introduction

The top quark, discovered in 1995 at the Tevatron [1,2], is the heaviest elementary particle known to-date. The lifetime of top quark is so short such that it decays before hadronization. By measuring the decay product of a top quark, one can study its properties, such as spin, polarization and mass can be determined.

Top quarks can be used to probe for new physics. The top quark pair and single top production processes are also major background to physics beyond standard model (BSM) searches. The Large Hadron Collider (LHC) is a energy frontier machine. The data collected LHC during the first years operation allow us to perform unprecedented tests and precision measurements on different top-quark properties. Detailed description of the general purpose detectors of LHC, can be found in the reports of ATLAS [3] and CMS [4].

2 Top Quark Properties

Various properties of the top quark production or decays are being studied at LHC. Those are to test the standard model (SM) predictions and good candles for new physics searches.

2.1 W-boson Helicity in Top Quark Decays

The W-boson helicity fractions in top quark decays are very sensitive to the tWb vertex couplings. Anomalous tWb couplings, which do not arise from the SM, would alter the value of one or more helicity fractions. The W-boson helicity fractions (F_R, F_L, and F_0) can be measured using the helicity angle θ^*, which is defined as the angle angle between the direction of the charged lepton in W rest frame and W direction in the top quark rest frame. Their relations can be written as: $\frac{1}{\Gamma}\frac{d\Gamma}{d\cos\theta^*} = \frac{3}{8}(1-\cos\theta^*)^2 F_L + \frac{3}{8}(1+\cos\theta^*)^2 F_R + \frac{3}{4}(\sin\theta^*)^2 F_0$, assuming $F_R + F_L + F_0 = 1$, where $F_x = \frac{\Gamma_x}{\Gamma}$. The latest result [7] is a combination of recent measurements by the ATLAS and CMS Collaborations using their data corresponding to integrated luminosities ranging from 35 pb^{-1} to 2.2 fb^{-1} collected at a center-of-mass energy of 7 TeV. The measured helicity fractions are $F_0 = 0.626 \pm 0.034(\text{stat.}) \pm 0.048(\text{syst.})$ and $F_L = 0.359 \pm 0.021(\text{stat.}) \pm 0.028(\text{syst.})$, which are in agreement with predictions from NNLO QCD.

CMS has published their latest 8 TeV result [8] done with a single top production topology using lepton plus two jets events. The measured helicity fractions are $F_0 = 0.720 \pm 0.039(\text{stat.}) \pm 0.037(\text{syst.})$ and $F_L = 0.298 \pm 0.028(\text{stat.}) \pm 0.032(\text{syst.})$. By assuming unitarity, one can get $F_R = -0.018 \pm 0.019(\text{stat.}) \pm 0.011(\text{syst.})$. The differences between the measurements and the SM predictions are within one sigma significance.

2.2 Top Quark Charge Asymmetry

The top quark charge asymmetry comes from the difference on the produced top-quark pair respect to their pseudo-rapidity (η) direction. For Tevatron experiments, protons are colliding on anti-protons. Any preferences on the produce top quark charge sign to the original colliding particle will cause an asymmetry, so-called forward-backward asymmetry. At LHC, protons are colliding on protons, only the interferences on the tree and box diagram as well as initial and final state interactions can cause the asymmetry under SM. Experimentally, one can see small differences on the distribution of differential cross section verses η. Some new physics, like axiguon, Z' or KK-gluon, can contribute and enhance the asymmetry.

An effort has been done by ATLAS and CMS to combine the $t\bar{t}$ charge asymmetry results [9] with lepton plus jets events collected at $\sqrt{s} = 7$ TeV. The asymmetry is measured as $A_C = 0.005 \pm 0.007(\text{stat.}) \pm 0.006(\text{syst.})$, which is in agreement with the prediction from the SM. Both ATLAS [10] and CMS also have their results using di-lepton events collcected at $\sqrt{s} = 7$ TeV by looking at the asymmetry on the produced top quarks and the charge sign of leptons from top-quarks decay. No significant deviation from SM is seen.

2.3 Top Quark Polarization and Spin Correlation

In the SM, top quarks are produced almost un-polarized. However, the spins are correlated due to its short lifetime. The small amount of polarization can be attributed to electroweak corrections to the QCD-dominated production process. New physics could affect both the spin correlation and polarization properties.

Both ATLAS and CMS have measured the $t\bar{t}$ pair polarization with events taking at $\sqrt{s} = 7$ TeV. The ATLAS result [12] is based on template fit on single lepton and di-lepton events. CMS uses lepton plus jet events to provide a background subtracted measurement [13], which unfolds the results back to parton level. The measurements are found to be agreed with SM predictions. On the spin correlation study, ATLAS and CMS have published results using 7 TeV data. ATLAS has a study [14] using their full 8 TeV data. The measured degree of correlation is $A_{\text{helicity}} = 0.38 \pm 0.04$, which agrees the SM prediction. This study also excludes super-symmetry top squarks with masses between the SM top quark mass and 191 GeV at the 95% confidence level (CL).

2.4 Top Quark FCNC Searches

The flavor-changing neutral current (FCNC) process is described by the penguin diagram. Comparing with the top-quark charged current process with tree diagram, FCNC with top is highly suppressed under SM at order of $O(10^{-15})$. Several models extend SM predict enhancements on the FCNC processes up to order of $O(10^{-3})$. Any detection of top quark decays or productions through the FCNC diagram would be a direct hint of physics beyond standard model (BSM).

FCNC Top Quark Decays and Productions

Searching for top-quarks decay into Zq has been performed since the LEP and Tevatron experiments. The current most stringent limit is given by the CMS study [15]. By looking at

$t\bar{t} \dashrightarrow WbZq \dashrightarrow bj\ell^+\ell^-\ell'$ trilepton events combining 7 TeV and 8 TeV data, the limit on $\mathcal{B}(t \to Zq)$ is set to be $< 0.05\%$ at 95% CL.

The search for FCNC can also be done through the single top-quark production processes. CMS has limits [16] on $\mathcal{B}(t \dashrightarrow Zu) < 0.51\%$ and $\mathcal{B}(t \dashrightarrow Zc) < 11.40\%$ as a complementary to the search with $t\bar{t}$ decays. ATLAS has the current best limits [17] on $\mathcal{B}(t \dashrightarrow gu) < 0.0031\%$ and $\mathcal{B}(t \to gc) < 0.016\%$ using a data corresponding to 14.2 fb^{-1} collected at 8 TeV. CMS also provides limits [18] on $\mathcal{B}(t \dashrightarrow \gamma u) < 0.0161\%$ and $\mathcal{B}(t \dashrightarrow \gamma c) < 0.182\%$. Currently no excess to the SM predictions is seen.

Search for $t \dashrightarrow Hq$ Decays

The Higgs particle was discovered with its mass measured as ~ 125.5 GeV, which is lighter than the mass of the top quark. Theoretically $t \dashrightarrow Hq$ decay is also an FCNC process and suppressed by GIM mechanism. The branching fraction of $t \dashrightarrow Hc$ is also predicted at order of $O(10^{-15})$ in SM. Some models, extending SM predicts, enhancement of this process up to detectable level for LHC.

ATLAS currently has the best limit [19] on the branching fraction of $t \dashrightarrow Hc$ with a direct search approach using $H \dashrightarrow \gamma\gamma$ events combining 7 TeV and 8 TeV data. The limit is give to as $\mathcal{B}(t \dashrightarrow Hc) < 0.79\%$ at 95% CL with $< 0.51\%$ expected. Meanwhile, a re-interpretation of CMS SUSY multi-lepton searches [20] provides a limit as $\mathcal{B}(t \dashrightarrow Hc) < 0.56\%$ by combining studies on $H \dashrightarrow WW^*$, $\tau\tau$, ZZ^* and $\gamma\gamma$ channels. The latest CMS result [21] with direct search approach on H decays into multi-lepton channels gives $\mathcal{B}(t \dashrightarrow Hc) < 0.93\%$ at 95% CL with $< 0.89\%$ expected. This corresponds to a bound on the top-charm flavor violating Higgs Yukawa couplings of $\sqrt{|\lambda^h_{tc}|^2 + |\lambda^h_{ct}|^2} < 0.18$. The observables used in the searches are shown in Fig. 1.

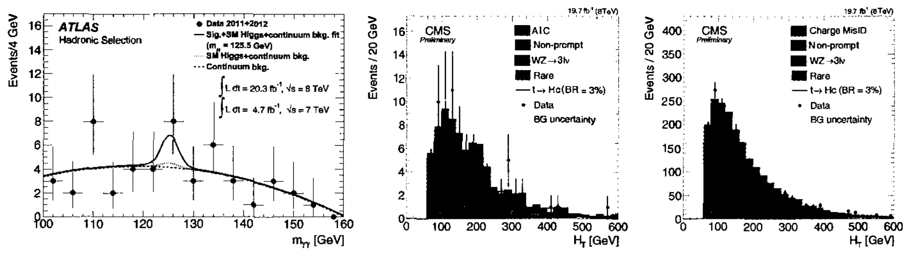

Figure 1 – Distribution of $m_{\gamma\gamma}$ for the selected events in the hadronic channel of the ATLAS $t \to Hc$ search (left). H_T distributions in the trilepton (middle) and same-sign dilepton (right) channels in the CMS $t \to Hc$ search.

3 Summary and Prospects

Top-quark mass measurements at the LHC by ATLAS and CMS have already reached the precision of the Tevatron results. Studies on various top quark properties, including W-boson helicity, charge asymmetries, spin correlation and polarization, as well as FCNC couplings, have been carried out and so far no significant deviations from SM predictions are seen. Therefore, precision measurements are needed for the search of possible new physics contributions.

ATLAS and CMS experiments are finishing up their studies with 7 and 8 TeV data and heading for the LHC restarts in summer of 2015 with increased energy and luminosity. This is a new milestone ahead and we are expecting more exciting results.

References

1. F. Abe, H. Akimoto et al., Observation of Top Quark Production in $p\bar{p}$ Collisions with the Collider Detector at Fermilab, Phys. Rev. Lett. **74**, 2626 (1995).
2. S. Abachi, B. Abbott et al., Observation of the Top Quark, Phys. Rev. Lett. **74**, 2632 (1995).
3. The ATLAS collaboration, The ATLAS experiment at the CERN Large Hadron Collider, JINST **3**, S08003 (2008).
4. The CMS collaboration, The CMS experiment at the CERN LHC, JINST **3**, S08004 (2008).
5. The CMS collaboration, Determination of the top-quark pole mass and strong coupling constant from the $t\bar{t}$ production cross section in pp collisions at $\sqrt{s}$ = 7 TeV, Phys. Lett. B **728**, 496 (2014).
6. The CMS collaboration, Measurement of the $t\bar{t}$ production cross section in the dilepton channel in pp collisions at $\sqrt{s}$=7 TeV, J. High Energy Phys. **11**, 067 (2012).
7. The ATLAS and CMS collaboration, Combination of the ATLAS and CMS measurements of the W-boson polarization in top-quark decays, ATLAS-CONF-13-033 (2013).
8. The CMS collaboration, Measurement of the W boson helicity in events with a single reconstructed top quark in pp collisions at $\sqrt{s}$ = 8 TeV, J. High Energy Phys. **01**, 053 (2015).
9. The ATLAS and CMS collaboration, Combination of ATLAS and CMS $t\bar{t}$ charge asymmetry measurements using LHC proton-proton collisions at $\sqrt{s}$ = 7 TeV, ATLAS-CONF-2014-012.
10. The ATLAS collaboration, Measurement of the charge asymmetry in dileptonic decays of top quark pairs in pp collisions at $\sqrt{s}$ = 7 TeV using the ATLAS detector, arXiv:1501.07383 (2015).
11. The CMS collaboration, Combination of ATLAS and CMS ttbar charge asymmetry measurements using LHC proton-proton collisions at 7 TeV, CMS-PAS-TOP-14-006 (2014).
12. The ATLAS collaboration, Measurement of Top Quark Polarization in Top-Antitop Events from Proton-Proton Collisions at $\sqrt{s}$ = 7 TeV Using the ATLAS Detector, Phys. Rev. Lett. **111**, 232002 (2013).
13. The CMS collaboration, Measurements of $t\bar{t}$ Spin Correlations and Top-Quark Polarization Using Dilepton Final States in pp Collisions at $\sqrt{s}$ = 7 TeV, Phys. Rev. Lett. **112**, 182001 (2014).
14. The ATLAS collaboration, Measurement of Spin Correlation in Top-Antitop Quark Events and Search for Top Squark Pair Production in pp Collisions at $\sqrt{s}$ = 8 TeV Using the ATLAS Detector, Phys.Rev.Lett. **114**, 142001 (2015).
15. The CMS collaboration, Search for flavor-changing neutral currents in top-quark decays $t \dashrightarrow Zq$ in pp collisions at $\sqrt{s}$=8 TeV, Phys.Rev.Lett. **112**, 171802 (2014).
16. The CMS collaboration, Search for Flavor Changing Neutral Currents in tZ events in proton-proton collisions at 7 TeV, CMS-PAS-TOP-12-021 (2013).
17. The ATLAS collaboration, Search for single top-quark production via FCNC in strong interactions in $\sqrt{s}$ = 8 TeV ATLAS data, ATLAS-CONF-2013-063 (2013).
18. The CMS collaboration, Search for anomalous single top quark production in association with a photon, CMS-PAS-TOP-14-003 (2014).
19. The ATLAS collaboration, Search for top quark decays $t \to qH$ with $H \to \gamma\gamma$ using the ATLAS detector, J. High Energy Phys. **06**, 008 (2014).
20. The CMS collaboration, A search for anomalous production of events with three or more leptons using 19.5/fb of $\sqrt{s}$=8 TeV LHC data CMS-PAS-TOP-13-034 (2013).
21. The CMS collaboration, Search for top quark decays via Higgs-boson-mediated flavor changing neutral currents in pp collisions at $\sqrt{s}$ = 8 TeV, CMS-PAS-TOP-13-017 (2015).

Single top production at the LHC

C. Escobar on behalf of the ATLAS and CMS Collaborations
Department of Physics & Astronomy, University of Pittsburgh, Pittsburgh, PA 1520 USA.
cescobar@cern.ch

A review of the recent results on measurements of cross-sections and top quark properties in single top quark processes, performed at the LHC by ATLAS and CMS is presented. The measurements are in good agreement with predictions and no deviations from Standard Model expectations have been seen so far.

1 Introduction

The top quark is the heaviest known Standard Model (SM) elementary particle. Its large mass means that it decays quickly without forming hadrons therefore offering the unique opportunity to study the properties of a "bare" quark. Because of this, top quark is fundamental for understanding physics in the SM and beyond. At the LHC [1], top quarks are produced predominantly in pairs via the flavour-conserving strong interaction, while an alternative process produces single top quarks through the weak interaction. Single top quark production is mediated through three channels: exchange of a virtual W boson in the t-channel or s-channel, and production of an on-shell W boson and a top quark in the Wt-channel.

This review focuses on the latest results on single top quark analyses performed by ATLAS [2] and CMS [3] in pp collisions at the LHC. This includes cross-section measurements at 8 TeV and measurements of properties in single top quark processes at 7 and 8 TeV.

2 Single top production cross-section measurement

At the LHC, in pp collisions at 8 TeV, the single top quark production cross-sections are calculated at next-to-leading order (NLO) in QCD with re-summed next-to-next-to-leading logarithmic (NNLL) accuracy. They are found to be $87.76^{+3.44}_{-1.91}$ pb for the t-channel [4], 22.37±1.52 pb for the Wt-channel [5] and 5.61±0.22 pb for the s-channel [6], where the uncertainties correspond to the sum in quadrature of the scale and the parton distribution function (PDF) uncertainties.

2.1 Measurement of the t-channel production cross-section

The event signature of the t-channel in the lepton+jets final state contains a charged lepton (e or μ), missing transverse momentum ($\not{E}_T$) and two jets where one originates from a b-quark (b-tagged jet) and the other from the spectator quark. At 8 TeV, CMS has performed an analysis using 19.7 fb^{-1} of the LHC data [7], exploiting the discriminating feature of the pseudorapidity of the non b-tagged jet ($|\eta_j|$) to measure the t-channel cross-section. Two signal (lepton charge dependent) regions and two control regions ($m(\ell\nu b) < 130$ GeV and $m(\ell\nu b) > 220$ GeV) are considered. Sources of systematic uncertainties are evaluated with pseudo-experiments. The cross-sections for top quark and top antiquark production extracted from a template fit are

53.8 ± 1.5 (stat.) ± 4.4 (syst.) pb and 27.6 ± 1.3 (stat.) ± 3.7 (syst.) pb, respectively. Accounting for correlations, the top-antitop cross-section ratio is measured to be $R_t = 1.95 \pm 0.10$ (stat.) ± 0.19 (syst.). The jet energy scale (JES) is the dominant source of systematic uncertainty for the cross-sections while for R_t, the PDF uncertainty is the largest one.

A fiducial t-channel cross-section measurement is provided by an ATLAS analysis using 20.3 fb^{-1} of the 8 TeV data [8]. A binned maximum likelihood fit is performed to the neural network (NN) output in the signal region where backgrounds are treated as nuisance parameters. The modelling of $t\bar{t}$ and W+jets is validated in dedicated control regions. The fiducial phase space is defined close to that of the reconstructed and selected data set. The particle-level objects are constructed from stable particles in the final state, with a very similar definition to the reconstructed objects. The fiducial cross-section within the detector acceptance is measured to be 3.37 ± 0.05 (stat.) ± 0.48 (syst.) pb. Source of systematic uncertainties are obtained from pseudo-experiments with dominant contributions coming from the JES and the signal generator. The fiducial measurement is extrapolated to the full phase space using different Monte Carlo generators. The inclusive cross-section is determined to be 82.6 ± 1.2 (stat.) ± 12.0 (syst.) pb, using aMC@NLO+Herwig [9,10].

2.2 *Observation of the Wt-channel production*

The Wt-channel event signature in the dilepton final state contains two high p_T leptons, large $\not{E}_T$ and one b-tagged jet. The Wt-channel production has been observed in CMS in this dilepton final state, using 12.2 fb^{-1} of the 8 TeV data [11]. A maximum likelihood fit is performed on a boosted decision tree (BDT) output over all lepton flavour combinations (ee, $e\mu$ or $\mu\mu$) and in different signal regions. The shapes for signal and backgrounds are taken from simulation. Sources of systematic uncertainties are treated as constrained nuisance parameters in the fit except for the luminosity and theory uncertainties which are unconstrained. The scale and the $t\bar{t}$ modelling are the dominant source of systematic uncertainties. A significance of 6.1σ (5.4σ) is observed (expected) for the signal. The cross-section is measured to be 23.4 ± 5.4 (stat. + syst.) pb.

A similar measurement is carried out in ATLAS, in the $e\mu$ final state, using 20.3 fb^{-1} of the 8 TeV data [12]. A fit to the BDT output is simultaneously performed in two regions. Templates for signal and backgrounds are taken from simulation and sources of systematic uncertainties evaluated by means of pseudo-experiments with the main contribution coming from the Wt-channel and $t\bar{t}$ modelling. The measurement has reached an observed (expected) significance of 4.2σ (4.0σ). The cross-section is determined to be 27.2 ± 2.8 (stat.) ± 5.4 (syst.) pb.

The results of the two experiments are combined [13] with the BLUE method. The theory modelling systematic uncertainties are considered fully correlated between CMS and ATLAS, while a 31% correlation is assigned to the luminosity and a 50% correlation is taken into account for the b-tagging uncertainty. The stability of the combination with these choices is verified by examining different correlation values. The combination leads to 25.0±1.4 (stat.)±4.5 (syst.) pb.

2.3 *Search for the s-channel production*

The s-channel signal is characterised by one high p_T isolated charged lepton (e or μ), $\not{E}_T$ and two b-tagged jets. Using 20.3 fb^{-1} and 19.3 fb^{-1} of the 8 TeV data, ATLAS [14] and CMS [15] have set upper limits of < 14.6 pb and < 11.5 pb with 95% CL on the s-channel cross-section, respectively. The observed (expected) significance is found to be 1.3σ (1.4σ) for ATLAS and 0.7σ (0.9σ) for CMS. Both analyses use a BDT discriminant constructed in the signal region and in the $t\bar{t}$ control region (requiring three jets, two of them being b-jets). The signal strength is extracted using a likelihood fit to the BDT outputs where the $t\bar{t}$ and W+jets backgrounds are constrained in the fit. The multijet background is determined using data-driven techniques. Sources of systematic uncertainties are evaluated using pseudo-experiments. The scale and JES uncertainties are the dominant contributions to the total uncertainty.

2.4 $|V_{\rm tb}|$ determination

Single top quark production allows a direct probe of the SM Wtb coupling at the production vertex. In particular, the production cross-section is proportional to the square of the CKM matrix element $|V_{\rm tb}|$. The extraction of $|V_{\rm tb}|$ from the single top quark cross-section measurements does not require assumptions about the number of quark generations or unitarity of the CKM matrix but assumes $|V_{\rm tb}| \gg |V_{\rm td}|, |V_{\rm ts}|$ (i.e. $\mathcal{BR}(t \to Wb) \approx 1$) and that the Wtb interaction is a SM-like left-handed weak coupling. Deviations from the SM may be indications of new physics that modifies the Wtb vertex coupling. The available measurements of single top quark production in the t-channel [7,8,16,17] and Wt-channel [11,12,13,18] allow determinations of $|V_{\rm tb}|$ with different levels of precision. The most precise measurement up to date is performed by CMS in the combination [7] of the $|V_{\rm tb}|$ measurements using the two t-channel cross-section measurements at 7 and 8 TeV, which achieves: $|V_{\rm tb}| = 0.998 \pm 0.041$ (4.1%).

3 Top quark properties in production and decay

3.1 Limits on anomalous couplings in Wtb vertex

Deviations from the SM in the Wtb vertex can be expressed in terms of the anomalous couplings, $V_{\rm L,R}$ and $g_{\rm L,R}$, presented in this effective Lagrangian [19,20]:

$$\mathcal{L}_{Wtb} = -\frac{g}{\sqrt{2}}\bar{b}\gamma^{\mu}\left(V_{\rm L}P_{\rm L} + V_{\rm R}P_{\rm R}\right)tW_{\mu}^{-} - \frac{g}{\sqrt{2}}\bar{b}\frac{i\sigma^{\mu\nu}q_{\nu}}{m_W}\left(g_{\rm L}P_{\rm L} + g_{\rm R}P_{\rm R}\right)tW_{\mu}^{-} + \text{h.c.} \qquad (1)$$

A direct search for the anomalous couplings is done in an analysis [21] carried out in CMS using 5.0 fb^{-1} of 7 TeV data. Two Bayesian NN (BNN) are used to discriminate between the SM t-channel and SM backgrounds and between anomalous hypothetic scenarios against all SM processes. The anomalous scenarios are simulated for $(V_{\rm L}, V_{\rm R})$ and $(V_{\rm L}, g_{\rm L})$ combinations where those couplings that are not present in the combination are set to zero. For each combination the two BNN discriminants are used as inputs in the statistical analysis. The observed (expected) limits at 95% CL are $|V_{\rm L}| > 0.92$ (0.88) and $|g_{\rm L}| < 0.09$ (0.06) for $(V_{\rm L}, g_{\rm L})$, and $|V_{\rm L}| > 0.90$ (0.88) and $|V_{\rm R}| < 0.34$ (0.39) for $(V_{\rm L}, V_{\rm R})$.

In addition, an indirect measurement in a cut-and-count analysis [22] is carried out in ATLAS using 4.7 fb^{-1} of 7 TeV data. A forward-backward asymmetry with respect the normal to the plane defined by the W boson momentum and the top quark polarization is used to probe the $\mathcal{CP}$-violating complex phase of $g_{\rm R}$. The measured value of the asymmetry is 0.031 ± 0.065 (stat.)$^{+0.029}_{-0.031}$ (syst.). Taking this measurement together with the theoretical prediction of the top quark polarisation of 0.9, the experimental limits on Im$(g_{\rm R})$ are determined to be $[-0.20, 0.30]$ at 95% CL.

3.2 Measurement of the W boson helicity fractions

Taking into account the differential decay rate of the decaying top quark, considering the angle θ_{ℓ}^{*} between the W boson momentum in the top quark rest frame and the momentum of the down-type decay fermion in the rest frame of the W boson, the contributions of right-handed ($F_{\rm R}$), left-handed ($F_{\rm L}$) and longitudinal (F_0) helicity fractions of the W boson are measured by CMS [23]. The 8 TeV data sample corresponds to an integrated luminosity of 19.7 fb^{-1} and all events containing a $t \to \ell b\nu$ interaction, including $t\bar{t}$ and single top processes, are considered as signal. The resulting $\cos\theta_{\ell}^{*}$ distribution is fitted to the data to extract, simultaneously, the W boson helicity fractions and the W+jets background contamination. The combination of the electron and muon channels yields $F_{\rm L} = 0.298 \pm 0.028$ (stat.) $\pm$ 0.032 (syst.), $F_0 = 0.720 \pm 0.039$ (stat.) ± 0.037 (syst.) and $F_{\rm R} = 0.018 \pm 0.019$ (stat.) ± 0.011 (syst.). These results are used to set exclusion limits on the real part of the Wtb anomalous couplings, $g_{\rm L}$ and $g_{\rm R}$, assuming $V_{\rm L} = 1$ and $V_{\rm R} = 0$.

3.3 Top quark polarization

In the SM, the top quark is highly polarised in the direction of the spectator quark in the t-channel process. Its spin is also correlated with the angular properties of the decay products. The angle between the charged lepton and non b-tagged jet (i.e. spectator jet) in the top quark rest frame (θ^*) is used in CMS to measure the top quark polarization [24]. The collected data sample at 8 TeV corresponds to 19.7 fb^{-1} and a BDT is used to purify the signal sample. The background-subtracted distribution of $\cos\theta^*$ is then unfolded to parton-level. A fit to the unfolded distribution leads to a top quark spin asymmetry of 0.41 ± 0.06 (stat.) $\pm\, 0.16$ (syst.) extracted from the combination of measurements in the electron and muon channels using the BLUE method. A top quark polarization of 0.82 ± 0.12 (stat.) $\pm\, 0.32$ (syst.) is then obtained under the assumption that the spin analysing power of a charged lepton is 100%.

4 Conclusions

The ATLAS and CMS collaborations have produced high precision cross-section, including fiducial, measurements and detailed studies of top quark properties using the delivered 7 and 8 TeV LHC data. The measurements are in good agreement with predictions and no hint for physics beyond the SM was observed so far in the top quark sector.

5 Acknowledgement

The author would like to thank the ATLAS and CMS collaborations for their incredible work in single top quark studies and also to the organizers for the kind invitation to this conference.

References

1. L. Evans and P. Bryant, JINST **3** (2008) S08001.
2. The ATLAS Collaboration, JINST **3** (2008) S08003.
3. The CMS Collaboration, JINST **3** (2008) S08004.
4. N. Kidonakis, Phys. Rev. D **83** (2011) 091503.
5. N. Kidonakis, Phys. Rev. D **82** (2010) 054018.
6. N. Kidonakis, Phys. Rev. D **81** (2010) 054028.
7. The CMS Collaboration, JHEP **1406** (2014) 090.
8. The ATLAS Collaboration, ATLAS-CONF-2014-007.
9. J. Alwall, M. Herquet, F. Maltoni, O. Mattelaer and T. Stelzer, JHEP **1106** (2011) 128.
10. G. Corcella *et al.*, JHEP **0101** (2001) 010.
11. The CMS Collaboration, Phys. Rev. Lett. **112** (2014) 23, 231802.
12. The ATLAS Collaboration, ATLAS-CONF-2013-100.
13. The ATLAS and CMS Collaborations, ATLAS-CONF-2014-052, CMS-PAS-TOP-14-009.
14. The ATLAS Collaboration, Phys. Lett. B **740** (2015) 118.
15. The CMS Collaboration, CMS-PAS-TOP-13-009.
16. The CMS Collaboration, JHEP **1212** (2012) 035.
17. The ATLAS Collaboration, Phys. Rev. D **90** (2014) 112006.
18. The CMS Collaboration, Phys. Rev. Lett. **110** (2013) 022003.
19. J. A. Aguilar-Saavedra, Nucl. Phys. B **812** (2009) 181.
20. J. A. Aguilar-Saavedra, Nucl. Phys. B **821** (2009) 215.
21. The CMS Collaboration, CMS-PAS-TOP-14-007.
22. The ATLAS Collaboration, ATLAS-CONF-2013-032.
23. The CMS Collaboration, JHEP **1501** (2015) 053.
24. The CMS Collaboration, CMS-PAS-TOP-13-001.

3.
Heavy Flavours

Introduction to Heavy Flavours

F. MAHMOUDI
Université de Lyon, Université Lyon 1, F-69622 Villeurbanne Cedex, France;
Centre de Recherche Astrophysique de Lyon, CNRS, UMR 5574, Saint-Genis Laval Cedex, F-69561, France; Ecole Normale Supérieure de Lyon, France
and
CERN Theory Division, Physics Department, CH-1211 Geneva 23, Switzerland

We present a short review of heavy flavours and the main challenges given the recent experimental developments.

1 Introduction

Many fundamental questions in particle physics are related to flavour. Among the most important open issues one can mention the hierarchy of quark masses, the absence of flavour changing neutral currents, the pattern of mixing angles of quarks, the origin of the baryon asymmetry in the Universe and the number of flavours and quarks. While there have been several attempts to provide answers to these questions, by considering for example continuous or discrete flavour symmetries, extra-dimension models or compositeness, no definite picture is yet attained. The quark sector is nevertheless well described through the Cabibbo-Kobayashi-Maskawa (CKM) formalism.

In this review, we will first briefly address the CKM mechanism and in particular the determination of V_{ub} for which there are discrepancies in the measurements. We will then move to indirect search for New Physics (NP) with the two main actors, which are tests of CP violation and studies of rare decays.

2 CKM formalism

In the Standard Model (SM), the mixing within the three generations of quarks is described by the CKM matrix. In the Wolfenstein parametrisation, it can be written as

$$V_{\rm CKM} = \begin{pmatrix} V_{ud} & V_{us} & V_{ub} \\ V_{cd} & V_{cs} & V_{cb} \\ V_{td} & V_{ts} & V_{tb} \end{pmatrix} = \begin{pmatrix} 1-\lambda^2/2 & \lambda & A\lambda^3(\rho+i\eta) \\ -\lambda & 1-\lambda^2/2 & A\lambda^2 \\ A\lambda^3(1-\rho-i\eta) & -A\lambda^2 & 1 \end{pmatrix} \tag{1}$$

which contains three CP conserving parameters and one CP violating phase, and is unitary. The results of two decades of Babar, Belle and LHCb in measuring the CKM parameters is summarised in Fig. 1, which confirms the unitarity of the CKM matrix, and shows that the CKM paradigm is fully consistent with the data.

One of the least known parameters of the CKM matrix is V_{ub}. Measurement of $|V_{ub}|$ is very challenging, but the precision is reduced to $\sim 10\%$ at B factories. The two main ways to measure $|V_{ub}|$ are based on inclusive semi-leptonic decays ($B \to X_u \ell \nu$) and exclusive semi-leptonic decays

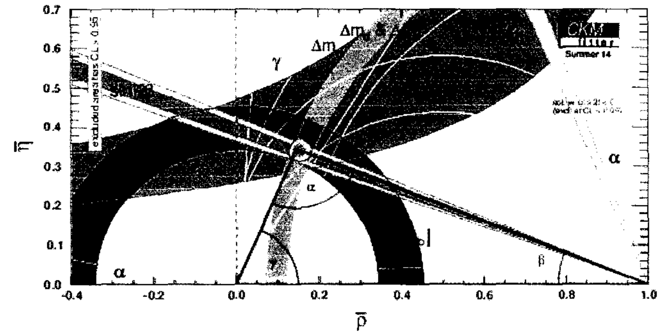

Figure 1 – Unitarity triangle in the $\bar{\rho} = \rho(1 - \lambda^2/2)$ vs. $\bar{\eta} = \eta(1 - \lambda^2/2)$ parameter plane[1].

$(B \to \pi \ell \nu)$. Both approaches provide independent measurements of $|V_{ub}|$. There is currently a discrepancy in the central values of about 3σ, but they have roughly the same precision. Both methods can be employed at a high luminosity B factory, and the experimental error in the determination of $|V_{ub}|$ will decrease with increasing integrated luminosity and improved analysis techniques. The inclusive and exclusive determinations of $|V_{ub}|$ have independent theoretical errors[2]. Concurrent reduction of this theoretical error is however more challenging. A summary of the current measurements is provided in Fig. 2.

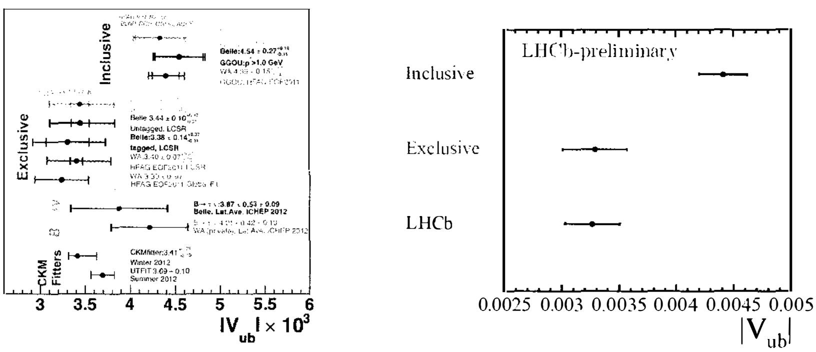

Figure 2 – Summary of the different measurements of $|V_{ub}|$ at B factories[3] (left panel), and comparison with the LHCb result[4] (right panel).

The current combination of $|V_{ub}|$ from inclusive decays using nine independent measurements of $B \to X_u \ell \nu$ gives[5]:

$$|V_{ub}| = (4.41 \pm 0.15(\text{exp})^{+0.15}_{-0.17}(\text{theory})) \times 10^{-3} , \tag{2}$$

where the experimental error is of the same order as the theoretical error. Conversely, the world average measurement of $|V_{ub}|$ from exclusive decays is[5]:

$$|V_{ub}| = (3.28 \pm 0.29) \times 10^{-3} . \tag{3}$$

Very recently, LHCb has also measured $|V_{ub}|$ using baryonic decays[6]. This is an important breakthrough, as it was thought for long that the measurement of $|V_{ub}|$ is impossible at hadron colliders. The most promising channels at LHCb are $\Lambda_b \to p\,\mu\nu$ and $B_s \to K^+\mu\nu$. $\Lambda_b \to p\,\mu\nu$ is more favourable due to smaller background with protons. Both decays have branching ratios of about $10^{-5} - 10^{-4}$, and precise lattice calculations of $\Lambda_b \to p, \Lambda_{(c)}$ form factors are now available [7]. Experimentally, such decays are challenging because of neutrino reconstruction. The main background comes from decays involving V_{cb}. The determination of $|V_{ub}|$ from $\Lambda_b \to p\,\mu\nu$ gives:

$$|V_{ub}| = (3.27 \pm 0.15(\text{exp}) \pm 0.17(\text{theory}) \pm 0.06(|V_{cb}|)) \times 10^{-3}\,, \tag{4}$$

which is 3.5σ below the inclusive measurement but agrees well with current exclusive world average, as can be seen in the right panel of Fig. 2.

V_{ub} is a particularly important CKM parameter since it is also related to the question of CP violation.

3 CP violation

CP violation is a key concept to explain the baryon asymmetry in the Universe. Since the CKM matrix is the only source of CP violation in the SM, any sign of extra CP violation would point to New Physics. As can be seen from Eq. (1), V_{ub} and V_{td} are the only CP violating CKM parameters in the SM. V_{ub} is probed directly in $b \to u$ transitions. V_{td} on the other hand involves a top quark and therefore is probed indirectly, for example in B_d mixings.

3.1 CP violation in $B_{(s)}$ mixings

The study of the $B_{(s)} - \bar{B}_{(s)}$ oscillations allows for indirect probe of CP violation in V_{td} (V_{ts}). B and $\bar{B}$ have different properties which come from the difference in the heavy and light eigenstates. Two important observables are the mass difference and the decay rate difference between the two eigenstates, which can be written as

$$\Delta M \equiv M_H - M_L = 2|M_{12}|\,, \qquad \Delta\Gamma \equiv \Gamma_L - \Gamma_H = 2|\Gamma_{12}|\cos\phi_q\,, \tag{5}$$

where M_{12} and Γ_{12} are respectively sensitive to the heavy (i.e. top quarks and New Physics) and light internal particles. The deviation from the SM is parametrised by Δ_q ($q = d, s$) in a generic way:

$$M_{12,q} = M_{12,q}^{SM} \times \Delta_q\,. \tag{6}$$

A complex Δ_q implies new source of CP violation, and $\phi_q \equiv \arg(\Delta_q)$ is the CP violating weak phase.

$B_{(s)}$ mixings are particularly studied using the semi-leptonic asymmetries (for example $B_{(s)} \to D_{(s)}\ell\nu$), which allows us to measure the quantity a_{sl}, related to the imaginary part of the ratio of Γ_{12} over M_{12}, or ϕ_q and Δ_q:

$$a_{\text{sl}}^q = \text{Im}\left(\frac{\Gamma_{12,q}}{M_{12,q}}\right) = \left(\frac{|\Gamma_{12,q}|}{|M_{12,q}|}\right)\frac{\sin(\phi_q^{SM} + \phi_q)}{|\Delta_q|}\,. \tag{7}$$

The measurements of a_{sl}^d and a_{sl}^s by LHCb [8,9] and a_{sl}^d by the B factories [10] are well in agreement with the SM predictions [11], while the measurement of these two quantities in combination with the dimuon charge asymmetry by the D0 experiment shows a deviation of more than 3σ from the SM prediction [12].

3.2 CP violation in $B_{(s)}$ decays

One way to probe more directly CP violation is to consider decays into neutral mesons. For example by comparing $B^- \to D^0K^-$ and $B^- \to \bar{D}^0K^-$ one can directly probe the difference between the D^0 and the $\bar{D}^0$. These decays correspond to different diagrams which are either sensitive to the CP conserving CKM parameters V_{cb} and V_{us}, or to V_{ub} and V_{cs}. Other channels can also be studied such as $B \to \phi K^{(*)}, K\pi$, $B_s \to KK, \pi\pi, K\pi, \phi\phi, J/\psi\,\phi$.

The way to derive a CP asymmetry is different when the initial meson is charged or neutral, because of the oscillations. For the charged mesons, the measurement consists of studying directly the decay with a positive charge and the decay with a negative charge, and computing a CP asymmetry, leading to a direct determination of this asymmetry:

$$A_{CP} \equiv \frac{\Gamma(M^+ \to f^+) - \Gamma(\bar{M}^- \to f^-)}{\Gamma(M^+ \to f^+) + \Gamma(\bar{M}^- \to f^-)} \,. \tag{8}$$

For neutral mesons, because of the oscillations, the determination is more complicated and is mostly indirect. The CP asymmetry is defined similarly to the case of charged mesons but it is time dependent because of the oscillations:

$$A_{CP}(t) \equiv \frac{\Gamma(M^0 \to f;t) - \Gamma(\bar{M}^0 \to f;t)}{\Gamma(M^0 \to f;t) + \Gamma(\bar{M}^0 \to f;t)} \,. \tag{9}$$

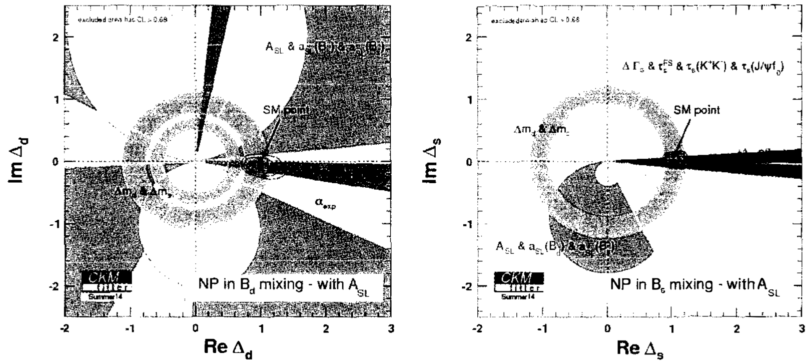

Figure 3 – Experimental determination of Δ_d from B_d mixings (left panel) and Δ_s from B_s mixings (right panel) by the CKMfitter collaboration [1]. The SM corresponds to $\Delta_{d,s} = 1$.

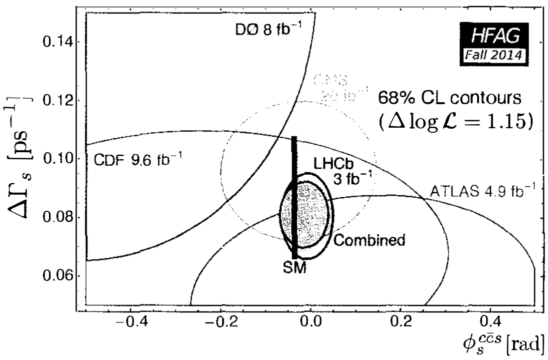

Figure 4 – Decay rate difference $\Delta\Gamma_s$ as a function of the new CP phase ϕ_s from analyses of the $b \to c\bar{c}s$ decays [1].

To summarise CP violation in the b sector, Fig. 3 shows the results of the CKMfitter collaboration for B_d and B_s mixings in Summer 2014. They correspond to a deviation by slightly more than 1σ in B_d mixings, and less than 1σ in B_s mixings. A combination of the results related to the decays of $b \to c\bar{c}s$ has also been performed by HFAG. Their results are presented in Fig. 4, which shows a good agreement with the SM, and that ϕ_s is compatible with the absence of new source of CP violation.

3.3 CP violation in charm physics

CP violation in charm physics is also very important, especially because it involves CKM matrix elements without CP violation. Hence, CP violation in the charm sector is expected to be very small. The idea is similar to CP violation in the b sector, where the $B_{(s)}$ mesons are replaced by $D_{(s)}$ mesons. CP violation in charm physics can be probed in both $D_{(s)}$ mixings and $D_{(s)}$ decays. For the decays, the typical channels are $D^0 \to K^+K^-$ and $\bar{D}^0 \to K^+K^-$, which probe V_{cs} and V_{us} and involve the $D^0 - \bar{D}^0$ oscillation (so time-dependent). There are many other channels with 2, 3 or 4 light mesons (pions or kaons). Another interesting observable that can be considered for D_0 decays is the difference of CP violation between $D^0 \to K^+K^-$ and $D^0 \to \pi^+\pi^-$, defined as:

$$\Delta A_{CP} \equiv A_{CP}(K^+K^-) - A_{CP}(\pi^+\pi^-) \,, \tag{10}$$

which is expected to be small.

Fig. 5 presents ΔA_{CP} as a function of A_{CP} using the combination of all the measurements from CDF, Babar, Belle and LHCb. The figure shows that A_{CP} is compatible with 0, while ΔA_{CP} is slightly smaller than expected.

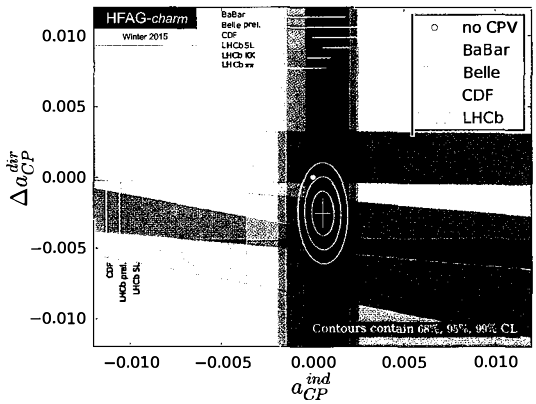

Figure 5 – ΔA_{CP} as a function of A_{CP} in the charm sector[10].

4 Rare decays

Another way to search indirectly for New Physics is through rare decays, which occur at loop level in the SM and are therefore very sensitive to NP effects. The theoretical framework for the calculation of rare decays is based on the effective field theory approach where the short distance (Wilson coefficients) and long distance (local operators) contributions are separated using Operator Product Expansion[13].

There have been several breakthroughs during the past few years, in particular with the first measurement of the $B_s \to \mu^+\mu^-$ branching ratio, and the measurement of clean angular observables in the $B \to K^*\mu^+\mu^-$ decay.

The branching ratio of $B_s \to \mu^+\mu^-$ can be calculated using

$$\begin{aligned} \mathrm{BR}(B_s \to \mu^+\mu^-) &= \frac{G_F^2\alpha^2}{64\pi^3} f_{B_s}^2 \tau_{B_s} m_{B_s}^3 |V_{tb}V_{ts}^*|^2 \sqrt{1 - \frac{4m_\mu^2}{m_{B_s}^2}} \\ &\times \left\{ \left(1 - \frac{4m_\mu^2}{m_{B_s}^2}\right) |C_S - C_S'|^2 + \left|(C_P - C_P') + 2\,(C_{10} - C_{10}')\frac{m_\mu}{m_{B_s}}\right|^2 \right\} , \end{aligned} \tag{11}$$

where C_{10} embeds the SM contribution, and C_S and C_P are scalar and pseudoscalar coefficients which can receive large contributions from NP. The C_i' denote the chirality flipped Wilson coefficients. f_{B_s} is the B_s decay constant which constitutes the largest source of uncertainty. The SM prediction for this branching ratio is $(3.54 \pm 0.27) \times 10^{-9}$, based on [14,15,16], which is in agreement with the combined CMS and LHCb measured value of $(2.8^{+0.7}_{-0.6}) \times 10^{-9}$ presented in [17]. The compatibility between the SM values and the experimental measurement sets strong constraints on New Physics models, in particular on supersymmetry [18], where the scalar and pseudoscalar contributions are enhanced approximately as $\tan^6\beta/M_A^4$.

The $B \to K^*\mu^+\mu^-$ decay also provides a multitude of observables sensitive to different helicity structures in the decay amplitude. Unfortunately, the theoretical predictions for the usual observables inherit large uncertainties from the hadronic form factors. This has led to the construction of a number of optimised observables as appropriate ratios of angular coefficients where the form factor uncertainties cancel at leading order, while having high sensitivity to NP effects [19]. LHCb has found a 2.9σ discrepancy with the SM predictions in two of the q^2 bins for one of these clean angular observables [20], namely in the bins $q^2 \in [4.0, 6.0]$ and $[6.0, 8.0]$ GeV^2 of the observable P_5', as can be seen in Fig. 6.

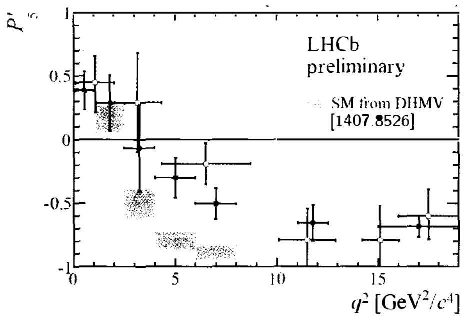

Figure 6 – LHCb experimental measurements of the P_5' observable [20] with 3 fb^{-1} of data (in black), compared to the 1 fb^{-1} results (in blue) and the theoretical predictions [21], as a function of q^2.

Another recent discrepancy measured by LHCb is the ratio R_K of the branching ratio of $B \to K\mu^+\mu^-$ over the one of $B \to Ke^+e^-$ for $q^2 \in [1, 6]$ GeV^2, which is a probe of lepton universality. This ratio is expected to be close to 1 in the SM [22], with uncertainties lower than 1%. The LHCb result is $0.745^{+0.090}_{-0.074}(\mathrm{stat.}) \pm 0.036(\mathrm{syst.})$ [23], showing a deficit of about 25%. This result is compared to the ones from Belle and Babar in Fig. 7.

Discrepancies in both $B \to K^*\mu^+\mu^-$ and $B \to K\ell^+\ell^-$ may be related to New Physics but a global fit of all the $b \to s\ell\ell$ observables shows that the discrepancy is smaller than 2σ if four Wilson coefficients or more are allowed to vary [24]. This is examplified in Fig. 8, where in the left panel a global fit to the Wilson coefficients $C_9, C_{10}, C_9', C_{10}'$ is compared to the results obtained

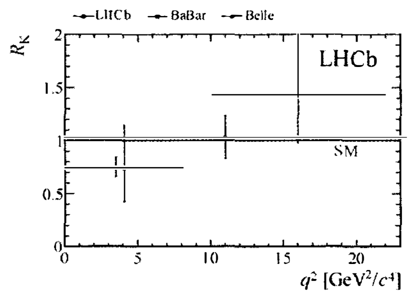

Figure 7 – LHCb, Babar and Belle experimental measurements of the R_K ratio, as a function of q^2 [23].

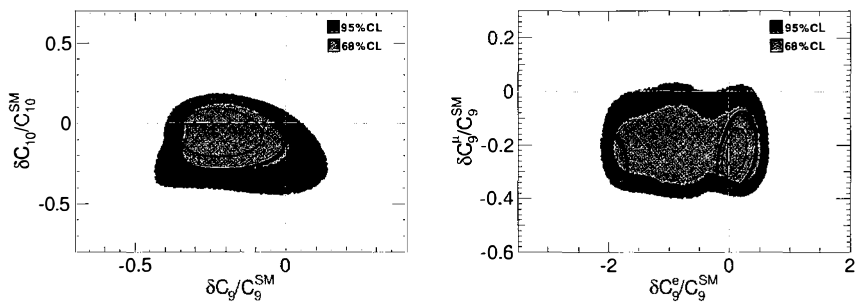

Figure 8 – Global fits to the $b \to s\ell\ell$ observables [24]. δC_i corresponds to the NP contribution to the Wilson coefficient C_i. The light (dark) blue zone shows the 68% (95%) C.L. region. In the left panel, the result of a global fit to $C_9, C_{10}, C_9', C_{10}'$ is compared to the result obtained if only C_9, C_{10} are varied (red and black contours). In the right panel, the result of a global fit to $C_9^{\mu}, C_9^{e}, C_9'^{\mu}, C_9'^{e}$ is compared to the result obtained if only C_9^{μ}, C_9^{e} are varied (red and black contours).

if only C_9, C_{10} are varied. Similarly, in the right panel, a global fit to the Wilson coefficients $C_9^{\mu}, C_9^{e}, C_9'^{\mu}, C_9'^{e}$ is shown and compared to the fit to C_9^{μ}, C_9^{e}.

While the current discrepancies are for the moment not significant enough to claim for any discovery, it is interesting to notice that a modification of the Wilson coefficient C_9^{μ} seems to provide a coherent answer favoured by the current results (see for example Refs. [25,26]).

5 Conclusions

Heavy flavour physics plays a major role in our understanding of the fundamental questions in particle physics. Several decades of B factory measurements and recently also the LHC experiments have provided impressive tests of the SM paradigms and parameters. More recent challenges of flavour physics are focused on finding indirect paths to New Physics, mainly through CP violating and rare decay observables. At the moment, the current experimental data do not point to new source of CP violation. On the other hand, there exist a few deviations with the SM predictions in the semi-leptonic rare decays, although not significant enough to be conclusive yet. The impressive progress in the theoretical calculations and lattice results in the recent years have been crucial in this context. The next runs of the LHC and a future high luminosity B factory are likely to provide more insight to settle the current discrepancies or point to New Physics phenomena.

Acknowledgments

The author is grateful to the organisers of Moriond QCD 2015 for the fruitful conference and for their invitation, and acknowledges partial support from Institut Universitaire de France.

References

1. CKMfitter, `http://ckmfitter.in2p3.fr/www/results/plots_ckm14/ckm_res_ckm14.html`
2. A. G. Akeroyd and F. Mahmoudi, *JHEP* **1010**, 038 (2010) [arXiv:1007.2757 [hep-ph]].
3. P. Urquijo, arXiv:1305.1234 [hep-ex].
4. R. Aaij *et al.* [LHCb Collaboration], arXiv:1503.07089 [hep-ex].
5. K. A. Olive *et al.* [Particle Data Group Collaboration], *Chin. Phys.* C **38**, 090001 (2014).
6. R. Aaij *et al.* [LHCb Collaboration], arXiv:1504.01568 [hep-ex].
7. W. Detmold, C. Lehner and S. Meinel, arXiv:1503.01421 [hep-lat].
8. R. Aaij *et al.* [LHCb Collaboration], *Phys. Lett.* B **728**, 607 (2014) [arXiv:1308.1048 [hep-ex]].
9. R. Aaij *et al.* [LHCb Collaboration], *Phys. Rev. Lett.* **114**, 041601 (2015) [arXiv:1409.8586 [hep-ex]].
10. Y. Amhis *et al.* [Heavy Flavor Averaging Group (HFAG) Collaboration], arXiv:1412.7515 [hep-ex].
11. A. Lenz and U. Nierste, arXiv:1102.4274 [hep-ph].
12. V. M. Abazov *et al.* [D0 Collaboration], *Phys. Rev. Lett.* **110**, 011801 (2013) [arXiv:1207.1769 [hep-ex]].
13. A. J. Buras, hep-ph/9806471.
14. F. Mahmoudi, *Comput. Phys. Commun.* **178**, 745 (2008) [arXiv:0710.2067 [hep-ph]]; *Comput. Phys. Commun.* **180**, 1579 (2009) [arXiv:0808.3144 [hep-ph]].
15. T. Hermann, M. Misiak and M. Steinhauser, *JHEP* **1312**, 097 (2013) [arXiv:1311.1347 [hep-ph]].
16. C. Bobeth, M. Gorbahn and E. Stamou, *Phys. Rev.* D **89**, 034023 (2014) [arXiv:1311.1348 [hep-ph]].
17. V. Khachatryan *et al.* [CMS and LHCb Collaborations], *Nature* **522**, 68 (2015) [arXiv:1411.4413 [hep-ex]].
18. A. Arbey, M. Battaglia, F. Mahmoudi and D. Martinez Santos, *Phys. Rev.* D **87**, 035026 (2013) [arXiv:1212.4887 [hep-ph]].
19. S. Descotes-Genon, J. Matias, M. Ramon and J. Virto, *JHEP* **1301**, 048 (2013) [arXiv:1207.2753 [hep-ph]].
20. LHCb Collaboration, LHCb-CONF-2015-002.
21. S. Descotes-Genon, L. Hofer, J. Matias and J. Virto, *JHEP* **1412**, 125 (2014) [arXiv:1407.8526 [hep-ph]].
22. G. Hiller and F. Kruger, *Phys. Rev.* D **69**, 074020 (2004) [hep-ph/0310219].
23. R. Aaij *et al.* [LHCb Collaboration], *Phys. Rev. Lett.* **113**, 151601 (2014) [arXiv:1406.6482 [hep-ex]].
24. T. Hurth, F. Mahmoudi and S. Neshatpour, *JHEP* **1412**, 053 (2014) [arXiv:1410.4545 [hep-ph]].
25. S. Descotes-Genon, J. Matias and J. Virto, *Phys. Rev.* D **88**, 074002 (2013) [arXiv:1307.5683 [hep-ph]].
26. G. Hiller and M. Schmaltz, *Phys. Rev.* D **90**, 054014 (2014) [arXiv:1408.1627 [hep-ph]].

Recent Heavy Flavor Physics Results from the Tevatron

Donatella Lucchesi on behalf of CDF and D0 Collaborations
Department of Physics and Astronomy and INFN, via Marzolo 8, 35131 Padova, Italy

The CDF and D0 experiments are continuing to analyze data collected at the Tevatron collider until 2011 with results on heavy flavor physics that exceed expectations. The study of CP violation in the charm system and the newest determinations of the forward-backward asymmetry in the b-hadron production are presented.

1 Introduction

Hadrons with b and c quarks were copiously produced at the $\sqrt(s) = 1.96$ TeV proton anti-proton Tevatron collider at Fermilab but since the inelastic cross section is a factor $10^3 - 10^4$ larger, detectors and online selections had to be optimized in order to identify and to reconstruct them. Detectors had to have a very good tracking and vertex resolution, a wide acceptance and good particle identification for electrons and muons, with in addition a highly selective trigger. The complete description of the CDF and D0 detectors can be found elsewhere [1].

2 CP Violation in Charm decay

To date, CP violation has been established in transitions of strange and bottom hadrons, studies in the interactions of charm quarks have shown no experimental evidence. Charm transitions are complementary to the processes involving K and B mesons, therefore measurements of CP violation in charm probe non Standard Model (SM) physics through charged-current couplings [2].

2.1 Direct CP violation in $D^+ \to K^-\pi^+\pi^+$ decay

The direct CP violation parameter in the Cabibbo-favored decay $D^+ \to K^-\pi^+\pi^+$ and charge conjugate, is defined as

$$A_{CP}(D^+ \to K^-\pi^+\pi^+) = \frac{\Gamma(D^+ \to K^-\pi^+\pi^+) - \Gamma(D^- \to K^+\pi^-\pi^-)}{\Gamma(D^+ \to K^-\pi^+\pi^+) + \Gamma(D^- \to K^+\pi^-\pi^-)}.$$

Experimentally, the A_{CP} is determined by measuring a raw charge asymmetry and by applying corrections to account for differences in the detection of the final state particles and in the production rates of D^+ and D^- mesons. D0 reconstructs D candidates in a sample of single muon and dimuon triggered events from all possible three-track combinations consistent with coming from a common vertex, significantly displaced respect to the primary vertex. The signal is separated from the background by using a log-likelihood ratio method that combines twelve individual variables into a single multivariate discriminant. The signal distributions are modeled using Monte Carlo simulation while the background shapes are taken from data using 1% of them chosen by randomly sampling the D candidates. The final result is [3]

$$A_{CP}(D^+ \to K^-\pi^+\pi^+) = [0.16 \pm 0.15(stat.) \pm 0.09(syst.)]\%.$$

2.2 Indirect CP violation in $D^0 \to K^-K^+$ and $D^0 \to \pi^-\pi^+$ decay

Decay-time-dependent rate asymmetries, $A_{CP}(t)$, of Cabibbo suppressed decays into CP eigenstates, such as $D^0 \to K^+K^-$ and $D^0 \to \pi^+\pi^-$ process for D^0 and $\bar{D^0}$ mesons, are among the most sensitive probes for CP violation in the charm sector [4]. The asymmetry receives contributions from any difference between D^0 and $\bar{D^0}$ decay amplitudes (direct CP violation) and from the oscillation probabilities between charm and anticharm mesons or interference between decays that follow, or not, an oscillation (indirect CP violation). Because of the slow D^0 mixing rate, $A_{CP}(t)$ ca be approximated to the first order as [5]

$$A_{CP}(t) \approx A_{CP}^{dir} - \frac{\langle t \rangle}{\tau} A_\Gamma \tag{1}$$

where $\langle t \rangle$ is the mean of the decay time and τ the CP averaged D^0 lifetime. A_{CP}^{dir} is the direct CP violation contribution that depends on the decay mode, while A_Γ is mostly due to indirect CP violation. D^0 candidates are reconstructed in the full dataset collected by CDF with the trigger on the hadronic decay of heavy flavor hadrons. D^0 are requested to come from the strong decay $D^{*+} \to D^0\pi^+$ and $D^{*-} \to \bar{D^0}\pi^-$ in order to identify the the initial D flavor through the charge of the low-momentum π meson. Data are divided in samples according to the initial flavor and the decay time, determined from the decay length of the D meson. In each sample the number of D^0 and $\bar{D^0}$ is obtained by fitting the invariant mass distribution and then used to construct the asymmetry. The equation 1 is finally used to measure [6]:

$$A_\Gamma(\pi^+\pi^-) = (-0.1 \pm 1.8(stat.) \pm 0.3(syst.)) \times 10^{-3},$$

$$A_\Gamma(K^+K^-) = (-1.9 \pm 1.5(stat.) \pm 0.4(syst.)) \times 10^{-3}$$

that combined give: $A_\Gamma = (-1.2 \pm 1.2) \times 10^{-3}$.

3 b-hadron Forward-Backward asymmetry

The study of forward-backward asymmetry, A_{FB}, in quark pair production has become very important since CDF has shown a discrepancy of the order of 3σ between the Standard Model expectations and the measured $t\bar{t}$ quark pair production [7]. The study of A_{FB} in $b\bar{b}$ quark pair production can help in understanding the origin of the asymmetry. In the SM $b\bar{b}$ quark production proceeds through the strong interactions $q\bar{q} \to b\bar{b}$ and $gg \to b\bar{b}$ neither of which contribute to A_{FB} in the leading-order but high order corrections can result in an asymmetry through the interference of initial-state and final-state radiative gluon diagrams, box diagram with the Born one and different amplitudes in flavor excitation of $q + g$ processes; there is also some contribution from the electro-weak production processes $q\bar{q} \to Z/\gamma^* \to b\bar{b}$. At the Tevatron $b\bar{b}$ production is dominated by the gluon fusion process which does not contribute to A_{FB}, therefore, when the full cross section is considered, the integrated asymmetry predicted by the SM is small.

3.1 Forward-backward asymmetry in Λ_b^0 baryon production

D0 studies the forward-backward production asymmetry of Λ_b^0 and $\bar{\Lambda}_b^0$ barions using the fully reconstructed decay chain $\Lambda_b^0 \to J/\psi\Lambda$, $J/\psi \to \mu^+\mu^-$, $\Lambda \to p\pi^-$ and its charge conjugate. The positive z-axis is chosen to be in the direction of the proton beam and therefore the forward direction corresponds to a Λ_b^0 particle emitted with $y > 0$ or a $\bar{\Lambda}_b^0$ particle emitted at $y < 0$ where the rapidity $y = ln((E + p_z)/(E - p_z))/2$. Candidate events are collected via the muon trigger by requiring a pair of oppositely charged muons with an invariant mass compatible with coming from a J/ψ. To form Λ_b^0 and $\bar{\Lambda}_b^0$ the J/ψ is combined with a Λ and $\bar{\Lambda}$ baryon candidate. The forward and backward production cross sections, $\sigma(F)$ and $\sigma(B)$, are extracted from fits to the invariant mass distributions of forward and backward candidates in four rapidity bins in the range $0.1 < |y| < 2$, rejecting the region $|y| < 0.1$ where the asymmetry may be diluted by forward-backward migration due to the finite y resolution. The rates are then used to calculate the asymmetry $A = (\sigma(F) - \sigma(B))/(\sigma(F) + \sigma(B))$ and the ratio, $R = \sigma(B)/\sigma(F)$ as function of the rapidity. The results are shown in figure 1 together with those from LHC. Data show a tendency of forward particles to be emitted at larger values of rapidity than their backward counterparts.

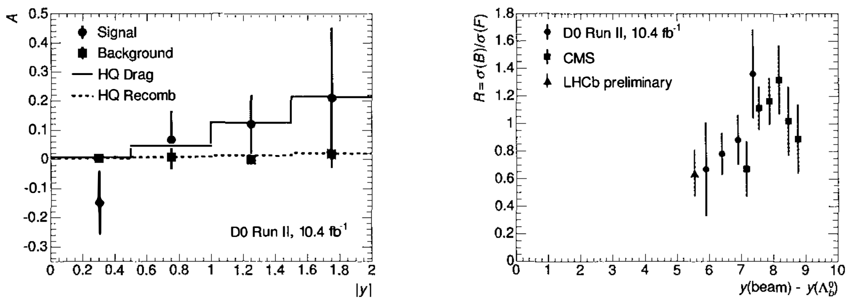

Figure 1 – Left: Measured A_{FB} versus rapidity $|y|$ compared to predictions obtained with two different models [8]. Right: Measured ratio of the backward to forward production cross section versus rapidity loss compared to those obtained by CMS and LHCb.

3.2 Forward-backward asymmetry in $b\bar{b}$ quark production

CDF has measured the forward-backward asymmetry in $b\bar{b}$ quark production in the high and low $b\bar{b}$ quark invariant mass. Several theorists have computed the SM prediction for $A_{FB}(b\bar{b})$ with different results, the most comprehensive calculations [9] have been tuned to match CDF analysis cuts.

Data collected with an inclusive jet trigger with energy thresholds at $E_T > 50, 70$, and $100GeV/c^2$ have been used to measure the asymmetry for $M_{b\bar{b}} > 150GeV/c^2$. Jets with b quark are identified by requiring a secondary vertex. The flavor of the b is determined by evaluating the charge of the jet calculated as the sum of the charge of the jet tracks averaged over the momentum. The sample composition in terms of b, c, and light quarks is obtained by fitting the tag mass, defined as the invariant mass of the tracks belonging to the secondary vertex using templates for the shape of each component obtained from Monte Carlo simulation and from data for light quarks. The measurement is corrected for the detector acceptance and mismeasurements, of which the most important is the jet energy that affects the dijet mass. To estimate the asymmetry at the hadron-jet level a Bayesian calculation is performed by using a model which includes, among the others, background distributions, the invariant mass resolution and the jet charge ambiguity. In figure 2 (left) is shown the the highest-probability-density credible intervals at 68% and 95% credibility for A_{FB} in each hadron-jet-level mass bin. The results are consistent with zero and with the predictions [9]. Axigluons with a mass of $200GeV/c^2$ are excluded but not the heavier one at $345GeV/c^2$.

The low $b\bar{b}$-jets invariant mass measurement is performed on the muon triggered data sample. The muon track has to be inside one of the two jets with $E_T > 20GeV/c$ with the second jet back

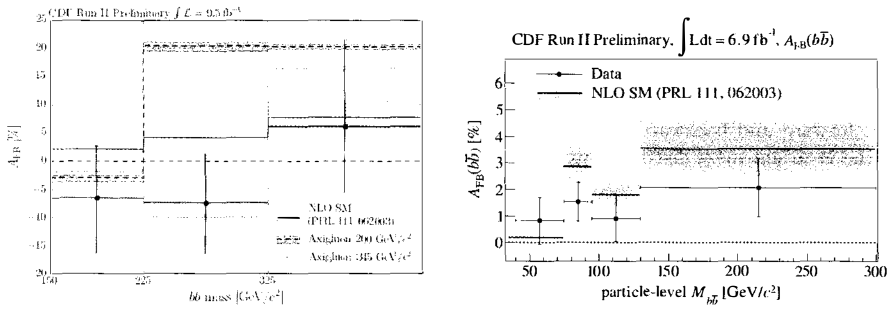

Figure 2 – Left: Measured A_{FB} as function of high $b\bar{b}$-jets invariant mass, the error bars represent the 68% credible intervals. Right: Measured A_{FB} as a function of particle-level low $M_{b\bar{b}}$.

to back to muon one. In addition to that both jets have to be identified as b jets by requiring a secondary vertex. The flavor of the b-jets is evaluated by using the charge of the muon after the correction for the $B^0 - \bar{B}^0$ mixing and the cascade decay $b \to c \to \mu$. The fraction of b quark on the muon jets is obtained by fitting the $P_{T,rel}$, the distribution of muon momentum with respect to the jet axis, while on the other jet the tag invariant mass is used. The $b\bar{b}$ fraction in each di-jets bin is evaluated by computing the average b fraction between its lowest and highest value. In order to extract A_{FB} at particle level the background is subtracted from the measured distributions and the acceptance of the CDF detector is taken into account using Monte Carlo simulation. The measured particle-level distribution, figure 2 (right), shows a tendency of the A_{FB} to increase with $M_{b\bar{b}}$ with a spike around Z pole mass similar to the theoretical prediction. The measured integrated asymmetry of $(1.2 \pm 0.7)\%$ is consistent with the prediction.

4 Conclusions

CDF and D0 have demonstrated unique capabilities for studying heavy flavor physics. No CP violation in the charm sector has been revealed. The study of $A_{FB}(b\bar{b})$ has ruled out an axigluon of mass 200 GeV/c^2 and shows a good agreement between theory and data.

References

1. D. Acosta et al. [CDF Collaboration], Phys. Rev. D 71, 032001 (2005); V. M. Abazov et al. [D0 Collaboration], Nucl. Instrum. Methods Phys. Res. A 565, 463 (2006).
2. S. Bianco, F.L. Fabbri, D. Benson, and I.I. Bigi, Riv. Nuovo Cim. 26N7, 1 (2003); G. Burdman and I. Shipsey, Annu. Rev. Nucl. Part. Sci. 53, 431 (2003); I. Shipsey, Int. J. Mod. Phys. A 21, 5381 (2006); M. Artuso, B. Meadows, and A.A. Petrov, Annu. Rev. Nucl. Part. Sci. 58, 249 (2008).
3. V. M. Abazov et al. [D0 Collaboration], Phys. Rev. D 90, 111102(R) (2014).
4. M. Golden and B. Grinstein, Phys. Lett. B 222, 501 (1989); A. Le Yaouanc, L. Oliver, and J.C. Raynal, Phys. Lett. B 292, 353 (1992); F. Buccella, M. Lusignoli, G. Miele, A. Pugliese, and P. Santorelli, Phys. Rev. D 51, 3478 (1995).
5. T. Aaltonen et al. [CDF Collaboration], Phys. Rev. D85, 012009 (2012).
6. T. Aaltonen et al. [CDF Collaboration], PRD-RC 90, 111103 (2014).
7. T. Aaltonen et al. [CDF Collaboration], Phys. Rev. D 87, 092002 (2013).
8. V.M. Abazov et al. [D0 Collaboration] Phys. Rev. D 91, 072008 2015.
9. B. Grinstein and C. W. Murphy, Phys.Rev.Lett. 111, 062003 (2013).

Measurements of Heavy Flavour Production at ATLAS and CMS

Leonid Gladilin (on behalf of the ATLAS and CMS Collaborations)
Lomonosov Moscow State University Skobeltsyn Institute of Nuclear Physics (SINP MSU), Moscow 119991, Russian Federation

Results of the ATLAS and CMS experiments on heavy flavour production at LHC, released or updated after the previous Moriond conference, are reviewed.

1 Introduction

Measurements of the non-prompt (from b-hadron decays) production of charmonium states probe production and hadronisation of b quarks, and decays of b-hadrons. Measurements of the bottomonium and prompt charmonium production probe a heavy quark pair production and its subsequent evolution into a bound state. The latter includes non-perturbative effects and can be described with colour-singlet (CS) and colour-octet (CO) contributions in the framework of non-relativistic QCD (NRQCD). In this framework, the non-perturbative evolution is described with long-distance matrix elements (LDME) tuned to experimental results. Associated production of a quarkonium and, e.g., another quarkonium or a gauge boson is potentially sensitive to the double parton scattering (DPS) contribution. Recent results on heavy quarkonium production obtained with the ATLAS [1] and CMS [2] detectors at the LHC are described in this note.

2 Recent results

The double-differential cross sections of the $J/\psi \to \mu^+\mu^-$ and $\psi(2S) \to \mu^+\mu^-$ mesons promptly produced in pp collisions at $\sqrt{s} = 7\,\mathrm{TeV}$ have been presented by CMS [3] as a function of transverse momentum, p_{T}, up to or beyond $p_{\mathrm{T}} = 100$ GeV in four rapidity, y, bins, as well as integrated over the $|y| < 1.2$. Figure 1 (left) compares the $\psi(2S)$ cross sections with the NRQCD calculation [4] with LDMEs tuned to lower-p_{T} LHC data. The prompt and non-prompt production cross-sections of the $\psi(2S) \to J/\psi\pi^+\pi^-$ production have been measured by ATLAS [5] in the rapidity range $|y| < 2.0$ for transverse momenta between 10 and 100 GeV. Figure 1 (right) compares the prompt $\psi(2S)$ production cross sections for three rapidity intervals with theoretical predictions. The next-to-leading-order (NLO) NRQCD predictions [6] describe the data satisfactorily across the full range of transverse momentum studied. Predictions from the colour evaporation model [7] are able to describe all but the the highest p_{T} region, where the production rates are significantly overestimated. The partial next-to-next-to-leading-order (NNLO*) colour-singlet calculations [8], in contrast, undershoot the data by an order of magnitude at the highest p_{T} studied. Predictions of the k_{T}-factorisation model [9] exhibit a softer p_{T} spectrum than observed and clearly undershoot the data in overall rate.

Figure 2 compares the non-prompt $\psi(2S)$ and $\chi_{c1/2}$ [10] production cross sections with theoretical predictions. In non-prompt $\psi(2S)$ production, both NLO general-mass variable-flavour-number scheme (GM-VFNS) calculations [11] and fixed-order next-to-leading-logarithm (FONLL) calculations [12] describe the data well, but a tendency is observed for the theory to predict a slightly harder

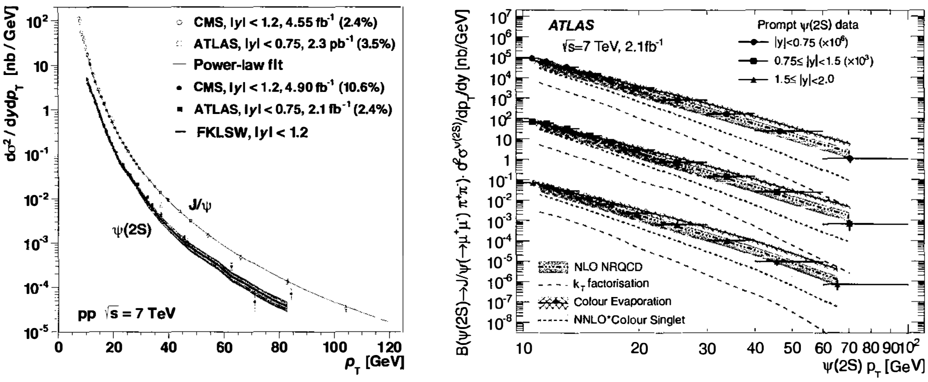

Figure 1 – Measured differential cross sections for prompt J/ψ and $\psi(2S)$ production as a function of p_{T}. Left: J/ψ and $\psi(2S)$ production cross sections integrated in the range $|y| < 1.2$ [3]. Right: $\psi(2S)$ production cross sections for three rapidity intervals [5]. The measured cross sections are compared with theoretical predictions.

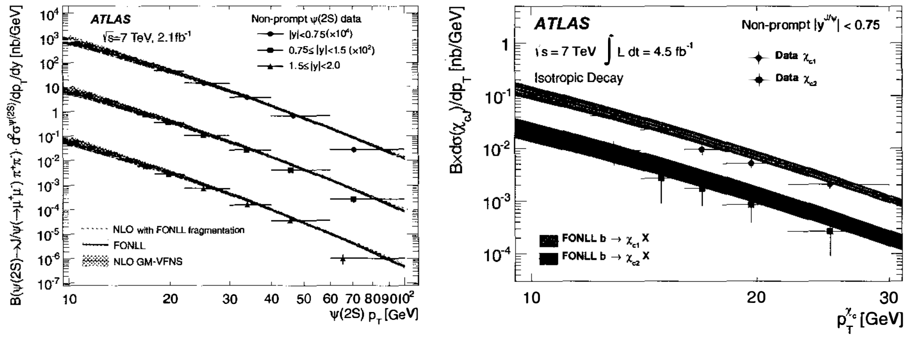

Figure 2 – Measured differential cross sections for non-prompt $\psi(2S)$ (left) [5] and χ_c (right) [10] production as a function of p_{T}. The measured cross sections are compared with theoretical predictions.

p_{T} spectrum than is measured in data. The measurements of non-prompt χ_c production generally agree well with predictions based upon the FONLL approach.

Measurements of the differential production cross sections as a function of p_T for the $\Upsilon(1S)$, $\Upsilon(2S)$, and $\Upsilon(3S)$ states in pp collisions at $\sqrt{s} = 7\,\mathrm{TeV}$ have been presented by CMS [13]. Figure 3 (left) compares the Υ production cross sections with the NLO NRQCD predictions [14]. The calculations describe the trends of the data for all three $\Upsilon(nS)$ states, including the feature that the $\Upsilon(3S)$ p_{T} spectrum is harder than those of the two lower-mass states. The production cross section ratio $\sigma(\chi_{b2}(1P))/\sigma(\chi_{b1}(1P))$ has been measured by CMS [15] by detecting the radiative decays to an $\Upsilon(1S)$ and a photon. Figure 3 (right) compares the measured cross section ratio, as a function of $p_{\mathrm{T}}^{\Upsilon}$, with a theoretical calculation based on the experimental $\sigma(\chi_{c2})/\sigma(\chi_{c1})$ cross section ratio extrapolated using NRQCD scaling rules [16]. The prediction is not fully consistent with the measurements.

A signal yield of 446 ± 23 events for the production of prompt J/ψ meson pairs has been observed by CMS[17] in pp collisions at $\sqrt{s} = 7\,\mathrm{TeV}$ using an integrated luminosity of about $4.7\,\mathrm{fb}^{-1}$. Differential cross sections have been obtained in bins of the J/ψ pair invariant mass (Fig. 4 (left)), the absolute rapidity difference between the two J/ψ mesons (Fig. 4 (right)), and the J/ψ pair transverse momentum. There is no evidence for the η_b resonance in the J/ψ pair invariant-

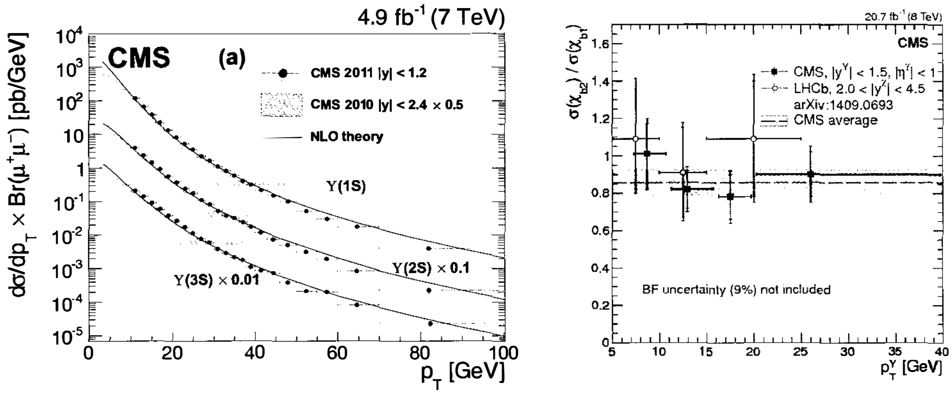

Figure 3 – Left: Measured differential cross sections for Υ production times di-muon branching fractions as a function of p_T [13]. The $\Upsilon(2S)$ and $\Upsilon(3S)$ measurements are scaled by 0.1 and 0.01, respectively, for display purposes. Right: The ratio of the χ_{b2} and χ_{b1} production cross sections as a function of $p_T(\Upsilon)$ [15]. The measurements are compared with theoretical predictions.

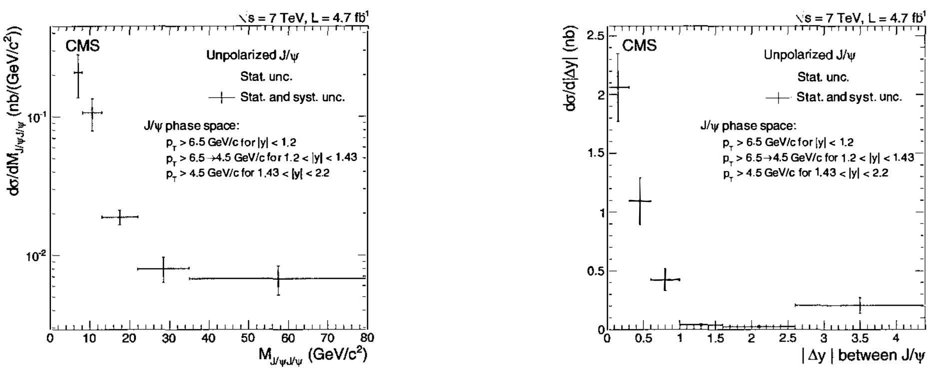

Figure 4 – Differential cross sections for prompt double J/ψ production as a function of the double J/ψ invariant mass (left) [17] and a function of the absolute rapidity difference between J/ψ mesons (right) [17]. The gray boxes represent statistical errors only, and the error bars represent statistical and systematic errors added in quadrature.

mass distribution above the background expectations derived from the η_b sideband regions. The differential cross section decreases rapidly as a function of $|\Delta y|$. However, a non-zero value is measured in the $|\Delta y|$ bin between 2.6 and 4.4, where the DPS contribution is expected to dominate.

The first observation and measurement of both associated Z + prompt J/ψ and Z + non-prompt J/ψ production has been performed by ATLAS [18] using $20.3\,\mathrm{fb}^{-1}$ of data collected in pp collisions at $\sqrt{s} = 8\,\mathrm{TeV}$. Production of a $J/\psi \to \mu^+\mu^-$ meson in association with a Z boson occurs approximately twice per million Z bosons. Measurements of the azimuthal angle between the Z boson and J/ψ meson (Fig. 5 (left)) suggest that both single-parton scattering and DPS contributions may be present in the data. The measured Z + prompt J/ψ production rates are compared (Fig. 5 (right)) to the leading order (LO) CS predictions [19] and to the NLO NRQCD predictions [20] for CS and CO prompt production processes. A higher production rate is predicted through colour-octet transitions than through colour-singlet processes, but the expected production rate from the sum of singlet and octet contributions falls approximately an order of magnitude short of the data.

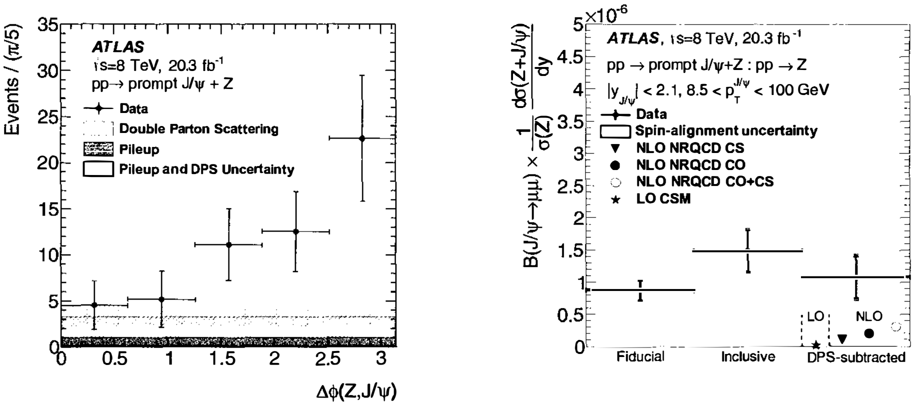

Figure 5 – Left: Azimuthal angle between the Z boson and the J/ψ meson for the prompt J/ψ production [18]. Right: Production cross-sections ratios of J/ψ in association with a Z boson, relative to inclusive Z production, for prompt J/ψ production [18]. The first point indicates the total integrated cross-section ratio measured in the defined fiducial volume, the second point shows the same quantity corrected for detector acceptance effects on the J/ψ reconstruction, and the third point illustrates the corrected cross-section ratio after subtraction of the double parton scattering contribution.

Acknowledgments

Participation in the conference was partly supported by the Russian Foundation for Basic Research, grant 15-02-08133.

References

1. ATLAS Collaboration, JINST 3 (2008) S08003.
2. CMS Collaboration, JINST 3 (2008) S08004.
3. CMS Collaboration, arXiv:1502.04155.
4. P. Faccioli et al., *Phys. Lett.* B **736**, 98 (2014), arXiv:1403.3970.
5. ATLAS Collaboration, *JHEP* **09**, 079 (2014), arXiv:1407.5532.
6. Y.-Q. Ma, K. Wang, K.-T. Chao, *Phys. Rev. Lett.* **106**, 042002 (2011), arXiv:1009.3655.
7. A. D. Frawley, T. Ullrich, R. Vogt, *Phys. Rept.* **462**, 125 (2008), arXiv:0806.1013.
8. J. Lansberg, *Eur. Phys. J.* C **61**, 693 (2009), arXiv:0811.4005.
9. S. Baranov, A. Lipatov, N. Zotov, *Phys. Rev.* D **85**, 014034 (2012), arXiv:1108.2856.
10. ATLAS Collaboration, *JHEP* **07**, 154 (2014), arXiv:1404.7035.
11. P. Bolzoni, B. A. Kniehl, G. Kramer, *Phys. Rev.* D **88**, 074035 (2013), arXiv:1309.3389.
12. M. Cacciari et al., *JHEP* **10**, 137 (2012), arXiv:1205.6344.
13. CMS Collaboration, arXiv:1501.07750.
14. B. Gong et al., *Phys. Rev. Lett.* **112**, 032001 (2014), arXiv:1305.0748.
15. CMS Collaboration, *Phys. Lett.* B **743**, 383 (2015), arXiv:1409.5761.
16. A. K. Likhoded, A. V. Luchinsky, S. V. Poslavsky, *Phys. Rev.* D **90**, 074021 (2014), arXiv:1409.0693.
17. CMS Collaboration, *JHEP* **09**, 094 (2014), arXiv:1406.0484.
18. ATLAS Collaboration, arXiv:1412.6428.
19. B. Gong et al., *JHEP* **03**, 115 (2013), arXiv:1210.2430.
20. S. Mao et al., *JHEP* **02**, 071 (2011), arXiv:1102.0398.

MEASUREMENT OF *CP*-VIOLATING PHASES IN B DECAYS AT LHCb

NAZIM HUSSAIN
On behalf of the LHCb Collaboration
Department of Physics, University of Oxford
Denys Wilkinson Building, Keble Road, Oxford, OX1 3RH, United Kingdom

A selection of recent LHCb results pertaining to measurements of the CKM unitarity triangle are presented. In these proceedings, I summarise a measurement of $\sin(2\beta)$, the most precise time-dependent *CP* violation measurement made at a hadron collider yet, as well as the latest LHCb γ combination, a measurement of greater precision than the B factories. Newly studied decays of the form $B^{\pm} \to [hh\pi^0]_D h^{\pm}$ that offer additional sensitivity to γ are also presented.

1 Introduction

The LHCb experiment has been instrumental in the study of *CP* violation. In the Standard Model, *CP* violation may manifest itself in three ways: in decays, in mixing and in the interference between mixing and decay. At LHCb, all three have been studied in B hadrons, emphasising the importance of B decays in measurements of *CP* violation.

In the CKM unitarity triangle, the angle β is defined as $\arg(-V_{cd}V_{cb}^*/V_{td}V_{tb}^*)$ and γ as $\arg(-V_{ud}V_{ub}^*/V_{cd}V_{cb}^*)$. Recent measurements of $\sin(2\beta)$ [1] are in disagreement with the average of direct measurements. Thus, further experimental study is required to understand these tensions. With regards to γ, it is the only angle of the CKM triangle that can be measured directly using tree-level decays. Hence, complementary measurements between tree and loop level processes can be used as tests for new physics. For such tests to be meaningful, though, experimental precision on direct γ measurements needs to be improved.

These proceedings will discuss some new results from LHCb pertaining to $\sin(2\beta)$, γ and their associated *CP* observables.

2 Measurement of *CP* violation in $B^0 \to J/\psi K_S^0$

Both a B^0 and a $\overline{B}^0$ can decay to the $J/\psi K_S^0$ final state. The interference between these decay amplitudes from direct decay and from decay after $\overline{B}^0$–B^0 mixing result in a time-dependent asymmetry that can be expressed as

$$\mathcal{A}(t) = \frac{S\sin(\Delta m t) - C\cos(\Delta m t)}{\cosh(\frac{\Delta\Gamma t}{2}) + A_{\Delta\Gamma}\sinh(\frac{\Delta\Gamma t}{2})}. \tag{1}$$

In this expression, Δm and $\Delta\Gamma$ are the mass and decay width differences between the mass eigenstates of the $\overline{B}^0$–B^0 system, while S, C and $A_{\Delta\Gamma}$ are *CP* observables. For this system, $\Delta\Gamma$ is negligible and thus the expression simplifies to only the numerator. In the dominant transition $b \to \bar{c}s$, *CP* violation in decay is expected to be negligible. This allows a measurement of S which is related to β via the relation $S = \sin(2\beta)$.

This measurement of CP violation using the $B^0 \to J/\psi K^0_S$ decay channel[2] uses 3 fb^{-1} of pp collision data from LHCb. This is an update to a 1 fb^{-1} analysis[3], however in addition to using the larger available data set, there is also use of an improved tagging procedure for distinguishing between B^0 and $\overline{B}^0$ candidates, in particular by exploiting an additional tagging algorithm. This same-side pion tagger (SSπ) determines the flavour content of the B meson by examining the charge of the pions produced in the fragmentation associated to the signal candidate production or in decays of excited B mesons to signal B mesons. The SSπ tagger supplements the opposite-side tagger (OS) used previously, where the B meson quark content is determined by using the charge of an electron or muon produced from semileptonic B decays, the charge of the kaon from the decay chain $b \to c \to s$, and the charge of the particles associated to the secondary vertex of the non-signal B meson decay. The improvement to tagging methods leads to an increased tagging power of greater than 25% compared to the previous LHCb measurement.

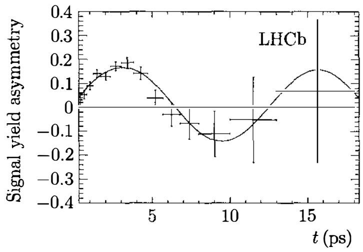

Figure 1 – The time-dependent $\overline{B}^0$–B^0 asymmetry. The binned signal yield asymmetry is shown in black and the curve is the fit projection of the PDF.

A multidimensional probability density function (PDF) is constructed using, among other variables, the reconstructed B meson mass, the decay time and tagging related observables. An unbinned fit to data is performed with this PDF (binned asymmetries are presented in Fig. 1) and the CP observables S and C are extracted and measured to be

$$S = 0.731 \pm 0.035\ (\mathrm{stat}) \pm 0.020\ (\mathrm{syst}), \quad C = -0.038 \pm 0.032\ (\mathrm{stat}) \pm 0.005\ (\mathrm{syst}). \tag{2}$$

When C is fixed to 0, the measurement of $\sin(2\beta)$ yields 0.746 ± 0.030 (stat). This result is the most precise time-dependent CP violation measurement made at a hadron collider to date.

3 LHCb γ Combination

The LHCb experiment has studied a variety of B decay channels with sensitivity to the CKM angle γ. A more precise measurement of γ can be achieved through the combination of these results. The decay channels considered in this combination[4] are: $B^\pm \to [hh]_D h^\pm$[5], $B^\pm \to [K\pi\pi\pi]_D h^\pm$[6], $B^\pm \to [K^0_S hh]_D K^\pm$[7], $B^\pm \to [K^0_S K\pi]_D K^\pm$[8], $B^0 \to [hh]_D K^{*0}$[9] and $B^0_s \to D_s^\mp K^\pm$[10], where h is either a kaon or a pion.

The combination is performed for the $B \to DK$ decay modes using a frequentist approach. In addition to the effects of D^0–$\overline{D}^0$ mixing, possible contributions from CP violation in the D^0 system (at first order) are considered as well. The results of the combination are presented in Fig. 2. The best-fit value of γ is found to be 72.9° and at the 68% confidence level (CL), γ is measured to be

$$\gamma = \left(73^{+9}_{-10}\right)^\circ . \tag{3}$$

This measurement is of greater precision than comparable legacy measurements made by the B factories.

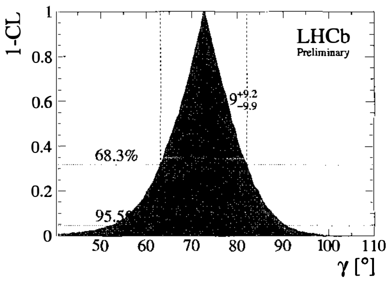

Figure 2 – Confidence level (CL) curve for the γ combination. The 1σ and 2σ CL bounds are indicated.

4 *CP* Violation in $B^{\pm} \to [hh\pi^0]_D h^{\pm}$ Decays

One of the ways in which LHCb is looking to improve its γ combination measurement is through the inclusion of new B decay modes. This analysis [11] is the first time the ADS [12,13] decays of the form $B^{\pm} \to [K\pi\pi^0]_D h^{\pm}$ and the quasi-GLW decays $B^{\pm} \to [\pi\pi\pi^0]_D h^{\pm}$, $B^{\pm} \to [KK\pi^0]_D h^{\pm}$ have been studied at LHCb. The $B^{\pm} \to [KK\pi^0]_D h^{\pm}$ final state has not previously been studied elsewhere.

In order to extract the *CP* observables, the $D \to K^+\pi^-\pi^0$ coherence factor and average strong-phase difference measured at CLEO-c [16] are taken as external inputs. Similarly, the $D \to \pi^+\pi^-\pi^0$ and $D \to K^+K^-\pi^0$ *CP* fractions [17] are also used.

The *CP* observables $R^{K\pi\pi^0}_{\mathrm{ADS(K)}}$ and $R^{K\pi\pi^0}_{\mathrm{ADS}(\pi)}$ are measured to be $0.0140 \pm 0.0047 \pm 0.0021$ and $0.00235 \pm 0.00049 \pm 0.00006$, respectively, where the first uncertainty is statistical and the second is systematic [a]. This analysis also marks the first observation of the suppressed decay $B^{\pm} \to [\pi^{\pm}K^{\mp}\pi^0]_D\pi^{\pm}$ (Fig. 3) and $B^{\pm} \to [K^+K^-\pi^0]_D\pi^{\pm}$ (Fig. 4) at the 5.3σ and greater than 10σ significance levels, respectively. First evidence of the $B^{\pm} \to [K^+K^-\pi^0]_D K^{\pm}$ decay is also seen at 4.5σ. Likelihood scans of γ with the parameters of interest r_B and δ_B, as seen in Fig. 5, place a bound of $r_B = 0.11 \pm 0.03$ at 1σ. These results will contribute to the overall precision of γ when combined with other measurements.

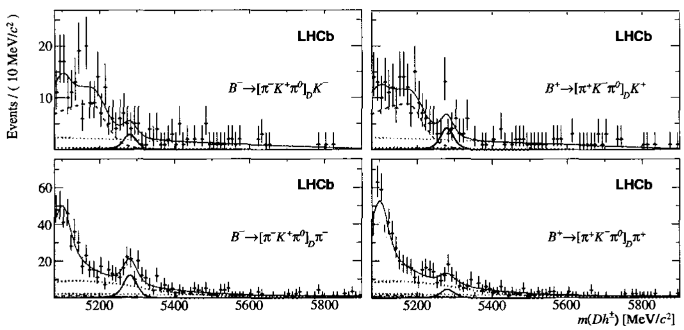

Figure 3 – Invariant mass distributions of $B^{\pm} \to [\pi^{\pm}K^{\mp}\pi^0]_D h^{\pm}$ candidates, separated by B hadron charge. $B^{\pm} \to DK^{\pm}$ ($B^{\pm} \to D\pi^{\pm}$) signal events are in the upper (lower) plots. The solid red curve represents $B^{\pm} \to DK^{\pm}$ events and the green curve represents $B^{\pm} \to D\pi^{\pm}$ events. The grey shape indicates partially reconstructed $B^{\pm}$ decays and the heavy dotted red curve indicates wrongly reconstructed D decays. The lightly dotted blue line represents the combinatorial component and the magenta line indicates contributions from partially reconstructed $B^0_s \to DK^{\mp}\pi^{\pm}$ decays where the pion is not reconstructed. The solid blue line represents the total PDF.

[a] These values have been updated since their original presentation at Moriond QCD.

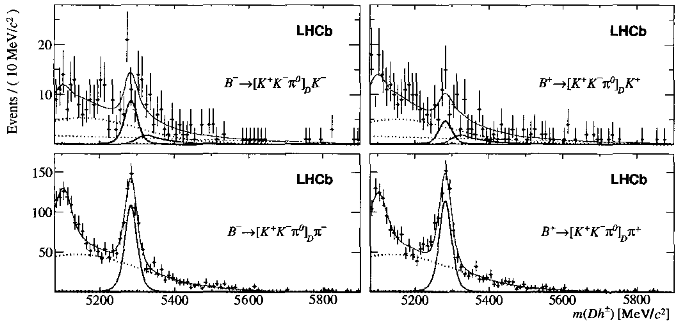

Figure 4 – Invariant mass distributions of $B^{\pm} \to [K^+K^-\pi^0]_D h^{\pm}$. The PDF descriptions are the same as in Fig. 3.

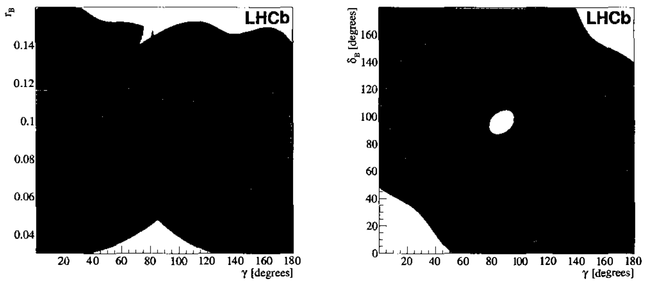

(a) Likelihood scan of r_B vs. γ.

(b) Likelihood scan of δ_B vs. γ

Figure 5 – The 1σ band is in light blue, the 2σ band is in dark blue and the 3σ band in white. The marker shows the results of the latest LHCb γ combination.

References

1. J. Charles *et al.*, arXiv:1501.0501.
2. LHCb Collaboration, R. Aaij *et al.*, arXiv:1503.07089.
3. LHCb Collaboration, R. Aaij *et al.*, *Phys. Lett.* B **721**, 24 (2013).
4. LHCb Collaboration, R. Aaij *et al.*, LHCb-CONF-2014-004.
5. LHCb Collaboration, R. Aaij *et al.*, *Phys. Lett.* B **712**, 203 (2012).
6. LHCb Collaboration, R. Aaij *et al.*, *Phys. Lett.* B **723**, 44 (2013).
7. LHCb Collaboration, R. Aaij *et al.*, *Nucl. Phys.* B **888**, 169 (2014).
8. LHCb Collaboration, R. Aaij *et al.*, *Phys. Lett.* B **733**, 36 (2014).
9. LHCb Collaboration, R. Aaij *et al.*, *Phys. Rev.* D **90**, 112002 (2014).
10. LHCb Collaboration, R. Aaij *et al.*, *JHEP* **11**, 060 (2014).
11. LHCb Collaboration, R. Aaij *et al.*, arXiv:1504.05442, submitted to *Phys. Rev.* D.
12. D. Atwood, I. Dunietz, and A. Soni, *Phys. Rev. Lett.* **78**, 3257 (1997).
13. D. Atwood, I. Dunietz, and A. Soni, *Phys. Rev.* D **63**, 036005 (2001).
14. M. Gronau and D. Wyler, *Phys. Lett.* B **265**, 172 (1991).
15. M. Gronau and D. London, *Phys. Lett.* B **253**, 483 (1991).
16. J. Libby *et al.*, *Phys. Lett.* B **731**, 197 (2014).
17. M. Nayak *et al.*, *Phys. Lett.* B **740**, 1 (2015).

Polarization study in B decays to vector meson final states

C.D. Lü[a] and Zhi-Tian Zou[b]
[a] *Institute of High Energy Physics, Chinese Academy of Sciences, Beijing 100049, China*
[a] *Department of Physics, Yantai University, Yantai 264005, China*

In the framework of perturbative QCD approach, the polarization and other observables of $B_{(s)} \to VV$ decays (V denoting vector meson) are reexamined. In order to resolve the polarization anomaly and the decay rate deficit problems, we adopt the updated distribution amplitudes of vector final states and keep the terms proportional to the $r_V^2 = m_V^2/m_B^2$ (m_V and m_B denote the masses of vector meson and B meson, respectively), especially in the denominators of penguin decay amplitudes. For most of the observables, the updated PQCD predictions are not only better than the former PQCD predictions but also in good agreement with the experimental data. The chiral enhanced penguin annihilation contribution and the hard-scattering emission contribution are the keys to interpret the polarization anomaly, such as $B \to \phi K^*$ and $B_s \to \phi\phi$ decay modes.

1 INTRODUCTION

Exclusive B_q (q=u;d;s) meson decays to vector final states have aroused a great interest for both theorists and in experiments[1,2,3,4]. These decays differ greatly from those modes involving scalar or pseudoscalar states, because the vector mesons can be produced in three polarization states. The polarization study is also interesting and important, apart from the study about branching ratios. Although, the underlying dynamics for B decays is extremely complicated, based on the naive factorization approach, a number of two-body hadronic B decays had been studied. Due to the shortcoming of this approach, for those penguin-dominant, color-suppressed decays, the predictions of branching ratios are below the current data. On the other hand, this approach can not account for the direct CP asymmetries, nor the transverse polarization fraction in penguin dominant $B_q \to VV$ decays. The perturbative QCD (PQCD) approach,[5,6] QCD factorization approach[7] and soft-collinear effective theory[8] overcome this shortcoming by including more QCD contributions in the heavy quark mass expansion.

In this letter, we reexamine the $B_q \to VV$ decays in the PQCD approach, although many of the $B_q \to VV$ decays were studied in the literature.[3,4] In the previous studies, the terms proportional to $r_V^2 = m_V^2/m_{B_q}^2$ have been omitted in the amplitudes, especially in the denominator of the propagators of virtual quarks and gluons, and transverse polarized amplitudes, which are suppressed by "r_V^2". In experimental side, more data for $B_q \to VV$ decays become available now, such as the branching fraction and the polarization fractions of $B_s \to \phi\phi$, which also call the new and updated PQCD study. After using the updated distribution amplitudes of the vector meson and keep these r_V^2 dependent terms, we bring the earlier PQCD predictions in better accord in terms of the measured observables in some problematic cases, such as the $B \to \phi K^*$ and $B_s \to \phi\phi$ decays. In the PQCD framework, penguin annihilation contribution is the key to understanding the polarization anomaly. Especially, the chirally enhanced (S-P) (S+P) penguin annihilation gives rise to large transverse polarizations. Together with the hard spectator-scattering contributions, this could help solve the transverse polarization puzzle in the penguin dominant $B_q \to VV$ decays.

2 FORMALISM

We shall revisit the $B_{(s)} \to VV$ decays in the PQCD approach, which is based on the k_T factorization[5,6,9]. The basic idea of PQCD approach is taking into account the transverse momentum k_T of valence quarks in the hadrons, and as a result, the end-point singularity in collinear factorization can be avoided. On the other hand, the transverse momentum can introduce additional energy scale which is the cause of the double logarithms in QCD correction. Fortunately, the double logarithms can be resummed through the renormalization group equation that results in the Sudakov form factor. This form factor effectively suppresses the end-point contribution of distribution amplitude of mesons in the small transverse momentum region, which makes the calculation in the PQCD approach reliable and consistent.

In hadronic $B_{(s)}$ decays, there are several typical scales, and expansions with respect to the ratios of the scales to be carried out. We can perturbatively calculate the electroweak physics higher than W boson mass scale. Using the renormalization group equation, we include the dynamics from m_W scale to m_b scale in the so-called Wilson coefficients. The physics between M_B scale and the factorization scale can be calculated perturbatively and included in the so-called Hard Kernel in the PQCD approach. The soft dynamics below the factorization scale is nonperturbative and described by the hadronic wave functions of mesons, which is universal for all decay modes. Finally, based on the factorization, the decay amplitude can be described as the following convolution of the the Wilson coefficients $C(t)$, the hard scattering kernel and the light-cone wave functions $\Phi_{M_i,(B)}$ of mesons[10],

$$\begin{aligned}\mathcal{A} \sim \quad & \int dx_1 dx_2 dx_3 b_1 db_1 b_2 db_2 b_3 db_3 \\ & \times Tr\left[C(t)\Phi_B(x_1,b_1)\Phi_{M_2}(x_2,b_2)\Phi_{M_3}(x_3,b_3)H(x_i,b_i,t)S_t(x_i)e^{-S(t)}\right], \qquad (1)\end{aligned}$$

where Tr denotes the trace over Dirac and colour indices, b_i is the conjugate variable of quark's transverse momentum k_{iT}, x_i is the momentum fractions of valence quarks and t is the largest energy scale in the hard part $H(x_i, b_i, t)$. The jet function $S_t(x_i)$ from the threshold resummation of the double logarithms $\ln^2 x_i$ smears the end-point singularities on x_i.[11] The Sudakov form factor $e^{-S(t)}$ from the resummation of the double logarithms suppresses the soft dynamics effectively i.e. the long distance contributions in the large b region[12].

3 RESULTS AND DISCUSSION

We update the PQCD computations in this work by including the improvements, such as (i) the values of the Gegenbauer moments in distribution amplitudes and the decay constants of initial and final states and (ii) the treatment of the terms which are proportional to the ratio "$r_V^2 = m_V^2/m_B^2$", especially those in the quark and gluon propagator and the transverse amplitudes. Comparing with the former PQCD computations, we find that the omitted the r_V^2 terms can change the real and imaginary parts of amplitudes to enhance the transverse contributions, which is the key to explain the polarization anomaly in $B \to K^*\phi$ and $B_s \to \phi\phi$ decays. The numerical results of these considered $B_q \to VV$ decays branching ratios, polarization fractions and other observables are displayed in ref. [13]. Here, we only list these well detected channels with our theoretical results and the experimental data in the Table 1.[13] One can notice that these decays are all penguin dominant and with large fraction of transverse polarization of order 0.5 or even bigger. In the PQCD approach, the annihilation type diagrams can be perturbatively calculated without introducing any new non-perturbative parameters, which is the key to predict the direct CP asymmetry[14] and the large transverse polarization. We find that the large transverse polarization fraction can be interpreted by the chirally enhanced annihilation transverse contributions, especially (S-P)(S+P) penguin annihilation contribution introduced by the QCD penguin operator O_6, which is not the usual current. For the (S-P)(S+P) penguin annihilation diagram, the polarization fraction satisfy

$$f_L \approx f_\parallel \approx f_\perp. \qquad (2)$$

Table 1: The updated branching ratio, percentage of longitudinal polarization f_L and transverse polarizations $f_\perp$, relative phase,$\phi_\parallel$(rad), $\phi_\perp$(rad), $\Delta\phi_\parallel(10^{-2}rad)$, $\Delta\phi_\perp(10^{-2}rad)$ and the CP asymmetry parameters A^0_{CP} and $A^\perp_{CP}$ in $B_{(s)} \to K^*\phi$,$B_s \to \phi\phi$ and $B_s \to \bar{K}^{*0}K^{*0}$ decays calculated in the PQCD approach.

Modes	$Br(10^{-6})$	$f_L(\%)$	$f_\perp$ (%)	$\phi_\parallel$	$\phi_\perp$
$B^0(K^{*0}\phi)$	$9.8^{+4.9}_{-3.8}$	$56.5^{+5.8}_{-5.9}$	$21.3^{+2.8}_{-2.9}$	$2.15^{+0.22}_{-0.19}$	$2.14^{+0.23}_{-0.19}$
Exp	9.8 ± 0.6	48 ± 3	24 ± 5	2.40 ± 0.13	2.39 ± 0.13
$B^+(K^{*+}\phi)$	$10.3^{+4.9}_{-3.8}$	$57.0^{+6.3}_{-5.9}$	$21.0^{+3.0}_{-3.0}$	$2.18^{+0.23}_{-0.19}$	$2.19^{+0.22}_{-0.20}$
Exp	10.0 ± 2.0	50 ± 5	20 ± 5	2.34 ± 0.18	2.58 ± 0.17
$B_s(\phi\phi)$	$16.7^{+8.9}_{-7.1}$	$34.7^{+8.9}_{-7.1}$	$31.6^{+3.5}_{-4.4}$	$2.01^{+0.23}_{-0.23}$	$2.00^{+0.24}_{-0.21}$
Exp	19 ± 5	34.8 ± 4.6	$36.5 \pm 4.4 \pm 2.7$	$2.71^{+0.31}_{-0.36} \pm 0.22$	
$B_s(\bar{K}^{*0}\phi)$	$0.39^{+0.20}_{-0.17}$	$50.0^{+8.1}_{-7.2}$	$24.2^{+3.6}_{-3.9}$	$1.95^{-0.21}_{-0.22}$	$1.95^{+0.21}_{-0.22}$
Exp	1.10 ± 0.29	$51 \pm 15 \pm 7$	$28 \pm 11 \pm 2$	$1.75 \pm 0.58 \pm 0.3$	
$B_s(K^{*0}\bar{K}^{*0})$	$5.4^{+3.0}_{-2.4}$	$38.3^{+12.1}_{-10.5}$	$30.0^{+5.3}_{-6.1}$	$2.12^{+0.21}_{-0.25}$	$2.15^{+0.22}_{-0.23}$
Exp	$28.1 \pm 4.6 \pm 5.6$	$31 \pm 12 \pm 4$	$38 \pm 11 \pm 4$		
	$A^{dir}_{CP}(\%)$	$A^0_{CP}(\%)$	$A^\perp_{CP}(\%)$	$\Delta\phi_\parallel$	$\Delta\phi_\perp$
$B^0(K^{*0}\phi)$	0.0	0.0	0.0	0.0	0.0
Exp		4 ± 6	-11 ± 12	11 ± 22	8 ± 22
$B^+(K^{*+}\phi)$	$-1.0^{+0.18}_{-0.26}$	$-0.60^{+0.12}_{-0.14}$	$0.75^{+0.23}_{-0.11}$	-5^{+12}_{-33}	-1
Exp	-1 ± 8	$17 \pm 11 \pm 2$	$22 \pm 24 \pm 8$	$7 \pm 20 \pm 5$	$19 \pm 20 \pm 7$
$B_s(\phi\phi)$	0.0	0.0	0.0	0.0	0.0
$B_s(\bar{K}^{*0}\phi)$	0.0	0.0	0.0	0.0	0.0
$B_s(K^{*0}\bar{K}^{*0})$	0.0	0.0	0.0	0.0	0.0

As a result, in PQCD approach, together with the hard-scattering emission diagrams, the penguin annihilation can explain the polarization anomaly measured in experiments.

Since the initial and the final state meson distribution amplitudes are the most important input parameters in the PQCD approach, our predictions of branching fractions for $B_s \to VV$ decays are similar as the predictions in ref.[4], as the distribution amplitudes we adopted here are similar to those used in ref.[4], except for the decays with ϕ meson in final states. For $B_s \to \phi\phi$ decay, the former predictions of branching ratio and polarization fraction do not agree with the data. After adopting the new distribution amplitudes and keeping the r_V^2 terms, the current predictions of all observables are in good agreement with the experimental data. Compared with other light vector mesons, the impact of r_V^2 terms is more pronounced, because the mass of ϕ is larger than other light vector mesons.

In order to quantify the r_V^2-dependent terms' influence, especially in the annihilation diagrams of penguin-dominant decay modes, we have listed the emission and annihilation type amplitudes, branching ratios, and transverse polarization fractions of the penguin-dominant $B^0 \to K^{*0}\phi$, $B_s \to \phi\phi$ decays and the tree-dominant decay $B^+ \to \rho^+\rho^0$ with and without the r_V^2 terms in Table 2.[13] One can find that for those penguin-dominant decays, the impact of the r_V^2 -dependent terms in the amplitudes of the annihilation part, as well as in the imaginary part of the emission diagrams, is numerically significant. we emphasize that the large penguin-annihilation type amplitude is the key to interpret the large transverse polarization fraction measured in experiments. When the $x_3 \to 1$ or $x_2 \to 0$, the r_V^2 -dependent term contributes a non-negligible imaginary part. As a result, for example $B_s \to \phi\phi$ decay, the branching ratios are reduced, while the transverse polarization fraction rise. On the contrary, for tree-dominant $B^+ \to \rho^+\rho^0$ decay, the impact of the r_V^2 terms on the traditional emission diagrams is tiny, as expected.

Table 2: Amplitudes (10^{-3}), branching ratios (10^{-6}) and the polarization fractions (%) with (and without) the r_V^2-dependent terms in the $B^0 \to K^{*0}\phi$, $B_s \to \phi\phi$ and $B^0 \to \rho^+\rho^0$ decays.

Modes		A^L	A^N	A^T	Br	f_L
$B^0 \to K^{*0}\phi(r_V^2)$	emission	-3.3+0.67i	-0.66+0.06i	0.64-0.05i	9.8	56
	annihilation	0.32-1.6i	-0.43+0.84i	0.42-0.83i		
$B^0 \to K^{*0}\phi$	emission	-3.0-0.09i	-0.71-0.012i	0.69+0.03i	15	70
	annihilation	-0.42-1.95i	0.05+1.28i	-0.11-1.38i		
$B_s \to \phi\phi(r_V^2)$	emission	-2.8+0.37i	-0.60+0.10i	0.60-0.08i	16.7	34.7
	annihilation	0.68-1.2i	-0.53+1.0i	0.53-1.0i		
$B_s \to \phi\phi$	emission	-2.6-0.02i	-0.64+0.03i	0.63-0.005i	26.6	45
	annihilation	-0.04-1.8i	0.18+1.8i	-0.15-1.7i		
$B^+ \to \rho^+\rho^0(r_V^2)$	emission	3.0+5.9i	0.28+0.33i	0.27-0.29i	13.5	98
	annihilation	~ 0	~ 0	~ 0		
$B^+ \to \rho^+\rho^0$	emission	2.8+5.8i	0.12+0.33i	-0.11-0.29i	13.3	99
	annihilation	~ 0	~ 0	~ 0		

4 SUMMARY

In this work, we have improved the PQCD predictions about $B_{(s)} \to VV$ decays, including the branching ratios, CP-asymmetries, and other observables, especially the polarization fractions. By adopting the new distribution amplitudes of vector mesons and keeping the r_V^2-dependent terms in the decay amplitudes especially in the transverse amplitudes, we note that, for those penguin dominant decays with polarization puzzle, our updated longitudinal polarization fractions agree well with the data, for example $B \to \phi K^*$ and $B_s \to \phi\phi$ decays. We emphasize that the (S-P)(S+P) penguin annihilation diagram is the key to interpret the polarization anomaly.

Acknowledgments

We thank A. Ali, X. Liu and Y. Li for excellent collaboration on this study. This research was supported in part by the National Science Foundation of China under the Grant Nos. 11447032, 11235005, 11375208, the Natural Science Foundation of Shandong province (ZR2014AQ013).

References

1. H. Y. Cheng and C. K. Chua, *Phys. Rev.* D **80**, 114008 (2009).
2. H. Y. Cheng and C. K. Chua, *Phys. Rev.* D **80**, 114026 (2009).
3. Y. Li and C. D. Lü, *Phys. Rev.* D **73**, 014024 (2006); H. W. Huang, C. D. Lü, T. Morii, Y. L. Shen, G. L. Song, and J. Zhu, *Phys. Rev.* D **73**, 014011 (2006); J. Zhu, Y. L Shen, and C. D. Lü, *Phys. Rev.* D **72**, 054015 (2005).
4. A. Ali, G. Kramer, Y. Li, C. D. Lü, Y. L. Shen, W. Wang, and Y. M. Wang,*Phys. Rev.* D **76**, 074018 (2007).
5. Y.Y.Keum, H. N. Li, and A. I. Sanda, *Phys. Lett.* B **504**, 6 (2001); *Phys. Rev.* D **63**, 054008 (2001).
6. C. D. Lü, K. Ukai, and M. Z. Yang, *Phys. Rev.* D **63**, 074009 (2001)
7. M. Beneke, G. Buchalla, M. Neubert and C. T. Sachrajda, Phys. Rev. Lett. 83, 1914 (1999); Nucl. Phys. B591, 313 (2000).
8. C. W. Bauer, D. Pirjol and I. W. Stewart, Phys. Rev. Lett. 87, 201806 (2001).
9. H. N. Li, Prog. Part. Phys. **51**, 85 (2003), and reference therein.
10. C. H. Chang and H. N. Li, *Phys. Rev.* D **55**, 5577 (1997); T. W. Teh and H. N. Li, *Phys. Rev.* D **56**, 1615 (1997).
11. H. N. Li, *Phys. Rev.* D **66**, 094010 (2002).
12. H. N. Li and B. Tseng, *Phys. Rev.* D **57**, 443 (1998).
13. Z. T. Zou, Ahmed. Ali, C. D. Lü, X. Liu, and Y. Li, *Phys. Rev.* D **91**, 054033 (2015).
14. B.-H. Hong, C.-D. Lü, Sci. China **G49**, 357-366 (2006), e-Print Archive: hep-ph/0505020

Studies of charmonium at BESIII

Wenbiao Yan (For BESIII Collaboration)
*Department of Modern Physics, University of Science and Technology of China,
96 JinZhai Road, Hefei, 230026, Anhui Province, China*

Using 2.25×10^8 J/ψ and 1.06×10^8 $\psi(3686)$ data samples with BESIII detector at BEPCII, upper limits of some charmonium rare decays are obtained at 90% confidence level. i.e., $Br(J/\psi \to \gamma\gamma) < 2.0 \times 10^{-7}$; $Br(J/\psi \to \gamma\phi) < 1.4 \times 10^{-6}$; $Br(J/\psi \to D_s^- e^+ \nu_e + c.c) < 1.3 \times 10^{-6}$; $Br(J/\psi \to D_s^{*-} e^+ \nu_e + c.c) < 1.8 \times 10^{-6}$; $Br(J/\psi \to D_s^- \rho^+ + c.c) < 1.3 \times 10^{-5}$; $Br(J/\psi \to \bar{D}^0 \bar{K}^{*0} + c.c) < 2.5 \times 10^{-6}$. The radiative transitions $\psi(3770) \to \gamma\eta_c$ and $\gamma\eta_c(2S)$ are also searched for $2.92\ pb^{-1}\psi(3770)$ data sets.

1 Introduction

The Charmonium in Quantum chromodynamics(QCD) is an analogy with positronium in Quantum electrodynamics. For charmonium above charm threshold, there are many missing states, and a large number of charmonium-like states are observed in final states with charmonium and light hadrons. A number of observed states do not fit into $c\bar{c}$ picture, and have some strange properties. Fot this part, one could find more detail in Kai Zhu's talk[1]. For charmonium below charm threshold, all states have been observed, and charm anti-charm potential model describes spectrum well. In this talk, I present recent results on rare and radiative decay of charmonium states below charm threshold by BESIII Collaboration.

2 Charmonium rare decays

Standard model(SM) has surved decades of experimental tests, but there are still room for physics beyond standard model. We could search for it at energy frontier , e.g. LHC; or at low energy collision with high luminosity. In this talk, I present results on searching for C-parity violation in $J/\psi \to \gamma\gamma$ and $\gamma\phi$ decays via $\psi(3686) \to \pi^+\pi^- J/\psi$.

Because charmonium decays are dominated by electromagnetic and strong interaction, weak decays are rare. we could search for some highly suppressed process at SM, an observation of these process maybe due to new physics. I show results on semileptonic weak decay and two body hadronic weak decay $J/\psi \to D_s^- e^+\nu_e + c.c$ and $J/\psi \to D_s^{(*)-} e^+\nu_e + c.c$; two-body hadronic weak decays $J/\psi \to D_s^- \rho^+ + c.c$ and $J/\psi \to \bar{D}^0 \bar{K}^{*0} + c.c.$

2.1 $J/\psi \to \gamma\gamma$ and $\gamma\phi$

The charge conjugation (C) operation transforms a particle into its antiparticle and vice versa. The C invariance is held in strong and electromagnetic interactions in SM. Evidence for C violation in the EM sector would immediately indicate physics beyond SM. Tests of C invariance in EM interactions have been carried out by many experiments. Untill now, no C-violating processes have been observed in electromagnetic interactions[2].

To search for C-parity violation process $J/\psi \to \gamma\gamma$[3] via $\psi(3686) \to \pi^+\pi^- J/\psi$ events are selected with topology $\gamma\gamma\pi^+\pi^-$. The invariant mass recoiling against $\pi^+\pi^-$, $M^{rec}_{\pi^+\pi^-}$ of candidate signal events is shown in Fig.1(a). A J/ψ signal is clearly observed, and is dominated by backgrounds. The main peaking backgrounds come from $\psi(3686) \to \pi^+\pi^- J/\psi$, $J/\psi \to \gamma\pi^0, \gamma\eta, \gamma\eta_c$ and 3γ $(\pi^0/\eta/\eta_c \to \gamma\gamma)$ The solid curve shows the fitting results and the dashed line indicates the nonpeaking backgrounds in Fig.1(a). According to fitted number of signal events, a upper limit on branching fraction $Br(J/\psi \to \gamma\gamma)$ is determined to be 2×10^{-7} at 90% confidence level, which is one order of magnitude more stringent than previous upper limit.

The C-parity violation process $J/\psi \to \gamma\phi$[3] via $\psi(3686) \to \pi^+\pi^- J/\psi$ events are studied with topology $\gamma K^+K^-\pi^+\pi^-$. The invariant mass of K^+K^- of selected events is displayed in Fig.1(b). The region between arrows contains about 90% of signal according to Monte Carlo(MC) simulation. An MC study shows that there are no peaking background contributions. In the Fig.1, the solid line shows the global fit results and the dashed line shows the background, a upper limit of $Br(J/\psi \to \gamma\phi) < 1.4 \times 10^{-6}$ is obtained at 90% confidence level in the first time.

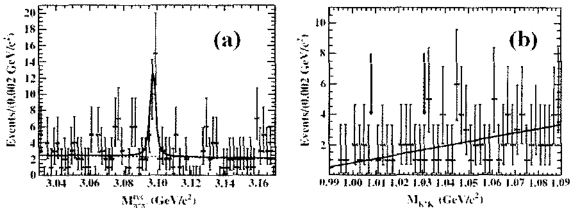

Figure 1 – $M^{rec}_{\pi^+\pi^-}$ spectrum for $J/\psi \to \gamma\gamma$ (left), The invariant mass of K^+K^- for $J/\psi \to \gamma\phi$ (right).

2.2 Semileptonic weak decays of J/ψ

Because mass of J/ψ is below open charm threshold, J/ψ can not decay into a pair of charmed mesons. However, J/ψ can decay into a single charmed meson via weak interaction[4], and are rare processes. Theoretical calculations predict $Br(J/\psi \to D_s^* l\nu)(l = e, \mu)$ to be 10^{-10} by using QCD sum rules and employing covariant light-front quark model [5]. However, The top-color models, the minimal supersymmetric SM with R-parity violation, or the two-Higgsdoublet model could enhance $Br(J/\psi \to D(\bar{D})X)$ (with X denoting any hadrons) with new interaction couplings [6].

For $J/\psi \to D_s^- e^+\nu_e + c.c$ candidate[7], the D_s meson is reconstructed via four decay modes, $D_s^- \to K^+K^-\pi^-$, $D_s^- \to K^+K^-\pi^-\pi^0$, $D_s^- \to K_s^0K^-$ and $D_s^- \to K_s^0K^+\pi^-\pi^-$. The undetected neutrino leads to missing energy $E_{miss} = E_{J/\psi} - E_{D_s^-} - E_{e^+}$ and missing momentum $\vec{p}_{miss} = \vec{p}_{J/\psi} - \vec{p}_{D_s^-} - \vec{p}_{e^+}$. The number of $J/\psi \to D_s^- e^+\nu_e + c.c$ event could be extracted with variable $U_{miss} = E_{miss} - |\vec{p}_{miss}|$. If signal events are correctly identified, U_{miss} is expected to peak around zero. Fig.2(a) shows U_{miss} distribution for four D_s decay modes in $J/\psi \to D_s^- e^+\nu_e + c.c$ candidates. The signal shapes obtained from MC simulations are shown with dashed curves. No significant excess of signal above background is observed in either mode. A simultaneous unbinned maximum likelihood fit is performed to determine event yields of four Ds decay modes, and a upper limit of $Br(J/\psi \to D_s^- e^+\nu_e + c.c) < 1.3 \times 10^{-6}$ at 90% confidence level.

For $J/\psi \to D_s^{*-}e^+\nu_e + c.c$ candidate [7], D_s and an additional photon are combined to reconstruct D_s^{*-}. With similar method for $J/\psi \to D_s^- e^+\nu_e + c.c$ analysis, a upper limit of $Br(J/\psi \to D_s^{*-}e^+\nu_e + c.c) < 1.8 \times 10^{-6}$ at 90% confidence level, which is set for the first time. The U_{miss} distributions for this decay chain are also shown in Fig.2(b).

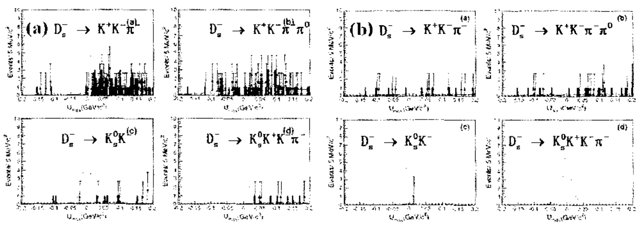

Figure 2 – U_{miss} distribution for $J/\psi \to D_s^- e^+\nu_e + c.c$ (left), U_{miss} distribution for $J/\psi \to D_s^{*-}e^+\nu_e + c.c$ (right)

2.3 Two-body hadronic weak decays of J/ψ

Branching fractions of rare processes $J/\psi \to D_s^-\rho^+ + c.c$ and $J/\psi \to \bar{D}^0\bar{K}^{*0} + c.c$ are to be $10^{-8} - 10^{-9}$ in a factorization model [8]. However, some models [9] with new physics could allow these processes to occur with branching fractions around 10^{-5}, which may be measurable in experiments.

For $J/\psi \to D_s^-\rho^+ + c.c$ process [10], in order to avoid large background contamination from J/ψ hadronic decays, D_s is identified with $D_s^- \to \phi e^-\nu_e$ and $\phi \to K^+K^-$. Because neutrinos are undetectable, the D_s^- is identified in distribution of mass recoiling against ρ^+ ($\rho^+ \to \pi^+\pi^0 \to \pi^+\gamma\gamma$). Fig.3(a) presents invariant mass of $\pi^+\pi^0$, where dots with error bars are experimental data, histograms represent distribution of signal MC events; vertical arrows show selection window for ρ. Mass distributions recoiling against of ρ prove that no excess of events above background is observed, and a upper limit of $Br(J/\psi \to D_s^-\rho^+ + c.c) < 1.3 \times 10^{-5}$ is obtained at 90% confidence level.

For $J/\psi \to \bar{D}^0\bar{K}^{*0} + c.c$ process [10], The $\bar{D}^0$ is reconstructed with $\bar{D}^0 \to K^+e^-\nu_e$. The invariant mass of $K^-\pi^+$ for $\bar{K}^{*0}$ and recoiling mass against of $\bar{K}^{*0}$ are shown in Fig.3(b). a upper limit of $Br(J/\psi \to \bar{D}^0\bar{K}^{*0} + c.c) < 2.5 \times 10^{-6}$ is obtained at 90% confidence level for the first time. These upper limits exclude new physics predictions which allow flavor-changing processes to occur with branching fractions around 10^{-5} but are still consistent with SM predictions.

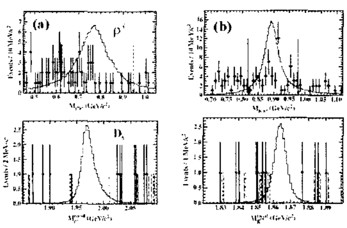

Figure 3 – Invariant mass of $\pi^+\pi^0$ and Mass distributions recoiling against of ρ for $J/\psi \to D_s^-\rho^+ + c.c$ process (left), Invariant mass of $K^-\pi^+$ for $\bar{K}^{*0}$ and recoiling mass against of $\bar{K}^{*0}$ for $J/\psi \to \bar{D}^0\bar{K}^{*0} + c.c$ process (right)

3 Search for $\psi(3770) \to \gamma\eta_c$ and $\gamma\eta_c(2S)$

The radiative transitions $\psi(3770) \to \gamma\eta_c$ and $\gamma\eta_c(2S)$ are supposed to be highly suppressed by selection rules, considering $\psi(3770)$ is predominantly the 1^3D_1 state. Because of non-vanishing photon energy, higher multipoles beyond leading one could contribute. Based on a $2.92pb^{-1}$ data set for $\psi(3770)$ study collected with BESIII detector at BEPCII, The radiative decay $\psi(3770) \to \gamma\eta_c$ and $\gamma\eta_c(2S)$ with $\eta_c/\eta_c(2S) \to K_s^0K^{\pm}\pi^{\pm}$, are searched [11], and compared with that of theory calculation with contributions from intermediate meson(IML) loop [12] and Lattice QCD prediction [13]. Fig.4 shows invariant-mass spectrum of $K_s^0K^{\pm}\pi^{\pm}$ for selected experimental events, together with estimated background events. In η_c and $\eta_c(2S)$ mass region, the estimated backgrounds can describe data well. Upper limits for $Br(\psi(3770) \to \gamma\eta_c) < 6.8 \times 10^{-4}$ and $Br(\psi(3770) \to \gamma\eta_c(2S)) < 2.0 \times 10^{-3}$ at 90% confidence level. In χ_{cj} mass region, a clear χ_{c1} signal are observed with $Br(\psi(3770) \to \gamma\chi_{c1}) = (2.33 \pm 0.65 \pm 0.43) \times 10^{-3}$. The measured $\Gamma(\psi(3770) \to \gamma\eta_c) < 19$KeV is consistent with $\Gamma_{IML} = 17.14^{+22.93}_{-12.03}$KeV [12] and $\Gamma_{LQCD} = 10 \pm 11$KeV [13]; $\Gamma(\psi(3770) \to \gamma\eta_c(2S)) < 55$KeV is consistent with $\Gamma_{IML} = 1.82^{+1.95}_{-1.19}$KeV [12].

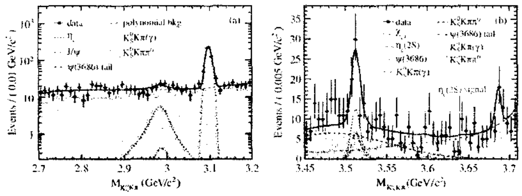

Figure 4 – Invariant-mass spectrum for $K_s^0K^{\pm}\pi^{\pm}$ from experimental data with estimated backgrounds and best-fit results superimposed in the (a) η_c and (b) $\chi_{c1} - \eta_c(2S)$ mass regions.

Acknowledgments

I would like to thank for support of National Natural Science Foundation of China (NSFC) under Contract No. 11475164; Joint Large-Scale Scientific Facility Funds of the NSFC and Chinese Academy of Science under Contract No. 11179007.

References

1. Kai Zhu, proceeding paper of this conference.
2. K.A. Olive et al., Chin. Phys. C 38, 090001 (2014).
3. M. Ablikim et al., BESIII Collaboration, *Phys. Rev.* D **90**, 092002 (2014).
4. M. A. Sanchis, *Phys. Lett.* B **280**, 299 (1992).
5. Y.-M.Wang, H. Zou, Z.-T.Wei, X.-Q. Li, and C.-D. Lu, Eur. Phys. J. C 54, 107 (2008).
6. X.-M. Zhang, High Energy Phys. Nucl. Phys. 25, 461 (2001); H.-B. Li and S.-H. Zhu, Chin. Phys. C 36, 932 (2012); C. Hill, Phys. Lett. B 345, 483 (1995).
7. M. Ablikim et al., BESIII Collaboration, *Phys. Rev.* D **90**, 112014 (2014).
8. Ramesh C. Verma, A.N. Kamal and Andrzej Czarnecki, *Phys. Lett.* B **252**, 690 (1990).
9. A. Datta, P. J. ODonnell, S. Pakvasa, and X. Zhang, Phys. Rev. D 60, 014011 (1999); X. Zhang, High Energy Phys. Nucl. Phys. 25, 461 (2001).
10. M. Ablikim et al., BESIII Collaboration, *Phys. Rev.* D **89**, 071101(R) (2014).
11. M. Ablikim et al., BESIII Collaboration, *Phys. Rev.* D **89**, 112005 (2014).
12. Gang Li and Qiang Zhao, *Phys. Rev.* D **84**, 074005 (2011).
13. Jozef J. Dudek, Robert G. Edwards and Christopher E. Thomas, *Phys. Rev.* D **79**, 094504 (2009).

EXOTIC CHARMONIUM-LIKE STATES AT BESIII

KAI ZHU
On behalf of BESIII collaboration
Institute of High Energy Physics, Beijing, 100049, China

The recent measurement results of exotic charmonium-like states, the so called XYZ particles, at BESIII have been presented. I mainly discussed the charged $Z_c(3900)$ state, its neutral partner, and possible excited states.

1 Introduction

Charmonium states are charm quark pair meson $c\bar{c}$, its spectrum can be calculated by potential model and the theoretical predictions are consistent with experimental results well. However, at the charmonium states region, recently some new states have been observed, and these so called XYZ particles cannot be assigned in the charmonium frame easily. On the other hand, the quantum chromodynamics (QCD) predicts that there are maybe exotic states rather than the usual baryon (qqq) and meson ($q\bar{q}$) states. They could be bound gluons (glueball), $q\bar{q}$-pair mixed with excited gluons (hybrids), multi-quark color singlet states such as: $q\bar{q}q\bar{q}$ (tetra-quark or molecular), $q\bar{q}q\bar{q}q$ (penta-quark), $q\bar{q}q\bar{q}q\bar{q}$ (six-quark or baryonium) and *et al.*. These newly found XYZ states are candidates of the exotic states.

BESIII detector is a magnetic spectrometer [1] located at BEPCII, which is a double-ring e^+e^- collider working at the center-of-mass energy from 2.0 to 4.6 GeV. Rich physics potential is at BESIII, that includes light hadron, charmonium, charm, and R & QCD physics. The cylindrical core of the BESIII detector consists of a helium-based main drift chamber (MDC), a plastic scintillator time-of-flight system (TOF), and a CsI(Tl) electromagnetic calorimeter (EMC), which are all enclosed in a superconducting solenoidal magnet providing a 1.0 T magnetic field . The solenoid is supported by an octagonal flux-return yoke with resistive plate counter muon identifier modules interleaved with steel. The acceptance of charged particles and photons is 93% over 4π solid angle. The momentum resolution of the charged particle at 1 GeV/c^2 is 0.5%, and the dE/dx resolution is 6%. The EMC measures photon energies with a resolution of 2.5% (5%) at 1 GeV in the barrel (endcaps). The time resolution of TOF is 80 ps in the barrel and 110 ps in the end caps. Till now, BESIII has collected about 0.6 B ψ' events, 1.3 B J/ψ events, 2.9 fb^{-1} $\psi(3770)$, and others including scan and continuum data, *et al.*. Above 4 GeV, it has collected about 5 fb^{-1} data mainly for the studies of XYZ states.

2 XYZ particles

A charged Z state named $Z_c(3900)$ is observed by BESIII [2] and Belle [3] via process $\pi^{\pm}(\pi J/\psi)^{\mp}$, and confirmed with CLEO-c's data [4]. The measured mass and width of the three experiments are shown in Table. 1. Analysis shows $Z_c(3900)$ is strongly coupled to $c\bar{c}$ as well as has electric charge, that indicates it is at least a 4−quarks state. Many interpretations are proposed, such as DD^* module, tetra-quark state, Cusp, and threshold effect, *et al.*, but none of them is a satisfied explanation yet.

Table 1: Masses and widths of the $Z_c(3900)$ and its neutral partner or excited states. The results are default from BESIII without explicit specification. For preliminary results from BESIII, only statistical uncertainties are shown here.

states	$M((MeV)$	Γ(MeV)
$Z_c(3900)$ (BESIII)	$3899.0 \pm 3.6 \pm 4.9$	$46 \pm 10 \pm 20$
$Z_c(3900)$ (Belle)	$3894.5 \pm 6.6 \pm 4.5$	$63 \pm 24 \pm 26$
$Z_c(3900)$ (CLEO-c data)	$3885 \pm 5 \pm 1$	$34 \pm 12 \pm 4$
$Z_c^0(3900)$	3894.8 ± 2.3	29.6 ± 8.2
$Z_c(3885)$ [single tag]	$3883.9 \pm 1.5 \pm 4.2$	$24.8 \pm 3.3 \pm 11.0$
$Z_c(3885)$ [double tag]	3884.3 ± 1.2	23.8 ± 2.1
$Z_c(4020)$	$4022.9 \pm 0.8 \pm 2.7$	$7.9 \pm 2.7 \pm 2.6$
$Z_c^0(4020)$	$4023.9 \pm 2.2 \pm 3.8$	fixed to $\Gamma(Z_c(4020))$
$Z_c(4025)$	$4026.3 \pm 2.6 \pm 3.7$	$24.8 \pm 5.6 \pm 7.7$

In order to reveal the nature of the Z_c state, BESIII systematically searched its other decay modes, its charge conjugated partner, and its excited states. Its neutral partner $Z_c^0(3900)$ has been found via $\pi^0 J/\psi$ spectrum. When BESIII searched another Z_c production mode via $\pi^{\pm}(D\bar{D}^*)^{\mp}$ [5] with a single D-tag method, the so called $Z_c(3885)$ is found. It's mass and width are consistent to the $Z_c(3900)$. This particle and its decay mode has been confirmed by BESIII with a double D-tag method. At higher mass region, a charged $Z_c(4020)$ is found via process $\pi^{\pm}(\pi h_c)^{\mp}$ [6], as well as its neutral partner via $\pi^0(\pi h_c)^0$. Close to $Z_c(4020)$, a charged $Z_c(4025)$ is found via process $\pi^{+}(D^*\bar{D}^*)^{\mp}$ [7]. The masses and widths of these states are listed in Table 1 too for comparison. BESIII also searched $Z_c \to \omega\pi$, however no significant signal has been observed, the upper limits of production cross sections are $\sigma(e^+e^- \to Z_c\pi,\ Z_c \to \omega\pi) < 0.27$ pb and < 0.18 pb at 90% credible level for the center-of-mass energies of 4.23 GeV and 4.26 GeV, respectively.

Due to their similar masses and widths, we may assume $Z_c(3900)$ and $Z_c(3885)$ are the same state Z_c, while $Z_c(4020)$ and $Z_c(4025)$ are same as an excited state Z_c'. For even higher Z_c excited state, Belle observed $Z_c(4200)$ [8] and $Z_c(4030)$ [9] via B decay ($\pi J/\psi$ and $\pi\psi'$), and $Z_c(4030)$ is confirmed by LHCb via $B^0 \to \psi'\pi K^+$ [10], as well as its J^P is determined as 1^+. In order to search Z_{cs}, Belle updated its previous K^+K^-J/ψ measurement to a Dalitz Plot analysis [11], however, no evident structure is found in $K^{\pm}J/\psi$ mass distribution under current statistics. Belle has observed $Z_b(10610)$ and $Z_b(10650)$ in $\pi^+\pi^-\Upsilon(nS)$ [12 13], $\pi^+\pi^-h_b(mP)$ [14] and $[B\bar{B}^*]^{\pm}\pi^{\mp}$ [15] final states. Due to above information, a Z family chart is proposed in Fig. 1.

$X(3872)$ was first observed via $B \to K(\pi^+\pi^-J/\psi)$ process by Belle [16], and its mass is close to the D^0D^{*0} threshold and its width very narrow. Its J^{PC} has been determined by CDF [17] and LHCb [18] to be 1^{++}. The partial width measurement shows that it takes a 50% chance to decay via open-charm channel and at the $O(\%)$ via charmonium. Since its discovery, many interpretations of its nature have been proposed, such as D^0D^{*0} module, hybrid, $\chi_{c1}(2P)$, and tetra-quark states, *et al.*. However no one is very satisfactory and more studies are needed to understand its nature . Recently BESIII reported a new production mode of $e^+e^- \to \gamma(\pi^+\pi^-J/\psi)$ [19], with data samples collected at center-of-mass energies from 4.009 to 4.420 GeV. Before BESIII's discovery, only in the pp collision and B decays $X(3872)$ has been found.

$X(3823)$ was firstly seen by Belle in $B \to \chi_{c1}\gamma K$ decays as a narrow peak in the invariant mass distribution of the $\chi_{c1}\gamma$ system [20]. Its properties are consistent with the $\psi_2(1^3D_2)$ charmonium state. At BESIII, $X(3823)$ is observed via $e^+e^- \to \pi^+\pi^-X(3823) \to \pi^+\pi^-\gamma\chi_{c1}$, and there is evidence that it is may from $Y(4260)$ decay.

In last decade, lots of Y states have been observed, for example $Y(4008)$, $Y(4260)$, $Y(4360)$,

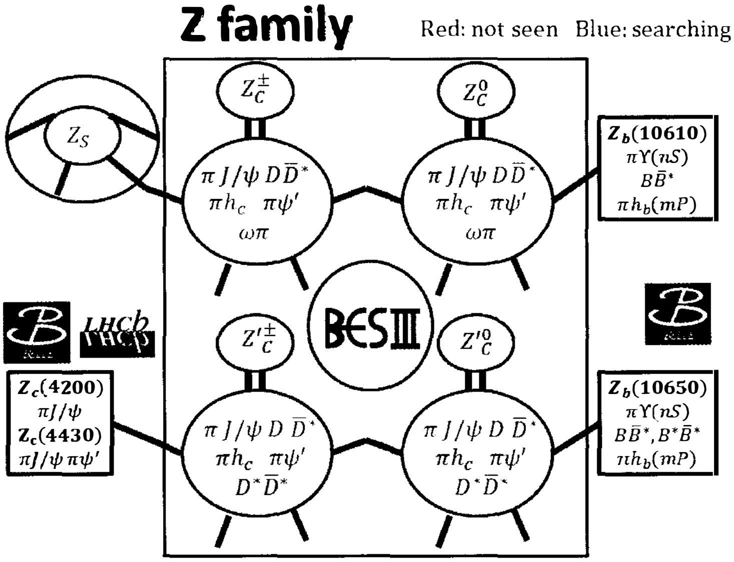

Figure 1 – A proposed Z family chart.

$Y(4630)$, and $Y(4660)$, *et al.*. They are produced via initial state radiative (ISR) processes in e^+e^- collision, that means they are vector states. However, the total number of these Y states is absolutely larger than that of the theoretical prediction by potential model for charmonium around this energy region. One thing is interesting that these Y states are only found in $\pi^+\pi^- J/\psi$ [21,22], $\pi^+\pi^-\psi(2S)$ [23], and $\Lambda_c^+\Lambda_c^-$ [24] final states, but no evidence from open charm, *i.e.*$Y \to D^{(*)}D^{(*)}$ [25,26,27].

At BESIII, abundant structures are observed in the cross section shapes from 4.0 to 4.6 GeV via different processes, that are from e^+e^- to $\pi^+\pi^- h_c$ [6], $\omega\chi_{c0}$ [28], $\eta J/\psi$, $\pi^0\pi^0 J/\psi$, $J/\psi\eta\pi^0$, $\pi^+\pi^-\gamma\chi_{c1}$, $\eta' J/\psi$, $\gamma\phi J/\psi$ and $\gamma\chi_{cJ}$. But the statistics are limited, then larger data samples are necessary and possible interferences need be considered to understand them correctly.

3 Summary

A relatively systematic study on exotic charmonium-like states, *i.e.*XYZ particles, has been performed at BESIII. Abundant and interesting results are obtained, and that has greatly improved our knowledge about these exotic states. However, the natures of the these exotic states are still mysterious, the relations between them are unclear, and some expected states and decay modes are missing. To shed light on the puzzles, more decay channels should be studied carefully, partial wave analysis (PWA) is needed to clarify their quantum number, *i.e.* J^{JC}, and a fine scan from 3.8 to 4.6 GeV at BESIII may be helpful. More results from BESIII will come soon with analyses are under way.

Acknowledgments

I am grateful to the Moriond2015 committee for the organization of this very nice conference.

References

1. M. Ablikim *et al.* [BESIII Collaboration], Nucl. Instrum. Meth. A **614**, 345 (2010) [arXiv:0911.4960 [physics.ins-det]].
2. M. Ablikim *et al.* [BESIII Collaboration], Phys. Rev. Lett. **110**, 252001 (2013) [arXiv:1303.5949 [hep-ex]].
3. Z. Q. Liu *et al.* [Belle Collaboration], Phys. Rev. Lett. **110**, 252002 (2013) [arXiv:1304.0121 [hep-ex]].
4. T. Xiao, S. Dobbs, A. Tomaradze and K. K. Seth, Phys. Lett. B **727**, 366 (2013) [arXiv:1304.3036 [hep-ex]].
5. M. Ablikim *et al.* [BESIII Collaboration], Phys. Rev. Lett. **112**, no. 2, 022001 (2014) [arXiv:1310.1163 [hep-ex]].
6. M. Ablikim *et al.* [BESIII Collaboration], Phys. Rev. Lett. **111**, no. 24, 242001 (2013) [arXiv:1309.1896 [hep-ex]].
7. M. Ablikim *et al.* [BESIII Collaboration], Phys. Rev. Lett. **112**, no. 13, 132001 (2014) [arXiv:1308.2760 [hep-ex]].
8. K. Chilikin *et al.* [Belle Collaboration], Phys. Rev. D **90**, no. 11, 112009 (2014) [arXiv:1408.6457 [hep-ex]].
9. S. K. Choi *et al.* [Belle Collaboration], Phys. Rev. Lett. **100**, 142001 (2008) [arXiv:0708.1790 [hep-ex]].
10. R. Aaij *et al.* [LHCb Collaboration], Phys. Rev. Lett. **112**, no. 22, 222002 (2014) [arXiv:1404.1903 [hep-ex]].
11. C. P. Shen *et al.* [Belle Collaboration], Phys. Rev. D **89**, no. 7, 072015 (2014) [arXiv:1402.6578 [hep-ex]].
12. A. Bondar *et al.* [Belle Collaboration], Phys. Rev. Lett. **108**, 122001 (2012) [arXiv:1110.2251 [hep-ex]].
13. I. Adachi [Belle Collaboration], arXiv:1105.4583 [hep-ex].
14. I. Adachi *et al.* [Belle Collaboration], Phys. Rev. Lett. **108**, 032001 (2012) [arXiv:1103.3419 [hep-ex]].
15. I. Adachi *et al.* [Belle Collaboration], arXiv:1209.6450 [hep-ex].
16. S. K. Choi *et al.* [Belle Collaboration], Phys. Rev. Lett. **91**, 262001 (2003) [hep-ex/0309032].
17. A. Abulencia *et al.* [CDF Collaboration], Phys. Rev. Lett. **98**, 132002 (2007) [hep-ex/0612053].
18. R. Aaij *et al.* [LHCb Collaboration], Phys. Rev. Lett. **110**, 222001 (2013) [arXiv:1302.6269 [hep-ex]].
19. M. Ablikim *et al.* [BESIII Collaboration], Phys. Rev. Lett. **112**, no. 9, 092001 (2014) [arXiv:1310.4101 [hep-ex]].
20. V. Bhardwaj *et al.* [Belle Collaboration], Phys. Rev. Lett. **111**, no. 3, 032001 (2013) [arXiv:1304.3975 [hep-ex]].
21. B. Aubert *et al.* [BaBar Collaboration], Phys. Rev. Lett. **95**, 142001 (2005) [hep-ex/0506081].
22. C. Z. Yuan *et al.* [Belle Collaboration], Phys. Rev. Lett. **99**, 182004 (2007) [arXiv:0707.2541 [hep-ex]].
23. X. L. Wang *et al.* [Belle Collaboration], Phys. Rev. Lett. **99**, 142002 (2007) [arXiv:0707.3699 [hep-ex]].
24. G. Pakhlova *et al.* [Belle Collaboration], Phys. Rev. Lett. **101**, 172001 (2008) [arXiv:0807.4458 [hep-ex]].
25. G. Pakhlova *et al.* [Belle Collaboration], Phys. Rev. D **77**, 011103 (2008) [arXiv:0708.0082 [hep-ex]].
26. K. Abe *et al.* [Belle Collaboration], Phys. Rev. Lett. **98**, 092001 (2007) [hep-ex/0608018].
27. G. Pakhlova *et al.* [Belle Collaboration], Phys. Rev. Lett. **100**, 062001 (2008) [arXiv:0708.3313 [hep-ex]].
28. M. Ablikim *et al.* [BESIII Collaboration], Phys. Rev. Lett. **114**, no. 9, 092003 (2015) [arXiv:1410.6538 [hep-ex]].

STUDY OF CHARMONIUM(-LIKE) STATES AT BABAR AND BELLE

RUSLAN CHISTOV [a]
National Research Nuclear University MEPhI (Moscow Engineering Physics Institute), Kashirskoye shosse 31, Moscow, 115409, Russia
and
Institute for Theoretical and Experimental Physics, B. Cheremushkinskaya 25, Moscow, 117218, Russia

We discuss recent results on charmonium-like states at B-factories. It includes brief overview of the Belle results on the charged charmonium-like states, update of the analysis of $e^+e^- \to \pi^+\pi^-\psi(2S)$ process at Belle and new results on a search for $X(4140)$ and $X(4270)$ decaying into $J/\psi\phi$ at BaBar.

1 Introduction

Experimental spectrum of $c\bar{c}$ states [1] below the $D\bar{D}$ threshold agrees well with theoretical predictions [2]. Until the B-Factories era [3] no evidences for the states which could shake conventional picture of charmonium were found.

12 years ago the Belle Collaboration discovered undreamed-of new particle, named $X(3872)$ [4], decaying into $J/\psi\pi^+\pi^-$, with a very narrow (for the state above the $D\bar{D}$ threshold) width ($\Gamma < 1.2$ MeV/c^2 @ 90% CL) and with the mass ($M = 3871.69 \pm 0.17$ MeV/c^2) which coincides within errors with the $D^{*0}\bar{D}^0$ threshold of (3871.8 ± 0.3) MeV/c^2. It should be noted that there is no expected from theory any charmonium level in the vicinity to this mass. After the discovery of $X(3872)$ and its confirmation by CDF, D0 and BaBar [1] many new particles were observed by BaBar and Belle [5]. Because of its unusual properties (mismatching with the predicted levels, large partial width of the non-$D\bar{D}^{(*)}$ decay modes and even non-mesonic or -baryonic quark content) they are called as charmonium-like (XYZ) states. All of these have inbreathed new life in heavy flavour physics and lead to the formation of its new branch - spectroscopy of XYZ states.

In this talk we discuss some recent results from B-factories Belle and BaBar concerning the charmonium-like states.

2 Recent results on Z^+'s: charged charmonium-like states at Belle

In 2007 by analyzing the $B \to \psi(2S)\pi^+K$ decays, new exotic state was observed by Belle [6]: charged state, named $Z(4430)^+$, decaying into $\psi(2S)\pi^+$. This state can not be an isospin singlet, conventional or hybrid state, its minimal quark content should be $|c\bar{c}u\bar{d}>$. In a year Belle observed two new charged charmonium-like states [7], $Z(4250)^+$ and $Z(4050)^+$, both decaying into another ordinary charmonium χ_{c1} and charged pion. Again these states were found in $B \to$ *charmonium* decay, this time $B \to \chi_{c1}\pi^+K$. By looking at the same B meson decays,

[a]Speaker, on behalf of the Belle Collaboration

BaBar did not confirm these charged charmonium-like states [8]. Meanwhile Belle made two updates on $Z(4430)^+$ with higher statistics: by using Dalitz plot analysis [9] and full four-dimensional amplitude analysis [10]. The existence of $Z(4430)^+$ itself and its parameters were confirmed. Moreover, in the latter analysis Belle obtained constraints on the possible J^P numbers of $Z(4430)^+$: the preferred hypothesis is 1^+.

Then two different experiments, BES III [11] and Belle [12], reported the observation of another charged charmonium-like state, $Z(3900)^+$, decaying into $J/\psi\pi^+$. Both experiments find it in $e^+e^- \to Y(4260)$ reaction, where $Y(4260)$ is reconstructed in $J/\psi\pi^+\pi^-$ final state. At last, LHCb [13] confirmed the production of $Z(4430)^+$ in B decays and measured its parameters together with the spin-parity to be in a good agreement with those obtained in the updated Belle analysis on $Z(4430)^+$. So the existence of new types of hadrons, charged charmonium-like states, which quark content differs from mesonic or baryonic, is confirmed.

Last year Belle continued a search for new candidates to Z^+ family. By performing a full four-dimensional amplitude analysis of 3-body decay $B \to J/\psi\pi^+K$ Belle observed another state decaying into $J/\psi\pi^+$, $Z(4200)^+$ [14] which preferred $J^P = 1^+$. This analysis also results in first evidence for $Z(4430)^+ \to J/\psi\pi^+$, the second decay mode of $Z(4430)^+$. Fig. 1 shows the $M^2(J/\psi\pi^+)$ projection of the Dalitz plot. The curves are the fit results with and without $Z(4200)^+$.

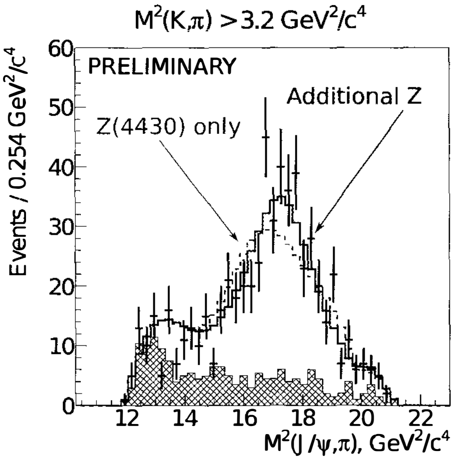

Figure 1 – Projection of the fit results with and without the $Z(4200)^+$.

Table 1 shows the masses and natural widths of all discussed here charged charmonium-like states. The exact nature of charged charmonium-like states remains unclear and there are several approaches towards their interpretation. New measurements are needed to test theoretical models and clarify Z^+'s nature.

3 Updated study of $e^+e^- \to \psi(2S)\pi^+\pi^-$ process at Belle

The $e^+e^- \to \psi(2S)\pi^+\pi^-$ process, first observed in ISR at BaBar [15] permitted to establish new unexpected chamonium-like states $Y(4360) \to \psi(2S)\pi^+\pi^-$. Then Belle confirmed this state and observed a new one in a higher mass, $Y(4660)$ [16]. Using the full data-set, BaBar confirmed thc existence of the second resonance [17]. Recently, using all available data Belle presented an update of its initial $e^+e^- \to \psi(2S)\pi^+\pi^-$ analysis [18]. The resulted accuracy in masses and widths for these Y's was improved. In this update, following the observation of charged charmonium-

Table 1: Experimental data on charged charmonium-like states.

State	Mass, Mev/c^2	Γ, MeV/c^2	Experiment and Decay Modes
$Z(4430)^+$	$4485 \pm 22^{+28}_{-11}$	200^{+41+26}_{-46-35}	$\psi(2S)\pi^+$, Belle [6]
	$4475 \pm 7^{+15}_{-25}$	$172 \pm 13^{+37}_{-34}$	$\psi(2S)\pi^+$, LHCb [13]
$Z(4050)^+$	$4051 \pm 14^{+20}_{-41}$	82^{+21+47}_{-17-22}	$\chi_{c1}\pi^+$, Belle [7]
$Z(4250)^+$	$4248^{+44+180}_{-29-35}$	$177^{+54+316}_{-39-61}$	$\chi_{c1}\pi^+$, Belle [7]
$Z(3900)^+$	$3899.0 \pm 3.6 \pm 4.9$	$46 \pm 10 \pm 20$	$J/\psi\pi^+$, BES III [11]
	$3894.5 \pm 6.6 \pm 4.5$	$63 \pm 24 \pm 26$	$J/\psi\pi^+$, Belle [12]
$Z(4200)^+$	4196^{+31+17}_{-29-13}	$370^{+70+70}_{-70-132}$	$J/\psi\pi^+$, Belle [14]

like state $Z(3900)^+ \to J/\psi pi^+$ in ISR $e^+e^- \to J/\psi\pi^+\pi^-$ events [12], Belle investigated the $\psi(2S)\pi^\pm$ mass spectrum for the events from the $Y(4360)$ mass region. New resonant structure at 4.05 GeV/c^2 is seen and its parameters were extracted to be $M = (4054 \pm 3 \pm 1)$ MeV/c^2 and $\Gamma = (45 \pm 11 \pm 6)$ MeV. The significance of the signal of this new charged charmonium-like state was obtained to be 3.5 σ.

4 Search for the X(4140) and X(4270) decaying into $J/\psi\phi$ at BaBar

Recently the XYZ list has been enriched by two new states decaying into $J/\psi\phi$. Both were found by analyzing the $B^+ \to J/\psi\phi K^+$ decays. One of them, $X(4140)$, was originally observed by CDF as a near-threshold peak with a significance of more than 5 σ in the $J/\psi\phi$ final state [19]. Later D0 published a 3.1 σ evidence for this state [20]. Belle searched for $X(4140)$ in $\gamma\gamma$ events and found no evidence for its production [21]. As for the LHC experiments, CMS confirms [22] the production of $X(4140)$ but LHCb do not [23]. All experiments that see $X(4140)$ also find evidence for the second peaking structure $X(4270)$ at higher $J/\psi\phi$ masses.

This year BaBar published results on their search for these two states in $B^+ \to J/\psi\phi K^+$ decays. No evidences were found for $X(4140)$ or $X(4270)$ (the significance is below 2σ for each resonance) [24]. Table 2 shows the results on a relative fraction $f = \mathcal{B}(B^+ \to XK^+) \times \mathcal{B}(X \to J/\psi\phi)/\mathcal{B}(B^+ \to J/\psi\phi K^+)$ for different experiments.

Further studies with increased statistics at LHC experiments will permit to obtain more information about these states and fix its status.

Table 2: Relative fractions of $X(4140)$ and $X(4270)$ in B^+ decays in different experiments.

Experiment	$f(4140)$, %	$f(4270)$, %
CDF	$14.9 \pm 3.9 \pm 2.4$	
D0	$21 \pm 8 \pm 4$	
CMS	$\approx 10 \pm 3$	
LHCb	< 7 @ 90% CL	< 8 @ 90% CL
BaBar	< 13.3 @ 90% CL	< 18.1 @ 90% CL

5 Summary

In this talk several recent results on charmonium-like states were presented from Belle and BaBar. New results constantly appear and theoretical models try to accommodate them and predict new states. Actively running BES III and LHC experiments as well as future Belle II experiment [?] will continue the studies of charmonium-like states, which have more complex internal structure than mesons or baryons.

Acknowledgments

R.C. would like to thank the Organizing Committee of 50^{th} Rencontres de Moriond for hospitality. This work is supported by the Russian Ministry of Education and Science contracts 14.A12.31.0006 and the Russian Foundation for Basic Research grant 14-02-01220.

References

1. K. A. Olive *et al.* (Particle Data Group), *Chin. Phys. C*, **38**, 090001 (2014).
2. M. B. Voloshin, *Prog. Part. Nucl. Phys.* **61**, 455-511 (2008).
3. A. J. Bevan *et al.* (BaBar and Belle Collaborations), *arXiv:1406.6311.*
4. S. K. Choi *et al.* (Belle Collaboration), PRL **91**, 262001 (2003).
5. S. L. Olsen, *Int. J. Mod. Phys. Conf. Ser.* **29**, 1460250 (2014); S. Godfrey and S. L. Olsen, *Ann. Rev. Nucl. Part. Sci.* **58**, 51 (2008).
6. S. K. Choi *et al.* (Belle Collaboration), *Phys. Rev. Lett.* **100**, 142001 (2008).
7. R. Mizuk *et al.* (Belle Collaboration), *Phys. Rev.* D **78**, 072004 (2008).
8. B. Aubert *et al.* (BaBar Collaboration), *Phys. Rev.* D **79**, 112001 (2009); J. P. Lees *et al.* (BaBar Collaboration), *Phys. Rev.* D **85**, 052003 (2012).
9. R. Mizuk *et al.* (Belle Collaboration), *Phys. Rev.* D **80**, 031104 (2009).
10. K. Chilikin *et al.* (Belle Collaboration), *Phys. Rev.* D **88**, 074026 (2013).
11. M. Ablikim *et al.* (BESIII Collaboration), *Phys. Rev. Lett.* **110**, 252001 (2013).
12. Z. Q. Liu *et al.* (Belle Collaboration), *Phys. Rev. Lett.* **110**, 252002 (2013).
13. R. Aaij *et al.* (LHCb Collaboration), *Phys. Rev. Lett.* **112**, 222002 (2014).
14. K. Chilikin *et al.* (Belle Collaboration), *Phys. Rev.* D **90**, 112009 (2014).
15. B. Aubert *et al.* (BaBar Collaboration), *Phys. Rev. Lett.* **98**, 212001 (2007).
16. J. P. Lees *et al.* (Belle Collaboration), *Phys. Rev.* D **86**, 051102R (2012).
17. B. Aubert *et al.* (BaBar Collaboration), *Phys. Rev.* D **89**, 111103 (2014).
18. X. L. Wang, C. Z. Yuan, C. P. Shen, P. Wang *et al.* (Belle Collaboration), *arXiv:1410.7641.*
19. T. Aaltonen *et al* (CDF Collaboration), *arXiv:1101.6058.*
20. V. M. Abazov *et al.* (D0 Collaboration), *Phys. Rev.* D **89**, 012004 (2013).
21. C. P. Shen *et al.* (Belle Collaboration), *Phys. Rev. Lett.* **104**, 112004 (2010).
22. S. Chatrchyan *et al.* (CMS Collaboration), *Phys. Lett.* B **734**, 261 (2014);
23. R. Aaij *et al.* (LHCb Collaboration), *Phys. Rev.* D **85**, 091103 (2012).
24. J. P. Lees *et al.* (BaBar Collaboration), *Phys. Rev.* D **91**, 012003 (2015).

HEAVY QUARK SPECTROSCOPY AT LHCb

Tomasz Skwarnicki
on behalf of the LHCb collaboration

Department of Physics, Syracuse University, Syracuse, NY 13244, USA

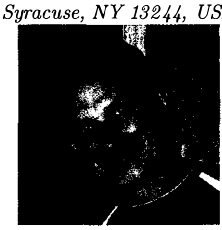

The analysis of 3.0 fb^{-1} of proton-proton collisions collected with the LHCb detector has yielded a broad range of results in spectroscopy of conventional and exotic hadrons with heavy quark(s) inside. We review the LHCb results which have been obtained over the last year.

1 Masses of the $\chi_b(3^3P_J)$ States

Long-lived heavy quarkonia states, $c\bar{c}$ and $b\bar{b}$, have played a key role in solidifying the quark model and in development of quantitative theoretical methods to describe hadrons; potential models early on, more recently NRQCD and lattice QCD. The triplet $3P$ $b\bar{b}$ states are among the most recently observed heavy-heavy mesons [1,2]. Because of their proximity to the open flavor threshold, it has been speculated that couplings to virtual $B^{(*)}\bar{B}^{(*)}$ pairs could drastically affect their masses and decay properties [3]. Furthermore, it has been proposed that the $\chi_b(3^3P_1)$ state could have a substantial component of an $I = 0$ $B\bar{B}^*$ molecule, X_b, analogous to the $I = 0$ $D\bar{D}^*$ molecule offered as an explanation for the $X(3872)$ state [4]. The LHCb collaboration has observed these states via direct production in pp collisions at the LHC, through their photon transitions to $\Upsilon(1,2,3^3S_1)$ states reconstructed

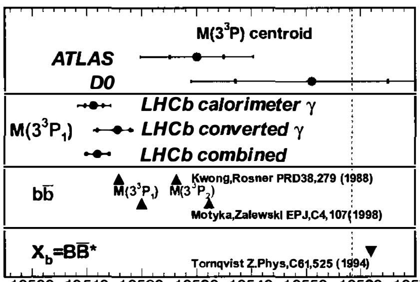

Figure 1 – Various measurements of the $\chi_b(3^3P_J)$ masses compared to the theoretical predictions. The vertical dashed line shows the open flavor threshold, $2M(B)$.

in the $\mu^+\mu^-$ final state. The results obtained with the transition photon detected in the EM calorimeter[5] and in the tracking system after a conversion to an e^+e^- pair[6] are consistent with each other. By fitting the data for the mass of the $\chi_b(3^3P_1)$ state, instead of the ill-defined mass centroid[1,2], the results are made easier to interpret. The average over these two determinations, $M(3^3P_1) = 10512.2 \pm 2.3$ MeV, has much improved errors over the previous measurements and is within a few MeV to the potential model predictions, some published 27 years, as illustrated in Fig. 1. Therefore, it appears that the coupled-channel corrections are either small or well absorbed into an effective $Q\bar{Q}$ potential adjusted to the experimental data on the other $b\bar{b}$ states. The measured ratios of the photon transition rates to different $\Upsilon(n^3S_1)$ states are also consistent with the potential model expectations.

2 Recent Results on the $X(3872)$ State

While the $\chi_b(3^3P_J)$ states discussed in the previous section are slightly below the $B\bar{B}^{(*)}$ threshold, the narrow $X(3872)$ state has a mass coinciding, within the experimental errors, with the $D^0\bar{D}^{*0}$ threshold (the inclusion of charge-conjugate states is implied in this article). Among the $c\bar{c}$ states, $\eta_c(2^1D_2)$ with $J^{PC} = 2^{-+}$ and $\chi_c(2^3P_1)$ with $J^{PC} = 1^{++}$ are expected to be in this mass range and narrow. In order to explain its mass it has also been proposed that the $X(3872)$ is a 1^{++} $D\bar{D}^*$ molecule. A tetraquark model of $X(3872)$ predicts $J^{PC} = 1^{++}$ as well. Previously, the LHCb collaboration ruled out 2^{-+} assignment in favor of 1^{++}, assuming that the lowest orbital angular momentum dominated the $X(3872) \to (\pi^+\pi^-)J/\psi$ decay[7]. The same assumption was done in the analysis of the CDF data, which had ruled out the other spin assignments[8]. This decay appears to proceed via the isospin violating $X(3872) \to \rho^0 J\psi$ decay with the phase-space limit coinciding with the ρ^0 pole mass, severely limiting the energy release Q in this decay. With small Q, the momentum of the $X(3872)$ decay products, p, is also small. Since the $c\bar{c}$ states are known to have a compact size, the impact parameter between the decay products, r, is expected to be small as well, making it difficult to generate substantial orbital angular momentum, $L = rp$. However, if the $X(3872)$ state has a significant molecular component, its size would be large, possibly enhancing higher L values. This calls for reanalysis of the data with no assumption about L, which could lead to a different J^{PC} assignment. A determination of the magnitude of higher L contributions for the correct J^{PC} is also of interest, since a substantial value would suggest an anomalously large size of the $X(3872)$ state. The LHCb has tripled the $X(3872)$ signal statistics in the $B^+ \to X(3872)K^+$, $X(3872) \to \rho^0 J/\psi$, $\rho^0 \to \pi^+\pi^-$, $J/\psi \to \mu^+\mu^-$ decay chain, and has

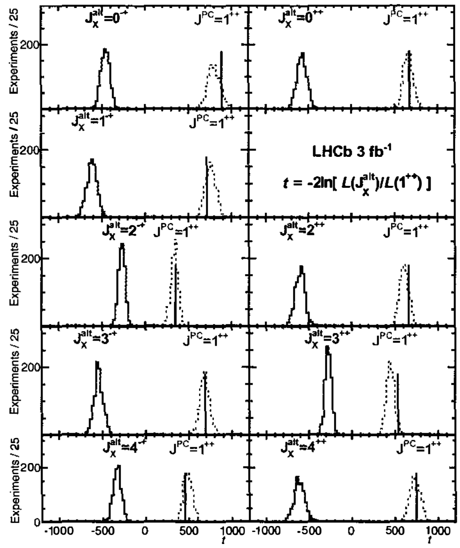

Figure 2 – Distributions of the likelihood-ratio test statistic, $t \equiv -2\ln[L(J_X^{\rm alt}))/L(1^{++})]$, for the simulated LHCb experiments under the $X(3872)$ $J^{PC} = J_X^{\rm alt}$ hypothesis (blue solid histograms) and under the favored $J^{PC} = 1^{++}$ hypothesis (red dashed histograms). The values of the test statistics for the LHCb data are shown by the solid vertical lines. The data prefer 1^{++} by about 16 standard deviations over the other assignments.

confirmed the $J^{PC} = 1^{++}$ assignment for the first time without any assumptions about L [9] (see Fig. 2). The $X(3872) \to \rho^0 J/\psi$ decay is dominated by S wave. A tight upper limit of 4% at 95% C.L. is set on the fraction of D wave.

The LHCb collaboration has also measured a ratio of radiative branching fractions, $R_{\gamma\psi} \equiv \mathcal{B}(X(3872) \to \gamma\psi(2^3S_1))/\mathcal{B}(X(3872) \to \gamma J/\psi(1^3S_1))$, which is considered to be a good probe of its internal composition [10]. If $X(3872)$ is the $\chi_c(2^3P_1)$ state, $R_{\gamma\psi}$ should be substantial because of a good overlap of the 2^3P_1 and 2^3S_1 wave functions (the same number of radial nodes) making the corresponding E1 matrix element larger than for the transition to the 1^3S_1 state. In the molecular model, there is no clear mechanism to enhance photon transitions to the radially excited state over the transitions to the ground state, which are phase-space preferred. Previously, the BaBar collaboration claimed $R_{\gamma\psi}$ to be large, albeit with the large errors [11]. The Belle collaboration, observed the transitions to the 1^3S_1 state with a better significance but found no evidence for the transitions to the 2^3S_1 state [12]. Within the large experimental errors the BaBar and Belle experiments did not disagree, but pointed towards the opposite conclusions. The LHCb has observed both transitions with the highest significance and measured $R_{\gamma\psi} = 2.48 \pm 0.64 \pm 0.29$, pointing to a substantial component of the 2^3P_1 $c\bar{c}$ bound state inside the $X(3872)$ meson, possibly mixing with the four-quark structures ($D^0\bar{D}^0$ molecule or cusp, tetraquark).

3 Resonant Character of the $Z(4430)^+$ State

The long lasting dispute about the nature of the $X(3872)$ illustrates the difficulties in distinguishing exotic four-quark formations from ordinary $c\bar{c}$ mesons for neutral states. This ambiguity does not exist for charged states decaying to charmonia. The first candidate of this type, $Z(4430)^+ \to \psi(2S)\pi^+$, was observed by Belle in the $B^0 \to \psi(2S)\pi^+K^-$ decays [13]. The BaBar collaboration could not confirm nor disprove the $Z(4430)^+$ state with nearly an equal number of observed B^0 decays [14]. The LHCb experiment has reconstructed an order of magnitude larger number of $B^0 \to \psi(2S)\pi^+K^-$ decays, and observed a 13.9σ significant $Z(4430)^+$ signal in the 4D amplitude analysis of invariant masses and decay angles [15]. The mass, width and $J^P = 1^+$ assignments agree with the latest results from the similar analysis by Belle, but are now established with much improved errors [16]. Thanks to the large data statistics, LHCb is able to probe the $Z(4430)^+$ amplitude without the Breit-Wigner ansatz. The Argand diagram exhibits a behavior typical of a resonant bound state, as shown in Fig. 3. This is the first demonstration of this type for an exotic hadron candidate. Possible theoretical interpretations of the $Z(4430)^+$ structure include a tetraquark [17], or a $D(2S)^+\bar{D}^0$ molecule [18,19]. Rescattering of pairs of excited D, D_s mesons has been also proposed [20], but rests on the speculation that the LHCb data could accommodate, within the fit uncertainties, the phase-running in the opposite

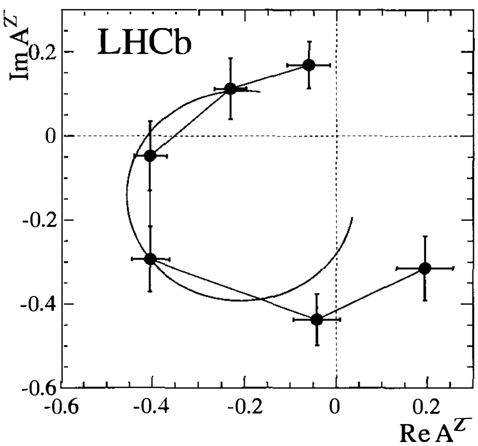

Figure 3 – Fitted values of the $Z(4430)^+$ amplitude in six $M(\psi(2S)\pi^+)^2$ bins, shown in an Argand diagram (connected points with the error bars, $M(\psi(2S)\pi^+)^2$ increases counter-clockwise). The red curve is the prediction from the Breit-Wigner formula with a resonance mass (width) of 4475 (172) MeV. Units are arbitrary.

direction to the resonance.

Recently, the LHCb collaboration has observed $B_s^0 \to \psi(2S)\pi^+K^-$ decays for the first time [21]. The $\psi(2S)\pi^+$ distribution does not exhibit peaking at the $Z(4430)^+$ mass. However, the B_s^0 signal statistics are at present insufficient to probe exotic hadron contributions to this decay at the level observed in the B^0 decays.

4 Results on Heavy-light Mesons

As illustrated in the previous two sections, interpretations of exotic hadron $Q\bar{Q}q\bar{q}$ candidates often invoke excitations of heavy-light mesons, $Q\bar{q}$ ($q = u, d, s$). Such bound states are relativistic. Their fine structure has to do with light-quark spin-orbit coupling, $\vec{j}_q = \vec{S}_q + \vec{L}$, rather than coupling of the total spin of two quarks to the orbital angular momentum characteristic for heavy-heavy mesons. Semi-relativistic potential models, HQET and lattice QCD calculations have been employed to predict heavy-light mass spectra. Many of the predicted excitations have not been yet observed. The LHCb collaboration has several new results on heavy-light spectroscopy.

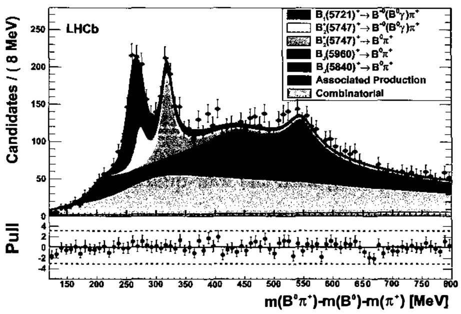

Figure 4 – Results of the simultaneous fit to $B^+\pi^-$ and $B^0\pi^+$ candidates in three p_T intervals, displayed for the highest p_T bin (> 2 GeV) of $B^0\pi^+$ mass.

A Dalitz analysis of the $B_s^0 \to \bar{D}^0K^-\pi^+$ decay resolved the previously observed $D_{sJ}^*(2860)^- \to \bar{D}^0K^-$ state to be an overlap of $J^P = 1^-$ and 3^- states, which are likely $1D_{1,3}$ $c\bar{s}$ states [22,23]. This is the first significant observation of a spin 3 meson produced in B decays. The spin of $D_{sJ}^*(2573)^-$ state is proved to be 2, in agreement with the $1P_2$ interpretation.

A similar Dalitz analysis of the $B^- \to \bar{D}^+K^-\pi^+$ decay, observed for the first time, confirms the spin 2 assignment to the $D_J^*(2460)^0$ meson ($1P_2$ candidate) [24]. Only a candidate for $1D_1$ state, $D_1^*(2760)^0$, is observed in the LHCb data with the present statistics.

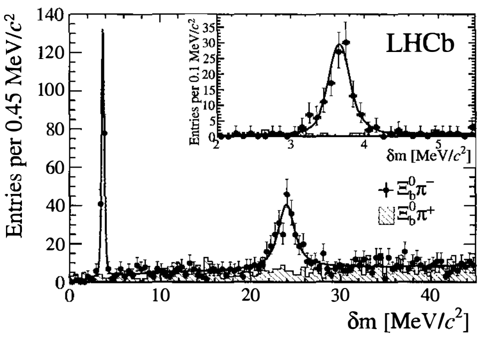

Figure 5 – Distribution of the mass difference, $\delta m \equiv M(\Xi_b^0\pi) - M(\Xi_b^0) - M(\pi)$, for right-sign (points with error bars) and wrong-sign (hatched histogram) $\Xi_b^0\pi^\pm$ candidates in data, together with the fit of the $\Xi_b^{\prime(*)-}$ (lower mass peak, enlarged in the inset) and the Ξ_b^{*-} (higher mass peak) states.

The LHCb also has new results on excitations of B mesons observed in $B^{+,0}\pi^{-,+}$ decays [25]. Candidates for B^+ and B^0 mesons are reconstructed in one of the decay modes with J/ψ or D in the final state. Since the $B\pi$ candidates are observed in prompt production, the backgrounds are high. Several peaks in $M(B\pi)$ spectra are observed. The backgrounds are a strong function of the transverse momentum of the candidates (p_T), therefore, simultaneous mass fits are performed in 3 different p_T intervals. In addition to the previously well established $B_1(5721)^{0,+}$, $B_2(5747)^{0,+}$ mesons ($1P_{1,2}$ $j_q = 3/2$

candidates), for which the mass and width measurements are improved, significant evidence for one or two peaks at higher mass is obtained, in the mass range expected for $2S_0$, $2S_1$ $j_q = 1/2$ states (Fig. 4).

5 Two New Beautiful and Strange Baryons

Spectroscopy of baryons with a b quark inside is still in its infancy, with many states expected in the lowest $L = 0$ $SU(3)_f$ multiplets of bqq system still unobserved. The LHCb collaboration has searched for bsq states via a full reconstruction of a cascade of the strong decay, $\Xi_b^{'(*)-} \to \Xi_b^0 \pi^-$, followed by the two weak decays, $\Xi_b^0 \to \Xi_c^+ \pi^-$, $\Xi_c^+ \to pK^-\pi^+$. Two new baryons are observed (Fig. 5), matching the expectations for the $\Xi_b^{'(*)-}$ ($J = 1/2$, $j_{qq}^P = 1^+$) and Ξ_b^{*-} ($J = 3/2$, $j_{qq}^P = 1^+$) states[26].

6 Summary

Highlights of the LHCb results in heavy quark spectroscopy over the past year include:

- The precision measurement of $\chi_b(3^3P_1)$ mass, and the measurement of ratios of photon transition rates to $\gamma\Upsilon(1,2,3^3S_1)$, which are consistent with the expectations for pure $b\bar{b}$ states in spite of their proximity to the $B\bar{B}$ threshold.
- The studies of the radiative decays of $X(3872)$ to $\gamma\psi(1,2^3S_1)$ and of orbital angular momentum in the $\rho^0 J/\psi$ decays, which point to a significant $\chi_c(2^3P_1)$ component.
- An amplitude analysis of the $Z(4430)^+ \to \psi(2^3S_1)\pi^+$ contribution to the $B^0 \to \psi(2^3S_1)\pi^+K^-$ decay confirms existence of this state. The magnitude and phase mass-variation are consistent with an exotic four-quark bound state.
- Many new results on heavy-light spectroscopy of the excitations of D_s, D and B mesons. Such studies are important for theoretical interpretations of exotic meson candidates in the heavy-heavy-light-light sector, which often invoke phenomena related to the heavy-light pairs.
- The observation of two new beautiful and strange baryons, which illustrates still largely untapped potential of conventional, and possibly exotic, baryon spectroscopy of heavy quarks at the LHC.

While many exotic hadron candidates have been observed in the heavy quark sector by many different experiments and colliders, a comprehensive theoretical understanding of these states is still lacking. In order to advance it, we are looking forward to obtaining larger data samples in the upcoming Run-II of the LHC and even larger gains in sensitivity with the upgraded LHCb detector in the years to follow.

References

1. G. Aad et al. Observation of a new χ_b state in radiative transitions to $\Upsilon(1S)$ and $\Upsilon(2S)$ at ATLAS. *Phys. Rev. Lett.*, 108:152001, 2012.
2. V.M. Abazov et al. Observation of a narrow mass state decaying into $\Upsilon(1S) + \gamma$ in $p\bar{p}$ collisions at $\sqrt{s} = 1.96$ TeV. *Phys. Rev.*, D86:031103, 2012.
3. J. Ferretti, G. Galat, and E. Santopinto. Quark structure of the $X(3872)$ and $\chi_b(3P)$ resonances. *Phys. Rev.*, D90:054010, 2014.
4. M. Karliner and J. L. Rosner. $X(3872)$, X_b, and the $\chi_{b1}(3P)$ state. *Phys. Rev.*, D91:014014, 2015.
5. R. Aaij et al. Study of χ_b meson production in pp collisions at $\sqrt{s}$=7 and 8 TeV and observation of the decay $\chi_b \to \Upsilon(3S)\gamma$. *Eur. Phys. J.*, C74:3092, 2014. LHCb-PAPER-2014-031.

6. R. Aaij et al. Measurement of the $\chi_b(3P)$ mass and of the relative rate of $\chi_{b1}(1P)$ and $\chi_{b2}(1P)$ production. *JHEP*, 10:088, 2014. LHCb-PAPER-2014-040.
7. R. Aaij et al. Determination of the $X(3872)$ meson quantum numbers. *Phys. Rev. Lett.*, 110:222001, 2013. LHCb-PAPER-2013-001.
8. A. Abulencia et al. Analysis of the quantum numbers J^{PC} of the $X(3872)$. *Phys. Rev. Lett.*, 98:132002, 2007.
9. R. Aaij et al. Quantum numbers of the $X(3872)$ state and orbital angular momentum in its $\rho^0 J/\psi$ decay. *Submitted to Phys. Rev. D Rapid Communications*, 2015. LHCb-PAPER-2015-015, arXiv:hep-ex/1504.06339.
10. R. Aaij et al. Evidence for the decay $X(3872) \to \psi(2S)\gamma$. *Nucl. Phys.*, B886:665, 2014. LHCB-PAPER-2014-008.
11. B. Aubert et al. Evidence for $X(3872) \to \psi(2S)\gamma$ in $B^\pm \to X(3872)K^\pm$ decays, and a study of $B \to c\bar{c}\gamma K$. *Phys. Rev. Lett.*, 102:132001, 2009.
12. V. Bhardwaj et al. Observation of $X(3872) \to J/\psi\gamma$ and search for $X(3872) \to \psi'\gamma$ in B decays. *Phys. Rev. Lett.*, 107:091803, 2011.
13. S.K. Choi et al. Observation of a resonance-like structure in the $\pi^\pm\psi'$ mass distribution in exclusive $B \to K\pi^\pm\psi'$ decays. *Phys. Rev. Lett.*, 100:142001, 2008.
14. B. Aubert et al. Search for the $Z(4430)^-$ at BaBar. *Phys. Rev.*, D79:112001, 2009.
15. R. Aaij et al. Observation of the resonant character of the $Z(4430)^-$ state. *Phys. Rev. Lett.*, 112:222002, 2014. LHCB-PAPER-2014-014.
16. K. Chilikin et al. Experimental constraints on the spin and parity of the $Z(4430)^+$. *Phys. Rev.*, D88:074026, 2013.
17. L. Maiani, F. Piccinini, A.D. Polosa, and V. Riquer. The $Z(4430)$ and a New Paradigm for Spin Interactions in Tetraquarks. *Phys. Rev.*, D89:114010, 2014.
18. L. Ma, X.-H. Liu, X. Liu, and S.-L. Zhu. Exotic Four Quark Matter: $Z_1(4475)$. *Phys. Rev.*, D90:037502, 2014.
19. T. Barnes, F.E. Close, and E.S. Swanson. Molecular Interpretation of the Supercharmonium State Z(4475). *Phys. Rev.*, D91:014004, 2015.
20. P. Pakhlov and T. Uglov. Charged charmonium-like $Z(4430)^+$ from rescattering in conventional B decays. 2014. arXiv:hep-ph/1408.5295.
21. R. Aaij et al. Observation of the decay $\overline{B}{}^0_s \to \psi(2S)K^+\pi^-$. *Submitted to Phys. Lett. B*, 2015. LHCb-PAPER-2015-010, arXiv:hep-ex/1503.07112.
22. R. Aaij et al. Observation of overlapping spin-1 and spin-3 $\bar{D}^0K^-$ resonances at mass 2.86 GeV/c^2. *Phys. Rev. Lett.*, 113:162001, 2014. LHCB-PAPER-2014-035.
23. R. Aaij et al. Dalitz plot analysis of $B^0_s \to \bar{D}^0K^-\pi^+$ decays. *Phys. Rev.*, D90:072003, 2014. LHCB-PAPER-2014-036.
24. R. Aaij et al. First observation and amplitude analysis of the $B^- \to D^+K^-\pi^-$ decay. *Phys.Rev.*, D91:092002, 2015. LHCB-PAPER-2015-007, arXiv:hep-ex/1503.02995.
25. R. Aaij et al. Precise measurements of the properties of the $B_1(5721)^{0,+}$ and $B_2^*(5747)^{0,+}$ states and observation of structure at higher invariant mass in the $B^+\pi^-$ and $B^0\pi^+$ spectra. *to appear in JHEP*, 2015. LHCB-PAPER-2014-067, arXiv:hep-ex/1502.02638.
26. R. Aaij et al. Observation of two new Ξ_b^- baryon resonances. *Phys. Rev. Lett.*, 114:062004, 2015. LHCb-PAPER-2014-061, arXiv:hep-ex/1411.4849.

Flavour Violation in a Class of two Higgs-Doublet Models

G. C. Branco
Departamento de Física and Centro de Física Teórica de Partículas (CFTP),
Instituto Superior Técnico (IST), U. de Lisboa (UL),
Av. Rovisco Pais, P-1049-001 Lisboa, Portugal.

We examine flavour violation in a class of two Higgs-Doublet models where there are FCNC at tree level, but naturally suppressed by a symmetry introduced at tree level. We examine how these class of models can satisfy the stringent constraints from experiment and discuss the prospects for discovering some of the flavour changing Higgs decays in the second run of the LHC at 13TeV.

1 Introduction

Higgs Flavour Violating Neutral Couplings (HFVNC) arise in Two Higgs Doublet Models (2HDM) [1] as well as in other extensions of the SM. There are very stringent experimental constraints on Flavour-Changing-Neutral-Currents (FCNC), so in order to be plausible, models with FCNC have to contain a mechanism to naturally suppress these couplings. In this talk, we analysed BGL models [2] which were suggested for the quark sector but then generalised [3] and extended to the lepton sector [4]. In the 2HDM there are in general three neutral scalars, in the Higgs basis they are denoted H^0, R and I, with H^0 having flavour diagonal couplings in the fermion eigenstate basis. On the contrary, R and I have HFVNC with a flavour structure which in general is arbitrary. The key feature of BGL models is the fact that the HFVNC of R and I are completely fixed in terms of V_{CKM} and U_{PMNS} matrix elements. Apart from the ratio $v2/v1 = \tan(\beta)$, no other free parameters are introduced. This is achieved in a natural way through the introduction of a discrete symmetry at the Lagrangian level. Therefore, BGL models and their flavour structure are stable under renormalisation. Apart from restricting the flavour structure of the Yukawa couplings, the symmetry also restricts the scalar potential in such a way that CP is not violated in the scalar sector, either explicitly or spontaneously. As a result, the pseudo-scalar field I and the charged scalars are physical fields, while the two other two neutral physical fields can be expressed in terms of H^0 and R through a single rotation.

Under the assumption that the Higgs particle discovered at LHC can be identified with H^0, we have studied in detail the experimental restrictions on BGL models, determining the mass ranges allowed for the new scalars [5]. In particular, we have shown that in some of the BGL models the masses of the scalar masses can be in the range of a few hundred GeV, therefore within the reach of LHC-13TeV.

2 Yukawa Interactions in BGL Models

The Yukawa interactions in two Higgs doublet models can be written :

$$\begin{aligned}\mathcal{L}_Y &= -\overline{Q_L^0}\,\Gamma_1\Phi_1 d_R^0 - \overline{Q_L^0}\,\Gamma_2\Phi_2 d_R^0 - \overline{Q_L^0}\,\Delta_1\tilde{\Phi}_1 u_R^0 - \overline{Q_L^0}\,\Delta_2\tilde{\Phi}_2 u_R^0 \\ &\quad -\overline{L_L^0}\,\Pi_1\Phi_1 l_R^0 - \overline{L_L^0}\,\Pi_2\Phi_2 l_R^0 - \overline{L_L^0}\,\Sigma_1\tilde{\Phi}_1\nu_R^0 - \overline{L_L^0}\,\Sigma_2\tilde{\Phi}_2\nu_R^0 + \text{h.c.},\end{aligned} \tag{1}$$

where Γ_i, Δ_i Π_i and Σ_i are matrices in flavour space. In order for the tree level FCNC to depend only on V_{CKM} , a flavour symmetry has to be introduced. Such a symmetry was introduced by Branco, Grimus and Lavoura [2], under which the fields transform in the following way:

$$Q_{Lj}^0 \to \exp(i\tau)\; Q_{Lj}^0 \;, \qquad u_{Rj}^0 \to \exp(i2\tau)u_{Rj}^0 \;, \qquad \Phi_2 \to \exp(i\tau)\Phi_2 \;, \tag{2}$$

where $\tau \neq 0, \pi$ while all other quark field transform trivially under the symmetry. The family index j can be chosen to be 1, 2, 3. One could also choose the d_R to transform non-trivially under the symmetry:

$$Q_{Lj}^0 \to \exp(i\tau)\; Q_{Lj}^0 \;, \qquad d_{Rj}^0 \to \exp(i2\tau)d_{Rj}^0 \;, \quad \Phi_2 \to \exp(-i\tau)\Phi_2 \;. \tag{3}$$

The symmetry of Eq. 2 leads to FCNC in the down sector, while the symmetry of Eq.3 leads to FCNC in the up sector. Taking into account the three possible choices for the index j, one has six different BGL type models in the quark sector. One encounters an entirely analogous situation in the lepton sector if one also includes Dirac mass terms for the neutrinos, so one has altogether thirty six different BGL models. Of course, in the leptonic sector FCNC are controlled by the U_{PMNS} matrix elements.

In order to analyse the physical implications of the three neutral scalars, it is useful to expand the neutral scalar field around their vevs $\phi_j^0 = \frac{1}{\sqrt{2}}(v_j + \rho_j + i\eta_j)$ and define the two following rotations:

$$\begin{pmatrix} H^0 \\ R \end{pmatrix} \equiv \begin{pmatrix} \cos\beta & \sin\beta \\ -\sin\beta & \cos\beta \end{pmatrix} \begin{pmatrix} \rho_1 \\ \rho_2 \end{pmatrix}; \qquad \begin{pmatrix} H \\ h \end{pmatrix} \equiv \begin{pmatrix} \cos\alpha & \sin\alpha \\ -\sin\alpha & \cos\alpha \end{pmatrix} \begin{pmatrix} \rho_1 \\ \rho_2 \end{pmatrix} \tag{4}$$

where $\tan(\beta) = v2/v1$. It is useful to write the Yukawa couplings in terms of the quark mass-eigenstates and the scalar fields in the Higgs basis :

$$\begin{aligned}\mathcal{L}_Y(\text{quark, Higgs}) &= -\frac{\sqrt{2}H^+}{v}\bar{u}\left(VN_d\gamma_R - N_u^\dagger\, V\gamma_L\right)d + \text{h.c.} - \\ -\frac{H^0}{v}\left(\bar{u}D_u u + \bar{d}D_d\, d\right) &- \frac{R}{v}\left[\bar{u}(N_u\gamma_R + N_u^\dagger\gamma_L)u + \bar{d}(N_d\gamma_R + N_d^\dagger\gamma_L)\, d\right] + \\ &+i\frac{I}{v}\left[\bar{u}(N_u\gamma_R - N_u^\dagger\gamma_L)u - \bar{d}(N_d\gamma_R - N_d^\dagger\gamma_L)\, d\right]\end{aligned} \tag{5}$$

The matrices N_d, N_u, fix the flavour structure of the the scalar couplings to fermions. In the BGL models with HFCNC in the down sector, N_d, N_u are given by:

$$(N_d)_{rs}(\text{up-type}) = \frac{v_2}{v_1}(D_d)_{rs} - \left(\frac{v_2}{v_1} + \frac{v_1}{v_2}\right)(V_{CKM}^\dagger)_{rj}(V_{CKM})_{js}(D_d)_{ss} \tag{6}$$

Note that no sum in j is implied. Particularising for the case $j = 3$, one has:

$$N_u(\text{up-type}) = -\frac{v_1}{v_2}\text{diag }(0, 0, m_t) + \frac{v_2}{v_1}\text{diag }(m_u, m_c, 0) \tag{7}$$

Entirely analogous equations hold for the case of BGL models with FCNC in the up sector.

3 Brief Discussion of Phenomenological Implications

Like any multi-Higgs extension of the SM, BGL models have to satisfy the stringent constraints of low energy phenomenology. A thorough analysis of the thirty six BGL models was done in [5] in the limit where the discovered scalar particle is identified with H^0. We imposed the present experimental constraints arising from various relevant flavour observables such as neutral meson mixings, $B \to X_s\gamma$, $l_j \to l_i\gamma$, as well as electroweak precision data. It was verified that in some of BGL models all phenomenological constraints are satisfied even for scalar masses of order a few hundred GeV, at the reach of the next round of LHC at 13TeV. Some of the BGL models allow for charged Higgs masses lower than 480 GeV which is the constraint derived from $b \to s\gamma$ on type II 2HDM [6] This results from the different dependence that these models have on $\tan(\beta)$

The fact that in some of the BGL models the masses of the neutral scalars may be relatively light in spite of the presence of FCNC, is due to the automatic suppression by small V_{CKM} elements. For example, in the case of up-type models, with $j = 3$, one can see from Eq. (6) that the tree-level neutral Higgs contribution to $K^0 - \overline{K^0}$ transition has an automatic suppression of $|V_{td}V_{ts}|^2$, which is a suppression of order λ^{10} in the amplitude where lambda stands for the Cabibbo parameter.

In the context of BGL models, there is the possibility that the Higgs particle h discovered at LHC is a mixture of H^0 and R parametrised by the angle $(\beta - \alpha)$. There are then HFVNC of h which depend on $\tan(\beta)$ and $\sin(\beta - \alpha)$. An important task is to find a region in the $\sin(\beta - \alpha)$ versus $\tan(\beta)$ plane where rare processes like $t \to ch$ and $h \to \mu\tau$ can occur at a rate sufficient to discover at LHC-13 TeV [7].

Acknowledgments

The author thanks the organisers of Rencontres de Moriond for the invitation to present this work and for the very stimulating atmosphere. The work presented in this Conference is partially supported by Fundação para a Ciência e a Tecnologia (FCT, Portugal) through the projects CERN/FP/123580/2011, PTDC/FIS-NUC/0548/2012, and CFTP-FCT Unit 777 (UID/FIS/00777/2013) which are partially funded through POCTI (FEDER), COMPETE, QREN and EU.

References

1. G. C. Branco, P. M. Ferreira, L. Lavoura, M. N. Rebelo, M. Sher and J. P. Silva, *Phys. Rept.* **516**, 1 (2012) [arXiv:1106.0034 [hep-ph]].
2. G. C. Branco, W. Grimus and L. Lavoura, *Phys. Lett.* B **380**, 119 (1996) [hep-ph/9601383].
3. F. J. Botella, G. C. Branco and M. N. Rebelo, *Phys. Lett.* B **687**, 194 (2010) [arXiv:0911.1753 [hep-ph]].
4. F. J. Botella, G. C. Branco, M. Nebot and M. N. Rebelo, *JHEP* **1110**, 037 (2011) [arXiv:1102.0520 [hep-ph]].
5. F. J. Botella, G. C. Branco, A. Carmona, M. Nebot, L. Pedro and M. N. Rebelo, *JHEP* **1407**, 078 (2014) [arXiv:1401.6147 [hep-ph]].
6. M. Misiak, H. M. Asatrian, R. Boughezal, M. Czakon, T. Ewerth, A. Ferroglia, P. Fiedler and P. Gambino *et al.*, *Phys. Rev. Lett.* **114**, no. 22, 221801 (2015) [arXiv:1503.01789 [hep-ph]].
7. F. J. Botella, G. C. Branco, M. Nebot and M. N. Rebelo, work in preparation.

RARE BEAUTY DECAYS AT LHCB

F. DETTORI [a]
CERN European Organization for Nuclear Research, Geneva (Switzerland)

In this contribution we review the most recent measurements of the LHCb experiment in the field of rare decays of B mesons. In particular the first observation of the $B_s^0 \to \mu^+\mu^-$ decay, the angular analysis of $B_d^0 \to K^*\ell^+\ell^-$ decays and the test of lepton universality in $B^+ \to K^+\ell^+\ell^-$ decays are presented.

1 Introduction

Rare decays of particles with b quarks are fundamental indirect probes for physics beyond the Standard Model (SM). The LHCb experiment is searching new physics in different channels with data collected in pp collisions at the LHC. The status of rare decay searches and measurements as of Moriond 2015 conferences is the following: no large deviation has been found in the most sensitive modes, however several discrepancies are present in various channels and observables. It appears clear the importance of fits to the full pattern of observables and of the possibility to probe many different final states. In this contribution we only review some of the recent measurements on rare b decays performed at LHCb.

2 Observation of the rare decay $B_s^0 \to \mu^+\mu^-$

The rare decays $B_s^0 \to \mu^+\mu^-$ and $B^0 \to \mu^+\mu^-$ are among the golden modes for the search of physics beyond the SM. In addition to the perturbative expansion suppression these decays are suppressed for helicity reasons. Therefore the branching fractions are predicted to be very small, at the level of $(3.66\pm0.23)\times10^{-9}$ and $(1.06\pm0.09)\times10^{-10}$ for the $B_s^0 \to \mu^+\mu^-$ and $B^0 \to \mu^+\mu^-$ respectively. [1]

In many new physics extensions of the SM, instead, this decay is enhanced or further suppressed, so that its branching fraction is sensitive to any modification to scalar or pseudoscalar couplings. The search for these decays has started long ago but only recently they have been strongly constrained. A first evidence for the $B_s^0 \to \mu^+\mu^-$ decay was obtained with 2fb^{-1} of pp collisions at LHC by the LHCb experiment [2]. This evidence was confirmed by the LHCb and CMS experiments with the full Run I data [3,4].

In order to improve the statistical precision, the two collaborations performed a combined analysis of the two datasets; a total of 3 fb^{-1} and 25 fb^{-1} of integrated luminosity collected by the LHCb and CMS experiments respectively, were analysed [5]. A simultaneous unbinned maximum likelihood fit was performed on the data, sharing observables and some nuisance parameters among the experiments. In particular, in addition to the branching fraction of the signal channels, the branching fraction of the $B^+ \to J/\psi K^+$ and the ratio of hadronisation fractions f_d/f_s, were shared.

[a] On behalf of the LHCb Collaboration

The fit to the combined data yielded a measurement of the $B_s^0 \to \mu^+\mu^-$ branching fraction of $\mathcal{B}(B_s^0 \to \mu^+\mu^-) = 2.8^{+0.7}_{-0.6} \times 10^{-9}$ with a signal significance corresponding to 6.2σ, representing the first observation of this decay. The $B^0 \to \mu^+\mu^-$ branching fraction was measured to be $\mathcal{B}(B^0 \to \mu^+\mu^-) = 3.9^{+1.6}_{-1.4} \times 10^{-10}$ with a signal significance of 3.2σ from the likelihood, cross-checked with the Feldman-Cousins method, which gave a 3.0σ significance, constituing a first evidence for the $B_s^0 \to \mu^+\mu^-$ decay. The invariant mass distribution for this fit and its confidence level contours are shown in Fig. 1. A separate fit to the ratio of the two branching fractions $\mathcal{R} = \frac{\mathcal{B}(B^0 \to \mu^+\mu^-)}{\mathcal{B}(B_s^0 \to \mu^+\mu^-)}$, yielded a measured value of $\mathcal{R} = 0.14^{+0.08}_{-0.06}$ consistent with the SM predictions at the 2.3σ level.

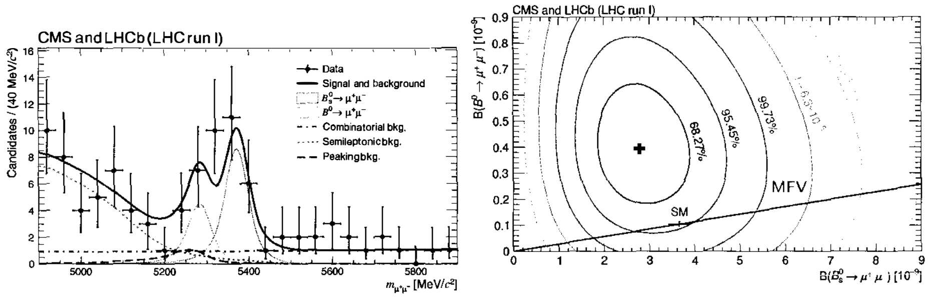

Figure 1 – On the left it is shown the distribution of the dimuon invariant mass for the six most significant bins of the combined analysis to LHCb and CMS data[5]. On the right the confidence level contours in the two dimensional plane of $\mathcal{B}(B^0 \to \mu^+\mu^-)$ versus $\mathcal{B}(B_s^0 \to \mu^+\mu^-)$.

3 Test of lepton universality using $B^+ \to K^+\ell^+\ell^-$ decays

One important test of the SM leptonic couplings comes from the measurement of lepton universality in $B^+ \to K^+\ell^+\ell^-$ decays. In particular the ratio of branching fractions $R_K = \int_{q^2_{min}}^{q^2_{max}} \frac{d\Gamma[\mathcal{B}(B^+ \to K^+\mu^+\mu^-)]}{dq^2} dq^2 / \int_{q^2_{min}}^{q^2_{max}} \frac{d\Gamma[\mathcal{B}(B^+ \to K^+e^+e^-)]}{dq^2} dq^2$ was measured by LHCb exploiting the full Run I luminosity of 3 fb^{-1} [6]. The measurement is performed by determining the relative yields of the rare decays $B^+ \to K^+\ell^+\ell^-$ with respect to the correspondent resonant channels $B^+ \to K^+J/\psi(\ell^+\ell^-)$ and correcting for efficiency ratios. The value of this observable is predicted to be 1 with very good uncertainty in the SM [7,8] and is therefore a stringent test of its lepton couplings; any significant deviation from unity can be interpreted as a sign of new physics contributions.

LHCb measured R_K for $B^+ \to K^+\ell^+\ell^-$ decays with $q^2 = m^2_{\ell^+\ell^-} \in [1, 6]\mathrm{GeV}^2/\mathrm{c}^4$. Different trigger strategies were used and the different measurements were compatible and combined. The final result obtained was $R_K = 0.745^{+0.090}_{-0.074}(\mathrm{stat}) \pm 0.036(\mathrm{syst})$, which is the most precise measurement to date of this quantity. This value of R_K is compatible with the SM predictions at a level of 2.6σ and stimulated some discussion from the theoretical point of view, which we do not review here; however as an example, it was suggested that if confirmed would point to new physics violating also the lepton flavour conservation. [9] Further tests of lepton universality and lepton flavour violation are being performed by the LHCb experiment in order to shed some light on this possibility.

4 Angular analysis of $B_d^0 \to K^*\ell^+\ell^-$ decays

The rare decays $B_d^0 \to K^*\ell^+\ell^-$ are not only sensitive probes of NP through their rates, but most prominently through their final state angular distributions. The angular distribution of the four final state particles can be fully characterized by q^2, defined as above, and by three angles $\Omega = (\theta_\ell, \theta_K, \phi)$ [10]. The CP averaged angular distribution for a q^2 bin can be written as:

$$\frac{1}{\mathrm{d}(\Gamma+\bar{\Gamma})/\mathrm{d}q^2}\frac{\mathrm{d}^3(\Gamma+\bar{\Gamma})}{\mathrm{d}\vec{\Omega}} = \frac{9}{32\pi}\Big[\frac{3}{4}(1-F_\mathrm{L})\sin^2\theta_K + F_\mathrm{L}\cos^2\theta_K + \frac{1}{4}(1-F_\mathrm{L})\sin^2\theta_K\cos 2\theta_\ell \quad (1)$$
$$-F_\mathrm{L}\cos^2\theta_K\cos 2\theta_\ell + S_3\sin^2\theta_K\sin^2\theta_\ell\cos 2\phi + S_4\sin 2\theta_K\sin 2\theta_\ell\cos\phi + S_5\sin 2\theta_K\sin\theta_\ell\cos\phi$$
$$+\frac{4}{3}A_\mathrm{FB}\sin^2\theta_K\cos\theta_\ell + S_7\sin 2\theta_K\sin\theta_\ell\sin\phi + S_8\sin 2\theta_K\sin 2\theta_\ell\sin\phi + S_9\sin^2\theta_K\sin^2\theta_\ell\sin 2\phi\Big]$$

where S_i, F_L and A_FB are CP-averaged observables. Any contribution of physics beyond the SM can modify the value of these observables and their dependence with q^2, so that these channels are sensitive to any change in the intermediate particles couplings.

In the following we summarize the most recent results from LHCb on the $B_d^0 \to K^*\ell^+\ell^-$ channels with ℓ being an electron or a muon.

4.1 $B_d^0 \to K^*e^+e^-$

An angular analysis to the $B_d^0 \dashrightarrow K^*e^+e^-$ channel was performed on the full Run I dataset of 3 fb^{-1} for events with very low q^2 ($\in [0.002, 1.120]\mathrm{GeV}^2/\mathrm{c}^4$) [11], being therefore sensitive to right handed currents in the intermediate photon exchange. Due to the small statistics, part of the dependence on the angle ϕ was cancelled by the variable transformation $\phi \dashrightarrow \phi + \pi$ for $\phi < 0$, so that four angular observables are measured: F_L, $A_T^{\Im}$, $A_T^{\Re}$ and $A_T^{(2)}$ [b].

The distributions of the three angles are shown in Fig. 2 superimposed with the full fit to the data and the various components. The results of the angular observables are reported in Table 1 and show good agreement with the SM prediction from Ref. [12]. The constraints from this decay to right handed currents are currently more precise than the ones from the correspondent radiative mode $B_d \to K^*\gamma$.

Table 1: Results on $B_d^0 \to K^*e^+e^-$ angular observables as measured by the LHCb experiment [11], compared to theoretical predictions from Ref. [12]

Observable	Measurement	SM prediction
F_L	$+0.16 \pm 0.06 \pm 0.03$	$+0.10^{+0.11}_{-0.05}$
$A_\mathrm{T}^{(2)}$	$-0.23 \pm 0.23 \pm 0.05$	$0.03^{+0.05}_{-0.04}$
$A_\mathrm{T}^{\Re}$	$+0.10 \pm 0.18 \pm 0.05$	$-0.15^{+0.04}_{-0.03}$
$A_\mathrm{T}^{\Im}$	$+0.14 \pm 0.22 \pm 0.05$	$(-0.2^{+1.2}_{-1.2}) \times 10^{-4}$

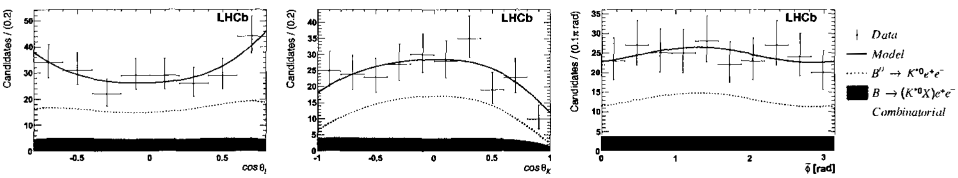

Figure 2 – Angular distributions for $B_d^0 \to K^*e^+e^-$ events as measured by LHCb, together with the various fit components (see legend).

[b] Where $A_T^{\Re} = \frac{4}{3}A_{FB}/(1-F_L)$, $A_T^{(2)} = \frac{1}{2}S_3/(1-F_L)$ and $A_T^{\Im} = \frac{1}{2}S_9/(1-F_L)$

4.2 $B_d^0 \to K^*\mu^+\mu^-$

The $B_d^0 \to K^*\mu^+\mu^-$ decay is a golden channel for the search of NP as to the already described sensitivity to various couplings adds the ease of detection of muons. LHCb has recently updated its previous study of this decay[13,14] by analysing the full dataset[15]. With respect to the previous results, owing to the enlarged statistics it was possible to perform a full angular analysis which allows to estimate all the CP-averaged observables simultaneously. Furthermore the fit was performed simultaneously also to the $K\pi$ mass in order to disentangle the S-wave component and the K^* resonance.

The fit to the angular observables was performed in bins of q^2 and the results are shown for selected observables in Fig 3. The full results are reported in Ref. [15] which also contains a full covariance matrix of the measured observables which allows to insert these measurements in global fits.

Most of the observables are in very good agreement with SM expectations. The observable A_{FB} is good agreement with the SM, though it is consistently below the prediction in several bins. The measurement of the observable $P_5' = S_5/\sqrt{F_L(1-F_L)}$ (less sensitive to form-factor effects[16]) is, consistently with previous publication [14], distant from the SM prediction in some bins. In particular the deviation corresponds to 2.9σ for both bins of $q^2 \in [4.0, 6.0]\mathrm{GeV}^2/\mathrm{c}^4$ and $\in [6.0, 8.0]\mathrm{GeV}^2/\mathrm{c}^4$, for a naively combined significance of 3.7σ.

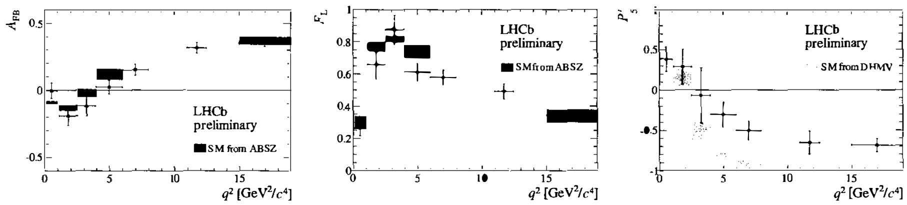

Figure 3 – Distributions of selected angular observables measured in the $B_d^0 \to K^*\mu^+\mu^-$ decay by LHCb[15]. Data points are shown in black while theoretical predictions are shown in purple and orange for Ref. [17,18] and Ref. [19], respectively.

References

1. Christoph Bobeth et al. *Phys. Rev. Lett.*, 112:101801, 2014. [hep-ph/1311.0903]
2. LHCb Collaboration, R. Aaij et al. *Phys. Rev. Lett.*, 110:021801, 2013. [hep-ex/1211.2674]
3. LHCb Collaboration, R. Aaij et al. *Phys. Rev. Lett.*, 111:101805, 2013. [hep-ex/1307.5024]
4. CMS Collaboration, Chatrchyan et al. *Phys. Rev. Lett.*, 111:101804, 2013. [hep-ex/1307.5025]
5. LHCb and CMS Collaborations, V. Khachatryan et al. *Nature*, 10.1038/nature14474, 2015. [hep-ex/1411.4413]
6. LHCb Collaboration, R. Aaij et al. *Phys.Rev.Lett.*, 113:151601, 2014. [hep-ex/1406.6482]
7. Gudrun Hiller and Frank Kruger. *Phys.Rev.*, D69:074020, 2004. [hep-ph/0310219]
8. Chris Bouchard et al. *Phys.Rev.Lett.*, 111(16):162002, 2013. [hep-ph/1306.0434]
9. Sheldon L. Glashow et al. *Phys.Rev.Lett.*, 114:091801, 2015. [hep-ph/1411.0565]
10. Wolfgang Altmannshofer et al. *JHEP*, 0901:019, 2009. [hep-ph/0811.1214]
11. LHCb Collaboration, R. Aaij et al. *JHEP*, 1504:064, 2015. [hep-ex/1501.03038]
12. Sebastian Jager and Jorge Martin Camalich. 2014. [hep-ph/1412.3183]
13. LHCb Collaboration, R. Aaij et al. *JHEP*, 1308:131, 2013. [hep-ex/1304.6325]
14. LHCb Collaboration, R Aaij et al. *Phys.Rev.Lett.*, 111:191801, 2013. [hep-ph/1308.1707]
15. LHCb Collaboration, LHCb-CONF-2015-002, Mar 2015.
16. Sébastien Descotes-Genon et al. *JHEP*, 1305:137, 2013. [hep-ph/1303.5794]
17. Wolfgang Altmannshofer and David M. Straub. 2014. [hep-ph/1411.3161]
18. Aoife Bharucha et al., [hep-ph/1503.05534] 2015.
19. Sébastien Descotes-Genon et al. *JHEP*, 1412:125, 2014. [hep-ph/1407.8526]

$B \to K^* \mu\mu$: theory interpretation or *A hitchiker's guide to* $B \to K^* \mu\mu$ *optimised observables*[a]

S. Descotes-Genon[1], L. Hofer[2], J. Matias[2] and J. Virto[3]

[1] *Laboratoire de Physique Théorique, CNRS/Univ. Paris-Sud (UMR 8627) 91405 Orsay Cedex, France*

[2] *Universitat Autònoma de Barcelona, 08193 Bellaterra, Barcelona*

[3] *Theoretische Physik 1, Naturwissenschaftlich-Technische Fakultät, Univ. Siegen, 57068, Germany*

We discuss the role and advantages of the different $B \to K^*\mu\mu$ optimised observables, defined to have little sensitivity to hadronic (form factor) input. We focus on the sensitivity of each observable to short-distance Wilson coefficients.

1 Motivation and interest of $B \to K^* \mu\mu$

Flavour-Changing Neutral Currents (FCNC) have been prominent tools in high-energy physics to search for new degrees of freedom, due to their quantum sensitivity to energies much higher than the external particles involved. In the current context where the LHC has discovered a scalar boson completing the Standard Model (SM) picture but no additional particles that would go beyond this framework, FCNC can be instrumental in order to determine in which direction to look for New Physics (NP). One particularly interesting instance of FCNC is provided by $b \to s\ell\ell$ and $b \to s\gamma$ transitions, which can be probed through various decay channels, currently studied in detail at the LHC, in particular at the LHCb and CMS experiments.

Indeed, recent experimental results have shown interesting deviations from the Standard Model. In 2013, the LHCb collaboration announced the measurement of angular observables describing the decay $B \to K^*\mu\mu$ in both regions of low and large-K^* recoils [1]. Two observables, P_2 and P_5', were in significant disagreement with the SM expectations in the large-K^* recoil region [2]. A few months later, an improved measurement of the branching ratio for $B \to K\mu\mu$ at large recoil turned out to be on the low side compared to theoretical expectations [3], as well as the branching ratios of $B \to K^*\mu\mu$ and $B_s \to \phi\mu\mu$ at low recoil [3,4,5]. Another measurement has also raised a lot of attention recently, namely $R_K = Br(B \to K\mu\mu)/Br(B \to Kee)$, measured by LHCb, and showing a significantly lower result than its SM prediction equal to 1 (up to a very good accuracy) [6]. In the Moriond 2015 conference, a new analysis of $B \to K^*\mu\mu$ was presented with an extended data set (3 fb^{-1}), confirming the pattern of deviations observed with a restricted set of data [7].

The presence of very different scales for the external states (at most $O(m_b)$) and the internal degrees of freedom ($O(M_W)$ or above) allows for model-independent analyses relying on the effective Hamiltonian approach. The latter is obtained by focusing on $b \to s$ transitions and integrating out all heavy degrees of freedom, leading to (in the case of the SM):

$$\mathcal{H}^{SM} = -\frac{4G_F}{\sqrt{2}} \left\{ V_{tb}V_{ts}^*[C_1 Q_1^c + C_2 Q_2^c + \sum_{i=3...10} C_i Q_i] + V_{tu}V_{us}^*[C_1(Q_1^c - Q_1^u) + C_2(Q_2^c - Q_2^u)] \right\} \quad (1)$$

[a] Based on talks given by J. Matias at Moriond 2015 Electroweak session and by S. Descotes-Genon at Moriond 2015 QCD session.

up to contributions suppressed by additional powers of m_b/M_W. The Wilson coefficients C_i describe the short-distance physics (function of $m_t, m_W \ldots$ in the SM) whereas the local operators Q_i correspond to long-distance physics involving only light/soft degrees of freedom. In this framework, $b \to s$ transitions are mainly described by $Q_7 = e/(4\pi)^2 \bar{s}\sigma^{\mu\nu}(1+\gamma_5)F_{\mu\nu}\, b$, related to the emission of a real or soft photon, $Q_9 = e^2/(4\pi)^2 \bar{s}\gamma_\mu(1-\gamma_5)b\ \bar{\ell}\gamma_\mu\ell$ involved in $b \to s\mu\mu$ via the emission of a Z boson or a hard photon, and $Q_{10} = e^2/(4\pi)^2 \bar{s}\gamma_\mu(1-\gamma_5)b\ \bar{\ell}\gamma_\mu\gamma_5\ell$ involved in $b \to s\mu\mu$ via the emission of a Z boson. The value of the Wilson coefficients can be obtained by matching the SM at a high-energy scale $\mu_0 = O(m_t)$ and evolving down at $\mu_{\text{ref}} = O(m_b)$ (usually 4.8 GeV, with typical values $C_7^{SM} = -0.29$, $C_9^{SM} = 4.1$, $C_{10}^{SM} = -4.3$).

The presence of NP can alter this picture by modifying the value of the Wilson coefficients $C_{7,9,10}$, but also by allowing new long-distance operators Q_i, which would be very suppressed or absent in the SM. This yields the chirally-flipped operators $Q_{7',9',10'}$ (obtained for instance by a heavy spin-1 boson coupling to right-handed fermions), scalar and pseudoscalar operators $Q_{S,S',P,P'}$ (induced, e.g., by the exchange of charged scalar or pseudoscalar Higgs-like bosons) or tensor operators $Q_{T,T'}$ (allowed in principle, but difficult to generate in viable models). These NP contributions are expressed as $C_i = C_i^{SM} + \delta C_i$ at μ_{ref}. An accurate extraction of short-distance physics requires a good understanding of long-distance physics, and in particular QCD effects. In some kinematic configurations (either low or large recoil of the K^* meson), one can use effective theories to separate soft and hard physics, in order to build observables with a limited sensitivity to hadronic uncertainties, or so-called optimised observables [8,9,10,11,12]. Additional studies have been performed in order to assess long-distance effects that could contribute, in particular the charm resonances and loop contributions, the form factors, and the power corrections in the effective-field theory approach [13,14,15]. These elements have been combined in global fits of $b \to s\ell\ell$ Wilson coefficients, with different sets of observables and statistical approaches [16,17,18]. They point towards a large negative contribution to C_9, amounting to 25% of its SM value, leaving open the possibility of large contributions to other Wilson coefficients.

Each optimised observable does play a different role in such fits, pulling the Wilson coefficients in different directions in order to increase the agreement of predictions with LHCb data compared to the SM result. We are going to review their role in this proceeding.

2 $B \to K^*\mu\mu$ observables: Optimised basis

Due to its particularly rich kinematics [19], the $B \to K^*\mu\mu$ decay provides 12 angular coefficients, corresponding to interferences between 8 transversity amplitudes, generally labelled in relation to the polarisation of the K^*-meson and/or the chirality of the dilepton pair ($A_{0,\perp,\|}^{L,R}$ and A_t, A_S). However, if lepton masses or scalars are not considered, not all angular coefficients carry independent information: the corresponding redundancies can be worked out thanks to the analysis of symmetries of the transversity amplitudes that leave the angular coefficients invariant [20,21]. In this scenario one can show that only 8 independent observables can be built, out of which 6 optimised observables can be chosen, namely $P_1, P_2, P_3, P_4', P_5', P_6'$. The remaining two observables can be chosen, for instance, to be the (differential) branching ratio and longitudinal polarisation. For a complete phenomenological description, the previous set of P-wave observables should be complemented with a set of S-wave independent observables [22,23,24] associated to $B \to K_0^*\mu^+\mu^-$ where K_0^* is a broad scalar resonance. We will now focus on the optimised observables of the P-wave sector, which exhibit the largest sensitivity to short-distance physics.

2.1 P_1 or A_T^2

The definition in terms of amplitudes is [8]

$$P_1 = A_T^{(2)} = \frac{|A_\perp|^2 - |A_\||^2}{|A_\perp|^2 + |A_\||^2} \tag{2}$$

where in this definition and all the following ones, it should be understood that each term has associated the corresponding CP conjugated term, with the notation $|A_i|^2 = |A_i^L|^2 + |A_i^R|^2 + |\bar{A}_i^L|^2 + |\bar{A}_i^R|^2$. Lepton, scalar and tensor terms are neglected. This observable is particularly suited to detect the presence of right-handed currents. The left-handed structure of the SM implies that the s quark produced in the decay of the b quark will be in a helicity state of $-1/2$ (neglecting the s-quark mass). The combination of the s quark with the spectator quark generates a K^*-meson with helicity -1 or 0, but not $+1$. The suppression of $H_{+1} = (A_\perp + A_\|)/\sqrt{2} \simeq 0$ implies $A_\perp \simeq -A_\|$ and consequently $P_1^{\rm SM} \simeq 0$. Deviations from this prediction would signal contributions from a new right-handed structure. In Table 1 we present how $\langle P_1\rangle_{[0.1,0.98]}$, $\langle P_1\rangle_{[6,8]}$ and $\langle P_1\rangle_{[15,19]}$ are affected by shifting one Wilson coefficient at a time. Only significant changes are indicated, and shifts improving the agreement with data are indicated in boldface. As expected, changing Wilson coefficients for SM operators (not carrying a right-handed structure) does not induce any sizeable shift. The first bin of P_1 exhibits the largest sensitivity to C_7'. Contrary to most observables, P_1 is also rather sensitive to New Physics at low recoil.

2.2 $\underline{P_4'}$

The definition is [11,12]

$$P_4' = \sqrt{2}\frac{\mathrm{Re}(A_0^L A_\|^{L*} + A_0^R A_\|^{R*})}{\sqrt{|A_0|^2(|A_\perp|^2 + |A_\||^2)}} \tag{3}$$

Together with P_5', this observable establishes bounds on P_1 or enters in consistency relations. In particular, the bound

$$P_5'^2 - 1 \le P_1 \le 1 - P_4'^2 \tag{4}$$

works very efficiently in two bins: [6,8] and low-recoil. In the first case, the preference of data for $P_4' \ge 1$ in the [6,8] bin requires $P_1 \le 0$, in agreement with 2015 data (notice that in 2013 data P_1 was positive in the bin [4.3,8.68]). In the second case, taking the central values of the low-recoil bin as an illustration, one finds that $-0.54 \le P_1 \le -0.44$ again in the right ballpark as compared to the measurement $P_1 \simeq -0.50$. Strictly speaking, this is a bound on the unbinned observables, but they can be adapted for binned observables in the case where the observables are slowly varying with q^2, providing important cross-checks among the LHCb measurements.

2.3 $\underline{P_2}$

The definition is [12,10]

$$P_2 = \frac{\mathrm{Re}(A_\|^L A_\perp^{L*} - A_\|^R A_\perp^{R*})}{|A_\perp|^2 + |A_\||^2} \tag{5}$$

This observable is the optimised and clean version of the forward-backward asymmetry, and it was originally [10] called $A_T^{re} = 2P_2$. It highlights the correlation among A_{FB} and F_L, with a low sensitivity to choices of form factors compared to these observables. Indeed, the prediction for A_{FB} and F_L depends strongly on the parametrisation of form factors used, and the ratio of errors between two commonly used parametrizations, for some bins of A_{FB} or F_L can be as large [25] as a factor 3 or 4. On the contrary, in the case of P_2, besides a shift in central values due to the different central value predictions of the form factors (induced by leading-order power corrections included in our predictions), the ratio of errors is near one showing its robustness and low dependence of this observable on the details of the parametrization.

The observable P_2 contains three relevant elements of information: the position of its zero q_0^2, the position q_1^2 of its maximum, and the value of P_2 at q_1^2. At leading order, assuming no

Table 1: Impact for a given observable of the shift of one of the Wilson coefficients by an amount δC_i (the other Wilson coefficients keeping their SM value). The first row corresponds to the variation due to a positive shift δC_i and the second row to a negative shift by the same amount. The changes improving the agreement of predictions with the 2015 LHCb data are written in boldface. Double "-" means variations below 0.03, only those in $\langle P_2\rangle_{[2.5,4]}$ are provided explicitly.

$\langle P_1\rangle_{[0.1,0.98]}$	$\lvert\delta C_7\rvert = 0.1$	$\lvert\delta C_9\rvert = 1$	$\lvert\delta C_{10}\rvert = 1$	$\lvert\delta C_{7'}\rvert = 0.1$	$\lvert\delta C_{9'}\rvert = 1$	$\lvert\delta C_{10'}\rvert = 1$
$+\lvert\delta C_i\rvert$	--	--	--	**−0.53**	−0.05	--
$-\lvert\delta C_i\rvert$	--	--	--	+0.52	+0.05	--
$\langle P_1\rangle_{[6,8]}$	$\lvert\delta C_7\rvert = 0.1$	$\lvert\delta C_9\rvert = 1$	$\lvert\delta C_{10}\rvert = 1$	$\lvert\delta C_{7'}\rvert = 0.1$	$\lvert\delta C_{9'}\rvert = 1$	$\lvert\delta C_{10'}\rvert = 1$
$+\lvert\delta C_i\rvert$	--	--	--	+0.11	+0.16	**−0.37**
$-\lvert\delta C_i\rvert$	--	--	--	**−0.12**	**−0.16**	+0.37
$\langle P_1\rangle_{[15,19]}$	$\lvert\delta C_7\rvert = 0.1$	$\lvert\delta C_9\rvert = 1$	$\lvert\delta C_{10}\rvert = 1$	$\lvert\delta C_{7'}\rvert = 0.1$	$\lvert\delta C_{9'}\rvert = 1$	$\lvert\delta C_{10'}\rvert = 1$
$+\lvert\delta C_i\rvert$	--	--	--	**+0.03**	**+0.15**	−0.14
$-\lvert\delta C_i\rvert$	--	--	--	−0.03	−0.11	**+0.19**
$\langle P_4'\rangle_{[6,8]}$	$\lvert\delta C_7\rvert = 0.1$	$\lvert\delta C_9\rvert = 1$	$\lvert\delta C_{10}\rvert = 1$	$\lvert\delta C_{7'}\rvert = 0.1$	$\lvert\delta C_{9'}\rvert = 1$	$\lvert\delta C_{10'}\rvert = 1$
$+\lvert\delta C_i\rvert$	**+0.04**	--	--	−0.11	−0.10	**+0.17**
$-\lvert\delta C_i\rvert$	−0.05	--	--	**+0.09**	**+0.10**	−0.20
$\langle P_4'\rangle_{[15,19]}$	$\lvert\delta C_7\rvert = 0.1$	$\lvert\delta C_9\rvert = 1$	$\lvert\delta C_{10}\rvert = 1$	$\lvert\delta C_{7'}\rvert = 0.1$	$\lvert\delta C_{9'}\rvert = 1$	$\lvert\delta C_{10'}\rvert = 1$
$+\lvert\delta C_i\rvert$	--	--	--	--	**−0.06**	+0.05
$-\lvert\delta C_i\rvert$	--	--	--	--	+0.04	**−0.08**
$\langle P_2\rangle_{[2.5,4]}$	$\lvert\delta C_7\rvert = 0.1$	$\lvert\delta C_9\rvert = 1$	$\lvert\delta C_{10}\rvert = 1$	$\lvert\delta C_{7'}\rvert = 0.1$	$\lvert\delta C_{9'}\rvert = 1$	$\lvert\delta C_{10'}\rvert = 1$
$+\lvert\delta C_i\rvert$	−0.31	−0.21	**+0.05**	−0.01	−0.01	−0.02
$-\lvert\delta C_i\rvert$	**+0.19**	**+0.15**	−0.04	−0.03	--	--
$\langle P_2\rangle_{[6,8]}$	$\lvert\delta C_7\rvert = 0.1$	$\lvert\delta C_9\rvert = 1$	$\lvert\delta C_{10}\rvert = 1$	$\lvert\delta C_{7'}\rvert = 0.1$	$\lvert\delta C_{9'}\rvert = 1$	$\lvert\delta C_{10'}\rvert = 1$
$+\lvert\delta C_i\rvert$	−0.07	−0.09	−0.06	--	--	--
$-\lvert\delta C_i\rvert$	**+0.11**	**+0.17**	**+0.05**	--	--	--
$\langle P_5'\rangle_{[.1,.98]}$	$\lvert\delta C_7\rvert = 0.1$	$\lvert\delta C_9\rvert = 1$	$\lvert\delta C_{10}\rvert = 1$	$\lvert\delta C_{7'}\rvert = 0.1$	$\lvert\delta C_{9'}\rvert = 1$	$\lvert\delta C_{10'}\rvert = 1$
$+\lvert\delta C_i\rvert$	**−0.07**	**−0.10**	**−0.08**	**−0.23**	+0.08	+0.09
$-\lvert\delta C_i\rvert$	+0.04	+0.11	+0.05	+0.16	**−0.07**	**−0.13**
$\langle P_5'\rangle_{[4,6]}$	$\lvert\delta C_7\rvert = 0.1$	$\lvert\delta C_9\rvert = 1$	$\lvert\delta C_{10}\rvert = 1$	$\lvert\delta C_{7'}\rvert = 0.1$	$\lvert\delta C_{9'}\rvert = 1$	$\lvert\delta C_{10'}\rvert = 1$
$+\lvert\delta C_i\rvert$	−0.11	−0.15	−0.10	−0.11	−0.06	**+0.21**
$-\lvert\delta C_i\rvert$	**+0.16**	**+0.28**	**+0.09**	**+0.15**	**+0.10**	−0.21
$\langle P_5'\rangle_{[6,8]}$	$\lvert\delta C_7\rvert = 0.1$	$\lvert\delta C_9\rvert = 1$	$\lvert\delta C_{10}\rvert = 1$	$\lvert\delta C_{7'}\rvert = 0.1$	$\lvert\delta C_{9'}\rvert = 1$	$\lvert\delta C_{10'}\rvert = 1$
$+\lvert\delta C_i\rvert$	−0.04	−0.07	−0.07	−0.08	−0.08	**+0.19**
$-\lvert\delta C_i\rvert$	**+0.07**	**+0.19**	**+0.09**	**+0.10**	**+0.11**	−0.18
$\langle P_5'\rangle_{[15,19]}$	$\lvert\delta C_7\rvert = 0.1$	$\lvert\delta C_9\rvert = 1$	$\lvert\delta C_{10}\rvert = 1$	$\lvert\delta C_{7'}\rvert = 0.1$	$\lvert\delta C_{9'}\rvert = 1$	$\lvert\delta C_{10'}\rvert = 1$
$+\lvert\delta C_i\rvert$	--	--	--	**−0.03**	**−0.11**	+0.12
$-\lvert\delta C_i\rvert$	--	+0.06	+0.03	+0.03	+0.10	**−0.14**

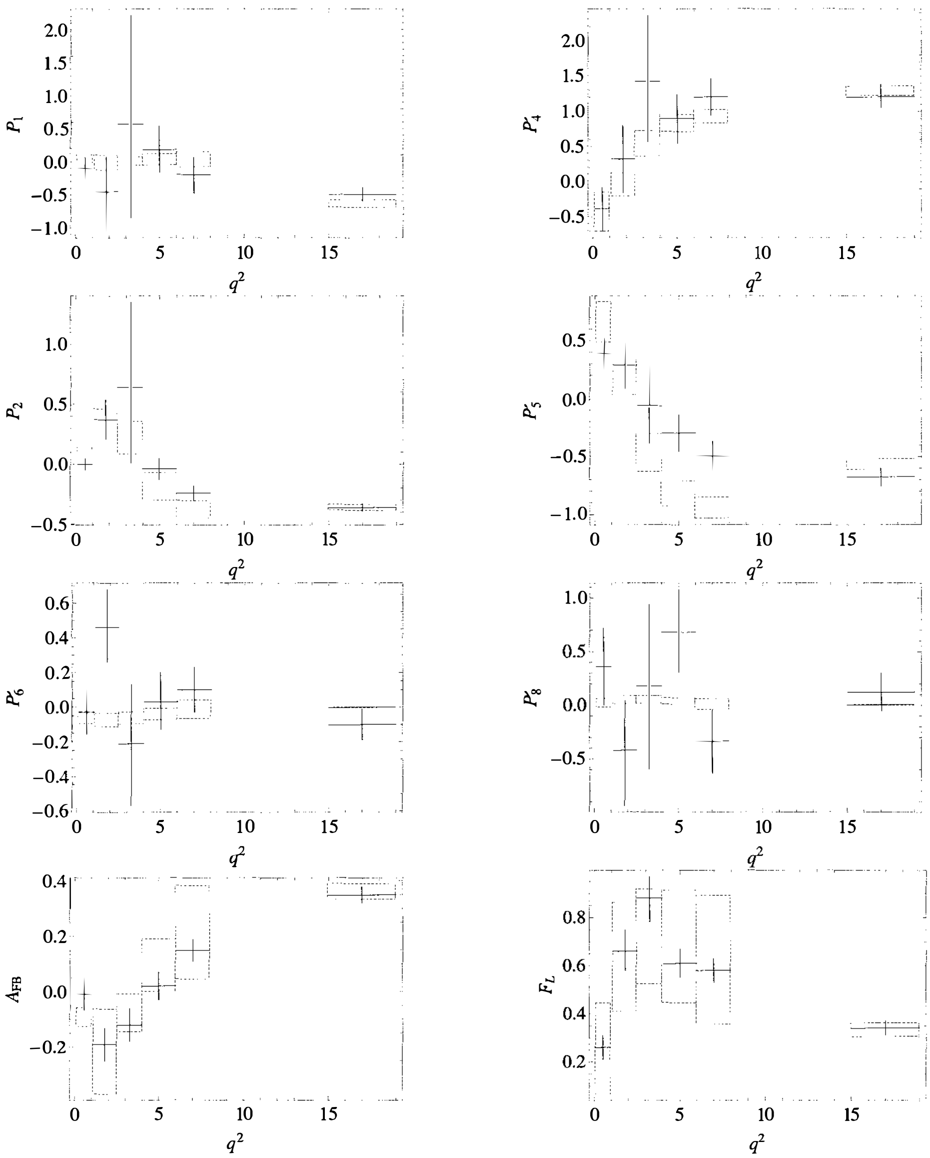

Figure 1 – Set of optimised $B \to K^* \mu\mu$ observables: crosses represent the latest LHCb results and boxes our SM predictions computed using KMPW form factors and including a long-distance charm contribution.

contribution from right-handed currents, i.e., $C_i' = 0$ the first two quantities are given by:

$$q_0^{2\,LO} = -2\frac{m_b M_B C_7^{\rm eff}}{C_9^{\rm eff}(q_0^2)} \quad \text{and} \quad q_1^{2\,LO} = -2\frac{m_b M_B C_7^{\rm eff}}{{\rm Re}C_9^{\rm eff}(q_1^2) - C_{10}} \tag{6}$$

where for the position of the maximum we have neglected a term of $\mathcal{O}({\rm Im}(C_9^{\rm eff})^2)$ following [22]. These expressions illustrate that a NP contribution to C_9 and C_7 would shift both the zero and the maximum of P_2, but with a different magnitude. The position of the maximum can be also shifted via a C_{10} contribution. It was found in [10,22] that a NP contribution to the SM Wilson coefficients $C_{7,9,10}$ can only shift the position of the maximum but not the value of the observable that is fixed at $P_2^{max} = 1/2$. On the contrary, the presence of NP contributions into the chirally flipped operators would reduce the maximum below 1/2, though not by a large amount. Unfortunately, a fluctuation of the $\langle F_L\rangle_{[2.5,4]}$ bin has induced a large experimental error in the corresponding bin of P_2, and the discussion remains inconclusive for the moment.

In Table 1 we show the sensitivity to shifts of Wilson coefficients in the [6,8] bin. The sensitivity of this observable to NP at low recoil is small. At large recoil, one should remark that the same shifts of the Wilson coefficients moving $\langle P_2\rangle_{[6,8]}$ towards data also improves the agreement of $\langle P_2\rangle_{[2.5,4]}$ with data (assuming that data is above the SM) except for C_{10} (whose impact is small in any case). On the other hand, chirally flipped coefficients (positive or negative) shift down the value of the observable in this bin (though by a relatively small amount).

Finally, P_2 offers further consistency checks based on the relation [26]

$$P_2 = \frac{1}{2}\left[P_4' P_5' + \sqrt{(-1 + P_1 + P_4'^2)(-1 - P_1 + P_5'^2)}\right]. \tag{7}$$

The first check stems from the reality of the square root in the previous equation. If we take a bin where $P_2 = -\epsilon$ (with $\epsilon > 0$), one must have

$$P_5' \leq -2\epsilon/P_4' \tag{8}$$

Considering the [6,8] bin and taking the central values $\langle P_2\rangle_{[6,8]} \sim -0.24 \equiv -\epsilon$ and $\langle P_4'\rangle_{[6,8]} \sim 1.20$, one obtains $\langle P_5'\rangle_{[6,8]} \leq -0.4$, in fair agreement with the measurement $\langle P_5'\rangle_{[6,8]} \sim -0.5$. More generally, eq. (8) implies a specific order [25] for $\langle P_2\rangle_{[6,8]}$ and $\langle P_5'\rangle_{[6,8]}$ which is nicely fulfilled by the current data. A similar reasoning holds in the [4,6] bin.

A second check is related to the zero in eq. (7). At the position q_0^2 of the zero of P_2 (or A_{FB}) the following relation should be fulfilled [26]:

$$[P_4'^2 + P_5'^2]_{q_0^2} = 1 - \eta(q_0^2) \tag{9}$$

with $\eta(q_0^2) = [P_1^2 + P_1(P_4'^2 - P_5'^2)]_{q^2=q_0^2}$. If we consider the [4,6] bin, $\langle P_2\rangle_{[4,6]}$ is close to zero. As an illustration, let us assume that q_0^2 is near the center of the bin, i.e., 5 GeV^2 (this will be measured with precision using the amplitude method analysis [27]). Considering the central values as a raw estimate to test this relation $\langle P_5'\rangle_{[4,6]} \sim -0.30$, $\langle P_4'\rangle_{[4,6]} \sim +0.90$ and $\langle P_1\rangle_{[4,6]} \sim +0.18$, the left-hand side of eq. (9) yields 0.90 while the right-hand side is 0.84. Even though there is a good agreement, let us remind again that this relation is valid for the unbinned observables and so the binning induces an error, besides the necessary inclusion of the error bars.

2.4 P_5'

The definition is [11,12]

$$P_5' = \sqrt{2}\frac{{\rm Re}(A_0^L A_\perp^{L*} - A_0^R A_\perp^{R*})}{\sqrt{|A_0|^2(|A_\perp|^2 + |A_\parallel|^2)}} \tag{10}$$

In the current data from LHCb, this observable exhibits the largest deviations with respect to the SM prediction in some bins, the so-called "anomaly" [2] illustrated in Fig. 1. Interestingly, this observable can receive large NP contributions without spoiling the good agreement of P_4' data with SM predictions: in Table 1 the large impact of a variation of C_9 in P_5' corresponds to a negligible effect on P_4' in the [6,8] bin.

Two mechanisms may enforce a larger impact of NP in P_5' with respect to P_4'. The first mechanism consists in weakening the suppression of the right-handed amplitudes with respect to the left-handed amplitudes, in order to profit from the relative minus sign between the two terms in the numerator of P_5' (compared to the plus sign in P_4'). The SM suppression of the right-handed amplitudes is due to the numerical coincidence $C_9^{\rm SM} \sim -C_{10}^{\rm SM}$, which is altered if only one of the two coefficients, say C_9, receives a NP contribution. The second mechanism consists in introducing a NP contribution reducing the size of $A_\perp^L$ in the numerator but keeping the other transversity amplitudes untouched, leading to a significant (minor) change in P_5' (P_4').

In Table 1 we show the sensitivity to shifts of Wilson coefficients for the [4,6], [6,8] and low-recoil bins. One notices the large sensitivity of $\langle P_5'\rangle_{[6,8]}$ to an additional $C_9^{\rm NP}$ as compared to $\langle P_4'\rangle_{[6,8]}$, in agreement with the data. Moreover, all Wilson coefficients have a large impact in this bin as compared to other bins and observables. Similar results are found for $\langle P_5'\rangle_{[4,6]}$. The first large-recoil bin exhibits an interesting sensitivity to C_7', even though lepton mass effects [24,28] affect this first bin (as well as other observables in the same bin). At low recoil, $\langle P_5'\rangle_{[15,19]}$ is more sensitive to NP than other observables in this region, but not as much as at large recoil.

2.5 P_3, P_6' and P_8'

The last optimised observables are defined as [11,12]

$$P_6' = -\sqrt{2}\frac{{\rm Im}(A_0^L A_\parallel^{L*} - A_0^R A_\parallel^{R*})}{\sqrt{|A_0|^2(|A_\perp|^2+|A_\parallel|^2)}} \quad P_8' = -\sqrt{2}\frac{{\rm Im}(A_0^L A_\perp^{L*} + A_0^R A_\perp^{R*})}{\sqrt{|A_0|^2(|A_\perp|^2+|A_\parallel|^2)}} \tag{11}$$

and

$$P_3 = -\frac{{\rm Im}(A_\parallel^{L*} A_\perp^L + A_\perp^R A_\parallel^{R*})}{|A_\perp|^2+|A_\parallel|^2} \tag{12}$$

They are mainly sensitive to phases (strong or weak, SM or beyond). A more direct test of new weak phases is the measurement of the $P_i^{\rm CP}$ observables [12]. Present data is compatible with the SM with large error bars including local fluctuations (up to 2 σ for some of the P_6' measurements) that are expected to disappear with more data. This set of observables also are required to fulfill bounds such as : $P_8'^2 - 1 \le P_1 \le 1 - P_6'^2$ (following the same reasoning as the bounds in [26]).

3 Conclusion

Optimised observables for $B \to K^*\mu\mu$ play a prominent role in the search for NP in $b \to s$ transitions. Several analyses have been performed, including some presented at this conference. Our own analysis following our earlier work [2] is under way [28], including experimental and theoretical correlations (they were not included in our results presented at the Moriond 2015 sessions). This study must be performed carefully in order to gauge the impact of correlations for the analysis at different levels (soft form factors, power corrections...).

We will consider the above optimised observables, as well as the branching ratios of $B \to K\mu\mu$, $B_s \to \mu\mu$, $B \to X_s\gamma$, $B \to X_s\mu\mu$, together with observables related to $B \to K^*\gamma$ ($S_{K^*\gamma}$ and A_I). The list of observables to be included is not closed yet: for instance, electronic modes should also be considered [29]. We will take advantage of new determinations of form factors [30] and improved studies of charm effects. This should yield a more complete picture of the Wilson coefficients describing radiative $b \to s$ transitions, and hopefully, this will allow us to disentangle Standard Model and New Physics contributions in these decays.

Acknowledgments

J.M. and L.H. acknowledge support from FPA2011-25948 and the grant 2014 SGR 1450. J.M. is supported in part by the Centro de Excelencia Severo Ochoa SEV- 2012-0234. J.V. is funded by the Deutsche Forschungsgemeinschaft (DFG) within research unit FOR 1873 (QFET).

References

1. R. Aaij *et al.* [LHCb Collaboration], Phys. Rev. Lett. **111** (2013) 191801 [arXiv:1308.1707 [hep-ex]].
2. S. Descotes-Genon, J. Matias and J. Virto, Phys. Rev. D **88** (2013) 074002 [arXiv:1307.5683 [hep-ph]].
3. R. Aaij *et al.* [LHCb Collaboration], JHEP **1406** (2014) 133 [arXiv:1403.8044 [hep-ex]].
4. R. Aaij *et al.* [LHCb Collaboration], JHEP **1307** (2013) 084 [arXiv:1305.2168 [hep-ex]].
5. R. R. Horgan, Z. Liu, S. Meinel and M. Wingate, Phys. Rev. Lett. **112** (2014) 212003 [arXiv:1310.3887 [hep-ph]].
6. R. Aaij *et al.* [LHCb Collaboration], Phys. Rev. Lett. **113** (2014) 151601 [arXiv:1406.6482 [hep-ex]].
7. The LHCb Collaboration [LHCb Collaboration], LHCb-CONF-2015-002, CERN-LHCb-CONF-2015-002; Ch. Langebruch's talk at Moriond 2015 Electroweak session.
8. F. Kruger and J. Matias, Phys. Rev. D **71** (2005) 094009 [hep-ph/0502060].
9. C. Bobeth, G. Hiller and D. van Dyk, JHEP **1007** (2010) 098 [arXiv:1006.5013 [hep-ph]].
10. D. Becirevic and E. Schneider, Nucl. Phys. B **854** (2012) 321 [arXiv:1106.3283 [hep-ph]].
11. S. Descotes-Genon, J. Matias, M. Ramon and J. Virto, JHEP **1301** (2013) 048 [arXiv:1207.2753 [hep-ph]].
12. S. Descotes-Genon, T. Hurth, J. Matias and J. Virto, JHEP **1305** (2013) 137 [arXiv:1303.5794 [hep-ph]].
13. A. Khodjamirian, T. Mannel, A. A. Pivovarov and Y.-M. Wang, JHEP **1009** (2010) 089 [arXiv:1006.4945 [hep-ph]].
14. J. Lyon and R. Zwicky, arXiv:1406.0566 [hep-ph].
15. S. Descotes-Genon, L. Hofer, J. Matias and J. Virto, JHEP **1412** (2014) 125 [arXiv:1407.8526 [hep-ph]] and references within.
16. W. Altmannshofer and D. M. Straub, Eur. Phys. J. C **73** (2013) 2646 [arXiv:1308.1501 [hep-ph]].
17. F. Beaujean, C. Bobeth and D. van Dyk, Eur. Phys. J. C **74** (2014) 2897 [Eur. Phys. J. C **74** (2014) 3179] [arXiv:1310.2478 [hep-ph]].
18. W. Altmannshofer and D. M. Straub, arXiv:1411.3161 [hep-ph]; D. Straub's talk at Moriond 2015 Electroweak session.
19. W. Altmannshofer *et al.* JHEP **0901** (2009) 019 [arXiv:0811.1214 [hep-ph]].
20. U. Egede, T. Hurth, J. Matias, M. Ramon and W. Reece, JHEP **1010** (2010) 056 [arXiv:1005.0571 [hep-ph]].
21. J. Matias, F. Mescia, M. Ramon and J. Virto, JHEP **1204** (2012) 104 [arXiv:1202.4266 [hep-ph]].
22. L. Hofer and J. Matias, arXiv:1502.00920 [hep-ph].
23. D. Becirevic and A. Tayduganov, Nucl. Phys. B **868** (2013) 368 [arXiv:1207.4004 [hep-ph]].
24. J. Matias, Phys. Rev. D **86** (2012) 094024 [arXiv:1209.1525 [hep-ph]].
25. S. Descotes-Genon, L. Hofer, J. Matias and J. Virto, arXiv:1503.03328 [hep-ph].
26. J. Matias and N. Serra, Phys. Rev. D **90** (2014) 3, 034002 [arXiv:1402.6855 [hep-ph]].
27. U. Egede, M. Patel and K. A. Petridis, arXiv:1504.00574 [hep-ph].
28. S. Descotes-Genon, L. Hofer, J. Matias and J. Virto, work in progress.
29. R. Aaij *et al.* [LHCb Collaboration], JHEP **1504** (2015) 064 [arXiv:1501.03038 [hep-ex]].
30. A. Bharucha, D. M. Straub and R. Zwicky, arXiv:1503.05534 [hep-ph].

What we learn from $SU(2) \times U(1)$ gauge invariance about model independent parametrization of new physics (in rare B decays)

RODRIGO ALONOSO, BENJAMIN GRINSTEIN[a] AND JORGE MARTIN CAMALICH
Physics Department, University of California, San Diego, 9500 Gilman Dr.
La Jolla, CA 92093-0319, USA

Effective field theory is ubiquitously used to parametrize the effects of new physics at low energies. When the new physics has a mass gap above the electroweak scale the effective theory is constrained by the requirements of gauge invariance under the electroweak group. We show this gives relations among the coefficients of the low energy effective Lagrangian. It also leads to relations between low and high energy processes. The results are used to severely constraint the Lagrangian for flavor changing neutral processes in rare B decays. In particular terms that can be used to explain the R_K anomaly are severely restricted.

1 Introduction

Now that the higgs boson has been discovered[1] it seems likely that the Standard Model (SM) of electroweak interactions is a good approximation to the correct description of physics at energies up to that of the electroweak scale. In fact, since the LHC has not seen new particles it is likely that any physics beyond the standard model (BSM) is characterized by a higher energy scale, $\Lambda > M_W$, or even $\Lambda \gg M_W$. Hence, for this talk we assume BSM physics is comprised of new degrees of freedom with a mass gap above the electroweak scale, and that the physics below that scale is described by an effective theory consisting of the SM supplemented by interactions that take the form of higher dimension operators characterized ("suppressed") by appropriate powers of the scale Λ. In so doing we are assuming that the electroweak gauge group, $SU(2) \times U(1)$ is linearly realized. There is a higgs doublet field, and its expectation value is responsible for the masses of electroweak vector bosons and of quarks and leptons.

If we are agnostic about BSM physics, and assume only that it is characterized by a scale Λ above that of the low energy physics characteristic of decays of B mesons, we can characterize the BSM interactions by terms in the Lagrangian of dimension higher than 4 suppressed by powers of the scale Λ. This effective Lagrangian description must comply with the requirements of unitarity (hermiticity of the Hamiltonian), locality, Lorentz invariance and symmetry under the unbroken gauge symmetry group, $SU(3)_c$ for color and $U(1)_{em}$ for electromagnetism. We will show,

[a]Speaker

by explicit construction, that this low energy effective theory can contain more independent interactions that a setup characterized by linearly realized electroweak symmetry below a scale $\Lambda \gg M_W$ allows.[2] We will do so only for a limited sector of the theory, that pertaining rare B decays. The method, of course, can be applied to other sectors of the low energy Lagrangian, say, rare K decays. But we have chosen the case of rare B decays both for concreteness and because it allows us to address some recent measurements that indicate deviations from SM expectations, such as in the ratio R_K of the rate for $B \to K\mu\mu$ and $B \to Kee$.

2 The low energy effective theory

The low energy EFT Lagrangian respects $SU(3)_c \times U(1)_{em}$ and is built from the SM content save for the heavier fields: W, Z and Higgs bosons, and the top quark. To leading order in $G_F = 1/(\sqrt{2}v^2)$ the effective Lagrangian for $\Delta B = 1$ processes is[3]

$$\mathcal{L}_{\text{eff}} = -\frac{4G_F}{\sqrt{2}} \sum_{p=u,c} \lambda_{ps}\left(C_1\mathcal{O}_1^p + C_2\mathcal{O}_2^p + \sum_{i=3}^{10} C_i\mathcal{O}_i\right), \tag{1}$$

with $\lambda_{ps} = V_{pb}V_{ps}^*$. The operators $\mathcal{O}_{1,2}^p$, $\mathcal{O}_{3,\ldots,6}$ and $\mathcal{O}_8$ do not contribute to $B_s \to l\bar{l}$ and their contribution to $B \to K^{(*)}l\bar{l}$ requires an electromagnetic interaction. We focus on the electromagnetic penguin, $\mathcal{O}_7 = \frac{e}{(4\pi)^2}\overline{m}_b[\bar{s}\sigma^{\mu\nu}P_R\, b]F_{\mu\nu}$ and the semileptonic operators, $\mathcal{O}_9 = \frac{e^2}{(4\pi)^2}[\bar{s}\gamma_\mu P_L b][\bar{l}\gamma^\mu l]$ and $\mathcal{O}_{10} = \frac{e^2}{(4\pi)^2}[\bar{s}\gamma_\mu P_L b][\bar{l}\gamma^\mu\gamma_5 l]$, where b, s, l stand for the bottom and strange quarks and a charged lepton, respectively, $F_{\mu\nu}$ is the photon field strength, and $P_{R,L} = (1 \pm \gamma_5)/2$.

In addition, BSM physics can generate chirally-flipped ($b_{L(R)} \to b_{R(L)}$) versions of these operators, $\mathcal{O}'_{7,\ldots,10}$, and also four scalar and two tensor operators,[4]

$$\mathcal{O}_S^{(\prime)} = \frac{e^2}{(4\pi)^2}[\bar{s}P_{R(L)}b][\bar{l}l],\; \mathcal{O}_P^{(\prime)} = \frac{e^2}{(4\pi)^2}[\bar{s}P_{R(L)}b][\bar{l}\gamma_5 l], \tag{2}$$

$$\mathcal{O}_T = \frac{e^2}{(4\pi)^2}[\bar{s}\sigma_{\mu\nu}b][\bar{l}\sigma^{\mu\nu}l],\; \mathcal{O}_{T5} = \frac{e^2}{(4\pi)^2}[\bar{s}\sigma_{\mu\nu}b][\bar{l}\sigma^{\mu\nu}\gamma_5 l]. \tag{3}$$

There are only two possible non-vanishing tensor operators because $(\bar{l}\sigma^{\mu\nu}P_R l)(\bar{s}\sigma_{\mu\nu}P_L b) = (\bar{l}\sigma^{\mu\nu}P_L l)(\bar{s}\sigma_{\mu\nu}P_R b) = 0$ identically. These, together with $\mathcal{O}_{7,9,10}$ and $\mathcal{O}'_{7,9,10}$ constitute the most general basis for the Lagrangian describing B_s (semi-)leptonic rare decays at order G_F. The 12 coefficients in the EFT Lagrangian of these distinct operators are *a priori* independent. As we will see, if our BSM assumptions hold the number is reduced to 8.

3 The High Energy Effective Lagrangian

We now assume the operators appearing in the effective Lagrangian are generated by physics at a scale $\Lambda \gg M_W$ so they are manifestly $SU(3)_c \times SU(2)_L \times U(1)_Y$ invariant. It is constructed from gauge fields, chiral fermions doublets $q_L = (u_L, d_L)^T$, $\ell_L = (\nu_L, l_L)^T$ and singlets u_R, d_R and e_R, and since we assume the symmetry is linearly realized, the Higgs doublet H. In the basis in which the down-type Yukawa matrix is diagonal we write $q_d = (u_{jL}V_{jd}^*, d_L)$, $q_s = (u_{jL}V_{js}^*, s_L)$ and $q_b = (u_{jL}V_{jb}^*, b_L)$.

For rare B decays the leading BSM corrections are from operators of dimension 6. The effective Lagrangian takes the form $\mathcal{L}_{BSM} = \frac{1}{\Lambda^2}\sum_i C_i Q_i$. The operators that are relevant to the study of rare (semi-)leptonic decays in the B_q system are either dipole-like, $Q_{dW} = g_2(\bar{q}_s\sigma^{\mu\nu}b_R)\tau^I H\, W_{\mu\nu}^I$, $Q_{dB} = g_1(\bar{q}_s\sigma^{\mu\nu}b_R)HB_{\mu\nu}$, $Q'_{dW} = g_2H^\dagger\tau^I(\bar{s}_R\sigma^{\mu\nu}q_b)W_{\mu\nu}^I$, $Q'_{dB} = g_1H^\dagger(\bar{s}_R\sigma^{\mu\nu}q_b)B_{\mu\nu}$, Higgs-current times fermion-current, $Q_{Hq}^{(1)} = \left(H^\dagger i\overleftrightarrow{D}_\mu H\right)(\bar{q}_s\gamma^\mu q_b)$,

$Q_{Hq}^{(3)} = H^\dagger i(\tau^I \overrightarrow{D}_\mu - \overleftarrow{D}_\mu \tau^I)H(\bar{q}_s \tau^I \gamma^\mu q_b)$, $Q_{Hd} = \left(H^\dagger i \overleftrightarrow{D}_\mu H\right)(\bar{s}_R \gamma^\mu b_R)$ or four-fermion,

$$
\begin{aligned}
Q_{\ell q}^{(1)} &= (\bar{\ell}\gamma_\mu \ell)(\bar{q}_s \gamma^\mu q_b), & Q_{\ell q}^{(3)} &= (\bar{\ell}\gamma_\mu \tau^I \ell)(\bar{q}_s \gamma^\mu \tau^I q_b), & Q_{ed} &= (\bar{l}_R \gamma_\mu l_R)(\bar{s}\gamma^\mu b_R), \\
Q_{\ell d} &= (\bar{\ell}\gamma_\mu \ell)(\bar{s}\gamma^\mu b_R), & Q_{qe} &= (\bar{q}_s \gamma_\mu q_b)(\bar{l}\gamma^\mu l_R), & Q_{\ell edq} &= (\bar{q}_s b_R)(\bar{l}_R \ell), \\
Q'_{\ell edq} &= (\bar{\ell}\, l_R)(\bar{s}_R q_b), & & & & \qquad (4)
\end{aligned}
$$

where color and weak-isospin indices are omitted and τ^I stand for the Pauli matrices in $SU(2)_L$-space.

This Lagrangian cannot be compared still with that of Eq. (1); one has to integrate out the heavy degrees of freedom, *i.e.*, Z, W, t and H, and run it down to μ_b. The first step yields four-fermion and dipole operators of the low energy EFT. Remarkably, no new tensor-like operators (3) appear after integration of W and Z bosons at leading order. By contrast, new contributions to the coefficients of $\mathcal{O}_{9,10}^{(\prime)}$ are indeed generated.

Explicitly, the connection with the Lagrangian of Eq. (1), at the scale M_W is, for scalar and tensor type operators,

$$
C_S^l = -C_P^l = \frac{4\pi^2}{e^2 \lambda_{ts}} \frac{v^2}{\Lambda^2} C_{\ell edq}, \quad C_S^{l\prime} = C_P^{l\prime} = \frac{4\pi^2}{e^2 \lambda_{ts}} \frac{v^2}{\Lambda^2} C'_{\ell edq}, \quad C_T = C_{T5} = 0. \tag{5}
$$

There are similar expression for the dipole and current-current type of leptonic operators which we have given elsewhere.[2] Equation (5) shows explicitly what has been advertised in the introduction: *(i)* Some operators cannot be generated in the EFT ($C_T = C_{T5} = 0$). *(ii)* There are correlations between nonvanishing coefficients ($C_S = -C_P$ and $C'_S = C'_P$). *(iii)* The contributions to some EFT coefficients may be subject to constraints arising purely from high energies (*e.g.*, $Q_{dW}^{(\prime)}$, $Q_{dB}^{(\prime)}$, Q_{Hq} and Q_{Hd} contribute to flavor-violating Z and H decays).

4 Some consequences in rare B decays

The branching fractions $\overline{\mathcal{B}}_{q\ell}$ for the decays $B_q^0 \to l^+ l^-$ have been precisely predicted.[5] The muonic modes have been recently measured by LHCb and CMS.[6] BSM physics gives deviations from unity in the ratios

$$
\overline{R}_{ql} = \frac{\overline{\mathcal{B}}_{ql}}{(\overline{\mathcal{B}}_{ql})_{\rm SM}} \simeq \frac{|C_S - C'_S|^2}{r_{ql}^2} + \left|1 - \frac{C_P - C'_P}{r_{ql}}\right|^2, \tag{6}
$$

where $r_{ql} = 2m_l(m_b + m_q)C_{10}^{SM}/m_{B_q}^2$. We neglect C'_{10} for simplicity. The decay rate is only sensitive to the differences $(C_P - C'_P)$ and $(C_S - C'_S)$ so the sums, $(C_P + C'_P)$ and $(C_S + C'_S)$, need to be constrained through other means. But using, from this work, Eq. (5) in Eq. (6):

$$
\overline{R}_{ql} \simeq \frac{|C_S - C'_S|^2}{r_{ql}^2} + \left|1 - \frac{C_S + C'_S}{r_{ql}}\right|^2. \tag{7}
$$

The resulting bounds are shown as contour plots in Fig. 1.

The scalar operators contribute to the total decay rates $B \to K^{(*)} l^+ l^-$, providing another experimental input to resolve degeneracies. In practice, however, any sensitivity is blurred by the SM contribution which depends on quite uncertain hadronic form factors[9]. As an example, the coefficient $I_6^c(q^2)$ in the angular distribution in the K^* mode is directly proportional to the combination $|C_S - C'_S|^2$, and it is a null test of the SM[10,9] but the contribution is suppressed by m_l so that the observable is not competitive with purely leptonic decays.

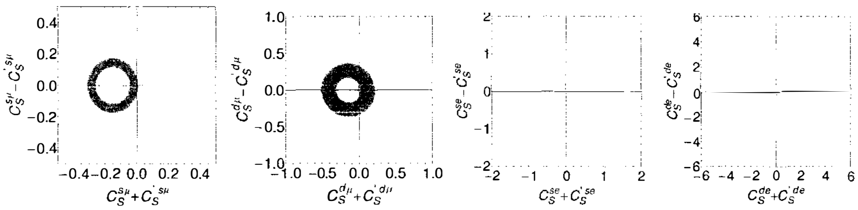

Figure 1 – Form left to right: limits at 68% and 95% C.L. on the scalar Wilson coefficients from $B_s \to \mu^+\mu^-$, $B_d \to \mu^+\mu^-$ and at 95% C.L. from $B_s \to e^+e^-$, $B_d \to e^+e^-$, using data from LHC [6,7] and the Tevatorn.[8]

Lepton (non)-universality. The LHCb collaboration[11] has reported

$$R_K \equiv \frac{\mathrm{Br}\,(B^+ \to K^+\mu\mu)}{\mathrm{Br}\,(B^+ \to K^+ee)} = 0.745^{+0.090}_{-0.074}(\mathrm{stat}) \pm 0.036(\mathrm{syst}). \tag{8}$$

in the [1, 6] GeV^2 bin. The deviation of R_K from unity has 2.6σ significance. Bobeth *et al*[4] show that sizable scalar operators may produce large effects in R_K. Our bounds from $B_q \to \ell\ell$ exclude the possibility of scalar operators accounting for (8): at 95% C.L. we find $0.982 < R_K < 1.007$.

In light of this and the absence of tensors, we conclude that a large lepton universality violation in R_K may only be produced by the operators $\mathcal{O}_9^{(\prime)}$ and $\mathcal{O}_{10}^{(\prime)}$. One possibility is a sizable and negative effect in C_9 affecting only the muonic mode, $\delta C_9^\mu = -1$, yielding $R_K \simeq 0.79$. In the next talk, S. Descotes-Genon will argue that $\delta C_9^\mu = -1$ is necessary to understand other aspects of the current $b \to s\mu\mu$ data set.[12]

Acknowledgments

This work was supported in part by DOE grant DE-SC0009919.

References

1. G. Aad *et al.* [ATLAS Collaboration], Phys. Lett. B **716** (2012) 1; S. Chatrchyan *et al.* [CMS Collaboration], Phys. Lett. B **716** (2012) 30
2. R. Alonso, B. Grinstein, and J. Martin Camalich, Phys. Rev. Lett. **113**, 241802 (2014)
3. B. Grinstein, M. J. Savage and M. B. Wise, Nucl. Phys. B **319**, 271 (1989); G. Buchalla, A. J. Buras and M. E. Lautenbacher, Rev. Mod. Phys. **68**, 1125 (1996); K. G. Chetyrkin, M. Misiak and M. Munz, Phys. Lett. B **400**, 206 (1997) [Erratum-ibid. B **425**, 414 (1998)]
4. C. Bobeth, G. Hiller and G. Piranishvili, JHEP **0712**, 040 (2007)
5. C. Bobeth, *et al.*, Phys. Rev. Lett. **112**, 101801 (2014)
6. R. Aaij *et al.* [LHCb Collaboration], Phys. Rev. Lett. **110**, 021801 (2013) *idem* **111**, 101805 (2013); S. Chatrchyan *et al.* [CMS Collaboration], Phys. Rev. Lett. **111**, 101804 (2013)
7. CMS and LHCb collaborations, CMS-PAS-BPH-13-007, LHCb-CONF-2013.
8. T. Aaltonen *et al.* [CDF Collaboration], Phys. Rev. Lett. **102** (2009) 201801
9. S. Jäger and J. Martin Camalich, JHEP **1305**, 043 (2013) [arXiv:1212.2263 [hep-ph]].
10. W. Altmannshofer, *et al* JHEP **0901**, 019 (2009)
11. R. Aaij *et al.* [LHCb Collaboration], arXiv:1406.6482 [hep-ex].
12. S. Descotes-Genon, J. Matias and J. Virto, Phys. Rev. D**88**, 074002 (2013); W. Altmannshofer and D. M. Straub, Eur. Phys. J. C**73** 2646 (2013); R. R. Horgan, *et al*,Phys. Rev. Lett. **112** 212003 (2014) F. Beaujean, C. Bobeth and D. van Dyk, arXiv:1310.2478;

Explaining the LHC flavour anomalies

ANDREAS CRIVELLIN
CERN Theory Division, CH-1211 Geneva 23, Switzerland

The LHC observed deviations from the Standard Model (SM) in the flavour sector: LHCb found a 4.3 σ discrepancy compared to the SM in $b \to s\mu\mu$ transitions and CMS reported a non-zero measurement of $h \to \mu\tau$ with a significance of 2.4 σ. Here we discuss how these deviations from the SM can be explained, focusing on two models with gauged $L_\mu - L_\tau$ symmetry. The first model contains two scalar doublets and vector-like quarks while the second one employs three scalar doublets but does not require vector-like fermions. In both models, interesting correlations between $b \to s\mu\mu$ transitions, $h \to \mu\tau$, and $\tau \to 3\mu$ arise.

1 Introduction

The LHC completed the SM by discovering the Brout–Englert–Higgs particle [1,2]. While no significant direct evidence for physics beyond the SM has been found, the LHC did observe 'hints' for new physics (NP) in the flavor sector, which are sensitive to virtual effects of new particles and can be used as guidelines towards specific NP models: $h \to \mu\tau$, $B \to K^*\mu^+\mu^-$, $B_s \to \phi\mu^+\mu^-$ and $R(K) = B \to K\mu^+\mu^-/B \to Ke^+e^-$. It is therefore interesting to examine if a specific NP model can explain these four anomalies simultaneously. In Refs. [3,4], two variants of such a model were presented, which we want to review here.

LHCb reported deviations from the SM predictions[5,6] (mainly in an angular observable called P_5' [7]) in $B \to K^*\mu^+\mu^-$ [8] with a significance of 2–3 σ. In addition, the measurement of $B_s \to \phi\mu\mu$ disagrees with the SM predictions by about 3 σ [9,10]. This discrepancy can be explained in a model independent approach by rather large contributions to the Wilson coefficient C_9 [11,12,9], i.e. an operator $(\bar{s}\gamma_\alpha P_L b)(\bar{\mu}\gamma^\alpha\mu)$, which can be achieved in models with an additional heavy neutral Z' gauge boson [13,14,15,16,17]. Furthermore, LHCb [18] recently found indications for the violation of lepton flavour universality in B meson decays

$$R(K) = \frac{B \to K\mu^+\mu^-}{B \to Ke^+e^-} = 0.745^{+0.090}_{-0.074} \pm 0.036\,, \tag{1}$$

which disagrees from the theoretically rather clean SM prediction $R_K^{\rm SM} = 1.0003 \pm 0.0001$ [19] by 2.6 σ. A possible explanation is again a NP contributing to $C_9^{\mu\mu}$ involving muons, but not electrons [20,21,22]. Interestingly, the value for C_9 required to explain $R(K)$ is of the same order as the one required by $B \to K^*\mu^+\mu^-$ [23,24]. The global fit to the $b \to s\mu\mu$ data presented at this conference gives a 4.3σ better fit to data for the assumption of NP in $C_9^{\mu\mu}$ only, compared to the SM fit [25].

Concerning Higgs decays, CMS measured a lepton-flavour violating (LFV) channel[26] $\mathrm{Br}[h \to \mu\tau] = (0.84^{+0.39}_{-0.37})$ which disagrees from the SM (where this decay is forbidden) by about 2.4σ. Most attempts to explain this decay rely on models with an extended Higgs sector [27,28,29,30,31]. One particular interesting solution employs a two-Higgs-doublet model (2HDM) with gauged $L_\mu - L_\tau$ [32].

2 The models

Our models under consideration are multi-Higgs-doublet models with a gauged $U(1)_{L_\mu - L_\tau}$ symmetry [32,a]. The $L_\mu - L_\tau$ symmetry with the gauge coupling g' is broken spontaneously by the vacuum expectation value (VEV) of a scalar Φ with $Q^{\Phi}_{L_\mu - L_\tau} = 1$, leading to the Z' mass $m_{Z'} = \sqrt{2}g'\langle\Phi\rangle \equiv g' v_\Phi$ and Majorana masses for the right-handed neutrinos.[b]

In both models at least two Higgs doublets are introduced which break the electroweak symmetry: Ψ_1 with $Q^{\Psi_1}_{L_\mu - L_\tau} = -2$ and Ψ_2 with $Q^{\Psi_2}_{L_\mu - L_\tau} = 0$. Therefore, Ψ_2 gives masses to quarks and leptons while Ψ_1 couples only off-diagonally to $\tau\mu$:

$$\mathcal{L}_Y \supset -\overline{\ell}_f Y_i^\ell \delta_{fi} \Psi_2 e_i - \xi_{\tau\mu} \overline{\ell}_3 \Psi_1 e_2 - \overline{Q}_f Y_{fi}^u \tilde{\Psi}_2 u_i - \overline{Q}_f Y_{fi}^d \Psi_2 d_i + \text{h.c.} \tag{2}$$

Here Q (ℓ) is the left-handed quark (lepton) doublet, u (e) is the right-handed up quark (charged lepton) and d the right-handed down quark while i and f label the three generations. The scalar potential is the one of a $U(1)$-invariant 2HDM [37] with additional couplings to the SM-singlet Φ, which most importantly generate the doublet-mixing term

$$V(\Psi_1, \Psi_2, \Phi) \supset 2\lambda\Phi^2\Psi_2^\dagger\Psi_1 \to \lambda v_\Phi^2 \Psi_2^\dagger \Psi_1 \equiv m_3^2 \Psi_2^\dagger \Psi_1 ,$$

that induces a small vacuum expectation value for Ψ_1 [32]. We define $\tan\beta = \langle\Psi_2\rangle/\langle\Psi_1\rangle$ and α is the usual mixing angle between the neutral CP-even components of Ψ_1 and Ψ_2 (see for example [37]). We neglect the additional mixing of the CP-even scalars with $\mathrm{Re}[\Phi]$.

Quarks and gauge bosons have standard type-I 2HDM couplings to the scalars. The only deviations are in the lepton sector: while the Yukawa couplings $Y_i^\ell \delta_{fi}$ of Ψ_2 are forced to be diagonal due to the $L_\mu - L_\tau$ symmetry, $\xi_{\tau\mu}$ gives rise to an off-diagonal entry in the lepton mass matrix:

$$m_{fi}^\ell = \frac{v}{\sqrt{2}} \begin{pmatrix} y_e \sin\beta & 0 & 0 \\ 0 & y_\mu \sin\beta & 0 \\ 0 & \xi_{\tau\mu}\cos\beta & y_\tau \sin\beta \end{pmatrix} . \tag{3}$$

It is this τ–μ entry that leads to the LFV couplings of h and Z' of interest to this letter. The lepton mass basis is obtained by simple rotations of (μ_R, τ_R) and (μ_L, τ_L) with the angles θ_R and θ_L, respectively:

$$\sin\theta_R \simeq \frac{v}{\sqrt{2}m_\tau}\xi_{\tau\mu}\cos\beta , \qquad \frac{\tan\theta_L}{\tan\theta_R} = \frac{m_\mu}{m_\tau} \ll 1 . \tag{4}$$

The angle θ_L is automatically small and will be neglected in the following.[c] A non-vanishing angle θ_R not only gives rise to the LFV decay $h \to \mu\tau$ due to the coupling

$$\frac{m_\tau}{v}\frac{\cos(\alpha-\beta)}{\cos(\beta)\sin(\beta)} \sin(\theta_R)\cos(\theta_R)\overline{\tau}P_R\mu h \equiv \Gamma^h_{\tau\mu}\overline{\tau}P_R\mu h , \tag{5}$$

[a] The abelian symmetry $U(1)_{L_\mu - L_\tau}$ is an anomaly-free global symmetry within the SM [33], and also a good zeroth-order approximation for neutrino mixing with a quasi-degenerate mass spectrum, predicting a maximal atmospheric and vanishing reactor neutrino mixing angle [34]. Breaking $L_\mu - L_\tau$ is mandatory for a realistic neutrino sector, and such a breaking can also induce charged LFV processes, such as $\tau \to 3\mu$ [35,36] and $h \to \mu\tau$ [32].

[b] Neutrino masses arise via seesaw with close-to-maximal atmospheric mixing and quasi-degenerate masses [32].

[c] Choosing $Q_{L_\mu - L_\tau} = +2$ for Ψ_2 would essentially exchange $\theta_L \leftrightarrow \theta_R$ [32], with little impact on our study.

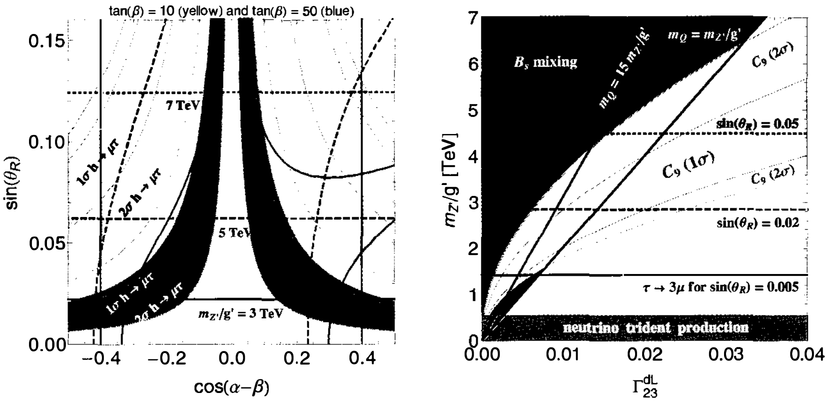

Figure 1 – Left: Allowed regions in the $\cos(\alpha-\beta)$–$\sin(\theta_R)$ plane. The blue (light blue) region corresponds to the 1σ (2σ) region of the CMS measurement of $h \to \mu\tau$ for $\tan\beta = 50$; yellow stands for $\tan\beta = 10$. The (dashed) red contours mark deviations of $h \to \tau\tau$ by 10% compared to the SM for $\tan\beta = 50$ (10). The vertical green lines illustrate the naive LHC limit $|\cos(\alpha-\beta)| \leq 0.4$, horizontal lines denote the 90% C.L. limit on $\tau \to 3\mu$ via Z' exchange. Right: Allowed regions for model 1 in the Γ_{23}^{dL}-$m_{Z'}/g'$ plane from $b \to s\mu^+\mu^-$ data (yellow) and B_s–$\overline{B}_s$ mixing (blue). For B_s–$\overline{B}_s$ mixing, (light) blue corresponds to ($m_Q = 15 m_{Z'}/g'$) $m_Q = m_{Z'}/g'$. The horizontal lines denote the lower bounds on $m_{Z'}/g'$ from $\tau \to 3\mu$ for $\sin(\theta_R) = 0.05,\ 0.02,\ 0.005$. The gray region is excluded by neutrino trident production.

in the Lagrangian, but also leads to off-diagonal Z' couplings to right-handed leptons

$$g' Z'_\nu \,(\bar{\mu}, \bar{\tau}) \begin{pmatrix} \cos 2\theta_R & \sin 2\theta_R \\ \sin 2\theta_R & -\cos 2\theta_R \end{pmatrix} \gamma^\nu P_R \begin{pmatrix} \mu \\ \tau \end{pmatrix}, \tag{6}$$

while the left-handed couplings are to a good approximation flavour conserving. $m_{Z'}/g'$ needs to be in the TeV range in order to suppress $\tau \to 3\mu$ if we want to explain $h \to \mu\tau$ [32] (see Fig. 1 (left)), which gives stronger bounds than neutrino trident production [15]. In order to explain the observed anomalies in the B meson decays, a coupling of the Z' to quarks is required as well, not inherently part of $L_\mu - L_\tau$ models.

3 Model 1: vector-like quarks

In order to couple the Z' to quarks we follow Ref. [15] and generate effective couplings via heavy vector-like quarks [38] charged under $L_\mu - L_\tau$. As a result, the couplings of the Z' to quarks are in principle free parameters and can be parametrized as:

$$g' \left(\bar{d}_i \gamma^\mu P_L d_j Z'_\mu \Gamma_{ij}^{dL} + \bar{d}_i \gamma^\mu P_R d_j Z'_\mu \Gamma_{ij}^{dR} \right). \tag{7}$$

In the limit of decoupled vector-like quarks with the quantum numbers of right-handed quarks, only C_9 is generated, giving a very good fit to data. The results are shown in the right plot of Fig. 1 depicting that for small values of Γ_{sb}^L and θ_R, $b \to s\mu^+\mu^-$ data can be explained without violating bounds from B_s–$\overline{B}_s$ mixing or $\tau \to 3\mu$. In the left plot of Fig. 2 the correlations of $b \to s\mu^+\mu^-$ and $h \to \mu\tau$ with $\tau \to 3\mu$ are shown, depicting that consistency with $\tau \to 3\mu$ requires large values of $\tan\beta$ (not being in conflict with any data as the decoupling limit is a type I model) and future searches for $\tau \to 3\mu$ are promising to yield positive results. While this model predict tiny branching ratios for lepton-flavour-violating B decays, these branching ratios can be sizable in generic Z' models in the presence of fine tuning in the B_s–$\overline{B}_s$ system [39].

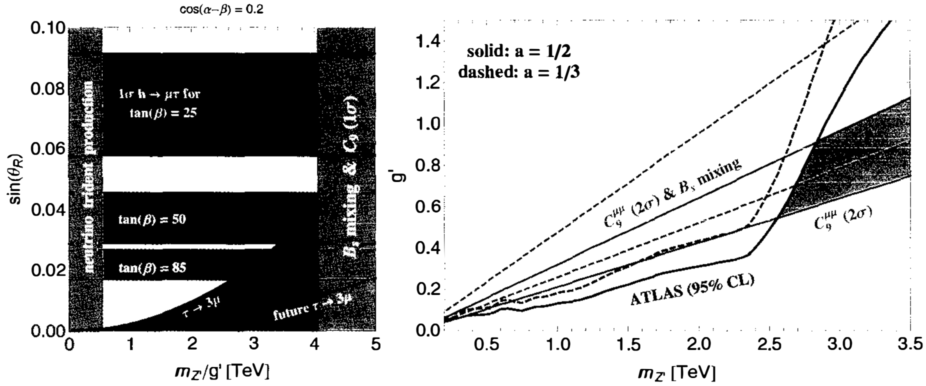

Figure 2 – Left: Allowed regions for model 1 in the $m_{Z'}/g'$–$\sin(\theta_R)$ plane: the horizontal stripes correspond to $h \to \mu\tau$ (1σ) for different $\tan\beta$ and $\cos(\alpha-\beta) = 0.2$, (light) blue stands for (future) $\tau \to 3\mu$ limits at 90% C.L. The gray regions are excluded by neutrino trident production or B_s–$\overline{B}_s$ mixing in combination with the $1\,\sigma$ range for C_9. Right: Limits for model 2 on $q\bar{q} \to Z' \to \mu\bar{\mu}$ from ATLAS (black, allowed region down right) and the $2\,\sigma$ limits on $C_9^{\mu\mu}$ to accommodate $b \to s\mu\mu$ data (allowed regions inside the red cone). Solid (dashed) lines are for $a = 1/2$ $(1/3)$. For $a = 1/2$, the green shaded region is allowed (similar for $a = 1/3$ using the dashed bounds).

4 Model 2: horizontal quark charges

In order to avoid the introduction of vector-like quarks, one can assign flavour-dependent charges to baryons as well[4]. Here, the first two generations should have the same charges in order to avoid very large effects in K–$\overline{K}$ or D–$\overline{D}$ mixing, generated otherwise unavoidably due to the breaking of the symmetry necessary to generate the measured Cabibbo angle of the CKM matrix. If we require in addition the absence of anomalies, we arrive at the following charge assignment for baryons $Q'(B) = (-a,\ -a,\ 2a)$, while leptons are still assigned $L_\mu - L_\tau$. Here $a \in \mathcal{Q}$ is a free parameter of the model with important phenomenological implications. In this model, one additional Higgs doublet, which breaks the flavour symmetry in the quark sector, is required compared to the model with vector-like quarks. In case the mixing among the doublets is small, the correlations among $h \to \mu\tau$, $b \to s\mu^+\mu^-$ and $\tau \to 3\mu$ are similar as in the model with vector-like quarks discussed in the last subsection (left plot of Fig. 2).

The low-energy phenomenology is rather similar to the one of the model with vector-like quarks (model 1), but the contributions to B_s–$\overline{B}_s$ mixing are directly correlated to B_d–$\overline{B}_d$ and K–$\overline{K}$ mixing, because all flavour violation is due to CKM factors. (These constraints are evaded for $a \lesssim 1$.) However, the implications concerning direct LHC searches are very different, as the Z' boson couples to quarks of the first generation and can be directly produced on-shell as a resonance in $p\bar{p}$ collisions. The resulting strong bounds are shown in right plot of Fig. 2, where they are compared to the allowed regions from B_s–$\overline{B}_s$ mixing and $b \to s\mu^+\mu^-$ data for different values of a.

5 Conclusions

In these proceedings we reviewed two variants of a model with a gauged $L_\mu - L_\tau$ symmetry which can explain all LHC anomalies in the flavour sector simultaneously: 1) a 2HDM with effective $Z'\bar{s}b$ couplings induced by heavy vector-like quarks, 2) a 3HDM with horizontal charges for baryons. The models can account for the deviations from the SM in $b \to s\mu^+\mu^-$ data and $h \to \mu\tau$ simultaneously, giving also the desired effect in $R(K)$. Due to the small values of the τ–μ mixing angle θ_R, sufficient to account for $h \to \mu\tau$, the Z' contributions to $\tau \to 3\mu$ are not in conflict with present bounds for large $\tan\beta$ in wide rages of parameter space. Interestingly, $b \to s\mu^+\mu^-$ data combined with B_s–$\overline{B}_s$ put a upper limit on $m_{Z'}/g'$ resulting in a lower limit on $\tau \to 3\mu$ if $\mathrm{Br}[h \to \mu\tau] \neq 0$: for lower values of $\tan\beta$ the current experimental bounds are reached and future sensitivities will allow for a more detailed exploration of the allowed parameter space. The possible range for the $L_\mu - L_\tau$ breaking scale further implies the masses of the Z' and the right-handed neutrinos to be at the TeV scale, potentially testable at the LHC with interesting additional consequences for LFV observables. While the low energy phenomenology of both models is rather similar, the variant with horizontal charges for baryons predicts sizable Z' production rates testable at the next LHC run.

Acknowledgments

We thank the organizers of the invitation to *Moriond QCD* and for the opportunity to present these results. A.C. is supported by a Marie Curie Intra-European Fellowship of the European Community's 7th Framework Programme under contract number (PIEF-GA-2012-326948).

1. Georges Aad et al. Observation of a new particle in the search for the Standard Model Higgs boson with the ATLAS detector at the LHC. *Phys.Lett.*, B716:1–29, 2012.
2. Serguei Chatrchyan et al. Observation of a new boson at a mass of 125 GeV with the CMS experiment at the LHC. *Phys.Lett.*, B716:30–61, 2012.
3. Andreas Crivellin, Giancarlo D'Ambrosio, and Julian Heeck. Explaining $h \to \mu^\pm\tau^\mp$, $B \to K^*\mu^+\mu^-$ and $B \to K\mu^+\mu^-/B \to Ke^+e^-$ in a two-Higgs-doublet model with gauged $L_\mu - L_\tau$. *Phys.Rev.Lett.*, 114:151801, 2015.
4. Andreas Crivellin, Giancarlo D'Ambrosio, and Julian Heeck. Addressing the LHC flavor anomalies with horizontal gauge symmetries. *Phys.Rev.*, D91:075006, 2015.
5. U. Egede, T. Hurth, J. Matias, M. Ramon, and W. Reece. New observables in the decay mode $B_{(d)} \to K^{*0}\ell^+\ell^-$. *JHEP*, 0811:032, 2008.
6. Wolfgang Altmannshofer, Patricia Ball, Aoife Bharucha, Andrzej J. Buras, David M. Straub, et al. Symmetries and Asymmetries of $B \to K^*\mu^+\mu^-$ Decays in the Standard Model and Beyond. *JHEP*, 0901:019, 2009.
7. Sebastien Descotes-Genon, Tobias Hurth, Joaquim Matias, and Javier Virto. Optimizing the basis of $B \to K^*\ell^+\ell^-$ observables in the full kinematic range. *JHEP*, 1305:137, 2013.
8. R Aaij et al. Measurement of Form-Factor-Independent Observables in the Decay $B^0 \to K^{*0}\mu^+\mu^-$. *Phys.Rev.Lett.*, 111(19):191801, 2013.
9. Ronald R. Horgan, Zhaofeng Liu, Stefan Meinel, and Matthew Wingate. Calculation of $B^0 \to K^{*0}\mu^+\mu^-$ and $B_s^0 \to \phi\mu^+\mu^-$ observables using form factors from lattice QCD. *Phys.Rev.Lett.*, 112:212003, 2014.
10. R.R. Horgan, Z. Liu, S. Meinel, and M. Wingate. Rare B decays using lattice QCD form factors. 2015.
11. Sebastien Descotes-Genon, Joaquim Matias, and Javier Virto. Understanding the $B \to K^*\mu^+\mu^-$ Anomaly. *Phys.Rev.*, D88(7):074002, 2013.
12. Wolfgang Altmannshofer and David M. Straub. New physics in $B \to K^*\mu\mu$? *Eur.Phys.J.*, C73(12):2646, 2013.
13. Rhorry Gauld, Florian Goertz, and Ulrich Haisch. On minimal Z' explanations of the $B \to K^*\mu^+\mu^-$ anomaly. *Phys.Rev.*, D89:015005, 2014.
14. Andrzej J. Buras, Fulvia De Fazio, and Jennifer Girrbach. 331 models facing new $b \to s\mu^+\mu^-$ data. *JHEP*, 1402:112, 2014.
15. Wolfgang Altmannshofer, Stefania Gori, Maxim Pospelov, and Itay Yavin. Quark flavor transitions in $L_\mu - L_\tau$ models. *Phys.Rev.*, D89(9):095033, 2014.
16. Christoph Niehoff, Peter Stangl, and David M. Straub. Violation of lepton flavour universality in composite Higgs models. 2015.

17. Sierra D. Aristizabal, Florian Staub, and Avelino Vicente. Shedding light on the $b \to s$ anomalies with a dark sector. 2015.
18. Roel Aaij et al. Test of lepton universality using $B^+ \to K^+\ell^+\ell^-$ decays. *Phys.Rev.Lett.*, 113(15):151601, 2014.
19. Christoph Bobeth, Gudrun Hiller, and Giorgi Piranishvili. Angular distributions of $B \to K\ell\ell$ decays. *JHEP*, 0712:040, 2007.
20. Rodrigo Alonso, Benjamin Grinstein, and Jorge Martin Camalich. $SU(2) \times U(1)$ gauge invariance and the shape of new physics in rare B decays. *Phys.Rev.Lett.*, 113(24):241802, 2014.
21. Gudrun Hiller and Martin Schmaltz. R_K and future $b \to s\ell\ell$ physics beyond the standard model opportunities. *Phys.Rev.*, D90(5):054014, 2014.
22. Diptimoy Ghosh, Marco Nardecchia, and S.A. Renner. Hint of Lepton Flavour Non-Universality in B Meson Decays. *JHEP*, 1412:131, 2014.
23. T. Hurth, F. Mahmoudi, and S. Neshatpour. Global fits to $b \to s\ell\ell$ data and signs for lepton non-universality. *JHEP*, 1412:053, 2014.
24. Wolfgang Altmannshofer and David M. Straub. State of new physics in $b \to s$ transitions. 2014.
25. Wolfgang Altmannshofer and David M. Straub. Implications of $b \to s$ measurements. 2015.
26. Vardan Khachatryan et al. Search for lepton-flavour-violating decays of the Higgs boson. 2015.
27. Avital Dery, Aielet Efrati, Yosef Nir, Yotam Soreq, and Vasja Susi. Model building for flavor changing Higgs couplings. *Phys.Rev.*, D90:115022, 2014.
28. Miguel D. Campos, A. E. Cárcamo Hernández, Heinrich Päs, and Erik Schumacher. Higgs $\to \mu\tau$ as an indication for S_4 flavor symmetry. 2014.
29. Alejandro Celis, Vincenzo Cirigliano, and Emilie Passemar. Disentangling new physics contributions in lepton flavour violating tau decays. 2014.
30. D. Aristizabal Sierra and A. Vicente. Explaining the CMS Higgs flavor violating decay excess. *Phys.Rev.*, D90:115004, 2014.
31. Chao-Jung Lee and Jusak Tandean. Lepton-Flavored Scalar Dark Matter with Minimal Flavor Violation. *JHEP*, 1504:174, 2015.
32. Julian Heeck, Martin Holthausen, Werner Rodejohann, and Yusuke Shimizu. Higgs $\to \mu\tau$ in Abelian and Non-Abelian Flavor Symmetry Models. *Nucl.Phys.*, B896:281–310, 2015.
33. X.G. He, Girish C. Joshi, H. Lew, and R.R. Volkas. NEW Z-prime PHENOMENOLOGY. *Phys.Rev.*, D43:22–24, 1991.
34. Pierre Binetruy, Stephane Lavignac, Serguey T. Petcov, and Pierre Ramond. Quasidegenerate neutrinos from an Abelian family symmetry. *Nucl.Phys.*, B496:3–23, 1997.
35. Gautam Dutta, Anjan S. Joshipura, and K.B. Vijaykumar. Leptonic flavor violations in the presence of an extra Z. *Phys.Rev.*, D50:2109–2115, 1994.
36. Julian Heeck and Werner Rodejohann. Gauged $L_\mu - L_\tau$ Symmetry at the Electroweak Scale. *Phys.Rev.*, D84:075007, 2011.
37. G.C. Branco, P.M. Ferreira, L. Lavoura, M.N. Rebelo, Marc Sher, et al. Theory and phenomenology of two-Higgs-doublet models. *Phys.Rept.*, 516:1–102, 2012.
38. Paul Langacker. The Physics of Heavy Z' Gauge Bosons. *Rev.Mod.Phys.*, 81:1199–1228, 2009.
39. Andreas Crivellin, Lars Hofer, Joaquim Matias, Ulrich Nierste, Stefan Pokorski, et al. Lepton-flavour violating B decays in generic Z' models. 2015.

A NEW LONG DISTANCE CONTRIBUTION TO $B^{\pm} \to K^{\pm}/\pi^{\pm}\ell^{+}\ell^{-}$ DECAYS

A. GUEVARA, G. LÓPEZ CASTRO, P. ROIG, S. L. TOSTADO
Departamento de Física, Cinvestav del IPN, Apdo Postal 14-740, 07000 Mexico DF. Mexico

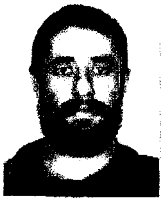

We have identified a missing long-distance (one-photon exchange) contribution to the $B^{\pm} \to K^{\pm}/\pi\ell^{+}\ell^{-}$ decays. Although it does not help to explain the anomaly measured by the LHCb Coll. in the ratio $R_K = \mathcal{B}(B^{\pm} \to K^{\pm}\mu^{+}\mu^{-})/\mathcal{B}(B^{\pm} \to K^{\pm}e^{+}e^{-}) \sim 0.75$ (2.6 σ deviation with respect to $R_K = 1 + \mathcal{O}(10^{-4})$ in the Standard Model), it provides a sizable contribution to the branching ratio of the $B^{\pm} \to \pi^{\pm}\ell^{+}\ell^{-}$ decays. The new decay mechanism gives rise to a measurable CP asymmetry, which is of order 1% in both channels. These predictions can be tested in forthcoming LHCb measurements. All the details can be seen in[1].

1 Introduction

In the search of a more fundamental description of interactions in nature, one has to look for effects that can not be described by the current theory of particle physics, namely the Standard Model (SM). A way to do this is studying the more suppressed processes in the SM, where a deviation from a precise SM prediction is expected to be more significant than in processes that are not suppressed. In order to claim that an effect comes from physics Beyond the SM (BSM) in a certain process, all the SM contribution have to be known and understood at the precision required by experiments. In $B^{\pm} \to K^{\pm}\ell^{+}\ell^{-}$ decays, LHCb[2] has measured the R_K ratio in the $[1,6]$ GeV^2 region of squared lepton pair invariant mass q^2, which is $R_K = 0.745^{+0.090}_{-0.074} \pm 0.036$, while the current SM prediction in the same energy range is[3] $R_K^{SM} = 1 + (3.0^{+1.0}_{-0.7}) \times 10^{-4}$, which takes into account only Short Distance (SD) contributions to the process. This LHCb measurement, together with a previous prediction[4] of lepton universality violation in another process due to purely kinematic effects, prompted us to study Long Distance (LD) contributions to the Branching Fraction of $B^{\pm} \to P^{\pm}\ell^{+}\ell^{-}$ decays, with $P = \pi, K$.

2 Short Distance contribution

In order to compute the SD amplitude to the $B^{-} \to K^{-}/\pi^{-}\ell^{+}\ell^{-}$ decay, we follow previous computations of such amplitude[3,5] using QCD Factorization (QCDF), where the effective weak hamiltonian

$$\mathcal{H}_{eff} = -\frac{G_F \alpha}{\sqrt{2}\pi} V_{q'b} V^*_{q'q} \sum_i C_i^q(\mu_s) O_i^q(\mu_s) \tag{1}$$

is used to compute this amplitude, where $q' = c, t$ and $q = d, s$. The main contributions to this process come from the operators with the vector and axial lepton current $O_9^q = (\bar{q}\gamma_\mu b_L)(\bar{\ell}\gamma^\mu \ell)$ and $O_{10}^q = (\bar{q}\gamma_\mu b_L)(\bar{\ell}\gamma^\mu \gamma_5 \ell)$, nevertheless at higher order in QCDF all the other operators will contribute, but less significantly than the former operators.

The leading contribution to the amplitude computed from this hamiltonian is the following

$$\mathcal{M}[B^- \to P^- \ell^+ \ell^-] = \frac{G_F \alpha}{\sqrt{2}\pi} V_{q'b} V^*_{q'q} \xi_P(q^2) p_B^\mu \left(F_V \bar{\ell}\gamma_\mu \ell + F_A \bar{\ell}\gamma_\mu \gamma_5 \ell \right), \tag{2}$$

where ξ_P is the soft form factor associated to the $B \to P$ transition, and the F_V and F_A are form factors that depend mainly on SD effects, which becomes evident when their dependence on the so called Wilson Coefficients ($C_1, ..., C_{10}$) is noticed. The q^2 dependence of the soft form factor can be obtained, for example, using Light Cone Sum Rules (LCSR) (for more details see[6]),

$$\xi_\pi(q^2) = \frac{0.918}{1 - q^2/(5.32 \text{ GeV})^2} - \frac{0.675}{1 - q^2/(6.18 \text{ GeV})^2} + \mathcal{P}_\pi(q^2) \tag{3a}$$

$$\xi_K(q^2) = \frac{0.0541}{1 - q^2/(5.41 \text{ GeV})^2} + \frac{0.2166}{[1 - q^2/(5.41 \text{ GeV})^2]^2} + \mathcal{P}_K(q^2) \tag{3b}$$

where it is fitted to dipole expressions, which are the main contributions to this form factor. The $\mathcal{P}_P(q^2)$ are polynomials on q^2, whose coefficients correspond to the Gegenbauer moments. The values of C_9 and C_{10} are taken from the NNLL calculation[7].

3 New Long Distance contribution

We focus on the same energy range LHCb uses, which excludes completely any charm quark contamination. The contributing Feynman diagrams are those of Fig.1; other contributions to this process from purely LD effects vanish due to electric charge conservation[8]. The left-hand-side diagram on Fig.1 is suppressed by a factor m_P^2/m_B^2 with respect to the right-hand-side diagram, so that we can neglect its contribution. The LD contributions for the process are obtained using Resonance Chiral Theory (RχT)[9].

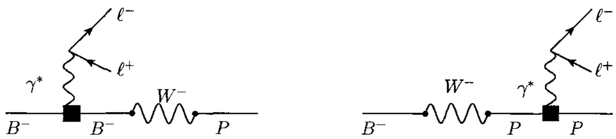

Figure 1 – New long distance contribution to the process, where the square is for structure dependent one-photon exchange. Other structure dependent contributions vanish due to gauge invariance.

The amplitude that we obtain from the leading contribution is

$$\mathcal{M}_{LD} = \sqrt{2} G_F V_{ub} V^*_{uq} f_B f_P \frac{e^2}{q^2} \frac{m_B^2}{m_B^2 - m_P^2} [F_P(q^2) - 1] p_B^\mu \bar{\ell}\gamma_\mu \ell, \tag{4}$$

which we see that has the same structure as the F_V part of the SD amplitude, so that it can be added as a correction to this form factor in the following way

$$F_V^{eff} = F_V + \frac{\kappa_P m_B^2}{q^2} \frac{F_P(q^2) - 1}{\xi_P(q^2)}, \tag{5}$$

where the $\kappa_P = -8\pi^2 \frac{V_{ub}V_{uq}^*}{V_{tb}V_{tq}^*}\frac{f_B f_P}{(m_B^2-m_P^2)}$ is a dimensionless constant $\mathcal{O}(10^{-2})$ times a CKM suppression factor which depends on the final P state. In Wolfenstein's parametrization, for $P=\pi$, κ is $\mathcal{O}(\lambda^0)$, while for $P=K$ is $\mathcal{O}(\lambda^2)$.

Our ignorance of the underlying dynamics is encoded in the $F_P(q^2)$ form factors, which can be seen in Fig.2. These are almost saturated by the lowest-lying light-flavor resonances (ρ, ω and ϕ), following different parametrizations for[11] $P=\pi$ and[12] $P=K$. We have also used phenomenological models by BaBar[13] as a test of our error. Their form factors are fitted using also heavier resonances. The almost perfect agreement on the peaks of the lightest resonances ensures a prediction with small error because the contribution of heavier resonances is negligible.

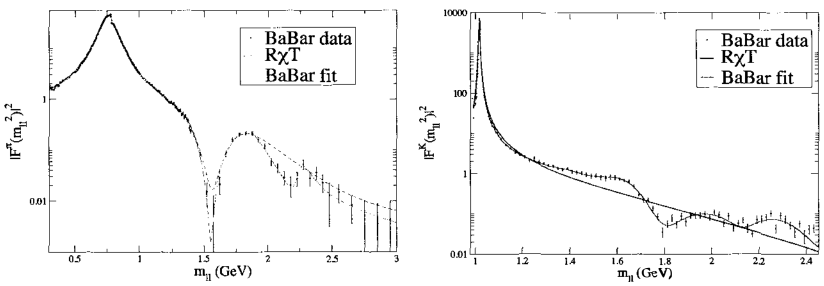

Figure 2 – Our form factor compared to data and BaBar fitted form factor for $P=\pi$ (left) and $P=K$ (right). The form factors depend on the dilepton pair invariant mass.

The invariant mass spectrum for both channels are shown in Fig.3, which shows this spectrum from kinematic threshold. The difference between $\ell = e, \mu$ becomes important at $q^2 \lesssim 0.3$ GeV^2.

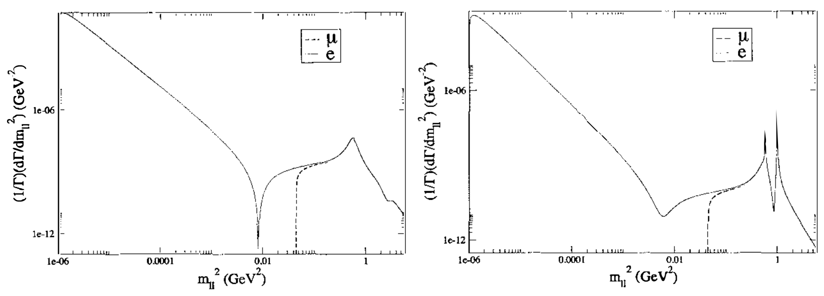

Figure 3 – New LD invariant mass spectrum from kinematic threshold for π (left) and K (right). In both plots, the spectrum of e^+e^- invariant mass overlaps with the $\mu^+\mu^-$ spectrum when $q^2 \gtrsim 0.3$ GeV^2; therefore, there is a negligible contribution to R_K.

We confirm that the LHCb range is free of hadronic pollution for $P=K$, as shown in Table 1; but for $P=\pi$ there is a significant pollution in the $[1,8]$ GeV^2 range. Comparing the LHCb measurement[14] to the SD contribution of the branching fraction in the whole kinematic range[15] we find a better agreement by adding our LD contribution, obtaining a value of $BR^{LD+SD} = (2.6^{+0.4}_{-0.3}) \times 10^{-8}$.

The LD contribution induces lepton universality deviations of $\mathcal{O}(10^{-5})$ in R_P. The different weak and strong phases of SD and LD contributions generate a CP asymmetry[1,16] $A_{CP} = \frac{\Gamma(B^+\to P^+l^+l^-)-\Gamma(B^-\to P^-l^+l^-)}{\Gamma(B^+\to P^+l^+l^-)+\Gamma(B^-\to P^-l^+l^-)}$, corresponding numerical results are shown in Table 2.

Table 1: LD, SD and their interference contributions to the branching ratio for both channels

	$P=\pi$	$P=\pi$	$P=K$
	$0.05 \leq q^2 \leq 8$ GeV^2	$1 \leq q^2 \leq 8$ GeV^2	$1 \leq q^2 \leq 6$ GeV^2
LD	$(9.16 \pm 0.15) \cdot 10^{-9}$	$(5.47 \pm 0.05) \cdot 10^{-10}$	$(1.70 \pm 0.21) \cdot 10^{-9}$
Interf	$(-2.62 \pm 0.13) \cdot 10^{-9}$	$(-2^{+2}_{-1}) \cdot 10^{-10}$	$(-6 \pm 2) \cdot 10^{-11}$
SD	$(9.83^{+1.49}_{-1.04}) \cdot 10^{-9}$	$(8.71^{+1.35}_{-0.90}) \cdot 10^{-9}$	$(1.90^{+0.69}_{-0.41}) \cdot 10^{-7}$

Table 2: CP Asymmetry for the different energy ranges for π and K.

	$q^2 \geq 1$ GeV^2	$q^2 \geq 4m_\mu^2$
$P=\pi$	$(2.5 \pm 1.5)\%$	$(14 \pm 2)\%$
$P=K$	$-(1.3 \pm 0.5)\%$	$-(0.5 \pm 0.5)\%$

4 Conclusions

Our analysis shows that BSM studies should be restricted to the [1,8] GeV^2 range for $P=\pi$; the effect of this new LD contribution could be measured in LHCb in the next run. It is also important to understand the current LHCb measurement of the branching fraction. In the case of $P=K$, there is not an important contribution for the branching fraction; this is because in the interference the peak of the ϕ resonance does not surpass the CKM suppression factor, contrary to the pure LD contribution. The A_{CP} we predict is an important effect that must be taken into account for BSM searches in both channels through this observable.

Acknowledgments

We thank Cinvestav, the organizing committee and Conacyt for financial support.

References

1. A. Guevara, G. López Castro, P. Roig and S. L. Tostado, arXvi:1503.06890 [hep-ph]
2. R. Aaij *et al* (LHCb coll.), *Phys. Rev. Lett.* **113**, 151601 (2014)
3. C. Bobeth *et al*, *JHEP* **0712**, 040 (2007)
4. P. Roig, A. Guevara, G. López Castro, *Phys. Rev.* D **88**, 033007 (2013)
5. A. Khodjamiriam *et al.* JHEP **1302**, 010 (2013)
6. P. Ball and R. Zwicky *Phys. Rev.* D **71**, 014015 (2005)
7. M. Beneke *et al.*, *Nucl. Phys.* B **612**, 25 (2001)
8. G. Ecker *et al*, *Nucl. Phys.* B **291**, 692 (1987)
9. G. Ecker, J. Gasser, A. Pich and E. de Rafael *Nucl. Phys.* B **321**, 311 (1989)
10. G. Amoros *et al.*, *Eur. Phys. J. C* **27**, 243 (2003)
11. D. Gómez Dumm and P. Roig, *Eur. Phys. J. C* **73**, 8,2528 (2013);
    O. Shekhovtsova *et al.*, *Phys. Rev.* D **86**, 113008 (2012)
12. E. Arganda *et al. JHEP* **0806**, 079 (2008)
13. J. P. Lees *et al.* (BaBar coll.), *Phys. Rev.* D **88**, 032013 (2013)
    J. P. Lees *et al.* (BaBar collaboration), *Phys. Rev.* D **86**, 032013 (2012)
14. R. Aaij *et al. JHEP* **12**, 125 (2012)
15. A. Ali *et al. Phys. Rev.* D **89**, 094021 (2014)
16. W. S. Hou, M. Kohda and F. Xu, Phys. *Phys. Rev.* D **90**, 1, 013002 (2014)

4.
QCD

RECENT QCD RESULTS FROM THE TEVATRON

P. SVOISKY, for the D0 and CDF Collaborations
Department of Physics, University of Oklahoma, 440 W. Brooks St.
Norman, OK 73019, USA

We present a variety of QCD related results from the CDF and D0 Collaborations made public during the last several months. Analyses from CDF include measurements of charged pion pair production in diffractive events and searches for potential glue-ball states, imposing new limits on Y(1S) production in association with W/Z bosons, and measurements of WW+jets production cross sections inclusively and versus the number of jets. D0 analyses feature a measurement of double J/ψ production and the effective cross section of double parton scattering, measurements of W+c, W+b inclusive cross sections, and a measurement of the ratio of Z+2b jets to Z+2jets cross sections.

1 Results

This collection of studies has been performed by the CDF and D0 high energy experiments using proton-anti-proton beams produced by the Fermilab Tevatron collider. The major goal of these studies is elucidating phenomena strongly dependent on the structure of the colliding nucleons and interaction of their constituent partons in the perturbative and non-pertubative regimes of quantum chromodynamics (QCD). The two detectors feature tracking systems, calorimetry, and muon spectrometers based on different technology and materials making the results from the two experiments complementary to each other. The relatively low trigger thresholds due to the nature of the colliding beams and relatively low pileup allow studies of the particle spectra either completely or partially inaccessible at the LHC experiments.

1.1 Measurement of central exclusive $\pi^+\pi^-$ production in $p\bar{p}$ collisions at $\sqrt{s} = 0.9$ and 1.96 TeV at CDF

Predictions of the theory of strong interactions between quarks and gluons, QCD, are most reliable in the perturbative regime of high momentum transfer or distance scales much smaller than the size of hadrons. This analysis selects scattering processes producing a pair of low transverse momentum (p_T) hadrons. Such processes are governed by non-perturbative physics.

The dataset is collected in proton-antiproton collisions at $\sqrt{s} = 0.9$ and 1.96 TeV [1]. Besides the pair of two central, $|\eta| < 1.3$ particles, the analysis looks for the absence of the detector activity above noise (rapidity gap) in all of the instrumented pseudorapidity region ($1.3 < |\eta| < 5.9$). Such process is expected to be dominated by double pomeron (DPE) exchange, where pomeron in Regge theory is a pair of gluons in a color-singlet state. The DPE acts as a quantum number filter for the central state, only allowing isotopic spin $I = 0$ and positive parity, C-parity, and G-parity, favoring states having valence gluons and no valence quarks, such as glueballs. Exclusive production of f_0, f_2, $X_{c0(2)}$, and $X_{b0(2)}$ mesons is also allowed.

The two central tracks, assumed to be pions, are studied in two subsets: with a requirement of $p_T > 0.4$ GeV and $p_T > 1.0$ GeV. The results are presented as differential cross sections $d\sigma/dM(\pi\pi)$ from $M(\pi\pi) > 1.0$ GeV in the first subset and from $M(\pi\pi) > 0.3$ GeV in the second subset. Fig. 1 shows the cross section for the first subset on the left and the second subset on the right. The data feature a peak centered at 1270 MeV consistent with $f_2(1270)$ meson with a shoulder on the high mass side presumably from $f_0(1370)$ meson. The states $f_0(1500)$ and $f_0(1710)$ are considered to be glueball candidates but their signal is complicated by mixing with quarkonium states.

The differential cross sections at the two energies are similar in shape, see Fig. 1, left. The ratio $R(0.9 : 1.96) = 1.284 \pm 0.039$ is shown below the left plot and is consistent with 1.3 expected from Regge phenomenology (in the case of elastic scattering, when both proton and anti-proton are intact), falling as $1/\ln(s)$. However, diffractive scattering is not excluded from the data, which supposedly raises the ratio up to $R(0.9 : 1.96) = 1.560 \pm 0.056$ at $M(\pi\pi) > 2.0$ GeV.

The right plot in Fig. 1 features a sharp drop at around 1.0 GeV where $f_0(980)$ and the K^+K^- threshold would occur. There is no sign of a prominent ρ^0 signal, which is expected as far as in DPE the process is forbidden and the photoproduction of ρ^0-mesons is small.

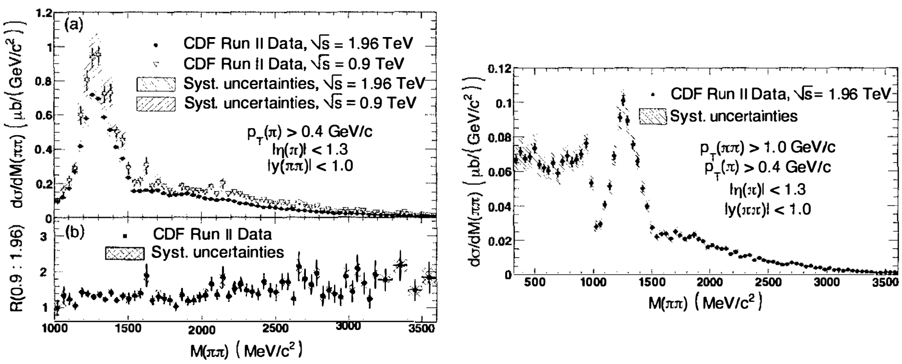

Figure 1 – Differential cross sections $d\sigma/dM(\pi\pi)$ for the $p_T > 0.4$ GeV subset (left) and $p_T > 1.0$ GeV subset (right).

1.2 Observation and studies of double J/ψ production at D0

Production of multiple quarkonium states provides insight into the parton structure of the nucleon [2]. There are also ongoing searches for new bound states of hadronic matter, such as tetraquarks. In $p\bar{p}$ collisions J/ψ mesons are produced either promptly (directly at the interaction point or as a radiative product of a heavier charmonium state) or non-promptly, as a decay of a detectably long-lived B hadron state. The double J/ψ meson production is predicted to have a substantial double parton scattering (DP) contribution and also be dominated by color singlet mechanism.

The analysis measures the prompt single J/ψ production cross section and prompt double J/ψ production cross section in order to extract $\sigma_{\text{eff}} = 1/2 \cdot \sigma(J/\psi)^2/\sigma(J/\psi J/\psi)$, a parameter related to an initial state parton spatial density distribution within a nucleon.

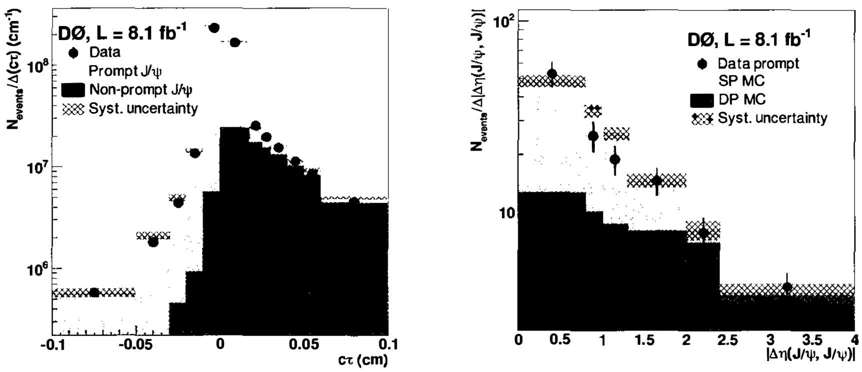

Figure 2 – Template fits of the J/ψ lifetime (left), and $\Delta\eta(J/\psi, J/\psi)$ (right) distributions.

The prompt fraction is extracted using a fit of prompt and non-prompt J/ψ production Monte Carlo templates of the J/ψ lifetime to data distribution, illustrated in the case of single J/ψ production in Fig. 2 (left). In the case of double J/ψ production both J/ψ mesons are used in the fit. The prompt fractions of the single J/ψ and double J/ψ productions are found to be equal to 0.814 ± 0.009 and 0.592 ± 0.101, respectively. The accidental continuous background is subtracted before the fits.

The analysis finds 160 ± 16 double J/ψ candidates after accidental background subtraction. The DP fraction is estimated using the template fits of DP and single parton (SP) Monte Carlo templates of the pseudorapidity difference between the two prompt J/ψ candidates, $\Delta\eta(J/\psi, J/\psi)$, to the data distribution, shown in Fig. 2 (right), and found to be equal to 0.42 ± 0.12.

After application of the detector, prompt fraction, accidental background, and DP fraction (in the case of double J/ψ production) corrections, the single prompt J/ψ fiducial cross section for $p_T^{J/\psi} > 4$ GeV is found to be $\sigma(J/\psi) = 23.9 \pm 4.6(stat) \pm 3.7(syst)$ nb, while the prompt double J/ψ DP production cross section is $\sigma_{DP}(J/\psi J/\psi) = 59 \pm 6(stat) \pm 22(syst)$ fb, and therefore $\sigma_{\text{eff}} = 4.8 \pm 0.5(stat) \pm 2.5(syst)$ mb. This value of σ_{eff} is significantly smaller than the value found in the previous measurements, which may indicate a smaller average distance between gluons than between quarks or between a quark or a gluon, in the transverse space.

1.3 Search for production of $\Upsilon(1S)$ in association with W/Z bosons at CDF

The standard model (SM) predictions for the cross sections of the ΥW and ΥZ production are very sensitive to the non-relativistic quantum-chromodynamic (NRQCD) models and especially to the numerical values of the long-distance matrix elements (LDME) of the probability for a $b\bar{b}$ quark pair to form a bottomonium state. Furthermore, significant excursions from the predicted SM rate would indicate the presence of new physics, such as supersymmetry.

This analysis studies either a 4-lepton sample, with 2 electrons or muons at high $p_T > 20, 15$ GeV, or 1 electron or muon at $p_T > 20$ GeV and transverse missing energy $\not{E}_T > 20$ GeV, and 2 low $1.5 < p_T < 15$ GeV muons [3]. The analysis observes 1 $\Upsilon + (W \to l\nu)$ candidate event and 1 $\Upsilon + (Z \to ll)$ candidate event with 1.2 ± 0.5 and 0.1 ± 0.1 estimated background events, respectively. Double parton scattering contribution is estimated not to exceed 15%. 95% CL limits are set on the $\Upsilon(1S)W$ production cross section, $\sigma(p\bar{p} \to \Upsilon W) < 5.6$ pb, and $\Upsilon(1S)Z$ production cross section, $\sigma(p\bar{p} \to \Upsilon Z) < 21$ pb, which are the most stringent bounds on these processes to date.

1.4 Measurements of the differential cross sections of W+c and W+b production at D0

W+c, W+b production represent significant backgrounds to rare SM processes, such as top quark pair production, single top quark, and W boson in association with a Higgs boson decaying into two b quarks. The dominant processes contributing to $W + c$-jet production are $qg \to Wc$ and $q\bar{q}' \to Wg$ followed by $g \to c\bar{c}$. The production cross section of the first process is sensitive to the s quark parton distribution function (PDF). For the first time, in this analysis, a significant contribution of the second process is allowed by not requiring a soft muon within a b or c-jet and an opposite sign of this muon with the one coming from the W boson decay[4].

The measured W+c, W+b inclusive differential cross sections vs the jet p_T are shown in Fig. 3 (W+c in the middle, W+b on the left, and W+c/W+b ratio on the right). We observe a significant excess of events above the NLO prediction in W+c cross section in the high jet p_T region, dominated by the $g \to c\bar{c}$ process.

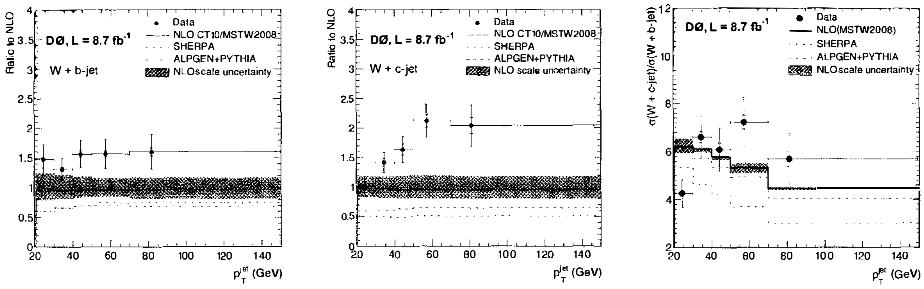

Figure 3 – Inclusive differential cross sections of $W + b$-jet (left), $W + c$-jet (middle), and $W + c/W + b$ ratio (right).

1.5 Measurements of the W^+W^- production at CDF and measurements of the ratio of the cross sections of $Z + 2b$-jet and $Z + 2$-jet production at D0

Both W^+W^- and $Z + 2b$-jets processes are significant, if not most important, backgrounds for the Higgs boson decay into W^+W^- and $b\bar{b}$, respectively. The W^+W^-+jets cross section is measured inclusively, differentially vs the number of additional jets, and differentially vs the jet E_T for the one additional jet selection[5].

The cross section for the leading background to the Higgs production with the decay to $b\bar{b}$, $Z + 2b$-jets is measured inclusively as a ratio to the higher statistics $Z + 2$-jets final state[6]. Important common systematic uncertainties cancel out in the ratio.

References

1. T. Aaltonen *et al.*, CDF Collaboration, arXiv: 1502.01391, and references therein.
2. V. M. Abazov *et al.*, D0 Collaboration, *Phys. Rev.* D **90**, 111101(R) (2014).
3. T. Aaltonen *et al.*, CDF Collaboration, *Phys. Rev.* D **91**, 052011 (2015).
4. V. M. Abazov *et al.*, D0 Collaboration, *Phys. Lett.* B **743**, 6-14 (2015).
5. T. Aaltonen *et al.*, CDF Collaboration, CDF Note 11098.
6. V. M. Abazov *et al.*, D0 Collaboration, *Phys. Rev.* D **91**, 052010 (2015).

α_s determination at NNLO*+NNLL accuracy from the energy evolution of jet fragmentation functions at low z

David d'Enterria[1], and Redamy Pérez-Ramos[2,3].
[1] *CERN, PH Department, CH-1211 Geneva 23, Switzerland*
[2] *Sorbonne Université, UPMC Univ Paris 06, UMR 7589, LPTHE, F-75005, Paris, France*
CNRS, UMR 7589, LPTHE, BP 126, 4 place Jussieu, F-75252 Paris Cedex 05, France

The QCD coupling α_s is extracted from the energy evolution of the first two moments (multiplicity and mean) of the parton-to-hadron fragmentation functions at low fractional hadron momentum z. Comparisons of the experimental e^+e^- and deep-inelastic $e^{\pm}$p jet data to our NNLO*+NNLL predictions, allow us to obtain $\alpha_s(m_Z^2) = 0.1205\pm0.0010^{+0.0022}_{-0.0000}$, in excellent agreement with the current world average determined using other methods at the same level of accuracy.

1 Introduction

For massless quarks and fixed number of colours, the only fundamental parameter of the theory of the strong interaction, quantum chromodynamics (QCD), is its coupling constant α_s. Starting from a value of $\Lambda_{QCD} \approx 0.2$ GeV, where the perturbatively-defined coupling diverges, α_s decreases with increasing energy Q following a $1/\ln(Q^2/\Lambda^2_{QCD})$ dependence. The current uncertainty on α_s evaluated at the Z mass, $\alpha_s(m_Z^2) = 0.1185\pm0.0006$, is $\pm0.5\%$ [1], making of the strong coupling the least precisely known of all fundamental constants in nature. Improving our knowledge of α_s is a prerequisite to reduce the uncertainties in perturbative-QCD calculations of all (partonic) cross sections at hadron colliders, and for precision fits of the Standard Model (α_s dominates e.g. the Higgs boson H$\to$ b$\bar{\text{b}}$ partial width uncertainty). It has also far-reaching implications including the stability of the electroweak vacuum [2] or the scale at which the interaction couplings unify.

Having at hand new independent approaches to determine α_s from the data, with experimental and theoretical uncertainties different from those of the other methods currently used, is crucial to reduce the overall uncertainty in the combined α_s world-average value [1]. In Refs. [3,4] we have presented a novel technique to extract α_s from the energy evolution of the moments of the parton-to-hadron fragmentation functions (FF) computed at approximate next-to-leading-order (NLO*) accuracy including next-to-next-to-leading-log (NNLL) resummation corrections. This approach is extended here to include full NLO, plus a set of NNLO, corrections. Our new NNLO*+NNLL theoretical results for the energy dependence of the hadron multiplicity and mean value of the FF are compared to jet fragmentation measurements in e^+e^- and deep-inelastic $e^{\pm}$p collisions, in order to extract a high-precision value of α_s.

2 Evolution of the parton-to-hadron fragmentation functions at NNLO*+NNLL

The distribution of hadrons in a jet is encoded in a fragmentation function, $D_{\mathrm{i}\to\mathrm{h}}(z,Q)$, which describes the probability that the parton i fragments into a hadron h carrying a fraction $z = p_{\mathrm{hadron}}/p_{\mathrm{parton}}$ of the parent parton's momentum. Usually one writes the FF as a function of the log of the inverse of z, $\xi = \ln(1/z)$, to emphasize the region of relatively low momenta that dominates the jet hadronic fragments. Starting with a parton at a given energy Q, its evolution to another energy scale Q' is driven by a branching process of parton radiation and splitting, resulting in a jet "shower", which can be computed perturbatively using the DGLAP [5] equations at large $z \gtrsim 0.1$, and the Modified Leading Logarithmic Approximation (MLLA) [6], resumming soft and collinear singularities at small z. Due to colour coherence and gluon radiation interference, not the softest partons but those with intermediate energies multiply most effectively in QCD cascades, leading to a final FF with a typical "hump-backed plateau" (HBP) shape as a function of ξ (Fig. 1), which can be expressed in terms of a distorted Gaussian:

$$D(\xi,Y,\lambda) = \mathcal{N}/(\sigma\sqrt{2\pi})\cdot e^{\left[\frac{1}{8}k-\frac{1}{2}s\delta-\frac{1}{4}(2+k)\delta^2+\frac{1}{6}s\delta^3+\frac{1}{24}k\delta^4\right]}\,,\ \text{with}\ \delta = (\xi-\bar{\xi})/\sigma, \tag{1}$$

where $\mathcal{N}$ is the average hadron multiplicity inside a jet, and $\bar{\xi}$, σ, s, and k are respectively the mean peak position, dispersion, skewness, and kurtosis of the distribution. The set of integro-differential equations for the FF evolution combining hard (DGLAP, MLLA, next-to-MLLA) and soft (DLA) radiation can be solved by expressing the Mellin-transformed hadron distribution in terms of the anomalous dimension γ: $D \simeq C(\alpha_s(t))\exp\left[\int^t \gamma(\alpha_s(t'))dt\right]$ for $t = \ln Q$, leading to a perturbative expansion in half powers of α_s: $\gamma \sim \mathcal{O}(\alpha_s^{1/2})+\mathcal{O}(\alpha_s)+\mathcal{O}(\alpha_s^{3/2})+\mathcal{O}(\alpha_s^2)+\mathcal{O}(\alpha_s^{5/2})+\cdots$. Corrections up to order $\alpha_s^{3/2}$ were computed for the first time in Ref. [3,4]. The full set of NLO $\mathcal{O}(\alpha_s^2)$ terms for the anomalous dimension, including the two-loop splitting functions, plus a fraction of the $\mathcal{O}(\alpha_s^{5/2})$ terms, coming from the NNLO expression for the α_s running, have now been computed [7]. Upon inverse-Mellin transformation, one obtains the energy evolution of the FF, and its associated moments, as a function of $\mathrm{Y} = \ln(E/\Lambda_{\mathrm{QCD}})$, for an initial parton energy E, down to a shower cut-off scale $\lambda = \ln(Q_0/\Lambda_{\mathrm{QCD}})$ for $N_f = 3,4,5$ quark flavors. The resulting formulae for the energy evolution of the moments depend on Λ_{QCD} as *single* free parameter. Particularly simple expressions are obtained in the limiting-spectrum case ($\lambda = 0$, i.e. evolving the FF down to $\mathrm{Q}_0 = \Lambda_{\mathrm{QCD}}$) motivated by the "local parton hadron duality" hypothesis for infrared-safe observables which states that the distribution of partons in jets are simply renormalized in the hadronization process without changing their HBP shape. Thus, by fitting the experimental hadron jet data at various energies to Eq. (1), one can determine α_s from the corresponding energy-dependence of its FF moments.

3 Data-theory comparison and α_s extraction

The first step of our procedure is to fit to Eq. (1) all existing jet FF data measured in e^+e^- and $e^\pm,\nu$-p collisions at $\sqrt{s} \approx$ 1–200 GeV (Fig. 1) in order to obtain the corresponding FF moments at each jet energy. Finite hadron-mass effects in the DG fit are accounted for through a rescaling of the theoretical (massless) parton momenta with an effective mass m_{eff} as discussed in Refs. [3,4]. The overall normalization of the HBP spectrum ($\mathcal{K}_{\mathrm{ch}}$), which determines the average charged-hadron multiplicity of the jet, is an extra free parameter in the DG fit which, nonetheless, plays no role in the final Λ_{QCD} value given that its extraction *just* depends on the *evolution* of the multiplicity, and not on its absolute value at any given energy.

Once the FF moments have been obtained, one can perform a combined fit of them as a function of the original parton energy (which in the case of e^+e^- corresponds to half the centre-of-mass energy $\sqrt{s}/2$ and, for DIS, to the invariant four-momentum transfer Q_{DIS}). The top panels of Fig. 2 show the energy evolution of the zeroth (multiplicity) and first (peak position, closely connected to the mean of the distribution) moments of the FF, computed at an increasingly higher level of accuracy (from LO to NNLO*). The hadron multiplicity and FF peak increase exponentially and logarithmically with energy, and the theoretical convergence of their evolutions are very robust as indicated by

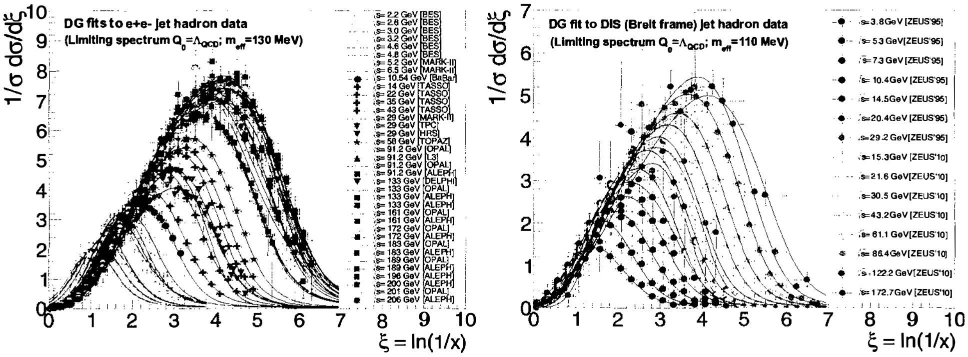

Figure 1 – Charged-hadron distributions in jets as a function of $\xi = \ln(1/z)$ measured in e^+e^- at $\sqrt{s} \approx$ 2–200 GeV (left) and $e^{\pm}$, ν-p (Breit frame, scaled up by ×2 to account for the full hemisphere) at $\sqrt{s} \approx$ 4–180 GeV (right), individually fitted to Eq. (1), with the hadron mass corrections (m_{eff} = 130,110 MeV) quoted.

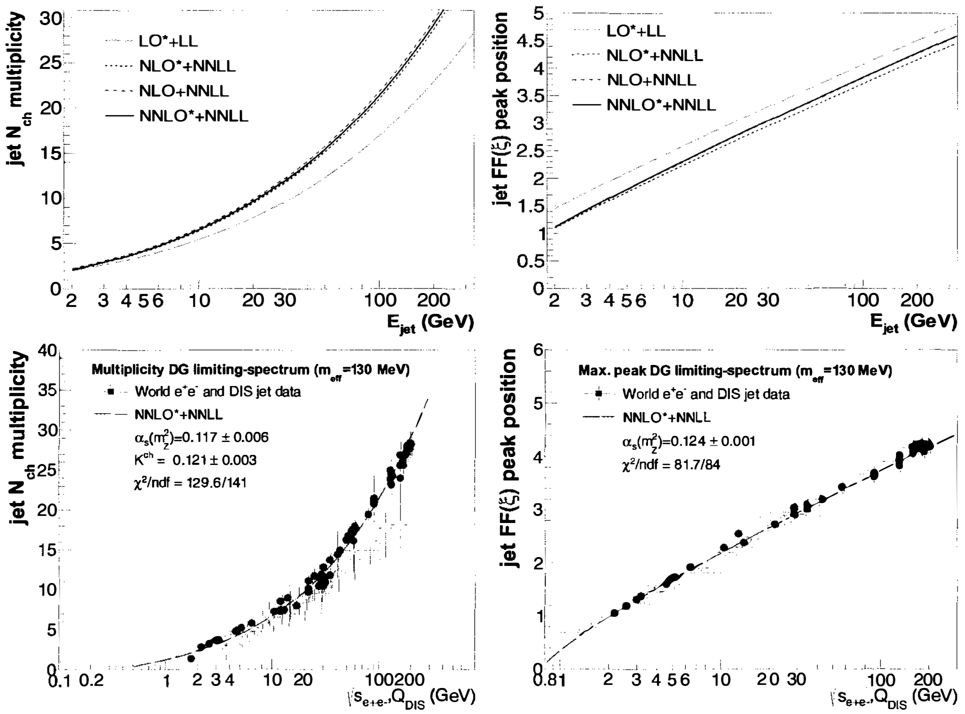

Figure 2 – Energy evolution of the jet charged-hadron multiplicity (left) and FF peak position (right). Top: Comparison of theoretical predictions at four levels of accuracy. Bottom: Fit of the experimental e^+e^- and DIS jet data to the NNLO*+NNLL predictions. The obtained $\mathcal{K}_{\text{ch}}$ normalization constant, the individual NNLO* $\alpha_s(\text{m}_Z^2)$ values, and the goodness-of-fit per degree-of-freedom χ^2/ndf, are quoted.

the small changes introduced by incorporating higher-order terms. The corresponding data-theory comparisons are seen in the bottom panels of Fig. 2. The NNLO*+NNLL limiting-spectrum ($\lambda = 0$) predictions for $N_f = 5$ active quark flavours[a], leaving Λ_{QCD} as a free parameter, reproduce very well

[a]The moments of the lowest-$\sqrt{s}$ data have a few-percent correction applied to account for the (slightly) different

the data. The most "robust" FF moment for the determination of $\Lambda_{\rm QCD}$ is the peak position $\xi_{\rm max}$ which is quite insensitive to most of the uncertainties associated with the extraction method (DG and energy evolution fits, finite-mass corrections)[4] as well as to higher-order corrections. The hadron multiplicities measured in DIS jets appear somewhat smaller (especially at high energy) than those measured in e^+e^- collisions, due to limitations in the FF measurement only in half (current Breit) $e^{\pm}$p hemisphere and/or in the determination of the relevant Q scale[4]. The value of $\alpha_s(m_Z^2)$ obtained from the combined multiplicity+peak fit yields $\alpha_s(m_Z^2) = 0.1205 \pm 0.0010$, where the error includes all sources of uncertainty discussed in Ref.[4]. An extra theoretical scale uncertainty of $^{+0.0022}_{-0.0000}$ should be added (this is a conservative estimate obtained only at NLO* accuracy[4]). In Fig. 3 we compare our extracted $\alpha_s(m_Z^2)$ value to all other NNLO results from the latest PDG compilation[1], plus that obtained from the pion decay factor[8], and the top-quark pair production cross sections[9]. The precision of our result ($^{+2\%}_{-1\%}$) is clearly competitive with the other measurements, with a totally different set of experimental and theoretical uncertainties. A simple weighted average of all these NNLO values yields: $\alpha_s(m_Z^2) = 0.1186 \pm 0.0004$, in perfect agreement with the central value of the current world-average, $\alpha_s(m_Z^2) = 0.1185 \pm 0.0006$, but with a 30% smaller uncertainty.

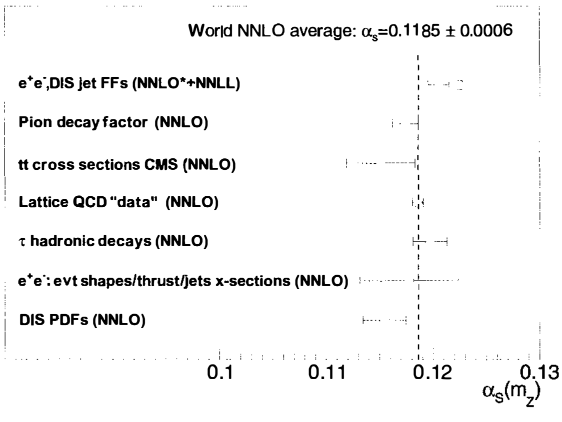

Figure 3 – Summary of α_s determinations using different methods at NNLO$^{(*)}$ accuracy. The dashed line and shaded (yellow) band indicate the current world-average and uncertainty (listed also on the top)[1].

We are grateful to Anatoly Kotikov and Gavin Salam for useful discussions. R. Pérez-Ramos thanks the support from the CERN TH Division where part of this work was carried out.

References

1. K. A. Olive *et al.* [Particle Data Group Collab.], *Chin. Phys.* C **38** (2014) 090001.
2. D. Buttazzo *et al.*, *JHEP* **1312** (2013) 089.
3. R. Pérez-Ramos and D. d'Enterria, JHEP **1408** (2014) 068; *Proceeds. Moriond QCD and High-Energy Interactions* 2014, pp. 315; arXiv:1408.2865 [hep-ph].
4. D. d'Enterria and R. Prez-Ramos, *Nucl. Phys. B Proc. Suppl.* to appear, arXiv:1410.4818 [hep-ph]; *EPJ Web Conf.* **90** (2015) 04001.
5. V.N. Gribov and L.N. Lipatov, *Sov. J. Nucl. Phys.* 15 (1972) 438; G. Altarelli and G. Parisi, *Nucl. Phys.* B 126 (1977) 298; Y.L. Dokshitzer, *Sov. Phys. JETP* 46 (1977) 641.
6. Y.L. Dokshitzer, V.A. Khoze and S. Troian, *Int. J. Mod. Phys.* A7 (1992) 1875.
7. R. Pérez-Ramos and D. d'Enterria, in preparation.
8. J. L. Kneur and A. Neveu, *Phys. Rev.* D **88** (2013) 7, 074025.
9. S. Chatrchyan *et al.* [CMS Collab.], *Phys. Lett.* B **728** (2014) 496.

(N_f = 3,4) evolutions below the charm and bottom production thresholds.

NLO QCD+EW automation and precise predictions for V+multijet production

S. Kallweit
Institut für Physik & PRISMA Cluster of Excellence, Johannes Gutenberg Universität, 55099 Mainz, Germany

J. M. Lindert[a], S. Pozzorini, M. Schönherr
Physik-Institut, Universität Zürich, Winterthurerstrasse 190, CH-8057 Zürich, Switzerland

P. Maierhöfer
Institute for Particle Physics Phenomenology, Durham University, Durham DH1 3LE, UK

In this talk we present a fully automated implementation of next-to-leading order electroweak (NLO EW) corrections in OpenLoops together with Sherpa and Munich. As a first application, we present NLO QCD+EW predictions for the production of positively charged W bosons in association with up to three jets and for the production of a Z boson or photon in association with one jet.

1 Introduction

The upcoming Run-II of the LHC will probe the Standard Model (SM) of particle physics at unprecedented energies and precision. At the TeV energy scale higher-order electroweak (EW) corrections can be strongly enhanced due to the presence of large Sudakov logarithms. Their inclusion in the experimental analyses will significantly enhance the sensitivity for new phenomena. Here we present a fully automated implementation of next-to-leading order (NLO) EW corrections, applicable to any process within the SM.

In the following, first we briefly review the recently accomplished automation of NLO EW corrections in OpenLoops[1], Sherpa[2] and Munich[3]. Subsequently, we present numerical results for W+multijet production and for Z-boson and photon production in conjunction with one jet. Due to the large cross sections and clean experimental signatures these processes represent an ideal laboratory to test the validity of theoretical methods and tools that are used for the simulation of a vast range of processes at the LHC. Furthermore, they are important backgrounds for top- and Higgs-physics and various searches for physics beyond the Standard Model including Dark Matter searches in the monojet channel.

Discussion and results presented here are partly based on [4], where more details can be found.

2 NLO QCD+EW automation in OpenLoops + Sherpa/Munich

The calculation of NLO QCD corrections for any SM process was already well established in the OpenLoops+Sherpa/Munich programs. This fully automated framework has now been extended to NLO EW calculations. More precisely, the new implementation allows for NLO calculations at any given Order $\alpha_s^n\alpha^m$, including all relevant QCD–EW interference effects. Full NLO

[a]Speaker

SM calculations that include all possible $\mathcal{O}(\alpha_s^{n+k}\alpha^{m-k})$ contributions to a certain process are also supported.

The OpenLoops [1] program generates all relevant matrix-element ingredients, i.e. one-loop amplitudes, tree amplitudes for Born and bremsstrahlung contributions, as well as colour-, charge-, gluon-helicity and photon-helicity correlations that are needed for infrared subtractions. The OpenLoops program is based on the Open Loops algorithm [5], which employs a recursion to construct loops as tree structures supplemented with full loop-momentum information. Combined with the Collier tensor reduction library [6] the employed recursion permits to achieve very high CPU performance and a high degree of numerical stability.

The kernel of the Open Loops recursion is universal and depends only on the Lagrangian of the model at hand. The algorithm is thus applicable to any process within any renormalizable theory. The implementation has successfully been applied to various precision studies at NLO QCD and the extension to NLO electroweak corrections has very recently been achieved. It required the implementation of all $\mathcal{O}(\alpha)$ EW Feynman rules in the framework of the numerical Open Loops recursion including counterterms associated with so-called R_2 rational parts [7] and with the on-shell renormalization of UV singularities [8]. Additionally for the treatment of heavy unstable particles the complex mass scheme has been implemented. For the convenience of the user the OpenLoops program is accompanied by a large process library including more than a hundred LHC processes – currently all at the NLO QCD level but the library will be extented to NLO EW soon.

All complementary tasks, i.e. the bookkeeping of partonic processes, the subtraction of IR singularities, and phase space integration, have been automated within Munich and Sherpa. Automated NLO EW simulations will be supported by future public releases of the employed tools.

3 W+multijet production

As a first highly non-trivial application we study the production of $W^+ + n$ jets with $n = 1, 2, 3$ at the LHC including NLO QCD and NLO EW corrections.

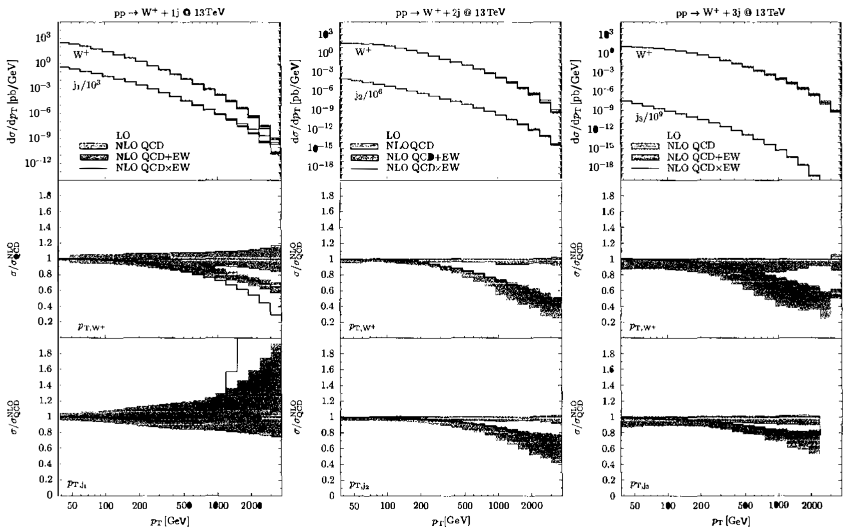

Figure 1 – Distributions in the transverse momentum p_T of the W^+ and the n-th jet for inclusive $W^+ + nj$ production with $n = 1$ (left), $n = 2$ (center), $n = 3$ (right) at $\sqrt{s} = 13$ TeV. Absolute LO (light blue), NLO QCD (green), NLO QCD+EW (red) and NLO QCD×EW (black) predictions (upper panel) and relative corrections with respect to NLO QCD (lower panels). The bands correspond to scale variations, and in the case of relative corrections only the numerator is varied.

In Fig. 1 we show differential distribution in the transverse momentum of the produced W^+ and the n-th jet. We use the anti-k_T jet clustering algorithmn with R=0.4 and require $p_{\rm T} > 30$ GeV and $|\eta| < 4.5$ for the jets. Besides LO predictions of $\mathcal{O}(\alpha_S^n\alpha)$ we show NLO QCD predictions including corrections of $\mathcal{O}(\alpha_S^{n+1}\alpha)$ and NLO QCD + EW predictions including $\mathcal{O}(\alpha_S^{n+1}\alpha)+\mathcal{O}(\alpha_S^n\alpha^2)$ corrections. Theoretical uncertainties are assessed by standard variations of the renormalization and factorization scales.[4] Besides QCD + EW predictions we also show factorized QCD $\times$ EW predictions were the NLO QCD predictions are multiplied with a NLO EW K-factor. A difference between the two approaches indicates uncertainties due to missing two-loop EW-QCD corrections. In the lower panel we show corrections with respect to the NLO QCD prediction. In the tail of the $p_{\rm T}$ distribution of the jet in $W+1$ jet production the NLO QCD corrections grow larger then a factor of 10 and the EW corrections turn positive. Together with the large scale uncertainties this is a clear indication for a poor perturbative convergence. Indeed, NLO corrections to inclusive $W+1$ jet production are dominated by dijet configurations radiating a relatively soft W, which are effectively of leading order. Such configurations appear already at LO for $W+2$ jet production (shown in the central plot), where the NLO QCD corrections are small and stable. Here, the EW corrections show a typical Sudakov behaviour and reach $-30(-60)\%$ and $-15(-25)\%$ at 1(4) TeV for the $p_{\rm T}$ of the W^+ and the 2nd jet respectively. A similar picture emerges for $W+3$ jet production (shown in the right plot).

In Fig. 2 we show differential distributions in $H_{\rm T}^{\rm tot}$ – the scalar sum of all final state transverse momenta for $W^+ + 1, 2, 3$j production. In order to improve the perturbative convergence in the case of $W^+ + 1$j production we employ a veto on a second jet if $\Delta\phi_{j_1j_2} > 3/4\pi$. Still, for very large $H_{\rm T}^{\rm tot}$ the QCD corrections to $W^+ + 1$j and $W^+ + 2$j production increase strongly, suppressing the impact of the EW corrections. Only for $W^+ + 3$j production the QCD corrections are stable in all of the considered range. However, here the EW corrections are still moderate and only increase beyond the NLO QCD scale uncertainties for $H_{\rm T}^{\rm tot}$ at the TeV scale.

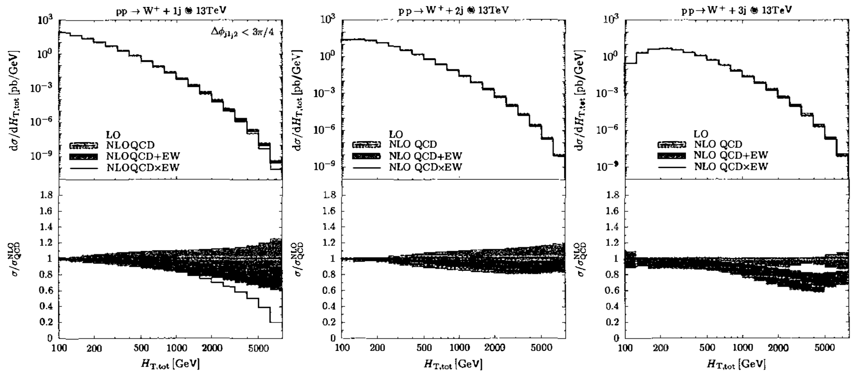

Figure 2 – Distributions in $H_{\rm T}^{\rm tot}$ for exclusive $W^+ + 1j$ (left), inclusive $W^+ + 2j$ (center) and inclusive $W^+ + 3j$ (right) production. Curves and bands as in Fig. 1.

4 Z/γ+jet production

As a second application we study the production of a Z boson or a photon in association with a jet at the LHC with $\sqrt{s} = 8$ TeV. The ratio of these processes differential in the $p_{\rm T}$ of the produced gauge bosons can be used to model $Z(\to \nu\bar{\nu}) + 1j$ production from a precise experimental measurement of $\gamma + 1j$ production, i.e. the dominant irreducible SM background in monojet searches for Dark Matter.

Results in the $p_{\rm T}$ of the produced weak gauge boson are shown in Fig. 3 with the same color coding and nomenclature as before. In the left and central plot results for $Z + 1j$ and $\gamma + 1j$

production are shown respectively. We require for the associated jet $p_{T,j} > 110$ GeV and $|\eta_j| < 2.4$ and veto a possible second jet with $p_{T,j} > 30$ GeV and $\Delta\phi_{j_1 j_2} > 2.5$. These cuts are in agreement with a setup employed by CMS in an upcoming monojet search. The NLO QCD corrections to both processes are almost identical at large transverse momentum of the produced gauge bosons $p_{T,V}$, while they differ slightly at small $p_{T,V}$ due to the finite mass of the produced Z. NLO QCD scale uncertainties are at the level of 10%. On the contrary, the EW corrections to $Z+1j$ production are enhanced compared to $\gamma+1j$ production and at 1 TeV they reach −20% and −8% respectively. In the right plot of Fig. 3 we show the ratio in $p_{T,V}$ of $Z+1j$ over $\gamma+1j$ production. This observable is fairly stable in the considered p_T range and QCD corrections are below 10%. However, EW corrections result in an almost constant shift of about 10% comparing the p_T-ratio at LO and NLO QCD + EW. Such a shift is consistent with the observed deviation presented by CMS at Moriond 2015 QCD (also shown in Fig. 6 of [9]).

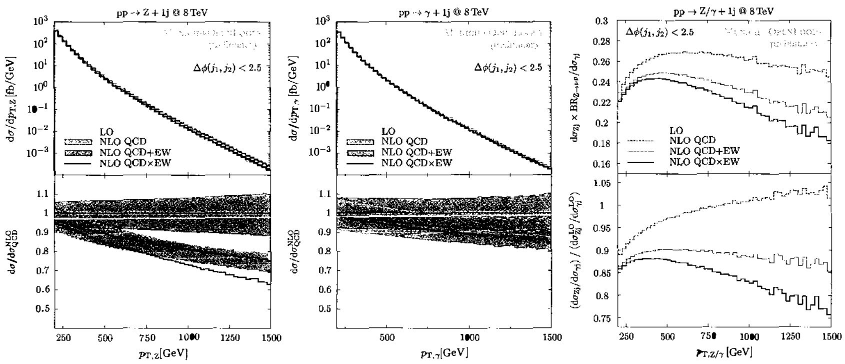

Figure 3 – Distributions in the transverse momenta of the Z boson (left) and of the photon (center) for $Z+1j$ and $\gamma+1j$ production at $\sqrt{s}=8$ TeV. Curves and bands as in Fig. 1. In the right plot the ratio of the p_T of the Z and the photon together with the relative corrections in the ratio with respect to the LO ratio are shown using the same color coding as before.

5 Conclusions

Recent progress in the automation of perturbative calculations within the OpenLoops +Munich/Sherpa frameworks has opened the door to NLO QCD+EW simulations for a vast range of Standard Model processes, up to high particle multiplicity, at current and future colliders. The large impact of NLO EW effects in V+multijet production at high energy demonstrates the relevance of these new tools for the upcoming Run-II of the LHC.

References

1. The OpenLoops one-loop generator by F. Cascioli, J. Lindert, P. Maierhöfer and S. Pozzorini is publicly available at `http://openloops.hepforge.org`.
2. T. Gleisberg et al., JHEP **0902** (2009) 007, [arXiv:0811.4622].
3. Munich—an automated parton level NLO generator by S. Kallweit. In preparation.
4. S. Kallweit et al., [arXiv:1412.5157].
5. F. Cascioli et al., Phys.Rev.Lett. **108** (2012) 111601, [arXiv:1111.5206].
6. A. Denner, S. Dittmaier, and L. Hofer, [arXiv:1407.0087].
7. M. Garzelli et al., JHEP **1001** (2010) 040, [arXiv:0910.3130].
8. A. Denner, Fortsch.Phys. **41** (1993) 307–420, [arXiv:0709.1075].
9. CMS Collaboration [CMS Collaboration], CMS-PAS-SMP-14-005.

NNLO corrections for LHC processes

Fabrizio Caola
CERN Theory Division, CH-1211, Geneva 23, Switzerland

To fully profit from the remarkable achievements of the experimental program at the LHC, very precise theoretical predictions for signal and background processes are required. In this contribution, I will review some of the recent progress in fully exclusive next-to-next-to-leading-order (NNLO) QCD computations. As an example of the phenomenological relevance of these results, I will present LHC predictions for $t-$channel single-top production and Higgs boson production in association with one hard jet.

1 NNLO computations: status and prospects

The impressive achievements of the LHC program at CERN, culminated with the discovery of the Higgs boson [1,2], allow us to scrutinize the Standard Model (SM) to a level of accuracy never seen before. Although interesting *per se*, the ultimate goal of such scrutiny is to find deviations from expected predictions which point to new physics beyond the standard model. So far, no significant deviation has been observed, indicating that new physics, if present, may be hiding in subtle effects. Disentangling such small deviations requires very good theoretical control on standard model predictions.

In general, computing perturbative corrections to a given process requires two steps. First, all relevant tree and loop amplitudes must be known. Second, a consistent framework to combine real and virtual corrections into finite predictions for physical observables is needed. In order for theoretical predictions to describe the complicate experimental environments in a reliable way, the framework must be able to cope with arbitrary (infra-red safe) fiducial cuts on the final state and be valid for any (infra-red safe) differential distribution. In other words, the framework should allow for fully exclusive predictions. This requirement proved to be very challenging to deal with and as a result for a a long time fully exclusive NNLO predictions were only available for process with a trivial color flow, like Higgs[3,4] or Drell-Yan production[5,6]. In the recent years however, thanks to a big effort in the theory community, significant progress has been made [7] and it is now possible, at least in principle, to deal with processes of arbitrary complexity. In practice, predictions for genuine $2 \to 2$ processes are now doable, and indeed in the recent past NNLO computations for top-quark[8], dijet[9], single-top[10] and Higgs plus Jet[11] started to appear.

To go beyond $2 \to 2$ processes, several issues must be addressed. First, two loop amplitudes must be computed. So far the state-of-the art is $2 \to 2$ amplitudes with up to one internal/external mass scale (like e.g. amplitudes for $pp \to t\bar{t}$ production [12]) or $2 \to 2$ amplitudes with up to two *external* mass scales (like e.g. amplitudes for $pp \to WZ$ production [13]). Going beyond that will require substantial improvements of our current technology. Second, to compute NNLO correction to $pp \to X$ one needs one-loop amplitudes for $pp \to X+$parton, and they have to be stable enough in the unresolved regime where the extra parton is very soft / collinear. In the recent past, we witnessed a lot of progress in automatic one-loop computations [14]. It is an interesting question whether the results obtained from these automatic tools are stable and efficient enough to cope with the demands of NNLO computations. Third, it is not clear if existing implementations of subtraction frameworks will *in practice* work with high multiplicity final states. Although all major conceptual issues have been now more or less solved, yet all existing computations require significant amount of computing resources to deal with $2 \to 2$ kinematics. It is hence far from obvious that the same frameworks will successfully handle genuine $2 \to 3$ and more complicated processes.

Fortunately, a lot of processes for which NNLO accuracy is desirable fall in the $2 \to 2$ category (see e.g. the Les Houches wish-list [15]). In the following, I will briefly illustrate the recent progress in NNLO computations and its phenomenological implications by discussing two of such processes, $t-$channel single top production and Higgs boson production in association with one hard jet.

2 NNLO predictions: phenomenological examples

$t-$channel single-top

The relevance of the top physics program at the LHC has already been discussed extensively in these proceedings. The main difference w.r.t. the Tevatron program is that at the LHC the signal yield for tops at the LHC is relatively large, thus allowing for very precise studies of this particle and its properties. At hadron colliders, tops can be produced both through strong interactions, which lead to $t\bar{t}$ pair production, and through weak interactions, which lead to single-top production. The cross-section for $t\bar{t}$ is larger, yet the yield for single-top is still sizable at the LHC. Moreover, measuring the single-top cross-section gives direct access to the V_{tb} CKM matrix element.

For single-top production, most of the cross-section comes from the so-called $t-$channel topology. NLO corrections to the total $t-$channel cross-section are known to be small, at the percent level. Naively, this would suggest per mill level NNLO corrections, well beyond the accuracy goal of actual measurements. Unfortunately, there are many indications that the smallness of NLO corrections to the total cross-section is accidental. Moreover, NLO corrections to more differential quantities can be as large as 20%. In order to achieve a percent level perturbative control, higher order predictions are thus needed.

NNLO corrections to $t-$channel single top, for stable tops, were computed in [10] using the five flavor number scheme in the factorized approximation. Using the MSTW2008 parton set, the NNLO total cross section for $m_t = 173.2$ GeV is $\sigma_{\rm NNLO} = 54.2^{+0.5}_{-0.2}$ pb, to be compared with the NLO prediction $\sigma_{\rm NLO} = 55.1^{+1.6}_{-0.9}$ pb and the LO one $\sigma_{\rm LO} = 53.8^{+3.0}_{-4.3}$ pb. Errors refer to scale variations of a factor of two around $\mu = m_t$. As anticipated, NNLO corrections are as large as the NLO ones. All these predictions are in excellent agreement with the current experimental measurement presented in these proceedings $\sigma_t = 53.85 \pm 9\%$. At NNLO, the residual perturbative uncertainty due to scale variation is greatly diminished compared to previous orders, thus making it basically irrelevant in the full budget of theoretical error, which is dominated by uncertainty on parameters like parton distribution functions or the $b-$quark mass. A thorough estimate of such uncertainties is currently under way. As we briefly mentioned before, NLO corrections can be significantly larger for more exclusive quantities. It is thus interesting to investigate whether NNLO corrections are enough to stabilize the perturbative expansion in these cases or not. An example is shown in Fig. 1, where the top $p_\perp$ cumulative cross-section is shown. Despite NLO corrections at high $p_\perp$ are very large and outside the LO uncertainty band, NNLO corrections are very stable throughout the full spectrum.

So far, NNLO predictions are only known for stable top. However, NNLO corrections to top decay are known [16]. Combining these results with the one just described will allow for a complete $pp \to t + X \to Wb + X$ NNLO computation, in the narrow width approximation. The result of such combination would be very interesting, as it will allow for a proper study of single-top production at the LHC in the actual measured fiducial region.

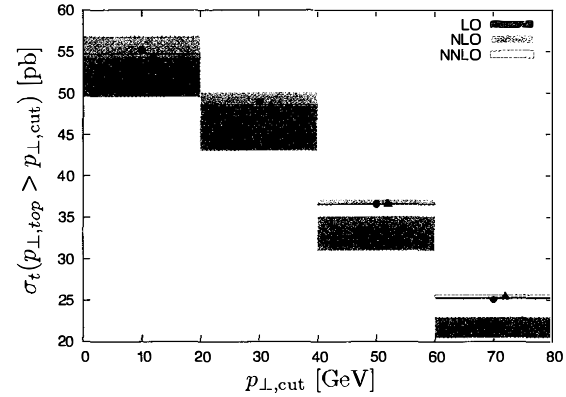

Figure 1 – Top $p_\perp$ cumulative cross-section at LO (red), NLO (green) and NNLO (blue). Colored bands represent scale variation uncertainty, in the range $\mu_r = \mu_f \in [m_t/2, 2m_t]$. See text for details.

2.1 Higgs boson production in association with one jet

Studying the properties of the recently found Higgs boson is clearly one of the main goals of the LHC experimental program. From a theoretical point of view, Higgs production at the LHC is quite hard to properly describe because the perturbative series has a poor convergence. For example, the NLO corrections for inclusive Higgs production in gluon fusion are as large as the LO rate. To obtain reliable predictions, computation of enough terms in the perturbative expansion is thus mandatory. For fully inclusive Higgs production, corrections up to N^{3}LO were recently computed[17]. Unfortunately, in most cases the knowledge of the total cross-section alone is not enough and more differential information is required. Predictions in these situations are much more involved, and as a consequence the theoretical control is much worse. A particularly interesting class of processes in this family are Higgs boson produced in association with one or more hard jets. On one hand a proper modeling of such processes is very important for experimental analysis in channels like the $H \to WW$ or $H \to \tau\tau$ where a jet-bin categorization is fundamental for increasing the sensitivity. Furthermore, Higgs boson in association with one hard jet gives direct access to the Higgs transverse momentum spectrum.

In this contribution I will present results of a recently completed computation of Higgs boson plus jet which includes all the ingredients relevant for reliable phenomenology at the LHC. More specifically, NNLO corrections are computed for the gg and qg channels, which are expected to account for about 99% of the total cross-section. The computation is carried out in the Higgs effective field theory where the top quark is integrated out and a point-like interaction ggH is considered. Such an approximation is reliable at the percent level up to transverse momenta of the order of $p_\perp \sim 150$ GeV [18]. Results are obtained using the NNPDF21LO, NNPDF23NLO and NNPDF23NNLO parton sets and values of α_s. We use the central scale $\mu_r = \mu_f = m_H = 125$ GeV. Jets are reconstructed using the anti-k_t algorithm with $p_\perp > 30$ GeV and $R = 0.5$. We find the total cross-section to be $\sigma_{\mathrm{LO}} = 3.9^{+1.7}_{-1.1}$ pb, $\sigma_{\mathrm{NLO}} = 5.6^{+1.3}_{-1.1}$ pb and $\sigma_{\mathrm{NNLO}} = 6.7^{+0.5}_{-0.6}$ pb at LO, NLO and NNLO respectively where the upper(lower) results are for the scale choices $\mu_r = \mu_f = m_H/2$ $(2m_H)$. NNLO corrections are sizable, around 20% on top of NLO, but smaller than the NLO ones indicating a convergence of the perturbative series. The residual uncertainty due to scale variation is significantly reduced to the $\sim 10\%$ level.

In Fig.2 the cumulative one-jet cross-section (left pane) and the Higgs $p_\perp$ spectrum in the 1-jet bin (right pane) are shown. These plots show a clear improvement of scale uncertainties also for more differential observables. The convergence of the perturbative series is reasonable:

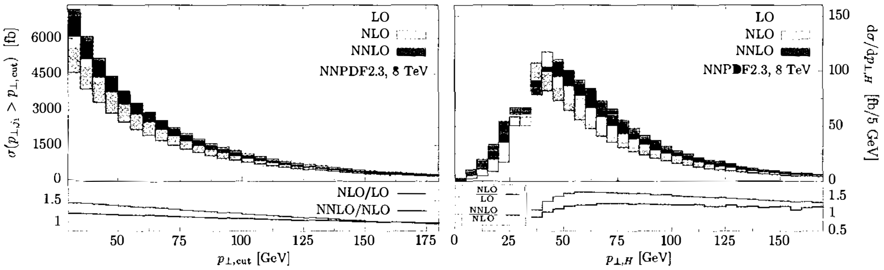

Figure 2 – Higgs plus jet total cumulative $p_{\perp,jet}$ cross-section (left) and Higgs boson $p_\perp$ spectrum in the 1-jet bin (right) at LO (yellow), NLO (green) and NNLO (blue). Colored bands represent scale variation uncertainty, in the range $\mu_r = \mu_f \in [m_H/2, 2m_H]$. In the lower pane, the ratio between consecutive perturbative orders for the scale choice $\mu = m_H$ is shown. See text for details.

while the LO and the NLO bands only partially overlap, the NLO/NNLO overlap is substantial. Interestingly enough, the NNLO to NLO ratio is not constant: the bulk of the corrections lies in the low $p_\perp$ region, while the NLO and NNLO curves tend to converge to the same value at high $p_\perp$.

3 Conclusion

The LHC program requires very accurate theoretical modeling of complex experimental environments. Such predictions are mandatory to scrutinize the structure of the Standard Model and hopefully find deviations pointing to new physics. An essential ingredients are refined higher order predictions for fully exclusive reactions. Thanks to a big effort in the theoretical community, first NNLO predictions for genuine $2 \to 2$ colorful processes recently started to appear. In this contribution, I illustrated the recent progress by showing accurate phenomenological predictions for $t-$channel single top and Higgs boson production in association with one jet at the LHC. These are only examples chosen among a rapidly growing number of processes computed to NNLO accuracy, which are pushing farther the boundaries for phenomenological studies at hadron colliders.

Acknowledgments

I thank the organizers for the invitation to present these results at *Moriond QCD 2015*. I would also like to thank M. Schulze, M. Brucherseifer, F. Petriello, R. Boughezal and especially K. Melnikov for their collaboration on the work presented in this contribution.

References

1. G. Aad *et al.* [ATLAS Collaboration], Phys. Lett. B 716 (2012) 1.
2. S. Chatrchyan *et al.* [CMS Collaboration], Phys. Lett. B 716 (2012) 30.
3. C. Anastasiou, K. Melnikov and F. Petriello, Phys. Rev. Lett. **93**, 262002 (2004).
4. S. Catani and M. Grazzini, Phys. Rev. Lett. **98**, 222002 (2007).
5. K. Melnikov and F. Petriello, Phys. Rev. D **74**, 114017 (2006).
6. S. Catani, L. Cieri, G. Ferrera, D. de Florian and M. Grazzini, Phys. Rev. Lett. **103**, 082001 (2009).
7. see e.g. A. Gehrmann-De Ridder, T. Gehrmann and E. W. N. Glover, JHEP **0509**, 056 (2005); S. Catani and M. Grazzini, Phys. Rev. Lett. **98**, 222002 (2007); S. Catani, L. Cieri, D. de Florian, G. Ferrera and M. Grazzini, arXiv:1311.1654 [hep-ph]; S. Weinzierl, JHEP

0303, 062 (2003); G. Somogyi, P. Bolzoni and Z. Trocsanyi, Nucl. Phys. Proc. Suppl. **205-206**, 42 (2010); M. Czakon, Phys. Lett. B **693**, 259 (2010); M. Czakon, Nucl. Phys. B **849**, 250 (2011); M. Czakon and D. Heymes, Nucl. Phys. B **890**, 152 (2014) and references therein.
8. M. Czakon, P. Fiedler and A. Mitov, Phys. Rev. Lett. **110**, no. 25, 252004 (2013); M. Czakon, P. Fiedler and A. Mitov, arXiv:1411.3007 [hep-ph].
9. A. Gehrmann-De Ridder, T. Gehrmann, E. W. N. Glover and J. Pires, Phys. Rev. Lett. **110**, no. 16, 162003 (2013); J. Currie, A. Gehrmann-De Ridder, E. W. N. Glover and J. Pires, JHEP **1401**, 110 (2014).
10. M. Brucherseifer, F. Caola and K. Melnikov, Phys. Lett. B **736**, 58 (2014).
11. R. Boughezal, F. Caola, K. Melnikov, F. Petriello and M. Schulze, JHEP **1306**, 072 (2013); X. Chen, T. Gehrmann, E. W. N. Glover and M. Jaquier, Phys. Lett. B **740**, 147 (2015).
12. P. Baernreuther, M. Czakon and P. Fiedler, JHEP **1402**, 078 (2014).
13. F. Caola, J. M. Henn, K. Melnikov, A. V. Smirnov and V. A. Smirnov, JHEP **1411**, 041 (2014); T. Gehrmann, A. von Manteuffel and L. Tancredi, arXiv:1503.04812; A. von Manteuffel and L. Tancredi, arXiv:1503.08835; F. Caola, J. M. Henn, K. Melnikov, A. V. Smirnov and V. A. Smirnov, JHEP **1506**, 129 (2015).
14. F. Cascioli, P. Maierhofer and S. Pozzorini, Phys. Rev. Lett. **108**, 111601 (2012); G. Cullen, H. van Deurzen, N. Greiner, G. Heinrich, G. Luisoni, P. Mastrolia, E. Mirabella and G. Ossola *et al.*, Eur. Phys. J. C **74**, no. 8, 3001 (2014); J. Alwall, R. Frederix, S. Frixione, V. Hirschi, F. Maltoni, O. Mattelaer, H.-S. Shao and T. Stelzer *et al.*, JHEP **1407**, 079 (2014).
15. `https://phystev.cnrs.fr/wiki/2013:groups:sm:nnlowishlist`
16. J. Gao, C. S. Li and H. X. Zhu, Phys. Rev. Lett. **110**, no. 4, 042001 (2013); M. Brucherseifer, F. Caola and K. Melnikov, JHEP **1304**, 059 (2013).
17. C. Anastasiou, C. Duhr, F. Dulat, F. Herzog and B. Mistlberger, Phys. Rev. Lett. **114**, no. 21, 212001 (2015).
18. R. V. Harlander, T. Neumann, K. J. Ozeren and M. Wiesemann, JHEP **1208**, 139 (2012).

Estimation of uncertainties from missing higher orders in perturbative calculations

E. Bagnaschi [1] [a]
[1]*DESY, Notkestraße 85, D22607 Hamburg, Germany*

In this proceeding we present the results of our recent study [2] of the statistical performances of two different approaches, Scale Variation (SV) and the Bayesian model of Cacciari and Houdeau (CH) [1] (which we also extend to observables with initial state hadrons), to the estimation of Missing Higher-Order Uncertainties (MHOUs) [4], in perturbation theory. The behavior of the models is determined by analyzing, on a wide set of observables, how the MHOU intervals they produce are successful in predicting the next orders. We observe that the Bayesian model behaves consistently, producing intervals at 68% Degree of Belief (DoB) comparable with the scale variation intervals with a rescaling factor r larger than 2 and closer to 4. Concerning SV, our analysis allows the derivation of a heuristic Confidence Level (CL) for the intervals. We find that assigning a CL of 68% to the intervals obtained with the conventional choice of varying the scales within a factor of two with respect to the central scale could potentially lead to an underestimation of the uncertainties in the case of observables with initial state hadrons.

1 Introduction

Precision phenomenology will be of primary importance for new physics searches during the upcoming second run of the LHC, since no strong hints of deviation from the Standard Model (SM) have emerged from the analysis of run-1 data. These analyses require accuracy not only in the experimental measurements (i.e. high statistics and strict control of systematic errors) but also in the SM theoretical predictions. When experimental and theoretical uncertainties are of the same order of magnitude, it becomes important to be able to assess quantitatively the importance of all sources of uncertainties. Concerning theoretical uncertainties, one of the most important classes is represented by the uncomputed higher-order contributions to the perturbative expansion of the observables. Traditionally, the community has estimated them by varying the unphysical scales that appear in the perturbative result (e.g. the renormalization scale and the factorization scale). This procedure has been used for many years and it allows a quick estimate of the effects of missing higher orders. However this method yields intervals that do not posses a strict statistical meaning, therefore making it difficult to integrate these uncertainties in more complex analyses of the experimental data. To solve some of the shortcomings of the SV procedure, Cacciari and Houdeau have recently proposed a new method, built using the framework of Bayesian statistics [1]. While not considered in this proceeding, it should be pointed out that the same problem has also been studied with a more mathematical oriented approach, using sequence transformation techniques, in ref. [4], where also the concept of MHOU was originally introduced.

In our study [2], we first try to address some of the drawbacks of the original CH framework, introducing a modified version, named $\overline{\text{CH}}$, which we also extend to observables with initial state hadrons. We then consider the two models, SV and $\overline{\text{CH}}$, and we analyze their performances on two wide set of observables, characterized by the presence/absence of hadrons in the initial state.

[a]emanuele.bagnaschi@desy.de

This allows us to test the consistency of the $\overline{\text{CH}}$ model, estimate a heuristic confidence level for the SV intervals and then compare the two prescriptions for the estimation of the MHOUs.

2 Models for the estimation of theoretical uncertainties

2.1 Scale variation

The first model we consider is the standard and widely used procedure of scale variation. Given an arbitrary perturbative observable O, characterized by a central hard scale Q, its truncated perturbative expansion

$$O_k(Q,\mu) = \sum_{n=l}^{k} \alpha_s^n(\mu) c_n(Q,\mu) \tag{1}$$

contains a residual dependence on the unphysical scales (e.g. the renormalization scale), which here we collectively represent with μ, that were introduced during the computation. This dependence is unphysical and will vanish if the observable were computed at all orders. Specifically, the functional dependence on μ of the expression given in eq. 1 is of higher order in α_s and it is governed by the renormalization group equation. The latter is such that varying the scales yields terms that are effectively part of the unknown higher-order contribution, multiplied by logarithmic factors of the ratio of the scales Q and μ. Due to these properties, it is customary to evaluate the degree of convergence of a perturbative expansion (i.e. the size of the missing higher-order terms) by varying the unphysical scales around their central value Q in the interval $[Q/r, rQ]$, where the rescaling factor r is usually chosen equal to 2. Several prescriptions for SV are adopted in the literature, differing in the details of how the uncertainty interval is constructed from the values obtained when the scales are varied (e.g. scanning vs taking the values at the extremes of the variation interval).

However the SV method has two drawbacks. First of all, the intervals obtained in this way have a priori no statistical meaning and therefore can not be included consistently in other analyses. Secondly, the value for the rescaling factor r, usually assumed to be two, is arbitrary and there are no clear-cut theoretical justifications to opt for a specific value over another.

2.2 The Cacciari-Houdeau Bayesian framework

As a second prescription, we consider the Bayesian framework developed by Cacciari and Houdeau[1], originally introduced to address the shortcomings of SV. One of the drawbacks of the original CH model is that its prediction for the uncertainty intervals depends on the expansion parameter chosen for the perturbative series of the observable. However, in perturbative QCD, the expansion parameter is not unambiguously defined. To address these issues, we introduce a parameter λ that reflects our ignorance of the optimal expansion parameter. Our expression for a generic observable, which starts at order l and it is known up to order k, is then given by

$$O_k = \sum_{n=l}^{k} \left(\frac{\alpha_s}{\lambda}\right)^n (n-1)!\, \lambda^n \frac{c_n}{(n-1)!} \equiv \sum_{n=l}^{k} \left(\frac{\alpha_s}{\lambda}\right)^n (n-1)!\, b_n, \tag{2}$$

where we have isolated a factor $(n-1)!$ in the expansion. The latter can be motivated from theory by looking at the behavior of the coefficients c_n for large n. The same priors of the original CH model are retained. Then, we extrapolate λ by measuring the performance of the model for a fixed λ value on a given set of observables. At a given order and for a given DoB, we calculate for each observable the corresponding uncertainty interval. Then we compute the success rate, defined as the ratio between the number of observables whose next-order is within the computed DoB interval over the total number of observables in the set. We define the optimal λ value to be such that the success rate is equal to requested DoB.

We then perform the extension to hadronic observables

$$O_k(\tau, Q) = \mathcal{L}(Q) \otimes \sum_{n=l}^{k} \alpha_s^n C_n(Q) \tag{3}$$

in two possible ways:

1. By performing the convolution integral in eq. 3 (using the same PDFs at all orders), extracting the perturbative coefficients by re-expanding in power of α_s with the same factors as in the non-hadronic case and then by feeding them to the same model.

2. By going to Mellin space, identifying the dominant [b] Mellin moment N^*, applying the $\overline{\mathrm{CH}}$ model to the coefficient function at this moment and then rescaling back the uncertainty interval to the observable in the physical space. This procedure is theoretically cleaner, since it does not involve non-perturbative physics coming from the PDF.

For our global analysis we opted for the first method, due to its simplicity and ease of use. However we have also applied the second approach to some observables, like $pp \to H$. In all cases the value of λ should be re-determined with the same procedure that was used for the observables without initial state hadrons. We denote the new value with λ_h.

3 Results

We consider two sets of observables, characterized by the presence or absence of hadrons in the initial state. The former set includes the R ratio, QCD sum rules, event shape observables, particle decays and splitting kernels. The latter contains Higgs and weak bosons production (also in association with jets), $t\bar{t}$ and $b\bar{b}$ production. For each observable in the set under study, we compute the MHOU at a given order k with a specific model and we compare with the prediction at order $k+1$. We define the success rate of the model as the ratio of the observables for which the $k+1$ order is inside the error band over the total number of observables in the set. In the case of the $\overline{\mathrm{CH}}$ model, this procedure is repeated for different DoBs and it is also used to determine λ at the same time, while for SV the algorithm is repeated for different values of r.

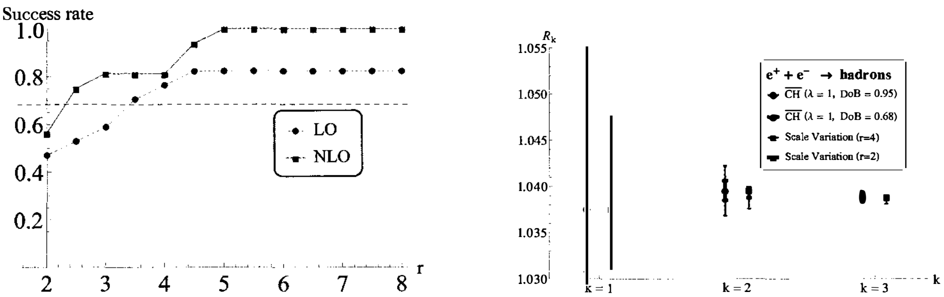

Figure 1 – On the left we show the results for the SV heuristic CL, for the non-hadronic observable set, considering the values assumed by the observable in the entire scale variation interval. On the right we show the comparison of the error bars, for $e^+e^- \to$ hadrons, produced by SV (red) and the $\overline{\mathrm{CH}}$ model (blue) for different values of r and DoB, respectively.

In the left plot of fig. 1, which shows the performance of SV for the non-hadronic observables, we notice that at LO (as expected) SV is poorly predictive of the next unknown-order up to $r = 3 - 4$, while at NLO we observe a heuristic 68% CL already for $r \simeq 2$. The comparison of

[b] We follow the observations, first appeared in ref. [3], on the analytic structure of the cross section in Mellin space and its dominant contributions.

the results for SV and $\overline{\mathrm{CH}}$ (with $\lambda = 1$, determined as explained above), on the right side of the same figure, allows us to compare the predictions from the two models for a specific observable, $e^+e^- \to$ hadrons. We see that the 68% DoB Bayesian intervals are slightly larger than the $r = 2$ SV intervals and comparable in size with the $r = 4$ ones.

In fig. 2, we show the same analysis of fig. 1 for the hadronic-observable set. From the left plot, we see that the SV intervals are less predictive than in the non-hadronic case and, even at NLO, a heuristic CL of 68% is obtained only for $r \simeq 4 - 5$, though the specific value depends whether one uses the NNLO PDF at all orders, or, as it is done in the plot, matches the PDF to the perturbative order of the computation. On the right, we show, as an example, the results for $pp \to H$. We see that, for this specific observable, the bands obtained with the $\overline{\mathrm{CH}}$ model[c] are systematically larger than the ones obtained with SV. We also observe that the two possible extensions to hadronic observables of the $\overline{\mathrm{CH}}$ model agree in their prediction for the MHOU.

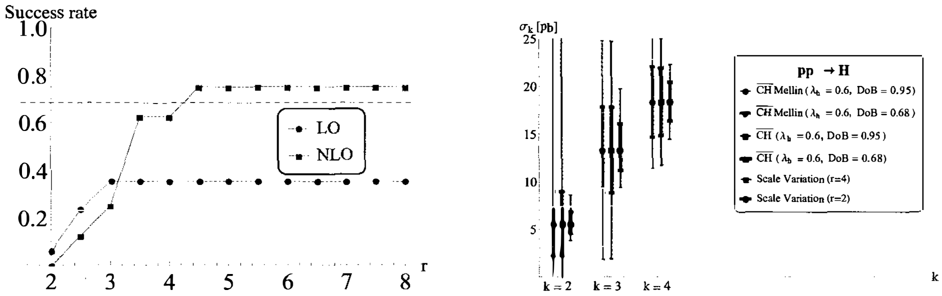

Figure 2 – On the left we show the results for the SV heuristic CL for the hadronic observable set, as a function of r, with order-matched PDFs and by considering only the observable values at the extremes of the scale variation interval. On the right we show the comparison of the error bars, for $pp \to H$, produced by SV (red) and the $\overline{\mathrm{CH}}$ model (blue and green) for different values of r and DoB, respectively.

4 Conclusions and outlook

We have performed a statistical study of the performances of the SV and $\overline{\mathrm{CH}}$ models. Concerning SV, we find that, for non-hadronic observables, a value of $r \simeq 2$ corresponds to a heuristic CL of about 68% at NLO. On the other hand, in the hadronic case, a larger value of r, between 4 and 5, is needed to reach the same confidence level (the precise value being dependent on the choice adopted for the PDFs). With respect to the $\overline{\mathrm{CH}}$ model, which we have also extended to hadronic observables, we find that a consistent determination of the value of λ is possible and that it leads to error bars that are of the same order of magnitude of the SV intervals, with a 68% DoB band usually slightly larger than the $r = 2$ and closer to the $r = 4$ SV interval. We have therefore shown that the $\overline{\mathrm{CH}}$ model can be reliably used to estimate MHOUs. Possible future improvements involve the introduction of a specific prior for the value of λ, to replace the current frequentist procedure, and the development of more refined models tailored on specific classes of observables, especially for the hadronic case.

References

1. M. Cacciari and N. Houdeau. JHEP **1109** (2011) 039 [arXiv:1105.5152 [hep-ph]].
2. E. Bagnaschi, M. Cacciari, A. Guffanti and L. Jenniches, JHEP **1502** (2015) 133 [arXiv:1409.5036 [hep-ph]].
3. M. Bonvini, S. Forte and G. Ridolfi. Nucl. Phys. B **847** (2011) 93 [arXiv:1009.5691 [hep-ph]].
4. A. David and G. Passarino, Phys. Lett. B **726** (2013) 266 [arXiv:1307.1843].

[c] In the hadronic case, we have found $\lambda_h \simeq 0.6$, reflecting systematically larger radiative corrections than in the non-hadronic one. Indeed smaller values of λ correspond to larger error bars in the $\overline{\mathrm{CH}}$ model.

Combining parton showers and NNLO matrix elements

S. Höche, Y. Li, S. Prestel[a]
Theory group, SLAC National Accelerator Laboratory,
Menlo Park, CA 94025, USA

In this talk, we discuss recent developments in combining parton showers and fixed-order calculations. We focus on the UN^{2}LOPS method for matching next-to-next-to-leading order computations to the parton shower, and we present results from SHERPA for Drell-Yan lepton-pair and Higgs-boson production at the LHC.

1 Introduction

With the LHC experiments entering the second long phase of data collection after the upgrade period, we expect that the Standard Model (SM) of particle physics will be probed in exquisite detail while searching for hints of phenomena beyond our current knowledge. A major role in this endeavor is played by parton-shower Monte Carlo programs, which allow to predict the full final-state kinematics on an event-by-event basis.

In this talk, we will briefly describe the evolution and status of combining fixed-order calculations with parton shower (PS) resummation, followed by comments on which state-of-the art merging schemes lend themselves to further improvements. We will then discuss how next-to-next-to-leading order (NNLO) accurate predictions can be included into event generators. Finally, we present results in the UN^{2}LOPS scheme [1,2] as implemented in SHERPA [3].

2 The story so far

Finding ways to combine accurate fixed-order calculations with parton showers has been a major topic in event generator development since the turn of the century. A decisive boost came from methods for merging multiple inclusive tree-level calculations by making them exclusive using Sudakov form factors derived from the parton shower [6,7,8]. Another breakthrough was the development of algorithms for matching parton showers to NLO QCD calculations [4].

All these methods have ambiguities and uncertainties. A particularly striking example of differences between NLO+PS matched results was presented in [5]: The prediction for the Higgs-boson transverse momentum distribution shown in this publication varies greatly with the matching scheme. Differences in the schemes are formally beyond the required NLO+PS accuracy. Their numerical size reveals, however, that more accurate and less variable calculations of the Higgs-boson + jet process must be included to make experimentally relevant predictions.

This can be achieved using methods for combining a sequence of multi-parton fixed-order calculations, often referred to as "multi-jet merging". Merging methods exist for tree-level [6] and NLO calculations [7,8]. They provide state-of-the art predictions for LHC Run-II. A comparison of NLO merging schemes in [9] has shown good agreement between different approaches. More importantly,

[a]Speaker

the agreement between theory and experiment is improved, and theoretical uncertainties may be reduced.

3 Moving towards NNLO accuracy

NLO multi-jet merging techniques have additional features compared to LO merging. For example, those real-emission corrections to $X + n$-jet production which lead to $n + 1$ well-separated jets above the merging scale need to be removed, since such configurations are already included by merging with the $n + 1$-jet calculation. In addition, the approximate virtual corrections included in the PS must, at $\mathcal{O}(\alpha_s^{n+1})$, be replaced by the full NLO result. A more subtle issue arises from additionally demanding the stability of inclusive jet cross sections [8,10]: In merged calculations, the emission probability is given by exact fixed-order matrix elements. In contrast, the resummed virtual corrections derive from the Sudakov factor of the parton shower. Upon integration over the radiative phase space, the two do not cancel, leading to a "unitarity violation".

This discrepancy can be removed using unitary merging techniques [8]. One of them is the so-called UNLOPS method. It allows, in a process-independent way, to add the precise difference between fixed-order real-emission matrix elements and their parton-shower approximations to the merged result. This is called the "subtract what you add" philosophy. In the UNLOPS scheme, it is possible to combine arbitrarily many NLO calculations, and include tree-level results when NLO calculations are not available. UNLOPS retains the merging scale as a *technical* parameter, since low merging scales – while desirable to use higher-order calculations over most of the phase space leads to inefficient event generation.

4 Combining NNLO calculations with parton showers

Although NLO merging yields accurate predictions for many multi-jet observables, it is desirable for some reactions to move beyond NLO accuracy. Such processes include reactions with large higher-order corrections, e.g. Higgs-boson production in gluon fusion, standard candles like Drell-Yan lepton pair production, and other phenomenologically important processes.

NNLO accurate matching to the parton shower has been achieved first in the MINLO approach [11]. The MINLO method [10] is based on matching the hard process plus one-jet NLO calculation to the parton shower, and supplement it with Sudakov form factors that account for the resummed virtual and unresolved higher-order corrections between the hard scale and the resolution scale of the jet. In its current implementation it uses analytic Sudakov factors derived for q_T resummation, which limits its applicability to hard processes with no light QCD jets in the final state. The genuine NNLO corrections are included through pre-tabulated phase-space dependent K-factors, which leads to fast event generation but makes the extension to processes with more complicated final states challenging.

Within the UN^{2}LOPS approach [1,2], a variant of UNLOPS, NNLO corrections associated with the emission of resolvable QCD radiation are treated as the hard process plus one additional jet at NLO. The remainder of the phase space is filled by a calculation for the hard process at NNLO, with a corresponding veto on any QCD activity. Both parts are separately finite, and parton shower matching is only needed for the first. To make the result physically meaningful, the separation cut must be smaller than the infrared cutoff of the parton shower. This requires very stable NLO matched calculations for the one-jet process. In contrast to the MINLO method, real-emission configurations do not receive a contribution from the NNLO K-factor.

Neither NNLOPS nor UN^{2}LOPS should be considered final a answer to NNLO+PS matching, but rather as a first step towards more general methods.

5 NNLO+PS matched results in SHERPA

We will now discuss some phenomenologically relevant results obtained with the UN^{2}LOPS matching as implemented in the SHERPA event generator. In order to control all aspects of the matched

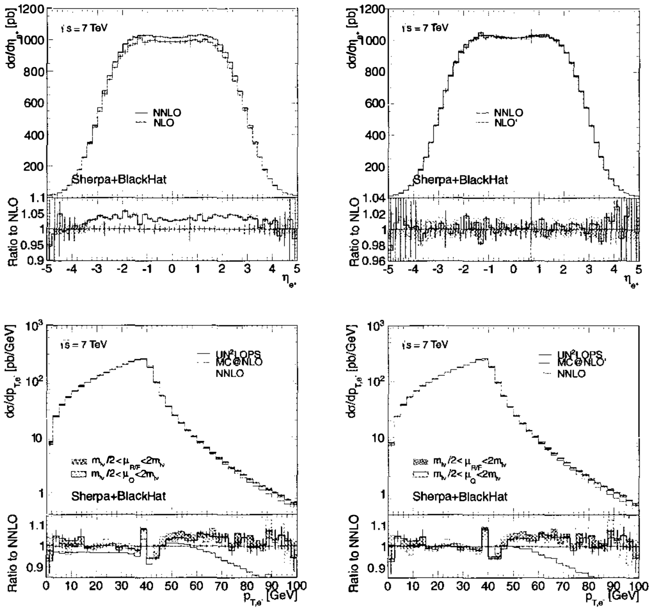

Figure 1 – Charged current Drell-Yan lepton pair production, for two different PDF choices. *Upper left*: Pseudorapidity of the positron at NLO and NNLO accuracy. NLO PDFs used in the NLO calculation. *Upper right*: Pseudorapidity of the positron. NNLO PDFs used in the NLO calculation. *Lower left*: $p_\perp$ of the positron. NLO PDFs used in MC@NLO. *Lower right*: $p_\perp$ of the positron. NNLO PDFs used in MC@NLO.

calculation, the full NNLO calculation using a $q_\perp$ cutoff method has been implemented in Sherpa itself. This technique is limited to processes without light jets in the hard process, a shortcoming that can in principle be remedied by using different techniques for performing the fixed-order NNLO calculation. The following plots, and the SHERPA plug-in containing the UN^{2}LOPS implementation are publicly available [14].

Figure 1 highlights an interesting feature of the NNLO corrections to neutral and charged current Drell-Yan lepton pair production. For inclusive observables, using a NNLO PDF for a NLO calculation reproduces the full NNLO calculation very well, both in normalization and in shape. This is clearly a very process-dependent statement, and it breaks down once an observable depends not only on the Born degrees of freedom, as shown in the lower right panel of Figure 1: In the phase space region which can only be accessed by giving the lepton-pair system transverse momentum ($p_T > 40$ GeV), the NNLO result cannot be mimicked by a NLO calculation. In this region the improvement obtained from UN^{2}LOPS is apparent.

The UN^{2}LOPS prescription has also been applied to [2]. Figure 2 exemplifies the residual uncertainties of the NNLO matched calculation in Higgs-boson production through gluon fusion. We use two different ways to include the Wilson coefficient for the ggh vertex [2]: A factorized matching scheme which is reminiscent of the POWHEG strategy, and an individual matching scheme that somewhat mimics the MC@NLO procedure. The results are as expected: The factorized approach leads to a harder tail in the $q_\perp$ distribution, whereas the individual matching has a softer tail and a small enhancement for medium $q_\perp$ values. The individual matching shows better agreement with the NNLO+NNLL result of the HqT program [13]. The uncertainty due to varying the parton shower starting scale becomes appreciable for small $q_\perp$ values, and is significantly larger than the resummation scale variation in HqT. This might be taken as indication that a more accurate parton shower would be beneficial.

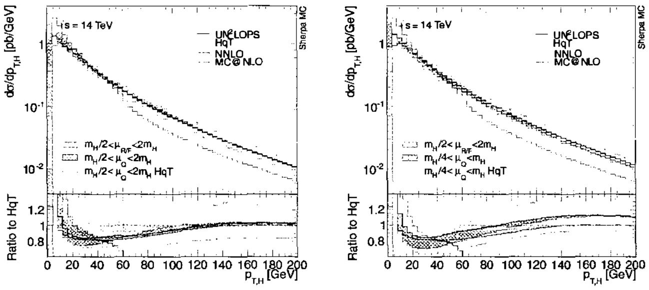

Figure 2 – Higgs boson $p_\perp$ spectrum in individual matching (left) and factorized matching (right).

6 Conclusions

We have reviewed the current status of matching and merging parton shower resummation and fixed order calculations. Some state-of-the-art NLO merging methods have recently been molded into NNLO matching methods. The prerequisite for these extensions was a well-defined one-jet cross section, which was then updated to NNLO accuracy for the inclusive process. Results of the UN^{2}LOPS scheme as implemented in SHERPA have been presented. This implementation includes new NNLO fixed-order calculations for (neutral and charged current) Drell-Yan lepton pair and (gluon-fusion initiated) Higgs-boson production. When applied to the Drell-Yan process, we find that the NLO results, when computed with NNLO PDFs, reproduce the full NNLO results for inclusive observables. For Higgs-boson production at NNLO+PS accuracy, two schemes were presented, highlighting some residual uncertainties of the matching.

Work supported by the US Department of Energy under contract DE–AC02–76SF00515.

References

1. S. Höche, Y. Li, S. Prestel. *Phys. Rev.*, D91(7):074015, 2015.
2. S. Höche, Y. Li, S. Prestel. *Phys. Rev.*, D90(5):054011, 2014.
3. T. Gleisberg, et al. *JHEP*, 02:007, 2009.
4. S. Frixione B. R. Webber. *JHEP*, 06:029, 2002. P. Nason. *JHEP*, 11:040, 2004. S. Frixione, P. Nason, C. Oleari. *JHEP*, 11:070, 2007.
5. S. Alioli, P. Nason, C. Oleari, E. Re. *JHEP*, 04:002, 2009.
6. S. Catani, F. Krauss, R. Kuhn, B. R. Webber. *JHEP*, 11:063, 2001. L. Lönnblad. *JHEP*, 05:046, 2002. M. L. Mangano, M. Moretti, R. Pittau. *Nucl. Phys.*, B632:343–362, 2002. F. Krauss. *JHEP*, 08:015, 2002. S. Höche, F. Krauss, S. Schumann, F. Siegert. *JHEP*, 05:053, 2009. K. Hamilton, P. Richardson, J. Tully. *JHEP*, 11:038, 2009. L. Lönnblad, S. Prestel. *JHEP*, 03:019, 2012. L. Lönnblad, S. Prestel. *JHEP*, 02:094, 2013.
7. N. Lavesson, L. Lönnblad. *JHEP*, 12:070, 2008. T. Gehrmann, S. Höche, F. Krauss, M. Schönherr, F. Siegert. *JHEP*, 01:144, 2013. S. Höche, F. Krauss, M. Schönherr, F. Siegert. *JHEP*, 04:027, 2013. R. Frederix, S. Frixione. *JHEP*, 12:061, 2012. S. Alioli, et al. *JHEP*, 09:120, 2013.
8. L. Lönnblad, S. Prestel. *JHEP*, 03:166, 2013. S. Plätzer. *JHEP*, 08:114, 2013.
9. J. Butterworth, et al. Les Houches 2013: SM Working Group Report. 2014.
10. K. Hamilton, P. Nason, C. Oleari, G. Zanderighi. *JHEP*, 05:082, 2013. K. Hamilton, P. Nason, G. Zanderighi. *JHEP*, 1210:155, 2012.
11. K. Hamilton, P. Nason, E. Re, G. Zanderighi. *JHEP*, 10:222, 2013. A. Karlberg, E. Re, G. Zanderighi. *JHEP*, 09:134, 2014. K. Hamilton, P. Nason, G. Zanderighi. *JHEP*, 05:140, 2015.
12. S. Catani, M. Grazzini. *Phys.Rev.Lett.*, 98:222002, 2007. S. Catani, L. Cieri, G. Ferrera, D. de Florian, M. Grazzini. *Phys.Rev.Lett.*, 103:082001, 2009.
13. G. Bozzi, S. Catani, D. de Florian, M. Grazzini. *Phys.Lett.*, B564:65–72, 2003. G. Bozzi, S. Catani, D. de Florian, M. Grazzini. *Nucl. Phys.*, B737:73–120, 2006. D. de Florian, G. Ferrera, M. Grazzini, D. Tommasini. *JHEP*, 11:064, 2011.
14. `http://www.slac.stanford.edu/~shoeche/pub/nnlo`.

QCD Amplitudes: new perspectives on Feynman integral calculus

Pierpaolo Mastrolia
Dipartimento di Fisica e Astronomia, Università di Padova, and INFN Sezione di Padova, via Marzolo 8, 35131 Padova, Italy.
Max-Planck Insitut für Physik, Föhringer Ring 6, 80805 München, Germany.

I analyze the algebraic patterns underlying the structure of scattering amplitudes in quantum field theory. I focus on the decomposition of amplitudes in terms of independent functions and the systems of differential equations the latter obey. In particular, I discuss the key role played by unitarity for the decomposition in terms of master integrals, by means of generalized cuts and integrand reduction, as well as for solving the corresponding differential equations, by means of Magnus exponential series.

1 Introduction

High energy particle collisions are the ideal framework for accessing new informations on matter constituents and forces of nature. The higher the energy of the colliding particles, the richer the landscape of the produced ones. The discovery of new physics interactions cannot be disentangled from the discovery of massive, *heavy* particles, emerging from collisions of ever increasing energy. On the other side, by increasing energy, also the probability of producing *many light* particles is enhanced. Therefore, advances in High Energy Particle Physics necessarily depend on our ability to describe the scattering processes involving *many* light and heavy *particles* at very high accuracy, hence they depend on our capability of evaluating Feynman diagrams. Beyond leading order (LO), Feynman diagrams represent challenging multidimensional/multivariate integrals, whose direct evaluation is often prohibitive, therefore the computation of scattering amplitudes beyond the LO is addressed in two stages: *i)* the decomposition in terms of a basis of functions, and *ii)* their evaluation of the elements of such a basis, called *master integrals* (MIs). In this contribution, I elaborate on the algebraic properties of Feynman integrals, which can be exploited for decomposing them in terms of MIs and for computing the latter. The techniques I discuss can be applied to generic amplitudes, and have a impact on high-accuracy prediction for collider physics, as well as for exploring the more formal aspect of quantum field theory.

Let us observe that amplitudes can be decomposed in terms of independent functions, exactly like a vector can be decomposed along basic directions. One needs a *basis* and a *projection* technique. The latter is necessary to extract the coefficients of the linear combination. *Factorization* is the basic idea we are going to elaborate on. Factorization is ubiquitous in the discovery of new mathematical and physical concepts. Complex numbers emerged from factorizing the simplest number we may think of, *i.e.* $1 = (-i)i$; quantum mechanics relies on the factorization of the identity matrix, $\mathbb{I} = \sum_n |n\rangle\langle n|$; Dirac equation emerged from factorizing the d'Alambertian operator, *i.e.* $\Box = (-i\partial\!\!\!/)(i\partial\!\!\!/)$. What does happen when amplitudes factorize?

Cutting a virtual particle and bringing it on the mass shell ($p^2 = m^2$), turned out to be a suitable projection technique yielding amplitudes decomposition. Why multiple-cuts are important? First, because multiple-cuts yield functions identification. Since any diagram is characterized by its internal lines, a given master diagram is univocally identified by a cut-diagram where all internal particles are on-shell. Moreover, when applied to amplitudes, multiple-cuts behave like *high-pass filters*, which isolate only the diagrams that have those internal lines to be cut, while the others are automatically discarded. Therefore, by considering all possible cuts of an amplitude, in a top-down procedure, from the maximum number of cuts to the lowest one, it is possible to build a (triangular) system of equations from which *all* coefficients can be determined.

2 Integrand decomposition

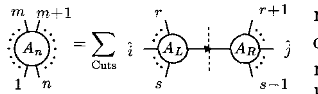

Figure 1 – Tree-level recurrence relation.

Tree-level scattering amplitudes obey a quadratic recurrence relation [1] (BCFW), depicted in Fig.1, whose derivation relies on Cauchy's residue theorem. Since tree amplitudes are rational functions of kinematic variables, the BCFW recurrence can be understood as due simply to partial fractioning [2], because *residue theorem applied to rational functions amounts to partial fractions.* Is that just accidental, and holding for tree-level amplitudes, or partial fractioning can be exploited also at higher orders?

The *integrand reduction algorithm* [3] had a dramatic impact on our ability of computing one-loop amplitudes. The basic idea lies in the existence of a relation between numerators and denominators of scattering amplitudes which can be used to decompose the integrands of one-loop amplitudes in terms of integrands of MIs. The amplitude decomposition in terms of MIs is then achieved after integrating the integrand decomposition. The coefficients of the MIs are a subset of the coefficients appearing in the decomposition of the integrands. Therefore, within the integrand reduction algorithm, coefficients can be determined simply by algebraic manipulation, with the great advantage of bypassing any integration.

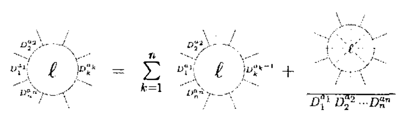

Figure 2 – (right) Multiloop integrand decomposition formula. A generic ℓ-loop integrand with a certain number of denominators, each raised to an arbitrary power, is expressed as combination of integrands where the power of a given denominator is reduced by one, plus a term corresponding to the residue, depicted by a cut diagram.

The idea behind the GoSam framework [4,5] is to combine automated diagram generation and algebraic manipulation with the integrand-level reduction. The code is very flexible and it has been employed in several applications at NLO QCD accuracy, studies of BSM scenarios, electroweak calculations, and recently also within NNLO calculations. It is interfaced to several MonteCarlo event generators, like SHERPA, HERWIG, AMC@NLO. In particular, GoSam was used to evaluate the NLO QCD correction to $pp \to Hjjj$ (in the infinite top-mass limit) [6], which was the subject of a recent new phenomenological analysis [7].

The extension of the integrand decomposition beyond one-loop has been proposed in [8], and refined in [9,10,11], where the unitarity-based decomposition of multi-loop integrands has been addressed as a polynomial decomposition problem, and systematized within the *multivariate* *polynomial division algorithm.* Accordingly, any generic multi-loop integral with n denominators, $\mathcal{I}_{12\ldots n} = \int d^d q_1 \cdots d^d q_m \; I_{12\ldots n}$, with $I_{12\ldots n} = N_{12\ldots n}/(D_1 \ldots D_n)$, can undergo an integrand decomposition by means of successive polynomial divisions (modulo Gröbner basis) between the numerator and the denominators, see Fig.2. The result of the decomposition reads as,

$$I_{12\ldots n} = \frac{\Delta_{12\ldots n}}{D_1 \ldots D_n} + \frac{\Delta_{2\ldots n}}{D_2 \ldots D_n} + \ldots + \frac{\Delta_{12\ldots n-1}}{D_1 \ldots D_{n-1}} + \ldots + \frac{\Delta_n}{D_n} + \ldots + \frac{\Delta_1}{D_1} \,, \tag{1}$$

where $\Delta_{i\ldots j}$ are the remainders of the iterated divisions (w.r.t. the Gröbner basis of the ideal $\langle D_i, \ldots, D_j \rangle$). Each residue $\Delta_{i\ldots j}$ is a polynomial in the components of the loop momenta not constrained by the cut $D_i = \ldots = D_j = 0$. Therefore, by integrating both sides, one obtains the decomposition of the original integral $\mathcal{I}_{12\ldots n}$ in terms of *independent integrals.* The integrand decomposition (1) implies that, exactly as it happens for the tree-level amplitudes, also the integrands of multi-loop amplitudes can be decomposed in terms of independent building blocks simply by *partial fractioning* !

While in the one-loop case the independent integrals are analytically known, in the multi-loop case, their classification and evaluation is an open problem.

3 Differential Equations and Feynman Integrals

The *method of differential equations* (DEs) [12,13,14], reviewed in [15,16,17], is one of the most effective techniques for computing dimensionally regulated multi-loop integrals.

In fact, any ℓ-loop integral $\mathcal{I}$ is a homogeneous function of external momenta p_i and masses m_i, whose degree $\gamma = \gamma(d, \ell)$ depends on the space-time dimensions $d = 4 - 2\epsilon$, on the number of loops ℓ, and on the powers of denominators. Therefore, one can write the Euler scaling equation,

$$\Big(\sum_i p_i \cdot \partial_{p_i} + \sum_j m_j^2 \, \partial_{m_j^2} \Big) \mathcal{I} = \gamma(d, \ell) \mathcal{I} \,, \tag{2}$$

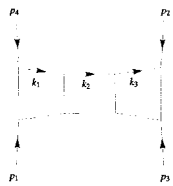

Figure 3 – (The three-loop ladder box diagram, with one off-shell leg: the solid lines stand for massless particles; the dashed line represents a massive particle. Momentum conservation is $\sum_{i=1}^4 p_i = 0$, with $p_i^2 = 0$ $(i = 1,\ 2,\ 3)$ and $p_4^2 = m_H^2$.

where $\partial_x \equiv \partial / \partial x$. Euler relation can be engineered to show that MIs obey linear systems of first-order differential equations (DEs) in the kinematic invariants, which can be used for the determination of their actual expression. By establishing an analogy between Schrödinger Equation in the interaction picture (in presence of an Hamiltonian with a linear perturbation) and systems of DEs for Feynman integrals (whose associated matrix is linear in ϵ) [18], we have recently proposed an algorithm to find the transformation matrix yielding to a *canonical* system [19], where the dependence on the dimensional parameter ϵ is factorized from the kinematic. In particular, we found that the canonical transformation can be obtained by means of Magnus exponential matrix [20]. The integration of canonical systems is simple, and the analytic properties of its solution are manifestly inherited from the associated matrix, that becomes the kernel of the representation of the solutions in terms of repeated integrations. The latter in fact are the coefficients of a Magnus (or alternatively Dyson) series expansion in ϵ. Magnus exponential is not unitary, as it happens in the quantum mechanical case, but the proposed method can be considered also inspired by unitarity.

3.1 *Applications*

We made use of Magnus theorem for the determination of non-trivial integrals, like the two-loop vertex diagrams for the electron form factors in QED and the two-loop box integrals for the $2 \to 2$ massless scattering [18], the two-loop corrections to the $pp \to Hj$, as well as for evaluating the three-loop ladder diagrams for $pp \to Hj$ (in the infinite top-mass approximation) [21], see Fig.3. The latter is a formidable calculation involving the solution of a system of 85 MIs. In this case, after identifying a set of MIs obeying a linear system of differential equations in $x = -s/m_H^2$ and $y = -t/m_H^2$, by means of a Magnus transform, the system can be brought in canonical form, reading as,

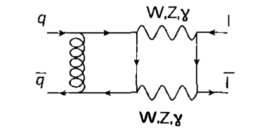

Figure 4 – Representative two-loop box diagram for QCD-EW corrections to $q\bar{q} \to \ell^+\ell^-$.

$$d\vec{\mathcal{I}}(x,y) = \epsilon \; A(x,y) \; \vec{\mathcal{I}}(x,y) \; , \tag{3}$$

where $\vec{\mathcal{I}}$ is the vector of MIs, and $df = \partial_x f dx + \partial_y f dy$. The matrix A is purely logarithmic, $A(x,y) = a_1 \ln(x) + a_2 \ln(1-x) + a_3 \ln(y) + a_4 \ln(1-y) + a_5 \ln(x+y) + a_6 \ln(1-(x+y))$, where the a_i ($i = 1, \dots, 6$) are 85×85 matrices whose entries are just rational numbers. The logarithmic form of A trivializes the solution, which can be written as a Dyson series in ϵ, where the coefficient of the series are combinations of Multiple Polylogarithms with uniform weight (where the weight increases as the order in ϵ does).

Boundary conditions are determined by imposing the regularity of the solutions in special kinematic configurations. Surprisingly, to fix the boundary values of all 85 MIs, only 2 simple integrals have to be independently provided.

Also, we have been considering the mixed EW-QCD corrections to Drell-Yan production at NNLO, whose representative diagram is depicted in Fig.4. Also in this case, Magnus exponential can employed to reach a canonical system for the 48 MIs drawn in Fig.5, in the variables $x = -s/m_V^2$ and $y = -t/m_V^2$, with $V = W, Z$ [22].

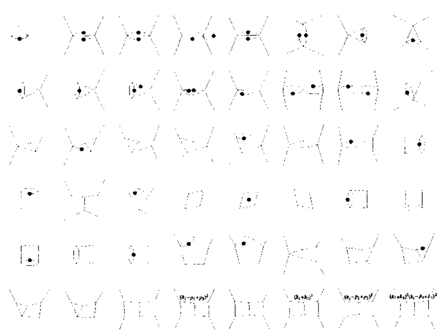

Figure 5 – Master integrals for $q\bar{q} \to \ell^+\ell^-$ at two-loop. Plane lines stands for massless particle, while dashed lines stands for massive particles.

4 Conclusions

In this contribution, I have analyzed the algebraic patterns underlying the structure of scattering amplitudes in gauge theory. *Unitarity* plays a central role in the context of evaluating scattering amplitudes. It not only inspired methods to perform the amplitudes decomposition, by means of unitarity-cuts, but it also suggested a technique for the evaluation of master integrals, by means of matrix exponentials, similar to the unitary time-evolution in quantum mechanics.

Acknowledgments

Supported by the Alexander von Humboldt Foundation, in the framework of the Sofja Kovalevskaja Award 2010, endowed by the German Federal Ministry of Education and Research.

References

1. Ruth Britto, Freddy Cachazo, and Bo Feng. New Recursion Relations for Tree Amplitudes of Gluons. *Nucl. Phys.*, B715:499–522, 2005.
2. Diana Vaman and York-Peng Yao. QCD recursion relations from the largest time equation. *JHEP*, 0604:030, 2006.
3. Giovanni Ossola, Costas G. Papadopoulos, and Roberto Pittau. Reducing full one-loop amplitudes to scalar integrals at the integrand level. *Nucl.Phys.*, B763:147–169, 2007.
4. Gavin Cullen, Nicolas Greiner, Gudrun Heinrich, Gionata Luisoni, Pierpaolo Mastrolia, et al. Automated One-Loop Calculations with GoSam. *Eur.Phys.J.*, C72:1889, 2012.
5. Gavin Cullen, Hans van Deurzen, Nicolas Greiner, Gudrun Heinrich, Gionata Luisoni, Pierpaolo Mastrolia, et al. $GOSAM$-2.0: a tool for automated one-loop calculations within the Standard Model and beyond. *Eur.Phys.J.*, C74(8):3001, 2014.
6. G. Cullen, H. van Deurzen, N. Greiner, G. Luisoni, P. Mastrolia, et al. Next-to-Leading-Order QCD Corrections to Higgs Boson Production Plus Three Jets in Gluon Fusion. *Phys.Rev.Lett.*, 111(13):131801, 2013.
7. Nicolas Greiner, Stefan Hoeche, Gionata Luisoni, Marek Schonherr, Jan-Christopher Winter, et al. Phenomenological analysis of Higgs boson production through gluon fusion in association with jets. 2015.
8. Pierpaolo Mastrolia and Giovanni Ossola. On the Integrand-Reduction Method for Two-Loop Scattering Amplitudes. *JHEP*, 1111:014, 2011.
9. Simon Badger, Hjalte Frellesvig, and Yang Zhang. Hepta-Cuts of Two-Loop Scattering Amplitudes. *JHEP*, 1204:055, 2012.
10. Yang Zhang. Integrand-Level Reduction of Loop Amplitudes by Computational Algebraic Geometry Methods. *JHEP*, 1209:042, 2012.
11. Pierpaolo Mastrolia, Edoardo Mirabella, Giovanni Ossola, and Tiziano Peraro. Scattering Amplitudes from Multivariate Polynomial Division. *Phys.Lett.*, B718:173–177, 2012.
12. A.V. Kotikov. Differential equations method: New technique for massive Feynman diagrams calculation. *Phys.Lett.*, B254:158–164, 1991.
13. Ettore Remiddi. Differential equations for Feynman graph amplitudes. *Nuovo Cim.*, A110:1435–1452, 1997.
14. T. Gehrmann and E. Remiddi. Differential equations for two loop four point functions. *Nucl.Phys.*, B580:485–518, 2000.
15. Mario Argeri and Pierpaolo Mastrolia. Feynman Diagrams and Differential Equations. *Int.J.Mod.Phys.*, A22:4375–4436, 2007.
16. Vladimir A. Smirnov. Analytic tools for Feynman integrals. *Springer Tracts Mod.Phys.*, 250:1–296, 2012.
17. Johannes M. Henn. Lectures on differential equations for Feynman integrals. *J.Phys.*, A48(15):153001, 2015.
18. Mario Argeri, Stefano Di Vita, Pierpaolo Mastrolia, Edoardo Mirabella, Johannes Schlenk, et al. Magnus and Dyson Series for Master Integrals. *JHEP*, 1403:082, 2014.
19. Johannes M. Henn. Multiloop integrals in dimensional regularization made simple. *Phys.Rev.Lett.*, 110:251601, 2013.
20. W. Magnus. On the exponential solution of differential equations for a linear operator. *Comm. Pure and Appl. Math.*, VII, 1954.
21. Stefano Di Vita, Pierpaolo Mastrolia, Ulrich Schubert, and Valery Yundin. Three-loop master integrals for ladder-box diagrams with one massive leg. *JHEP*, 1409:148, 2014.
22. Roberto Bonciani, Stefano Di Vita, Pierpaolo Mastrolia, and Ulrich Schubert. work in progress.

Colour connection and the doubly-heavy hadron production in e^+e^- annihilations

LI, Shi-Yuan
School of Physics, Shandong University, Jinan, 250100, P.R. China

The colour connection of the parton system is an important bridge to connect the perturbative phase and the hadronic phase in high energy collisions. We discuss the colour connections with a simple example, *i.e.*, four heavy quark system in e^+e^- annihilation, emphasizing on a special one, which is necessary for the doubly heavy baryon and tetraquark productions. We then investigate the hadronization effects with the help of various hadronization models. The global properties related to a certain colour connection are not sensitive to hadronization models. We also simply mention how to search for the doubly heavy hadrons in B factories by the help of the event shape in the end of the paper.

In high energy collisions, the produced final state partons transit into hadrons after hadronization. This is one of the most important processes for understanding the non-perturbative quantum chromodynamics and the confinement mechanism. e^+e^- annihilation has the advantage that the hadronization results can be compared with the experimental data directly to extract informations of hadronization because of no hadrons in the initial states. To embed the parton system into a hadronization model, it is necessary to specify the concrete colour connection. However, the colour connection for one multiparton system is not unique. Some clues can be obtained by analyzing the decomposition of the colour space of the final partons [1,2,3,4,5]. One of the interesting and important examples is the four-heavy-quark system ($QQ'\bar{Q}\bar{Q}'$), in which many phenomena related to QCD properties can be studied, *e.g.*, the (re)combination of quarks in the production of special hadrons, the influence of soft interaction on the reconstruction of intermediate particles (such as $W^{\pm}$), *etc.*, most of which are more or less related to the colour connections among these four quarks. In Ref. [4], the interesting decompositions of the colour space of the $QQ'\bar{Q}\bar{Q}'$ system in e^+e^- annihilation have been discussed, which are

$$\begin{aligned}&(3_Q \otimes 3_{Q'}) \otimes 3^*_{\bar{Q}} \otimes 3^*_{\bar{Q}'} = 3^*_{QQ'} \otimes 3^*_{\bar{Q}} \otimes 3^*_{\bar{Q}'} \oplus \cdots, \quad or \\ &3_Q \otimes 3_{Q'} \otimes (3^*_{\bar{Q}} \otimes 3^*_{\bar{Q}'}) = 3_Q \otimes 3_{Q'} \otimes 3_{\bar{Q}\bar{Q}'} \oplus \cdots,\end{aligned} \tag{1}$$

where 3 and 3* denote the triplet and anti-triplet representations of the $SU_c(3)$ Group respectively, and the subscripts correspond to the relevant (anti)quark. When two (anti)quarks in colour state 3*(3) attract each other to form a(n) '(anti)diquark' and the invariant mass is sufficiently small, it can hadronize into a(n) (anti)baryon (tetraquark). The hadronization is a 'branching' process via the creation of quarks from vacuum by the strong interactions within the system. In this process, if taking $cc\bar{c}\bar{c}$ as an example, the diquark (cc) combines with a quark q (antidiquark $\bar{q}\bar{q}'$) to form Ξ^+_{cc} [6,7] (T_{cc} [8]). To balance the quantum numbers of colour and flavour, an antiquark/diquark must be simultaneously created from vacuum. To branch them further, more quark pairs and diquark pairs must be created from vacuum via the interactions among the quark system. Such a cascade process will proceed until the end of time when most of the 'inner energy' of the entire system is transformed into the kinematical energies and masses of the produced hadrons. Each of two newly created quarks (antidiquarks) combines with each of the primary $\bar{c}$ quarks to respectively hadronize into two open charmed hadrons, which can be described by an assigned concrete hadronization model (for details, see [9,10,11,12]). In Ref. [4], we adopted the Lund String Model [9,10], and to clearly describe the colour configuration mentioned above, a three-jet event shape is considered. It needs to be emphasized that the above description of the hadronization picture and the event shape have no dependence on hadronization models. However, we want to study to what extent different hadronization models interplay with this kind of colour connection. For this purpose, we also employ Quark Combination Model [13,14] to deal with the hadronization of the remnant partons besides Ξ_{cc}^{+} (T_{cc}). As other hadronization models, Quark Combination Model successes in reproducing experimental data of $e^+e^- \to h's$ and $pp(\bar{p}) \to h's$ processes. As a matter of fact, the baryon to meson ratio [15,16] and constituent quark number scaling of elliptic flow v_2 [17] measured at RHIC experiments can be naturally understood. Furthermore, compared with other hadronization models, Quark Combination Model can be easily used to deal with the hadronization of the hidden quarks [18,19].

The details of the application of the hadronization can be found in Ref. [4]. As for Ξ_{cc}^{+} production, the complementary antiquark can produce an antibaryon by combining with an antidiquark, and the balancing diquark pair is broken by the interactions within the remaining system and then each of two quarks becomes connected to the primary $\bar{c}$ quark to form two $q'\bar{c}$ colour singlet systems. The fragmentation of the heavy diquark can be described by the Peterson formula [20]

$$f(z) \propto \frac{1}{z(1 - 1/z - \epsilon_Q/(1-z))^2}, \tag{2}$$

where ϵ_Q is a free parameter which is expected to scale between flavors as $\epsilon_Q \propto 1/m_Q^2$. The fragmentation of the complementary (anti)quark can be described with the help of standard fragmentation function [21] as well as the analytical formulation employed in PYTHIA [10]

$$f(z) \propto z^{-1}(1-z)^a exp(-bm_\perp^2/z), \tag{3}$$

where a and b are free parameters, as can be found in Ref. [10].

The hadronization of the remaining $q'\bar{c}$ systems is described by the hadronization models. In the framework of Quark Combination Model [13,14], Quark Production Rule and Quark Combination Rule are adopted to describe the hadronization in a colour singlet system, a simple Longitudinal Phase Space Approximation is used to obtain the momentum distribution for primary hadrons in its own system, and then this hadronization scheme is extended to the multi-parton states.

For the center-of-mass energy set to Z^0 pole, we investigated the hadronization effects on jets. To demonstrate the hadronization effects, the transverse-momentum (with respect to the thrust axis) distributions of Ξ_{cc}^{+}, are calculated. The absolute values of the distributions more or less depend on the parameters in Eq. (2), (3) and the entire hadronization. Once data are available at the future relevant experiments, *e.g.*, International Linear Collider, the Higgs factory and Z^0 factory, *etc.*, the fragmentation functions and/or the parameters can be tuned according to the comparison with data. The details can be found in our recent papers mentioned above.

In the special colour connection discussed here, each of two newly created quarks and one primary $\bar{c}$ are connected by the colour flow tube, while there is no colour flow between two primary $\bar{c}$ quarks. So after hadronization, the produced hadrons will mainly distribute along two colour flow and almost no hadrons emerge in the phase-space between two primary $\bar{c}$ quarks. This is so-called 'string effect' and the corresponding event shape is not sensitive to which hadronization model is used. To show this effect (event shape), We choose the more symmetric three-jet events by requiring that the angle between any two jets is larger than $\pi/2$. Because of momentum conservation, all three jet momenta must be in the same plane ($\mathcal{P}$) in the e^+e^- center-of-mass frame [25]. To obtain $\vec{k}_i'$ in the plane $\mathcal{P}$, the three-momentum of each final-state particle $\vec{k}_i$ is projected onto one of the three regions between the jets. The three-momentum of the jet that contains Ξ_{cc}^+ is chosen to be the x axis. The angle between $\vec{k}_i'$ and the x axis is the azimuthal angle ϕ of the corresponding particle. We can then calculate the final particle-number (energy) distribution $1/N\, dN/d\phi$ $(1/E\, dE/d\phi)$. The corresponding results are obviously similar for various hadronization models. This can help to justify our understanding on the hadronization described above.

Therefore the study of colour connections is important for understanding nonperturbative QCD. The future relevant experiments, *e.g.*, International Linear Collider, the Higgs factory and Z^0 factory, *etc.*, can provide opportunities for this study. Moreover, it is well known that the hadronization model should be universal for different hadronization processes. So LSM and QCM, *etc.*, can also be applied in other hadronization processes, *e.g.*, pp collision in Large Hadron Collider (LHC) and DIS. For the case that four-quark system emerges which has large rapidity gap with other clusters, the hadronization effects can also be studied by QCM when suitable observables introduced, *e.g.*, the ratio of baryon to meson of Eq. (**??**). In addition, cc can be regarded as a coloured cluster, so if a similar heavy coloured particle [26,27] beyond Standard Model is produced at LHC, our method can provide useful hints to investigate the related hadronization phenomena.

As has mentioned above, the doubly heavy hadron is the key trigger for the colour connection we discussed in this paper. So it is very crucial to investigate the progress of the experiments. In the hadroproduction process of charged hyperon beam on nuclear targets, a resonance decaying into $\Lambda_c^+ K^- \pi^+$ [?] and pD^+K^- is observed by the SELEX Collaboration. The resonance could be one of doubly charmed hadrons, Ξ_{cc}^+ baryon. However, in the following studies of the $\Lambda_c^+ K^- \pi^+$ mass spectrum at B factories, both Barbar and Belle have yet not found this resonance. A search performed by FOCUS Collaboration in the photoproduction process gives no evidence, either. Recently, LHCb Collaboration look for Ξ_{cc}^+ in the decay channel $\Lambda_c^+ K^- \pi^+$ in pp collisions, and find no signal. In an improved search with more data and additional decay modes, Belle Collaboration again fail to give positive evidence. The production mechanism for doubly charmed baryons seems intriguing.

All the above mentioned experiments have used the $\Lambda_c^+ K^- \pi^+$ channel to search for Ξ_{cc}^+. The number of reconstructed Λ_c^+ in BaBar (~ 600000) and that in FOCUS (~ 19500) are both much larger than that in SELEX (~ 1650), but only SELEX observes doubly charmed baryon. This fact forces people to suspect whether Ξ_{cc}^+ can be produced only in hadroproduction with hyperon beams. It is necessary to perform more exploration at Belle and BaBar to dispel the suspicion. In e^+e^- annihilation, the cross sections do not prefer the forward direction as in high energy hadronic interactions. The 4π spectrometers can record most of the reaction processes. If we improve the method to veto the background and/or fluctuations for the measurement, we are possible to get a signal or a stronger exclusion.

In e^+e^- annihilation, one must have two pairs of $c\bar{c}$ to produce Ξ_{cc}^+. The lowest order partonic process is $e^+e^- \to c\bar{c}c\bar{c}$. One $c\bar{c}$ pair is produced via the virtual photon, and the other $c\bar{c}$ pair is then produced via the virtual gluon splitting which is emitted from one of the quark/antiquark lines. When these two c's are close to each other in phase space, they can hadronize into Ξ_{cc}^+. Otherwise, all the charm quarks/antiquarks will hadronize into singly charmed hadrons. The latter case also belongs to the background. The quark and the gluon propagators together determine the phase space configuration. This apparent feature suggests that the generation of Ξ_{cc}^+ associates with the three-jet like event shape: a cc jet, one $\bar{c}$ jet close to it, while the other $\bar{c}$ jet almost in the opposite direction. Therefore, one may experimentally identify such three jets first, then reconstruct Λ_c^+ only in the cc jet (and the nearside $\bar{c}$ jet if not well separated), and then search for doubly charmed baryons employing these Λ_c^+, K^-'s and π^+'s only in the same jet. By such an investigation, those Λ_c^+'s as well as K^-'s and π^+'s which apparently belong to the awayside $\bar{c}$ jet could be vetoed. The essential question is how to identify these three jets. In this work we find that in most cases the cc jet is the most energetic one, while the awayside $\bar{c}$ jet is the second. Further more, these three jets belong to three energy regions almost without overlap, which means that all these three jets can be well identified. All the particles (like those Λ_c^+'s, K^-'s and π^+'s) belong to the awayside $\bar{c}$ jet can be vetoed from the construction of Λ_c^+ as well as Ξ_{cc}^+. This method can also suppress the background process by orders of magnitude. We hope the forthcoming B factory experiments can provide an improved answer. The details of this part can be found from [5].

References

1. Qun Wang and Qu-Bing Xie, Phys. Rev. D **52**, 1469, 1995.
2. Qun Wang, G. Gustafson and Qu-Bing Xie, Phys. Rev. D **62** 054004, 2000.
3. W. Han, S. -Y. Li, Z. -G. Si and Z. -J. Yang, Phys. Lett. B **642**, 62 (2006).
4. Y. Jin, S. -Y. Li, Z. -G. Si, Z. -J. Yang and T. Yao, Phys. Lett. B **727**, 468 (2013).
5. Y. Jin, S. Y. Li, Y. R. Liu, Z. G. Si and T. Yao, Phys. Rev. D **89**, no. 9, 094006 (2014).
6. J. P. Ma and Z. G. Si, Phys. Lett. B **568** (2003) 135.
7. J. Jiang, X. -G. Wu, S. -M. Wang, J. -W. Zhang and Z. -Y. Fang, Phys. Rev. D 87, **054027** (2013).
8. S. Zouzou, B. Silvestre-Brac, C. Gignoux, J. M. Richard, Z. Phys. C **30**, 457 (1986).
9. B. Andersson, 'The Lund Model' (Cambridge University Press, 1998), and references therein.
10. T. Sjostrand, P. Eden, C. Friberg, L. Lonnblad, G. Miu, S. Mrenna and E. Norrbin, Comput. Phys. Commun. **135**, 238 (2001).
11. G. Marchesini and B. R. Webber, Nucl. Phys. B **238**, 1, 1984; B. R. Webber, Nucl. Phys. B **238**, 492, 1984.
12. G. Corcella et al., JHEP 0101, 010, 2001.
13. Si Z G, Xie Q B, Wang Q. Commun Theor Phys, 1997, 28: 85-94; Si Z G, Xie Q B. High Ener Phys and Nucl Phys, 1999, 23: 445-458.
14. Xie Q B, Liu X M. Quark production rule in e^+e^- annihilation to two jets. Phys Rev D, 1988, 38: 2169-2177
15. Adler SS *et al.*, Phys. Rev. Lett. **91**, 172301 (2003).
16. Adams J *et al.*, arXiv:nucl-ex/0601042; Long H, J. Phys. G **30**, 193 (2004).
17. S. S. Adler *et al.* [PHENIX Collaboration], Phys. Rev. Lett. **91**, 182301 (2003); J. Adams *et al.* [STAR Collaboration], Phys. Rev. Lctt. **92**, 052302 (2004); J. Adams *et al.* [STAR Collaboration], Phys. Rev. Lett. **95**, 122301 (2005).
   18
18. T. Han, Z. Si, K. M. Zurek and M. J. Strassler, JHEP **0807**, 008 (2008).
19. R. Essig, P. Schuster and N. Toro, Phys. Rev. D **80**, 015003 (2009).
20. C. Peterson, D. Schlatter, I. Schmitt and P. Zerwas, Phys. Rev. D **27** (1983) 105.
21. S. Albino, B. A. Kniehl and G. Kramer, Nucl. Phys. B **725**, 181 (2005).
22. Xie Q B, in Proceedings of the XIXth International Symposium on Multi-particle Dynamics 1988, edited by D. Schiff and J. Tran Thanh Van (World Scientific, Singapore 1988), P. 369, and the references therein.
23. W. Han, S. -Y. Li, Y. -H. Shang, F. -L. Shao and T. Yao, Phys. Rev. C **80** (2009) 035202.
24. JADE Collaboration, W. Bartel et al., Z. Phys. C **33**, 23 (1986); S. Bethke, Habilitation thesis, LBL 50-208 (1987).
25. J. R. Ellis, M. K. Gaillard and G. G. Ross, Nucl. Phys. B **111** (1976) 253 [Erratum-ibid. B **130** (1977) 516].
26. Y. Kats and M. J. Strassler, JHEP **1211**, 097 (2012).
27. C. Y. Chen, A. Freitas, T. Han and K. S. M. Lee, arXiv:1410.8113 [hep-ph].

Quantization of the QCD string with a helical structure

Š.Todorova-Nová
Institute of Nuclear and Particle Physics, Charles University,
V Holešovičkách 2, 180 00 Prague, Czech Republic

The quantum properties of a helixlike shaped QCD string are studied in the context of the semiclassical Lund fragmentation model. It is shown how simple quantization rules combined with the causality considerations in the string fragmentation process describe the mass hierarchy of light pseudoscalar mesons. The quantized helix string model predicts observable quantum effects related to the threshold behavior of the intrinsic transverse momentum of hadrons, and of the minimal transverse momentum difference between adjacent hadrons. The numerical fit of the properties of the QCD field breaking into ground state hadrons agree with values obtained recently in the theory of knotted chromoelectric flux tubes.

1 Introduction

The concept of the QCD string with a helical structure has been introduced in [1] and some of its potential explored in [2]. The model has been shown to decribe the experimentally established correlations between the longitudinal and transverse momentum components of hadrons measured by DELPHI at LEP [3] and the azimuthal ordering of hadrons, recently observed by ATLAS at LHC [4].

2 Space-time properties of helical string model

In the transition from the 1-dimensional Lund string to a 3-dimensional helix-shaped string, it is necessary to reconsider some of the model properties. The basic assumption of a string modelling the confining QCD field with a constant string tension ($\kappa \sim 1\mathrm{GeV/fm}$) remains unchanged. However, the use of light-cone coordinates is no longer appropriate, as the trajectory of partons in the model is allways bended by the interaction with the field.

In the case of slowly varying field, the string can be approximated by an ideal helix with radius R and constant pitch $\mathrm{d}\Phi/\mathrm{dz}$, where Φ stands for the azimuthal angle (helix phase) and z is the space coordinate parallel to the string axis. Movement of a parton along the string can be thus described with the help of the longitudinal coordinate z and the folded transverse coordinate.

Following a string breakup at $[Re^{i\Phi_B}, z_B, t_B]$ into a pair of massless partons created at rest, the partons will move along the string and acquire the momentum

$$p_{||}(t) = \pm\kappa\beta\ c\ (t - t_B) \tag{1}$$
$$p_T(t) = \pm\kappa R(e^{i\omega c(t-t_B)} - e^{i\Phi_B}) \tag{2}$$

The longitudinal velocity of partons β is related to the angular velocity ω

$$\beta = \sqrt{1 - (R\omega)^2}, \tag{3}$$

(the light-cone coordinates are recovered in the limit case $R\omega = 0$) .

The momentum of a direct hadron created by adjacent string breakups at $[Re^{i\Phi_i}, z_i, t_i]$, $[Re^{i\Phi_j}, z_j, t_j]$ is

$$E_h = \tfrac{\kappa}{\beta}|(z_i - z_j)| = \tfrac{\kappa}{\beta}|\Delta z|, \tag{4}$$
$$p_{h,||} = \kappa\beta(t_i - t_j) = \kappa\beta\Delta t, \tag{5}$$
$$p_{h,T} = \kappa R(e^{i\Phi_i} - e^{i\Phi_j}), \tag{6}$$

and its mass is

$$m_h = \kappa\sqrt{(\Delta z/\beta)^2 - (\beta\Delta t)^2 - (2R\sin\Delta\Phi/2)^2}. \tag{7}$$

There is a fundamental difference (well illustrated by Eq. 7) between the helical string model and the standard Lund string model in what concerns the causality relation between breakup vertices.

In the standard Lund string model, the creation of a massive direct hadron requires a space-like distance between breakup vertices ($\beta = 1, m_h > 0 \Rightarrow |\Delta z| > |\Delta t|$). The mass spectrum of hadrons is included in the model with the help of external parameters. Arguably, it is the absence of the cross-talk between hadron-generating adjacent string breakups which prevents the model from developing physics scenarios investigating the origin of the hadron mass hierarchy.

The situation is different in the case of the helical string model, where a time-like distance between breakup vertices is possible. In order to explore the causal properties of the model, the time-like distance between adjacent breakup vertices will be imposed in the following. If the information (about a breakup of the string at a given point) is allowed to pass along the string only, the space-time distance between adjacent vertices becomes negligible (to the extent we have neglected the parton masses) which means the propagating parton essentially triggers the following break-up and the mass of the outcoming hadron is (note that in this case $\Delta z = \beta\Delta t$)

$$m_S(\Delta\Phi) = \kappa R\sqrt{(\Delta\Phi)^2 - (2\sin\Delta\Phi/2)^2}. \tag{8}$$

It is interesting to see that the longitudinal momentum is factorized out from the equation and that the hadron mass depends on the transverse properties of the string shape only. To obtain a discrete mass spectrum, it is sufficient to introduce quantization of the transverse coordinate $R\Phi$ (to be discussed in the following section).

3 Mass spectra

Let's assume the string quantization is realized through the quantization of the transverse coordinate

$$R\Phi \Rightarrow \mathrm{nR}\Delta\Phi = \mathrm{n}\xi, (\mathrm{n} = 1, 2, ..) \tag{9}$$

and that the n=1 case corresponds to the lightest hadron, the π meson.

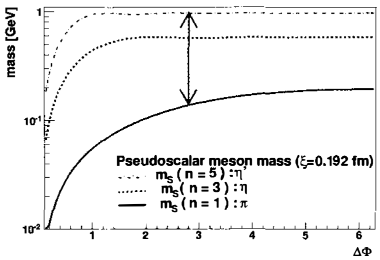

$\kappa\xi$ [MeV]	κ R [MeV]	$\Delta\Phi$
192.5 ± 0.5	68 ± 2	2.82 ± 0.06
meson	PDG mass [MeV]	model [MeV]
π	135 - 140	137
η	548	565
η'	958	958

Figure 1 – Left: The predicted masses of light pseudoscalar mesons as function of helix phase difference $\Delta\Phi$, for fixed $R\Delta\Phi$=0.192 fm rad. Right: Best fit of the parameters of the pion ground state obtained from the mass spectrum of light pseudoscalar mesons. The η mass is reproduced within a 3% margin which serves as the base of uncertainty for R, $\Delta\Phi$ parameters.

Eq. 8 is particularly interesting for the study of light meson mass hierarchy because it describes the narrow pseudoscalar states (PS) decaying into an odd number of pions

$$PS \quad \rightarrow \mathrm{n}\pi,\ \mathrm{n} = (1), 3, 5, .. \tag{10}$$
$$m(PS) \quad = \kappa\sqrt{(\mathrm{n}\xi)^2 - (2\xi/\Delta\Phi)^2 \sin^2(\mathrm{n}\Delta\Phi/2)}. \tag{11}$$

The results of the best fit matching the Eq. 11 to experimentally measured data [5] are shown/listed in Fig 1 [6]. Despite the fact that the simultaneous fit of 2 unknowns (R, $\Delta\Phi$) from 3 hadronic states is overconstrained, a common solution describing the properties of the ground state is found. The π, $\eta(548)$ and $\eta'(958)$ masses are reproduced by Eq. 11 with precision better than 3% using ξ = 0.192 fm and $\Delta\Phi$=2.8 (for κ =1 GeV/fm).

It is worth mentioning that the estimated effective radial size of the helix string (68±2 MeV) turns out to be in agreement with the estimate of the confinment scale $\Lambda_{tube} = 65.16 \pm 0.61$ MeV obtained from the fit of J^{++} spectra modelled via tight topological QCD knots [7].

The possibility for the string to interact across loops is one of the most intriguing features of the model : the mass spectrum of n-loop string piece (obtained from the knowledge of the parameters of the quantized helix string) is closely correlated with the emergence of new particle types (Fig. 2) .

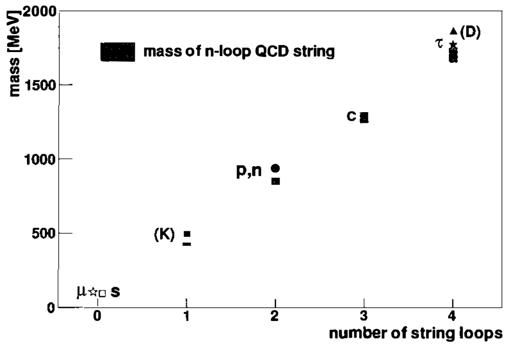

Figure 2 – The mass spectrum of particles carrying a new quantum number compared with the mass of a helix-shaped QCD string with parameters derived from experimental data. The open and bound quark states are included (s-K, c-D).

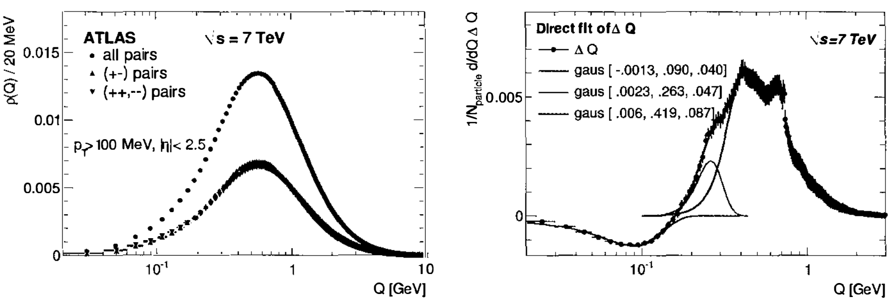

Figure 3 – Left: Corrected 2-particle spectra as function of the momentum difference Q. Right: Subtracted spectra $\Delta Q = Q^{+-} - Q^{\pm\pm}$ revealing the Q($^{+-}$) threshold and the double gaussian structure predicted by the model.

4 Predicted observable quantum effects

The quantization of the helix string implies a quantization of the momentum difference between adjacent hadrons. Since the local charge conservation forbids the production of adjacent like-sign charged hadron pairs in the fragmentation process, the quantum effects can play a large role in the correlation phenomena with a significant difference between particle pairs with like-sign and unlike-sign charge combination.

The quantized model of the helical string predicts existence of a threshold in the minimal momentum difference between pairs of adjacent direct hadrons at $Q^{+-} \sim 0.26$ GeV and production of close pairs of like-sign pions at $Q^{\pm\pm} \sim 0.09$ GeV in case the string fragments into a chain of ground-state hadrons [6]. The enhanced production of the close pairs of like-sign pions is readily observed in the data and traditionally attributed to the Bose-Einstein effect. The model of the helix-like shaped QCD string offers an alternative explanation of the origin of these correlations, which would be the result of quantum coherence in the string fragmentation. Indeed, the measured Q spectra recently published by the ATLAS Collaboration [8] reveal a double-gaussian structure which agrees very well with the model predictions (Fig.3). Further measurements should be performed to explore the presumed link between production of ground state hadron chains and the appearance of correlations.

References

1. B. Andersson *et al.*, *J.High Energy Phys.* **09**, 014 (1998).
2. Š.Todorova-Nová, *Phys. Rev.* D **86**, 034001 (2012).
3. DELPHI Coll., *Z. Phys.* C **73**, 11 (1996).
4. ATLAS Coll., *Phys. Rev.* D **86**, 052005 (2012).
5. Particle Data Group, *Phys. Rev.* D **86**, 010001 (2012).
6. Š.Todorova-Nová, *Phys. Rev.* D **89**, 015002 (2014).
7. R.V.Buniy *et al.*, *Phys. Rev.* D **89**, 054513 (2014).
8. ATLAS Coll., [arXiv:1502.07947] submitted to EPJC.

Multiparticle Dynamics and Pion Production in a Flux Tube

Andrew V. Koshelkin
Moscow Institute for Physics and Engineering, Kashirskoye shosse., 31, 115409 Moscow, Russia

Cheuk-Yin Wong
Physics Division, Oak Ridge National Laboratory, Oak Ridge, TN 37830, USA

By compactifying $QCD_4 \to QCD_2$, we consider the dynamics of quark and gluons in the 2D flux tube. In the case of a linear transverse confining potential, the quark and gluon states are found to be 2D oscillator-like eigenstates. On the basis of the obtained eigenstates, we obtain the momentum distributions of quarks and gluons in the 2D flux tube. We use these distributions of quarks and gluons to calculate the p_T distribution of pions in the quark-antiquark channel.

1 Introduction

The quark-gluon string, arising between a quark and an antiquark, is an effective method to study hadron processes (see, for example, Ref.[1]). The string model concept is utilized in the string model of hadrons[2] and the string fragmentation model of particle production[3,4]. The one-dimensional string model is an idealization of a more realistic three-dimensional flux-tube. It has the limitations that it pertains mainly to the dynamics along the longitudinal direction and cannot describe the dynamics in the transverse directions. To describe the transverse dynamics, it is necessary to restore the string to the original two-dimensional flux-tube form and examine the structure and the states of quanta in the flux tube. The knowledge of the states in the flux tube provide useful information for the investigation of the transverse momentum distribution of the produced particles, for which a wealth of information have been collected recently[6,7,8,9,10,11,12].

In the string fragmentation model, a produced q-$\bar{q}$ parton pairs are described as residing within the string. Such a description presumes the confinement of these produced partons inside the tube. Hence, it is reasonable to envisage that within the string models, quarks and gluons in the QCD 4-dimensional space-time are subject to transverse confinement. We can describe the property of transverse quark confinement in terms of a confining scalar interaction $S(\mathbf{r}_\perp)$ in transverse coordinates $\mathbf{r}_\perp$, with the quark mass function described by $m(\mathbf{r}_\perp) = m_0 + S(\mathbf{r}_\perp)$ where m_0 is the quark rest mass.

Previously, we show from action integral that under the assumption of transverse confinement and longitudinal dominance, QCD_4 in (3+1) dimensional space-time can be approximately compactified into QCD_2 in (1+1) dimensional space-time[5]. In such a process, we find the equations of motion for quarks in the flux tube, and the relation between the coupling constant $g_{2\mathrm{D}}$ in QCD_2 and the coupling constant $g_{4\mathrm{D}} = g$ in QCD_4. We shall use these equations of motion to get the quark and gluon wave functions.

2 Equations of Motion for Transverse Dynamics of Quarks

The transverse dynamics of quarks and gluons in the flux tube picture is governed by transverse functions $G_{\pm}(\mathbf{r}_{\perp})$ which are in the fermion $\Psi(x)$ and gauge fields $A^a_\mu(x^0, x^3, \vec{r}_\perp)$:

$$\Psi(x) = \frac{1}{\sqrt{2}} \begin{pmatrix} G_+(\mathbf{r}_\perp)\,(f_+(x^0;x^3) + f_-(x^0;x^3)) \\ -G_-(\mathbf{r}_\perp)\,(f_+(x^0;x^3) - f_-(x^0;x^3)) \\ G_+(\mathbf{r}_\perp)\,(f_+(x^0;x^3) - f_-(x^0;x^3)) \\ G_-(\mathbf{r}_\perp)\,(f_+(x^0;x^3) + f_-(x^0;x^3)) \end{pmatrix}, \quad A^a_\mu(x^0, x^3, \vec{r}_\perp) = \sqrt{\sum_{\sigma=\pm1} |G_\sigma(\vec{r}_\perp)|^2 A^a_\mu(x^0, x^3)},$$

The functions $G_+(\mathbf{r}_\perp)$ and $G_-(\mathbf{r}_\perp)$ satisfy the following equations[5]

$$\begin{aligned} (p_1 + ip_2)G_+(\mathbf{r}_\perp) &= (m(\mathbf{r}_\perp) + \lambda^2)G_-(\mathbf{r}_\perp), \\ (p_1 - ip_2)G_-(\mathbf{r}_\perp) &= (\lambda^2 - m(\mathbf{r}_\perp))G_+(\mathbf{r}_\perp), \end{aligned} \tag{1}$$

where

$$p_1 \mp ip_2 \quad = \quad e^{\mp i\varphi}\left[i\frac{d}{dr} \pm \frac{1}{r}\frac{d}{d\varphi}\right], \tag{2}$$

and λ^2 plays the role of the squared eigenenergy of the fermion.

In the case of the axisymmetric potential

$$m(\mathbf{r}_\perp) = \kappa|\mathbf{r}_\perp|, \tag{3}$$

where the parameter κ can be interpreted as the flux tube tension, the functions $G_{\pm}(\mathbf{r}_\perp)$ can be approximately expressed in terms of the wave function of the two-dimensional oscillator $\Psi_{\Lambda n\sigma}(\xi, \varphi)$:

$$G_\sigma(\mathbf{r}_\perp) = \sqrt{\frac{2i^{(1-\sigma)}\kappa n!}{\Gamma(\Lambda - \sigma/2 + n + 1)}}\frac{e^{i(\Lambda-\sigma/2)\varphi}}{\sqrt{2\pi}}e^{-\xi/2}\xi^{(\Lambda-\sigma/2)/2}L_n^{(\Lambda-\sigma/2)}(\xi); \; \sigma = \pm 1, \tag{4}$$

where $\xi = \kappa r_\perp^2$, φ is the azimuth angle in the plane of the vector $\vec{r}_\perp$, the functions $L_n^a(z)$ are the Laguerre polynomials. The corresponding eigenvalues are

$$\lambda^2 \;\equiv \epsilon^2(\Lambda n\sigma) = \kappa[4n + 2(\Lambda - \sigma/2) + 2]. \tag{5}$$

In formulas (4) and (5), n is nonnegative integer, Λ is semi-integer, both negative and positive.

3 Quark distribution

Eqs.(4) - (5) allow us to calculate the p_T distribution of quarks in the flux tube in the potential (3). A direct calculation gives the momentum distribution of quark as

$$\frac{dN_q(p)}{(2\pi)^3 d^3p} = \sum_{\Omega=-\infty, n=0, \sigma=\pm}^{+\infty} \Psi_{\Omega n\sigma}(\vec{p}_\perp)\;\Psi^*_{\Omega n\sigma}(\vec{p}_\perp)\;\frac{n_{\Omega,n,\sigma}(p_z)}{\varepsilon_{\Omega,n,\sigma}(p_z)}, \quad \varepsilon^2_{\Omega,n,\sigma}(p_z) = \lambda^2 \;\equiv \epsilon^2(\Lambda n\sigma) + p_z^2 \tag{6}$$

where $n_{\Omega,n,\sigma}(p_z)$ is the occupation number , $\Psi_{\Omega n\sigma}(\vec{p}_\perp)$ is the wave function (4) in the momentum representation. We assume that the occupancy numbers are given the Fermi-Dirac distribution with the zeroth chemical potential.

$$n_{\Omega,n,\sigma,p}(\vec{p}) = \frac{1}{1+e^{\frac{\epsilon_{\Omega,n,\sigma,p}}{T}}}, \tag{7}$$

where T is the temperature in the flux tube. Then, after the calculation according to Eq.(6), we obtain the quark distribution:

$$\frac{dN_q(p)}{d^3p} = \frac{8N_cN_f\sqrt{\pi}}{\kappa_q^{3/2}} \sum_{s=0}^{\infty} (-1)^s \int_0^{\infty} dt\; e^{-t^2p_z^2/4\kappa_q}\; e^{-\frac{(1+s)^2\kappa_q}{t^2T^2}}\; \frac{e^{-p_\perp^2/\kappa_q \tanh(t^2/4)}}{\sinh(t^2/2)} . \tag{8}$$

4 Gluon distribution

The gluon distribution is given by the formula

$$\frac{dN_g(p)}{d^3p} = (A_\mu^a)^\dagger(\vec{p}_\perp)\; A_a^\mu(\vec{p}_\perp)\; \frac{n_g(\vec{p})}{E(p_z)}, \tag{9}$$

where $A_a^\mu(\vec{p}_\perp)$ is the transverse part of the gluon field in the momentum representation, M is the effective mass of a gluon[5], $n_g(\vec{p})$ is the Bose-Einstein distribution function with the zeroth chemical potential, and $E^2(p_z) = p_z^2 + M^2$. The calculation lead to

$$\frac{dN_g(p)}{d^3p} = \frac{8N_gN_p}{\kappa_q\sqrt{{p_z}^2+M^2}} \left\{ \sum_{s=0}^{\infty} (-1)^s \int_0^{\infty} \frac{dt}{t} \exp\{-\frac{(1+s)^2\kappa_q}{t^2T^2}\} \frac{\exp[-\frac{p_\perp^2 \tanh(t^2/4)}{\kappa_q}]}{\sinh(t^2/2)} \right\} \times \frac{1}{\exp\left(\frac{\sqrt{{p_z}^2+M^2}}{T}\right)-1}, \tag{10}$$

where $N_g = 8$ is the number of the gluon kinds, $N_p = 2$ is the number of gluon polarizations.

5 Pion production from quark and antiquark

The provability of pion production from quark and antiquark can be written as

$$dP(\vec{p}) = (2\pi)^4 < |M(p_1,p_2;p)|^2 > \delta(p-p_1-p_2) \frac{d^3p}{2E(p)\,(2\pi)^3} \frac{d^3p_1}{(2\pi)^3} \frac{d^3p_2}{(2\pi)^3}, \tag{11}$$

where $E(p)$ and p are the energy 4-momentum of a pion, whereas p_i are the 4-momenta of the quark and anti-quark which consist of the pion. The matrix element $M(p_1,p_2;p)$ can be diagrammatically presented as follows:

$-M(p_1,p_2;p) =$

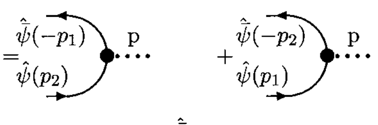

(12)

where the solid lines mean a quark, $\hat{\psi}(p)$ and antiquark $\hat{\bar{\psi}}(-p)$, respectively, while the dotted line is a pion. Normalizing $\hat{\psi}(p)$ and $\hat{\bar{\psi}}(-p)$ by a number of particles, we obtain the from Eq.(11)

$$\frac{2E(p)dN_{qq\pi}(\vec{p}_\perp,p_z)}{d^3p_\perp} \cong 2E(p) \int \frac{d^3p_1}{(2\pi)^3} \frac{d^3p_2}{(2\pi)^3} \delta^{(3)}(\vec{p}-\vec{p}_1-\vec{p}_2) \sum_{\nu,\mu} \Big(|\psi_\nu(\vec{p}_1)|^2\; |\bar{\psi}_\mu(\vec{p}_2)|^2 n_\nu(\vec{p}_1)\bar{n}_\mu(\vec{p}_2) + |\psi_\mu(\vec{p}_1)|^2\; |\bar{\psi}_\nu(\vec{p}_2)|^2 n_\mu(\vec{p}_1)\bar{n}_\nu(\vec{p}_2) \Big), \tag{13}$$

where $dN_{qq\pi}(\vec{p}_\perp, p_z)/d^3p$ is the number of pions per unit volume in the momentum space, $\psi_\mu(\vec{p}_i)$ is the quark wave function, and $n_\mu(\vec{p}_i)$ is the quark occupancy number. The corresponding barred symbols refer to anti-quarks. The subscript μ enumerates the states of quarks and anti-quarks.

We consider both quarks and antiquarks to be in thermal equilibrium and distributed according to the Fermi-Dirac formula with the zeroth chemical potential (7). When $\psi_\mu(\vec{p}_i) = \Psi_{\Lambda n\sigma}(\xi, \varphi)\chi_\sigma$ and $n_{\Omega,n,\sigma,p}(\vec{p})$ as given by Eqs.(4) and (7), we obtain after direct calculations

$$\frac{E(p)dN_{qq\pi}(\vec{p}_\perp, p_z)}{d^3p} = \frac{48E(p)}{\pi^{7/2}\kappa_q^{3/2}} \sum_{s_1=0}^{\infty} (-1)^{s_1} \int_0^\infty dt_1\, e^{-\frac{(1+s_1)^2\kappa_q}{t_1^2T^2}} \sum_{s_2=0}^{\infty} (-1)^{s_2} \int_0^\infty dt_2\, e^{-\frac{(1+s_2)^2\kappa_q}{t_2^2T^2}}$$
$$\times \frac{\exp\{-\frac{(t_1^2t_2^2)p_z^2}{4\kappa_q(t_1^2+t_2^2)}\}}{(t_1^2+t_2^2)^{1/2}} \frac{\exp\{-(\frac{p_\perp^2}{\kappa_q})\frac{\tanh(t_1^2/4)\tanh(t_2^2/4))}{\tanh(t_1^2/4)+\tanh(t_2^2/4)}\}}{\sinh(t_1^2/2)\sinh(t_2^2/2)\left(\tanh(t_1^2/4)+\tanh(t_2^2/4)\right)}. \quad (14)$$

Setting $p_z = 0$ we obtain the p_T distribution of pion rate from quark and antiquark at central rapidity. Let us take κ_q =1 Gev/fm and T = 160 MeV. Then, the numerical calculation of the p_T distribution according to Eq.(14) at $p_z = 0$ gives that the pion p_T distribution three orders less in a magnitude than the experimental results[11] on high energy $p-p$ collisions, even at the rather small $p_T \sim 0.5$ GeV. This means that the leading contributions to the pion rate from quark and antiquarks is significantly small.

6 Conclusion

On the basis of the $QCD_4 \to QCD_2$ compactification[5] the fermion and gluon state in the axial symmetric potential confining are studied in detail. The spectrum of the eigenvalues and eigenvectors of such state is calculated. The derived spectrum appears to be the quasi 2D-harmonic oscillator one in its structure. It is found that the obtained rate of pions at central rapidity in pp collisions from quark and antiquarks is significantly less than the experimental result of Ref. [11].

References

1. C. Y. Wong, *Introduction to High-Energy Heavy-Ion Collisions*, World Scientific Publisher, 1994.
2. N. Isgur and J. Paton, Phys. Rev. D**31**, 2910 (1985).
3. A. Casher, J. Kogut, and L. Susskind, Phys. Rev. D10, 732 (1974).
4. B. Andersson, G. Gustafson, G. Ingelman, and T. Sjöstrand, Phys. Rep. **97**, 31 (1983);
5. A. V. Koshelkin, C. Y. Wong, Phys. Rev. **D86**, 125026 (2012).
6. B. I. Abelev *et al.* (STAR Collaboration), Phys. Rev. C **75** (2007) 064901 .
7. A. Adare *et al.* (PHENIX Collaboration), Phys. Rev. D **83** (2011) 024909, 052004 and 064903.
8. G. Aad *et al.* (ATLAS Collaboration), New J. Phys. **13** (2011) 053033.
9. V. Khachatryan *et al.* (CMS Collaboration), JHEP **02** (2010) 041 and Phys. Rev. Lett. **105** (2010) 022002.
10. V. Khachatryan *et al.* (CMS Collaboration), JHEP **08** (2011) 086.
11. K. Aamodt *et al.* (ALICE Collaboration), Phys. Lett. B **693** (2010) 53; Eur. Phys. J. C **71** (2011) 1594 and 1655.
12. C. Y. Wong and G. Wilk, Acta Physica Polonica B42, 2047 (2012).
13. C. Y. Wong, R. C. Wang, and C. C. Shih, Phys. Rev. D **44**, 257 (1991).

Assuming Regge trajectories in holographic QCD: from OPE to Chiral Perturbation Theory

Luigi Cappiello[1,2],Giancarlo D'Ambrosio*[2,3] and David Greynat[1,2]

*Speaker

[1]*Dipartimento di Scienze Fisiche, Universitá di Napoli "Federico II", Napoli, Italia*

[2]*INFN-Sezione di Napoli, Via Cintia, 80126 Napoli, Italia*

[3]*CERN Theory Division, CH-1211 Geneva 23, Switzerland*

The Soft Wall model in holographic QCD has Regge trajectories but wrong operator product expansion (OPE) for the two-point vectorial QCD Green function. We correct analytically this problem and describe the axial sector and chiral symmetry breaking. The low energy chiral parameters, F_π and L_{10}, are well described analytically by the model in terms of Regge spacing and QCD condensates. The model nicely supports and extends previous theoretical analyses advocating Digamma function to study QCD two-point functions in different momentum regions.

1 Introduction

QCD Green functions are well described as an interpolation from the IR region, chiral perturbation theory (CHPT) and perturbative QCD region, but it is phenomenologically and theoretically interesting to go beyond this simple matching, for instance by implementing Regge trajectories [1]. Since Veneziano's model several authors have proposed to describe two point functions with Digamma functions [2], which produce a Regge spectrum and an OPE in the euclidean region. Also, a phenomenological matching among the various regions has been proposed [3]. We believe that there are theoretical motivations to insist on having Regge trajectories, *i.e.* a progression for the spectrum like $M_V(n)^2 \propto n$, and arrange for QCD OPE of the vector and axial vector two-point function

$$\Pi_{V,A}(Q^2) \underset{Q^2\to\infty}{\sim} \frac{N_c}{24\pi^2}\ln\left(\frac{\Lambda_V^2}{Q^2}\right) + \frac{\alpha_s\left\langle G^2\right\rangle}{24\pi}\frac{1}{Q^4} - \frac{14\pi}{9}c_{V,A}\,\alpha_s\,\left\langle\bar{\psi}\psi\right\rangle^2\frac{1}{Q^6} \tag{1}$$

with $c_V = 1$ and $c_A = -{}^{11}/_{7}$. We should then be able to take into account the difference appearing at order ${}^{1}/_{Q^6}$ in the OPE expansion of the vector and axial correlators. QCD literature [1,3] has addressed the issue to predict

$$F_\pi^2 = 2\,\mathsf{Res}\left[\Pi_{LR}\left(Q^2\right),0\right] \qquad \text{and} \qquad L_{10} = \frac{1}{2}\frac{\mathrm{d}}{\mathrm{d}Q^2}\left[Q^2\Pi_{LR}(Q^2)\right]\Big|_{Q^2=0}, \tag{2}$$

by phenomenologically matching the OPE to the pion and lowest mesons (ρ and a_1) with Regge resonances. A good knowledge of the three regions of QCD also leads to address properly the issue of duality violations in tau and b-decays and pion form factor [4]. Holographic QCD has: *i)* Hard Wall models (HW) good IR, chiral perturbation theory, and UV parton log, but Kaluza Klein NOT Regge and *ii)* Soft Wall model (SW): Regge and UV parton log plus terms in ${}^{1}/_{Q^2}$

but no χPT predictions. A recent review of those models and their relations with light front holographic QCD is Ref. [5]. Our idea in Rcf. [6] is that a correct OPE is pertinent for the study of the low Q^2 limit of $\Pi_{LR}(Q^2) = 1/2(\Pi_V - \Pi_A)$ allowing us to extract the chiral constants in eq. (2).

Indeed, in the SW model the AdS metric, $1/z$, is deformed by the presence of a scalar, $\Phi(z)$, the dilaton, describing confinement scale and hence Regge spacing: the effective metric is $w_0(z) = e^{-\Phi(z)}/z$ with $\Phi(z) = \kappa^2 z$. The equation of motion for the vectorial field associated expressed in its Fourier transform $f_V(z)$ becomes, [7]

$$\partial_z^2 f_V + \partial_z \left[\ln w_0(z)\right] \partial_z f_V + q^2 f_V = 0 \,, \tag{3}$$

This turns in an *harmonic-oscillator-like* problem, up to the $1/z$ term, for the eigenvalue problem $q^2 = M_V(n)^2$

$$\partial_z^2 \phi_n - \left(\frac{1}{z} + 2\kappa^2 z\right) \partial_z \phi_n + M_V(n)^2 \phi_n = 0 \,, \tag{4}$$

and leading to the two-point function expressed in terms of a Digamma function ψ,

$$Q^2 \Pi_V^{(0)}(Q^2) = -\frac{2\kappa^2}{g_5^2} \left(\frac{Q^2}{4\kappa^2}\right) \left[\gamma_E + \psi\left(\frac{Q^2}{4\kappa^2} + 1\right)\right] \,, \tag{5}$$

Practically, the same solution suggested in the past in 4D QCD models [2].

2 The vectors, the axials and chiral symmetry breaking

We propose to modify the dilaton perturbatively for z small adding a polynomial in z, $B(\sqrt{\theta} z)$. The damage for z large should be cured by the fact that Regge is dynamically obtained: θ is an auxiliary parameter ordering the expansion to match the OPE. Our proposal to have a correct OPE turns in a set of perturbative differential equations for f_V,

$$\partial_z^2 f_V - \partial_z \left[\frac{1}{z} + 2\kappa^2 z + b_2 \theta z^2 + b_4 \theta^2 z^4 + b_6 \theta^3 z^6\right] \partial_z f_V + q^2 f_V = 0 \,, \tag{6}$$

with a corresponding solution for the vector two-point function

$$\Pi_V = \Pi_V^{(0)} + \theta \Pi_V^{(1)} + \theta^2 \Pi_V^{(2)} + \theta^3 \Pi_V^{(3)} + \mathcal{O}(\theta^4) \,, \tag{7}$$

which takes the form (where $\mathcal{P}$ is a polynomial)

$$Q^2 \Pi_V^{(n)}(Q^2) = \sum_{k=0}^{n} \mathcal{P}_{k,n}\left(\frac{Q^2}{4\kappa^2}\right) \psi^{(k)}\left(\frac{Q^2}{4\kappa^2}\right) \,. \tag{8}$$

The coefficients b_n of the polynomial $B(\sqrt{\theta} z)$ are obtained by imposing that the large euclidean expansion of eq. (8) coincides with the QCD one eq. (1). The spectrum is Figure 1 while $\Pi_V^{(0)}$ is in eq. (5) and more specifically $\Pi_V^{(1)}$ and $F_V(n)^2$ are

$$\Pi_V^{(1)}(Q^2) = \sum_{n=0}^{\infty} \frac{F_V(n)^2}{Q^2 + M_V(n)^2} = \frac{b_2}{4\kappa^2 g_5^2} \left(\frac{4\kappa^2}{Q^2}\right) \left[1 + \left(\frac{Q^2}{4\kappa^2}\right) - \left(\frac{Q^2}{4\kappa^2}\right)^2 \psi'\left(\frac{Q^2}{4\kappa^2}\right)\right] \,, \tag{9}$$

with

$$\frac{F_V(n)^2}{4\kappa^2} = (1 - 6n)\left(\frac{3}{4}\frac{\langle \mathcal{O}_4 \rangle}{\kappa^4} - \frac{5}{32}\frac{\langle \mathcal{O}_6 \rangle_V}{\kappa^6}\right) - \frac{75}{32}\frac{\langle \mathcal{O}_6 \rangle_V}{\kappa^6} n^2 \,. \tag{10}$$

We use the same dilaton $\Phi(z)$ and polynomial $B(\sqrt{\theta}z)$, and, consistently with the AdS prescription for chiral symmetry breaking, we add a scalar field with the vacuum profile

$$\left(\frac{v(\sqrt{\theta}z)}{z}\right)^2 = \beta_0 + \beta_2 z^2\theta + \beta_4 z^4\theta^2 + \beta^* z\delta(z)\,, \tag{11}$$

where in Ref. [6], compared to typical HW or SW metric in Ref.[9], we have added $\beta_0 = 4\kappa^2/g_5^2$ and also a contact term $\beta^* z\delta(z)$. Based on the phenomenological relation

$$M_{a_1}^2 = 2\, M_\rho^2\,, \tag{12}$$

we reconcile the axial spectrum in Figure 2 with the phenomenological one as a shifted vectorial one leading to

$$\Pi_A(Q^2) = \Pi_V(Q^2 + 4\kappa^2) + \begin{pmatrix}\text{Corrections to obtain OPE}\\ \text{involving } \beta_{2k} \text{ coefficients}\end{pmatrix}\,. \tag{13}$$

Also the contact term β^* is needed in order to obtain the correct OPE.

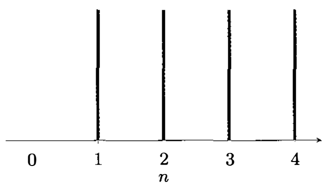

Figure 1 – Vectorial spectrum

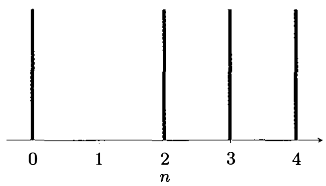

Figure 2 – Axial spectrum

3 The chiral constants

Now we believe that equations (2), ruling F_π and L_{10}, are theoretically more clean than those of $\Pi_{V,A}$:

$$F_\pi^2 = \frac{N_c\kappa^2\left(180\zeta(3) + 191 - 41\pi^2\right)}{72\pi^2} + \frac{5\left(\pi^2 - 10\right)}{2}\frac{\langle\mathcal{O}_4\rangle}{\kappa^2} - \frac{45\left(\pi^2-10\right)}{56}\frac{\langle\mathcal{O}_6\rangle_V}{\kappa^4}\,, \tag{14}$$

using $N_c = 3$, $\kappa = \sqrt{1.43/4}\,\mathrm{GeV} \simeq 0.6\,\mathrm{GeV}$[8] and the values of the condensates $\langle\mathcal{O}_4\rangle = (-0.635\pm 0.04)\cdot 10^{-3}\,\mathrm{GeV}^4$ and $\langle\mathcal{O}_6\rangle_V = (14\pm 3)\cdot 10^{-4}\,\mathrm{GeV}^6$ from [3], we obtain

$$F_\pi \simeq \sqrt{4099.9 + 579 + 1147.8}\,\mathrm{MeV} \simeq 76\ (\pm 3)_{\text{ext.}}\ \mathrm{MeV}\,, \tag{15}$$

the error in (15) are coming from the errors quoted for σ and the condensates [a]. While for L_{10}

$$L_{10} = \frac{N_c(8010\zeta(3) + 495 - 585\pi^2 - 46\pi^4)}{8640\pi^2} + \frac{-72\zeta(3) - 12 + 11\pi^2}{64}\frac{\langle\mathcal{O}_4\rangle}{\kappa^4} + \frac{5[5216\zeta(3) + 67 - 33\pi^2]}{1792}\frac{\langle\mathcal{O}_6\rangle_V}{\kappa^6}\,, \tag{16}$$

$$10^3 L_{10} \simeq -4.6 - 0.8 + 0.1 \simeq -5.3\,(\pm 1)_{\text{ext.}}\ \cdot \tag{17}$$

Both are in incredible good agreement with experiments. Particularly interesting is F_π where numerically all chiral symmetry breaking effects ($\beta_0, \beta_2, \beta_4$ and β^*) are relevant see Figures 3 and 4.

[a] Let us notice that if we had made the choice for $\sigma \simeq 0.9\,\mathrm{GeV}^2$ as in [7] the values obtained would have been $F_\pi \simeq 80$ MeV and $10^3 L_{10} \simeq 80$ MeV and $10^3 L_{10} \simeq -6.2$ which remain quite acceptable too.

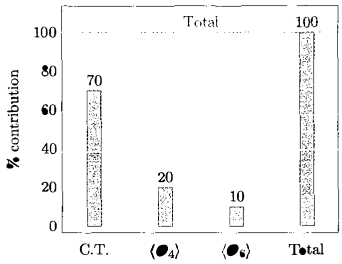

Figure 3 – Relative contributions to F_π^2

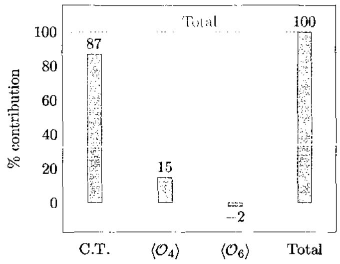

Figure 4 – Relative contributions to L_{10}

4 Conclusions

We think that it is important to realize chiral properties from a Regge theory analytically. Our results are phenomenologically very interesting (see Section 3) even if more work is needed. Somewhat maybe this work is on the spirit of Coleman Witten theorem that in large N_c established chiral symmetry breaking if there is confinement: we have followed their prescription but differently from their assumptions we show that several chiral breaking symmetry mechanisms are needed.

Acknowledgments

We thank the organizers for the invitation to *Moriond QCD* 2015 in particular Pr. Maria Krawczyk and the secretariat in particular Mrs. Vera de Sa-Varanda.

References

1. S. Peris, M. Perrottet and E. de Rafael, "Matching long and short distances in large N(c) QCD", JHEP **9805**, 011 (1998)
2. M. A. Shifman, *Quark-hadron duality*, hep-ph/0009131. Published in the Boris Ioffe Festschrift 'At the Frontier of Particle Physics Handbook of QCD', ed. M. Shifman (World Scientific, Singapore, 2001).
3. M. Golterman and S. Peris, "Large N(c) QCD meets Regge theory: The Example of spin one two point functions" JHEP **0101**, 028.
4. C. A. Dominguez, "Pion form-factor in large N(c) QCD", Phys. Lett. B **512**, 331 (2001)
5. S. J. Brodsky, G. F. de Teramond, H. G. Dosch and J. Erlich, "Light-Front Holographic QCD and Emerging Confinement", arXiv:1407.8131 [hep-ph].
6. L. Cappiello, G. D'Ambrosio and D. Greynat, arXiv:1505.01000 [hep-ph].
7. A. Karch, E. Katz, D. T. Son and M. A. Stephanov, "Linear confinement and AdS/QCD", Phys. Rev. D **74**, 015005 (2006).
8. P. Masjuan, E. Ruiz Arriola and W. Broniowski, "Reply to "Comment on "Systematics of radial and angular-momentum Regge trajectories of light nonstrange $q\bar{q}$-states?"", Phys. Rev. D **87**, no. 11, 118502 (2013)
9. H. J. Kwee and R. F. Lebed, "Pion Form Factor in Improved Holographic QCD Backgrounds", Phys. Rev. D **77**, 115007 (2008)
10. O. Cata, M. Golterman and S. Peris, "Duality violations and spectral sum rules", JHEP **0508**, 076 (2005).

Discretization effects in $N_c = 2$ QCD and Random Matrix Theory [a]

Mario Kieburg[1,2], Jacobus Verbaarschot [2],
Savvas Zafeiropoulos[2,3b]
[1] Fakultät für Physik, Universität Bielefeld, Postfach 100131, 33501 Bielefeld, Germany
[2] Department of Physics and Astronomy, Stony Brook University, NY 11794-3800, USA
[3] Institut für Theoretische Physik, Goethe-Universität Frankfurt,
Max-von-Laue-Str. 1, 60438 Frankfurt am Main, Germany

We summarize the analytical solution of the Chiral Perturbation Theory for the Hermitian Wilson Dirac operator of $N_c = 2$ QCD with quarks in the fundamental representation. Results have been obtained for the quenched microscopic spectral density, the distribution of the chiralities over the real modes and the chiral condensate. The analytical results are compared with results from a Monte Carlo simulation of the corresponding Random Matrix Theory.

1 Introduction

The case of $SU(2)$ QCD with fundamental quarks has attracted a great deal of interest in the past decades since it is a very interesting theory per se but it also shares many of the salient properties of $SU(3)$ QCD, such as confinement and chiral symmetry breaking. An important difference between $SU(2)$ and $SU(3)$ is that $SU(2)$ is pseudoreal, so that for an even number of flavors it is not hindered by the notorious sign problem at non zero chemical potential. Therefore, it is in an interesting playground for finite density studies, and one can study the phase diagram of $SU(2)$ QCD in the $T - \mu$ plane [1,2] and get some insight in the qualitative properties of the phase diagram of QCD. One can get an understanding of the systematics but one needs to bear in mind that the two theories have quantitative differences. For $SU(2)$ QCD the baryons are of bosonic nature and as a result this theory has a superfluid phase that is not encountered in ordinary QCD. Moreover, for beyond the Standard Model studies dedicated to the search of the conformal window, it has been shown that one can enter the conformal window with considerable less flavors compared to the $SU(3)$ theory [3]. All these non-perturbative studies have been mainly through lattice simulations employing one of the most prominent discretizations, that of Wilson fermions. This discretization explicitly breaks chiral symmetry and consequently the low lying part of the Dirac spectrum gets affected in a very particular way.

We study the discretization (cutoff) effects on the Dirac spectrum by employing the methods of Wilson Chiral Perturbation Theory (WchPT) and Wilson Random Matrix Theory (WRMT). This work extends previous work on $SU(3)$ QCD [4,5,6,7,8,9] and we point out the similarities and the differences among the two theories.

---

[a] Talk presented at the 50th Rencontres de Moriond (QCD and High Energy Interaction Session), La Thuile, 24 March 2015.
[b] Speaker.

2 Wilson chPT

Initially we concentrate on the study of the Hermitian Wilson Dirac operator $D_5 = \gamma_5 D_W$ where D_W is given by

$$D_W = \frac{1}{2}\gamma_\mu(\nabla_\mu + \nabla^*_\mu) - \frac{a}{2}\nabla_\mu\nabla^*_\mu. \tag{1}$$

We work in the $\epsilon-$ regime of WchPT where the mass m, the axial mass z and the lattice spacing a scale with the lattice volume such that the quantities

$$mV\Sigma, \quad zV\Sigma, \quad \text{and} \quad a^2VW_8 \tag{2}$$

are kept fixed (Σ is the chiral condensate and W_8 is the leading LEC). In this regime the partition function of WchPT factorizes and its mass dependence is given by a unitary matrix integral since the fluctuations of the zero momentum pions dominate completely the ones with non-zero momentum. The chiral partition function for N_f flavors reads[10]

$$Z_{N_f}(m, z; a) = \int_{SU(2N_f)/Sp(2N_f)} dU\, e^{\frac{m}{2}\Sigma V \mathrm{Tr}(U+U^\dagger)+\frac{z}{2}\Sigma V \mathrm{Tr}(U-U^\dagger)-a^2VW_8\mathrm{Tr}(U^2+U^{\dagger 2})}. \tag{3}$$

To access the spectral properties of the Dirac operator we employ the supersymmetric method. Adding an additional fermionic quark as well as an additional bosonic quark, with source terms in the mass as well as in the axial mass, one can differentiate with respect to these sources and compute the Green's function of this theory in the standard way. By setting the source terms to zero one recovers the original partition function. In this proceeding we present our results graphically and we refer the reader to the original work for detailed derivations[9].

The first spectral observable that we consider is the quenched resolvent of D_5 defined as

$$G_5(m, z) = \frac{1}{V}\mathrm{Tr}\frac{1}{D_5 + z} \tag{4}$$

whose discontinuity yields the spectral density of D_5

$$\rho_5(\lambda) = \frac{1}{\pi}\mathrm{Im}G_5(\lambda + i\epsilon). \tag{5}$$

The spectral density of D_5 for $N_c = 2$ exhibits a striking difference compared to $N_c = 3$ QCD. We see that there is a non-uniform convergence to the continuum limit[11] since there is a discontinuous jump by a factor of $1/\sqrt{2}$ which is persistent for arbitrarily small values of the lattice spacing as it is clearly shown in Fig. 1.

At the moment we have not been able to derive analytical results for the real eigenvalue density of D_W but we have obtained stringent upper and lower bounds of this distribution. The first distribution has been coined as the distribution of chiralities over the real modes of D_W and is defined as

$$\rho_\chi(\lambda) = \sum_{\lambda_W \in \mathbb{R}} \delta(\lambda + \lambda_W)\mathrm{sign}[\langle\lambda_W|\gamma_5|\lambda_W\rangle], \tag{6}$$

and together with

$$\rho_5(\lambda_5 = 0, m; a) = \left\langle \sum_k \delta(\lambda^5_k(m)) \right\rangle = \left\langle \frac{\delta(\lambda^W_k + m)}{|\langle k|\gamma_5|k\rangle|} \right\rangle, \tag{7}$$

we have the following inequality for the density $\rho_{\mathrm{real}}(\lambda)$ of the real modes of D_W,

$$\rho_\chi(\lambda) \le \rho_{\mathrm{real}}(\lambda) \le \rho_5(\lambda_5 = 0, m = \lambda). \tag{8}$$

In Fig. 2 we see that for large values of the lattice spacing these distributions are bounding the real eigenvalue density from above and below. While for values of a close to zero we see that ρ_χ is a very good approximation of ρ_{real} .

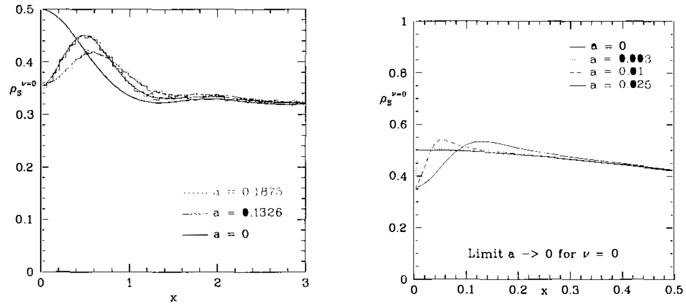

Figure 1 – The spectral density of D_5 for $z = 0, m = 0$ and values of a as in the legend of the figures. We see that the spectral density at zero virtuality jumps by a factor $1/\sqrt{2}$ when $a \neq 0$. The solid curves denote the analytical results while the histograms represent the data of a simulation of 10^5 200×200 random matrices. On the RHS we see the discontinuous behavior of ρ_5 for very small values of a.

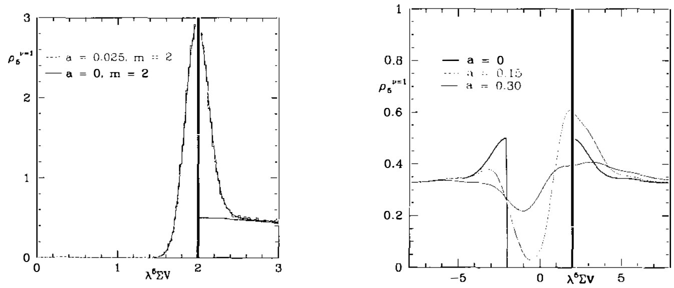

Figure 2 – In the left figure we show the spectral density of D_5 for $\nu = 1$, $m = 2$ and $a = 0.025$, and in the right figure we display the spectral density of D_5 for $\nu = 1$, $m = 2$ and $a = 0$ (black), $a = 0.15$ (green) and $a = 0.3$ (red). The numerical results (histogram) are compared to the analytical result (curve). Also shown are the results for $a = 0$ (black curve) with a δ-peak at $\lambda_5 \Sigma V = 2$. The δ peak corresponding to the zero modes gets broadened with a width proportional to the lattice spacing a. It is interesting to see that for larger values than $a = 0.3$ the peak of the zero modes has almost completely dissolved.

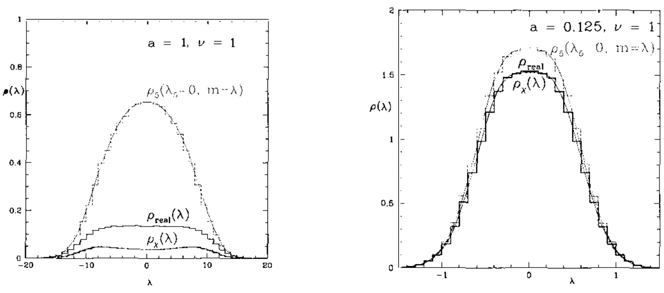

Figure 3 – The distribution of the chiralities (blue curves) and the inverse chiralities (red curves) over the spectrum of D_5 compared to Monte Carlo simulations for $\nu = 1$, $a = 1$(left) and $a = 0.125$(right). The density ρ_{real} of the real eigenvalues of D_W (black histogram) is always bounded by ρ_χ and $\rho_5(\lambda_5 = 0)$ and can be accurately approximated by ρ_χ for small values of the lattice spacing. The analytical results are in agreement with Monte-Carlo simulations (blue and red histograms).

3 Conclusions

We have studied the microscopic spectrum of the Wilson Dirac operator for QCD with two colors and quarks in the fundamental representation. The discretization effects for $SU(2)$ QCD are mostly similar to the case of $SU(3)$ QCD. As we have seen from the figures, the main effects are the broadening of the topological peak and the tail states that enter the gap of the Hermitian Dirac operator. Also in this case the gap closes when entering the Aoki phase. Similarly to the case of ordinary QCD additional real eigenvalues could potentially be an issue in the context of $SU(2)$ QCD. These originate from the collision of complex conjugate pairs which eventually enter the real axis, and on average, we have $a^{\nu+1}$ additional real eigenvalues when we are restricted sufficiently close to the continuum limit. However, note that the suppression of these modes (for $\nu \neq 0$) is not as strong as for ordinary QCD [6]. Another noteworthy property also found for QCD with three colors is that based on the Hermiticity properties of the Dirac operator one can pinpoint [9] the sign of W_8. In our conventions when taking into account only W_8 in our analysis we conclude that it should have a positive sign. The sign of W_8 is important because it controls if the theory enters or not the Aoki phase. Our results provide an analytical handle on the smallest eigenvalues of the Wilson Dirac operator which could potentially seriously compromise the Monte Carlo simulation if they become almost zero. One needs to point out that the absence of level repulsion from the origin for the case of two-color QCD makes this effect much more severe compared to $SU(3)$ QCD.

Acknowledgments

The authors wish to thank Gernot Akemann and Kim Splittorff for helpful comments. MK and SZ are financially supported by the Alexander-von-Humboldt Foundation. JV and SZ are supported by U.S. DOE Grant No. DE-FG-88ER40388 and MK is also partially financially supported by the CRC 701: *Spectral Structures and Topological Methods in Mathematics* of the Deutsche Forschungsgemeinschaft. SZ is particularly grateful to the organizers of Moriond QCD 2015 for their financial support as well as the opportunity to present the above results in this exciting and stimulating conference.

References

1. J. B. Kogut, D. K. Sinclair, S. J. Hands and S. E. Morrison, Phys. Rev. D **64**, 094505 (2001) [hep-lat/0105026].
2. S. Cotter, P. Giudice, S. Hands and J. I. Skullerud, Phys. Rev. D **87**, no. 3, 034507 (2013) [arXiv:1210.4496 [hep-lat]].
3. K. Rummukainen, AIP Conf. Proc. **1343**, 51 (2011) [arXiv: 1101.5875 [hep-lat]].
4. P. H. Damgaard, K. Splittorff, and J. J. M. Verbaarschot, Phys. Rev. Lett. **105**, 162002 (2010) [arXiv: 1001.2937 [hep-th]].
5. G. Akemann, P. H. Damgaard, K. Splittorff and J. J. M. Verbaarschot, Phys. Rev. D **83**, 085014 (2011) [arXiv:1012.0752 [hep-lat]].
6. M. Kieburg, J. J. M. Verbaarschot and S. Zafeiropoulos, Phys. Rev. Lett. **108**, 022001 (2012) [arXiv:1109.0656 [hep-lat]].
7. M. Kieburg, J. J. M. Verbaarschot and S. Zafeiropoulos, PoS LATTICE **2012**, 209 (2012) [arXiv:1303.3242 [hep-lat]].
8. M. Kieburg, J. J. M. Verbaarschot and S. Zafeiropoulos, Phys. Rev. D **88**, 094502 (2013) [arXiv:1307.7251 [hep-lat]].
9. M. Kieburg, J. J. M. Verbaarschot and S. Zafeiropoulos, arXiv:1505.01784 [hep-lat].
10. S. R. Sharpe and R. L. Singleton, Phys. Rev. D **58**, 074501 (1998) [arXiv: hep-lat/9804028].
11. J. J. M. Verbaarschot, Nucl. Phys. B **426**, 559 (1994) [hep-th/9401092].

ON MULTIPLE GLUON EXCHANGE WEBS

M. HARLEY
Higgs Centre for Theoretical Physics, University of Edinburgh, Edinburgh EH9 3FD, Scotland

I present an overview of the study of infrared singularities through the eikonal approximation and the concept of webs. Our work reveals the interesting structure of an infinite subclass of webs, Multiple Gluon Exchange Webs. We find that they can be expressed as sums of products of functions depending upon only a single cusp angle, spanned by a simple basis of functions, and conjecture that this structure will hold to all orders.

1 Introduction

The scattering amplitudes of gauge theories suffer from so called infrared (IR) singularities where massless particles carry vanishing momenta. However, observables obtained from such theories are rendered finite by an intricate cancellation of IR singularities coming from real and virtual contributions order-by-order in the perturbative series. It is therefore necessary to compute these singularities in order to develop subtraction algorithms for Monte Carlo phase-space integration and for the resummation of large-logarithmic corrections to particular collider observables. The study of IR singularities also has interesting implications for the theoretical study of non-abelian gauge theories. Being simpler to calculate than complete scattering amplitudes, their study promises to further our understanding of the mathematical structure of scattering amplitudes deep into their perturbative expansion.

At present, for general kinematics, the IR singularities of QCD are known up to three loop order for two hard partons [1] and up to two loops for multiparton scattering [2]. Our goal is to push this forward to a full determination of the three loop soft anomalous dimension. In the following, we shall be focusing on the virtual IR singularities of QCD amplitudes, where all hard partons are massive. This solves a more general problem than a massless treatment, for example the singularities of amplitudes containing top quarks, while allowing the IR singularities of amplitudes containing hard massless particles to be reproduced by taking the lightlike limit of the relevant partons. When all are taken to the lightlike limit, this will allow us to determine corrections to the sum-over-dipoles formula for multiparton scattering of massless hard partons at three loops [3].

2 Eikonal Approximation and Factorisation

In order to study IR singularities at high loop-order without the overburdening complications inherent to full amplitudes we make some approximations. We note that a virtual gluon carrying no momentum can not possibly affect the spin or momentum of the emitting hard partons, allowing us to discard such information from our calculation. In doing so we find that the IR singularities of massive scattering amplitudes are mapped one-to-one with the singularities of Wilson line correlation functions,

$$S = \langle \Phi_{\beta_1}(0,\infty) \otimes \Phi_{\beta_2}(0,\infty) \otimes \ldots \otimes \Phi_{\beta_n}(0,\infty) \rangle \, . \tag{1}$$

Here the scaleless velocities, β_i, are defined by $p_i = Q\beta_i$ for each hard parton momentum p_i and for an arbitrary scale Q. A Wilson line is defined by,

$$\Phi_{\beta_i}(a,b) = \mathcal{P}\exp\left(\mathrm{i}g_s\int_a^b ds\,\beta_i\cdot A(s\beta_i)\right), \tag{2}$$

where, $\mathcal{P}$ indicates ordering of colour matrices along the path and $A_\mu = A_\mu^a T_i^a$ is the gauge field in the representation of the parton i. This can be thought of as replacing the hard, coloured partons with classical, straight-line, semi-infinite radiators of soft gluons, carrying only a direction and colour information. This is known as the Eikonal approximation. Interestingly, in discarding scale from the problem we will find that even in the renormalized QCD theory, we have introduced new ultraviolet (UV) poles at the cusps where Wilson lines meet. We are thus required to renormalize the soft function,

$$S_{\text{ren.}}(\alpha_{ij},\alpha_s(\mu_R^2),\mu,m) = Z(\alpha_{ij},\alpha_s(\mu_R^2),\epsilon,\mu)S(\alpha_{ij},\alpha_s(\mu_R^2),\epsilon,m)\,, \tag{3}$$

where α_{ij} are related to the cusp angles through,

$$\frac{2\beta_i\cdot\beta_j}{\sqrt{\beta_i^2\beta_j^2}} = -\alpha_{ij} - \frac{1}{\alpha_{ij}}\,, \tag{4}$$

$\alpha_s(\mu_R^2)$ is the renormalised strong coupling, ϵ is the dimensional regularisation parameter and μ is the renormalisation scale. To calculate the UV singularities of S it is necessary to introduce some infrared regulator, m, in order to disentangle the UV and IR poles beyond one loop. When an IR regulator is not present, however, all loop diagrams contributing to S will be scaleless Feynman integrals in dimensional regularisation and therefore zero. This implies that a cancellation must be occurring between the UV and IR divergences, hence in determining Z we also obtain the IR poles of $S_{\text{ren.}}$,

$$S_{\text{ren.}}(\alpha_{ij},\alpha_s(\mu_R^2),\mu) = Z(\alpha_{ij},\alpha_s(\mu_R^2),\epsilon,\mu)\,. \tag{5}$$

Therefore, we are able to express the amplitude in a factorized form,

$$\mathcal{M}(p_i/\mu,\alpha_s(\mu_R^2),\epsilon) = Z(\alpha_{ij},\alpha_s(\mu_R^2),\mu,\epsilon)\;H(p_i/\mu,\alpha_s(\mu_R^2))\,, \tag{6}$$

where H is known as the hard function, a matching coefficient which can be determined at each order by computing the full amplitude, and all of the infrared singularities are contained within the renormalisation factor.

3 Non-abelian Exponentiation in Multiparton Scattering

A renormalisation group equation for the soft function can be deduced from Eq. (3),

$$\frac{d}{d\ln\mu^2}S_{\text{ren.}} = -\Gamma S_{\text{ren.}}\,, \tag{7}$$

defining Γ, the well known 'soft anomalous dimension'. Eq. (7). The solution of this equation implies exponentiation of $S_{\text{ren.}}$. There is an independent interpretation of exponentiation which is entirely diagrammatic as was first realised in the context of QED [4], generalised to the non-Abelian case in the context of Wilson loops [5], and in then later generalised further to the multi-leg case [6]. In the case of the cusp (two Wilson lines), the exponent is simply the sum of all irreducible diagrams, in the sense that they cannot be separated into subdiagrams by cutting Wilson lines alone. Such diagrams are known as webs. In multiparton scattering, however, the situation is more complicated owing to non-trivial colour flow at the hard interaction vertex. Here, the notion of webs is generalised to encompass sets of (possibly reducible) diagrams related by permutation of ordering of gluon emissions along the lines.

Webs in both the cusp and multiparton processes appear in the exponent with an 'exponentiated colour factor' (ECF), rather than the conventional colour factors of each diagram. In the multiline case a web, W, can be expressed according to,

$$W = \sum_{D,D'} C(D) R_{DD'} \mathcal{F}(D') \tag{8}$$

where D, D' index the diagrams in the web, $C(D)$ and $\mathcal{F}(D)$ are the diagram colour and kinematic factors, respectively, and $R_{DD'}$ is a mixing matrix which can be determined using the methods produced in [6,7]. It has been proven that ECFs are always given by colour factors of fully connected diagrams [7].

4 Subtracted webs

As mentioned above, we can determine the IR singularities of the soft function by renormalising the Wilson line correlator. Considering the multiplicative renormalisation of the soft function in eq. (3), the renormalisation factor, Z, can also be expressed as an exponential of counterterms. As Z and S are both matrix valued in multiparton scattering, we are required to use the Baker-Campbell-Hausdorff formula to find the exponent of $S_{\text{ren.}}$. Along with the physical stipulation that the anomalous dimension itself is finite, this allows us to express Γ in terms of the coefficients of the Laurent series of the webs at each order in α_s,

$$w = \sum_{n=1}^{\infty} w^{(n)} \alpha_s^n = \sum_{n=1}^{\infty} \sum_{k=-n}^{\infty} w^{(n,k)} \alpha_s^n \epsilon^k \,. \tag{9}$$

We can then write [8] the perturbative expansion of the anomalous dimension $\Gamma = -2\sum_{n=1}^{\infty} n\overline{w}^{(n)}\alpha_s^n$, where we define 'subtracted webs',

$$\begin{aligned}
\overline{w}^{(1)} &= w^{(1,-1)}\,, && (10)\\
\overline{w}^{(2)} &= w^{(2,-1)} + \frac{1}{2}\left[w^{(1,-1)}, w^{(1,0)}\right], && (11)\\
\overline{w}^{(3)} &= w^{(3,-1)} - \frac{1}{2}\left[w^{(1,0)}, w^{(2,-1)}\right] - \frac{1}{2}\left[w^{(2,0)}, w^{(1,-1)}\right] \\
&\quad -\frac{1}{6}\left[w^{(1,0)}, \left[w^{(1,-1)}, w^{(1,0)}\right]\right] + \frac{1}{6}\left[w^{(1,-1)}, \left[w^{(1,-1)}, w^{(1,1)}\right]\right]. && (12)\\
&\dots
\end{aligned}$$

The contents of the commutators in each subtracted web are composed of the subdiagrams of the web $w^{(n,-1)}$. Subtracted webs have several useful properties lacking in webs such as independence of the IR regulator and a corresponding restoration of crossing symmetry, which is broken by IR regularisation.

5 Multiple Gluon Exchange Webs

After having discussed webs in general we now wish to restrict ourselves to the simplest class of webs contributing to the multiparton soft anomalous dimension. Multiple Gluon Exchange Webs (MGEWs) comprise only webs which have gluons exchanged directly between Wilson lines, lacking gluon self-interaction away from the Wilson lines. Since we are interested in the soft anomalous dimension we shall consider subtracted MGEWs, which in general [9] have the structure,

$$\overline{w}^{(n)} = \left(\prod_{i=1}^{n} r(\alpha_i)\right) \sum_j c_j^{(n)} \int_0^1 \left[\prod_{k=1}^{n} dx_k \left(\frac{1}{x_k - \frac{1}{1-\alpha_k}} - \frac{1}{x_k + \frac{\alpha_k}{1-\alpha_k}}\right)\right] \mathcal{G}_j(\{x_i\})\Theta_j(\{x_i\})\,, \tag{13}$$

where $c_j^{(n)}$ the connected ECFs described in section 3, $\mathcal{G}_j$ are the subtracted web kernels corresponding to each of these colour factors, $r(\alpha) = (1+\alpha^2)/(1-\alpha^2)$ and $\Theta_j(\{x_i\})$ are the residual Heaviside functions left from the ordering of gluons on the Wilson lines. The subtracted web kernel can be obtained algorithmically following the methodology outlined in [9].

Based on physical constraints on the analytic structure of subtracted webs it has been conjectured [10] that subtracted MGEWs should be expressible as sums of products of functions of a single angle. Thus giving them a structure remarkably similar to that found in the cusp anomalous dimension [11]. Though generally the diagrams contributing to a subtracted MGEW contain multiple-polylogarithms, $\mathcal{G}_j$ is composed of only sums of products of logarithms in every subtracted web thus far considered[9], lending further evidence to this conjecture. Moreover, we find that all subtracted MGEWs can be expressed in terms of a remarkably simple basis of functions,

$$M_{k,l,m}(\alpha) = \frac{1}{r(\alpha)}\int_0^1 dx \left(\frac{1}{x-\frac{1}{1-\alpha}} - \frac{1}{x+\frac{\alpha}{1-\alpha}}\right)\ln^k\left(\frac{q(x,\alpha)}{x^2}\right)\ln^l\left(\frac{x}{1-x}\right)\ln^m \widetilde{q}(x,\alpha)\,, \quad (14)$$

where,

$$\ln q(x,\alpha) = \ln\left(1-(1-\alpha)x\right) + \ln\left(1-\left(1-\frac{1}{\alpha}\right)x\right), \quad (15)$$

$$\ln \widetilde{q}(x,\alpha) = \ln\left(1-(1-\alpha)x\right) - \ln\left(1-\left(1-\frac{1}{\alpha}\right)x\right). \quad (16)$$

which we have confirmed to hold in all subtracted MGEWs up to three loops, and even in the case of two four loop examples. We conjecture that this basis will fit all subtracted MGEWs[9]. It still remains to fully understand the simple analytic structure of subtracted MGEWs and prove the above conjectures. We are also continuing to take strides towards an understanding of webs in general, and are progressing towards a calculation of the multiparton three loop soft anomalous dimension in general kinematics. More generally, this research goes beyond the computation of higher order corrections and aims at exploring the all-order structure of IR singularities in gauge theories and the associated physics.

Acknowledgments

Many thanks go to my collaborators Giulio Falcioni, Einan Gardi, Lorenzo Magnea and Chris White. This work was supported by The University of Edinburgh.

References

1. A. Grozin, J.M. Henn, G.P. Korchemsky, P. Marquard, *Phys. Rev. Lett.* **114**, 6 (2015)
2. S.M. Aybat, L.J. Dixon, and G.F. Sterman, *Phys. Rev. Lett.* **97**, 072001 (2006); S.M. Aybat, L.J. Dixon, and G.F. Sterman, *Phys. Rev.* D **74**, 074004 (2006)
3. E. Gardi, L. Magnea, JHEP **0903**, 079 (2009); T. Becher, M. Neuber, JHEP **0906**, 081 (2009); T. Becher, M. Neuber, *Phys. Rev. Lett.* **102**, 162001 (2009)
4. D.R. Yennie, S.C. Frautschi, H. Suura, Annals. Phys. **13**, 379-452 (1961)
5. J.G.M. Gatheral, *Phys. Lett.* B **133**, 90 (1983); J. Frenkel, J.C. Taylor, *Nucl. Phys.* B **246**, 231 (1984)
6. E. Gardi, E. Laenen, G. Stavenga, C.D. White, JHEP **1011**, 155 (2010)
7. E. Gardi, J. Smillie, C.D. White, JHEP **1103**, 079 (2011).
8. E. Gardi, J. Smillie, C.D. White, JHEP **1109**, 114 (2011).
9. G. Falcioni, E. Gardi, M. Harley, L. Magnea, C.D. White, JHEP **1410**, 10 (2014)
10. E. Gardi, JHEP **1404**, 044 (2014).
11. J.M. Henn, T. Huber, JHEP **1203**, 101 (2012); JHEP **1211**, 058 (2012); JHEP **1309**, 147 (2013)

Small-radius jets to all orders

Matteo Cacciari
Université Paris Diderot, Paris, France
Sorbonne Universités, UPMC Univ Paris 06, UMR 7589, LPTHE, F-75005, Paris, France
CNRS, UMR 7589, LPTHE, F-75005, Paris, France

Frédéric Dreyer
Sorbonne Universités, UPMC Univ Paris 06, UMR 7589, LPTHE, F-75005, Paris, France
CNRS, UMR 7589, LPTHE, F-75005, Paris, France

Mrinal Dasgupta
Consortium for Fundamental Physics, School of Physics & Astronomy, University of Manchester, Manchester M13 9PL, United Kingdom

Gregory Soyez
IPhT, CEA Saclay, CNRS URA 2306, F-91191 Gif-sur-Yvette, France

Gavin Salam[a]
CERN, PH-TH, CH-1211 Geneva 23, Switzerland

With hadron colliders continuing to push the boundaries of precision, it is becoming increasingly important to have a detailed understanding of the subtleties appearing at smaller values of the jet radius R. We present a method to resum all leading logarithmic terms, $\alpha_s^n \ln^n R$, using a generating functional approach, as was recently discussed in Ref. [1] . We study a variety of observables, such as the inclusive jet spectrum and jet vetoes for Higgs physics, and show that small-R effects can be sizeable. Finally, we compare our calculations to existing ALICE data, and show good agreement.

1 Introduction

Jets are collimated bunches of particles produced by fragmentation of a quark or gluon.[2] They emerge from a variety of processes, such as scattering of partons in colliding protons, hadronic decays of massive particles (W, Z, H, t) and radiative gluon emissions. They are widely used as proxies for hard quarks and gluons. A precise understanding of jet processes at hadron colliders is critical in a wide variety of scenarios, such as background discrimination in Higgs production.

1.1 Jet algorithms

A jet definition includes a jet algorithm mapping final state particle momenta to jet momenta, the parameters required by the algorithm and a recombination scheme. Moreover, a jet definition should also be simple to implement in experimental analyses and theoretical calculations. It should yield finite cross sections at any order in perturbation theory and be relatively insensitive to hadronisation.

[a] On leave from CNRS, UMR 7589, LPTHE, F-75005, Paris, France

Most jet definitions used at hadron colliders are based on sequential recombination algorithms, which cluster pairs that are closest in a metric defined by the divergence structure of the theory. This requires an external parameter, the jet radius R, specifying up to which point separate partons are recombined into a single jet.

1.2 Perturbative properties of jets

Jet properties will be affected by gluon radiation and $g \to q\bar{q}$ splitting. In particular, emissions beyond the reach of the jet algorithm will reduce the jet energy.

We can calculate in the small-R limit the average energy difference between the hardest final state jet and an initial quark, considering gluon emissions outside of the jet. We find

$$\langle \Delta z \rangle_q^{\text{hardest}} = \int^{\mathcal{O}(1)} \frac{d\theta^2}{\theta^2} \int dz (\max[z, 1-z] - 1) \times \frac{\alpha_s}{2\pi} p_{qq}(z) \Theta(\theta - R)$$
$$= \frac{\alpha_s}{\pi} C_F \left(2\ln 2 - \frac{3}{8} \right) \ln R + \mathcal{O}(\alpha_s), \quad (1)$$

We notice the appearance of logarithmic terms of the form $\alpha_s \ln R$, which in the limit $\alpha_s \ln R \sim \mathcal{O}(1)$ will spoil the convergence of the perturbative series, requiring resummation to all orders. This limit is of relevance for example in extreme environments, such as heavy ion collisions, where values down to $R = 0.2$ are used,[8,9,10,11,12] and jet substructure tools such as filtering[15] and trimming[16] which resolve small-R subjets (with $R_{\text{sub}} = 0.2 - 0.3$) within moderate or large-R jets. Furthermore, even for the most common choice of the jet radius, $R = 0.4 - 0.5$[17,18], higher order corrections could be sizable, and small-R resummation could bring interesting insights into their effect.

We aim therefore to resum all leading logarithmic (LL) terms $\alpha_s^n \ln^n R$ in the limit of small-R, for a wide variety of observables.

2 Method

We use generating functionals $Q(x,t)$, $G(x,t)$ to encode the parton content when resolving an initial quark or gluon with momentum fraction x on an angular scale defined through a variable $t > 0$, where

$$t = \int_{R^2}^{1} \frac{d\theta^2}{\theta^2} \frac{\alpha_s(p_t\theta)}{2\pi} \sim \frac{\alpha_s}{2\pi} \ln \frac{1}{R^2}. \quad (2)$$

The evolution of a quark or gluon can then be described by two coupled differential equations. For an initiating quark, we have

$$\frac{dQ(x,t)}{dt} = \int dz\, p_{qq}(z) \left[Q(zx,t)\, G((1-z)x,t) - Q(x,t) \right], \quad (3)$$

while for an initiating gluon the evolution is described by

$$\frac{dG(x,t)}{dt} = \int dz\, p_{gg}(z) \left[G(zx,t) G((1-z)x,t) - G(x,t) \right]$$
$$+ \int dz\, n_f\, p_{qg}(z) \left[Q(zx,t) Q((1-z)x,t) - G(x,t) \right]. \quad (4)$$

These evolution equations allow us to resum observables to all orders numerically. They effectively exploit angular ordering.

3 Observables

We now present a few key observables of current interest where small-radius effects have been studied in detail.

3.1 *Microjet vetoes in Higgs production*

Jet veto resummation for Higgs production contain terms of the form

$$\alpha_s^m \ln^{2m} \frac{Q}{p_t} + \text{subleading} \tag{5}$$

Among the subleading terms, there are small-R enhanced terms such as

$$\alpha_s^{m+n} \ln^m \frac{Q}{p_t} \ln^n \frac{1}{R^2} + \dots \tag{6}$$

which have been suspected of playing an important role, and have been calculated to first order by several groups, [19,20,21] as well as numerically to second order. [22 b]

These small-R terms can be accounted for by an overall factor $\mathcal{U}$ that multiplies the jet veto efficiency, where $\mathcal{U}$ has the form

$$\begin{aligned} \mathcal{U} &\equiv P(\text{no microjet veto})/P(\text{no primary parton veto}) \\ &= \exp\left[-\frac{4\alpha_s(p_t)C}{\pi}\ln\frac{Q}{p_t}\int_0^1 dz\, f^{\text{hardest}}(z, t(R,p_t))\ln z\right], \end{aligned} \tag{7}$$

where we defined $f^{\text{hardest}}(z)$ the probability that the hardest microjet carries a momentum fraction z.

We extend therefore the calculation of small-R corrections in jet vetoes to all orders, and implement this result in JetVHeto [19]. The jet veto efficiency obtained is shown in figure 1.

The higher order small-R terms lead to a small shift in central value. But more noticeable is the change at low p_t of the bands calculated from scale variations, which grow larger. We attribute this to a non-trivial interplay between two classes of logarithms, of Q/p_t and R, where adding the small-R terms reveals uncertainties that are otherwise missed.

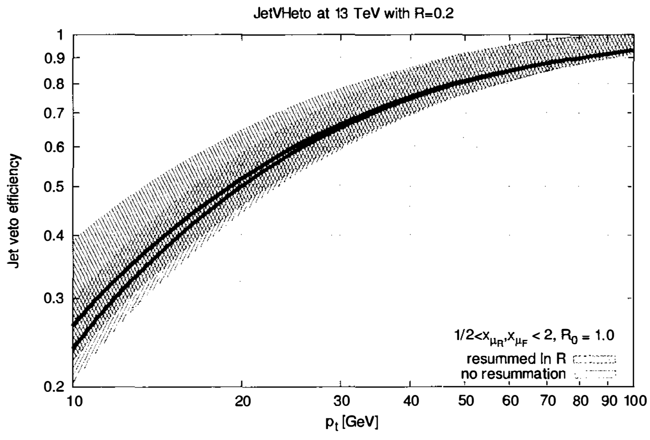

Figure 1 – Jet veto efficiency at 13 TeV with $R = 0.2$, in green (blue) without (with) small-R resummation

[b] The values in the first version of Ref. [22] were in disagreement with our analytical calculations, but this was corrected in arXiv-v3.

3.2 Inclusive jet spectrum

The jet spectrum can be obtained from the convolution of the inclusive microjet fragmentation function with the inclusive partonic spectrum from hard $2 \to 2$ scattering

$$\frac{d\sigma_{\text{jet}}}{dp_t} = \sum_i \int_{p_t} \frac{dp'_t}{p'_t} \frac{d\sigma_i}{dp'_t} f^{\text{incl}}_{\text{jet}/i}(p_t/p'_t, t), \tag{8}$$

where $f_{\text{jet}/i} \equiv \sum_j f_{j/i}$, and we define, for an initial parton i, $f^{\text{incl}}_{j/i}(z,t)$ the inclusive distribution of microjets of flavour j, at an angular scale t, carrying a momentum fraction z of the parton's momentum.

If we assume that the partonic spectrum is dominated by a single flavour i and that its p_t dependence is of the form $d\sigma_i/dp_t \sim p_t^{-n}$, then

$$\frac{d\sigma_{\text{jet}}}{dp_t} \simeq \frac{d\sigma_i}{dp_t} \int_0^1 dz\, z^{n-1} f^{\text{incl}}_{\text{jet}/i}(z,t) \equiv \frac{d\sigma_i}{dp_t} \langle z^{n-1} \rangle_i^{\text{incl}}, \tag{9}$$

Small-R effects are therefore enhanced by a $\ln n$ factor

$$\sim \alpha_s \ln \frac{1}{R^2} \ln n. \tag{10}$$

At the LHC, typical n values for the partonic spectrum range from about 4 at low p_t, to 7 or even larger at high p_t.

In figure 2, we show a comparison of the NLO prediction supplemented with small-R logarithms with existing ALICE data for the inclusive jet spectrum with $R = 0.2$. Here hadronisation is calculated using an analytic model [23], and the theoretical error bands are obtained from the envelope of the $0.5 < x_{\mu_R}, x_{\mu_F} < 2$ and $1 < R_0 < 1.5$ variations, as well as an estimation of hadronisation uncertainties.

At small values of the jet radius, the small-R resummation improves agreement with the data, and reduces the scale dependence of the NLO prediction.

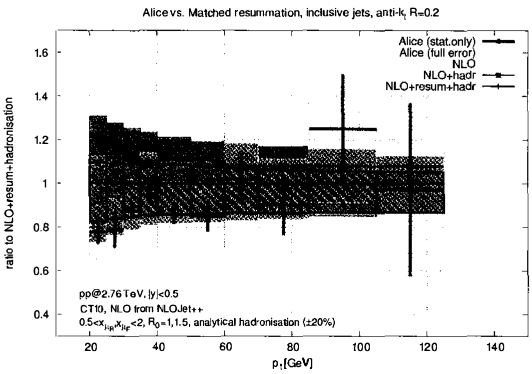

Figure 2 – Comparison of the matched resummation (blue) with ALICE data (red).

Acknowledgments

Some of the results presented here correspond to work in progress. This work has been supported by the ILP LABEX (ANR-10-LABX-63) supported by French state funds managed by the ANR within the Investissements d'Avenir programme under reference ANR-11-IDEX-0004-02.

References

1. M. Dasgupta, F. Dreyer, G. P. Salam and G. Soyez, arXiv:1411.5182 [hep-ph].
2. G. F. Sterman and S. Weinberg, Phys. Rev. Lett. **39** (1977) 1436.
3. S. Catani, Y. L. Dokshitzer, M. Olsson, G. Turnock and B. R. Webber, Phys. Lett. B **269** (1991) 432.
4. S. Catani, Y. L. Dokshitzer, M. H. Seymour and B. R. Webber, Nucl. Phys. B **406** (1993) 187.
5. M. Cacciari, G. P. Salam and G. Soyez, JHEP **0804** (2008) 063 [arXiv:0802.1189 [hep-ph]].
6. Y. L. Dokshitzer, G. D. Leder, S. Moretti and B. R. Webber, JHEP **9708** (1997) 001 [hep-ph/9707323].
7. M. Wobisch and T. Wengler, In *Hamburg 1998/1999, Monte Carlo generators for HERA physics* 270-279 [hep-ph/9907280].
8. M. Ploskon [STAR Collaboration], Nucl. Phys. A **830** (2009) 255C [arXiv:0908.1799 [nucl-ex]].
9. Y. S. Lai [PHENIX Collaboration], arXiv:0911.3399 [nucl-ex].
10. B. Abelev *et al.* [ALICE Collaboration], JHEP **1403** (2014) 013 [arXiv:1311.0633 [nucl-ex]].
11. G. Aad *et al.* [ATLAS Collaboration], arXiv:1406.2979 [hep-ex].
12. S. Chatrchyan *et al.* [CMS Collaboration], Phys. Rev. C **90** (2014) 024908 [arXiv:1406.0932 [nucl-ex]].
13. B. Abelev *et al.* [ALICE Collaboration], Phys. Lett. B **722** (2013) 262 [arXiv:1301.3475 [nucl-ex]].
14. S. Chatrchyan *et al.* [CMS Collaboration], arXiv:1406.0324 [hep-ex].
15. J. M. Butterworth, A. R. Davison, M. Rubin and G. P. Salam, Phys. Rev. Lett. **100** (2008) 242001 [arXiv:0802.2470 [hep-ph]].
16. D. Krohn, J. Thaler and L. -T. Wang, JHEP **1002** (2010) 084 [arXiv:0912.1342 [hep-ph]].
17. G. Aad *et al.* [ATLAS Collaboration], arXiv:1406.0076 [hep-ex].
18. S. Chatrchyan *et al.* [CMS Collaboration], JINST **6** (2011) P11002 [arXiv:1107.4277 [physics.ins-det]].
19. A. Banfi, P. F. Monni, G. P. Salam and G. Zanderighi, Phys. Rev. Lett. **109** (2012) 202001 [arXiv:1206.4998 [hep-ph]].
20. F. J. Tackmann, J. R. Walsh and S. Zuberi, Phys. Rev. D **86** (2012) 053011 [arXiv:1206.4312 [hep-ph]].
21. T. Becher, M. Neubert and L. Rothen, JHEP **1310** (2013) 125 [arXiv:1307.0025 [hep-ph]].
22. S. Alioli and J. R. Walsh, JHEP **1403** (2014) 119 [arXiv:1311.5234 [hep-ph]].
23. M. Dasgupta, L. Magnea and G. P. Salam, JHEP **0802** (2008) 055 [arXiv:0712.3014 [hep-ph]].


LA THUILE
60
20
5

Forward dijet production and improved TMD factorization in dilute-dense hadronic collisions

Sebastian Sapeta
CERN PH-TH, CH-1211, Geneva 23, Switzerland

We study inclusive dijet production at small x in hadronic collisions. We extend the High Energy Factorization (HEF) framework outside its kinematic window, where the transverse momentum imbalance of the dijets system is comparable to the transverse momenta of the individual jets, to the case of arbitrarily small transverse momentum imbalance. That involves generalizing the Transverse Momentum Dependent (TMD) factorization formula for dijet production to the case of finite N_c and with one of the incoming gluons being off-shell. We discuss the features of this new generalized TMD factorization and relate it to the colour-ordered amplitude formalism.

1 Introduction

Forward dijet production at the LHC offers a unique chance to study QCD dynamics in the regime of small x. By requiring the two jets to be produced in the forward direction one creates an asymmetric situation, in which one of the incoming hadrons is probed at large x, while the other is probed at a very small momentum fraction. Since the number of gluons grows rapidly with decreasing x, the above corresponds to collisions of dilute-dense systems.

This interesting kinematic regime faces various challenges with the most fundamental question concerning the factorization of short- and long-distance dynamics. The standard collinear factorization is not applicable in this case as the dependence on the transverse momentum of the low-x gluon in the target, k_t, cannot be neglected. The latter comes from the fact that at low x, the gluon distribution does not fall quickly with k_t, and a significant part of the contribution to the integrated gluon distribution comes from the region $k_t \gg 0$ [1].

The process of interest is shown schematically in Fig. 1. The energy fractions of the incoming parton from the projectile, x_1, and the gluon from the target, x_2, can be expressed in terms of rapidities and transverse momenta of the produced jets

$$x_1 = \frac{1}{\sqrt{s}}\left(|p_{1t}|e^{y_1} + |p_{2t}|e^{y_2}\right), \qquad x_2 = \frac{1}{\sqrt{s}}\left(|p_{1t}|e^{-y_1} + |p_{2t}|e^{-y_2}\right). \tag{1}$$

In the limit of forward jets production, one obtains

$$y_1, y_2 \gg 0 \qquad \Longrightarrow \qquad x_1 \sim 1 \quad \text{and} \quad x_2 \ll 1, \tag{2}$$

hence the target is probed at very low energy fractions and therefore is consists predominantly of gluons with non-vanishing transverse momenta. The target gluon's transverse momentum, k_t, is related to the transverse momenta of the outgoing jets, p_{1t} and p_{2t}, as well as the azimuthal distance, $\Delta\phi$, between the jets

$$|k_t|^2 = |p_{1t} + p_{2t}|^2 = |p_{1t}|^2 + |p_{2t}|^2 + 2|p_{1t}||p_{2t}|\cos\Delta\phi\,. \tag{3}$$

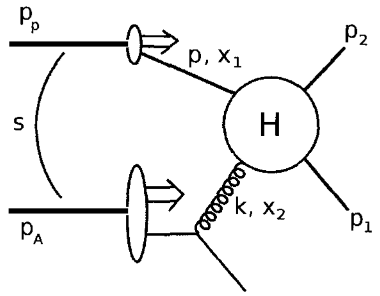

Figure 1 – Inclusive dijet production in dilute-dense collision. The blob H represents hard scattering and the solid lines coming out of H represent partons, which can be either quarks or gluons.

Since the target A is probed at low x_2, the dominant contributions come from the subprocesses in which the incoming parton on the target side is a gluon

$$qg \to qg\,, \qquad gg \to q\bar{q}\,, \qquad gg \to gg\,. \tag{4}$$

2 High energy factorization and generalized TMD factorization

Two approaches to dijet production at small x have been used so far: the high energy factorization (HEF) [2], valid in the limit $Q_s \ll |k_t| \sim |p_{1t}|, |p_{2t}|$, and the transverse momentum dependent (TMD) factorization [3], justified in the range $Q_s \ll |k_t| \ll |p_{1t}|, |p_{2t}|$. Here, Q_s is the so-called saturation scale marking the transition between linear and non-linear regimes of QCD.

The HEF formula for inclusive forward dijet production reads [4]

$$\frac{d\sigma^{pA\to\text{dijets}+X}}{dy_1dy_2d^2p_{1t}d^2p_{2t}} = \frac{1}{16\pi^3(x_1x_2s)^2}\sum_{a,c,d} x_1 f_{a/p}(x_1,\mu^2)\,\overline{|\mathcal{M}_{ag^*\to cd}|}^2\mathcal{F}_{g/A}(x_2,k_t)\frac{1}{1+\delta_{cd}}\,, \tag{5}$$

where $\mathcal{F}_{g/A}(x_2,k_t)$ is the unintegrated gluon distribution in a dense target A, the same that enters the F_2 structure function formula in deep inelastic scattering. The other parton distribution, $f_{a/p}(x_1,\mu^2)$, is a standard collinear PDF of a projectile. The matrix element $\overline{|\mathcal{M}_{ag^*\to cd}|}^2$ is calculated with the incoming gluon kept off-shell using a special set of rules that guarantee gauge invariance of the result [2,5]. The limitation of the HEF formula (5) lies in the fact that it breaks down when the gluon's transverse momentum k_t (or equivalently the transverse momentum imbalance between the two jets) gets much smaller than the average transverse momentum of the jets. Hence, this formula is in principle applicable away from the non-linear regime of the target A and it is not valid in the strict saturation domain.

The TMD formula for our process of interest, so far obtained only in the large-N_c limit [3], takes the form

$$\frac{d\sigma^{pA\to\text{dijets}+X}}{dy_1dy_2d^2p_{1t}d^2p_{2t}} = \frac{\alpha_s^2}{(x_1x_2s)^2}\sum_{a,c,d} x_1 f_{a/p}(x_1,\mu^2)\sum_i H^{(i)}_{ag\to cd}\mathcal{F}^{(i)}_{ag}(x_2,k_t)\frac{1}{1+\delta_{cd}}\,. \tag{6}$$

We see that factorization in a strong sense does not hold in this case and it is replaced by generalized factorization with several unintegrated gluon distributions, $\mathcal{F}^{(i)}_{ag}(x_2,k_t)$, accompanied by corresponding hard factors $H^{(i)}_{ag\to cd}$. The hard factors were so far calculated in the limit of vanishing gluon's transverse momentum [3] and the k_t dependence is present in Eq. (6) only via the unintegrated gluon distributions. The generalized TMD formula (6) has the advantage that it can be used to study the saturation domain where $|k_t| \sim Q_s$. It breaks down however when $|k_t|$ becomes comparable to the average jet transverse momentum, which corresponds to $\Delta\phi \ll \pi$, *c.f.* Eq. (3).

3 Improved TMD factorization

We have reconciled the two complementary approaches to forward dijet production, presented in the previous section section, into a unified framework that we call *improved TMD factorization* [6]. This new framework is valid in the limit $Q_s \ll |p_{1t}|, |p_{1t}|$ with an arbitrary value of $|k_t|$. Moreover, it profits from a number of improvements, as compared to HEF and generalized TMD descriptions, which include: (i) full N_c dependence in the hard factors, (ii) restored k_t dependence in the hard factors, and, (iii) reduced number of TMDs and the corresponding hard factors, which leads to a simpler form of the factorization formula.

The improved factorization formula for inclusive dijet production takes the form

$$\frac{d\sigma^{pA\to \text{dijets}+X}}{d^2P_t d^2k_t dy_1 dy_2} = \frac{\alpha_s^2}{(x_1x_2s)^2}\sum_{a,c,d} x_1 f_{a/p}(x_1,\mu^2)\sum_{i=1}^{2} K^{(i)}_{ag^*\to cd}\Phi^{(i)}_{ag\to cd}\frac{1}{1+\delta_{cd}}\,, \tag{7}$$

where $K^{(i)}_{ag^*\to cd}$ are the new hard factors and $\Phi^{(i)}_{ag\to cd}$ are the corresponding, new gluon TMDs. The hard factors retain full dependence on gluon's k_t and are summarized in a concise form in Table 1, where, in addition to the standard Mandelstam variables (*c.f.* Fig. 1 for notation)

$$\hat{s} = (p_1+p_2)^2\,, \qquad \hat{t} = (p-p_2)^2\,, \qquad \hat{u} = (p-p_1)^2\,, \tag{8}$$

we introduced their barred versions, defined only with the longitudinal component of the off-shell gluon

$$\bar{s} = (x_2p_A+p)^2\,, \qquad \bar{t} = (x_2p_A-p_1)^2\,, \qquad \bar{u} = (x_2p_A-p_2)^2\,. \tag{9}$$

The results of Table 1 were obtained using two different methods of calculation. The first method followed the original technique developed in the HEF formulation [2] and consisted of using standard Feynman rules in axial gauge with a special choice of the gauge vector, $n = p_A$, and the polarization vector of the off-shell gluon $\epsilon^0_\mu = i\sqrt{2}\,x_2p_{A\mu}/|k_t|$. This procedure is sufficient to render the result gauge invariant for a class of axial gauges in the high energy limit.

The second independent calculation relied on the frameworks of colour ordered amplitudes and helicity methods. Each $2\to 2$ amplitude in one of the three channels (4) is represented as a sum of two, gauge invariant subamplitudes corresponding to different colour flows. The squared amplitude consists of four terms, which however turn out be multiplied by only two unique colour structures. In terms of factorization formula, that means that only two TMDs are need in each channel, which results in the structure of the improved TMD factorization formula presented in Eq. (7).

Table 1: The hard factors accompanying the gluon TMDs $\Phi^{(i)}_{ag\to cd}$ entering the improved TMD factorization formula (7). The Mandelstam variables are defined according to Eqs. (8) and (9).

$K^{(i)}_{gg^*\to gg}$	$\frac{N_c}{C_F}\frac{(\bar{s}^4+\bar{t}^4+\bar{u}^4)(\bar{u}\hat{u}+\bar{t}\hat{t})}{\bar{t}\hat{t}\bar{u}\hat{u}\bar{s}\hat{s}}$	$-\frac{N_c}{2C_F}\frac{(\bar{s}^4+\bar{t}^4+\bar{u}^4)(\bar{u}\hat{u}+\bar{t}\hat{t}-\bar{s}\hat{s})}{\bar{t}\hat{t}\bar{u}\hat{u}\bar{s}\hat{s}}$
$K^{(i)}_{gg^*\to q\bar{q}}$	$\frac{1}{2N_c}\frac{(\bar{t}^2+\bar{u}^2)(\bar{u}\hat{u}+\bar{t}\hat{t})}{\bar{s}\hat{s}\hat{t}\hat{u}}$	$\frac{1}{4N_c^2C_F}\frac{(\bar{t}^2+\bar{u}^2)(\bar{u}\hat{u}+\bar{t}\hat{t}-\bar{s}\hat{s})}{\bar{s}\hat{s}\hat{t}\hat{u}}$
$K^{(i)}_{qg^*\to qg}$	$-\frac{\bar{u}\,(\bar{s}^2+\bar{u}^2)}{2\bar{t}\hat{t}\hat{s}}(1+\frac{\bar{s}\hat{s}-\bar{t}\hat{t}}{N_c^2\,\bar{u}\hat{u}})$	$-\frac{C_F}{N_c}\frac{\bar{s}(\bar{s}^2+\bar{u}^2)}{\bar{t}\hat{t}\hat{u}}$

Hence, the improved factorization has a simpler form than the generalized TMD formula of Eq. (6). The new TMDs, $\Phi^{(i)}_{ag\to cd}$, are related to the old TMDs, $\mathcal{F}^{(i)}_{ag}$, as follows

$$\begin{aligned}
\Phi^{(1)}_{gg\to gg} &= \frac{1}{2N_c^2}(N_c^2\mathcal{F}^{(1)}_{gg} - 2\mathcal{F}^{(3)}_{gg} + \mathcal{F}^{(4)}_{gg} + \mathcal{F}^{(5)}_{gg} + N_c^2\mathcal{F}^{(6)}_{gg})\,,\\
\Phi^{(2)}_{gg\to gg} &= \frac{1}{N_c^2}(N_c^2\mathcal{F}^{(2)}_{gg} - 2\mathcal{F}^{(3)}_{gg} + \mathcal{F}^{(4)}_{gg} + \mathcal{F}^{(5)}_{gg} + N_c^2\mathcal{F}^{(6)}_{gg})\,,
\end{aligned}$$

$$\Phi^{(1)}_{qg\to qg} = \mathcal{F}^{(1)}_{qg}\,, \qquad \Phi^{(2)}_{qg\to qg} = \frac{1}{N_c^2-1}\left(-\mathcal{F}^{(1)}_{qg} + N_c^2\mathcal{F}^{(2)}_{qg}\right)\,,$$
$$\Phi^{(1)}_{gg\to q\bar{q}} = \frac{1}{N_c^2-1}\left(N_c^2\mathcal{F}^{(1)}_{gg} - \mathcal{F}^{(3)}_{gg}\right)\,, \quad \Phi^{(2)}_{gg\to q\bar{q}} = -N_c^2\mathcal{F}^{(2)}_{gg} + \mathcal{F}^{(3)}_{gg}\,.$$

Both of the above calculations, the one using traditional approach and the one employing colour ordered amplitude formalism, lead to identical results for the hard factors and the new TMDs. Our formulae reduce to the generalized TMD results if the hard factors are taken in the limit of $k_t \to 0$ and only the leading N_c part is kept. Also, the HEF factorization and the collinear factorization are recovered in the respective limits.

4 Summary

We discussed the problem of theoretical description of the forward-forward dijet production in dilute-dense hadronic collisions. Our main result consists of a new, improved TMD factorization formula (7), which unifies two complementary theoretical frameworks commonly used in the literature: the high energy factorization [2] and the generalized TMD factorization [3].

The improved TMD framework is valid for the jet transverse momenta $|p_{1t}|, |p_{2t}| \gg Q_s$ and an arbitrary value of the incoming gluon transverse momentum, k_t. Our result incorporates full N_c dependence and complete k_t dependence in the hard factors and it is written in terms of a minimal set of the gluon TMDs. Hence, it constitutes a robust framework for studies of saturation domain with hard objects.

Acknowledgments

We thank the organizers of the 50$^{\text{th}}$ Rencontres de Moriond for the opportunity to present these results and for financial support. The studies described here were performed in collaboration with Piotr Kotko, Krzysztof Kutak, Cyrille Marquet, Elena Petreska and Andreas van Hameren.

References

1. K. Kutak and S. Sapeta, *Phys. Rev.* D **86**, 094043 (2012).
2. S. Catani, M. Ciafaloni and F. Hautmann, *Nucl. Phys.* B **366**, 135 (1991).
3. F. Dominguez, C. Marquet, B.-W. Xiao and F. Yuan, *Phys. Rev.* D **83**, 105005 (2011).
4. M. Deak, F. Hautmann, H. Jung and K. Kutak, *JHEP* **0909**, 121 (2009).
5. A. van Hameren, P. Kotko and K. Kutak, *JHEP* **1212**, 029 (2012).
6. P. Kotko, K. Kutak, C. Marquet, E. Petreska, S. Sapeta and A. van Hameren, arXiv:1503.03421 [hep-ph].

5.
New Phenomena

Strong Production SUSY Searches at ATLAS and CMS

Z.L. Marshall on behalf of the ATLAS and CMS Collaborations
Physics Division, Lawrence Berkeley National Laboratory, 1 Cyclotron Road, Berkeley CA, United States of America

The results of searches for strongly-produced supersymmetry at the Large Hadron Collider by the ATLAS and CMS collaborations are presented. Several of the historically strongest zero- and one-lepton final state searches have been updated to include multi-bin fits and combinations. In addition, new two-lepton final state search results are shown from CMS and ATLAS, which show 2.6 and 3.0 standard deviation excesses, respectively, above the standard model expectation, albeit in different regions of phase space. Both collaborations have also shown new searches that cover areas uncovered by previous searches, in both searches for light stops and searches for stealth supersymmetry.

1 Introduction

Supersymmetry (SUSY)[1,2,3], one popular extension of the Standard Model (SM), is the target of a diverse search programme at the Large Hadron Collider. This paper details the progress that ATLAS[4] and CMS[5], two general-purpose detectors, have made in searching for strongly-produced SUSY in data collected at $\sqrt{s} = 8$ TeV in 2012. Strongly-produced SUSY includes the production of gluinos (squarks), the superpartners of SM gluons (quarks), which decay in one or more steps to the lightest SUSY particle (LSP), typically a stable neutral particle that is also a dark matter candidate (e.g. the lightest neutralino, $\tilde{\chi}_1^0$, or the gravitino, $\tilde{G}$). The signatures of these events include jets, missing transverse momentum ($E_{\mathrm{T}}^{\mathrm{miss}}$), and frequently leptons.

The previous searches for SUSY in 0- and 1-lepton final states, detailed in Section 2 have introduced combinations and fits in order to extend their reach up to 1.35 TeV in gluino mass. New searches in dilepton final states by ATLAS and CMS, described in Section 3, have shown moderate 3.0 and 2.6 σ (respectively) excesses. Section 4 highlights some new searches that target particularly difficult-to-search regions of phase space. Finally, conclusions and prospects are given in Section 5.

2 Combinations and Fits

Using a large number of published and preliminary searches for strongly produced Supersymmetry, ATLAS and CMS are extending search limits on squarks and gluinos by combining multiple independent searches and by performing more complex fits of the available data[6,7,8,9,10]. Conceptually, combinations and fits are the same; one can imagine a combination of 0-, 1-, and 2-lepton individual search regions as a fit of the lepton multiplicity distribution, for example. A combination can provide stronger limits in the case of a single signal hypothesis. These fits and combinations rely on a detailed understanding of correlations between background estimates and systematics and require that the channels being combined are non-overlapping. As many of the searches were designed to provide the strongest limits in each individual channel, rather than being amenable to a straightforward combination, significant work may be involved when combining multiple searches[11].

Search limits are often shown in terms of "simplified models," unphysical models in which a subset of SUSY particles are included at masses accessible to the LHC. The other SUSY particles are decoupled and the decay modes are restricted, so that the models can be described with only a few parameters. Although in these simplified models quite high masses can be excluded, by introducing additional particles and decay modes these limits may weaken significantly.

Combinations provide the greatest benefit when the searches being combined have comparable sensitivity. This may occur in a "transition region" between the regions of phase space for which each individual search was optimized – although neither search is optimal, together they can still provide a strong limit. An example is shown in Figure 1, where ATLAS has designed two complimentary searches in different final states that have comparable sensitivity to a gluino, in a SUSY model where the gluino decays through a $\tilde{\chi}^0_2$ and sleptons or neutralinos, producing a final state that may contain a large number of leptons[6]. The combination of searches with exactly one and two or more leptons provides a reach 50–100 GeV stronger than either search alone. CMS have performed a similar combination in searches for bottom squarks, with complimentary searches targetting different regions of phase space[10].

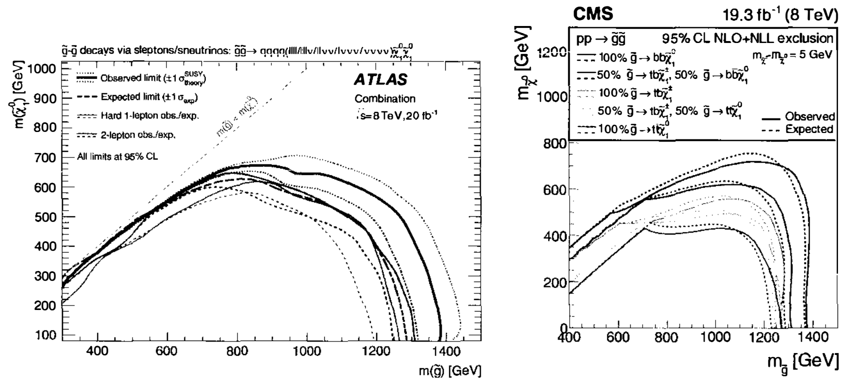

Figure 1 – The results of a combination of two ATLAS searches[6] (left) and several CMS searches[7] (right) for gluino production. The exclusion limits combine several final states to provide strong, generic limits.

Combinations also allow generic limits to be derived that are less dependent on the details of the final state. For example, CMS has set limits on gluino production, with the gluino decaying to $b\bar{b}\tilde{\chi}^0_1$ or $t\bar{t}\tilde{\chi}^0_1$ at varying rates[7]. Such decays can populate exlusively 0-lepton final states ($b\bar{b}\tilde{\chi}^0_1$) or provide a significant number of leptons ($t\bar{t}\tilde{\chi}^0_1$). The limits, shown in Figure 1, demonstrate the exclusion of a 1200 GeV gluino independent of the relative rates of these two decays. Similarly, ATLAS has set limits on stop production, with the stop decaying to either an on-shell or off-shell top at different rates[9]. The different decays can have significantly different kinematics that affect the searches' limits.

3 Dilepton Searches

Both ATLAS and CMS have recently published searches for SUSY in dilepton final states[12,13]. Both have separate analyses targeting signals with the production of Z-bosons, where the signal includes a peak in the dilepton mass ($m_{\ell\ell}$) spectrum, and signals with the production of an intermediate slepton, where the signal has an "edge" in the dilepton mass spectrum. In both cases, the signal produces events with two electrons (ee) or two muons ($\mu\mu$). Both ATLAS and CMS require some jet activity and large $E_{\mathrm{T}}^{\mathrm{miss}}$ in the events, although the details of the requirements differ. The results of these searches are shown in Figure 2.

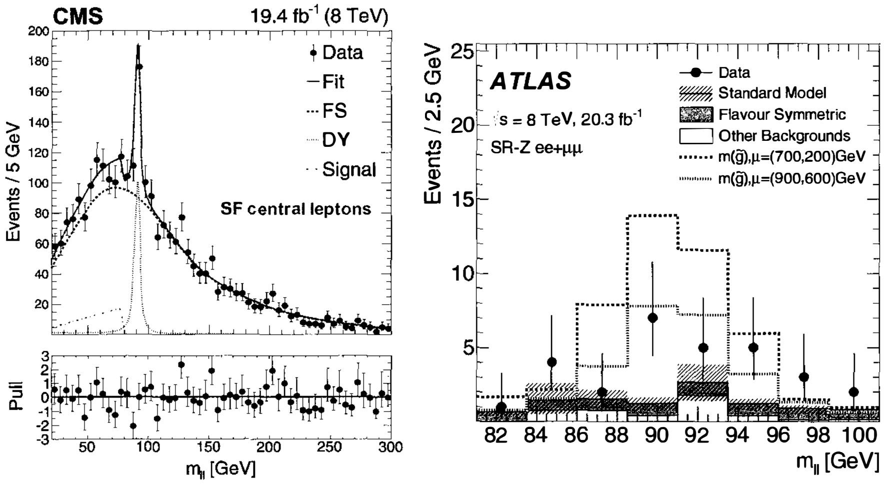

Figure 2 – The results of the CMS dilepton SUSY search[13] (left) and the ATLAS dilepton search in events with a Z boson[12] (right).

Both searches rely on data-driven methods for the estimation of the dominant backgrounds. In both cases, the $t\bar{t}$, WW, and $Z \to \tau\tau$ backgrounds are determined from a sample of events with an electron (e) and a muon (μ), with small corrections applied to estimate these backgrounds in the ee and $\mu\mu$ channels. CMS uses two methods for the estimation of the Z/γ^* background: a template method using events with an isolated γ, and a method that examines the balance of the Z p_{T} and that of the jet activity in the event. In the general gauge mediation SUSY models studied by ATLAS, neither of these background estimation techniques are applicable. Instead, ATLAS uses a jet smearing method to estimate the same background, cross-checked with simulated events. This method is less sensitive to the details of the signal model but suffers from significant extrapolation uncertainties. Nonetheless, the Z/γ^* background in both searches is small in the regions of interest.

Including all systematic uncertainties, CMS observes a 2.4σ local excess of the data over the background in events with low $m_{\ell\ell}$ (2.6σ when considering only central leptons). The excess observed is consistent with a 350-400 GeV sbottom. ATLAS have performed a search in a similar region of phase space and observe no similar excess. Although the two experiments differ in methodology, the searches should be sensitive to the same signal.

ATLAS observes a 3.0σ excess in events with a Z boson. The excess is consistent with a 900 GeV gluino and is present in both dielectron and dimuon events. Although CMS observes no similar excess, the searches have sufficiently different event selection that the ATLAS excess cannot be excluded by the published CMS results.

4 Exploring Difficult Regions of Phase Space

By exploiting new ideas and carefully designed searches, ATLAS and CMS are both exploring regions of phases space that had previously proven extremely difficult to explore.

It was previously believed that the stop could have a mass only slightly larger than that of the top quark, and its decay would only be observable via a small increase in the top production cross section, which is not predicted in QCD with sufficient precision. ATLAS has recently published a search for the stop just above the top mass using both the cross section and the spin correlations in the top quark decays[14]. As the top squarks have spin 0, the distribution of the opening angle between the two leptons in a dileptonic decay differs between the top squarks and the SM top quarks. By using the normalization of the distribution as well as the shape, a stop quark with $m_t < m_{\tilde{t}} < 191$ GeV is excluded. The normalization and shape contribute equally to the strength of the limit. With a growing set of searches based on spin properties, it may soon be possible to exclude a top squark with mass near the top mass.

A set of models known as "stealth" SUSY, were introduced as models that might be particularly difficult to find at the LHC. These models introduce a scalar in the decay chain that results in additional particles in the final state, but lower $E_{\mathrm{T}}^{\mathrm{miss}}$. By exploiting the relatively high jet multiplicity in these events and searching in events with either leptons or photons in the final state, CMS has produced limits on these models on squarks up to 1100 GeV, comparable to the limits on standard SUSY models[15]. Other variants of these "stealth" models populate different final states, but with well-targeted searches it maybe possible to exclude many of them.

5 Conclusions and Outlook

ATLAS and CMS are completing a detailed and broad search programme for strongly produced SUSY with the 8 TeV data that were collected in 2012. Many searches have been combined, in order to provide even stronger limits. Recent dilepton searches from both ATLAS and CMS show interesting excesses, and the data to be collected in 2015 should be sufficient to demonstrate whether these were large statistical fluctuations or the first hints of new physics. The experiments have also addressed several SUSY scenarios that are particularly challenging experimentally, demonstrating that with new ideas limits can be set on even rather stubborn signal models.

The next run of the LHC, at a center of mass energy of 13 TeV, should provide even stronger limits on strongly-produced SUSY. ATLAS has produced a number of projections for the strength of searches after initial 13 TeV data taking[16]. Even with conservative assumptions about systematic uncertainties, these projections indicate that only a small amount of data, in some cases 1 fb^{-1}, is needed before the current limits will be exceeded. These data may be sufficient to finally resolve the question of whether natural strong SUSY is realized in nature.

References

1. J. Wess and B. Zumino, Nucl. Phys. B **70** (1974) 39.
2. S. Dawson, E. Eichten, and C. Quigg, Phys. Rev. D **31** (1985) 1581.
3. S. P. Martin, in *Perspectives on Supersymmetry II*, G. L. Kane, ed., volume 21, p. 1. World Scientific, 2010. arXiv:hep-ph/9709356.
4. The ATLAS Collaboration, JINST **3** (2008) S08003.
5. The CMS Collaboration, JINST **3** (2008) S08004.
6. The ATLAS Collaboration, JHEP **04** (2015) 116. arXiv:1501.03555.
7. The CMS Collaboration, Phys. Rev. D **91** (2015) 052018. arXiv:1502.00300.
8. The CMS Collaboration, Phys. Lett. B **745** (2015) 5. arXiv:1412.4109.
9. The ATLAS Collaboration, ATLAS-CONF-2015-010 (2015).
10. The CMS Collaboration, CERN-PH-EP-2015-055 (2015), Accepted by JHEP. 1503.08037.
11. The ATLAS Collaboration, ATLAS-CONF-2015-011 (2015).
12. The ATLAS Collaboration, CERN-PH-EP-2015-038 (2015), Submitted to Eur. Phys. J. C. arXiv:1503.03290.
13. The CMS Collaboration, JHEP **04** (2015) 124. arXiv:1502.06031.
14. The ATLAS Collaboration, Phys. Rev. Lett. **114**, 142001 (2015). arXiv:1412.4742.
15. The CMS Collaboration, Phys. Lett. B **743** (2015) 503. arXiv:1411.7255.
16. The ATLAS Collaboration, ATL-PHYS-PUB-2015-005 (2015).

Searches for weakly produced SUSY at LHC

S. Folgueras for the CMS and ATLAS Collaborations
Departmento de Física, Universidad de Oviedo,
C/Calvo Sotelo s/n, 33005, Oviedo, Spain

A summary of the different searches for weakly produced SUSY by both CMS and ATLAS is presented here. A review on the methodology of these searches, including event selection, background suppression and estimation methods, etc is covered. Other searches at the LHC already probe squarks and gluino masses up to 1.4 TeV, such scenario, may favour electroweak production of charginos and neutralinos, that will produce many-lepton final states accompanied by E_T^{miss} and very little hadronic activity. Latest searches include Higgs boson in the decay and exploits VBF associated production to probe scenarios with very small mass splittings.

1 Introduction

SUSY models are a possible extension to the very successful standard model (SM) that provides a solution to many problems such as fine-tuning and the unification of the couplings. The search for SUSY has become a major goal and one of the highest priorities searches for both ATLAS [1] and CMS [2].

While most of LHC searches focus on strong production of SUSY with larger cross sections, electroweak production of SUSY may be the key to new physics, as the squarks and gluinos may be too heavy to be produced at LHC energies. The decay chain will produce sleptons (or W,Z and h bosons) and lead to multiple-lepton final states with little hadronic activity and significant missing transverse energy (E_T^{miss}) from the lightest-supersymetric particle (LSP).

As the production cross-section is very small, many final states are combined together targeting different production mechanisms to reach enough sensitivity for new physics. A summary of the different searches performed by CMS and ATLAS Collaborations will be shown in these proceedings.

2 Signature

Very clean lepton signatures with low hadronic activity are expected in the final state when assuming direct chargino-neutralino production with both light and heavy sleptons. In the second case, the chargino/neutralino decays directly to W,Z or h bosons. Three lepton final states [3,4] are yielded naturally by most of these models, however, under certain conditions, two lepton signatures could be more sensitive, i.e. when the mass splitting is small. On top of the multilepton selection, a Z-veto is generally applied to suppress background from diboson production, a (b)jet-veto is applied to suppress $t\bar{t}$ background. Signal regions are defined in bins of E_T^{miss}, $M_{T(2)}$ and m_{ll}. Two remaining backgrounds have to be estimated: non-prompt lepton backgrounds are estimated using different data-driven techniques. Irreducible diboson backgrounds are estimated using simulation. Control regions are used for MC validation.

3 Chargino-neutralino production

Previous searches from both CMS and ATLAS have looked for chargino-neutralino production decaying via sleptons or W,Z bosons (if the sleptons are too heavy). Many final states were used to probe electroweak production of charginos and neutralinos: the three leptons [3,4] final state is the most natural signaturc. If thc mass splitting between the particles is small, the sensitivity of the three-lepton analysis is very poor, however some of this efficiency can be recovered by dilepton final sates (both opposite-sign [5] and same-sign [3]). Finally, depending on the considered model, a final state with multiple taus can be hugely favoured, therefore a dedicated tau search [6] is also particularly sensitivc to these scenarios.

The Higgs discovery opened up a new possibility in electroweak production of SUSY, the neutralino could decay, not only into sleptons, or W/Z bosons, but also into a Higgs boson, leading to many new different final states that could be used to probe for electroweak production, both considering a light or a heavy LSP.

Considering different Higgs-decay-modes, various searches targeting chargino-neutralino production will be summarized. A W boson is produced in the chargino decay chain, while the neutralino decays to a Higgs boson and the LSP.

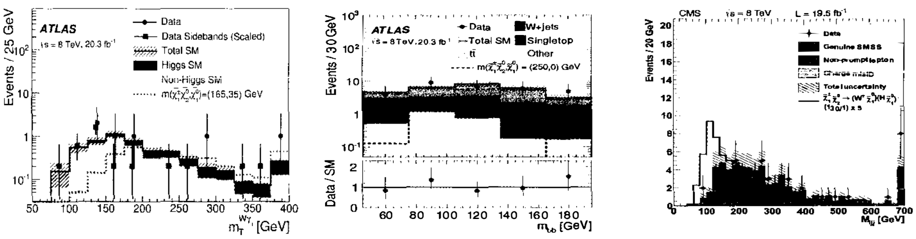

Figure 1 – Transverse mass distribution in the $\gamma\gamma$+lepton search [7] (left), m_{bb} distribution in the single-lepton search [7] (middle) and m_{ljj} for the same-sign search [3] (right). All three searches target $\tilde{\chi}_1^{\pm}\tilde{\chi}_2^0 \rightarrow hW^{\pm}\ \tilde{\chi}_1^0\tilde{\chi}_1^0$.

3.1 $\gamma\gamma$ lepton search

When the Higgs decays to two photons, the final state consists of two photons and a lepton. The signal region is defined using the transverse mass as a discriminating variable. The transverse mass is calculated with respect to the lepton in CMS [8] case and with respect one photon for ATLAS [7] case.

Non-SM Higgs backgrounds are estimated using a fit on the sidebands of the diphoton invariant mass distribution.

3.2 Single lepton search

To target the $h \rightarrow b\bar{b}$ final state, events with a lepton (coming from the W) and two b-jets from the Higgs decay are selected. The search strategy divides the signal region into E_T^{miss}[3] and m_{CT}, m_T bins [7] and looks for a resonance in the m_{bb} spectrum.

Background is estimated from MC, however, scveral control regions are used to constrain normalization and validation regions are used test background modelling.

3.3 Same-sign search

For searching in the $h \rightarrow WW$ channel, events with two same-sign leptons, no b-jets and 1,2 or 3 jets are selected. Extra cuts on E_T^{miss} and m_{T2} are then applied to remove background contribution in the CMS search [3] while ATLAS [7] uses extra cuts on E_T^{miss}, $|\Delta\eta|$, m_T and m_{eff}.

The search strategy is very similar, looking for a peak in the low m_{ljj} region.

3.4 Combination

As no significant excess over the Standard Model predictions is seen in either channel, a combination of all these searches together with the previous multilepton result[4,6,3] to set limits on chargino-neutralino production when $\tilde{\chi}_2^0 \to h\tilde{\chi}_1^0$. Chargino masses up to 250 (210) GeV are probed in ATLAS(CMS) search.

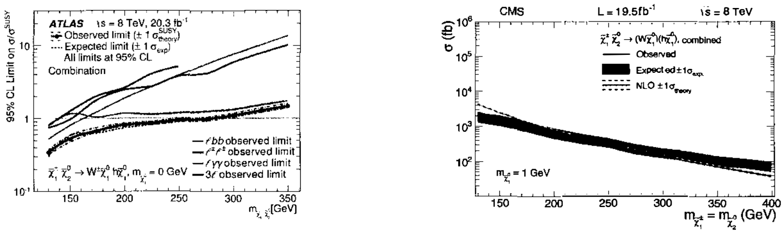

Figure 2 – Left: Observed (solid line) and expected (dashed line) 95% CL upper limits on the cross section normalised by the simplified model prediction as a function of the common mass $m_{\tilde{\chi}_1^\pm \tilde{\chi}_2^0}$ for $\tilde{\chi}_1^0 = 0$ GeV for the ATLAS combination [7]. Right: Observed and expected 95% CL upper limits on the cross section as a function of the mass $m_{\tilde{\chi}_1^\pm \tilde{\chi}_2^0}$ for $\tilde{\chi}_1^0 = 1$ GeV for CMS combination [8]. In both cases, the solid band around the expected limit represents the one-standard-deviation interval.

4 Electroweak production of SUSY with VBF production

More recent searches exploit the VBF topology, allowing a complementary route to probe the electroweak production sector, specially when trying to reach very compressed scenarios that are not accessible with more classic searches.

4.1 Photon + E_T^{miss} search

Events with one or two photons, no lepton, two VBF jets (large $|\Delta\eta|$ gap between the two jets) and E_T^{miss} are selected in this analysis [9]. Signal regions are designed on top of this selection to fully exploit the VBF topology, the invariant mass $|\Delta\eta|$ of the dijet system is used for the search region definition.

Background processes are mainly multijets and γ+jets, they are estimated directly from data control regions. Having found no significant excess over the SM expectations, limits are set for a various of LSP and NLSP masses in a GSMB model where the Higgs boson decays to a pair of neutralinos. Although the analysis was optimized for the one photon+E_T^{miss} signature, most stringent limits arise from the di-photon search.

4.2 Two lepton search

In this CMS analysis [10], events with 2 leptons, E_T^{miss} and two VBF jets (large $|\Delta\eta|$ gap between the two jets) are selected. A broad excess in the tails of the invariant mass distribution of the two jets will be an indication for new physics.

Main background for this search arises from $t\bar{t}$, V + jets, diboson and QCD, although the tight VBF requirements on the two jets reject most of the backgrounds produced via strong interaction. Simulation is used for estimating the remaining background processes and control-regions in data are used to constrain normalization of each process.

No excess over the SM prediction is seen in data and limits on chargino-neutralino production both decaying to staus, for different mass splitting and LSP masses are set. Chargino masses up to 250 GeV are excluded for a model with chargino-neutralino production, decaying to staus for a given mass splitting of ($m_{\tilde{\tau}} - m_{\tilde{\chi}_1^\pm} = 5$ GeV) and a massless LSP.

5 Summary

A wide variety of searches for weakly produced SUSY have been shown. Current CMS and ATLAS searches probe chargino and neutralino masses up to 700 GeV. Latest searches include Higgs bosons in the decays, probing chargino masses up to 250 GeV. More recent searches also look for weakly produced SUSY in association with two VBF jets, allowing to probe much compressed scenarios up to chargino masses of 250 GeV. The higher energy at the LHC will open up a whole new regime to look for SUSY. Figure 3 shows a the summary of all the searches performed by both collaborations.

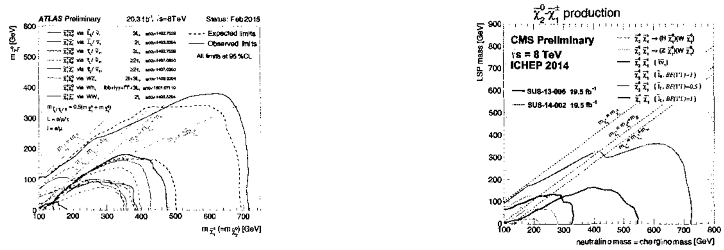

Figure 3 – Summary of ATLAS [11] (left) and CMS [12] (right) searches of electroweak production of charginos and neutralinos based of 20 fb^{-1} of pp collision data at $\sqrt{s}$ = 8 TeV. Exclusion limits at 90% confidence level are shown in the chargino-neutralino mass plane for several decay modes of the charginos and neutralinos.

References

1. ATLAS Collaboration. The ATLAS experiment at the CERN LHC. *JINST*, 3:S08003.
2. CMS Collaboration. The CMS experiment at the CERN LHC. *JINST*, 3:S08004, 2008.
3. CMS Collaboration. Searches for electroweak production of charginos, neutralinos, and sleptons decaying to leptons and W, Z, and Higgs bosons in pp collisions at 8 TeV. *Eur.Phys.J.*, C74(9):3036, 2014.
4. ATLAS Collaboration. Search for direct production of charginos and neutralinos in events with three leptons and missing transverse momentum in $\sqrt{s}$ = 8TeV *pp* collisions. *JHEP*, 1404:169, 2014.
5. ATLAS Collaboration. Search for direct production of charginos, neutralinos and sleptons in final states with two leptons and missing transverse momentum in *pp* collisions at $\sqrt{s}$ = 8 TeV. *JHEP*, 1405:071, 2014.
6. ATLAS Collaboration. Search for the direct production of charginos, neutralinos and staus in final states with at least two hadronically decaying taus and missing transverse momentum in *pp* collisions at $\sqrt{s}$ = 8 TeV. *JHEP*, 1410:96, 2014.
7. ATLAS Collaboration. Search for direct pair production of a chargino and a neutralino decaying to the 125 GeV Higgs boson in $\sqrt{s}$ = 8 TeV *pp* collisions. *arXiv*, 1501.07110, 2015.
8. CMS Collaboration. Searches for electroweak neutralino and chargino production in channels with Higgs, Z, and W bosons in pp collisions at 8 TeV. *Phys.Rev.*, D90(9):092007.
9. ATLAS Collaboration. Search for exotic Higgs-boson decays in events with at least one photon, missing transverse momentum, and two forward jets produced in $\sqrt{s}$ = 8 TeV pp collisions. Technical Report ATLAS-CONF-2015-001, Feb.
10. CMS Collaboration. Search for electroweak SUSY with VBF tagging. Technical Report CMS-PAS-SUS-14-005, 2015.
11. `https://twiki.cern.ch/twiki/bin/view/AtlasPublic/SupersymmetryPublicResults`.
12. `https://twiki.cern.ch/twiki/bin/view/CMSPublic/PhysicsResultsSUS`.

Thinking outside the beamspot: Other SUSY searches at the LHC (long-lived particles and R-parity violation)

H.W. Wulsin
for the ATLAS and CMS collaborations
Department of Physics, The Ohio State University,
191 West Woodruff Ave., Columbus OH, 43210, USA

Supersymmetric particles that are long-lived or violate R-parity could evade many conventional searches for supersymmetry. This talk presents the latest results of searches for supersymmetry with long-lived particles or R-parity violation performed by the ATLAS and CMS collaborations using ~20 fb^{-1} of proton-proton collisions at center-of-mass energy of 8 TeV delivered by the LHC.

1 Overview

Supersymmetry (SUSY) is an attractive theory because it could provide solutions to two big unsolved mysteries in particle physics: the identity of a dark matter particle and the stability of the Higgs mass against quantum corrections at very high energy scales. Many searches for SUSY have been performed, but no evidence of its existence has yet been found. Supersymmetric particles with long lifetimes could evade many conventional SUSY searches, which typically require the physics objects of interest to have a transverse impact parameter less than about a millimeter. R-parity violating SUSY particles could also evade many SUSY searches, which commonly require a large amount of missing transverse energy $E_{\mathrm{T}}^{\mathrm{miss}}$. To cover these gaps, dedicated searches that target long-lived particles and R-parity violation have been performed with data collected by the ATLAS [1] and CMS [2] experiments, in most cases using ~20 fb^{-1} of $\sqrt{s}$ = 8 TeV proton-proton collisions delivered by the LHC in 2012. No significant excesses above the background expectation are observed, and limits are placed on a variety of models.

The searches presented here cover a wide variety of signatures, including jets, leptons, photons, and tracks. These signatures depend on whether the supersymmetric particle is neutral or charged, and in what region of the detector it decays: the tracker, calorimeters, muon system, or outside the detector entirely. In general there are few standard model backgrounds that can mimic these signatures, but these searches have to confront unusual backgrounds from sources such as detector noise, cosmic rays, and reconstruction failure modes. The simulation is typically unable to describe these processes accurately, so the backgrounds are usually estimated with data-driven techniques.

2 Neutral long-lived particles decaying to jets, leptons, or photons

A search for displaced dijets [3] requires two jets, each with at least one track, originating from a common displaced vertex. There are many ways to produce such a signature, including a single displaced jet with final state radiation, a decay to 3 or more jets, or a decay to leptons, which are included as jets. The dominant background is from QCD multijets, which is reduced by placing requirements on the number of prompt tracks and the fraction of energy they carry, as well as on a likelihood discriminant that combines four variables associated with the vertex and cluster information. The remaining background is estimated by using uncorrelated data sideband control regions. Two events are observed in a loose search region and one event is observed in a tight search region, both consistent with expectations. Limits are set on hidden valley models and on RPV SUSY for decay lengths of millimeters to several meters; an example is given in Fig. 1.

If the long lived particle decays in the hadronic calorimeter, it would produce the signature of a trackless jet, a narrow jet with few associated tracker tracks and very little energy deposited in the electromagnetic calorimeter. A search for such particles [4] estimates the dominant QCD multijets background from the data. In the search region, 24 events are observed, consistent with the expectation, and limits are set on a hidden valley model in terms of the decay length of the valley pion ranging from tens of centimeters to tens of meters; an example is given in Fig. 1.

Another search [5] selects events with two displaced vertices close to a jet, each with at least five tracks, with the vertices either in the tracker or in the muon system. The backgrounds from fake vertices are estimated from data control regions, and are predicted to be two events or less for five different event topologies. Limits are set on a hidden valley scalar boson Z' and on stealth SUSY, with sensitivity to decay lengths between tens of centimeters and tens of meters; an example is given in Fig. 1.

There are also models that predict a long-lived particle that decays predominantly into light leptons, producing collimated jets of electrons, muons, or both. A search [6] requires two such lepton jets in the event, each of which is isolated from other tracks, and also separated from each other in the azimuthal angle. The observation is consistent with the expectation, and limits are placed on a dark photon model with a maximum sensitivity to decay lengths of several centimeters.

A search for a long-lived particle that decays to two opposite-sign, same-flavor leptons [7] suppresses the large contribution from Drell-Yan processes by placing cuts on the transverse impact parameter of the two leptons. The additional background is estimated with a data control region in which dilepton momentum is opposite the flight direction from the primary to the secondary vertex. Zero events are observed in the control region as well as in the signal region, and limits are set on a hidden valley model and on RPV SUSY. This search using inner-tracker tracks has recently been combined with a search that uses only muon tracks [8]; an example is given in Fig. 1.

ATLAS has performed searches for displaced vertices [9] within 30 cm of the beamspot in three dilepton channels and four multitrack channels. Vertices close to any detector material are vetoed in order to suppress the background from nuclear interactions. In all seven search channels, the main backgrounds originate from unrelated tracks or leptons that cross at a large angle to give a displaced vertex. In the multitrack channels, the vertex is required to have an invariant mass of at least 10 GeV and at least 5 tracks. The backgrounds are predicted to be less than one event, and no events are observed in any of the search channels. Limits are placed on split SUSY, RPV, and general GMSB.

A CMS search [10] motivated by a Displaced SUSY model selects events with an electron and a muon of opposite sign, each displaced, but not necessarily originating from a common

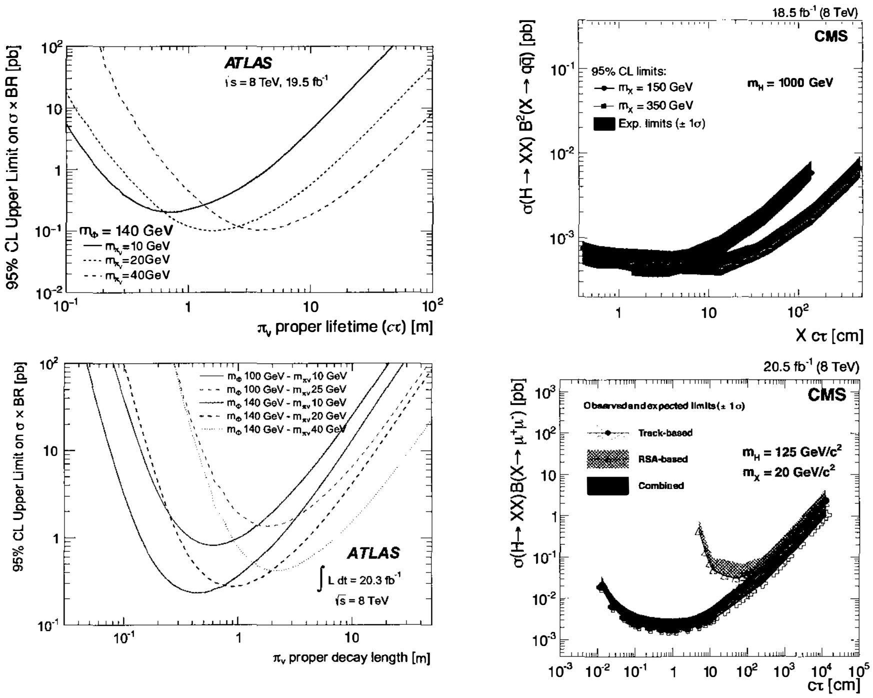

Figure 1 – Limits are placed on hidden valley models with a long-lived neutral particle, based on the signature of two jets from a common vertex (upper left [5] and upper right [3]), two trackless jets (lower left [4]), and two opposite-sign leptons from a common vertex (lower right [8]).

vertex. This search defines three exclusive signal regions based on the lepton transverse impact parameter, in the range of 0.2 mm to 2 cm. In the first region there are 19 observed events, and in the other two regions there are no observed events. These observations are consistent with the background predictions, and limits are placed on the stop lifetime and mass with a maximum sensitivity for a stop lifetime of about 2 cm.

If the long-lived particle decays to a photon it can be identified by the fact that the photon does not point back to the primary vertex and that it arrives late at the calorimeter. A search for displaced/delayed photons [11] exploits the pointing and timing resolution of the ATLAS detector's liquid argon calorimeter. The signal region is defined as two high-energy photons with large $E_{\mathrm{T}}^{\mathrm{miss}}$, and the search is performed in the two-dimensional plane of the longitudinal impact parameter and calorimeter arrival time. A low-$E_{\mathrm{T}}^{\mathrm{miss}}$control region is used to estimate the background. Limits are set on the GMSB model with a maximum sensitivity to lifetimes of about 2 ns.

3 Charged long-lived particles

If the long-lived particle is charged and has sufficiently low kinetic energy, it may come to rest in the detector. After some time, it may then decay. A CMS search for stopped particles [12] selects events with a calorimeter cluster that is asynchronous with the proton-proton collisions. The search sample corresponds to 281 hours of trigger livetime. The backgrounds in this search arise from processes that are uncorrelated with the proton-proton collisions, such as beam halo muons, cosmic rays, and HCAL noise. Ten events are observed, consistent with the expectation, and limits are placed on the gluino and stop masses for over 13 orders of magnitude. A similar search has been performed by ATLAS [13].

A long-lived charged particle can also be identified if it does not come to rest in the detector and escapes the detector, based on the fact that it is moving slowly. A search for such particles [14] identifies tracks with large ionization energy loss dE/dx in the pixel tracker or late timing measurements in the calorimeter or the muon system. Based on these measurements, the mass of the particle is reconstructed, which for signal is much larger than for Standard Model particles. The main background is from muons that have mismeasured dE/dx or timing information, and it is estimated by sampling the relevant distributions from data control regions. No excess is observed over the expectations, and limits are set on GMSB sleptons, LeptoSUSY squarks and gluinos, charginos, and R-hadrons. A related search [15] measures dE/dx from multiple subsystems and places limits on particles with a charge between 2 and 6 times the charge of the electron. A search for metastable charged particles [16] uses dE/dx measurements from the ATLAS pixel tracker and places limits on R-hadrons with lifetimes between 1 and 10 ns, stable gluinos (see Fig. 2), and stable and metastable charginos. Searches for particles with anomalous dE/dx measurements have also been performed by CMS [17].

A search for charged long-lived particles is also performed using a disappearing track signature, that of a high-p_T isolated track with several missing hits in the outer layers of the tracker and little energy deposited in the calorimeters [18]. The backgrounds in this search are estimated with tag and probe methods, and arise from reconstruction failure modes: unidentified electrons or muons, tracks with mismeasured momenta, or fake tracks. Two events are observed, consistent with the expectations, and limits are placed on the chargino mass and lifetime, with maximum sensitivity to lifetimes of several nanoseconds, as shown in Fig. 2. A similar search has been performed by ATLAS [19].

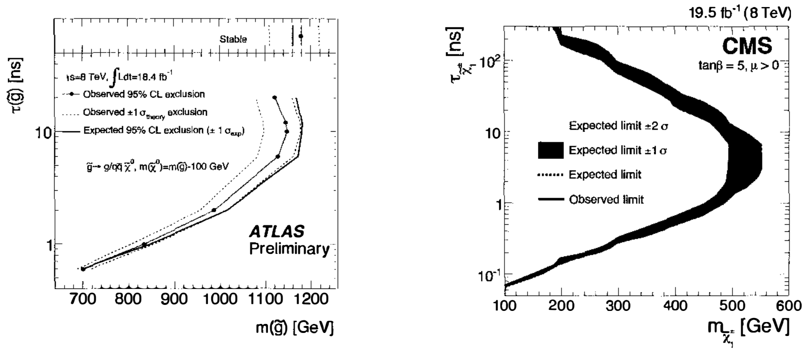

Figure 2 – Limits on charged metastable particles are placed using dE/dx information [16] (left) and by identifying disappearing tracks [18] (right).

4 R-parity violating prompt decays

A search for RPV SUSY in multijet final states [20] uses two strategies, a jet-counting analysis that looks for an excess of ≥ 6 or ≥ 7 jet events, with 0-2 b-jets, and an analysis based on the total jet mass, which is defined as the scalar sum of masses of the four leading large-radius jets, which would be formed from accidental substructure. The background is estimated from signal-depleted data control regions, in the jet-counting analysis by extrapolating with a scale factor from simulation, and in the total jet mass analysis by constructing the total jet mass from single jet mass templates. No excess above the prediction is observed, and limits are placed in the plane of gluino-neutralino masses.

Another RPV search[21] looks for a lepton flavor violating resonance of $e^{\pm}\mu^{\mp}$, $e^{\pm}\tau^{\mp}$, or $\mu^{\pm}\tau^{\mp}$. The search places lower limits on the τ-sneutrino mass between 1.7 - 2.0 TeV and on the Z' vector boson between 2.2 - 2.5 TeV, depending on the channel.

Finally, a search [22] is performed for pair-produced scalar tops that decay via an R-parity-violating coupling to a final state with two opposite-sign leptons of any flavor and 2 b-jets. The signal signature is two lepton-b-quark resonances with a similar mass. Limits are placed on the scalar top mass between 0.5 and 1 TeV in the framework of a $B-L$ extension of the Standard Model.

5 Reinterpretations

There are two new reinterpretations of searches that place constraints on long-lived particles. ATLAS reinterprets a prompt SUSY search for jets and $E_{\mathrm{T}}^{\mathrm{miss}}$and sets mass limits on gluinos with lifetimes of up to over a microsecond[23]. A CMS analysis[24] parameterizes the signal efficiencies of its searches for heavy stable charged particles, allowing a recasting in terms of the pMSSM and other models.

Acknowledgments

I thank the members of the ATLAS and CMS collaborations for producing the results presented in this talk, the CERN accelerator division for the excellent operation of the LHC, and the many funding agencies that support these experiments.

References

1. ATLAS Collaboration, "The ATLAS experiment at the CERN LHC", *JINST* **3**, S08003 (2008).
2. CMS Collaboration, "The CMS experiment at the CERN LHC", *JINST* **3**, S08004 (2008).
3. CMS Collaboration, "Search for long-lived neutral particles decaying to quark-antiquark pairs in proton-proton collisions at $\sqrt{s}=8$ TeV", *Phys. Rev.* D **91**, 012007 (2015).
4. ATLAS Collaboration, "Search for pair-produced long-lived neutral particles decaying in the ATLAS hadronic calorimeter in pp collisions at $\sqrt{s}=8$ TeV", *Phys. Lett.* B **743**, 15 (2015), arXiv:1501.04020.
5. ATLAS Collaboration, "Search for long-lived, weakly-interacting particles that decay to displaced hadronic jets in proton-proton collisions at $\sqrt{s}=8$ TeV with the ATLAS detector", arXiv:1504.03634.
6. ATLAS Collaboration, "Search for long-lived neutral particles decaying into lepton jets in proton-proton collisions at $\sqrt{s}=8$ TeV with the ATLAS detector", *J. High Energy Physics* **11**, 88 (2014).
7. CMS Collaboration, "Search for long-lived particles that decay into final states containing two electrons or two muons in proton-proton collisions at $\sqrt{s}=8$ TeV", *Phys. Rev.* D **91**, 052012 (2015), arXiv:1411.6977.
8. CMS Collaboration, "Search for long-lived particles that decay into final states containing two muons, reconstructed using only the CMS muon chambers", CMS-PAS-EXO-14-012.
9. ATLAS Collaboration, "Search for massive, long-lived particles using multitrack displaced vertices or displaced lepton pairs in pp collisions at $\sqrt{s}=8$ TeV with the ATLAS detector", arXiv:1504.05162.
10. CMS Collaboration, "Search for displaced supersymmetry in events with an electron and a muon with large impact parameters", *Phys. Rev. Lett.* **114**, 061801 (2015).

11. ATLAS Collaboration, "Search for nonpointing and delayed photons in the diphoton and missing transverse momentum final state in 8 TeV pp collisions at the LHC using the ATLAS detector", *Phys. Rev.* D **90**, 112005 (2014).
12. CMS Collaboration, "Search for decays of stopped long-lived particles produced in proton-proton collisions at $\sqrt{s} = 8$ TeV", *Eur. Phys. J. C* **75**, 151 (2015), arXiv:1501.05603.
13. ATLAS Collaboration, "Search for long-lived stopped R-hadrons decaying out of time with pp collisions using the ATLAS detector", *Phys. Rev.* D **88**, 112003 (2013).
14. ATLAS Collaboration, "Searches for heavy long-lived charged particles with the ATLAS detector in proton-proton collisions at $\sqrt{s} = 8$ TeV", *J. High Energy Physics* **01**, 068 (2015).
15. ATLAS Collaboration, "Search for heavy long-lived multi-charged particles in pp collisions at $\sqrt{s} = 8$ TeV using the ATLAS detector", arXiv:1504.04188.
16. ATLAS Collaboration, "Search for metastable heavy charged particles with large ionisation energy loss in pp collisions at $\sqrt{s} = 8$ TeV using the ATLAS experiment", ATLAS-CONF-2015-013.
17. CMS Collaboration, "Searches for long-lived charged particles in pp collisions at $\sqrt{s} = 7$ and 8 TeV", *J. High Energy Physics* **7**, 122 (2013), arXiv:1305.0491.
18. CMS Collaboration, "Search for disappearing tracks in proton-proton collisions at $\sqrt{s} =$ 8 TeV", *J. High Energy Physics* **01**, 096 (2015), arXiv:1411.6006.
19. ATLAS Collaboration, "Search for charginos nearly mass degenerate with the lightest neutralino based on a disappearing-track signature in pp collisions at $\sqrt{s} = 8$ TeV with the ATLAS detector", *Phys. Rev.* D **88**, 112006 (2013).
20. ATLAS Collaboration, "Search for massive supersymmetric particles decaying to many jets using the ATLAS detector in pp collisions at $\sqrt{s} = 8$ TeV", arXiv:1502.05686.
21. ATLAS Collaboration, "Search for a heavy neutral particle decaying to $e\mu$, $e\tau$, or $\mu\tau$ in pp collisions at $\sqrt{s} = 8$ TeV with the ATLAS detector", arXiv:1503.04430.
22. ATLAS Collaboration, "A search for $B - L$ R-Parity violating scalar top decays in $\sqrt{s} =$ 8 TeV pp collisions with the ATLAS experiment", ATLAS-CONF-2015-015.
23. ATLAS Collaboration, "Limits on metastable gluinos from ATLAS SUSY searches at $\sqrt{s}$ = 8 TeV", ATLAS-CONF-2014-037.
24. CMS Collaboration, "Constraints on the pMSSM, AMSB model and on other models from the search for long-lived charged particles in proton-proton collisions at $\sqrt{s} = 8$ TeV", arXiv:1502.02522.

Looking for supersymmetry: $\sim 1\,\mathrm{TeV}$ WIMP and the power of complementarity in LHC and dark matter searches

K. KOWALSKA, L. ROSZKOWSKI,[a] E.M. SESSOLO, S. TROJANOWSKI, A.J. WILLIAMS
BayesFITS Group, National Centre for Nuclear Research,
Hoża 69, 00-681 Warsaw, Poland

Some doubts have been expressed about low energy supersymmetry (SUSY) following the first run of the LHC. In this talk I will try to present a more upbeat view based on data, rather than theoretical expectations. In particular, I will make the following points: (a) in my opinion the most attractive candidate for dark matter (DM) is now the lightest neutralino with mass around 1 TeV and with well defined properties (a nearly pure higgsino); (b) this DM candidate will be nearly fully tested in forthcoming one-tonne DM underground search detectors; (c) the CMSSM will be nearly fully tested in the next few years by a combination of expected data from LHC experiments and from direct DM searches, as well as potentially also by the Cherenkov Telescope Array; (d) fine tuning, which is very large in simple models like the CMSSM, can be significantly reduced (even down to 1 in 20) with properly selected boundary conditions at the unification scale; (e) the $(g-2)_\mu$ anomaly can be accommodated not only in the context of the general MSSM but also of some unified SUSY models with some superpartners to be within reach of the LHC.

The outcome of the first run of the LHC has brought some sense of confusion and disappointment to the "new physics" community. Not even a remotely convincing hint of any signature of physics beyond the Standard Model (SM) emerged. In particular, direct limits on superpartner masses were pushed up significantly and, in the case of colored particles, reached and exceeded the ballpark of 1 TeV, except for the stops. Likewise, in flavor violating processes measured at the LHC and elsewhere SM predictions agree well with experimental data, again implying that any potential new physics contributions have to be suppressed, most likely by the large mass scale of new physics states. In particular, the measurements by LHCb and then also CMS of $\mathrm{BR}\,(\mathrm{B_s} \to \mu^+\mu^-)$, both agreeing with SM expectations suggest that the pseudoscalar Higgs boson is at or beyond 1 TeV, thus setting the scale for the heavy Higgs sector of the MSSM.

These negative results (from the point of view of new physics searches) were actually independently reinforced by emerging properties of the Higgs boson discovered by ATLAS and CMS. Its couplings to SM fermions and gauge bosons came out to be SM-like, thus suggesting that the other MSSM Higgs bosons are heavy, and decouple.

Of course, one can take the "I believe in what I can see" approach that the SM has been confirmed in light of the above and there is simply no new physics beyond the SM, at least up to the few TeV scale. I believe that it is too quick to jump to such conclusions. Firstly, the discovery of the Higgs boson is consistent not only with the SM but also with the frameworks that predict a SM-like Higgs boson, in particular with the MSSM. Secondly, apart from its many well known theoretical puzzles, the SM lacks explanations for big cosmological questions: dark

[a]Speaker. On leave of absence from the University of Sheffield.

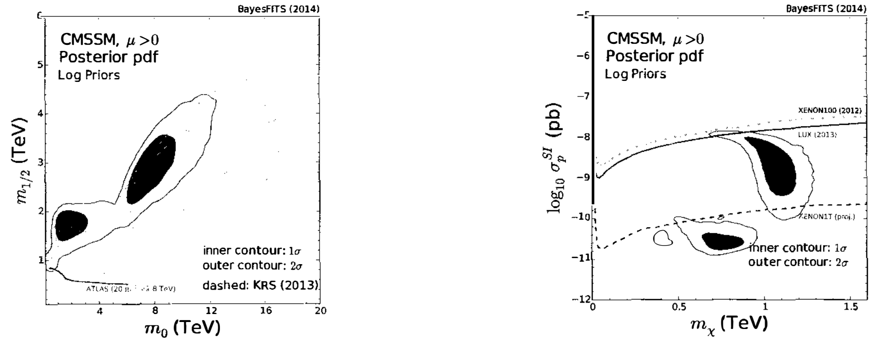

Figure 1: Left: Marginalized 2-dim. posterior pdf in the (m_0, $m_{1/2}$) plane of the CMSSM for $\mu > 0$, constrained by the experiments listed in Table 1 of Ref. [1]. The 68% credible regions are shown in dark blue, and the 95% credible regions in light blue. The solid red line shows the ATLAS combined 95% CL exclusion bound. Right: Marginalized 2D posterior pdf in the (m_χ,$\sigma_p^{\rm SI}$) plane for the CMSSM constrained by the experiments listed in Table 1 of Ref. [1]. The current LUX (solid red) and XENON100 (dash-dot gray) are also shown as well as projected 1-tonne (dash magenta) limits. Both figures are taken from Ref. [1].

matter, baryogenesis, cosmic inflation, etc. Thirdly, within the framework of low energy SUSY, the mass of the Higgs boson of around 125 GeV requires large radiative corrections from the stop sector at, or above, the 1 TeV scale. In SUSY in the context of GUTs, where soft SUSY breaking parameters are unified, this sets the scale for the SUSY breaking scale $M_{\rm SUSY}$ in the multi- TeV regime, again consistent with direct SUSY search limits and flavor processes.

An additional important, and robust, constraint on SUSY parameter space is provided by requiring that the relic density of the lightest neutralino assumed to be DM agrees with the experimentally determined value in the Universe. Since in constrained SUSY models this calculated quantity tends to be too large, it can be satisfied only in some specific regions of parameter space. The outcome is illustrated in the case of the CMSSM in the left panel of Fig. 1 (taken from Ref. [1], which is an update of Ref. [2]) where I present 1- and 2σ (credible) regions of Bayesian total posterior probability (pdf).[b] In the allowed bottom left corner, just above the red line marking the current strongest limit from ATLAS, one can recognize a "tiny" stau-coannihilation region (SC), which appears at only 2σ, followed, at larger m_0 and $m_{1/2}$, by an A-funnel (AF) region (1σ region occupying about 30% of total Bayesian probability). In both of them the neutralino is bino-like which in the pre-LHC era was considered to be the most attractive WIMP solution.

Finally, at multi-TeV m_0 and $m_{1/2}$ one can clearly see the largest (about 70%) high probability region which I will call a $\sim$ 1 TeV higgsino DM region (1TH) since in this region the lightest neutralino is higgsino-like and its mass is set by the μ-parameter and is close to 1 TeV in order to produce correct relic abundance. For comparison, in the left panel of Fig. 1 dotted lines show the previously favored regions based on the data available before 2013. [2]

The $\sim$ 1 TeV higgsino DM region is a new region relative to the pre-LHC studies of constrained SUSY models which explored much lower values of m_0 and $m_{1/2}$, up to some 4 TeV and 2 TeV, respectively, [3] although the existence of such a region in constrained SUSY was pointed out back in 2009, in the pre-LHC era, in the framework of the NUHM. [4] Remarkably, in this region the correct relic density is achieved simply by the μ-parameter being close to 1 TeV. No

[b]Due to space limitation in this writeup I only summarize some of our main results and cite only our relevant papers. I skip the description of the procedure and of the constraints adopted in deriving our numerical results. The reader is referred to our papers for a detailed presentation of our analysis and a list of references.

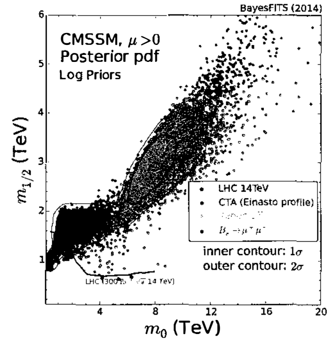

Figure 2: Complementarity of achivable experimental exploration of the CMSSM parameter space by LHC direct searches for SUSY (blue), BR $(B_s \to \mu^+\mu^-)$ (magenta), one tonne DM search detectors (orange) and CTA (green). The solid inner and outher contours show the respective 68% and 95% credible regions of the marginalized 2D posterior in the m_0 and $m_{1/2}$ plane of the CMSSM with $\mu > 0$. Taken from Ref. [1].

special mechanisms for reducing the relic density are required, unlike in the SC or AF regions. In this sense the 1TH region is most natural. All one needs is large enough bino, and wino, mass. In constrained models like the CMSSM this is achieved in regions of large enough $m_{1/2}$.

In the likelihood function that we used in our Bayesian analysis and numerical scans all relevant constraints were actually included – they are listed in Table 1 of Ref. [1] where also the numerical procedure used in performing our scans is described – but it is primarily the Higgs mass value and the DM relic abundance that determine the shape of the favored regions. Some role is also played by direct limits on superpartner masses (which we include in our likelihood function through an approximate but accurate procedure described in Ref. [2]) in setting a lower limit on $m_{1/2}$ (and thus reducing the importance of the SC region to the mere 2σ level) and by the updated measurements of BR $(B_s \to \mu^+\mu^-)$ in giving more "weight" to the AF region relative to a previous study[2] and by current upper limits on $\sigma_p^{\rm SI}$ in basically ruling out the mixed neutralino DM region, characteristic of the hyperbolic branch/focus point region.

The result shown in Fig. 1 for the case of the CMSSM is actually much more general. It applies both to unified, as well as phenomenological models, with gaugino masses taken above the higgsino mass of $\sim 1\,\mathrm{TeV}$.[5] In the right panel of Fig. 1 the favored regions shown in the left panel are mapped onto the $(m_\chi, \sigma_p^{\rm SI})$ plane. From left to right, we can see the "tiny" SC region (at 2σ only), followed by the AF region and, the largest 1TH DM region. For comparison we show also the current upper limits on $\sigma_p^{\rm SI}$ from LUX and Xenon100 which exclude the mixed neutralino DM region of HB/FP at a few hundred GeV.

The emerging picture looks to me highly encouraging. The most attractive $\sim 1\,\mathrm{TeV}$ higgsino DM region falls basically all within the reach of upcoming one tonne detectors, like Xenon-1T which is expected to produce new results by 2017 or so. This will provide the most robust way of exploring this region. This region should be independently probed within expected sensitivity reach of the forthcoming CTA due to start in 2018 or so, from observations of diffuse radiation, assuming 500 hours of observation time plus a steep enough DM density profile (close to the Einasto profile) towards the Galactic Center. (This being the case in simple constrained models, in phenomenological scenarios like the pMSSM there is, however, more freedom.[5])

This can be seen in Fig. 2 which also shows an impressive complementarity of DM search experiments (both direct and indirect in CTA) with LHC searches for signatures of SUSY. Both the SC and the AF regions will be probably beyond the reach of one tonne DM detectors but are expected to be accessible to the LHC14. The first of them will hopefully be explored by direct detection searches for SUSY. In the AF region, on the other hand, the superpartners are too heavy to be detected at the LHC. Fortunately, a precise enough, but achievable (at the level of $5-7\%$ of both experimental and theory error) determination of BR $(B_s \to \mu^+\mu^-)$, if it comes out to be consistent with SM predictions, would rule out most of the AF region.

I will now briefly comment on two additional issues. The first is about so-called fine-tuning (FT) and is linked to "naturalness". At $M_{\rm SUSY} \gtrsim 1\,{\rm TeV}$ FT is expected to be significant and indeed in the CMSSM it is now very large, even in excess of 1 in 3000. However, by making a suitable choice of mass relations at the GUT scale among soft parameters and also by linking μ to m_0 one can reduce FT in unified SUSY down to even 1 in 20.[6]

The final point is about the $(g-2)_\mu$ anomaly which suggests that the measured value of $(g-2)_\mu$ is over 3σ above SM estimates. Explaining it in terms of SUSY would require low enough smuon and (at least one) neutralino and/or muon sneutrino and (at least one) chargino masses. It is therefore no surprise that one fails to reproduce $\delta\,(g-2)_\mu$ in simple constrained SUSY models where slepton are unified with squarks, while in the general MSSM this can be easily done. Hence there is "common wisdom" that constrained SUSY is incompatible with the $(g-2)_\mu$ anomaly. However, this is not quite true. One way is to simply disunify sleptons and squarks, another, less known, is to disunify gauginos. Some such possible constrained SUSY models with relaxed boundary conditions at the GUT scale have been shown to reproduce $\delta\,(g-2)_\mu$ with the bonus that some light enough states must appear there and be for the most part accessible to LHC14. In other words, if the $(g-2)_\mu$ anomaly is real then either some light SUSY states will be seen at the LHC or those models will be ruled out.[7]

In conclusion, I've pointed out some distinct and well motivated phenomenological scenarios that can be put to a definitive experimental test at the LHC and in DM searches. While waiting for new data, and remaining open to surprises, I believe we have good reasons to remain optimistic. Long ago, before the LHC era began, I formulated the conjecture: "Low energy SUSY cannot be experimentally ruled out. It can only be discovered. Or else abandoned." Indeed, while some specific SUSY models could in principle be excluded, I could not think of any experimental measurement that can be made in currently available facilities that could rule out low energy SUSY as a framework. We should be able to know which way our field will go hopefully within the next few years.

References

1. L. Roszkowski, E. M. Sessolo and A. J. Williams, JHEP **1408**, 067 (2014) [arXiv:1405.4289 [hep-ph]].
2. K. Kowalska, L. Roszkowski and E. M. Sessolo, JHEP **1306**, 078 (2013) [arXiv:1302.5956 [hep-ph]].
3. A. Fowlie, M. Kazana, K. Kowalska, S. Munir, L. Roszkowski, E. M. Sessolo, S. Trojanowski and Y. L. S. Tsai, Phys. Rev. D **86**, 075010 (2012) [arXiv:1206.0264 [hep-ph]].
4. L. Roszkowski, R. Ruiz de Austri, R. Trotta, Y. L. S. Tsai and T. A. Varley, Phys. Rev. D **83**, no. 1, 015014 (2011) [Phys. Rev. D **83**, no. 3, 039901 (2011)] [arXiv:0903.1279 [hep-ph]].
5. L. Roszkowski, E. M. Sessolo and A. J. Williams, JHEP **1502**, 014 (2015) [arXiv:1411.5214 [hep-ph]].
6. K. Kowalska, L. Roszkowski, E. M. Sessolo and S. Trojanowski, JHEP **1404**, 166 (2014) [arXiv:1402.1328 [hep-ph]].
7. K. Kowalska, L. Roszkowski, E. M. Sessolo and A. J. Williams, JHEP **1506**, 020 (2015) [arXiv:1503.08219 [hep-ph]].

Searches for other non-SUSY new phenomena at the LHC

E. Kajomovitz
on behalf of the ATLAS and CMS Collaborations
Department of Physics, Duke University
Durham, NC 27708, USA

The ATLAS and CMS collaborations collected datasets of approximately 20 fb^{-1} of pp collisions at $\sqrt{s}$ = 8 TeV produced by the LHC during the Run-1 period. The collaborations performed a thorough analysis of these datasets searching for physics phenomena beyond the Standard Model. These conference proceedings summarize the results of a selection of searches targeting non-Supersymmetry phenomena.

1 Introduction

The substantial dataset of approximately 20 fb^{-1} of pp collisions at $\sqrt{s}$ = 8 TeV collected by the ATLAS [1] and CMS [2] collaborations during the Run-1 period of the LHC provided an unprecedented opportunity to search for phenomena beyond the Standard Model (SM). A thorough signature-driven search program targeting non-Supersymmetry extensions to the SM was executed by both collaborations. The collaborations used phenomenological models as benchmarks to optimize the event selection criteria and to interpret the data. These conference proceedings summarize the results of a selection of these searches, including searches for new massive resonances decaying to SM particles, searches for new phenomena in the angular distributions of dijet events, searches for vector-like partners of the third generation quarks, and searches for heavy neutrinos.

2 Searches for heavy resonances

Several extensions to the SM predict the existence of new resonances with masses at the TeV scale, for example, models with an extended gauge sector, models with warped extra dimensions, models with excited quarks, and compositeness models.

The CMS Collaboration searched for new phenomena in the invariant mass distribution of dijet events [3]. In this search, jets were constructed with the "wide-jet" technique that aims to include the complete radiation pattern of gluons by seeding the jet building with narrow jets and including objects within a distance of $\Delta R = \sqrt{\Delta\eta^2 + \Delta\phi^2} < 1$ of the narrow jet seeds, where η is the pseudo-rapidity, and ϕ is the azimuthal angle. To improve the sensitivity of the search to signals decaying to final states including bottom quarks, the selected events were classified according to their b-tag multiplicity. The background of this search was estimated using an empirical parametric model that assumes a smoothly and steeply falling dijet mass distribution for background events. The search was sensitive not only to new narrow resonances, but also to wide resonances and quantum blackholes. No significant discrepancies with respect to the SM background were observed and exclusion limits were set in the context of specific models, excluding string resonances with masses below 5.0 TeV; excited quarks below 3.5 TeV; scalar diquarks below 4.7 TeV; W' bosons below 1.9 TeV or between 2.0 and 2.2 TeV; Z' bosons below 1.7 TeV; Randall-Sundrum gravitons [4,5] below 1.6 TeV; excited bottom quarks, with masses below 1.2 or 1.6 TeV depending on their decay properties; axigluons and colorons with masses below 3.6 TeV; color-octet scalars with a mass below 2.5 TeV, and lower bounds between 5.0 and 6.3 TeV are set on the masses quantum black holes depending on the fundamental Planck scale and the number of extra dimensions of the quantum black hole production model.

CMS also searched for new physics in the dilepton mass spectra with $\mu\mu$ and ee final states [6]. The search was sensitive to resonant and non-resonant new phenomena. The resonant analysis used an unbinned maximum likelihood analysis, while the non-resonant analysis used cut-and-count approach. The dominant background to this search was Drell-Yan Z/γ production. The backgrounds were estimated using Next to Leading Order (NLO) simulation to determine the shape of the spectrum, and a data Control Region (CR) to determine the overall normalization. No significant deviations with respect to the SM were observed and exclusion limits were set on Sequential Standard Model Z' resonances lighter than 2.9 TeV, a superstring-inspired Z' lighter than 2.57 TeV, and Randall-Sundrum Kaluza-Klein gravitons with masses below 2.7, 2.4, and 1.3 TeV for couplings of 0.10, 0.05, and 0.01, respectively. Within the non-resonant analysis lower limits were established on M_{S}, the scale characterizing the onset of quantum gravity, which range from 3.3 to 4.9 TeV when the number of additional spatial dimensions varies from 3 to 7, and lower limits on Λ, the energy scale parameter for a contact interaction within the left-left isoscalar model; for dimuons the limits were set at 12.0 (15.2) TeV for destructive (constructive) interference, and for dielectrons the limits were set at 13.5 (18.3) TeV for destructive (constructive) interference.

ATLAS searched for high mass resonances in the invariant mass spectra of $\tau\tau$ final states [7], motivated by the possibility of lepton-flavor dependent new phenomena. This search used both leptonically and hadronically decaying τ leptons. A kinematic variable based on the transverse mass of the reconstructed τ's and missing transverse momentum, $E_{\mathrm{T}}^{\mathrm{miss}}$, was used as a proxy to the actual invariant mass of the $\tau\tau$ system. A cut-and-count approach was followed where the cut values were optimized for different sought after signals. No significant discrepancies with respect to the SM were observed and limits on the inclusive production cross section times branching ratio of a new Z' decaying to $\tau\tau$ were set as a function of the Z' mass, excluding new Z' with SM couplings decaying to $\tau\tau$ with masses up to 2 TeV.

CMS and ATLAS also searched for new heavy resonances decaying to a vector boson and a Higgs boson. ATLAS searched for these resonances using the decay of the Higgs boson to bottom quarks and non-hadronic decays of the vector bosons [8] targeting resonance masses between 0.3 and 1.9 TeV. In this search the data were classified according to the lepton and b-tagging multiplicity in the selected events. CMS searched for these resonances focus in a higher resonance mass regime covering from 0.8 to 2.5 TeV, and used the decays of the Higgs boson to τ leptons in conjunction with the hadronic decay of a Z boson [9], or the decay of the Higgs boson to b quarks and the leptonic decay a W boson [10]. To reconstruct and select hadronically decaying Z bosons, CMS used large-R jets, groomed to discard jet components from pileup and underlying event interactions, their mass and jet sub-structure properties. For the reconstruction and selection of the hadronically decaying Higgs bosons CMS also used large-R groomed jets in conjunction with the b-tagging multiplicity of associated narrow jets, and to reconstruct and select Higgs bosons decaying to τ leptons both leptonic and hadronic τ lepton decay modes were used. No significant deviations with respect to the SM prediction were observed by any of the analyses, and the results of these searches were interpreted with the Heavy Vector Triplet [11] phenomenological model as a benchmark. Under this model, ATLAS and CMS excluded minimal composite Higgs models (model B) with new resonance masses up to 1.5 TeV.

3 Searches in the angular distributions of dijet events

The angular distribution of jets relative to the beam axis in events with high dijet invariant mass are sensitive to the presence of new forces interacting with quarks and to the existence internal structure for quarks. CMS [12] and ATLAS [13] searched for new physics in dijet angular distributions analyzing the distribution of $\chi = e^{|y_1 - y_2|}$, where y_i is the rapidity of the leading or sub-leading jet in the event in bins of dijet mass. Both collaborations compared the data to NLO SM model predictions including electroweak (EW) corrections and no significant deviations with respect to these predictions were observed. The results by ATLAS and CMS were interpreted as 95% CL lower limits on the scale of a new contact interaction between 8 and 12 TeV depending on the interaction model. CMS also interpreted the results as 95% CL lower limits on the scale of a virtual graviton exchange in the Arkani-Hamed-Dimopolous-Dvali (ADD) [14,15] model of extra dimensions between 6 and 8 TeV depending on the number of extra dimensions.

4 Searches for vector-like quarks

Several extensions to the SM introduce new fermion partners to the third generation quarks for which both chiralities transform in the same way under the SM gauge groups as a means to explain the lightness of the Higgs boson mass. These new states, commonly referred to as vector-like quarks (VLQ), could be produced at the LHC; light VLQs would be produced dominantly in pairs in strong interaction processes, while heavy VLQs would be produced singly in weak interaction processes. The decays products of the VLQs can involve top and bottom quarks, and Higgs and vector bosons, depending on the flavor, mass, and couplings of these new quarks.

ATLAS and CMS searched for VLQ in different final states. ATLAS used events with b-tagged jets, and two same sign leptons or three leptons [16]. The analysis defined eight different signal regions optimized according to the lepton multiplicity, number of b-tagged jets, $E_{\mathrm{T}}^{\mathrm{miss}}$, and the scalar sum of transverse momenta of the different objects reconstructed in the event. The signal regions were optimized for different VLQ signals, and were also sensitive to the presence of other non-VLQ new phenomena such as four-top production, chiral bottom quarks, and flavor changing Higgs couplings. CMS searched for VLQ partners of the bottom quark in events with at least three leptons [17]. In this analysis, the events were classified according to the lepton multiplicity and flavor, including τ leptons, b-tagging multiplicity, and kinematic quantities. ATLAS searched for VLQ partners of the b quark in events with an isolated lepton, large $E_{\mathrm{T}}^{\mathrm{miss}}$, and at least one b-tagged jet [18]. The analysis targeted the decay of the new VLQ to a top quark and a W boson using multivariate analysis methods, but had sensitivity to other VLQ signatures. CMS searched for VLQ partners of the top quarks decaying to a top quark and a Higgs boson in the fully hadronic channel [19]. In this analysis, boosted decays of the top quark and the Higgs boson were reconstructed and tagged using large-R jets, b-tagging and jet sub-structure information, and the analysis proceeded using a likelihood constructed from the mass of the Higgs boson candidate and a kinematic variable that characterized the hadronic activity in the event. No significant deviations with respect to the SM predictions were observed by ATLAS or CMS and both collaborations set lower limits on the mass of VLQ and their couplings to the Higgs, and vector bosons.

5 Searches for heavy neutrinos

The observation of neutrino oscillations has provided evidence that neutrinos have masses. The "seesaw" mechanism can explain the smallness of the SM neutrino masses. In the simplest "seesaw" model, the mass of the SM neutrinos is given by $m_\nu \sim y_\nu^2 v^2 / m_N$, where y_ν is a Yukawa coupling between the SM neutrino and the Higgs field, v is the Higgs vacuum expectation value, and m_N is the mass of a new heavy neutrino state, N. In this model, N is a Majorana particle, and hence processes that violate lepton number are possible. At the LHC, these heavy neutrino states, N, could be produced through the charged weak interaction together with a charged lepton, and decay to a W and a lepton.

CMS and ATLAS searched for heavy neutrinos in events with leptons and jets. The CMS search used events with two same sign muons and jets [20]. In this search, the hadronic decay mode of the W resulting from the N decay was chosen to increase the signal selection efficiency. No significant deviation with respect to the SM expectation was observed, and heavy Majorana neutrinos with masses between 40 and 500 GeV were excluded depending on their coupling with the μ lepton. ATLAS searched for heavy neutrinos in events with two same sign leptons and two jets [21]. In this search, no significant deviation from the SM expectation was observed, and exclusion limits on heavy neutrinos between 100 and 500 GeV were set depending on the coupling between the heavy neutrino and the SM charged leptons.

6 Summary

These proceedings presented a selection of signature driven searches for physics beyond the SM performed with approximately 20 fb^{-1} of *pp* collisions at $\sqrt{s}$ = 8 TeV, collected during the Run-1 period of the LHC, by ATLAS and CMS collaborations. In the searches presented no significant deviations with respect to the SM expectation were observed, and exclusion limits were set on different benchmark models.

References

1. ATLAS Collaboration, *JINST* **3**, S08003 (2008).
2. CMS Collaboration, *JINST* **3**, S08003 (2008).
3. CMS Collaboration, *Phys. Rev.* D **91**, 052009 (2015).
4. L. Randall and R. Sundrum, *Phys. Rev. Lett.* **83**, 3370 (1999).
5. T. Han, J. Lykken, and R. Zhang, *Phys. Rev.* D **59**, 105006 (1999).
6. CMS Collaboration, *JHEP* **04**, 025 (2015).
7. ATLAS Collaboration, submitted to *JHEP* , arXiv:1502.07177 (2015).
8. ATLAS Collaboration, submitted to *Eur. Phys. J.* C , arXiv:1503.08089 (2015).
9. CMS Collaboration, submitted to *Phys. Lett.* B , arXiv:1502.04994 (2015).
10. CMS Collaboration, CMS-PAS-EXO-14-010
11. D. Pappadopulo, A.Thamm, R. Torre, A. Wulzer, *JHEP* **09**, 060 (2014).
12. CMS Collaboration, accepted by *Phys. Lett.* B , arXiv:1411.2646 (2014).
13. ATLAS Collaboration, accepted by *Phys. Rev. Lett.* , arXiv:1504.00357 (2015).
14. N. Arkani-Hamed, S. Dimopoulos, and G. Dvali, *Phys. Rev.* D **59**, 086004 (1999).
15. N. Arkani-Hamed, S. Dimopoulos, and G. Dvali, *Phys. Lett.* B **429**, 263 (1998).
16. ATLAS Collaboration, submitted to *JHEP* , arXiv:1504.04605 (2015).
17. CMS Collaboration, CMS-PAS-B2G-13-003
18. ATLAS Collaboration, submitted to *Phys. Rev.* D , arXiv:1503.05425 (2015).
19. CMS Collaboration, submitted to *JHEP* , arXiv:1503.01952 (2015).
20. CMS Collaboration, submitted to *Phys. Lett.* B , arXiv:1501.05566 (2015).
21. ATLAS Collaboration, to be submitted to *JHEP*, CERN-PH-EP-2015-070 (2015).

Electroweak baryogenesis in a scale invariant model and Higgs phenomenology

Kaori Fuyuto[1] and Eibun Senaha[1,2 a]

[1]*Department of Physics, Nagoya University, Nagoya 464-8602, Japan,*
[2]*Department of Physics and Center for Mathematics and Theoretical Physics, National Central University, Taoyuan, 32001, Taiwan*

We study the electroweak phase transition and the critical bubble in the scale-invariant two Higgs doublet model taking the recent LHC data into account. The sphaleron energy in this model is evaluated for the first time. It is found that the strong first-order electroweak phase transition is the inevitable consequence to be consistent with the observed 125 GeV Higgs boson. In such a case, the signal strength of the Higgs decay to two gammas and the triple Higgs boson coupling could deviate from the SM values by -10% and $+82\%$, respectively.

1 Introduction

Establishment of the Higgs sector is one of the primary issues in particle physics. In 2012, a scalar boson was discovered at the Large Hadron Collider (LHC), and the mass of the particle has been determined with 0.2% accuracy, $m_H = 125.09 \pm 0.21$ (stat.) $\pm$ 0.11 (syst.) GeV [1]. Clarifying the properties of the particle is as important as its discovery since the discovered particle must have the important roles if it is really the Higgs boson, namely, the origins of the mass generation and the electroweak symmetry (EW) breaking. The experimental proof of the former is possible by measuring the Higgs boson couplings to the gauge bosons and the fermions precisely, and the LHC experiment is now accessing those couplings. The latter can be clarified by reconstructing the Higgs potential. In particular, the measurement of the triple Higgs boson coupling is enormously important since it can exist only after EW symmetry is broken. So far, we know much less about the Higgs potential.

The EW symmetry can be broken if a tachyonic mass arise, which applies in the standard model (SM). On the other hand, as pointed out by Coleman and Weinberg[2], quantum corrections could also induce the EW symmetry breaking in massless theories. One of the cosmological implications of such classical scale-invariant theories is that the EW phase transition (PT) is first order, which is needed for successful EW baryogenesis (BG)[3]. As explicitly demonsrated by Funakubo et al, the scale-invariant two Higgs doublet model (SI-2HDM) accommodates the strong first-order EWPT[4]. However, in their analysis the masses of the Higgs boson and the top quark were not fixed to their observed values since those particles were not discovered at that time.

In this talk, we update the previous analysis in the light of the LHC data, and briefly discuss the phenomenological consequences in connection with Higgs physics.[5]

[a]speaker

2 Model

The Higgs potential in the SI-2HDM is given by [6]

$$V_0 = \frac{\lambda_1}{2}(\Phi_1^\dagger\Phi_1)^2 + \frac{\lambda_2}{2}(\Phi_2^\dagger\Phi_2)^2 + \lambda_3(\Phi_1^\dagger\Phi_1)(\Phi_2^\dagger\Phi_2) + \lambda_4(\Phi_1^\dagger\Phi_2)(\Phi_2^\dagger\Phi_1) + \left[\frac{\lambda_5}{2}(\Phi_1^\dagger\Phi_2)^2 + \text{h.c.}\right], \quad (1)$$

where the mass terms are forbidden by the classical scale invariance, and Z_2 symmetry is imposed to avoid the Higgs-mediated flavor-changing neutral current processes at tree level. From the stationary conditions, one gets

$$\tan^2\beta = \left(\frac{v_2}{v_1}\right)^2 = \sqrt{\frac{\lambda_1}{\lambda_2}}, \quad \sqrt{\lambda_1\lambda_2} + \lambda_{345} = 0, \quad (2)$$

where $v_1 = v\cos\beta$ and $v_2 = v\sin\beta$ with $v \simeq 246$ GeV, and $\lambda_{345} = \lambda_3 + \lambda_4 + \lambda_5$. We analyze the radiative EW symmetry breaking along the flat direction using the Gildener-Weinberg method[7]. The tree-level effective potential is

$$V_0(\varphi_1, \varphi_2) = \frac{\lambda_1}{8}\varphi_1^4 + \frac{\lambda_2}{8}\varphi_2^4 + \frac{\lambda_{345}}{4}\varphi_1^2\varphi_2^2, \quad (3)$$

where $\varphi_{1,2}$ are the classical background fields. Eq. (2) indicates that the energy of the minimum of V_0 is zero. Furthermore, from Eq. (2), it follows that the determinant of the mass matrix of the CP-even Higgs bosons is zero. Therefore, the tree-level potential has the flat direction. The massless scalar is the consequence of the classical scale invariance. The Higgs boson mass is generated after the EW symmetry is broken. Explicitly, one finds

$$m_h^2 = \frac{1}{8\pi^2 v^4}\left[m_H^4 + m_A^4 + 2m_{H^\pm}^4 + 6m_W^4 + 3m_Z^4 - 12(m_t^4 + m_b^4)\right]. \quad (4)$$

Note that m_h^2 becomes negative if the heavy Higgs bosons (H, A, $H^\pm$) are absent.

3 Sphaleron and Critical bubble

In the EWBG mechanism, the baryon number (B) is created by expanding Higgs bubbles. B can survive after the EWPT if the sphaleron process in the broken phase is quenched. Here, as the sphaleron decoupling condition, we adopt $\Gamma_B^{(b)}(T) \simeq (\text{prefactor})e^{-E_{\text{sph}}(T)/T} < H(T)$, where $\Gamma_B^{(b)}$ denotes the sphaleron rate in the broken phase, which is exponentially suppressed by $E_{\text{sph}}(T)/T$, with $E_{\text{sph}}(T)$ being the sphaleron energy at a temperature T. $H(T)$ is the Hubble parameter at T. We parametrize the sphaleron energy as $E_{\text{sph}}(T) = 4\pi v(T)\mathcal{E}(T)/g_2$, where g_2 denotes the SU(2) gauge coupling constant. The sphaleron decoupling condition is then takes the form

$$\frac{v(T)}{T} > \frac{g_2}{4\pi\mathcal{E}(T)}\left[42.97 + \text{log corrections}\right] \equiv \zeta_{\text{sph}}(T). \quad (5)$$

The log corrections mainly come from the fluctuation determinants about the sphaleron configuration, which will be dropped in our numerical evaluation of ζ_{sph} since they are subleading. We evaluate v_C/T_C and $\zeta_{\text{sph}}(T_C)$ numerically, where T_C is a temperature at which the effective potential has two degenerate vacua, and v_C is the Higgs vacuum expectation value at T_C. (For a recent study on $\zeta_{\text{sph}}(T_C)$ in the SM with a real singlet scalar, see Ref. [8].)

If the supercooling is large, the use of the above criterion would not be appropriate. As is done in the previous study, we also estimate a nucleation temperature (T_N), which is defined by

$$\Gamma_N(T_N)/H^3(T_N) = H(T_N), \quad (6)$$

where Γ_N is the bubble nucleation rate per unit volume per unit time at T_N. It should be emphasized that it is impossible to convert the entire region into the broken phase by only one

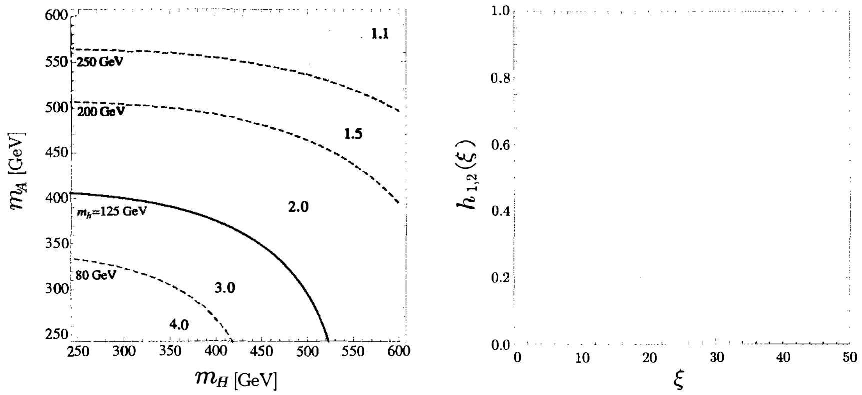

Figure 1 – (Left panel) Contours of m_h and v_C/T_C in the $(m_H,\ m_A)$ plane. The solid line in black represents $m_h = 125$ GeV. The each contour in white shows $v_C/T_C = 1.1$, 1.5, 2.0, 3.0 and 4.0 from top to bottom. (Right panel) The bubble wall profile at T_N.

bubble nucleated within the horizon volume. Therefore, the nucleation temperature defined by Eq. (6) should be thought as an upper bound of the temperature at which the EWPT developes.

In studying Eqs. (5) and (6), we use the following resummed effective potential

$$V_{\rm eff}(\varphi,T) = \sum_i n_i \left[\frac{\bar{M}_i^4(\varphi,T)}{64\pi^2}\left(\log\frac{\bar{M}_i^2(\varphi,T)}{\bar{\mu}^2} - c_i\right) + \frac{T^4}{2\pi^2} I_{B,F}\left(\frac{\bar{M}_i^2(\varphi,T)}{T^2}\right)\right], \tag{7}$$

with $I_{B,F}(a^2) = \int_0^\infty dx\ x^2 \log\left(1 \mp e^{-\sqrt{x^2+a^2}}\right)$, where $\bar{M}_i^2(\varphi,T)$ are the field-dependent boson masses with thermal corrections [5].

4 Results

In the left panel of Fig. 1, m_h and v_C/T_C are plotted in the (m_H, m_A) plane. As seen from Eq. (4), m_h goes up according as the heavy Higgs boson masses increase. The black solid line corresponds to $m_h = 125$ GeV. In other words, the 125 GeV Higgs predicts the scale of the heavy Higgs bosons. We overlay v_C/T_C denoted by the white contours. From top to bottom, $v_C/T_C = 1.1$, 1.5, 2.0, 3.0 and 4.0. It is concluded that the 125 GeV Higgs boson inevitably leads to the strong first-order EWPT in the SI-2HDM.

In the right panel of Fig. 1, the bubble wall profile at T_N is shown. Unlike the minimal supersymmetric SM case [9], the bubble wall width is thinner in the SI-2HDM.

As a benchmark, we take $m_H = m_A = m_{H^\pm} = 382$ GeV. Our findings are listed in Table 1. The sphaleron decoupling condition is satisfied at T_N. In this case, the signal strength of the Higgs boson decay to 2 gammas ($\mu_{\gamma\gamma}$) is reduced by 10% owing to the charged Higgs boson loop [10], and the deviation of the hhh coupling from the SM value ($\Delta\lambda_{hhh}$) is about +82%. The more detailed discussions on the phenomenology may be found in Refs. [11,12].

5 Summary

In this talk, the EWPT and the critical bubble in the SI-2HDM were revisited in the light of the LHC data. We also estimated the sphaleron decoupling condition in this model for the first time. To be consistent with 125 GeV Higgs boson, the EWPT is inevitably strongly first order. Some of phenomenological consequences of this model are $\mu_{\gamma\gamma} = 0.1$ and $\Delta\lambda_{hhh} = +82.1\%$.

Table 1: The results in our benchmark scenario ($m_H = m_A = m_{H^\pm} = 382$ GeV) are summarized . For the evaluation of the cutoff scale Λ, $\tan\beta = 1$ is chosen as a reference value.

v_C/T_C	211 GeV/91.5 GeV = 2.31
$\zeta_{\rm sph}(T_C)$	1.23
v_N/T_N	229 GeV/77.8 GeV = 2.94
$\zeta_{\rm sph}(T_N)$	1.20
$E_{\rm cb}(T_N)/T_N$	151.7
κ_V	1.0
κ_f	1.0
$\mu_{\gamma\gamma}$	0.90
$\Delta\lambda_{hhh}$	82.1%
Λ	6.3 TeV

Acknowledgments

E.S. thanks the organizers for their kind invitation and great hospitality at the workshop. E.S. is supported in part by the Ministry of Science and Technology of R. O. C. under Grant No. MOST 104-2811-M-008-011. The work of K.F. is supported by Research Fellowships of the Japan Society for the Promotion of Science for Young Scientists, No. 15J01079.

References

1. Georges Aad et al. Combined Measurement of the Higgs Boson Mass in *pp* Collisions at $\sqrt{s} = 7$ and 8 TeV with the ATLAS and CMS Experiments. 2015.
2. Sidney R. Coleman and Erick J. Weinberg. Radiative Corrections as the Origin of Spontaneous Symmetry Breaking. *Phys.Rev.*, D7:1888–1910, 1973.
3. V.A. Kuzmin, V.A. Rubakov, and M.E. Shaposhnikov. On the Anomalous Electroweak Baryon Number Nonconservation in the Early Universe. *Phys.Lett.*, B155:36, 1985.
4. Koichi Funakubo, Akira Kakuto, and Kazunori Takenaga. The Effective potential of electroweak theory with two massless Higgs doublets at finite temperature. *Prog.Theor.Phys.*, 91:341–352, 1994.
5. Kaori Fuyuto and Eibun Senaha. Sphaleron And Critical bubble in a scale invariant model : ReAnalysis. 2015.
6. Kenzo Inoue, Akira Kakuto, and Yoshimasa Nakano. Perturbation Constraint on Particle Masses in the Weinberg-Salam Model With Two Massless Higgs Doublets. *Prog.Theor.Phys.*, 63:234, 1980.
7. Eldad Gildener and Steven Weinberg. Symmetry Breaking and Scalar Bosons. *Phys.Rev.*, D13:3333, 1976.
8. Kaori Fuyuto and Eibun Senaha. Improved sphaleron decoupling condition and the Higgs coupling constants in the real singlet-extended standard model. *Phys.Rev.*, D90(1):015015, 2014.
9. Koichi Funakubo and Eibun Senaha. Electroweak phase transition, critical bubbles and sphaleron decoupling condition in the MSSM. *Phys.Rev.*, D79:115024, 2009.
10. Ilya F. Ginzburg, Maria Krawczyk, and Per Osland. Two Higgs doublet models with CP violation. 2002.
11. Christopher T. Hill. Is the Higgs Boson Associated with Coleman-Weinberg Dynamical Symmetry Breaking? *Phys.Rev.*, D89(7):073003, 2014.
12. G.C. Dorsch, S.J. Huber, K. Mimasu, and J.M. No. Echoes of the Electroweak Phase Transition: Discovering a second Higgs doublet through $A_0 \to ZH_0$. *Phys.Rev.Lett.*, 113(21):211802, 2014.

Searches for Dark Matter and Extra Dimensions at the LHC

Z. Demiragli for the CMS and ATLAS collaborations
Massachusetts Institute of Technology,
Department of Physics, 77 Massachusetts Ave
Cambridge, MA, United States

The CMS [1] and ATLAS [2] collaborations at the Large Hadron Collider have collected approximately 20fb^{-1} of pp collision data with center-of-mass energy of 8 TeV and have performed targeted searches for Dark Matter and Extra Dimensions. No significant deviations from the standard model prediction have been observed. A summary of the latest experimental results is presented here.

1 Introduction

Although, the Standard Model (SM) describes remarkably well everything we see in the laboratory experiments, it is not an entirely satisfactory theory to explain all that we see in nature. For example, the SM Higgs sector is highly unnatural. Higher-order corrections to the Higgs boson mass are proportional to an arbitrary cut-off scale and are referred to as quadratic divergences. If the cut-off scale is high, the corrections become large compared with the on-shell mass of the Higgs boson. This is often called the fine-tuning or hierarchy problem of the SM. Furthermore, results from many astrophysical observations strongly indicate the existence of a Dark Matter (DM) particle that does not interact via the strong or electromagnetic forces, and with a velocity not close to that of light. However, no such particle has been observed in the laboratory. In this conference proceedings, latest experimental results addressing the experimental signatures of the mentioned mysteries from the CMS and ATLAS experiments with approximately 20/fb of pp collision data collected with center-of-mass energy of 8 TeV are presented.

2 Searches for Dark Matter

At the Large Hadron Collider (LHC), one can search for DM particles that are pair produced in pp collisions. These studies are sensitive to low DM masses smaller than 10 GeV, and therefore provide information complementary to direct DM searches, which are more sensitive to larger DM masses. Since DM particles do not interact in the detector, the main signature of DM pair production at colliders is large missing transverse momentum (MET). Initial-state radiation (ISR) of jets, photons, Z, or W bosons, are used to tag DM pair production at colliders.

The interaction between the SM and the DM particles is mediated by a virtual particle mediator. If this mediator is heavier than the typical energy transfer at the LHC, an effective theory description is used to describe the process. If the mediator responsible for coupling of the SM and DM particles is light enough to be produced at the LHC, then a simplified theory description is used. The sensitivity of LHC searches tends to be independent of the mass of the DM particle and similar for spin independent and spin dependent couplings, which therefore provides an excellent complementarity to direct detection experiments.

2.1 *Dark Matter in Association with Mono jet/γ*

Both CMS and ATLAS experiments have performed a search for pair-produced dark matter association with an initial state radiated jet or photon using approximately 20/fb of $\sqrt{s}$ =8 TeV data. The events were accepted if there was a large energy jet/photon and also significant MET. To suppress various backgrounds, events with any additional hadronic or leptonic activity were vetoed. The number of observed events is found to be consistent with the standard model prediction. Limits are placed on the DM-nucleon scattering cross section using an effective theory description and on the the mass suppression scale ($M^* = M_{med}/\sqrt{g_q g_\chi}$) using a simplified theory description as shown in Fig. 1. Limits for other interaction forms can be found in the CMS and ATLAS publications[3 4 5 6].

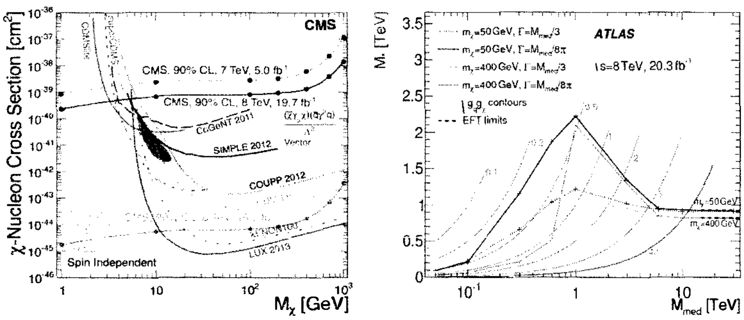

Figure 1 – CMS (left)[3] upper limits on the DM-nucleon cross section, at 90% CL, plotted against DM particle mass and compared with previously published results, and ATLAS (right)[4] observed limits on the mass suppression scale assuming vector interactions and a DM mass of 50 GeV and 400 GeV.

Apart from mono jet searches, events with at least two jets and no isolated leptons are also studied[7]. For such events, the razor variables are used to quantify the transverse balance of the jet momenta. The study is performed separately for events with and without jets originating from b quarks. The observed data yields are consistent with the expected background predictions, however the sensitivity was found to be comparable to a mono jet search.

2.2 *Dark Matter in Association with Mono Vector Boson*

For W boson radiation there is interference between the diagrams in which the W boson is radiated from the u quark or the d quark. In the case of equal coupling, the interference is destructive and gives a small W boson emission rate. If, however, the up-type and down-type couplings have opposite signs to give constructive interference, the relative rates of gluon, photon, W or Z boson emission can change dramatically, such that mono-W-boson production is the dominant process.

Both CMS and ATLAS collaborations also search for DM in association with a vector boson in leptonic[8] or hadronic final states[9]. The ATLAS collaboration searches for a hadronic large jet containing subjets consistent with a W or Z boson whereas CMS experiment uses transverse mass as search variable and considers leptonic state only. In both searches, the data are consistent with the standard model expectations. Limits are set on the mass scale in effective field theories that describe the interaction of DM and SM particles.

2.3 *Dark Matter in Association with Heavy Quark(s)*

For a scalar interaction between dark matter particles and gluons, the coupling strength is proportional to the mass of the quark. Therefore final states with bottom and top quarks are the most sensitive to these operators.

Both in CMS and ATLAS collaborations such final states [10 11 12 13] have been searched in final states containing large MET and high-momentum jets of which one or more are identified as jets containing b-quarks. Final states with top quarks are selected by requiring a high jet multiplicity and in some cases a single lepton. The data are found to be consistent with the SM expectations and limits are set on the mass scale of effective field theories that describe scalar and tensor interactions between DM and SM particles.

3 Searches for Extra Dimensions

Arkani-Hamed, Dimopolous, and Dvali (ADD) in 1998 proposed a model to solve the hierarchy problem of the SM with finite-sized extra dimensions in space beyond the three known dimensions. In this framework the SM particles are confined to 4-dimensional space-time where gravity is free to propagate into all extra dimensions which leads to the dilution of gravity. Furthermore, due to the compactness of the extra dimensions, Kaluza-Klein towers of excited graviton states occur which lead to enhanced cross section in signatures like diphotons.

3.1 High-mass Diphoton Resonances

Searching for high-mass diphoton resonances is an excellent way to observe the RS graviton, because of the larger branching ratio of the graviton decaying to photons and superior energy resolution of photons compared to the dijet case. ATLAS experiment has performed a search [14] looking for large mass diphoton resonances. The observed diphoton mass distribution is compared to the background prediction, and no significant excess of events over the background is found and exclusion limits are set on the cross section and the branching ratio as a function of graviton mass as shown in Fig. 2 .

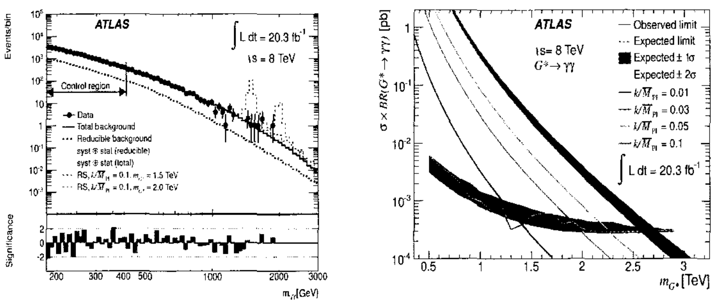

Figure 2 – Observed invariant mass distribution of diphoton events (left) and expected and observed upper limits on the cross section and the branching ratio as a function of graviton mass(right).

3.2 Resonant Top Quark Pair Production

Various extensions of the Randall-Sundrum model with extra dimensions predict Kaluza-Klein excitations of gluons or gravitons, both of which can have enhanced couplings to ttbar pairs. CMS has performed this search [15] in 5 different final states with various jet substructure techniques such as subjet b-tagging which led to 50% improvement in sensitivity. The ATLAS experiment performed a search [16] in semi leptonic final state in boosted and resolved categories. Results from both of the experiments are shown in Fig. 3

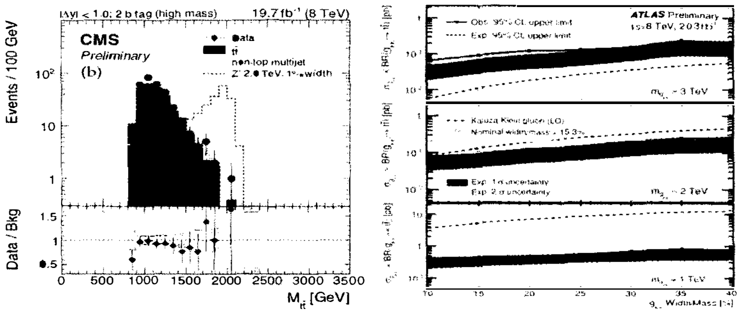

Figure 3 – Events from the CMS search (left) have two subjet b-tags. The uncertainty includes all the statistical and systematic uncertainties. The ratio of data/background is shown below. ATLAS (right) observed and expected upper limits on the cross-section times the branching ratio as a function of the width of KK gluon.

3.3 Lepton Flavor Violating Decays of Heavy Resonances

CMS has performed the first search [17] for quantum black holes decaying into the $e\mu$ final state. This is the search for heavy state with lepton flavor violation in interactions involving charged leptons. No evidence for physics beyond the SM is observed, exclusion limit are set ranging from 2.36 TeV to 3.63 TeV.

3.4 WW/WZ Resonances Decaying to a Lepton, Neutrino and Jet

ATLAS has performed a search for [18] narrow diboson resonances decaying to WW or WZ in the hadronic and leptonic final state using split filter substructure technique. And CMS has performed a similar search in the semi leptonic channel as well [19]. No evidence for resonant diboson production is observed, and resonance masses below 700 GeV are excluded at 95% confidence level for the spin-2 Randall-Sundrum bulk graviton.

References

1. CMS Collaboration, JINST **3**, S08004 (2008).
2. ATLAS Collaboration, JINST **3**, S08003 (2008).
3. CMS Collaboration, arXiv:1408.3583, submitted to EPJC.
4. ATLAS Collaboration, arxiv:1502.01518, submitted to EPJC.
5. CMS Collaboration, arXiv:1410.8812, submitted to PLB.
6. ATLAS Collaboration, PRD **91**, 012008 (2015).
7. CMS Collaboration, PAS EXO14-004.
8. CMS Collaboration, arXiv:1408.2745, submitted to Phys. Rev. D.
9. ATLAS Collaboration, PRL **112**, 041802 (2014)
10. CMS Collaboration, arXiv:1410.1149, submitted to Phys. Rev. Let.
11. ATLAS Collaboration, EPJC **75**, 79 (2015).
12. CMS Collaboration, arXiv:1504.03198, submitted to JHEP.
13. ATLAS Collaboration, EPJC **75**, 92 (2015)
14. ATLAS Collaboration, arXiv:1504.05511, submitted to Phys. Rev. D.
15. CMS Collaboration, CMS-PAS-B2G-13-008.
16. ATLAS Collaboration, ATLAS-CONF-2015-009.
17. CMS Collaboration, CMS-PAS-EXO-13-002.
18. ATLAS Collaboration, arXiv:1503.4677, submitted to EPJC.
19. CMS Collaboration, CMS-PAS-EXO-12-021.

MOVING BEYOND EFFECTIVE FIELD THEORY IN DARK MATTER SEARCHES AT COLLIDERS

GREG LANDSBERG
Department of Physics, Brown University, 182 Hope St, Providence, RI 02912, USA

In the past few years, the interest to collider searches for direct dark matter (DM) production has been growing exponentially. A variety of "Mono-X" signatures have been considered, where X stands for a probe particle recoiling against DM particles, which allows for the event to be triggerable. So far, the analysis of these signatures has been largely carried out in the framework of effective field theory (EFT), which allows for a comparison of the collider searches with searches in direct detection experiments. Unfortunately, as it has been recently pointed out by a number of authors, the EFT approach has severe limitations and may result in drastically underestimated or overestimated reach. I'll discuss these limitations and the new ideas in interpreting the collider searches for DM.

1 Introduction

Effective field theory (EFT) has been an important tool to study various processes where a detailed description of the interaction and its carrier is either unknown or model-dependent. The EFT is used to parameterize our ignorance of the fine details of the process and has been successfully applied to a number of cases, including Fermi's model of muon decay and searches for compositeness. It is therefore logical that the original theoretical papers [1,2,3] that proposed the initial-state radiation (ISR) tagging to detect dark matter production (DM) at colliders, relied on the EFT description of the scattering process in order to allow for a comparison of the sensitivity of these searches with that for direct detection (DD) experiments. A classical example of such a collider process is production of a single jet recoiling against a pair of DM particles that escape the detection, resulting in a spectacular "monojet" signature. Similar, "monophoton" signature is also possible in the case of a photon ISR.

Unfortunately, as has been realized recently, the use of EFT in this particular case is subject of a number of explicit and implicit assumptions, and important constraints, which severely limit the applicability of the EFT approach, sometimes to the point when it becomes all but useless. In this particular application, the EFT often fails in all three possible ways:

- As an "E" — not being effective in probing certain regions of parameter space;

- As an "F" — sometimes not even dealing with realistic fields; and
- As a "T" — not even holding as a viable theory.

The goal of these proceedings is to illustrate the limitations of the EFT approach and discuss more constructive ways of comparing the DM reach of collider experiments with that of the DD experiments, and potentially also with the reach of indirect detection experiments. Such a proper comparison would become particularly important if a significant excess in any of these experiments is seen.

2 EFT formalism and assumptions

Collider experiments are capable of setting limits on production cross section of DM particles in ISR-triggered processes, e.g. production of monojets[4,5]. These limits only require theoretical calculations, which properly describe the ISR process. While next-to-leading-order calculations are available for many such processes, often leading-order precision with an extra jet emission included in the matrix elements, suffices, making it relatively easy to calculate collider cross sections. The real issue comes when collider limits are being translated into limits on DM-nucleon scattering cross section, which is the variable used by DD experiments to represent their results. Note that fundamentally the process responsible for pair production of DM particles at colliders is the same as for the DM-nucleon scattering, or annihilation of a pair of DM particles used in indirect detection experiments. Assuming that the former process is mediated via an s-channel exchange of a certain particle, which we will refer to as the "mediator", the process is completely described by four parameters: the masses of the DM particle (m) and the mediator (M), and the two couplings of the mediator to quarks (g_q) and DM particles (g_χ), see Fig. 1 (left). (A similar diagram can be drawn to describe collider DM pair production via a t-channel exchange of a mediator, with the caveat that in this case the mediator must be a colored particle.) In order to compare the s-channel collider process with the t-channel DM-nucleon scattering, we "contract" the s-channel exchange in the EFT four-point interaction vertex, as shown in Fig. 1 (right), which then can be used to describe both. In order to perform this contraction we move from three fundamental parameters M, g_q, and g_χ to a single parameter Λ, the EFT cutoff, thus losing the full information about the underlying process, which is an inherent feature of the EFT approach.

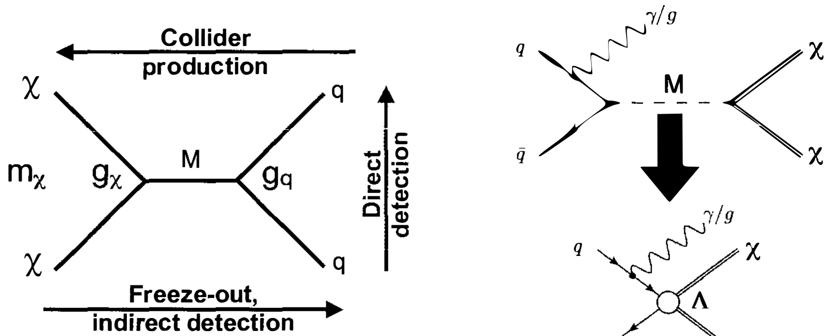

Figure 1 – Left: Feynman diagram of dark matter interaction with quarks via exchange of a mediator. Right: "contraction" of the s-channel mediator exchange diagram for the monojet or monophoton production into an EFT four-point interaction.

One can now directly equate the amplitude squared of the s-channel exchange in the limit of a heavy mediator ($M^2 \gg q^2$ in the event) with the one from the effective four-point interaction, which for, e.g. a mediator with scalar couplings, yields:

$$\left|\frac{ig_q g_\chi}{q^2 - M^2}(\bar{q}q)(\bar{\chi}\chi)\right|^2 \approx \left|\frac{-ig_q g_\chi}{M^2}(\bar{q}q)(\bar{\chi}\chi)\right|^2 = \left|\frac{1}{\Lambda^2}(\bar{q}q)(\bar{\chi}\chi)\right|^2,$$

leading to a crucial expression: $\frac{1}{\Lambda^2} = \frac{g_q g_\chi}{M^2}$.

The EFT approach is strictly valid for $q^2 \ll M^2$, which implies (from the kinematics of the s-channel exchange) $M^2 > (2m)^2$. Furthermore, in order for theory to be calculable, each of the two mediator couplings has to be less than $\sqrt{4\pi}$. Combining these two inequalities with the expression for Λ, we obtain: $2m < M < \Lambda\sqrt{g_q g_\chi} < 4\pi\Lambda$, or $\Lambda > \frac{m}{2\pi}$, which leads to an important conclusion that the validity region of the EFT grows when one deals with light DM. Similar validity regions in case of non-scalar couplings can be found, e.g. in Ref. [7] The case of light DM is particularly important for colliders as the sensitivity of DD experiments to light DM is reduced due to low-momentum recoil, and since for very light DM ($m < 10$ GeV), the DD experiments will soon reach the solar neutrino floor. Nevertheless, it's important to keep in mind that the above inequality really corresponds to the case when all the EFT assumptions break down spectacularly, and actual validity region really corresponds to $\Lambda \gg \frac{m}{2\pi}$.

The most tricky scenario is the case of a light mediator, for which EFT certainly fails. This case was explicitly studied in one of the early phenomenological papers on collider searches [8], with an explicit use of the s-channel exchange diagram instead of the EFT approach. In this case, collider searches offer an increased sensitivity to the DM production as they can produce light mediator on-shell, and hence the production cross section receives a resonant enhancement. However, the problem with the approach taken in Ref. [8] is that it treats the mediator width as a free parameter, whereas one can't do this, as the width of the mediator depends on the $3\sum_q g_q^2 + g_\chi^2 + ...$, and if even one of the couplings approaches the $\sqrt{4\pi}$ limit, the width becomes comparable to the mass of the mediator, independent on how small the other coupling is. Since a single-resonance exchange description stops being physically reasonable for mediators that broad, this seemingly correct approach can still give incorrect comparison with the DD experiments [9].

3 Beyond the EFT

Given this situation, it is clear that EFT, while a convenient way to simplify the problem, has too many hidden caveats and simply does not allow for a fair comparison between the collider and DD experiments. The key to the proper comparison is to treat the problem as fundamentally four-dimensional and represent the reach of both the DD and collider experiments in various planes given by a pair of these parameters (e.g., M and m), with the other two (in this case g_q and g_χ) being fixed to certain values, which can be scanned. In order to do this, one could use simplified models of DM, which assume certain type of couplings of the mediator to quarks and DM particles, e.g., vector or axial vector. Given that the number of such models is quite limited, one could rather easily span the relevant DM model space with just a handful of simplified models with s-channel or t-channel mediator exchange. Similar simplified model approach is successfully and broadly used in supersymmetry searches at the LHC. This is the approach advocated in the recent work [6,10] coming from the two groups of experimentalists and theorists (the first one generally affiliated with the CMS experiment, whereas the second one – with ATLAS). Both ATLAS and CMS are now transitioning to this approach to be used in the LHC Run 2.

Figure 2 (left) shows how the limits set using a simplified model with axial-vector couplings of the mediator to both DM particles and quarks compare with the limits from the EFT approach based on the CMS monojet analysis [4], as well as with the limit from the LUX experiment [11] in the canonical plane of DM-nucleon scattering cross section vs. the DM particle mass. While for relatively large couplings $g_q = g_\chi = 1.45$ the EFT results are close to those from the simplified model calculations up to DM particle mass of about 300 GeV, for smaller values of couplings the EFT grossly underestimates the LHC reach for light DM and grossly overestimates it for relatively heavy DM. Figure 2 (right) shows the projection of the CMS monojet analysis for LHC Run 2 and High-Luminosity LHC, as well as projected sensitivity of the next generation of DD experiments, in the more relevant plane of M vs. m, for the case of axial-vector mediator couplings. One can see a nice complementarity between the reach of the two types of experiments, with LHC winning over DD experiments for the case of small couplings and relatively heavy mediators and in the case of very light DM particles (with the mass less than about 5 GeV), while DD experiments offering higher reach for rather heavy DM with the mass above 200-400 GeV. Similar comparison is possible with indirect detection experiments.

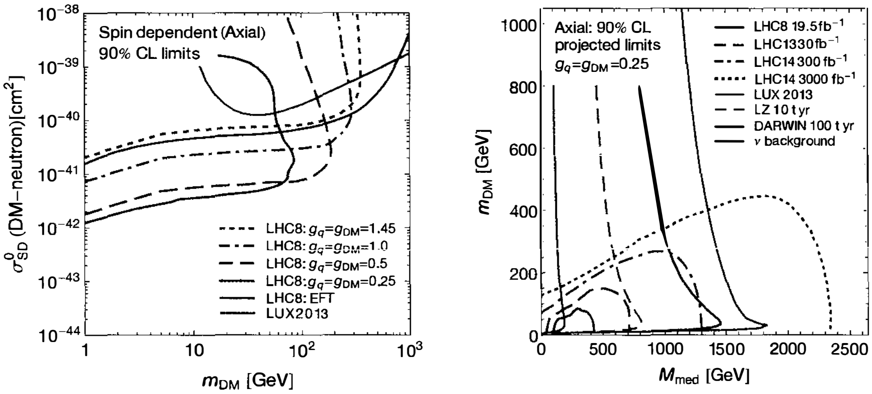

Figure 2 – Left: comparison of the EFT-based and simplified model limits on the DM-neutron scattering. Right: Comparison of the projected reach of the LHC and next generation of DD experiments. From Ref. [6]

To conclude, the simplified model approach allows for a fair comparison of the DM reach of different types of experiments and provides a more clear and advantageous way to present the results of future collider searches.

Acknowledgments

This work is partially supported by the DOE Award No. DE-SC0010010-003376. The author is grateful to the Imperial College, London CMS group for organizing and supporting the brainstorming workshop on dark matter at colliders, which sparkled this work and Ref. [6]

References

1. M. Beltran *et al.*, JHEP **09** (2010) 037; arXiv:1002.4137.
2. J. Goodman *et al.*, Phys. Lett. B **695** (2011) 185, arXiv:1005.1286.
3. Y. Bai, P.J. Fox, and R. Harnik, JHEP **12** (2010) 048, arXiv:1005.3797.
4. CMS Collaboration, arXiv:1408.3583.
5. ATLAS Collaboration, arXiv:1502.01518.
6. S. Malik *et al.*, Phys. Dark Universe **03** (2015) 003, arXiv:1409.4075.
7. N. Zhou, D. Berge, and D. Whiteson, Phys. Rev. D **87** (2013) 095013, arXiv:1302.3619.
8. P.J. Fox *et al.*, Phys. Rev. D **85** (2012) 056011, arXiv:1109.4398.
9. O. Buchmueller, M. J. Dolan and C. McCabe, JHEP **01** (2014) 025, arXiv:1308.6799.
10. J. Abdallah *et al.*, arXiv:1409.2893.
11. LUX Collaboration, Phys. Rev. Lett. **112** (2014) 091303, arXiv:1310.8214.

6.
Electroweak
Structure functions
Light quark

Inclusive W, Z and W/Z+jets production at the LHC

Sabine Lammers
Department of Physics, Indiana University,
727 E Third Street, Bloomington, IN. 47401

A review of recent W, Z and W/Z+jets (including heavy flavor) production measurements at the ATLAS and CMS experiments is given.

1 Introduction

Run I of the LHC has been extremely productive for improved understanding of EW and QCD physics. The measurements presented here are only a very small subset of the Run I results from the ATLAS [1] and CMS [2] experiments, but indicate the new level of kinematic reach as well as the high level of precision these types of measurements have achieved.

2 Inclusive W and Z production

Inclusive measurements of W and Z production are important tests of the EW and QCD theories. Direct measurements of W and Z properties at high precision can be compared with predictions calculated to NNLO in the strong coupling constant [3,4]. Moreover, these measurements are important input to searches with W and Z backgrounds. The measurements of boson transverse energy [5,7] is sensitive to the p_T distribution of partons in the proton and initial state gluon radiation, and is, as such, a sensitive test of QCD.

ATLAS has recently measured the transverse energy of the Z boson to high precision [7]. Z bosons are selected in data in a region where the reducible backgrounds can be minimized. Remaining irreducible backgrounds are less than 1% of the entire data sample, and are comprised of taus, W, diboson, $t\bar{t}$ and multijet events. These backgrounds are simulated with Monte Carlo, apart from multijet, which is simulated using a data-driven technique. The backgrounds are subtracted, and the data are unfolded to particle level in three rapidity regions and using three different definitions of the final state kinematics: Born, bare and dressed.

The Born-level results are compared to a variety of theory predictions. The comparison to a calculation with resummed multiple and collinear gluon emissions as implemented in Resbos is shown in Figure 1. CT10 PDFs are used for the theory predictions, and the theory uncertainties are dominated by PDF and scale uncertainties. The uncertainty on the data is significantly smaller than the theory uncertainties, and less than 1% throughout most of the p_T region measured. The breakdown of the experimental uncertainties for $Z \to e^+e^-$ results is shown in Figure 1. Taking account all the sources of theoretical uncertainty, the data is marginally in agreement with Resbos predictions. The precision of the data should be useful in constraining future theoretical development. Measurements of the transverse energy of the W boson are performed using a similar

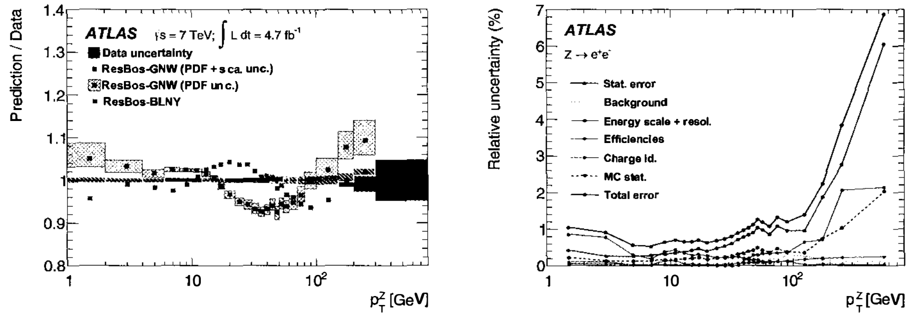

Figure 1 – Left: ratio of the predicted and measured Z-boson transverse momentum; right: breakdown of the experimental uncertainties on the Zp_T in the electron decay channel.

approach. A much larger multijet background makes this measurement more challenging, and the current experimental uncertainties on the W p_T cross section vary from 3-25% [9].

3 W/Z production in association with jets

Measurements of W and Z bosons in association with jets are important processes for studying perturbative QCD, and are used to validate the main backgrounds to many other Standard Model measurements and beyond the Standard Model (BSM) searches. The Run I dataset has allowed for measurements of up to 7 associated jets [8,10], including heavy flavor production [12,13]. ATLAS has published an extensive set of measurements of W+jets, confronting the data with NLO fixed-order QCD calculations, resummed calculations and matched matrix element + parton shower programs (MEPS) using data collected at $\sqrt{s}$ = 7 TeV. These measurements examine jet transverse energies up to 1 TeV, and are made in 40 different variables to examine the QCD dynamics in detail.

CMS has published extensive measurements of Z+jets observables, using 20 fb^{-1} of data collected at $\sqrt{s}$ = 8 TeV. This large dataset allows for double differential measurements. Figure 2 shows the differential cross section measurement $\frac{d^2\sigma}{dp_T(j1)dy(j1)}$, which measures the dependence of the cross section on leading jet p_T in bins of the leading jet rapidity y. The measurements are in reasonable agreement with the predictions from Sherpa and MadGraph, which are both MEPS programs.

In order to profit from reduced uncertainties, the ATLAS collaboration has published measurements of the ratio R_{jets} $\frac{W+jets}{Z+jets}$. The measurements probe the difference between the kinematics of the jet system recoiling against the W or Z boson. A very good description of the data by NLO pQCD is found, within the 1-15% experimental uncertainties over all jet bins ($n \leq 4$) considered.

Another set of ratio measurements have been recently released by CMS, which analyze $\frac{Z/\gamma^*+jets}{\gamma+jets}$, the ratio of a Z boson or virtual photon produced in association with jets to real photon production in association with jets [14]. This ratio is expected to be constant above a p_T region where Z boson mass effects are important. It can also test for potential large log effects at high energy, which are not always included in the perturbative calculations used for comparisons with data. The data are compared to predictions calculated by BlackHat and MadGraph simulations 3. It is interesting that both LO Madgraph and NLO Blackhat predict a larger ratio plateau in the high p_T tail than is seen in the data.

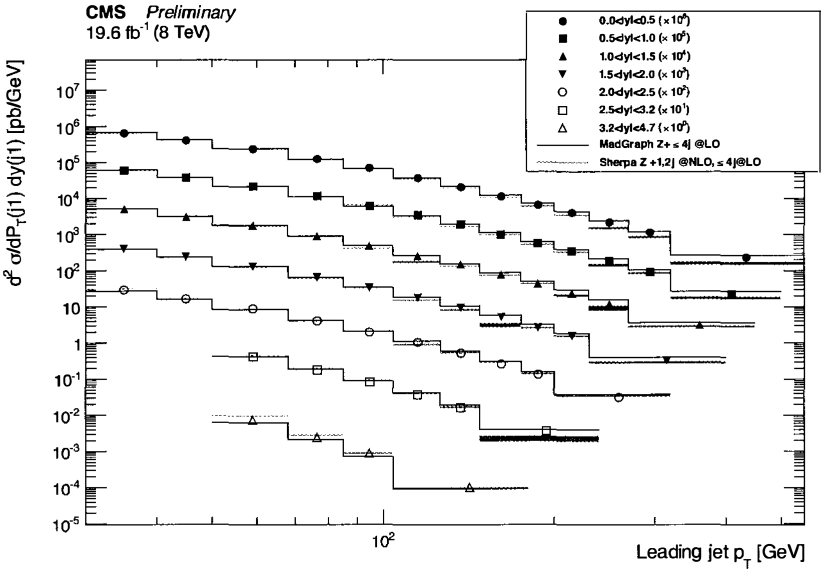

Figure 2 – The double differential cross section of $Z+\geq 1$ jet events as a function of leading jet p_T and leading jet rapidity y. The data are compared to LO predictions from Madgraph and NLO predictions from Sherpa.

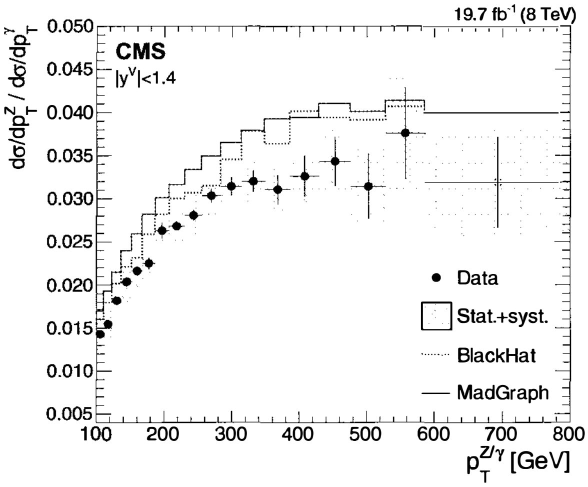

Figure 3 – The ratio of differential cross sections for inclusive Z and γ production as a function of the p_T of the boson. Data are compared to LO predictions from Madgraph and NLO predictions from Blackhat.

4 Z production in association with b-jets

The ATLAS and CMS collaborations have recently released measurements of Z bosons produced in association with b-quark jets[12,13]. $Z+b$ production is sensitive to the b-quark content of the proton; $Z+2b$ production is an important background to many Higgs and BSM searches. Fiducial cross sections from both experiments are in reasonable agreement with predictions by NLO pQCD.

An example from ATLAS is shown in Figure 4.

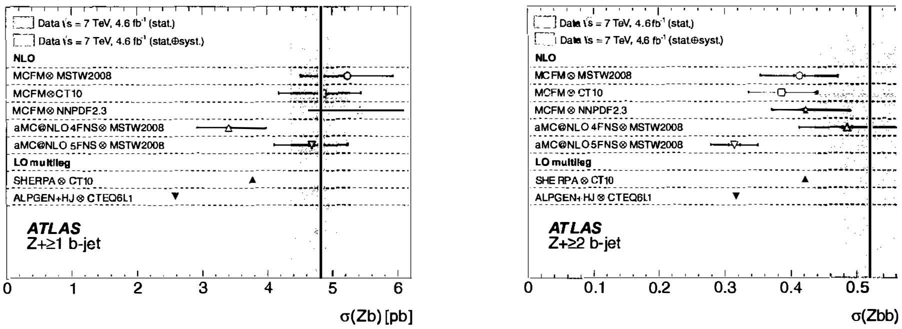

Figure 4 – Fiducial cross sections for Z+b (left) and Z+bb (right) production compared to a variety of theoretical predidctions.

References

1. ATLAS Collaboration, JINST **3** **S08003** (2008).
2. CMS Collaboration, JINST **3** **S08004** (2008).
3. R. Gavin, Y. Li, F. Petriello and S. Quackenbush, Comput. Phys. Commun. **182** (2011) 2388 [arXiv:1011.3540 [hep-ph]].
4. S. Catani, L. Cieri, G. Ferrera, D. de Florian and M. Grazzini, Phys. Rev. Lett. **103** (2009) 082001 [arXiv:0903.2120 [hep-ph]].
5. CMS Collaboration, [arXiv:1504.03511 [hep-ex]].
6. CMS Collaboration, Phys. Rev. D **85** (2012) 032002 [arXiv:1110.4973 [hep-ex]].
7. ATLAS Collaboration, JHEP **1409** (2014) 145 [arXiv:1406.3660 [hep-ex]].
8. CMS Collaboration, Phys. Rev. D **91** (2015) 5, 052008 [arXiv:1408.3104 [hep-ex]]. CMS-PAS-SMP-14-009.
9. CMS Collaboration, CMS-PAS-SMP-13-006
10. ATLAS Collaboration, Eur. Phys. J. C **75** (2015) 2, 82 [arXiv:1409.8639 [hep-ex]].
11. ATLAS Collaboration, Eur. Phys. J. C **74** (2014) 12, 3168 [arXiv:1408.6510 [hep-ex]].
12. ATLAS Collaboration, JHEP **1410** (2014) 141 [arXiv:1407.3643 [hep-ex]].
13. CMS Collaboration, JHEP **1406** (2014) 120 [arXiv:1402.1521 [hep-ex]].
14. CMS Collaboration, [arXiv:1505.06520 [hep-ex]].
15. ATLAS Collaboration, New J. Phys. **16** (2014) 11, 113013 [arXiv:1407.0800 [hep-ex]].

ELECTROWEAK PHYSICS AND QCD AT LHCB

D. JOHNSON
On behalf of the LHCb collaboration
CERN, Geneva, Switzerland

Data collected by the LHCb experiment allow proton structure functions to be probed in a kinematic region beyond the reach of other experiments, both at the LHC and further afield. In these proceedings the significant impact of LHCb Run 1 measurements on PDF fits is recalled and recent LHCb results, that are sensitive to PDFs, are described.

1 Measuring parton distribution functions at LHCb

The current experimental knowledge of proton structure functions carries large uncertainties, which are often the limiting factor in theoretical predictions for Standard Model (SM) processes and those beyond it (BSM). This strongly motivates the continued experimental study of processes that provide sensitivity to parton distribution functions (PDFs).

PDFs are typically parameterised using two kinematic variables, Q^2 and Bjorken x, corresponding to the squared interaction energy and the fraction of the nucleon's momentum carried by the parton, respectively. By consequence of the forward LHCb detector geometry, results obtained using LHCb data allow constraints to be placed on PDFs in kinematic regions that are inaccessible to those from other experiments at HERA and at the LHC.

A significant effect is seen in PDF fits[1] even when employing only a small selection of LHCb Run 1 results. These proceedings describe three recently published studies of heavy vector boson production at LHCb which will constrain PDF fits further. In addition, a new analysis of Υ photoproduction is presented, with particular sensitivity to the gluon PDF at low x.

2 Forward production of heavy vector bosons in 7 and 8 TeV pp collisions

Three analyses of pp collisions in LHCb are considered: W boson production at 7 TeV[2]; Z boson production, reconstructed in the e^+e^- decay mode at 8 TeV[3]; and 7 TeV Z boson production associated with a b-jet, where the Z decays to the dimuon final state[4]. There are several common components to these analyses. Final state muons and electrons are required to lie in the pseudorapidity range between 2 and 4.5 and to have a p_{T} greater than 20 GeV/c^2. In addition, most of these measurements benefit from a very precise integrated luminosity measurement[5], with a relative precision of 1.7% for 7 TeV data and 1.2% for 8 TeV data[a].

The first study exploits the full 7 TeV pp LHCb data sample corresponding to an integrated luminosity of 1 fb^{-1}. A single, high-p_{T} muon is required to be reconstructed. It must be well isolated, reducing background from hadronic QCD processes, and have a small impact parameter with respect to the primary vertex, suppressing background from leptonic τ and semi-leptonic heavy flavour decays. Events containing a second muon with large transverse momentum (p_{T})

[a] The $Z + b$-jet production cross-section relies on an earlier determination, with 3.5% relative uncertainty.

are rejected in order to reduce $\gamma^*/Z \to \mu^+\mu^-$ background. The final sample contains 806,094 $W^\pm$ candidates. A fit to the candidate p_T distribution is carried out in eight pseudorapidity ranges in order to identify remaining contributions from muons originating in $K^\pm$ or $\pi^\pm$ decays, other electroweak boson decays or from decaying heavy flavour, and the overall sample purity is found to be approximately 77%. The tag-and-probe method is employed to determine reconstruction efficiencies from samples of $Z \to \mu^+\mu^-$ decays, which are also used to determine selection efficiencies, after correcting for the difference in muon p_T. The integrated luminosity uncertainty dominates the systematic uncertainty for the $\sigma_{W\to\mu\nu}$ cross-section measurements, and is followed by the uncertainty on the muon reconstruction efficiencies. Both of these uncertainties cancel in the ratio, however, and in that case the main source of uncertainty arises from the template descriptions used in the fit to candidate p_T.

The total cross-sections (Figure 1(a)) and differential cross-sections (Figure 1(b)) demonstrate good agreement between the data and a range of SM next-to-next-to-leading order (NNLO) calculations.

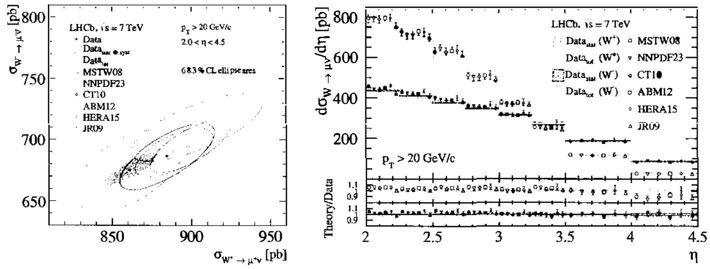

(a) Total cross-section.

(b) Differential cross-section.

Figure 1 – Total (a) and differential (b) cross-section measurements for W^+ and W^- production in pp collisions at 7 TeV.

The second result described concerns Z boson production reconstructed in the $Z \to e^+e^-$ channel, using the 8 TeV pp data set which corresponds to an integrated luminosity of $2\,\mathrm{fb}^{-1}$. This result extends a previous previous analysis using only 7 TeV pp collisions [6] and is an attractive extension to the $Z \to \mu^+\mu^-$ channel, offering a statistically independent measurement with considerably different systematic uncertainties. The 65,552 $Z \to e^+e^-$ candidates are selected requiring that the electrons should have a well-reconstructed momentum in the spectrometer and be associated to tracks leaving significant deposits in the electromagnetic calorimeter but not in the hadronic calorimeter. Nevertheless the principal background arises from randomly combined misidentified hadrons and is modelled using a sample of same-sign electron pairs reconstructed in data.

Since the electrons pass through a significant amount of detector material, and the effect of irrecoverable bremsstrahlung occurring before the electrons pass the magnet is considerable, there is significant uncertainty on the measurement of their momenta. Although some energy correction is achieved using associated calorimeter deposits, momenta are still degraded by approximately 25%. Consequently, the result is presented in terms an angular variable $\phi^* \approx p_\mathrm{T}/M$ and boson rapidity, y_Z, instead of p_T and y_Z. The largest systematic uncertainty, 1.6%, arises from the limited knowledge of electron tracking efficiencies and is obtained by comparing the efficiencies observed in simulation and data.

The measured differential cross-sections are shown in Figure 2. Figure 2(a) demonstrates the good agreement of theoretical predictions with LHCb data, down to Bjorken-$x \approx 10^{-6}$, for a range of PDF sets. In Figure 2(b) the agreement is evident between theoretical predictions using different methods to treat soft gluon emissions [7,8,9].

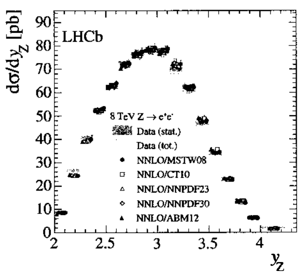

(a) Differential cross-section as a function of y_Z.

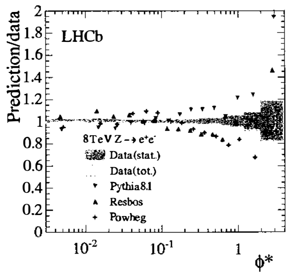

(b) Ratio of predicted and measured cross-section as a function of ϕ^*.

Figure 2 – Differential Z boson production cross-sections in 8 TeV pp collisions, reconstructed in the $Z \to e^+e^-$ channel. In (a) the differential production cross-section is shown as a function of Z rapidity whereas in (b) the ratio of prediction to measurement is shown as a function of the angular variable $\phi^* \approx p_T/M$.

The third study concerns the production of Z bosons in association with a beauty quark and uses data collected in 7 TeV pp collisions, corresponding to an integrated luminosity of $1\,\text{fb}^{-1}$. The measurement is normalised to the earlier LHCb measurement of Z boson production in association with a light jet [10] and forms a benchmark measurement to constrain backgrounds in SM Higgs analyses and BSM searches. The Z boson is reconstructed through its decay to $\mu^+\mu^-$ in the same way as the Z in the first analysis described in these proceedings. The associated jet is reconstructed using a particle flow algorithm with the following inputs: charged tracks and calorimeter clusters for neutral particles where deposits associated with charged tracks are subtracted. An anti-k_T clustering algorithm is employed with distance parameter equal to 0.5. The identification of b-jets is achieved by searching for 2-, 3- and 4-particle secondary vertices (SV) within the reconstructed jet, with the characteristic topology and kinematics expected for b-hadron decays. A fit, shown in Figure 3(a), is performed to the corrected invariant-mass of the secondary vertex using templates for light, charm and beauty jets, and 72 ± 15 $Z+b$-jet candidates are identified with jet $p_T > 10\,\text{GeV}/c$. The reconstruction efficiencies obtained in the Z+jet analysis are applied to this study, and the extra b-tagging efficiency is studied using simulated samples. This additional efficiency determination is the largest source of systematic uncertainty, along with that arising from the fit to SV corrected invariant-mass.

The measured cross-section is shown in Figure 3(b). Comparison is made with MCFM calculations [11] using massless and massive b-quarks at various orders of perturbative expansion, and good agreement with the data is seen in each case.

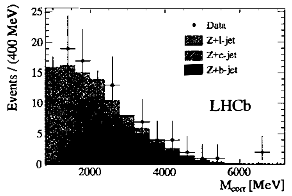

(a) Fit to SV corrected mass.

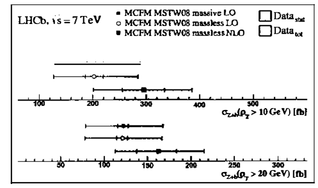

(b) Cross-section.

Figure 3 – Separation between Z production in association with light, charm and beauty jets is obtained through a fit to the invariant mass of a secondary vertex reconstructed within the jet, shown in (a). The resulting $Z+b$-jet production cross-section is compared to various theoretical predictions in (b) and good agreement is seen.

3 Exclusive production of heavy flavour states in diffractive interactions

Exclusive photoproduction occurs when a state is produced by low-p_T, colourless exchange of a pomeron and photon between the incoming protons, without dissociation of the protons or additional gluon radiation. Such processes can be perturbatively calculable and are sensitive to the square of the gluon PDF down to Bjorken-x of 1.5×10^{-5}. Since the photon-proton interaction energy depends exponentially on the produced meson rapidity, the forward geometry of LHCb allows the exploration of a new kinematic region compared to earlier measurements of exclusive Υ photoproduction at HERA.

The experimental signature of these processes is simple: two well-reconstructed muons and little other detector activity are required. Background from radiative χ_b decays are quantified in data. The background from inclusive Υ production where the additional activity occurs outside the LHCb acceptance is quantified by fitting the Υ p_T^2 spectrum, for which exclusive production templates are derived using the SuperChiC generator [12]. This fit is the source of the largest systematic uncertainties. These will be reduced in Run 2 by virtue of the recent addition of forward shower counters, extending the pseudorapidity coverage around LHCb [13]. The measured production cross-section for the $\Upsilon(1S)$ is shown in Figure 4(a) and the derived photo-production cross-section is given in Figure 4(b). Good agreement with perturbative predictions made at next-to-leading order is observed and the new kinematic region probed with the LHCb result is indicated.

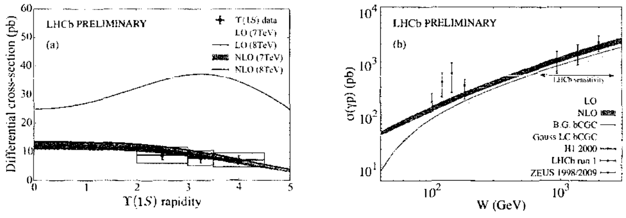

(a) Differential cross-section (b) Photo-production cross-section

Figure 4 – The differential cross-section as a function of rapidity, measured for $\Upsilon(1S)$ photoproduction, is shown in (a) and the derived photoproduction cross-section as a function of photon-proton interaction energy, W, is shown.

References

1. S. Alekhin, J. Bluemlein and S. Moch, *Phys. Rev.* D **89**, 054028 (2014).
2. LHCb collaboration, R. Aaij *et al.*, *JHEP* **12**, 079 (2014).
3. LHCb collaboration, R. Aaij *et al.*, `arXiv:1503.00963`, submitted to *JHEP.*
4. LHCb collaboration, R. Aaij *et al.*, *JHEP* **01**, 064 (2015).
5. LHCb collaboration, R. Aaij *et al.*, *JINST* **9**, P12005 (2014).
6. LHCb collaboration, R. Aaij *et al.*, *JHEP* **02**, 106 (2013).
7. T. Sjostrand, S. Mrenna and P. Skands, *JHEP* **05**, 026 (2006).
8. P. Nason, *JHEP* **11**, 040 (2004).
9. G.A. Ladinsky and C.P. Yuan, *Phys. Rev.* D **50**, 4239 (1994).
10. LHCb collaboration, R. Aaij *et al.*, *JHEP* **01**, 033 (2014)
11. J.M. Campbell and R. Ellis, *Nucl. Phys. Proc.* **557**, 205 (2010)
12. L.A. Harland-Lang, V.A. Khoze, M.G. Ryskin and W.J. Stirling, *EPJC* **69**, 179 (2010)
13. FSC Team (CMS), HERSCHEL Team (LHCb), M. Albrow, P. Collins, and A. Penzo, *Int. J. Mod. Phys. A* **29**, 1446018 (2014)

Jet production at HERA

D. BRITZGER
(On behalf of the H1 and ZEUS Collaborations)
DESY – Notkestraße 85, D-22607 Hamburg, Germany

New results on the measurements of jet cross sections and the hadronic final state in $e^{\pm}p$ collisions by the H1 and ZEUS experiments at HERA are presented. These are measurements of inclusive jet, dijet and trijet production as well as the production of $D^{*\pm}$ mesons in deep-inelastic scattering (DIS). Furthermore new measurements of the production of exclusive dijet cross sections as well as inclusive dijet cross sections in diffractive DIS and in diffractive photoproduction are presented.

1 Introduction

At the HERA collider in Hamburg, Germany, electrons were collided with protons at a centre-of-mass energy of 319 GeV. The two multi-purpose experiments H1 and ZEUS collected data until 2007 with an integrated luminosity of about $0.5\,\mathrm{fb}^{-1}$ per experiment. Several years after data taking, both experiments have successively refined their analysis techniques and now have achieved the final precision of their data with, for instance, a precision of the measurement of the jet energy scale of 1 %.

2 Recent results of jet production measurements at HERA

2.1 Measurement of multijet production in neutral current DIS

In the neutral current DIS (NC DIS) kinematic region of $150 < Q^2 < 15000\,\mathrm{GeV}^2$ and $0.2 < y < 0.7$, where Q^2 denotes the exchanged photon virtuality and y being the inelasticity, a simultaneous measurement of inclusive jet, dijet and trijet production, so-called multijet production, has been performed by H1 [1]. Furthermore, multijets normalised to the respective NC DIS cross section have been measured, which benefit from cancellation of the normalisation uncertainties and a significant reduction of many other systematic uncertainties. Jets are found using the k_T or the anti-k_T jet algorithm in the Breit frame and are required to have a transverse momentum exceeding $P_T^{\mathrm{jet}} > 7\,\mathrm{GeV}$. The invariant mass of the two leading jets must further exceed $M_{12} > 16\,\mathrm{GeV}$ for dijet and trijet production.

The measurement features an updated calibration of the measurement of the jet energy, which is based on calibration constants for jets derived using neural networks, as well as a multi-dimensional regularised unfolding method for the correction of detector effects. The latter is composed of a simultaneous unfolding of the three jet measurements together with the NC DIS cross sections where the statistical correlations are considered, thus also enabling to measure the normalised multijet production. The data are compared to predictions in next-to-leading order QCD (NLO) including corrections for hadronisation effects, and studying different parametrisations of the proton. The ratio of normalised k_T-jet cross sections to their NLO predictions is displayed in figure 1 as function of P_T in different Q^2 bins, where P_T represents the transverse momentum of the jet,

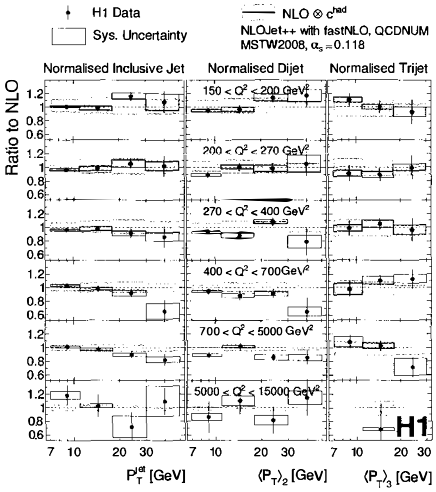

Figure 1 – Ratio of normalised jet cross sections to NLO QCD predictions as a function of Q^2 and transverse momenta observables.

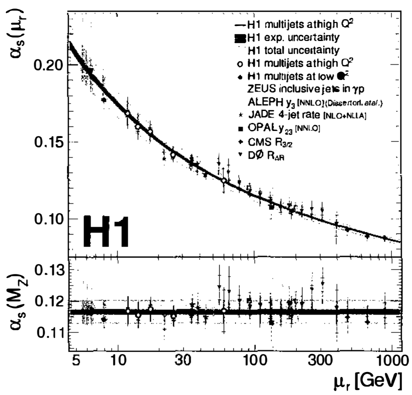

Figure 2 – Values of $\alpha_s(M_Z)$ (and corresponding values of $\alpha_s(\mu_r)$) extracted from the normalised multijet cross sections at different values of μ_r compared to values extracted from other jet data. The prediction for the running using the value of $\alpha_s(M_Z) = 0.1165\,(8)_{\rm exp}\,(38)_{\rm pdf,theo}$ is also shown.

$P_T^{\rm jet}$, in case of inclusive jets or the average transverse momentum, $< P_T^{\rm jet} >_2$ ($< P_T^{\rm jet} >_3$), of the two (three) leading jets in case of dijet (trijet) production. The data are in general found to be well described by the theoretical predictions and the precision of the data is considerably better than that of the NLO calculations, in particular for normalised jet cross sections.

The measurements are used to extract values of the strong coupling constant $\alpha_s(M_Z)$, where the simultaneous extraction from the normalised multijet measurement yields the best experimental precision of 0.7 % with a value of $\alpha_s(M_Z)|_{k_t} = 0.1165\ (8)_{\rm exp}\ (38)_{\rm PDF,theo}$, where 'exp' denotes the total experimental uncertainty, 'PDF,theo' the uncertainty from the PDFs and orders beyond NLO. Values of $\alpha_s(M_Z)$ are further determined at different values of the renormalisation scale μ_r and are compared in figure 2 to values from other jet measurements. The values are found to be consistent with the other values and also to be in good agreement with the expectations for the running from the renormalisation group equation. The value of $\alpha_s(M_Z)$ is the most precise value ever derived at NLO from jet data recorded in a single experiment.

2.2 Trijet production in DIS

The ZEUS experiment has measured[2] the production of inclusive trijets in the NC DIS kinematic region of $125 < Q^2 < 120000\,{\rm GeV}^2$ and $0.2 < y < 0.6$, where jets are found using the k_T cluster algorithm and are required to exceed a transverse momentum in the Breit frame of $E_{\rm T,B}^{\rm jet} > 8\,{\rm GeV}$. The double-differential measurement based on an integrated luminosity of $295\,{\rm pb}^{-1}$ exhibits good agreement with predictions in NLO QCD.

2.3 Exclusive dijets in diffractive DIS

The ZEUS experiment has measured[3] the production of exclusive dijets in diffractive DIS for $Q^2 > 25\,{\rm GeV}$ and for $\gamma^* p$ centre-of-mass energies in the range $90 < W < 250\,{\rm GeV}$. The exclusive dijet events, with jet transverse momenta greater than 2 GeV, have been reconstructed in the centre-of-mass system frame using the exclusive k_T algorithm. The normalised cross section is

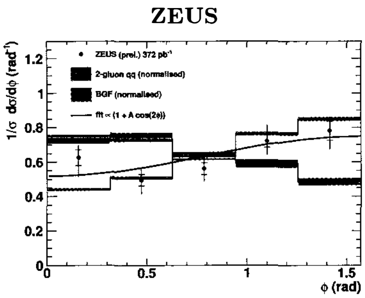

Figure 3 – The normalised differential cross section for the production of exclusive dijets as function of ϕ. The cross section is parameterised with a simple function and compared to two different theoretical models.

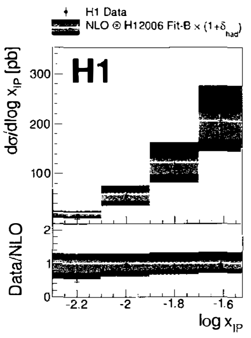

Figure 4 – Diffractive dijet differential cross section as a function of the fractional proton longitudinal momentum loss, $\log x_{I\!P}$, compared to NLO predictions.

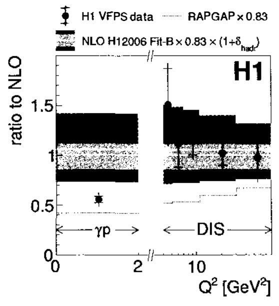

Figure 5 – Diffractive dijet cross sections in the PHP and DIS regime normalised to the NLO calculation as a function of Q^2.

given as a function of the angle ϕ, and is shown in figure 3, where ϕ is defined by the γ^*-dijet plane and the γ^*-$e^{\pm}$ plane in the rest frame of the diffractive final state. The comparison of the shape to theoretical predictions based on the Two-Gluon-Exchange model or the Resolved-Pomeron model exhibits a preference for the former, which is further supported by the study of a parameterised function as motivated by theory.

2.4 Inclusive dijet production in diffractive DIS (LRG)

The H1 experiment has presented a measurement [4] of single- and double-differential dijet production cross sections in diffractive DIS ($4 < Q^2 < 100\,\mathrm{GeV}^2$), where diffractive events are identified by requiring a large rapidity gap (LRG), i.e. an empty interval in rapidity between the high-mass hadronic final state and the elastically scattered proton or its low-mass excitation. The fully unfolded measurement investigates the kinematic range of the fractional proton longitudinal momentum loss of $x_{I\!P} < 0.03$, by identifying k_T-jets with a minimum transverse momentum of 5.5 and 4.5 GeV of the leading and subleading jet, respectively. The comparison to NLO QCD predictions, employing diffractive parton distribution functions (DPDF), exhibits a good agreement as shown in figure 4, while theoretical uncertainties from higher orders beyond NLO and from the DPDFs overshoot the experimental precision in a wide kinematical region.

The double-differential data is further used to determine the value of the strong coupling constant for the first time in diffractive DIS processes to $\alpha_s(M_Z) = 0.119\,(4)_{\mathrm{exp}}\,(12)_{\mathrm{theo}}$, thus illustrating the good agreement of theory to data and showing the experimental uncertainties to be significantly smaller than the uncertainties of the theory predictions.

2.5 Measurement of dijet production in diffractive DIS and photoproduction with a leading proton

Diffractive hadron-hadron interactions are found to be suppressed as compared to NLO predictions which are based on DPDFs obtained from HERA. Dijet production in diffractive photoproduction (PHP) allows the process to be studied in a similar environment to that of two interacting hadrons, where in the past discrepancies between the ZEUS and H1 measurements were a subject of debate.

The H1 experiment has presented measurements of unfolded differential dijet production cross sections in diffractive PHP ($Q^2 < 2\,\mathrm{GeV}^2$) as well as in diffractive DIS ($4 < Q^2 < 80\,\mathrm{GeV}^2$) in the kinematic range of $0.01 < x_{I\!P} < 0.024$ [5]. The leading final state proton is tagged in the H1 Very Forward Proton Spectrometer (VFPS) 220 m away from the interaction point, thus providing a complementary experimental method to previous analyses in PHP and DIS, which were based on the LRG method. The DIS dijet data are found to be well described by NLO predictions using DPDFs. In PHP, NLO predictions convoluted with DPDFs and photon PDFs overestimate the measured total cross sections, as shown in figure 5. However, the shapes of the investigated differential cross sections are described within the experimental and theoretical uncertainties. A detailed study of cross section ratios and double-ratios to NLO predictions or parton-shower improved leading-order MC predictions, where one profits from cancellations of uncertainties, confirms the previous H1 measurements based on the LRG method, while now possible contributions from proton-dissociative processes alone are excluded as an explanation for the observed suppression.

2.6 *Measurement and combination of D^* cross sections*

The H1 and ZEUS collaborations have combined their measurements of the production of $D^{*\pm}$ mesons in NC DIS in the range $5 < Q^2 < 1000\,\mathrm{GeV}^2$ and $0.02 < y < 0.7$ into a common dataset[6]. This effort yields measurements as function of the transverse momentum, $p_T(D^*)$ (see fig. 6), the pseudorapidity and inelasticity of the of the D^* meson, as well as of Q^2 and y, with significantly reduced experimental uncertainties compared to a single dataset, since the measurements benefit from increased statistical precision as well as from the uncorrelated systematic uncertainties of the two experiments. The combination exhibits that the individual datasets are consistent and the data are found to be reasonably well described by predictions in NLO QCD, while the combined data yields a much higher precision than the NLO predictions. The combination is further extended to data taken during the HERA-I period which extends the kinematic range down to $Q^2 > 1.5\mathrm{GeV}^2$ and the double-differential cross sections obtained as function of Q^2 and y are also well described by NLO predictions.

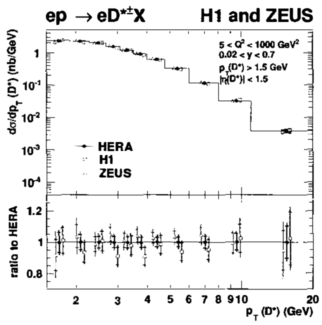

Figure 6 – Differential D^* production cross section as function of the transverse momentum of the D^* meson, $p_T(D^*)$. Data from the H1 and ZEUS experiments are shown together with the combined D^* production cross section.

3 Summary

Several new results on measurements of the hadronic final state in $e^{\pm}p$ collisions from HERA have been presented. In general good agreement between standard model expectations and data is observed, while the experimental uncertainties of the analyses presented here are often smaller than uncertainties on the predictions. Though, dijet production in diffractive photoproduction is not satisfactorily described by NLO predictions. The study of exclusive dijets in diffractive DIS sheds new light on the production principle of diffractive events. The H1 multijet measurements yields the most precise extraction of the strong coupling constant from jet cross sections reported so far.

References

1. V. Andreev *et al.* [H1 Collaboration], *Eur. Phys. J.* C **2**, 65 (2015) [arXiv:1406.4709]
2. ZEUS Collaboration, ZEUS preliminary, ZEUS-prel-14-008
3. ZEUS Collaboration, ZEUS preliminary, ZEUS-prel-14-004
4. V. Andreev *et al.* [H1 Collaboration], *JHEP* **1503**, 092 (2015) [arXiv:1414.0928]
5. V. Andreev *et al.* [H1 Collaboration], *JHEP* **1505**, 056 (2015) [arXiv:1502.01683]
6. H. Abramowicz *et al.* [H1 and ZEUS Collaborations], subm. to *JHEP* [arXiv:1503.06042]

HERAFitter - An Open Source framework to determine PDFs

Stefano Camarda
DESY - Notkestraße 85 D-22607 Hamburg Germany
On behalf of the HERAFitter Collaboration.

The `HERAFitter` project provides a framework for the determination of parton distribution functions (PDFs), and tools for assessing the impact of new data on PDFs. In this contribution, `HERAFitter` is used for a QCD analysis of the legacy measurements of the W-boson charge asymmetry and of the Z-boson production cross sections, performed at the Tevatron collider in Run II by the D0 and CDF collaborations. The Tevatron measurements are included in a PDF fit performed at next-to-leading order, and compared to the predictions obtained using other PDF sets from different groups. The measurements are in good agreement with NLO QCD theoretical predictions. The Tevatron data provide significant constraints on the d-valence quark distribution.

1 Introduction

According to the factorisation theorem, cross sections in hadron collisions are calculated by convoluting short distance partonic reactions with parton distribution functions (PDFs). Discovery of physics beyond the Standard Model at hadron colliders relies on the precise knowledge of the proton structure. Moreover, PDFs are among the dominant uncertainties for the measurement of the W mass, and for $gg \to H$ production. `HERAFitter` [1] provides a framework for the investigation of various methodologies in PDF fits, and tools for assessing the impact of new data on PDFs. It is widely used by the LHC experiments to improve the sensitivity of new measurements to PDFs. Full information about the project, downloads and documentation can be found at *herafitter.org.* A schematic view of a PDF fit, as implemented in `HERAFitter`, is shown in Fig. 1

In this contribution, `HERAFitter` is used to perform a QCD analysis of the Tevatron Run II legacy measurements of the W-boson charge asymmetry and of the Z-boson production cross sections [2]. At the Tevatron proton-antiproton collider, the production of W and Z bosons is dominated by valence-quark interactions. Whereas the primary source of information on the proton PDFs comes from deep-inelastic scattering (DIS), Drell-Yan production of W and Z bosons in proton-antiproton collisions can provide additional information, particularly on the d-valence quark PDFs.

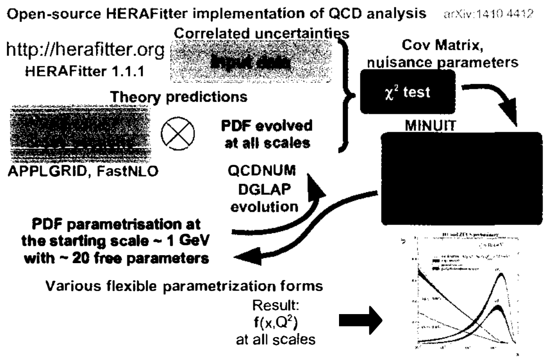

Figure 1 – Schematic representation of a PDF fit in HERAFitter.

2 Tevatron W and Z measurements and QCD settings

The most recent measurements of W-boson charge asymmetry and Z-boson inclusive production performed in Run II of the Tevatron collider are considered. They include the Z-boson differential cross section as a function of rapidity, measured by D0 [3]; the Z-boson differential cross section as a function of rapidity, measured by CDF [4]; the charge asymmetry of muons as a function of rapidity in $W \to \mu\nu$ decays, measured by D0 [5]; the W-boson charge asymmetry as a function of rapidity, measured by CDF [6]; the W-boson charge asymmetry as a function of rapidity, measured by D0 [7]. Besides the Tevatron W- and Z-boson measurements, the HERA I combined measurements of the inclusive DIS neutral- and charged-current cross sections measured by the H1 and ZEUS experiments [8] are used.

In general, the correlation model of the experimental uncertainties recommended by the Tevatron experiments is adapted and followed in the QCD analysis, with the exception of the experimental systematic uncertainties related to trigger and lepton identification efficiencies, which are treated as uncorrelated bin-to-bin.

The QCD analysis and PDF extraction is performed with the open-source framework HERAFitter. The charm mass is set to $m_c = 1.38$ GeV, as estimated from HERA charm production cross section [9], and the bottom mass to $m_b = 4.75$ GeV. The strong-interaction coupling constant at the Z boson mass, $\alpha_s(M_Z)$, is set to 0.118, and two-loop order is used for the running of α_s.

The PDFs for the gluon, u-valence, d-valence, $\bar{u}$, $\bar{d}$ quark densities are parametrised at the input scale of $Q_0^2 = 1.7$ GeV^2. The contribution of the s-quark density is taken to be proportional to the $\bar{d}$-quark density by setting $x\bar{s}(x) = r_s x\bar{d}(x)$, with $r_s = 1.0$. The strange and anti-strange quark densities are taken to be equal: $x\bar{s}(x) = xs(x)$.

The impact of a new data set on a given PDF set can be quantitatively estimated with a profiling procedure [10]. The profiling is performed using a χ^2 function which includes both the experimental uncertainties and the theoretical uncertainties arising from PDF variations:

$$\chi^2(\boldsymbol{\beta}_{\mathbf{exp}}, \boldsymbol{\beta}_{\mathbf{th}}) = \sum_{i=1}^{N_{\rm data}} \frac{\left(\sigma_i^{\rm exp} + \sum_j \Gamma_{ij}^{\rm exp}\beta_{j,\rm exp} - \sigma_i^{\rm th} - \sum_k \Gamma_{ik}^{\rm th}\beta_{k,\rm th}\right)^2}{\Delta_i^2} + \sum_j \beta_{j,\rm exp}^2 + \sum_k \beta_{k,\rm th}^2 . \quad (1)$$

The correlated experimental and theoretical uncertainties are included using the nuisance parameter vectors $\boldsymbol{\beta}_{\mathbf{exp}}$ and $\boldsymbol{\beta}_{\mathbf{th}}$, respectively. Their influence on the data and theory predictions is described by the $\Gamma_{ij}^{\rm exp}$ and $\Gamma_{ik}^{\rm th}$ matrices. The index i runs over all $N_{\rm data}$ data points, whereas the index j (k) corresponds to the experimental (theoretical) uncertainty nuisance parameters.

The measurements and the uncorrelated experimental uncertainties are given by σ_i^{exp} and Δ_i, respectively, and the theory predictions are σ_i^{th}.

3 Results

A QCD fit analysis performed on the Tevatron W- and Z-boson data, together with the HERA I data, is used to assess the impact of the Tevatron data on PDFs. The profiling is used to assess the impact of the Tevatron data on various PDF sets.

The optimal functional form for the PDF fit, which corresponds to 15 free parameters, is found through a *parametrisation scan*, and is used for a fit to the HERA I data only, and for a fit to the HERA I and Tevatron W- and Z-boson data. Table 1 shows the χ^2_{min} per degrees of freedom (dof) of the fit to the HERA I and Tevatron W- and Z-boson data. The contribution to the total χ^2_{min} of each data set, referred to as *partial* χ^2, is also shown. The partial χ^2 per number of points of each of the Tevatron and HERA I data set is close to unity.

Table 1: Results of a 15-parameters fit to the to the HERA I and Tevatron W- and Z-boson data. The contribution to the total χ^2_{min} of each data set and the corresponding number of points are shown.

Data set	χ^2 / number of points
HERA I	515 / 550
D0 $d\sigma(Z)/dy$	23 / 28
CDF $d\sigma(Z)/dy$	33 / 28
D0 muon charge asymmetry in $W \to \mu\nu$	12 / 10
CDF W charge asymmetry in $W \to e\nu$	15 / 13
D0 W charge asymmetry in $W \to e\nu$	16 / 14
Total χ^2_{min} / dof	615 / 628

The central value and the uncertainties of the PDFs are evaluated with MC replicas [11]. Figure 2 shows the comparison of the PDFs extracted with the MC replica method by fitting the HERA I data, and by fitting the HERA I and Tevatron W- and Z-boson data. A significant reduction of the PDF uncertainties is observed in the fit which includes the Tevatron W- and Z-boson measurements, in particular for the d-valence quark.

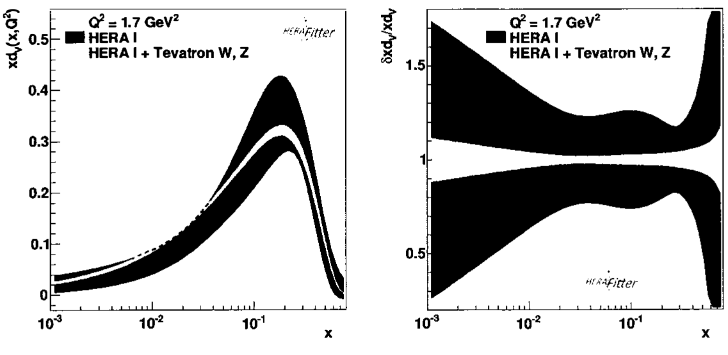

(a) (b)

Figure 2 – (a) PDFs at the starting scale $Q^2 = 1.7$ GeV^2 as a function of Bjorken-x for d_v determined with a fit to the HERA I data (blue), and with a fit to the HERA I and Tevatron W- and Z-boson data (yellow). (b) Relative PDF uncertainties.

The impact of the Tevatron W- and Z-boson measurements on the CT10nlo[12] and MMHT2014[13] is assessed by profiling. The uncertainties of the CT10nlo PDFs are scaled to 68% confidence limit. The compatibility of the Tevatron data with the CT10nlo, MMHT2014 and NNPDF3.0[14] sets is tested by evaluating the χ^2 function of Eq. (1). The partial χ^2 per number of points of each of the Tevatron data set, and the total χ^2 / dof, are close to unity for all the PDFs.

The CT10nlo and MMHT2014 PDFs are profiled to the Tevatron W- and Z-boson data. The results of the profiling on the relative uncertainty of the d-valence PDF are shown in Fig. 3. Significant reduction of the uncertainty is observed for both sets.

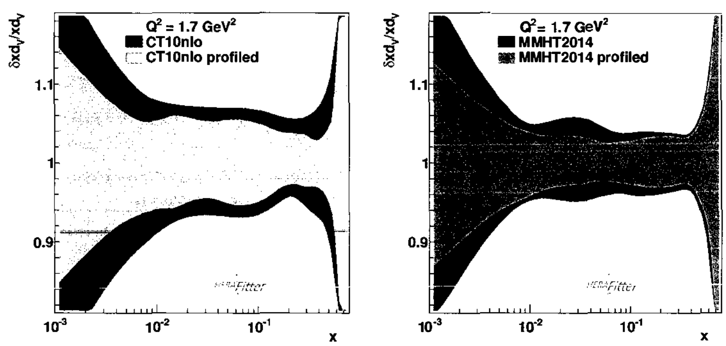

(a) (b)

Figure 3 – Relative uncertainties of the d-valence PDF at the scale $Q^2 = 1.7$ GeV^2 as a function of Bjorken-x before and after profiling for the (a) CT10nlo and (b) MMHT2014 PDFs.

Tables of the Tevatron measurements, with updated correlation model, and corresponding APPLGRID theoretical predictions[15] are publicly available at *herafitter.org.*

References

1. HERAFitter Collaboration, S. Alekhin *et al.* arXiv:1410.4412 [hep-ph].
2. HERAFitter Collaboration, S. Camarda *et al.* arXiv:1503.05221 [hep-ph].
3. D0 Collaboration, V. Abazov *et al. Phys. Rev. D* **76** (2007) 012003.
4. CDF Collaboration, T. A. Aaltonen *et al. Phys. Lett. B* **692** (2010) 232–239.
5. D0 Collaboration, V. M. Abazov *et al. Phys. Rev. D* **88** (2013) 091102.
6. CDF Collaboration, T. Aaltonen *et al. Phys. Rev. Lett.* **102** (2009) 181801.
7. D0 Collaboration, V. M. Abazov *et al. Phys. Rev. Lett.* **112** no. 15, (2014) 151803.
8. H1 and ZEUS Collaborations, F. Aaron *et al. JHEP* **1001** (2010) 109.
9. H1 and ZEUS Collaborations, H. Abramowicz *et al. Eur. Phys. J. C* **73** (2013) 2311.
10. H. Paukkunen and P. Zurita *JHEP* **1412** (2014) 100.
11. S. Forte, L. Garrido, J. I. Latorre, and A. Piccione *JHEP* **0205** (2002) 062.
12. J. Gao *et al. Phys. Rev. D* **89** no. 3, (2014) 033009.
13. L. Harland-Lang, A. Martin, P. Motylinski, and R. Thorne arXiv:1412.3989 [hep-ph].
14. The NNPDF Collaboration, R. D. Ball *et al.* arXiv:1410.8849 [hep-ph].
15. T. Carli *et al. Eur. Phys. J. C* **66** (2010) 503–524.

Hadronic physics with light quarks at BABAR and Belle

A. Hafner (for the BABAR and Belle collaboration)
Insitut für Kernphysik, J.J.-Becherweg 45,
Johannes Gutenberg-Universität Mainz, Germany

The anomalous magnetic moment of the muon $(g-2)_\mu$ is one of the most precisely measured quantities in particle physics (0.54 ppm). There is a long-standing discrepancy of 3-4 standard deviations between the direct measurement of $(g-2)_\mu$ and its theoretical evaluation. This theoretical prediction is subdivided into three contributions: QED, weak and hadronic. The QED and weak parts can be determined in perturbative approaches with very high precision. Thus, the hadronic uncertainty dominates the total theoretical uncertainty. Within the hadronic uncertainty, the largest contribution stems from the vacuum polarization term, which can be evaluated with the measurement of the inclusive hadronic cross section in e^+e^- annihilation. The second largest contribution to the hadronic uncertainty stems from the so-called Light-by-Light amplitudes. They have to be evaluated via theoretical models. These models require transition form factor measurements as input. Existing and future measurements of the relevant hadronic cross sections and transition form factors are presented.

1 Introduction

There are various ways to test the Standard Model (SM) of particle physics. Many approaches include searches for new particles or phenomena at the high energy frontier. Another approach is to measure SM observables with high precision and compare the measurement to the SM prediction. One particular test at this high precision frontier is the measurement of the anomalous magnetic moment of the muon $a_\mu = 0.5 \cdot (g-2)_\mu$. On the one hand, it is one of the most precisely measured observables in particle physics (0.54 ppm) [1]. On the other hand, there is a discrepancy of 3-4 standard deviations between the direct measurement of $(g-2)_\mu$ and its theoretical evaluation [2,3].

This theoretical prediction is subdivided into three contributions: QED, weak and hadronic. The QED and weak parts can be determined in perturbative approaches with very high precision[4]. At low energies perturbation theory cannot be used to calculate the hadronic contribution a_μ^{had}. Thus, the hadronic uncertainty dominates the total theoretical uncertainty. Within the hadronic uncertainty, the largest contribution stems from the vacuum polarization (VP) term. It is possible to relate this contribution $a_\mu^{\mathrm{had,VP}}$ via a dispersion relation to hadronic cross sections, which typically are measured in e^+e^- energy scan experiments at low energies. The study of the Initial State Radiation (ISR) events at flavor-factories allows independent measurements of exclusive hadronic cross sections. Here, high statistics e^+e^- experiments running at a fixed center-of-mass (c.m.) energy access processes at lower effective c.m. energies by studying events with a high energy photon emitted from the initial state. The use of this technique at high luminosity ϕ- and B-factories has been discussed in detail in Refs.[5,6,7]. The second largest contribution to the hadronic uncertainty stems from the so-called hadronic Light-by-Light (LbL) amplitudes. They have to be evaluated via theoretical models. These models require transition form factor measurements as input.

The most recent relevant exclusive hadronic cross section and transition form factor measurements are presented in the following.

2 Meson-Photon transition form factors

The uncertainty of the hadronic LbL contribution[8], $\Delta a_\mu^{\mathrm{had,LbL}} = 2.6 \cdot 10^{-10}$, to the theoretical estimate of $(g-2)_\mu$ is larger than the expected uncertainties of the upcoming direct $(g-2)_\mu$ measurements, $\sim 1.5 \cdot 10^{-10}$ [9,10]. The LbL estimates can be improved with experimental input, especially from photon-meson transition form factors (TFF). Here, the contribution of the π^0 TFF is dominating.

2.1 π^0-photon transition form factor

Measurements of the π^0 TFF are shown in Fig. 1 (left)[11,12,13,14]. BABAR agrees with CLEO in the region $4\,\mathrm{GeV}^2 < Q^2 < 9\,\mathrm{GeV}^2$. However, it clearly exceeds the expected asymptotic limit by pQCD: $\lim_{Q^2\to\infty} F(Q^2) = \sqrt{2} f_\pi$, taking into account systematic uncertainties of the efficiency (2.5%), background (0.3 – 6.0%), mostly due to $e^+e^- \to e^+e^-\pi^0\pi^0$, and additional model uncertainty (1.5%). The recent measurement by Belle with similar systematic uncertainties is in disagreement with *BABAR* at large Q^2, but also exceeds the asymptotic prediction. The slope, however, is in better agreement with pQCD.

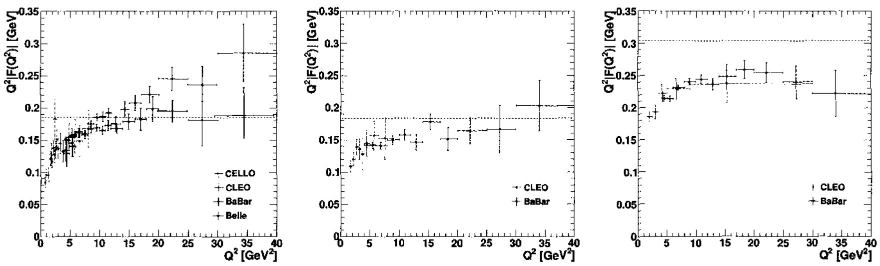

Figure 1 – Meson-Photon TFFs for the π^0 (left), η (middle), and η' (right) mesons of various experiments[11,12,13]. The dashed lines represent the asymptotic limit expected by pQCD.

2.2 η/η'-photon transition form factors

The η TFF measurement as a function of momentum transfer Q^2 from *BABAR*[11] and CLEO[14] is shown in Fig. 1 (middle). For *BABAR* the systematic uncertainty is 2.9%, dominated by model and π^0 reconstruction uncertainties of the $\eta \to \pi^+\pi^-\pi^0$ final state

The $\eta' \to \pi^+\pi^-\eta$[11], with $\eta \to \gamma\gamma$ measurements are shown in Fig. 1 (right). The *BABAR* systematic uncertainty of 3.5% is dominated by model and η reconstruction uncertainties. The η'-TFF stays below the asymptotic expectation.

More data is needed in order to solve this puzzling situation for the TFFs at large Q^2 and as input for $a_\mu^{\mathrm{had,LbL}}$ at small Q^2, especially for the π^0 final state.

3 Hadronic cross sections

The dominant contribution to the hadronic part of $(g-2)_\mu$ stems from the VP, requiring hadronic cross section measurements as input. The measurements of the dominating ($\sim$ 75%) $e^+e^- \to \pi^+\pi^-$ cross section has been performed with excellent precision and thus additional contributions with kaons and multihadronic final states are relevant.

3.1 $\sigma(e^+e^- \to K\bar{K})$

Recently, the $e^+e^- \to K^+K^-$ final state has been published by *BABAR*[15], see Fig. 2. In the ϕ peak region, this measurement is in agreement within 2 standard deviations to the CMD2[16] and SND[17] data. At larger cms energies (right) a different shape in comparison to SND is observed.

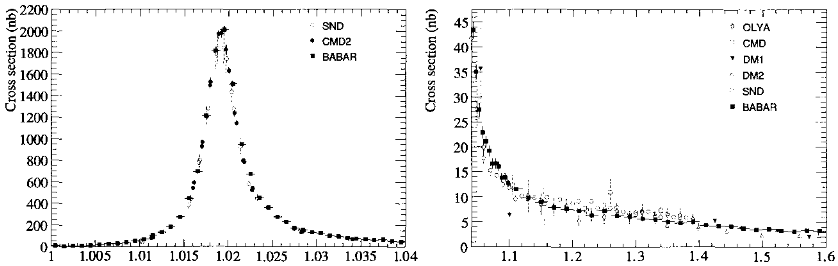

Figure 2 – Cross section of $e^+e^- \to K^+K^-$ in (left) and above (right) the ϕ peak region.

In Fig. 3 (left), the invariant $K^0_S K^0_L$-mass distribution by the *BABAR*[18] experiment in the ϕ peak region is shown, from which the partial electronic width of ϕ to $K^0_S K^0_L$ is extracted. This observable is in agreement with the CMD2[19] result. At larger energies, Fig. 3 (right), a clear structure is visible, which might be due to the $\phi(1680)$ resonance.

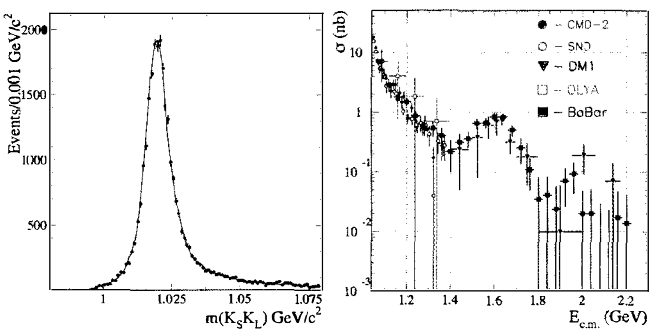

Figure 3 – Left: invariant $K^0_S K^0_L$-mass distribution by the *BABAR* experiment in the ϕ region. Right: cross section of $e^+e^- \to K^0_S K^0_L$ above the ϕ region.

3.2 Multihadronic final states

In Fig. 4, we see the first measurement of the hadronic cross section of the $K^0_S K^0_L \pi^+\pi^-$ (left), $K^0_S K^0_S \pi^+\pi^-$ (middle), and $K^0_S K^0_L K^+K^-$ (right) final states measured by *BABAR*. This will allow for the first time the direct extraction of the $(g-2)_\mu$ contribution of these final states. Up to date the value has been estimated by means of isospin relations.

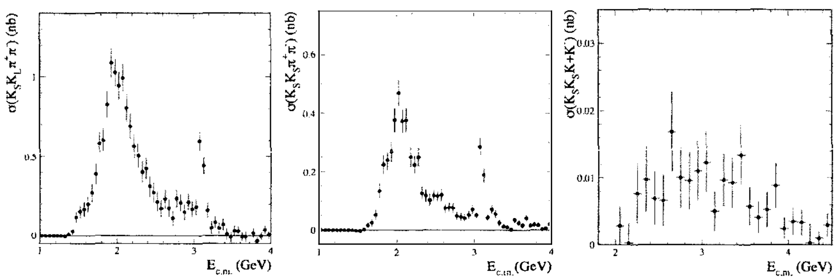

Figure 4 – Hadronic cross section of the $K_S^0K_L^0\pi^+\pi^-$ (left), $K_S^0K_S^0\pi^+\pi^-$ (middle), and $K_S^0K_L^0K^+K^-$ (right) final states measured by BABAR.

4 Conclusion and outlook

Including hadronic cross section and TFF measurements the remaining difference between theoretical prediction and measured value of 3.0-3.5 standard deviations [2,3] for the muon anomaly still poses an open question and requires further studies. The measurements of $K\bar{K}(\pi^+\pi^-/K^+K^-)$ await to be included into the world averages. Additional direct $(g-2)_\mu$ measurements [9,10] and hadronic cross section and TFF measurements will help to shed more light in the observed difference.

Acknowledgments

I want to thank the organizers for the warm hospitality and the excellent organization of this beautiful conference in La Thuile.

References

1. G.W. Bennett *et al.* (Muon g-2 Collaboration), Phys. Rev. D **73**, 072003 (2006).
2. M. Davier *et al.*, Europ. Phys. J. C **71**, 1515 (2011).
3. T. Teubner *et al.*, Nucl. Phys. Proc. Suppl. **218**, 225 (2011).
4. F. Jegerlehner and A. Nyffeler, Phys. Rept. **477**, 1 (2009).
5. A.B. Arbuzov *et al.*, JHEP **9812**, 009 (1998).
6. S. Binner, J.H. Kühn, K. Melnikov, Phys. Lett. B **459**, 279 (1999).
7. M. Benayoun *et al.*, Mod. Phys. Lett. A **14**, 2605 (1999).
8. J. Prades *et al.*, arXiv:0901.0306, (2009).
9. G. Venanzoni, (Fermilab E989 Coll.), Nucl. Phys. Proc. Suppl. **225-227**, 277-281 (2012).
10. T. Mibe, (J-PARC g-2 Collaboration), Nucl. Phys. Proc. Suppl. **218**, 242-246 (2011).
11. B. Aubert *et al.* (BABAR Collaboration), PRD **80**, 052002 (2009); PRD **84**, 052001 (2011).
12. S. Uehara *et al.* (Belle Collaboration), Phys. Rev. D **86**, 092007 (2012).
13. H. J .Behrend *et al.* (CELLO Collaboration), Z. Phys. C **49**, 401 (1991).
14. J. Gronberg *et al.* (CLEO Collaboration), Phys. Rev. D **57**, 33 (1998).
15. B. Aubert *et al.* (BABAR Collaboration), PRD **70**, 072004 (2004), PRD **71**, 052001 (2005), PRD **73**, 052003 (2006), PRD **73**, 012005 (2006), PRD **76**, 092006 (2007), PRD **76**, 092005 (2007), PRD **76**, 012008 (2007), PRD **77**, 092002 (2008), PRL **103**, 231801 (2009), PRD **85**, 112009 (2012), PRD **86**, 032013 (2012), PRD **88**, 032013 (2013), PRD **89**, 092002 (2014).
16. R.R. Akhmetshin *et al.* (CMD Collaboration), Phys. Lett. B **669**, 217-222 (2008).
17. M.N. Achasov *et al.* (SND Collaboration), Phys. Rev. D **76**, 072012 (2007).
18. J.P. Lees *et al.* (BABAR Collaboration), PRD **89**, 092002 (2014).
19. R.R. Akhmetshin *et al.* (CMD-2 Collaboration) Phys. Lett. B **466**, 385 (1999), Erratum-ibid. B **508**, 217-218 (2001).

FISRT OBSERVATION AND STUDY OF $K^{\pm} \to \pi^{\pm}\pi^0 e^+e^-$ DECAY AT THE NA48/2 EXPERIMENT

M.H. MISHEVA [a]
Joint Institute for Nuclear Research, Dubna, Russia

A sample of almost 2000 $K^{\pm} \to \pi^{\pm}\pi^0 e^+e^-$ rare decays with a background contamination below 3% is observed for the first time by the NA48/2 experiment at CERN/SPS. The preliminary branching ratio in the full kinematic region is obtained to be $BR(K^{\pm} \to \pi^{\pm}\pi^0 e^+e^-) = (4.06 \pm 0.17) \times 10^{-6}$ by analyzing the data set recorded in 3-month NA48/2 run during 2003. The measured value is in agreement with the theoretical prediction within one standard deviation.

1 Introduction

The $K^{\pm} \to \pi^{\pm}\pi^0 e^+e^-$ decay proceeds through virtual photon exchange which undergoes internal conversion into electron-positron pair, i.e. $K^{\pm} \to \pi^{\pm}\pi^0\gamma^* \to \pi^+\pi^0 e^+e^-$. Two possible mechanisms can lead to this rare kaon decay mode: Inner Bremsstrahlung (IB), where the γ^* is emitted by one of the charged mesons and Direct Emission (DE), when γ^* is radiated off at the weak vertex of the intermediate state of the process. The $K^{\pm} \to \pi^{\pm}\pi^0 e^+e^-$ amplitude consists of two terms: the dominant long-distance IB contribution (pure electric part) and the DE component (electric and magnetic parts). As a result, the differential decay width is a sum of IB, DE and (electric and magnetic) interference terms.

Detailed study of the various contributions to the amplitude of the considered rare process has been performed in the Ref. [1] whereas Ref. [2] provides identification of each dynamical contribution by a Dalitz plot analysis using a specifc set of kinematical variables. The $K^{\pm} \to \pi^{\pm}\pi^0 e^+e^-$ differential decay width with respect the invarant masses of the dilepton and dipion systems has been also calculated in both the kaon rest of frame and in the (e^-e^+) center-of-mass [3].

The first observation of the $K^{\pm} \to \pi^{\pm}\pi^0 e^+e^-$ decay and a preliminary result of the first experimental measurement of its branching fraction, using $K^{\pm} \to \pi^{\pm}\pi^0_D$ with $\pi^0_D \to e^+e^-\gamma$ as a

[a] on behalf of the NA48/2 Collaboration: G. Anzivino, R. Arcidiacono, S. Balev, J.R. Batley, M. Behler, S. Bifani, C. Biino, A. Bizzeti, B. Bloch-Devaux, G. Bocquet, N. Cabibbo, M. Calvetti, N. Cartiglia, A. Ceccucci, P. Cenci, C. Cerri, C. Cheshkov, J.B. Chèze, M. Clemencic, G. Collazuol, F. Costantini, A. Cotta Ramusino, D. Coward, D. Cundy, A. Dabrowski, P. Dalpiaz, C. Damiani, M. De Beer, J. Derré, H. Dibon, L. DiLella, N. Doble, K. Eppard, V. Falaleev, R. Fantechi, M. Fidecaro, L. Fiorini, M. Fiorini, T. Fonseca Martin, P.L. Frabetti, L. Gatignon, E. Gersabeck, A. Gianoli, S. Giudici, A. Gonidec, E. Goudzovski, S. Goy Lopez, M. Holder, P. Hristov, E. Iacopini, E. Imbergamo, M. Jeitler, G. Kalmus, V. Kekelidze, K. Kleinknecht, V. Kozhuharov, W. Kubischta, G. Lamanna, C. Lazzeroni, M. Lenti, L. Litov, D. Madigozhin, A. Maier, I. Mannelli, F. Marchetto, G. Marel, M. Markytan, P. Marouelli, M. Martini, L. Masetti, E. Mazzucato, A. Michetti, I. Mikulec, N. Molokanova, E. Monnier, U. Moosbrugger, C. Morales Morales, D.J. Munday, A. Nappi, G. Neuhofer, A. Norton, M. Patel, M. Pepe, A. Peters, F. Petrucci, M.C. Petrucci, B. Peyaud, M. Piccini, G. Pierazzini, I. Polenkevich, Yu. Potrebenikov, M. Raggi, B. Renk, P. Rubin, G. Ruggiero, M. Savrié, M. Scarpa, M. Shieh, M.W. Slater, M. Sozzi, S. Stoynev, E. Swallow, M. Szleper, M. Valdata-Nappi, B. Vallage, M. Velasco, M. Veltri, S. Venditti, M. Wache, H. Wahl, A. Walker, R. Wanke, L. Widhalm, A. Winhart, R. Winston, M.D. Wood, S.A. Wotton, O. Yushchenko, A. Zinchenko, M. Ziolkowski.

normalisation channel, are reported in the present work.

2 NA48/2 beam and detector system

Two simultaneous $K^{\pm}$ beams were produced by 400 GeV/c protons from the CERN/SPS impinging on a beryllium target. Opposite charge particles with a central momentum of (60±3)GeV/c were selected by an achromatic system consisting of two dipole magnet pairs and a collimator between them. The small transverse size (~1cm) of the kaon beams was achieved by a system of quadropole magnets. The kaon beams passed through cleaning and defining collimators before entering the decay volume housed in a 114 m long evacuated tank closed by 0.3% radiation lengths thick Kevlar window. The momenta (p) and positions of the charged decay products were measured in a magnetic spectrometer composed of four drift chambers and a dipole magnet. It was followed by a scintillator hodoscope consisting of two planes segmented into horizontal and vertical strips achieving a very good ~150 ps time resolution. A liquid krypton calorimeter (LKr), 27 radiation length thick, was used to measure electromagnetic deposits (E) and to identify electrons through their E/p ratio. Additional detector elecments as the hadron calorimeter, the muon and the photon veto counters were not used the present analysis. A detailed description of the NA48/2 detector set-up is available in Ref. [4].

3 $K^{\pm} \to \pi^{\pm}\pi^{0}e^{+}e^{-}$ selection and reconstruction

$K^{\pm} \to \pi^{\pm}\pi^{0}e^{+}e^{-}$ (denoted as $K_{\pi\pi ee}$ below) event candidates are reconstructed from exactly three charged tracks and two photons, forming a neutral pion, pointing to a common vertex in the fiducial decay volume. The charged track is identified as electron/positron if its E/p ratio is greater than 0.85, and as a charged pion if the E/p ratio is lower than 0.85. Two independent clusters without associated track in the LKr (γ-candidates), with energy more than 3 GeV and distance to the adjacent clusters greater than 10 cm are required to identify the two photons which reconstruct the nominal neutral pion mass within ± 10 MeV/c^2. The invariant mass of the charged pion, the electron, the positron and the reconstructed neutral pion is computed and is requested to be in the range (0.484 - 0.504) GeV/c^2 (± 10 MeV/c^2 from the nominal PDG $K^{\pm}$ mass [5]).
Two kaon decay modes are identified as background sources: $K^{\pm} \to \pi^{\pm}\pi^{0}_{\gamma\gamma}\pi^{0}_{D}$ ($K_{3\pi_D}$), where one of the neutral pions is subjected to a Dalitz decay $\pi^{0}_{D} \to e^{+}e^{-}\gamma$; $K^{\pm} \to \pi^{\pm}\pi^{0}_{D}$ ($K_{2\pi_D}$) and its radiative decay – $K^{\pm} \to \pi^{\pm}\pi^{0}_{D}\gamma$ ($K_{2\pi_D\gamma}$). The suppression of the $K_{3\pi_D}$ background events is achieved by requiring the squared invariant mass of the dipion system to be greater than 0.120 GeV^2/c^4. The invariant mass of the electron, the positron and one of the photons reconstructing the π^0 is demanded to be ± 7 MeV/c^2 away from the nominal mass of the neutral pion in order to reject $K_{2\pi_D(\gamma)}$ background contamination.
The data sample collected in a 3-month run in 2003 has been analysed. The number of the $K^{\pm} \to \pi^{\pm}\pi^{0}e^{+}e^{-}$ candidates in the signal region is 1916 while the overall background is below 3% and composed of (26 ± 5.1) $K_{2\pi_D(\gamma)}$ and (30 ± 5.5) $K_{3\pi_D}$ events (Fig. 1). All background contributions are estimated with the help of Monte Carlo simulations generated for each kaon mode.

4 Branching ratio measurement

The $K^{\pm} \to \pi^{\pm}\pi^{0}e^{+}e^{-}$ branching ratio (BR) is determined as:

$$BR(s) = \frac{N_s - N_b}{N_n} \cdot \frac{A_n \cdot \epsilon_n}{A_s \cdot \epsilon_s} \cdot BR(n),$$

where N_s is the number of the signal candidates (1916), N_b is the number of the estimated background events (55.8±7.4), A_s and ϵ_s are the geometrical acceptance and the trigger efficiency

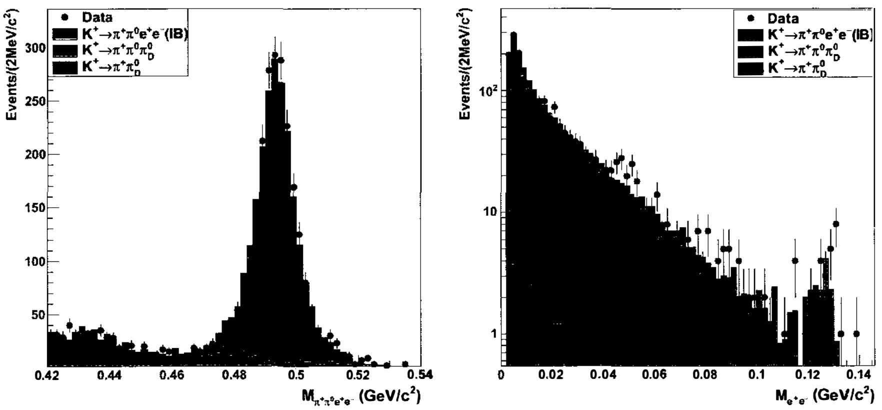

Figure 1 – Left: Invariant mass distribution of the $K^{\pm} \to \pi^{\pm}\pi^{0}e^{+}e^{-}$ reconstructed candidates before the final mass selection ((494 ± 10) MeV/c^2). Right: Invariant mass of the $(e^{-}e^{+})$-pair. Simulated signal events are plotted in red while the simulated background $K_{3\pi_D}$ and $K_{2\pi_{D(\gamma)}}$ events are superimposed in green and blue, respectively. The data distribution (black dots with error bars) is compatible with the sum of the simulated signal and background events.

of the signal. The "N_n, A_n, ϵ_n" notations are the corresponding quantities for the normalisation channel $K^{\pm} \to \pi^{\pm}\pi^{0}_{D}$ decay. The normalisation branching ratio $BR(n) = (2.425 \pm 0.076) \times 10^{-3}$ is the world average taken from [5]. The acceptances are obtained by MC simulations: $\sim 0.58\%$ for the signal mode and $\sim 3.6\%$ for the normalisation channel. The trigger efficiencies (ϵ_s and ϵ_n) are similar ($\sim 98\%$), determined from control data sample.

4.1 Normalisation channel

Both the signal and the normalisation kaon modes are selected concurrently by using the same trigger logic. A common event reconstruction is considered as much as possible aiming partial cancellation of systematic effects such as particle identification and trigger inefficiencies.
The event selection of the $K^{\pm} \to \pi^{\pm}\pi^{0}_{D}$ mode follows the same set of requirements used for the signal except for the π^{0}-reconstruction and background suppression parts. In case of $K_{2\pi_D\gamma}$, the neutral pion is reconstructed by demanding only one γ-candidate cluster, well separated from the adjecent clusters and with energy greater than 3 GeV, to be in time within 5ns with the electron and positron. The only background source for the normalisation channel is the $K^{\pm} \to \pi^{0}_{D}\mu^{\pm}\nu_{\mu}$ ($K_{\mu 3_D}$). Almost 6.715 million $K_{2\pi_D}$ candidates are selected with $K_{\mu 3_D}$ background contamination smaller than 0.1%.

4.2 Signal mode acceptance

The acceptances of the signal, the normalisation and the background channels are computed by GEANT3-based[6] Monte Carlo (MC) simulations which included the full detector and material description, stray magnetic fields, beamline simulation and local detector imperfections.
The MC simulation for the different $K_{\pi\pi ee}$ contributions – the IB, the DE and the electric interference, have been generated on the basis of the theoretical description given in Ref.[2]. The magnetic interference is not taken into account in the present measurement. The total $K_{\pi\pi ee}$ geometrical acceptance is calculated by using the theoretical fractions of different contributions[2]

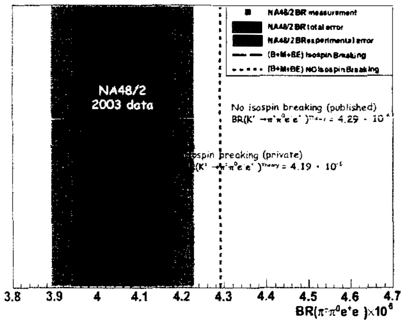

Figure 2 – The $K^{\pm} \to \pi^{\pm}\pi^{0}e^{+}e^{-}$ branching ratio obtained by the NA48/2 2003 data sample is plotted with its experimental error (shaded blue band) and its total error (shaded green band). The total error included statistical, systematic and external errors. The small dashed line represents the theoretical prediction of the $BR(K_{\pi\pi ee})$ with no isospin breaking published in Ref. [2]. The big dashed line shows the expected branching ratio with isospin breaking (thanks to the authors of Ref. [2], private communication). The experimental value of the $BR(K_{\pi\pi ee})$ is in a very good agreement with the theoretical predictions (within one standard deviation).

as the present data sample is not large enough to measure them:

$$A_s = \frac{A^{IB} + A^{DE} \cdot Frac_{DE}^{theory} + A^{El.Int.} \cdot Frac_{El.Int.}^{theory}}{1 + Frac_{DE}^{theory} + Frac_{El.Int.}^{theory}}.$$

As radiative corrections to the $K_{\pi\pi ee}$ mode are not available, the signal MC simulation included the following effects: the classical Coulomb attraction/repulsion between charged particles and the real photon(s) emission as implemented in the PHOTOS package [7].

5 Results

A sample of 1860 genuine $K^{\pm} \to \pi^{\pm}\pi^{0}e^{+}e^{-}$ events has been collected by NA48/2 Collaboration analysing the 2003 data sample. The preliminary result of the $K_{\pi\pi ee}$ branching ratio is obtained:

$$BR(K^{\pm} \to \pi^{\pm}\pi^{0}e^{+}e^{-}) = (4.06 \pm 0.10_{stat.} \pm 0.06_{syst.} \pm 0.13_{ext.}) \times 10^{-6},$$

where systematic errors include uncertainties on acceptance, particle identification, trigger efficiencies and radiative corrections. External error originates from the normalization mode BR uncertainties and it is the dominant error in the present result (Fig.2).

Acknowledgments

I am very grateful to O. Cata, G. D'Ambrosio and S. Gevorkyan for all interesting and fruitful discussions that we have had.

References

1. H. Pichl, *Eur. Phys. J. C* **20**, 371 (2001)
2. L.Cappiello *et al.*, *Eur. Phys. J. C* **72**, 1872 (2012); *Erratum-ibid. C* **72** , 2208 (2012)
3. S. Gevorkyan, M.H. Misheva, *Eur.Phys.J. C* **74**, 2860 (2014)
4. NA48: V. Fanti *et al.*, *Nucl. Instrum. Methods A* **574**, 433 (2007)
5. PDG: K.A. Olive *et al.* (Particle Data Group), *Chin. Phys. C* **38**, 090001 (2014)
6. GEANT3 Detector Description and Simulation Tool, CERN Program Library Long Writeup W5013 (1994).
7. E. Barberio and Z. Was (PHOTOS), *Comp. Phys. Comm.* **79**, 291 (1994).

7.
Heavy Ion

Geometry and Collective Behavior in Small Systems from PHENIX

Julia Velkovska for the PHENIX collaboration
Department of Physics and Astronomy, Vanderbilt University, PMB 401807, Nashville, TN 37235, USA

Recent results from particle correlations in high multiplicity p+Pb collisions at LHC and d+Au collisions at RHIC indicate that collective phenomena similar to those found in collisions between two large nuclei may also be present in small systems. To test competing theoretical interpretations of the data, the PHENIX experiment used collisions with differing initial geometries, such as ^{3}He+Au and d+Au, in order to control the strength of the possible collective effects. We present the first measurements of elliptic v_2 and triangular v_3 flow in high multiplicity ^{3}He+Au collisions at $\sqrt{s_{NN}}$=200 GeV. Sizable v_2 and v_3 values are observed, as expected from geometric considerations. The results are compared to a variety of theoretical predictions. Models based on hydrodynamic flow are in good agreement with the data.

1 Introduction

A key feature of the Quark-Gluon Plasma (QGP) produced in high-energy collisions between two heavy nuclei at the Relativistic Heavy Ion Collider (RHIC) and the Large Hadron Collider (LHC) is the formation of a system that behaves collectively as a nearly perfect fluid. Initial anisotropies in the energy density deposition in the collision zone are manifested through the system evolution and translated into final-state azimuthal anisotropies of the produced particles. Turning this signature off by varying the system size or the beam energy is essential for understanding the properties of the QGP and how the strongly coupled liquid emerges. It has long been considered that in small systems such as $p+p$, p+A, or d+A, equilibration can not be achieved and therefore the system cannot exhibit collective behavior. However, recent results from the LHC [1,2,3,4] and RHIC [5,6] challenge this paradigm. In high multiplicity p+Pb collisions, the correlations were shown to involve all produced particles [7], which is indicative of fluid formation. Mass ordering in the correlation strength, characteristic of hydrodynamic flow, has been observed both at RHIC and LHC energies in high-multiplicity d+Au and p+Pb collisions [6,8]. While many of the observed features can be explained with formation of small droplets of QGP which then expand hydrodynamically [9], alternative explanations involving novel initial-state glasma diagrams have also been shown to produce non-trivial particle correlations [10]. To test these competing theories the PHENIX experiment studied d+Au, and ^{3}He+Au collisions in order to control the initial size and shape of the interaction zone. In the case of collective final-state effects the latter system is expected to have enhanced triangular flow pattern [11]. We report on the first measurement of elliptic and triangular flow in high-multiplicity ^{3}He+Au collisions at $\sqrt{s_{NN}}$=200 GeV.

2 Experimental Details and Results

The collective flow can be studied by measuring two- or multi-particle correlations, or by measuring the correlation of the observed particles with a global symmetry plane that is defined event-by-event. In A+A collisions the collective flow induces a characteristic structure in the two-particle correlations in relative pseudorapidity ($\Delta\eta$) and azimuthal angle ($\Delta\phi$) known as "the ridge". The ridge extends over a long range in $\Delta\eta$ and is concentrated around $\Delta\phi \approx 0$. The observation of the ridge in high-multiplicity $p+p$ and p+Pb collisions at the LHC [1,2,3,4] gave the first indications that collective phenomena may exist in smaller systems. Although the PHENIX experiment does not have a wide acceptance in pseudorapidity, the presence of a ridge could be tested using charged particles detected in the PHENIX central arms that subtend $|\eta| < 0.35$, and the Beam-Beam Counters (BBC) or the Muon Piston Calorimeters (MPC) that cover forward and backward pseudorapidity and provide a pseudorapidity separation of at least 2.75 units. The results from the two-particle correlations measured in $p+p$ collisions, and the 0-5% most central d+Au [6] and ^{3}He+Au collisions at $\sqrt{s_{NN}}$=200 GeV are shown in Fig. 1. The correlations in $p+p$ collisions exhibit a peak at $\Delta\phi = \pi$ presumably dominated by particle production in jets that are back-to-back azimuthally. Particles produced within a single jet would yield a peak at $\Delta\phi = 0$, but the pseudorapidity separation between the particles of $\Delta\eta > 2.75$ eliminates this contribution. On the other hand, in the central d+Au, and ^{3}He+Au collisions the correlations contain a peak at $\Delta\phi = 0$, which indicates that a ridge-like structure is present in these systems.

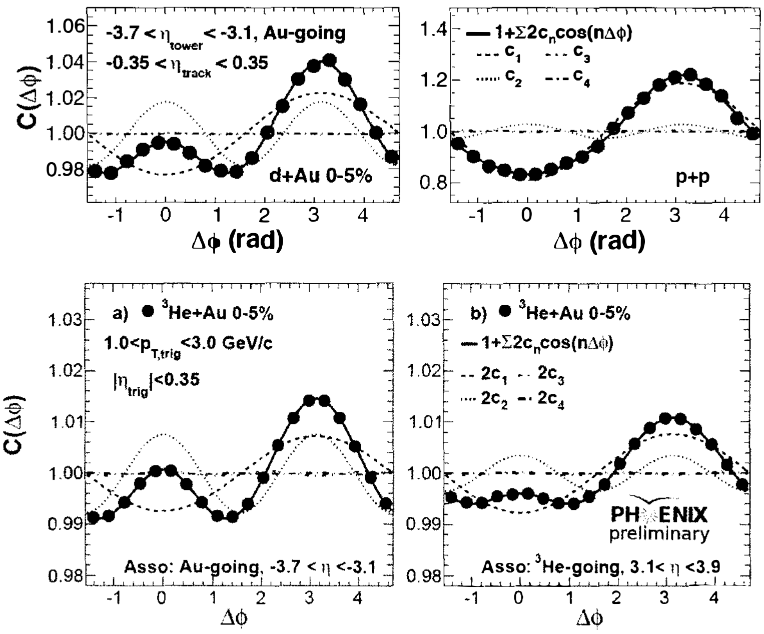

Figure 1 – Two-particle correlations in $p+p$ collisions, and the 0-5% most central d+Au and ^{3}He+Au collisions at $\sqrt{s_{NN}}$=200 GeV. Charged particles detected in the PHENIX central-arm spectrometers covering $|\eta| < 0.35$ are correlated with towers of energy or charge detected in the forward detectors MPC and BBC. A near-side ($\Delta\phi = 0$) peak is seen in the d+Au and ^{3}He+Au collisions, indicating a ridge formation.

The azimuthal anisotropy of produced particles can be quantified by the Fourier coefficients v_n in the expansion of the particles' distribution as: $dN/d\phi \propto 1 + \sum_{n=1} 2v_n \cos(n(\phi - \Psi_n))$, where n is the order of the harmonic, ϕ is the azimuthal angle of particles of a given type, and Ψ_n is the azimuthal angle of the n^{th} order event plane. The elliptic (v_2) and triangular (v_3) flow for inclusive charged hadrons produced at mid-rapidity $|\eta| < 0.35$ are measured with respect to Ψ_2 and Ψ_3 event planes reconstructed in the South MPC, located in the Au-going direction in the pseudorapidity region $-3.7 < \eta < -3.1$. The results for the 5% most central events are shown in Fig. 2. In both d+Au and ^{3}He+Au collisions, sizable elliptic flow is detected. The higher order moment v_3 was found to be consistent with zero in the d+Au system, which has small initial triangularity. In the ^{3}He+Au collisions significant third order eccentricity is present in the initial state of the collision and finite v_3 is measured, as theoretically predicted [11].

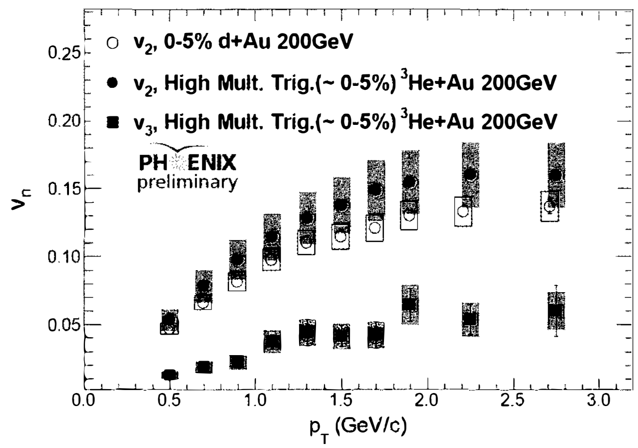

Figure 2 – Elliptic (v_2) and triangular (v_3) anisotropies as a function of p_T for inclusive charged hadrons at midrapidity in 0-5% central ^{3}He+Au collisions (filled symbols) and d+Au (open symbols) at $\sqrt{s_{NN}}$=200 GeV. In the d+Au measurement [6] the third order coefficient v_3 is consistent with zero. Error bars are statistical, and shaded bars and open rectangles represent the systematic uncertainties.

In Fig. 3 the v_2 and v_3 measurements in central ^{3}He+Au collisions are compared to theoretical calculations [12,13,14,15]. Several different approaches to modeling the initial energy density in the collisions and the pre-equilibrium dynamics are employed, and then followed by viscous hydrodynamic evolution [12,13,14]. The resulting elliptic and triangular anisotropies are compatible with the experimental results. In another approach [15], the initial energy density leads to string excitations from which partons emerge via a mechanism referred as string melting. Next, the system evolves through a parton cascade, partons coalesce into hadrons, and hadrons rescatter in a hadronic cascade. This microscopic approach also yields results compatible with the data. Calculations that are based solely on initial-state glasma diagrams [10] are not yet available for the ^{3}He+Au system.

3 Summary and Outlook

The PHENIX experiment has measured azimuthal anisotropies in particle emission in high-multiplicity d+Au and ^{3}He+Au collisions. The measured elliptic anisotropies are of similar magnitude in the two systems, while the triangular flow is sizable only in the ^{3}He+Au collisions, as expected from the initial geometry of the collision zone. Models incorporating hydrodynamic flow are in good agreement with the data and may indicate that droplets of QGP with small viscosity are being formed in the small collision systems. In 2015 the PHENIX experiment collected data from high-multiplicity p+p and p+A collisions. The forthcoming results will provide a full suite of geometries

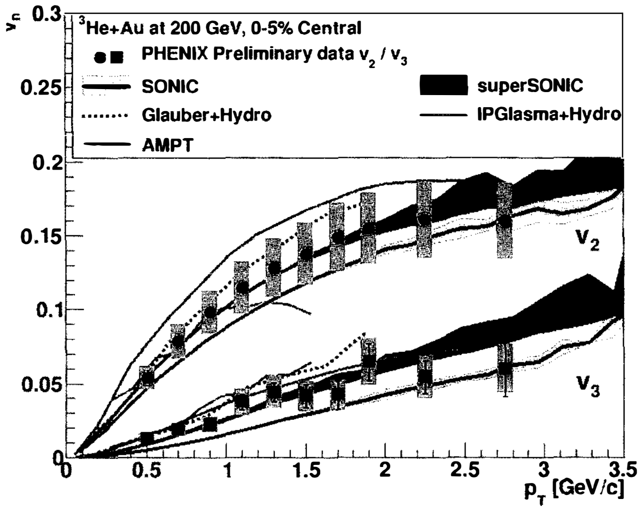

Figure 3 – Elliptic (v_2) and triangular (v_3) anisotropies as a function of p_T for inclusive charged hadrons at midrapidity in 0-5% central ^{3}He+Au collisions at $\sqrt{s_{NN}}$=200 GeV are compared to several theoretical models[12,13,14,15].

in order to constrain the origin of the observed anisotropies.

Acknowledgments

The author acknowledges the support of USA Department of Energy Grant No. DE-FG05-92ER40712 for participation in Moriond QCD 2015.

References

1. V. Khachatryan *et al (CMS Collaboration), JHEP* **1009**, 091 (2010)
2. S. Chatrchyan *et al (CMS Collaboration), Phys. Lett.* B **724**, 213 (2013)
3. G. Aad *et al (ATLAS Collaboration), Phys. Rev. Lett.* **110**, 182302 (2013)
4. B. Abelev *et al (ALICE Collaboration), Phys. Lett.* B **719**, 29 (2013)
5. A. Adare *et al (PHENIX Collaboration), Phys. Rev. Lett.* **111**, 212301 (2013)
6. A. Adare *et al (PHENIX Collaboration), Phys. Rev. Lett.* **114**, 192301 (2015)
7. V. Khachatryan *et al (CMS Collaboration)*,arXiv:1502.05382, accepted in *Phys. Rev. Lett.*
8. B. Abelev *et al (ALICE Collaboration), Phys. Lett.* B **726**, 164 (2013)
9. P. Bozek, and W. Broniowski, *Phys. Rev.* C **88**, 014903 (2012)
10. K. Dusling and R. Venugopalan, *Phys. Rev. Lett.* **108**, 262001 (2012)
11. J. L. Nagle *et al, Phys. Rev. Lett.* **113**, 112301 (2014)
12. P. Romatschke, arXiv:1502.04745
13. P. Bozek and W. Broniowski, *Phys. Lett.* B **747**, 135 (2015)
14. B. Schenke and R. Venugopalan, *Nucl. Phys.* A **931**, 1039 (2014)
15. J. D. O. Koop *et al,* arXiv:1501.06880

Beam Energy Scan Results from STAR

Bingchu Huang for the STAR collaboration
Department of Physics, 845 W Taylor St, M/C 273
Chicago, IL, USA 60607

The STAR experiment has collected data in Au+Au collisions in the Beam Energy Scan (BES) program at the Relativistic Heavy Ion Collider (RHIC). We present some selected recent results from STAR, which may be related to the turn-off signatures of quark-gluon-plasma (QGP), first order of phase transition, and critical point searches.

1 Introduction

The most successful theory to describe the strong force interaction is Quantum Chromodynamics (QCD). Exploring the QCD phase diagram, which is usually illustrated by temperature, T, vs. baryon chemical potential, μ_B, is one of the most important goals of heavy-ion collision experiments [1]. The phase diagram shows a partonic phase at high temperature and low μ_B at top RHIC energy. Assuming a thermalized system is reached in heavy-ion collisions, the T and μ_B can be varied by changing the collision energy [2]. Thus, we can explore the phase diagram and search for possible phase transition from partonic to baryonic degree-of-freedom dominant phase.

Lattice QCD [3] calculations show a rapid crossover at μ_B=0, and several QCD based models [4] suggest a first-order transition at large μ_B. The end point of the first-order phase transition is called the QCD Critical Point (CP). Searching for the first order phase boundary and QCD CP becomes the major goal of RHIC Beam Energy Scan (BES) program. The well established QGP signatures at 200 GeV are expected to turn off when the T and μ_B are crossing the phase boundary. Theoretically, the fluctuation of conserved quantities (net-baryon, net-charge and net-strangeness) would be enhanced near the QCD critical point.

2 Results

There are many interesting observables to search for the turn-off of QGP signatures and the critical point. Here we select the results of freeze-out parameters, first and second coefficients (v_1, v_2) of the Fourier expansion of angular distributions, net proton higher moments, and dielectron productions.

2.1 Freeze-out parameters

There are two types of freeze-out usually discussed in heavy-ion collisions, chemical freeze-out and kinetic freeze-out. The stage after the collisions when the inelasetic interactions stop is referred to as chemical freeze-out. The chemical freeze-out temperature T_{ch} and baryon chemical potential μ_B can be extracted by the statistical thermal models which have successfully described the experimental data for many different beam energies [1].

After the chemical freeze-out, the elastic interactions last for some time till the distance becomes large enough. The system is said to have undergone kinetic freeze-out. The transverse momentum p_T spectra of the produced particles remain unchanged, thus we can extract kinetic temperature and collective velocity from the spectra by a blast-wave model fit [1]. Figure 1 shows the chemical and kinetic freeze-out parameters from fit. The T_{ch} has a small dependence on μ_B for most central Au+Au collisions. It is nearly constant above 19.6 GeV, and increases from 7.7 to 19.6 GeV which is consistent with a model prediction from Ref. [5]. The T_{kin} has an anti-correlation with collective velocity $< \beta >$, lower in central collision and/or at higher collision energies. It suggests increased hadronic interactions in central and higher collision energies.

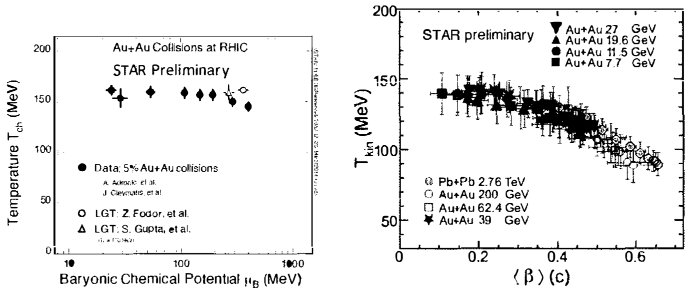

Figure 1 – Left: The chemical freeze-out temperature as a function of baryonic chemical potential μ_B. Right: The kinetic freeze-out temperature as a function of collective flow velocity $< \beta >$.

2.2 Directed flow v_1 and Elliptic flow v_2

The directed flow v_1 is considered as one of the most promising observables for the search of a first order phase transition, as it carries the early collision information and is sensitive to the Equation of State (EoS) [6]. Figure 2 left shows the directed flow slope dv_1/dy at mid-rapidity as a function of $\sqrt{s_{NN}}$ for anti-proton, proton, and net protons. The net-proton measurements show a decreasing trend of dv_1/dy from 7.7 to 11.5 GeV, with a minimum between 11.5 and 19.6 GeV [7]. Then it is monotonically increasing towards higher energies. The result is different from UrQMD calculations which do not contain first order phase transition. Hydrodynamic calculations predict such a minimum of dv_1/dy in the presence of a first order phase transition, however, the expected minimum is at lower energy than we observed.

The elliptic flow v_2 is the second order harmonic of the azimuthal particle distribution relative to the reaction plane. It probes the early stage of the reaction because it is formed by the pressure gradient of the created hot medium of the collisions. The number-of-constituent-quark (NCQ) scaling of v_2 at top RHIC energy is a signature of the QGP phase. Figure 2 right shows the difference in v_2 of particles and corresponding anti-particles as a function of beam energy [8]. The v_2 difference between particles and anti-particles is observed as an increasing trend when collision energy decreases. The difference between particles and anti-particles suggests that the NCQ scaling is broken. However, some models can qualitatively explain the data without a phase transition [9].

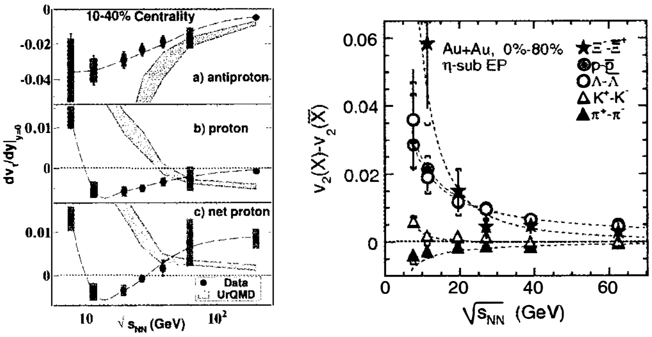

Figure 2 – Left: dv_1/dy at mid-rapidity as a function of $\sqrt{s_{NN}}$ for 10-40 % central Au+Au collisions for (a) anti-protons, (b) protons, and (c) net-protons. Right: Difference in v_2 between particles and anti-particles as a function of the collision energies in 0-80 % Au+Au collisions.

2.3 *Higher moments of net-proton distributions*

The correlation length of particles is expected to diverge when the T-μ_B trajectory of a system comes close or passes a QCD critical point. The divergence leads to a significant increase of event-by-event fluctuations of observables that are sensitive to the correlation length compared with variance. It was suggested to study the higher moment distributions of conserved quantities, such as net-baryon, net-charge, and net-strangeness. In Fig. 3, the net-proton moment products $\kappa\sigma^2$ and $S\sigma$ as a function of beam energy are shown in different centralities[10]. For peripheral (70-80%) and mid-central (30-40%) collisions, the $\kappa\sigma^2$ are close to unity and the $S\sigma$ show strong monotonic increase with decreasing energy. For 0-5% most-central collisions, the $\kappa\sigma^2$ start to deviate from unity and show deviation below unity at 19.6 and 27 GeV. Then it increases towards lowest beam energy 7.7 GeV. The $S\sigma$ of 0-5% centrality shows a large drop at 7.7 GeV. However, there are only statistical errors shown in the figure, and systematical uncertainties, which are dominated by the efficiency correction and the particle identification, are being studied.

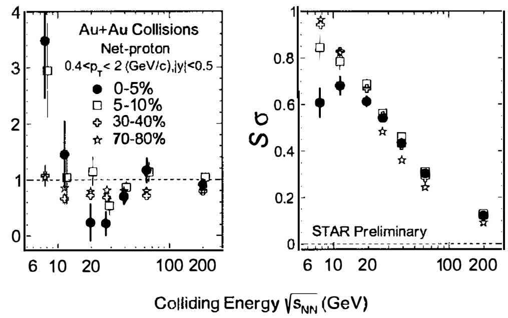

Figure 3 – Energy dependence of efficiency corrected cumulant ratios $\kappa\sigma^2 = C_4/C_2$ and $S\sigma = C_3/C_2$ of net-proton distributions in Au+Au collisions at different centralities (0-5%, 5-10%, 30-40%, 70-80%).

2.4 *Dielectron production*

Dielectron is produced through the whole evolution of the fireball created in the collisions, and it has minimal interactions when traveling through the medium. It contains the information from QGP thermal radiations, such as QGP temperature, and in-medium modifications of particles, such as ρ and heavy flavor quarks which may have a possible link to chiral symmetry restoration.

Figure 4 (left) shows the di-electron excess spectra with hadronic cocktail subtracted and acceptance corrected for 0-80% Au+Au collisions at 200 and 19.6 GeV[11]. The result of 19.6 GeV is compared with model calculations incorporating a broadened ρ spectral function and thermal dilepton rates in the QGP and hadron-gas (HG) phases convoluted with a fireball evolution [12]. The model can describe the low mass region of dielectron spectra over a wide range of energies at STAR quite well. The integrated yields of low mass dielectrons is sensitive to the lifetime of the hot medium. The yield would be larger if the medium interaction lasts longer. Therefore, we compare the yields of dilepton excess scaled by charged particle density to the theoretical lifetimes that are used to calculate the dielectron spectra in the model [13]. It shows fair consistency in the right frame of Fig. 4, which might indicate the longer lifetime in central than that in peripheral Au+Au collisions. However, the deviation is only about 2σ. More data are needed in further studies.

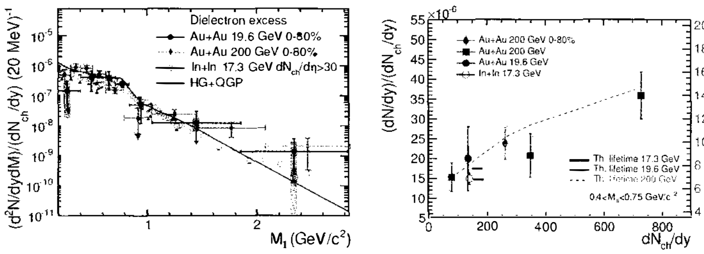

Figure 4 – Left: Dielectron excess invariant mass spectra in 0-80% Au+Au at 19.6 and 200 GeV. Right: Integrated yields of the normalized dilepton excesses as a function of dN_{ch}/dy.

3 Summary and outlook

STAR has produced many important results from the Beam Energy Scan program at RHIC. Freeze-out parameters, collective motions, net-proton higher moments and dielectron production have been shown. There are non-monotonic behaviors observed for directed flow v_1 and higher moments of net-proton. In the future, a BES phase II at RHIC with increased luminosity and upgraded detectors will improve statistical and systematic uncertainties of current measurements.

References

1. J. Adams et al. (STAR Collaboration), Nucl. Phys. **A 757**, 102 (2005), nucl-ex/0501009.
2. A. Andronic, P. Braun-Munzinger, and J. Stachel, Nucl. Phys. **A 772**, 167 (2006), nucl-th/0511071; J. Cleymans and K. Redlich, Phys. Rev. **C 60**, 054908 (1999), nucl-th/9903063; F. Becattini, J. Manninen, and M. Gazdzicki, Phys.Rev. **C 73**, 044905 (2006), hep-ph/0511092.
3. Y. Aoki, G. Endrodi, Z. Fodor, S. Katz, and K. Szabo, Nature **443**, 675 (2006), hep-lat/0611014; M. Cheng, N. Christ, S. Datta, J. van der Heide, C. Jung, et al., Phys.Rev. **D 77**, 014511 (2008), 0710.0354.
4. M. Asakawa and K. Yazaki, Nucl.Phys. **A 504**, 668 (1989); A. Barducci, R. Casalbuoni, S. De Curtis, R. Gatto, and G. Pettini, Phys.Lett. **B 231**, 463 (1989); A. Barducci, R. Casalbuoni, S. De Curtis, R. Gatto, and G. Pettini, Phys. Rev. **D 41**, 1610 (1990).
5. A. Andronic et al., Nucl. Phys. **A 834**, 237 (2010); J. Cleymans et al., Phys. Rev. **C 73**, 034905 (2006).
6. J. Brachmann et al., Phys. Rev. **C 61**, 024909 (2000); L. P. Csernai *et al.*, Phys. Lett. **B 458**, 454 (1999); H. Stocker, Nucl. Phys. **A 750**, 121 (2005).
7. L. Adamczyk *et al.,* Phys. Rev. Lett. **112**, 162301 (2014).
8. L. Adamczyk *et al.,* Phys. Rev. Lett. **110**, 142301 (2013).
9. J.C. Dunlop, M.A. Lisa, P. Sorensen, Phys. Rev. **C 84** (2011) 044914.
10. X. Luo, for the STAR Collaboration, arXiv:1503.02558.
11. L. Adamczyk et al., arXiv:1501.0534.
12. R. Rapp, J. Wambach, H. van Hees, arXiv:0901.3289v1 [hep-ph]; R. Rapp, Phys. Rev. C 63 (2001) 054907.
13. R. Rapp and H. van Hees, arXiv: 1411.4612.

HARD PROBES AT ATLAS

V.N. POZDNYAKOV for the ATLAS Collaboration
Joint Institute for Nuclear Research, Veksler and Baldin Laboratory of High Energy Physics, Joliot-Curie 6, 141980 Dubna, Moscow region, Russia

Recent experimental results on hard probes in Pb+Pb and p+Pb collisions from the ATLAS Collaboration at the LHC are presented. They include electroweak boson production in Pb+Pb where the scaling with nuclear thickness was observed; Z production in p+Pb showing an excess of Z at Pb-direction rapidity; direct modification of the jet fragmentation function in central Pb+Pb events was observed and the nuclear modification factor R_{AA} was measured as 0.8 in peripheral events and 0.5 in central ones.

1 Introduction

Ultra-relativistic heavy-ion collisions at the Large Hadron Collider (LHC) provide a fruitful tool to study dense matter created at extreme temperatures. It is expected that strongly interacting matter takes the state of quark-gluon plasma (QGP) and the partons generated in hard-scattering processes during the initial stages of nuclear collisions have to lose their energy when passing through the QGP. Both RHIC and LHC experiments have observed a suppression of charged hadron yields at high transverse momenta in heavy-ion collisions and jet suppression as well [1]. The ATLAS experiment [2] has an extensive heavy-ion program to take advantage of this opportunity.

The LHC carried out two Pb+Pb runs which took place in 2010 and 2011 at $\sqrt{s_{NN}}$=2.76 TeV per colliding nucleon pair and one p+Pb run in 2013 at $\sqrt{s_{NN}}$=5.02 TeV.

Results on heavy-ion collision studies are presented in terms of event centrality which reflects the overlap volume (impact parameter) of the two colliding nuclei. Collisions with a small (large) impact parameter are referred to as central (peripheral). The overlap volume is closely related to the average number of participant nucleons which scatter inelastically in each nuclear collision, $\langle N_{part} \rangle$, and to the average number of binary collisions between the nucleons of the colliding nuclei, $\langle N_{coll} \rangle$. Equivalently, $\langle N_{coll} \rangle$ may be defined as the average nuclear thickness function, $\langle T_{AA} \rangle$, multiplied by the total inelastic pp cross section. Glauber model calculations relate centrality to $\langle N_{part} \rangle$ and $\langle N_{coll} \rangle$, following the procedure described in the paper [3].

This document presents results of the inclusive jet and electroweak boson measurements obtained by the ATLAS experiment. These results give additional insight into behavior of jets in the QGP and confirm that electroweak boson production rates scale with the number of binary collisions.

2 Z and W production in Pb+Pb collisions

An understanding of any phenomenon on the energetic color-charge carriers propagating through a medium produced in the heavy ion collisions requires measuring the unmodified production rates of the particles before they lose energy. The appropriate candidates to perform such measurements are particles that do not interact via the strong force. The ATLAS experiment measured Z [4] and W [5] boson production in Pb+Pb collisions using the lepton decay channels.

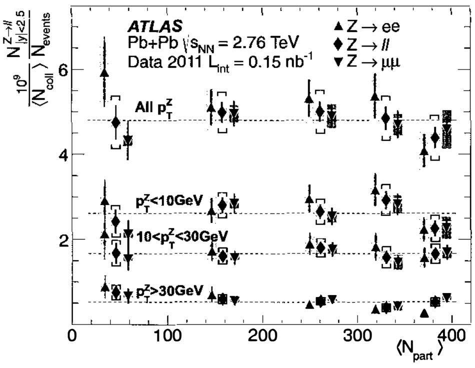

Figure 1 – Centrality dependence of Z boson yields divided by $\langle N_{coll} \rangle$ [4].

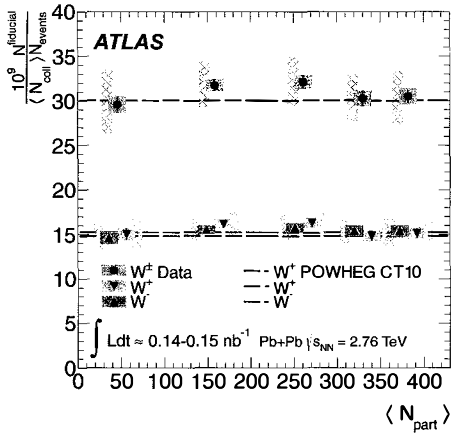

Figure 2 – W boson production yield per binary collision as a function of the mean number of participants $\langle N_{part} \rangle$ for W bosons [5].

To examine the expected binary collision scaling of the data, the Z boson per-event yields, divided by $\langle N_{coll} \rangle$, were measured and shown in Figure 1 as a function of $\langle N_{part} \rangle$, in several p_T^Z bins. It is seen that the electron and muon decay modes are consistent within their uncertainties for all p_T^Z and centrality regions. Within the statistical significance of the data sample, the Z boson per-event yield obeys binary collision scaling.

Figure 2 presents the W boson production yield per binary collision for each charge separately as well as inclusively as a function of $\langle N_{part} \rangle$ for the combined data. Comparisons to QCD NLO predictions [6] are also shown. The NLO predictions are consistent with the data for both the charge ratio and production yields.

3 Z production in p+Pb interactions

The study of p+Pb collisions is utilized at the LHC in order to differentiate between initial and final state effects in heavy-ion collisions under the assumption that the hot and dense QCD state cannot be formed in such collisions and all measured effects on the particles should originate from the initial state of the nucleus. This assumption was challenged by the very first results from p+Pb collisions at $\sqrt{s_{NN}}$ = 5.02 TeV produced by the LHC in 2012.

The study of the Z boson production in p+Pb collisions is a way to compare the initial state effects between the p+Pb and Pb+Pb collisions. The yields of Z bosons measured as function of their transverse momentum and rapidity are sensitive to any initial state nuclear effects.

The ATLAS experiment measured rapidity differential cross-section [7] shown in Figure 3 alongside the baseline model with Z boson production modeled via the incoherent superposition of many nucleon-nucleon collisions. Unlike the model, the data are not symmetric about the centre of mass, but express a relative excess at backward (Pb-going beam direction) rapidity. CT10 PDF [6] expectations shown in Figure 3 are scaled to have the total cross-section predicted by MSTW2008 PDF [8] at NNLO. This asymmetry in central events (not shown here) is more pronounced than in peripheral events which are roughly symmetric.

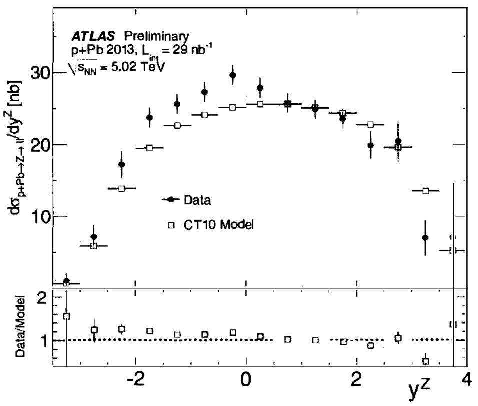

Figure 3 – The $d\sigma/dy$ distributions for $Z \rightarrow l^+l^-$ in the data compared with CT10 [7]. The lower panel is their ratio. The bars indicate statistical uncertainty and the shaded boxes systematic uncertainty.

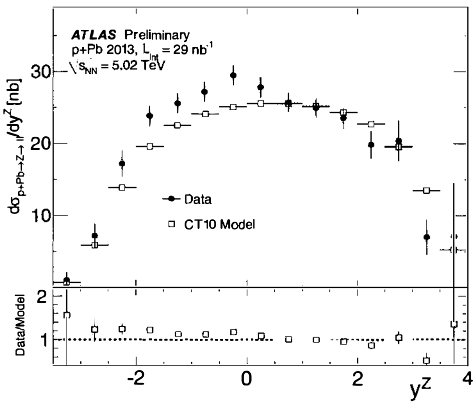

Figure 4 – Jet R_{AA} as a function of jet p_T [9]. The fractional luminosity and $\langle T_{AA} \rangle$ uncertainties are indicated separately by shaded boxes. The boxes, bands and error bars indicate uncorrelated and correlated systematic and statistical uncertainties, respectively.

4 Nuclear modification factor for jets in Pb+Pb interactions

Hard scattering processes occurring in hadron collisions produce high transverse momentum partons. In case of heavy-ion collisions, partons propagate through the produced medium and lose their energy. This results in so-called jet quenching phenomenon. The partonic energy loss can be probed through jet production rate suppression relative to *pp* collisions, where there are no quenching effects. Hard scattering rates are enhanced in central collisions - the larger nuclei overlap results in a higher integrated luminosity of partons able to participate in hard scattering processes. Thus these hard scattering rates are expected to be proportional to the nuclear overlap function.

The suppression is quantified by the nuclear modification factor R_{AA} - the ratio of the jet yield in heavy-ion collisions to that in *pp* interactions divided by total number of heavy-ion events and average nuclear thickness function $\langle T_{AA} \rangle$.

The measured jet R_{AA} as a function of jet p_T is shown in Figure 4 for different domains of collision centrality and jet rapidity [9]. In most central events (0-10% of event centrality) and along all jet rapidity intervals, the R_{AA} is around 0.5, that is the jets are suppressed by factor two. The jet nuclear modification factor, obtained from these measurements shows a weak rise with jet p_T and a slope that varies with collision centrality, while no significant slope is observed in the most peripheral collisions.

5 Inclusive jet charged particle fragmentation functions in Pb+Pb collisions

Jet quenching effect can both soften the spectrum of the momentum of hadrons inside the jet and decrease the total energy of the reconstructed jet. A description of jet quenching phenomenon requires measurements of both the single-jet suppression (shown in previous section) and the jet fragments.

The ATLAS experiment measured the jet fragmentation function $D(p_T)$ [10] for the charged-particles with the transverse momentum above 2 GeV produced within an angular range $\Delta R = 0.4$. Here, $\Delta R = \sqrt{\Delta\phi^2 + \Delta\eta^2}$ where $\Delta\phi$ ($\Delta\eta$) is the difference in azimuthal angles (pseudorapidities) between the charged particle and jet direction.

Figure 5 shows ratios of $D(p_T)$ distributions for the events from six centrality bins to those in the peripheral, 60-80% centrality bin. Jets used for the fragmentation measurements presented

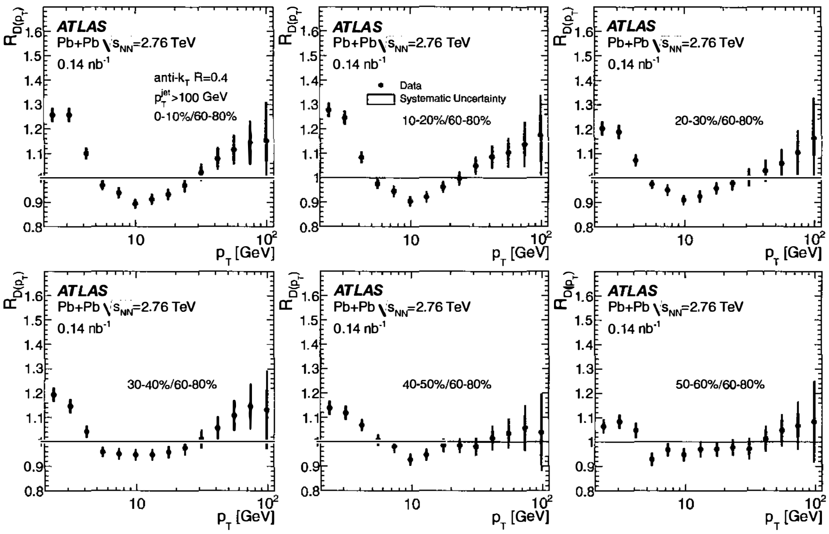

Figure 5 – Ratios of unfolded D($p_{\rm T}$) distributions in different collision centrality bins to those in peripheral (60-80%) collisions, D($p_{\rm T}$) $|_{\rm cent}$ / D($p_{\rm T}$) $|_{60-80}$, for R = 0.4 jets [10]. The error bars on the data points indicate statistical uncertainties while the yellow shaded bands indicate systematic uncertainties.

here were required to have $p_{\rm T}^{\rm jet}$ > 100 GeV and they were reconstructed by anti-k$_T$ algorithm with distance parameter value R=0.4. The ratios in Figure 5 show an enhancement at low p_T, a suppression at intermediate $p_{\rm T}$, and an increase above one at large $p_{\rm T}$ of the charged particles.

In summary, this paper presents the ATLAS experiment results for the electroweak boson production in Pb+Pb where the scaling with nuclear thickness was observed; Z production in p+Pb showing the scaling with $\langle T_A \rangle$ and an excess of Z at Pb-direction rapidity was found; direct modification of the jet fragmentation function in central Pb+Pb events was observed and nuclear modification factor R_{AA} was measured to be 0.8 in peripheral events and 0.5 in central ones.

References

1. PHENIX Collaboration, S.S. Adler *et al.* Phys. Rev. Lett. **93** (2004) 152302; ATLAS Collaboration, Phys. Lett. **B697** (2011) 294; CMS Collaboration, Eur. Phys. J. **C72** (2012) 1945.
2. ATLAS Collaboration, JINST **3** (2008) S08003.
3. ATLAS Collaboration, Phys. Lett. **B710** (2012) 363.
4. ATLAS Collaboration, Phys. Rev. Lett. **110** (2013) 022301.
5. ATLAS Collaboration, Eur. Phys. J. **C75** (2015), 23.
6. H.-L. Lai *et al.*, Phys. Rev. D82, 074024 (2010).
7. ATLAS Collaboration, *Z boson production in p+Pb collisions at* $\sqrt{s_{NN}} = 5.02$ *TeV with the ATLAS detector at the LHC*, ATLAS-CONF-2014-020 (2014). http://cds.cern.ch/record/1702971.
8. A. Martin, W. Stirling, R. Thorne, and G. Watt, Eur. Phys. J.C 63 (2009) 189.
9. ATLAS Collaboration, Phys. Rev. Lett. **114** (2015) 072302.
10. ATLAS Collaboration, Phys. Lett. **B739** (2014) 320.

Flow measurements in p+Pb and their comparison with Pb+Pb at ATLAS

Krzysztof W. Wozniak on behalf of the ATLAS Collaboration
Institute of Nuclear Physics, PAS, ul. Radzikowskiego 152, 31-342 Krakow, Poland

Particle anisotropic flow observed in the collisions of heavy nuclei is one of the signals of creation of the Quark-Gluon Plasma. The analysis of p+Pb collisions at $\sqrt{s_{\mathrm{NN}}} = 5.02$ TeV provides an opportunity to study the interactions between nucleons in a much smaller volume, but unlike the pp collisions, affected by nuclear effects. This report describes measurements of flow harmonics, v_1 to v_4, and their dependence on event centrality and particle transverse momentum.

1 Introduction

In the collisions of heavy nuclei a large energy is released in a relatively small volume, comparable with the overlap of the nuclei. Strong interactions of partons in the resulting Quark-Gluon Plasma lead to collective expansion of the system. The initial shape of the volume is reflected in the correlations between produced particles. In the p+Pb collisions the overlap volume is small and the creation of a QGP is thus not expected, but effects of collisions of the incoming proton with more than one nucleon are present. This allows the study of particle production and correlations in a system more complicated than that in pp collisions.

In 2012 and 2013, the Large Hadron Collider provided the p+Pb collisions at the energy of $\sqrt{s_{\mathrm{NN}}} = 5.02$ TeV which were measured using the ATLAS detector [?]. Charged particles are reconstructed in the $|\eta| < 2.5$ range in the Inner Detector comprised of several layers of silicon pixel sensors and silicon strips sensors surrounded by the Transition Radiation Tracker. The centrality of the collision is determined using signals from Forward Calorimeters (FCal), covering $3.1 < |\eta| < 4.9$, but in the presented p+Pb studies the total reconstructed number of charged-particle tracks is also used to characterize the event activity.

The particle anisotropic flow is studied using the Fourier expansion of the distribution of the azimuthal angle of tracks relative to the event plane. In the case of p+Pb events with relatively low multiplicities equivalent methods based on two- or more particle correlations are more appropriate. For pairs of particles, the coefficients $v_{n,n}$ are defined according to the formula:

$$\mathrm{d}N_{\mathrm{pairs}}/\mathrm{d}\Delta\phi \sim 1 + \sum 2v_{n,n}^2 \cos(n\Delta\phi) \tag{1}$$

where $\Delta\phi$ is the difference between the azimuthal angles of particles forming a pair. The coeficients $v_{n,n}$ depend on the transverse momenta, $p_{\mathrm{T}}^{\mathrm{a}}$ and $p_{\mathrm{T}}^{\mathrm{b}}$, of the particles in the pair. In the absence of non-flow effects they are related to the flow harmonics, v_n, by the formula:

$$v_{n,n}(p_{\mathrm{T}}^{\mathrm{a}}, p_{\mathrm{T}}^{\mathrm{b}}) = v_n(p_{\mathrm{T}}^{\mathrm{a}})v_n(p_{\mathrm{T}}^{\mathrm{b}}). \tag{2}$$

In p+Pb collisions, the correlations originating from jets, mini-jets and resonance decays dominate. Their contribution is the largest for pairs close in pseudorapidity, thus in the analysis the pairs with $|\Delta\eta| < 2$ are excluded. In addition, it is necessary to subtract the remaining recoil component, estimated from the most peripheral collisions [?].

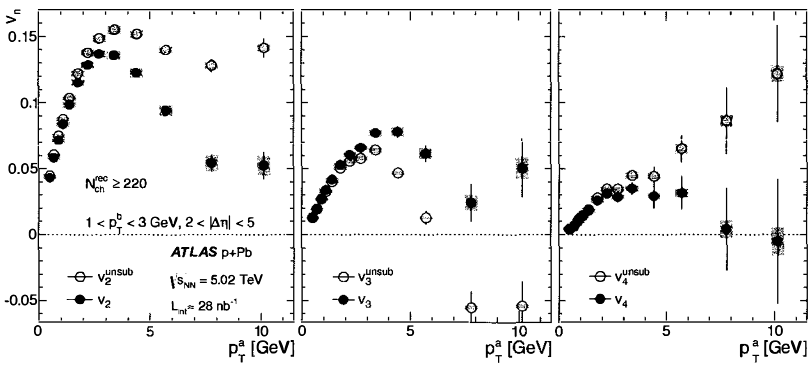

Figure 1 – The Fourier harmonics v_n, $n = 2 - 4$, as a function of p_T^a, obtained for the central collisions with $N_{ch}^{rec} \geq 220$ from the correlation functions before (open circles) and after (full circles) recoil subtraction [?]. Only particle pairs with $|\Delta\eta| > 2$ and $1 < p_T^b < 3$ with varying p_T^a were used. The statistical and systematic uncertainties are shown as error bars and shaded boxes, respectively.

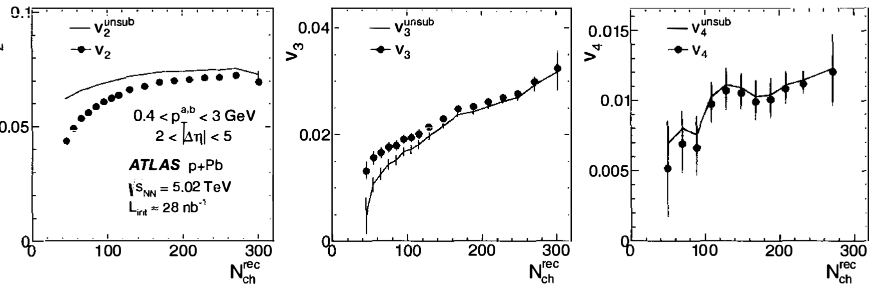

Figure 2 – The centrality dependence of v_n, $n = 2 - 4$, represented as a function of the number of reconstructed charged particles, N_{ch}^{rec}, for particle pairs with $0.4 < p_T^{a,b} < 3$ and $2 < |\Delta\eta| < 5$. The v_n values before and after recoil subtraction [?] are shown as lines and symbols, respectively. The statistical and systematic uncertainties of v_n are presented separately as error bars and shaded boxes, while in the case of v_n^{unsub} only the total combined error is shown.

2 Results

The largest anisotropic flow in p+Pb collisions is observed in the most central events, characterized by the highest activity, and selected according to the transverse energy registered in the Forward Calorimeters in the Pb-going side of the ATLAS detector, ΣE_T^{Pb}, or the multiplicity of reconstructed charged particles, N_{ch}^{rec}. The dependence of the flow harmonics on the transverse momentum for such events is shown in Fig. ??. The harmonics increase with p_T reaching a maximum at 3-4 GeV. In this region the results obtained with and without recoil subtraction start to deviate significantly. The corrected coefficients decrease for large p_T, while the v_n^{unsub} without recoil subtraction do not follow a common pattern: v_2^{unsub} values do not change much for large p_T, v_3^{unsub} decreases rapidly while v_4^{unsub} continues the increasing trend. The maximal values of the corrected v_n are decreasing with n.

The magnitude of the flow harmonics can be studied after integration over the $0.4 < p_T < 3$ GeV range where the uncertainties of the recoil subtraction are the smallest. Such integrated v_2, v_3 and v_4 values as a function of event multiplicity are presented in Fig. ??. All flow harmonics

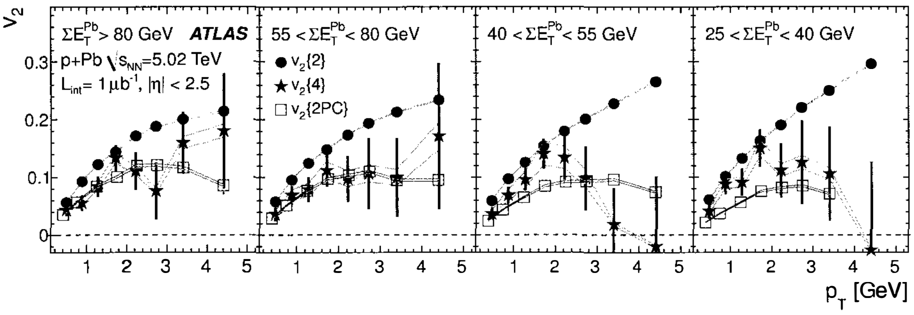

Figure 3 – The elliptic flow calculated from the two-particle correlations, $v_2\{2\mathrm{PC}\}$ (squares), using the two-particle cumulants, $v_2\{2\}$ (circles), and four-particle cumulants, $v_2\{4\}$ (stars), as a function of transverse momentum in four different activity intervals ?. $v_2\{2\mathrm{PC}\}(p_\mathrm{T}^\mathrm{a})$ was obtained after integrationg over $0.5 < p_\mathrm{T}^\mathrm{b} < 4$ GeV. The statistical and systematic uncertainties are shown as error bars and shaded boxes, respectively.

shown there increase with event centrality, the strongest increase is observed for v_3, while v_2 seems to saturate at the largest multiplicities.

The elliptic flow calculated from two-particle correlations, $v_2\{2\mathrm{PC}\}$, is compared in Fig. ?? with those from the cumulants method ($v_2\{2\}$ and $v_2\{4\}$) ? for several centrality classes (in this case selected according to the value of the transverse energy registered in the Forward Calorimeter on the Pb-going side, $\Sigma E_\mathrm{T}^\mathrm{Pb}$). $v_2\{2\}$, which contains non-flow contributions from two-particle correlations, is much larger than $v_2\{2\mathrm{PC}\}$ and $v_2\{4\}$. Similar values of $v_2\{2\mathrm{PC}\}$ and $v_2\{4\}$ confirm that two-particle correlations are predominantly short-range and can be suppressed either by neglecting pairs with $|\Delta\eta| < 2$ in $v_2\{2\mathrm{PC}\}$ or explicitly in $v_2\{4\}$.

The comparison of flow harmonics in p+Pb collisions at $\sqrt{s_\mathrm{NN}} = 5.02$ TeV and Pb+Pb collisions ? at $\sqrt{s_\mathrm{NN}} = 2.76$ TeV, for events with similar multiplicities ?, needs to account for the energy difference between these data. The mean transverse momentum is lower in the latter case so, for the comparison, the p_T in Pb+Pb collisions has to be rescaled and $v_n(p_\mathrm{T}/1.25)$ has to be used ?. After that a very good agreement of $v_3(p_\mathrm{T})$ is reached, while for $v_2(p_\mathrm{T})$ and $v_4(p_\mathrm{T})$ an additional scaling of the magnitude of flow harmonics from Pb+Pb collisions by a factor of 0.66 is necessary ?. This larger magnitude in the peripheral Pb+Pb collisions used for comparison is due to the elongation of the overlap area of nuclei that is not present in p+Pb collisions.

The dipolar flow, v_1, is studied separately, as it has quite different characteristics than the other harmonics. The $v_{1,1}^\mathrm{unsub}$ coefficient before recoil subtraction has negative values (Fig. ??, left panel). The correction introduces substantial changes, especially for large p_T^a and p_T^b, for which the initially negative coefficients become positive (Fig. ??, right panel). The $v_{1,1}(p_\mathrm{T}^\mathrm{a})$ dependences have very different slopes (both negative and positive) for different p_T^b ranges. However, $v_{1,1}$ always changes sign at the same value of $p_\mathrm{T}^\mathrm{a} \approx 1.5$ GeV. The dependence on p_T^b range disappears in the dipolar flow, v_1, calculated as

$$v_1(p_\mathrm{T}^\mathrm{a}) = v_{1,1}(p_\mathrm{T}^\mathrm{a}, p_\mathrm{T}^\mathrm{b}) \;/\; v_1(p_\mathrm{T}^\mathrm{b}) \tag{3}$$

where

$$v_1(p_\mathrm{T}^\mathrm{b}) = \pm\sqrt{|v_{1,1}(p_\mathrm{T}^\mathrm{b}, p_\mathrm{T}^\mathrm{b})|} \tag{4}$$

with the positive sign of $v_1(p_\mathrm{T}^\mathrm{b})$ for $p_\mathrm{T}^\mathrm{b} > 1.5$ GeV and negative otherwise. In Fig. ??, left panel, one can see that for events with largest multiplicities, $N_\mathrm{ch}^\mathrm{rec} \geq 220$, for all p_T^b ranges the $v_n(p_\mathrm{T}^\mathrm{a})$ values are very similar. There is also no indication on any dependence of $v_1(p_\mathrm{T}^\mathrm{a})$ on event multiplicity, at least for $N_\mathrm{ch}^\mathrm{rec} \geq 140$ (Fig. ??, right panel). The absolute values and properties of v_1 in p+Pb collisions $\sqrt{s_\mathrm{NN}} = 5.02$ TeV are very similar to those for Pb+Pb collisions ? at

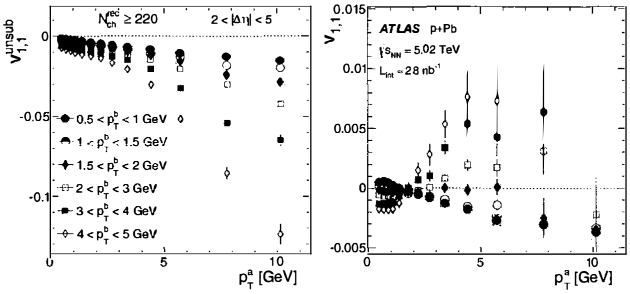

Figure 4 – The first-order harmonic of two-particle correlations, $v_{1,1}$, before (left panel) and after (right panel) recoil subtraction, as a function of p_T^a obtained for the central events with $N_{ch}^{rec} \geq 220$ using different p_T^b ranges [?]. The statistical and systematic uncertainties are shown as error bars and shaded boxes, respectively.

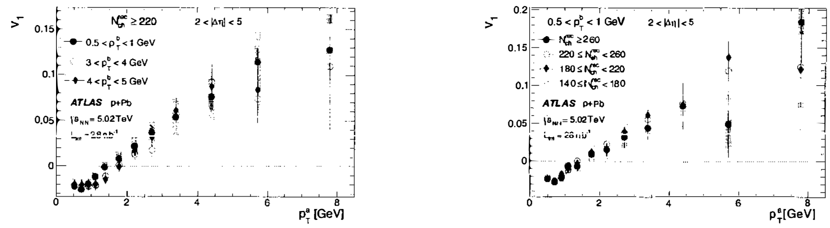

Figure 5 – The dipolar flow, v_1, as a function of p_T^a [?]: (left panel) for events with $N_{ch}^{rec} \geq 220$, in several different p_T^b ranges and (right panel) for events with different multiplicities in the single range $0.5 < p_T^b < 1$. The statistical and systematic uncertainties are shown as error bars and shaded boxes, respectively.

$\sqrt{s_{NN}}$ = 2.76 TeV, only the p_T value at which v_1 crosses zero is slightly lower, due to lower energy of Pb+Pb collisions.

3 Summary

In two-particle correlations analysis of the p+Pb collisions at $\sqrt{s_{NN}}$ = 5.02 TeV significant long-range correlations are observed. The v_2, v_3 and v_4 coefficients increase with event multiplicity, while the magnitude of the v_n decreases with n. There is a remarkable similarity of the p_T dependence of these harmonics in p+Pb and Pb+Pb collisions with similar multiplicities. The dipolar flow coefficient v_1 increases approximately linearly with p_T crossing zero at $p_T \sim 1.5$ GeV.

Acknowledgments

This work was supported in part by the National Science Center grants DEC-2011/03/B/ST2/02631, DEC-2013/08/M/ST2/00320 and by PL-Grid Infrastructure.

References

1. ATLAS Collaboration, *JINST* **3**, S08003 (2008).
2. ATLAS Collaboration, *Phys. Rev.* C **90**, 044906 (2014).
3. ATLAS Collaboration, *Phys. Lett.* B **725**, 60 (2013).
4. ATLAS Collaboration, *Phys. Rev.* C **86**, 014907 (2012).
5. G. Basar and D. Teaney, arXiv:1312.6770 [nucl-th].

Soft physics and collective phenomena in p–Pb collisions from ALICE

E. Leogrande, on behalf of the ALICE Collaboration
Universiteit Utrecht, The Netherlands
emilia.leogrande@cern.ch

New ALICE results concerning soft physics and collective phenomena in p–Pb collisions at $\sqrt{s_{NN}} = 5.02$ TeV are briefly discussed. First, the particle-multiplicity dependence of the flow coefficients v_2 and v_3 derived via multiparticle cumulants is reviewed. Then, results on the multiplicity dependence of jet-like two-particle correlation structures are shown. Finally, p–Pb femtoscopic radii of the pion-emitting source are compared with different colliding systems, such as pp and Pb–Pb.

1 Introduction

Heavy-ion collisions have provided striking evidences for the existence of collective phenomena involved in particle production [1]. Sources of collectivity can be several: a common source of produced particles, rescattering between constituents and/or hydrodynamics. The latter seems rather successful in describing heavy-ion results.
Lately, collective phenomena have been investigated also in p–Pb collisions. Given the multiplicity reached in this collision system (high multiplicity p–Pb is comparable to peripheral Pb–Pb), the "fireball" (if present) is expected to be small. Initial state fluctuations, then, are foreseen to play an important role.
Surprisingly, p–Pb and Pb–Pb collisions have revealed interesting similarities. As first astonishing results, the double ridge [2,3,4] and the mass ordering of the v_2 of pions, kaons and protons [5] from two-particle correlations have raised the question whether collective effects are also present in such small systems.
New measurements from ALICE investigating the multiplicity dependence of soft physics observables in p–Pb collisions are presented in these proceedings: flow coefficients v_2 and v_3 from multiparticle cumulants [6] (2), jet-like two-particle correlations [8] (3) and femtoscopic radii of the pion-emitting source [13,14] (4).

2 Multiplicity dependence of flow coefficients v_2 and v_3

As collectivity is a correlation between many particles, multi-particle correlation methods are used to investigate it. Multi-particle azimuthal correlations, though, also contain contributions from jets and resonances. An effective approach to reduce such contributions is the use of multi-particle cumulants $c_n\{m\}$ [a], which can be qualitatively depicted as standard correlators averaged over all the events. The effectiveness of this approach increases with a higher number of correlated particles m, since all non-flow contributions up to $m-1$ are removed, and/or with a larger pseudo-rapidity gap between them.

[a] n is the order, m is the number of correlated particles.

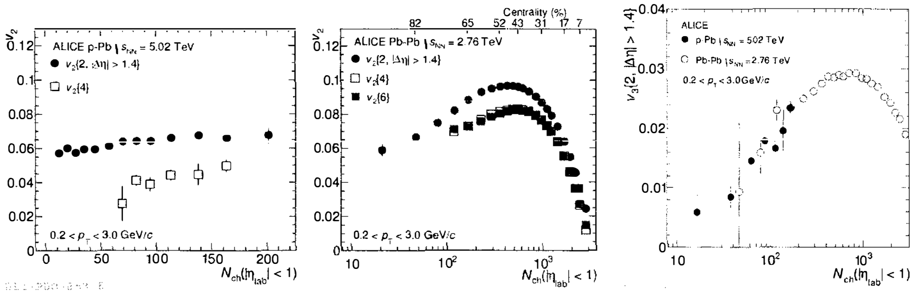

Figure 1 – Midrapidity multiplicity dependence of v_2 in p–Pb (left) and in Pb–Pb (middle) and v_3 (right) in p–Pb and Pb–Pb.[6]

From the cumulants, one can directly calculate the flow coefficients [7]: for instance, the relationship between the second-order two-particle cumulant and the elliptic flow is $v_2\{2\} = \sqrt{c_2\{2\}}$.

Figure 1 shows the v_2 in p–Pb (left panel) and Pb–Pb (middle panel) and the v_3 (right panel) in p–Pb and Pb–Pb as a function of midrapidity ($|\eta_{lab}| < 1$) charged particle multiplicity in the range $0.2 < p_T < 3.0$ GeV/c. As expected, the $v_2\{4\}$ values are systematically lower than the $v_2\{2\}$ ones, since non-flow contributions up to the third order are removed. A first remarkable observation is the agreement between $v_2\{4\}$ and $v_2\{6\}$ in Pb–Pb collisions, supporting the picture of collectivity. We then observe that $v_2\{2\}$ and $v_2\{4\}$ in p–Pb are smaller that $v_2\{2\}$ and $v_2\{4\}$ in Pb–Pb at similar multiplicities. On the contrary, v_3 does not differ between p–Pb and Pb–Pb in the overlapping multiplicity region. This would suggest that the v_3 could be mainly dominated by a common physics process in the two collision systems.

3 Multiplicity dependence of jet-like two-particle correlations

The long-range two-particle correlations in p–Pb collisions have been extensively studied [2,5]. However, useful information for the physical interpretation of the double-ridge structure comes also from the jet-like structure, which emerges in both long- and short-range correlations. Jet-like two-particle correlations create a peak in the near side ($\Delta\varphi$=0,$\Delta\eta$=0) and an elongated structure in $\Delta\eta$ in the away side ($\Delta\varphi = \pi$). Therefore, to extract these jet-like contributions in the near side it is enough to apply a $\Delta\eta$ cut and to subtract the long-range ($1.2 < |\Delta\eta| < 1.8$) from the short-range ($|\Delta\eta| < 1.2$) correlations. On the away side, though, the jet- and ridge-like contributions are mixed together. However, one can mirror the near-side long-range correlations in the away-side and subtract them from the total correlations in the away-side. The underlying assumption is that the double ridge is symmetric around $\Delta\varphi = \pi/2$. The effects due to the non-symmetric v_3 affect the away side only. The yields of the jet-like peaks extracted using this technique are then studied as a function of multiplicity.

A useful way of characterizing the multiplicity is by classifying events according to multiplicity classes, which are defined as percentile intervals of the multiplicity distribution measured with a specific detector [9]. The $0-5\%$ class corresponds to the highest multiplicity, while the $95-100\%$ to the lowest one.

In Fig. 2 the near-side per-trigger yield evaluated in $0.7 < p_{T,assoc} < p_{T,trig} < 5$ GeV/c is presented as a function of multiplicity class measured with the forward detector V0-A [10]. The red points are obtained after the aforementioned subtraction of long-range correlations is performed. Their flatness in $0-60\%$ can be interpreted as if higher multiplicity events are not built up by a higher number of associated particles per trigger particle (i.e. per minijet[b]), but rather by a

[b]Minijets are jets in the low-p_T region, where QCD is non perturbative.

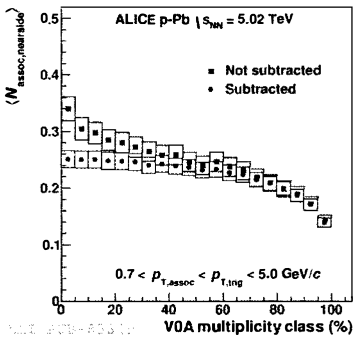

Figure 2 – Multiplicity dependence of per-trigger jet-yields with (red points) and without (black points) long-range correlation subtraction.[8]

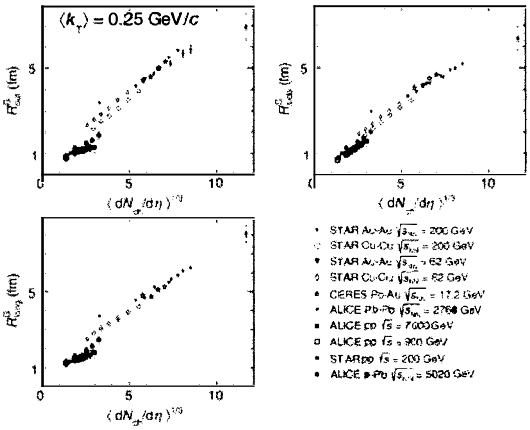

Figure 3 – Femtoscopic radii in three directions (*out, side, long*) as a function of the cube root of the measured charged-particle multiplicity density for many collision energies and systems.[13]

higher number of minijets per event. This is compatible with a model of minijets stemming from incoherent fragmentation of multiple parton interactions (MPIs). The black points, instead, are obtained if the long-range correlations are also included and they show an increasing trend with multiplicity. Thus, this is a possible hint of a different physical origin for jet- and ridge-like phenomena.

4 Femtoscopic radii of the pion-emitting source

One of the observables characterizing the bulk collective system is the size of the particle-emitting region at freeze-out, which can be extracted for pions from femtoscopic techniques [11,12].
Two-pion correlation functions are extracted [13] as a function of the momentum difference of the pair $\mathbf{q}$ in three different directions (*long* along the beam axis, *out* along the pair transverse momentum, *side* perpendicular to the other two). Femtoscopic effects become important for $\mathbf{q}$ below 0.4 GeV/c.
The radii extracted with a Gaussian fit of the correlation functions in the three directions are shown in Fig. 3 as a function of $\langle dN_{ch}/d\eta\rangle^{1/3}$, since it has been observed that they scale roughly

with the cube root of the measured charged-particle multiplicity density for many collision energies and initial system sizes. In fact, the pp, p–Pb and Pb–Pb radii evolve linearly with it, but with a significantly different scaling. The p–Pb radii agree with the pp ones at low multiplicities, but they diverge at higher multiplicities. Consistent results are found with a three-pion cumulants analysis [14], where radii in p–Pb are observed to be 5-15% higher than in pp and 35-55% lower than in Pb–Pb.

5 Conclusions

The soft physics observables in p–Pb collisions measured by ALICE add new information for the interpretation of results such as the double ridge in two-particle correlations, and in general for addressing the question whether collectivity is formed in such small systems. The multiparticle cumulants method has proven to be very effective in isolating genuine correlations among many particles. At similar multiplicity, the elliptic flow v_2 obtained in p–Pb is observed to be smaller than in Pb–Pb, while the triangular flow v_3 overlap, suggesting for the latter a common physics process in the two collision systems. A study of the jet-like correlations above the double ridge and of the minijet-yield evolution with multiplicity has shown that jet- and ridge-like phenomena likely arise from different physical mechanisms and are additive. This analysis also allows for a better characterization of the particle production in terms of minijets and multiple parton interactions. Finally, femtoscopic techniques grant the possibility of estimating the size of the source of pion emission and of comparing it among different collision energies and systems. In p–Pb, it is found to be larger than in pp, though comparable at low multiplicities, and smaller than in Pb–Pb. The combination of these results provide a strong challenge and constraints for theoretical models.

References

1. U. W. Heinz and R. Snellings, *Annu. Rev. Part. Sci. 63* (2013) 123-151.
2. ALICE Collaboration, *Phys. Lett.* B **719**, 29 (2013).
3. CMS Collaboration, *Phys. Lett.* B **718**, 795 (2013).
4. ATLAS Collaboration, *Phys. Rev. Lett.* **110**, 182302 (2013).
5. ALICE Collaboration, *Phys. Lett.* B **726**, 164 (2013).
6. ALICE Collaboration, *Phys. Rev.* C **90**, 054901 (2014).
7. A. Bilandzic, R. Snellings and S. Voloshin, *Phys. Rev.* C **83**, 044913 (2011).
8. ALICE Collaboration, *Phys. Lett.* B **741**, 38 (2014).
9. ALICE Collaboration, arXiv:1412.6828 (2014).
10. ALICE Collaboration, *JINST* **3**, S08002 (2008).
11. R. Lednicky, *Nucl. Phys.* A **774**, 189 (2006).
12. M. Lisa, S. Pratt, R. Soltz, U. Wiedemann, *Annu. Rev. Part. Sci. 55* (2005) 311.
13. ALICE Collaboration, *Phys. Rev.* C **91**, 034906 (2015).
14. ALICE Collaboration, *Phys. Lett.* B **739**, 139 (2014).

PARTON ENERGY LOSS AND PARTICLE PRODUCTION AT HIGH MOMENTA FROM ALICE

R. A. BERTENS for the ALICE collaboration
Institute for Subatomic Physics, Utrecht University
Princetonplein 5, 3508 TA Utrecht, The Netherlands

Partons, produced in the early stages of heavy-ion collisions, lose energy while propagating through the collision medium. This energy loss can be studied by comparing particle yields in different systems (pp, p–Pb, Pb–Pb). In addition, particle yields in different systems can be used to study hadronization mechanisms.

1 Introduction and analysis

The heavy-ion program at ALICE is aimed at studying strongly interacting matter in ultra-relativistic nuclear collisions where the formation of a Quark-Gluon Plasma (QGP), a deconfined state of quarks and gluons, is expected [1]. Hard partons that propagate through this matter are predicted to lose energy via (multiple) scattering and gluon radiation. As a result, p_{T} spectra of final state hadrons and jets will be modified with respect to yields derived from a simple superposition of incoherent proton-proton collisions. This modification, quantified by the *nuclear modification factor*, R_{AA}, is used to study parton energy-loss mechanisms and medium properties. Disentangling energy-loss signatures from initial state nuclear effects which may also modify transverse momentum spectra - such as nuclear PDF shadowing[2] - requires a comparison of the R_{AA} to the nuclear modification factor for proton-nucleus collisions, called R_{pA}. These proceedings give an overview of recent ALICE results on the nuclear modification factor for Pb–Pb collisions as well as p–Pb collisions.

ALICE[3] is a general-purpose heavy-ion experiment at CERN. Its central barrel includes an Inner Tracking System (ITS), Time Projection Chamber (TPC), Transition Radiation (TRD) and Time Of Flight (TOF) detector used for tracking (ITS, TPC) and identification (TPC, TOF, TRD) of charged particles. At high momenta (> 1 GeV/c) identification is complemented by a small acceptance ring imaging Cherenkov detector. Neutral mesons are reconstructed using an electromagnetic calorimeter; muons with a forward muon spectrometer.

The nuclear modification factor R_{AA} is defined as

$$R_{\mathrm{AA}} = \frac{\mathrm{d}^2 N_{\mathrm{AA}}/\mathrm{d}p_{\mathrm{T}}\mathrm{d}\eta}{\langle T_{\mathrm{AA}}\rangle \cdot \mathrm{d}^2\sigma_{\mathrm{pp}}/\mathrm{d}p_{\mathrm{T}}\mathrm{d}\eta} \tag{1}$$

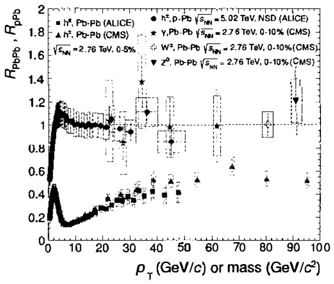

Figure 1 – Chared hadron R_{AA} in central collisions and R_{pA} at mid-rapidity[6].

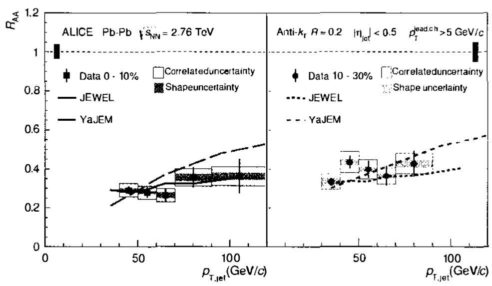

Figure 2 – R_{AA} of $R = 0.2$ full jets in central and mid-peripheral collisions compared energy-loss models[9].

where $d^2N_{AA}/dp_Td\eta$ represents the differential particle yield in nucleus-nucleus collisions and $d^2\sigma_{pp}/dp_Td\eta$ is the cross-section in proton-proton collisions. The nuclear overlap function $\langle T_{AA}\rangle$ is derived from a Glauber model[4] and proportional, in each centrality class, to the number of binary collisions $\langle N_{coll}\rangle$. At high p_T and in the absence of medium effects the R_{AA} is expected to be 1; at low momenta, the spectral shape is dominated by soft processes and such a scaling is not expected to hold[5]. As QGP formation is not predicted in pA collisions, R_{pA} (measured similarly) can be used to disentangle (cold) nuclear effects from QGP effects.

2 R_{AA} and R_{pA} of (identified) particles and jets

Fig. 1 shows the charged particle R_{AA} measured at $\sqrt{s_{NN}} = 2.76$ TeV in central collisions compared to the charged hadron R_{pA} at $\sqrt{s_{NN}} = 5.02$ TeV and the R_{AA} of particles which are *not* sensitive to QCD dynamics (γ, $W^{\pm}$, Z^0). R_{AA} of the γ, $W^{\pm}$ and Z^0 is 1 within uncertainties, confirming the $\langle N_{coll}\rangle$ scaling. The suppression of the charged hadron yield ($R_{AA} < 1$) in Pb–Pb collisions is not seen in p–Pb collisions ($R_{pA} = 1$), which indicates that the suppression in Pb–Pb collisions is a result of final state effects, most likely parton energy loss. Similar behavior is observed in the R_{AA} of jets, shown in Fig. 2. The suppression of the jet yield indicates strong out-of-cone radiation of jet energy for central and semi-central collisions. Comparisons to jet energy-loss models JEWEL[7] and YaJEM[8] show a qualitative agreement (χ^2 of 0.368 and 1.690 respectively[9]) with the data. Models based on gluon saturation[10,11] (Fig 3, top panel) and nPDF shadowing[12,13] (lower panel) predict small initial state nuclear effects at mid-rapidy in p–Pb collisions; this is confirmed by data as the measured R_{pA} is in agreement with unity for $p_T > 4$ GeV/c.

The R_{AA} and p_T spectra of identified particles can be used to study hadronization mechanisms. Fig. 4 show the ratio of proton to pion spectra and kaon to pion spectra in Pb–Pb and pp collisions. For $p_T < 5$ GeV/c the Pb–Pb ratios are strongly enhanced with respect to the pp measurement. This enhancement is consistent with a common velocity boost[14] (radial flow) which leads to a mass-dependent modification of the p_T spectra. The Kraków and EPOS[15,16] models, based on a hydrodynamic collision medium, are in better agreement with the data than the Fries[17] model, which assumes recombination as the dominant hadronization mechanism. In central collisions, the ϕ-meson spectrum (not shown, see[18]) is similar in shape to the proton spectrum, supporting the dominance of radial flow as the ϕ is a meson with a mass close to the proton mass. At high momenta (> 10 GeV/c) the particle ratios in pp and Pb–Pb collisions are equal, indicating vacuum-like hadronization through fragmentation.

Fig. 5 shows the R_{pA} of identified hadrons ($\pi^{\pm}$, $K^{\pm}$, $p\bar{p}$ and $\Xi\bar{\Xi}$, the latter reconstructed in the $\Xi \rightarrow \Lambda + \pi$ channel). For $p_T > 10$ GeV/c the R_{pA} is consistent with unity (and therefore no final state effects); at intermediate momenta however, a mass ordering similar to that in Pb–Pb

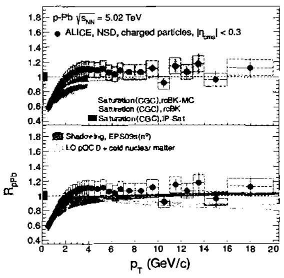

Figure 3 – Charged hadron R_{pA} compared to different models [6].

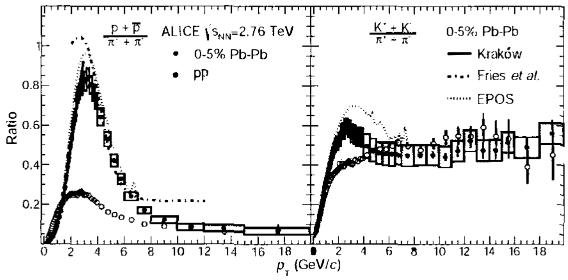

Figure 4 – Particle ratios in pp and central Pb–Pb collisions [14]. Theoretical predictions refer to Pb–Pb collisions.

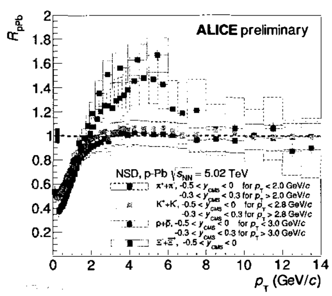

Figure 5 – R_{pA} of identified hadrons at mid-rapidity.

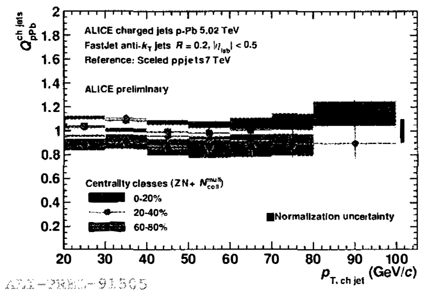

Figure 6 – Q_{pA} of charged $R = 0.2$ jets with the Zero Degree Calorimeter centrality estimate.

collisions is observed, prompting the question of whether or not this ordering is the result of collective behavior in small systems.

3 Centrality dependence in small systems: Q_{pPb}

To characterize dynamics of small systems more precisely, a 'centrality'-dependent nuclear modification factor, Q_{pPb}, is introduced in p–Pb collisions. Multiplicity fluctuates strongly for a given impact parameter [19], leading to a biased Q_{pPb} when centrality and $\langle N_{\mathrm{coll}}\rangle$ are derived directly from the number of tracks in the same η range. This is illustrated in Fig. 7, where such a measurement (points) is compared to a model (lines) comprising incoherent PYTHIA [20] events coupled to Glauber geometry. The observed agreement shows that the centrality dependence of the Q_{pPb} is an artifact of multiplicity fluctuations and *not* a result of nuclear effects.

Separating the centrality determination and the estimate of the $\langle N_{\mathrm{coll}}\rangle$ in η is expected to suppress the bias from multiplicity fluctuations. Fig. 8 shows the Q_{pPb} measured by estimating the centrality via Zero Degree Calorimeters (situated 116 m from the interaction point) and deriving $\langle N_{\mathrm{coll}}\rangle$ from the charged particle multiplicity at mid(left)- or forward(right) rapidities using VZERO scintillators [3]. In both figures, Q_{pPb} shows no centrality dependence and is in agreement with unity above $p_{\mathrm{T}} \approx 10$ GeV/c.. The same is seen in Fig. 6 where Q_{pPb} of jets is shown - the agreement with unity at high p_{T} in all centrality classes confirms that the jet suppression seen in Pb–Pb collisions is a medium effect.

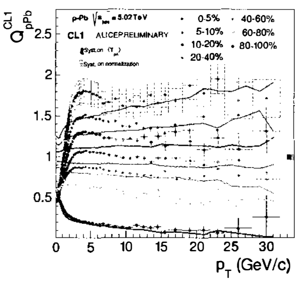

Figure 7 – Q_{pPb} with multiplicity at mid-rapidity as a centrality estimator [19].

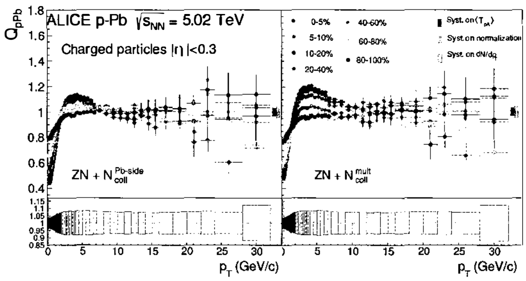

Figure 8 – Q_{pPb} with Zero Degree Calorimeter as centrality estimator for two $\langle N_{coll} \rangle$ estimates [19].

4 Conclusion

The nuclear modification factor of hadrons and jets is measured in Pb–Pb and p–Pb collisions. A strong suppression is observed in Pb–Pb, but not in p–Pb measurements, confirming that partons lose energy in the medium that is formed in the collision. The R_{AA} shows that relative energy loss decreases with increasing parton momenta.

From ratios of identified particle spectra it is concluded that mass rather than recombination determines the shape of spectra at low p_T, whereas at higher p_T fragmentation is likely to be the dominant hadronization mechanism. The R_{pA} of identified hadrons exhibits a mass ordering similar to the one observed in Pb-Pb, raising interesting questions about the observation of collective effects in small systems.

References

1. S.A. Bass, M. Gyulassy, H. Stoecker, W.J. Greiner, *J. Phys.* G **25** (1999)
2. D. de Florian, R. Sassot, *Phys. Rev.* D **69**, 074028 (2004)
3. K. Aamodt *et al.* (ALICE Coll.), *JINST* **3**, S08002 (2008)
4. M. Miller, K. Reygers, S. Sanders, P. Steinberg, *Annu. Rev. Nucl. Part. S.* **57**, 205 (2007)
5. B. Abelev *et al.* (ALICE Coll.) *Phys.Lett.* B **720**, 52-62 (2013)
6. B. Abelev *et al.* (ALICE Coll.) *PRL* **110**, 082302 (2013)
7. K. C. Zapp, *Phys.Lett.* B **735** (2014)
8. T. Renk, *Phys.Rev.* C **88**, 014905 (2013)
9. B. Abelev *et al.* (ALICE Coll.) arXiv:1502.01689 [nucl-ex]
10. P. Tribedy and R. Venugopalan, *Phys. Lett.* B **710**, 125 (2012)
11. J. L. Albacete, A. Dumitru, H. Fujii, and Y. Nara, *Nucl. Phys.* A **897**, 1 (2013)
12. I. Helenius, K. J. Eskola, H. Honkanen, and C. A. Salgado, *JHEP.* **07**, 073 (2012)
13. Z.-B. Kang, I. Vitev, and H. Xing, *Phys. Lett.* B **718**, 482 (2012)
14. B. Abelev *et al.* (ALICE Coll.) *Phys. Lett.* B **736**, 196-207 (2014)
15. P. Bozek, I. Wyskiel-Piekarska, *Phys. Rev.* C **85**, 064915 (2012)
16. K. Werner, I. Karpenko, M. Bleicher, T. Pierog, S. Porteboeuf-Houssais, *Phys. Rev.* C **85**, 064907 (2012)
17. R. J. Fries, B. Müller, C. Nonaka, and S. A. Bass, *PRL* **90**, 202303 (2003)
18. B. Abelev *et al.* (ALICE Coll.) *Phys. Rev.* C **91**, 024609 (2015)
19. B. Abelev *et al.* (ALICE Coll.) arXiv:1412.6828 [nucl-ex]
20. T. Sjostrand, S. Mrenna, and P. Z. Skands, *JHEP* **0605**, 026 (2006)

HEAVY QUARKS AND QUARKONIA FROM PHENIX

M. MAKEK for the PHENIX COLLABORATION
Department of Physics, Faculty of Science, University of Zagreb, Bijenička 32,10000 Zagreb, Croatia

The PHENIX experiment at the Relativistic Heavy Ion Collider has studied production of open and closed heavy flavor using a broad set of observables in various collision systems, p+p, d+Au, Cu+Cu, Cu+Au, Au+Au, U+U, with some of the measurements repeated at different beam energies. Such a rich set of results is important to disentangle the effects of the cold and the hot nuclear matter. We present the recent results on J/Ψproduction in Cu+Au collisions and Υ measurement in Au+Au collisions at $\sqrt{s_{NN}}$=200 GeV, where suppression of the yields compared to p+p collisions was observed, with a rapidity dependent asymmetry found for the former system. We also present the results of the open heavy flavor production in Au+Au collisions at $\sqrt{s_{NN}}$=62 GeV, measured through the single electron channel, where we found an enhancement of the yield and a non-zero elliptic flow. Finally, we report the newly extracted $b\bar{b}$ cross-section measured in d+Au collisions at $\sqrt{s_{NN}}$=200 GeV.

1 Introduction

Heavy flavor probes, i.e. hadrons carrying charm or bottom quarks, are powerful tools to study nuclear matter under extreme conditions. Since the heavy quarks are mainly produced in the initial hard scattering of partons, they are subject to signatures from all phases of evolution of nuclear collisions. Some of the heavy quark-antiquark pairs form bound quarkonia states and some hadronize into particles with one heavy quark or antiquark, denoted as open heavy flavor.

Signatures of the quark-gluon plasma (QGP) formation, such as suppression of the quarkonia yields or sequential melting of bound charmonium or bottomonium states have been established, however the extraction of medium properties from these observations is not easy, since many competing mechanisms can result in enhancement or suppression of the yields. The modification of yields in nuclear collisions is quantified by the ratio to the yields in p+p collisions, scaled by the number of expected binary collisions, N_{coll}. This ratio is known as the nuclear modification factor:

$$R_{AA} = \frac{1}{N_{coll}} \frac{d^2N_{AA}/dydp_T}{d^2N_{pp}/dydp_T} \tag{1}$$

In addition to QGP effects, the heavy quark production can be modified in the nuclear target, by the so called cold nuclear matter (CNM) effects such as modification of parton density functions in a nucleus (nPDF), initial state parton energy loss, Cronin effect or quarkonium breakup in hadronic medium. To disentangle those effects, measurements of different collision systems at different energies are desirable. The PHENIX experiment capitalizes on RHIC's capabilities to provide such collisions systems. Here we report four recent results, which address the above-mentioned topics.

2 Recent results

2.1 J/Ψ in Cu+Au collisions at $\sqrt{s_{NN}}$=200 GeV

The asymmetric collisions use the fact that the CNM effects will have a different rapidity dependence - e.g. parton distribution modifications should be different at backward and forward rapidities due to the asymmetric masses of the colliding nuclei. In addition, the different path length of the J/Ψ in the colliding nuclei should affect the magnitude of the initial state energy loss and $c\bar{c}$ breakup in nuclear collisions. PHENIX measured Cu+Au collisions at $\sqrt{s_{NN}}$= 200 GeV during the 2012 run. The J/Ψ particles were measured in the $J/\Psi \to \mu^+\mu^-$ channel in two rapidity regions $1.2 < y < 2.2$ (forward, Cu-going) and $-2.2 < y < -1.2$ (backward, Au-going). The obtained nuclear modification factor[1] in the two regions is shown in Fig. 1 (left), along with the results from Au+Au collisions[2] for reference. The observed suppression is systematically larger for forward rapidities, which one would not expect in the QGP, where the suppression should be higher in the backward region with a larger particle density. More insight can be obtained from the forward-to-backward R_{AA} ratio, shown in Fig. 1 (right). It is in a fair agreement with the expectations from a model of cold nuclear matter effects[3,4], based on EPS09 nPDFs and $c\bar{c}$ breakup cross section. Hence, one can conclude that the CNM effects are primarily responsible for the forward/backward suppression asymmetry.

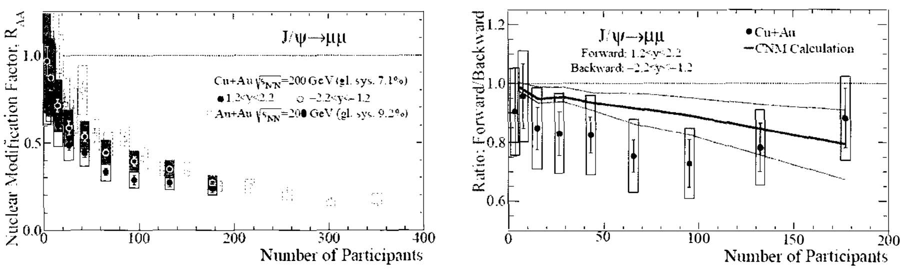

Figure 1 – Left is the nuclear modification factor, R_{AA}, as a function of number of collision participants, N_{part}. Values for J/Ψat forward (Cu-going) rapidity are shown as closed circles and at backward (Au-going) rapidity as open circles[1]. Data from Au+Au collisions[2] are also shown for reference. Right is the ratio of forward-to-backward rapidity (Cu-going/Au-going) J/Ψ yields, together with a model[3,4] of the cold nuclear matter contributions.

2.2 Υ in Au+Au collisions at $\sqrt{s_{NN}}$=200 GeV

The Υ is an excellent probe of QGP temperature since its three states (1S, 2S, 3S) have different binding energies, the higher mass states being more loosely bound. Hence the hot medium will more strongly dissociate the more loosely bound states. However, the regeneration of quarkonia in QGP directly competes with the suppression from the dissociation. In principle, the regeneration can happen by coalescence from independent b and $\bar{b}$ quarks or by their recombination from the original dissociated quarkonium. However, the former has a negligible probability at RHIC energies since the average number bottom quark pairs in a collision is much smaller than one. The latter is a small effect at RHIC energies[5].

PHENIX has measured the nuclear modification of the combined Υ (1S+2S+3S) states in Au+Au collisions $\sqrt{s_{NN}}$= 200 GeV at mid-rapidity ($|y| < 0.35$), where the Υ particles were reconstructed through the $\Upsilon \to e^+e^-$ channel. The result[6] is shown in Fig. 2, along with the measurement of the same collision system by STAR[7] and the measurement of Pb+Pb collision at $\sqrt{s_{NN}}$=2.76 TeV by CMS[8]. The result is consistent with the full suppression of the 2S and 3S states at this energy.

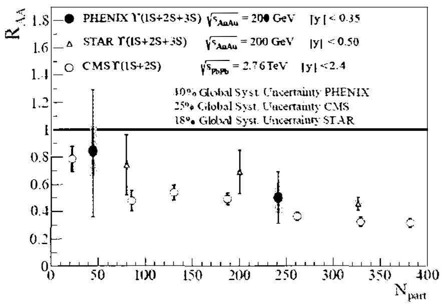

Figure 2 – Nuclear modification factor measured by PHENIX[6] as a function of N_{part} compared to STAR result[7] for Au+Au at $\sqrt{s_{NN}}$=200 GeV and CMS result[8] for Pb+Pb collision at $\sqrt{s_{NN}}$= 2.76 TeV.

2.3 Open heavy flavor in Au+Au collisions at $\sqrt{s_{NN}}$=62 GeV

PHENIX has measured open heavy flavor at mid-rapidity using electrons from semi-leptonic decays of hadrons containing one heavy quark. These electrons are identified by subtracting the cocktail of photonic electrons from the integral electron yield. While the results[9] from Au+Au collisions at $\sqrt{s_{NN}}$=200 GeV indicated a suppression in the most central events, compared to N_{coll} scaled p+p collisions, the new result[10] from Au+Au collision at $\sqrt{s_{NN}}$=62 GeV shows a systematic enhancement as depicted in Fig. 3 (left), although with large uncertainties. One could speculate that this difference in modification can be due to a larger Cronin enhancement and smaller energy loss at the lower energy. We have also determined the elliptic flow of the heavy flavor electrons and compared it to models[11,12], which describe it well for transverse momenta below 2 GeV/c, as shown in Fig. 3 (right).

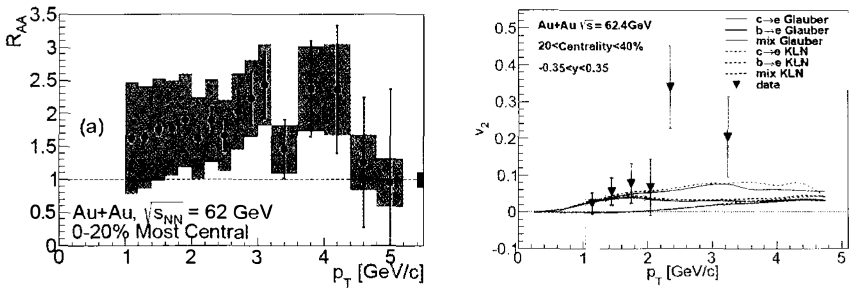

Figure 3 – Left is the nuclear modification factor, R_{AA} for electrons from heavy-flavor decays in 0-20% central Au+Au collisions at $\sqrt{s_{NN}}$= 62.4 GeV[10]. Right is the heavy-flavor electron v_2 in Au+Au collisions at $\sqrt{s_{NN}}$= 62.4 GeV[10] compared with models[11,12]. The R_{AA} is calculated using the ISR p+p baseline[13,14,15].

2.4 $b\bar{b}$ cross-section from d+Au collision at $\sqrt{s_{NN}}$=200 GeV

In addition to single electrons, the open heavy flavor at mid-rapidity can be accessed through the dielectron (e^+e^-) channel. The heavy flavor yield is obtained by subtracting the cocktail of pseudoscalar and vector mesons along with the Drell-Yan contribution from the invariant dielectron yield. The remaining yield is fit with the simulated shape of open charm and bottom decays. The simulations were done using two different generators, Pythia[16] and MC@NLO[17] and both describe the data[18] reasonably well, as demonstrated in Fig. 4. The cross-section for the $c\bar{c}$ could not be extracted due to strong model dependence of the generators, but this model

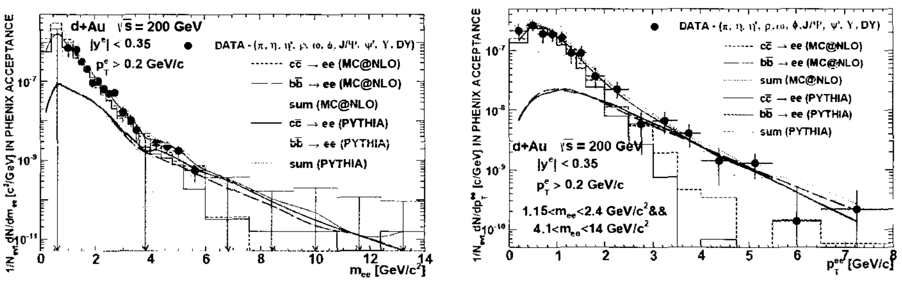

Figure 4 – The left panel compares the mass dependence of e^+e^-pair yield with Pythia[16] and MC@NLO[17] calculations and the right panel shows the comparison for the p_T dependence. The gray region in the left panel is not used for the fitting and is excluded from the p_T projection[18].

dependence was shown to be negligible[18] for the $b\bar{b}$, since it is kinematically smeared out due to the large b quark mass. Hence, we report the invariant cross section for the $b\bar{b}$ production in d+Au collisions at $\sqrt{s_{NN}}$=200 GeV of $\sigma_{b\bar{b}}^{dAu} = 1.27 \pm 0.28(\mathrm{stat}) \pm 0.46(\mathrm{syst})$ mb or in terms of nucleon-nucleon equivalent cross section $\sigma_{b\bar{b}}^{NN} = 3.4 \pm 0.8(\mathrm{stat}) \pm 1.1(\mathrm{syst})\ \mu$b.

3 Summary

PHENIX has added four new results to the very rich set of heavy flavor measurements. The measurements of quarkonia, J/Ψ, and Υ show they are suppressed in nuclear collisions compared to p+p collisions, as expected at energies of $\sqrt{s_{NN}}$=200 GeV. In addition, the results of the asymmetric Cu+Au collisions offer the possibility of disentangling the CNM effects from those of the QGP. The open heavy flavor measured through the dielectron channel allowed the extraction of the $b\bar{b}$ cross section from the d+Au collisions at $\sqrt{s_{NN}}$=200 GeV. At lower energy, $\sqrt{s_{NN}}$=62 GeV, we observed an enhancement of the open heavy flavor yield measured by single electrons and a non-zero elliptic flow.

References

1. A. Adare *et al* (PHENIX Collaboration), *Phys. Rev.* C **90**, 064908 (2014).
2. A. Adare *et al* (PHENIX Collaboration), *Phys. Rev.* C **84**, 054912 (2011).
3. J. L. Nagle *et al*, *Phys. Rev.* C **84**, 044911 (2011).
4. K. J. Eskola, H. Paukkunen and C. A. Salgado, *J. High Energy Phys.* **04**, 065 (2009).
5. A. Emerick, X. Zhao and R. Rapp, *Eur. Phys. J.* A **48**, 72 (2012).
6. A. Adare *et al* (PHENIX Collaboration), *Phys. Rev.* C **91**, 024913 (2015).
7. L. Adamczyk *et al* (STAR Collaboration), *Phys. Lett.* B **735**, 127 (2014).
8. S. Chatrchyan *et al* (CMS Collaboration), *Phys. Rev. Lett.* **109**, 222301 (2012).
9. A. Adare *et al* (PHENIX Collaboration), *Phys. Rev.* C **90**, 034903 (2014).
10. A. Adare *et al* (PHENIX Collaboration), *Phys. Rev.* C **91**, 044907 (2015).
11. S. Cao, G.-Y. Qin, S. A. Bass and B. Mueller, *Nucl. Phys.* A **904-905**, 653c-656c (2013).
12. S. Cao, Private communication.
13. M. Basile *et al*, *Il Nuovo Cimento* A **65**, 421 (1981).
14. F. W. Busser *et al*, *Nucl. Phys.* B **113**, 189 (1976).
15. P. Perez *et al*, *Phys. Lett.* B **112**, 260 (1982).
16. T. Sjostrand, S. Mrenna and P. Z. Skands, *J. High Energy Phys.* **05**, 026 (2006).
17. S. Frixione and B. Webber, *J. High Energy Phys.* **06**, 029 (2002).
18. A. Adare *et al* (PHENIX Collaboration), *Phys. Rev.* C **91**, 014907 (2015).

QUARKONIA AND HEAVY-FLAVOUR RESULTS FROM ALICE

M. GAGLIARDI for the ALICE Collaboration

Università degli Studi and Sezione INFN, Torino, Italy

Quarkonia and heavy flavour are important probes of the hot and dense QCD medium formed in high-energy heavy-ion collisions, through the modification of their yields and kinematical distributions. Measurements of their production in proton-nucleus collisions are crucial for the interpretation of heavy-ion results, as they allow one to study cold nuclear matter effects. Quarkonia and heavy-flavour production in Pb–Pb collisions at the LHC is measured in ALICE at both forward and mid-rapidity, by exploiting several experimental techniques. The main results obtained in Pb–Pb and p–Pb collisions are presented.

1 Introduction

The ALICE [1] experiment at the Large Hadron Collider (LHC [2]) studies QCD matter in ultra-relativistic heavy-ion (Pb–Pb) collisions at energy densities much larger than that of ordinary nuclear matter. Under these conditions, finite temperature QCD calculations on the lattice (see e.g. [3]) predict a transition to a deconfined state of matter known as Quark-Gluon Plasma (QGP). Heavy-flavour particles (open-charm and open-beauty hadrons) are a major tool for probing the properties of the QGP. They are sensitive to the medium density, through the mechanism of in-medium parton energy loss, which causes modifications of the momentum distributions in Pb–Pb collisions with respect to those in pp. The sensitivity of heavy quarks to collective effects in the medium can be studied via the azimuthal angle distribution of heavy-flavour particles in non-central collisions (elliptic flow). Quarkonium production suppression by colour screening was one of the first signatures proposed for the QGP [4]. Charmonium (re)generation due to the recombination of initially uncorrelated c and $\bar{c}$ quarks may also become relevant at LHC energies [5]. In p–Pb collisions, where no long-lived QGP is expected to be formed, heavy-flavour and quarkonium production can be affected by cold nuclear matter (CNM) effects, in both the initial and the final state. Since these effects are also present in Pb–Pb collisions, their measurement in p–Pb collisions is crucial for the interpretation of the results. Heavy-flavour particles produced at mid-rapidity ($|y| < 0.9$) are detected in ALICE by full reconstruction of D-meson decay topologies with displaced vertices, and by measuring the spectra of electrons from decays of heavy-flavour hadrons. At forward rapidity ($2.5 < y < 4$), their production is studied via their semi-muonic decays. Quarkonium production is measured at mid-rapidity via di-electron decays and at forward rapidity via di-muon decays; for both channels, the acceptance extends down to transverse momentum $p_{\mathrm{T}} = 0$.

2 Heavy-flavour results

2.1 Highlights from Pb–Pb collisions

The D-meson nuclear modification factor (R_{AA}) in Pb–Pb collisions [6] is shown as a function of p_{T} in Fig. 1, left, for two centrality classes. A suppression by a factor up to 5 in central collisions is observed for $p_{\mathrm{T}} > 5$ GeV/c. The R_{AA} of electrons and muons [7] from heavy-flavour decays is shown in Fig. 1, right, where a suppression by about a factor of 3 is observed. The pattern and the magnitude of the suppression are very similar for mid- (electrons) and forward (muons) rapidity. Measurements (not shown) of the elliptic flow of D mesons [9] and leptons from heavy-flavour decays show non-zero v_2 at intermediate p_{T} in semi-central collisions, pointing to a participation of charm quarks in the collective expansion of the medium. Theoretical models struggle to reproduce simultaneously the heavy-flavour R_{AA} and v_2 [9].

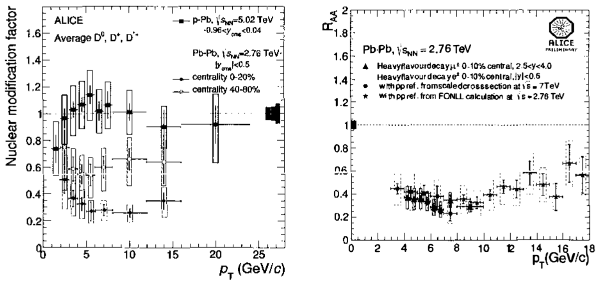

Figure 1 – Left: D-meson nuclear modification factor as a function of p_{T} in p–Pb and Pb–Pb collisions [6 8]. Right: nuclear modification factor of muons [7] and electrons in Pb–Pb collisions as a function of p_{T}.

2.2 Results from p–Pb collisions

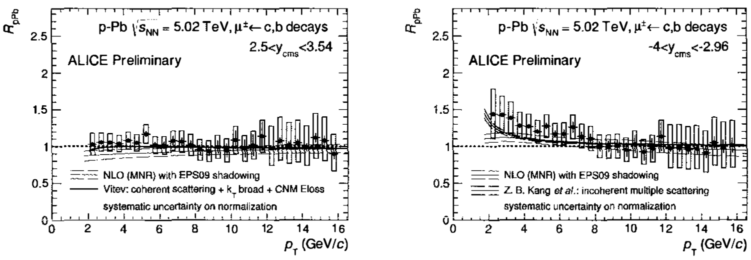

Figure 2 – Nuclear modification factor of muons from heavy-flavour decays in p–Pb collisions as a function of p_{T} at forward (left) and backward (right) rapidity, compared to theoretical models.

The nuclear modification factor R_{pPb} of D mesons in p–Pb collisions [8] is shown in Fig. 1, left. It is compatible with unity, and reproduced within uncertainties by perturbative QCD (pQCD) calculations including CNM effects such as shadowing and energy loss, or Colour Glass Condensate [8] (not shown). The R_{pPb} of muons from heavy-flavour decays is shown as a function of p_{T} in Fig. 2 for two different rapidity ranges: backward (Pb-going direction) and forward (p-going direction). The R_{pPb} of electrons at mid-rapidity is shown in Fig. 3, left. For both electrons and muons, the results are compatible with no suppression, and are reproduced by

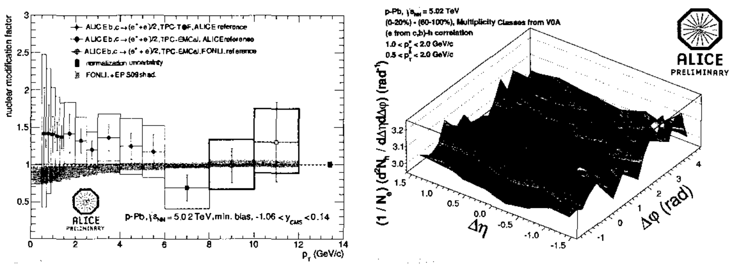

Figure 3 – Left: nuclear modification factor of electrons from heavy-flavour decays in p–Pb collisions as a function of p_{T} at mid-rapidity, compared to a theoretical calculation. Right: heavy-flavour electron-hadron correlation function in azimuth and pseudo-rapidity, for $1 < p_{\mathrm{T}}^{\mathrm{e}} < 2$ GeV/c and for the 0-20% multiplicity class, after subtraction of the 60-100% class.

pQCD calculations including CNM effects. These results suggest that the nuclear modifications of heavy-flavour production seen in Pb–Pb collisions are due to effects from the hot and dense medium. Figure 3, right, shows the azimuthal correlations between electrons from heavy-flavour decays and charged hadrons, in the trigger-particle (electron) transverse momentum range $1 < p_{\mathrm{T}}^{\mathrm{e}} < 2$ GeV/c and for the highest event-activity class, after subtraction of the lowest class to remove jet-like correlations. A double-ridge structure (not seen at higher $p_{\mathrm{T}}^{\mathrm{e}}$) appears, similar to what was observed for hadron-hadron correlations [10]. These results point to the presence of collective effects in p–Pb collisions, although a solid theoretical interpretation is not yet available.

3 Quarkonium results

3.1 Highlights from Pb–Pb collisions

The J/ψ R_{AA} at forward rapidity in Pb–Pb collisions [11] is shown as a function of p_{T} in Fig. 4, left. A suppression is observed, more pronounced at high p_{T} and relatively small at low p_{T}. Such a p_{T} dependence, not observed in lower-energy experiments at the Relativistic Heavy Ion Collider where a constant R_{AA} was observed [12], is compatible with models where part of the J/ψs are produced via (re)generation in the QGP or at the phase boundary (see references in [11]). Such a hypothesis is corroborated by a hint of non-zero J/ψ v_2 at intermediate p_{T} in semi-central collisions [14] (not shown). Figure 4, right, shows the Υ(1S) R_{AA} at forward rapidity as a function of the number of participants in Pb–Pb collisions [15]. A suppression is observed, larger than expected from suppression of feed-down from higher-mass resonances alone. The measured suppression is larger than the one observed at mid-rapidity by the CMS experiment [16].

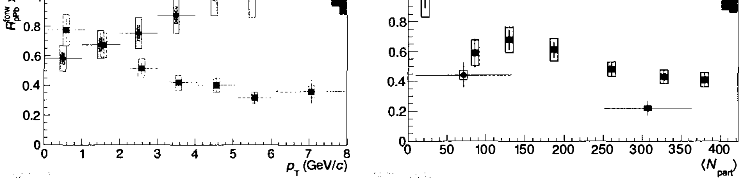

Figure 4 – Left: J/ψ nuclear modification factor as a function of p_{T} in Pb–Pb collisions [11], compared to the product of the backward- and forward-rapidity R_{pPb} [13]. Right: Υ(1S) nuclear modification factor in Pb–Pb collisions as a function of the number of participants, compared to the CMS result [16 15].

3.2 Results from p–Pb collisions

The J/ψ $R_{\rm pPb}$ [17] in two rapidity ranges is shown in Fig. 5, left. The results are compatible with no suppression at backward rapidity and slight suppression at forward rapidity, in agreement with models including shadowing and energy loss. Assuming factorisation of CNM effects, one can compare R_{AA} with the product of $R_{\rm pPb}$ in the forward and backward regions, as a function of $p_{\rm T}$ (Fig. 4, left). It emerges that the magnitude and trend of the suppression in Pb–Pb collisions are not accounted for by CNM effects alone, and can hence be ascribed to the hot and dense medium. The ψ(2S) $R_{\rm pPb}$ [18] in two rapidity ranges is shown in Fig. 5, left. At backward rapidity, the observed suppression is significantly larger than that of J/ψ. An event-activity-dependent analysis (not shown) has shown that the suppression occurs in the most "central" collisions. A possible explanation for such observations is the suppression of the ψ(2S) resonance by interaction with co-moving particles [19]. The Υ(1S) $R_{\rm pPb}$ [20] in two rapidity ranges is shown in Fig. 5, right. The suppression is compatible with that of J/ψ in the same ranges. Models including shadowing and energy loss tend to overestimate $R_{\rm pPb}$ at backward rapidity.

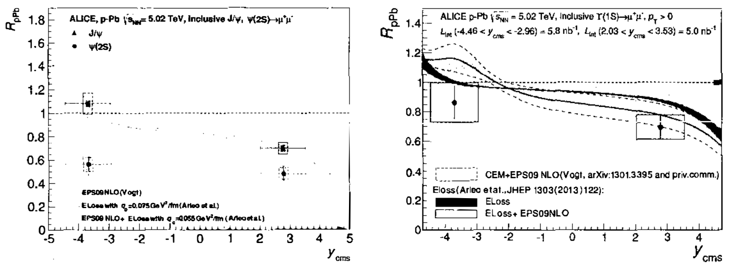

Figure 5 – Nuclear modification factor of J/ψ, ψ(2S) (left) and Υ(1S) (right) in p–Pb collisions [17 18 20], compared to theoretical models.

References

1. K. Aamodt et al. [ALICE Collaboration], *JINST* **3** S08002 (2008).
2. L. Evans et al., *JINST* **3** S08001 (2008).
3. F. Karstch, BNL-NT-06/2 (`hep-lat/0601013`).
4. T. Matsui and H. Satz, *Phys. Lett.* B **178** 416 (1986).
5. P. Braun-Munzinger and J. Stachel, *Phys. Lett.* B **490** 196 (2000).
6. B. Abelev et al. [ALICE Collaboration], *JHEP* **1209** 112 (2012).
7. B. Abelev et al. [ALICE Collaboration], *Phys. Rev. Lett.* **109** 112301 (2012).
8. B. Abelev et al. [ALICE Collaboration], *Phys. Rev. Lett.* **113** 232301 (2014).
9. B. Abelev et al. [ALICE Collaboration], *Phys. Rev.* C **90** 034904 (2014).
10. B. Abelev et al. [ALICE Collaboration], *Phys. Lett.* B **719** 29 (2013).
11. B. Abelev et al. [ALICE Collaboration], *Phys. Lett.* B **734** 314 (2014).
12. A. Adare et al. [PHENIX Collaboration], *Phys. Rev.* C **84** 054912 (2011).
13. B. Abelev et al. [ALICE Collaboration], `arXiv:1503.07179 [nucl-ex]` (2015).
14. B. Abelev et al. [ALICE Collaboration], *Phys. Rev. Lett.* **111** 162301 (2013).
15. B. Abelev et al. [ALICE Collaboration], *Phys. Lett.* B **738** 361 (2014).
16. S. Chatrchyan et al. [CMS Collaboration], *Phys. Rev. Lett.* **109** 222301 (2012).
17. B. Abelev et al. [ALICE Collaboration], *JHEP* **1402** 073 (2014).
18. B. Abelev et al. [ALICE Collaboration], *JHEP* **1412** 073 (2014).
19. E. Ferreiro, `arXiv:1411.0549 [hep-ph]` (2014).
20. B. Abelev et al. [ALICE Collaboration], *Phys. Lett.* B **740** 105 (2015).

The origin of thermal component in the transverse momentum spectra in high energy hadronic processes

A.A. Bylinkin
Laboratory of High Energy Physics, Moscow Institute of Physics and Technology, Institutsky per. 9, Dolgoprudny, Russia

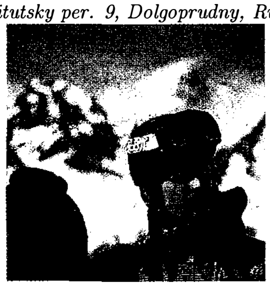

The transverse momentum spectra of hadrons produced in high energy collisions can be decomposed into the two components: the exponential ("thermal") and the power ("hard") ones. Recently, the H1 Collaboration has discovered that the relative strength of these two components in Deep Inelastic Scattering depends drastically upon the global structure of the event - namely, the exponential component is absent in the diffractive events characterized by a rapidity gap. We discuss the possible origin of this effect, and speculate that it is linked to the mechanism of confinement. Specifically, we argue that the thermal component is produced in the fragmentation of the color string due to the effective event horizon introduced by confinement, in analogy to the Hawking-Unruh effect. In diffractive events, the t-channel exchange is color-singlet and there is no fragmenting string – so the thermal component is absent. Analyzing the data on non-diffractive pp collisions, we find that the slope of the thermal component of the hadron spectrum is proportional to the saturation momentum that drives the deceleration in the color field, and thus the Hawking-Unruh temperature.

The transverse momentum spectra of hadrons produced in high energy collisions can be accyrately described by the sum of power ("hard") and exponential ("soft") components. The hard component is well understood as resulting from the high momentum transfer scattering of quarks and gluons, and their subsequent fragmentation. The "soft" one is ubiquitous in high energy collisions and has the appearance of the thermal spectrum – but its origin remains mysterious to this day. Indeed, while in nuclear collisions one may expect thermalization to take place, it is hard to believe that thermalization can occur in such processes as Deep-Inelastic Scattering or e^+e^- annihilation. Moreover, not only the transverse momentum spectra but also the abundances of hadrons in these elementary processes appear approximately thermal [1,2,3].

The universal thermal character of hadron transverse momentum spectra and abundances in all high energy processes can hardly be a coincidence and begs for a theoretical explanation. One attempt to understand it is based on the hypothesis that confinement is associated with an event horizon for colored particles. The quantum effects then produce the thermal spectra of hadrons, similarly to the Hawking evaporation of black holes or Unruh radiation. The color string stretching between the colored fragments in a high energy collision contains the longitudinal chromoelectric field. This field deccelerates the colored fragments producing a Rindler event horizon. Quantum fluctuations in the vicinity of the event horizon then result in the thermal production [4,5,6]. A novel prospective on this phenomenon is offered by the holographic gauge/gravity correspondence, in which high energy collisions lead to the creation of trapped surfaces (with corresponding event horizons) in the bulk AdS space [7,8,9,10]. In string approach, the inelastic processes are accompanied by deceleration, and thus the thermal emission [11,12,13].

The effective temperature of the hadron spectrum in this picture is proportional to deccel-eration that is driven by the confining chromoelectric field. The strength of the chromoelectric field at low collision energies is determined by the string tension. At high energies, the quantum evolution effects come into play, increasing the number of gluons in the wave functions of the colliding hadrons; therefore the chromoelectric field becomes stronger.

An economic and theoretically consistent way to describe this phenomenon is offered by the parton saturation [14], or color glass condensate [15], picture. In this approach the density of partons in the transverse plane inside hadrons, and thus the strength of the color field after the hadron collision, is parameterized by the saturation momentum $Q_s(s,\eta)$ that depends on the c.m.s. collision energy squared s and (pseudo-)rapidity η. The decceleration a then appears proportional to the value of the saturation momentum, $a \sim Q_s$. The temperature of the radiation from the resulting Rindler event horizon is thus given by [4]

$$T_{th} = c\,\frac{Q_s}{2\pi}, \tag{1}$$

where c is a constant of order one; in [5] an estimate $c \simeq 1.2$ was given.

The dependence of the saturation momentum on c.m.s. energy squared s and pseudo-rapidity η is given by

$$Q_s^2(s;\pm\eta) = Q_s^2(s_0;\eta=0)\left(\frac{s}{s_0}\right)^{\lambda/2} \exp(\pm\lambda\eta); \tag{2}$$

where $\lambda \simeq 0.2 \div 0.3$ is the intercept (see e.g. [16]). In the saturation scenario, Q_s is the only dimensionful parameter, so the transverse momentum spectra $F(p_T)$ have to scale as a function of dimensionless variable p_T/Q_s [17,18]:

$$F(p_T) = F(p_T/Q_s); \tag{3}$$

for massive hadrons of mass m, we have to replace $p_T \to m_T = \sqrt{p_T^2+m^2}$.

In ref. [19] it was found that the following parameterization describes well the hadron transverse momentum distribution in hadronic collisions and deep-inelastic scattering:

$$\frac{d\sigma}{p_T dp_T} = A_{therm}\exp\left(-m_T/T_{th}\right) + \frac{A_{hard}}{(1+\frac{m_T^2}{T^2\cdot n})^n}, \tag{4}$$

The typical charged particle spectrum fitted to this function (4) is shown in the Fig. 1.

Within the framework described above, the parameter T is the saturation momentum, $Q_s = T$, and the effective temperature T_{th} is proportional to Q_s as well, as given by (1). Therefore, basing on the picture outlined above, we expect the linear relation between T_{th} and T. Remarkably, such linear relation $T = (4.26 \pm 0.15)\cdot T_{th}$ has also been observed in [19].

Moreover, since the presence of the thermal component signals deceleration in longitudinal color fields, we can now understand a striking experimental observation [21]: in diffractive events characterized by a rapidity gap, the thermal component in the hadron transverse momentum spectrum is absent. In our present framework, this is a straightforward consequence of the color-singlet t-channel exchange that is responsible for diffraction – in this case there is no fragmenting string – and thus no deceleration.

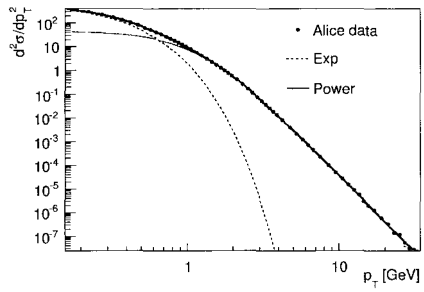

Figure 1 – Charged particle spectrum fitted to the function (4): the red (dashed) curve shows the exponential term and the green (solid) one stands for the power-like term.

Let us now check whether the relation between T_{th} and T is indeed linear. Since the variations of the temperature-like parameters T and T_{th} as a function of pseudorapidity are expected from (2), it is desirable to exclude their influence when studying the dependences of these parameters on the c.m.s. energy in a collision. This is possible if one combines only the data in more or less the same pseudorapidity intervals. Hence we look first at ISR [22], PHENIX [23], ALICE [24] and UA1 [20] data in the most central ($|\eta| < 0.8$) pseudo-rapidity region.

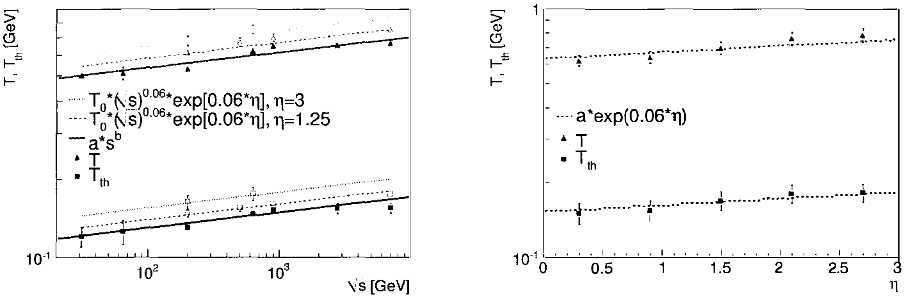

Figure 2 – Variations of the T, T_{th} parameters of (4) obtained from the fits to the experimental data (full points) as function of c.m.s. energy $\sqrt{s}$ in a collision and the measured pseudorapididty region η. Solid lines show power-law fits (2) of these variations. In addition, open points show parameters for the data measured in different pseudorapidity intervals with dashed and pointed lines showing predictions calculated according to (2).

The figure 2 shows the resulting from this analysis values of T and T_{th} as a function of c.m.s. energy in a collision. One can describe the energy dependence by the power-law fits (2) shown in figure 2:

$$T = 409 \cdot (\sqrt{s})^{0.06}\ MeV, \quad T_{th} = 98 \cdot (\sqrt{s})^{0.06}\ MeV. \tag{5}$$

We find a rather good agreement between the values extracted from the fit (4) of experimental data and expected on the basis of (2). Remarkably, from (5) one can again notice the linear relation between T and T_{th} with the proportionality coefficient 4.16 ± 0.2, which is not far from $(2\pi)/1.2 \simeq 5.23$ predicted in [5], so c is definitely of order 1.

To study the variations of T and T_{th} parameters as a function of pseudorapidity one can use the data published by the UA1 experiment [20] which are presented by charged particle spectra in five pseudorapidity bins, covering the total rapidity interval $|\eta| < 3.0$. Figure 2 shows how the parameters T and T_{th} vary with pseudorapidity together with the lines standing for the exponential behaviour predicted from eq. (2) with $\lambda = 0.12$ as obtained from the fits (5) to the experimental data. Though the data measured by the UA1 experiment have been measured only in five pseudorapidity intervals, one can clearly notice the growth of T and T_{th} values, which is also in a good qualitative agreement with the formula (2). Further precise measurements on double differential charged particle spectra should be performed at LHC to test the observed behaviour.

In addition, figure 2 shows UA1[20,25], BRAHMS[26] and CMS[27] data measured under different experimental conditions. In these measurements the pseudo-rapidity interval was much wider than in[22,23,24]. Therefore, one can compare the parameter values obtained from the fits of these data (open points in figure 2) to the values calculated according to (2) with $\lambda = 0.12$, T^0 and T^0_{th} taken from (5) and η taken as the mean value of the measured pseudorapidity interval. Rather good agreement between these predictions and the experimental data can be observed from figure 2 further supporting the proposed behaviour described by eq. (2).

We hope that our analysis sheds some light on the origin of the thermal component in hadron production. The established proportionality of the parameters describing the "thermal" and "hard" components of the transverse momentum spectra supports the theoretical picture in which the soft hadron production is a consequence of the quantum evaporation from the event horizon formed by deceleration in longitudinal color fields. The absence of the thermal component in diffractive interactions lend further support to our interpretation. It will be worthwhile to extend this analysis to other high energy processes. Future precise measurements at LHC are needed to further study the proposed picture for hadron production.

References

1. F. Becattini *et al.* Eur. Phys. J. C **56**, 493 (2008) [arXiv:0805.0964 [hep-ph]].
2. F. Becattini *et al.* Eur. Phys. J. C **66**, 377 (2010) [arXiv:0911.3026 [hep-ph]].
3. A. Andronic *et al.* Phys. Lett. B **675**, 312 (2009) [arXiv:0804.4132 [hep-ph]].
4. D. Kharzeev and K. Tuchin, Nucl. Phys. A **753**, 316 (2005) [hep-ph/0501234].
5. D. Kharzeev, E. Levin and K. Tuchin, Phys. Rev. C **75**, 044903 (2007) [hep-ph/0602063].
6. P. Castorina *et al.* Eur. Phys. J. C **52**, 187 (2007) [arXiv:0704.1426 [hep-ph]].
7. S. Lin and E. Shuryak, Phys. Rev. D **77**, 085013 (2008) [hep-ph/0610168].
8. D. M. Hofman and J. Maldacena, JHEP **0805**, 012 (2008) [arXiv:0803.1467 [hep-th]].
9. S. S. Gubser *et al.* Phys. Rev. D **78**, 066014 (2008) [arXiv:0805.1551 [hep-th]].
10. Y. Hatta and T. Matsuo, Phys. Rev. Lett. **102**, 062001 (2009) [arXiv:0807.0098 [hep-ph]].
11. A. Stoffers and I. Zahed, Phys. Rev. D **87**, 075023 (2013) [arXiv:1205.3223 [hep-ph]].
12. G. Basar *et al.* Phys. Rev. D **85**, 105005 (2012) [arXiv:1202.0831 [hep-th]].
13. E. Shuryak and I. Zahed, Phys. Rev. D **89**, 094001 (2014) [arXiv:1311.0836 [hep-ph]].
14. L. V. Gribov, E. M. Levin and M. G. Ryskin, Phys. Rept. **100**, 1 (1983).
15. L. D. McLerran and R. Venugopalan, Phys. Rev. D **49**, 2233 (1994) [hep-ph/9309289];
16. D. Kharzeev and E. Levin, Phys. Lett. B **523**, 79 (2001) [nucl-th/0108006].
17. J. Schaffner-Bielich *et al.* Nucl. Phys. A **705**, 494 (2002) [nucl-th/0108048].
18. L. McLerran *et al.* Acta Phys. Polon. B **41**, 1917 (2010) [arXiv:1006.4293 [hep-ph]].
19. A. A. Bylinkin *et al.* Phys. Atom. Nucl. **75** (2012) 999 [arXiv:1008.0332 [hep-ph]].
20. G. Bocquet *et al.* [UA1 Collaboration], Phys.Lett.B**366**:434-440,1996
21. A. A. Bylinkin and A. A. Rostovtsev, arXiv:1404.7302 [hep-ph].
22. K. Alpgard *et al.* [UA5 Collaboration], Phys. Lett. B **112** (1982) 183.
23. A. Adare *et al.* [PHENIX Collaboration], Phys. Rev. C **83** (2011) 064903
24. B. B. Abelev *et al.* [ALICE Collaboration], Eur. Phys. J. C **73** (2013) 2662.
25. C. Albajar *et al.* [UA1 Collaboration], Nucl. Phys. B **335** (1990) 261.
26. I. Arsene *et al.* [BRAHMS Collaboration], Phys. Rev. Lett. **98** (2007) 252001
27. V. Khachatryan *et al.* [CMS Collaboration], Phys. Rev. Lett. **105** (2010) 022002

MAGNETIC WILSON LOOP IN THE CLASSICAL FIELD OF HIGH-ENERGY HEAVY-ION COLLISIONS

E. PETRESKA
Centre de Physique Théorique, École Polytechnique,
91128 Palaiseau, France
and
Departamento de Física de Partículas and IGFAE, Universidade de Santiago de Compostela,
15782 Santiago de Compostela, Spain

This talk gives a brief review of the calculation of the expectation value of a magnetic Wilson loop in the transverse plane of ultra-relativistic heavy-ion collisions. The average of the Wilson loop is determined in the first moments after the impact.

1 Introduction

A complete description of high-energy collisions requires a precise understanding of the initial conditions. The initial conditions are given by the nuclear structure of the participants in the collision, as well as by the structure of the matter formed in the first moments after the impact. How the system evolves at later times depends on the fluctuations in these first two stages. These conditions are the point of interest of many recent works attempting to explain the transition of the collision system from a quantum state far from equilibrium, before the interaction, to the Quark Gluon Plasma that is believe to be formed in experiments at the Large Hadron Collider and the Relativistic Heavy Ion Collider.

In this talk we present the calculation of the expectation value of a spatial Wilson loop in the initial time of heavy-ion collisions. The computations are based on the Color Glass Condensate (CGC) theory for nuclear structure at high energies. The starting concept in the CGC theory is the classical description of the gauge fields, i.e. the McLerran-Venugopalan (MV) model for a large nucleus [1]. The form of the classical field of the individual nuclei before the collision and of the resulting field [2], as well as the form of the chromo-electric and chromo-magnetic fields formed at early times [3], have been calculated previously. We place a non-Abelian magnetic Wilson loop in the transverse plane normal to the longitudinal component of the chromo-magnetic field and compute its average. The numerical result gives an area law behaviour of the loop and indicates a presence of positive and negative domains of chromo-magnetic flux in the plane of the loop [4]. The fluctuations of the chromo-magnetic flux may be viewed as uncorrelated vortices with a typical radius $\sim 0.8/Q_s$. Q_s denotes the saturation momentum which is the scale where the gluon field exhibits non-linear dynamics [5]. A perturbation theory without screening gives a leading non-trivial term proportional to the square of the area of the loop [6].

In the MV model one assumes a momentum scale that separates the partons in the wave function of the nucleus: the partons with large longitudinal momentum act as static sources for the degrees of freedom with a small longitudinal momentum fraction x. The color charge squared per unit transverse area, μ^2, scales as $\mu^2 \sim \Lambda_{QCD}^2 A^{1/3}$, where A is the nucleon number. The momentum μ drives the running of the strong coupling constant, $\alpha_s(\mu^2)$, so for a nucleus with large A the coupling is small and parton distribution functions can be calculated perturbatively. The transverse gluon density in a large, Lorentz contracted, ultra-relativistic nucleus is high and the gauge fields are approximated as classical fields. Their form is obtainable from the classical Yang-Mills equations of motion. Quantum corrections are implemented by including a non-linear small-x evolution of the wave function of the nuclei.

In the picture of classical fields, the solutions of the Yang-Mills equations for a collision of two nuclei are the following. Before the impact, both, the gauge fields of the target and the projectile are a (different) gauge transformation of the vacuum. They are the non-Abelian analogue of the Weizsäcker-Williams field and in light-cone gauge their form is:

$$\alpha_m^i = \frac{i}{g} U_m \, \partial^i U_m^\dagger \quad , \quad \partial^i \alpha_m^i = g \rho_m \; . \tag{1}$$

The subscript m, with values 1 and 2, denotes the projectile and the target respectively. Introducing the gauge potential as

$$\Phi_m = -\frac{g}{\nabla_\perp^2} \rho_m \; , \tag{2}$$

the solution to (1) can be written as [2]:

$$\alpha_m^i = \frac{i}{g} e^{-ig\Phi_m} \partial^i e^{ig\Phi_m} \; . \tag{3}$$

In the forward light cone one needs to solve the equations of motion with two color currents representing the sources in the two nuclei, and with boundary conditions on the light cone. Analytical solution has been found only at proper time $\tau = \sqrt{t^2 - z^2} = 0$ [2]. The resulting transverse field is a sum of two pure gauge fields: $A^i = \alpha_1^i + \alpha_2^i$.

At $\tau = 0$ the transverse components of the chromo-magnetic and chromo-electric fields are zero. The longitudinal components are [3]:

$$E_z = ig[\alpha_1^i, \alpha_2^i] \; , \quad B_z = ig\epsilon^{ij}[\alpha_1^i, \alpha_2^j] \; , \quad (i,j = 1,2) \; . \tag{4}$$

where ϵ^{ij} is the antisymmetric tensor.

2 Magnetic Wilson loop in the classical field of heavy-ion collisions

The non-Abelian Wilson loop is gauge invariant and is defined as an exponential of an integration of the gauge field matrices, A^μ, ordered along the path. The magnetic Wilson loop is given by:

$$M(R) = \mathcal{P} \exp\left(ig \oint dx^i A^i\right) = \mathcal{P} \exp\left[ig \oint dx^i \left(\alpha_1^i + \alpha_2^i\right)\right] \; , \tag{5}$$

with R the radius of the loop. Note that $M(R) \equiv \mathbb{1}$ if evaluated in the field of a single nucleus (α_1^i or α_2^i) as those are pure gauges.

In [4] it was shown that the expectation value of the magnetic Wilson loop in the field A^i produced in a collision of two nuclei is proportional to the exponent of the area A of the loop:

$$W_M(R) = \frac{1}{N_c} \langle \mathrm{tr}\, M(R) \rangle \sim \exp\left(-\sigma_M A\right) \; . \tag{6}$$

Here, σ_M is the magnetic string tension. For the SU(2) gauge group its value was estimated to be $\sigma_M \simeq 0.12 Q_s^2$ from the fit to the lattice data. The result (6) was obtained for areas $A \gtrsim 2/Q_s^2$. It indicates that the structure of the chromo-magnetic flux at such scales corresponds to uncorrelated vortex fluctuations. This is shown in fig. 1 for proper time $\tau = 0$. For comparison,

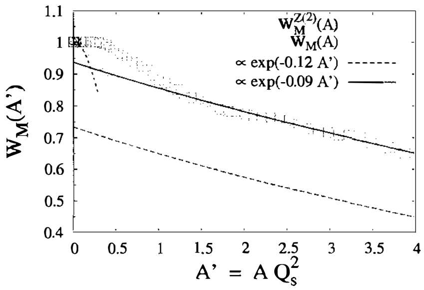

Figure 1 – Expectation value of the magnetic flux loop right after a collision of two nuclei (time $\tau = +0$) as a function of its area $A' \equiv A\,Q_s^2$. We define $Q_s^2 = (C_F/2\pi)\,g^4\mu^2$. Symbols show numerical results for $SU(2)$ Yang-Mills on a 4096^2 lattice; the lattice spacing is set by $g^2\mu_L = 0.0661$. The solid and dashed lines represent fits over the range $4 \geq A' \geq 2$. The short dotted line shows $\cos 2A'$ for $A' < 0.3$.

in the same figure we plot he expectation value of the $Z\,(N_c)$ part of the loop. The two fits have a similar behaviour, confirming the independent domain structure of the flux.

The expectation value in (6) refers to averaging over the color charge distributions in each nucleus. For large nuclei the color sources are treated as random variables with Gaussian probability distribution. Physical observables are then averaged with a Gaussian (McLerran-Venugopalan) action:

$$S_{\rm eff}[\rho^a] = \frac{1}{2}\int d^2\mathbf{x}\left[\frac{\rho_1^a(\mathbf{x})\rho_1^a(\mathbf{x})}{\mu_1^2} + \frac{\rho_2^a(\mathbf{x})\rho_2^a(\mathbf{x})}{\mu_2^2}\right] , \tag{7}$$

where μ^2 is the color charge squared per unit area, related to the saturation scale via $Q_s^2 \sim g^4\mu^2$.

To obtain $W_M(R)$ we need to determine the deviation of A^i from a pure gauge:

$$W_M(R) \simeq \frac{1}{N_c}\left\langle {\rm tr}\ \exp\left(-\frac{1}{2}\left[X_1, X_2\right]\right)\right\rangle \simeq 1 - \frac{1}{2N_c}\left\langle g^2h^2\right\rangle , \tag{8}$$

where:

$$g^2h^2 = \frac{1}{8}f^{abc}f^{\bar{a}\bar{b}c}X_1^aX_1^{\bar{a}}X_2^bX_2^{\bar{b}} \quad \text{with :} \quad X_m = ig\oint dx^i\alpha_m^{ai}t^a . \tag{9}$$

f^{abc} are the structure constants of the special unitary group and h^2 corresponds to a four gluon vertex of the fields. In addition, we expand the fields α^i from eq. (3) perturbatively in terms of the coupling constant:

$$\alpha_m^i = -\partial^i\Phi_m + \frac{ig}{2}\left(\delta^{ij} - \partial^i\frac{1}{\nabla_\perp^2}\partial^j\right)\left[\Phi_m, \partial^j\Phi_m\right] + \mathcal{O}\left(\Phi_m^3\right) . \tag{10}$$

A non-trivial result for the Wilson loop gives the term of quadratic order: $\alpha^{i,a} \sim gf^{abc}\Phi^b\partial^i\Phi^c$:

The expectation value $\langle h^2\rangle$ that enters in the expression for the magnetic loop involves the fields of both nuclei. The leading diagram is shown in fig. 2 corresponds to two sources, for both projectile and target, whose field is evaluated at second order in the gauge potential. The final result we obtain for the expectation value of the magnetic Wilson loop for classical fields α^i:

$$W_M(R) \simeq 1 - \frac{\pi^2N_c^6}{64(N_c^2-1)^3}\frac{Q_{s1}^4Q_{s2}^4}{\Lambda^4}A^2 . \tag{11}$$

In this result, A is the area of the loop, and Q_{s1} and Q_{s2} are the saturation scales of the projectile and the target, respectively. We use the relation:

$$Q_s^2 = \frac{g^4C_F}{2\pi}\mu^2 , \qquad \text{where :} \qquad C_F = \frac{N_c^2-1}{2N_c} . \tag{12}$$

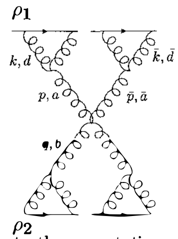

Figure 2 – Classical contribution to the expectation value of the magnetic Wilson loop.

The cut-off Λ regulates the infrared divergence of the integrals over the gluon momentum k shown in diagram 2. It sets the mass scale for the gluon propagator.

The perturbative result for the expectation value of the magnetic Wilson loop gives a first non-trivial contribution that is proportional to the square of the area, and therefore does not reproduce the numerical result. The analytical expansion of the magnetic loop holds only for small areas, and not in the onset of area law behaviour. A term proportional to the area of the loop would involve single powers of the target's and projectile's saturation scales: $\sim A\, Q_{s1} Q_{s2}$ [4]. However, Gaussian contractions can only give powers of Q_{s1}^2 and Q_{s2}^2:

$$\langle \rho_m^a(\mathbf{x})\, \rho_m^b(\mathbf{y}) \rangle = \mu_m^2 \delta^{ab} \delta(\mathbf{x} - \mathbf{y}) \sim Q_{s_m}^2 \;, \tag{13}$$

and therefore a term $\sim A^2$. Area law scaling of the Wilson loop presumably requires resummation of screening effects [7]. "Naive" perturbation theory cannot capture the presence of screening corrections.

In summary, the magnetic Wilson loop at proper time zero in heavy-ion collisions shows an area law behaviour which indicates a presence of independent domains of magnetic flux. The perturbative result for the average of the loop gives a term proportional to the area squared.

Acknowledgments

I thank the organizers of the Rencontres de Moriond 2015 for the opportunity to present this talk and for the financial support enabling me to attend the conference. I thank my collaborators Adrian Dumitru and Yasushi Nara with whom this work was done.

References

1. L. D. McLerran and R. Venugopalan, *Phys. Rev.* D **49**, 2233 (1994), *Phys. Rev.* D **49**, 3352 (1994); Y. V. Kovchegov *Phys. Rev.* D **54**, 5463 (1996)
2. A. Kovner, L. D. McLerran and H. Weigert, *Phys. Rev.* D **52**, 6231 (1995), *Phys. Rev.* D **52**, 3809 (1995);
3. D. Kharzeev, A. Krasnitz and R. Venugopalan, *Phys. Lett.* B **545**, 298-306 (2002); R. J. Fries, J. I. Kapusta and Y. Li, nucl-th/0604054; T. Lappi and L. McLerran, *Nucl. Phys.* A **772**, 200 (2006)
4. A. Dumitru, Y. Nara, E. Petreska, *Phys. Rev.* D **88**, 054016 (2013)
5. L. V. Gribov, E. M. Levin and M. G. Ryskin, Phys. Rept. **100**, 1 (1983); A. H. Mueller and J. W. Qiu, *Nucl. Phys.* B **268**, 427 (1986)
6. E. Petreska, *Phys. Rev.* D **89**, 057501 (2014)
7. A. Dumitru, H. Fujii and Y. Nara, *Phys. Rev.* D **88**, 031503 (2013)

8.
Celebrating the 50$^{\text{th}}$ Moriond

EARLY DAYS DISCOVERIES AND MORIOND

K. GOULIANOS
The Rockefeller University, 1230 York Avenue, New York, NY 10065-6399, USA

Launched into particle physics space in 1966, the Moriond conference has been extremely successful in providing a forum for young and mature physicists alike, both experimentalist and theorists, to report results and discuss ideas for future research. Having attended 22 of the past "Morionds" since 1976, I present my reminiscences of the early days of Moriond.

1 Introduction

I am honored to be invited to speak on *Early Days Discoveries and Moriond* in the 50th Moriond celebration session. My experience is based on the conferences listed in Fig.1.

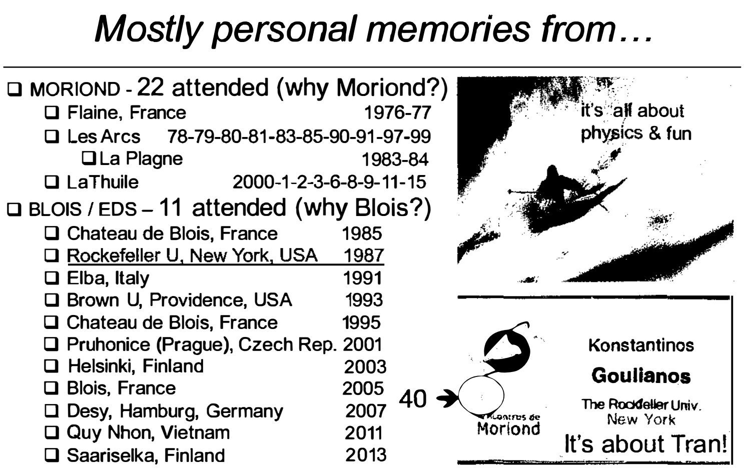

Figure 1 – Moriond-Blois Conferences I attended.

Figure 1, as well as the other figures in this paper, has been extracted from the talk I presented at the conference. The original text and images of the talk were obtained either from files produced in a web search of from my own personal files (e.g., my talk at Moriond 1976).

There are two items in this figure that need to be explained:

Why Blois? The creation of the Blois (EDS, Elastic and Diffractive Scattering) conference series highlights the genius of Tran (Jean Tran Thanh Van), the creator of Moriond. When he sensed that the subject of EDS was growing fast, he created a branch dedicated to it. He wisely decided to hold the EDS series not in a ski resort, like the Moriond, but in some interesting non-ski-oriented city, in order to widen the participation of groups around the world as local hosts. Blois, France, was the first such place.

Conference name-tag. This is my first Moriond's name-tag: note the "40" inside the (red) circle. In the interest of saving money to make the Moriond more affordable, Tran collected all name-tags at the end of a conference for recycling. I had to beg him to let me keep mine, citing my service in advertising the conference in a Moriond legacy talk that I had given.

Figure 2 shows that the strong mountain sun can turn one's hair from brown-black to white. No need for a hair dresser to make you respectable by bleaching your hair, just go to Moriond!

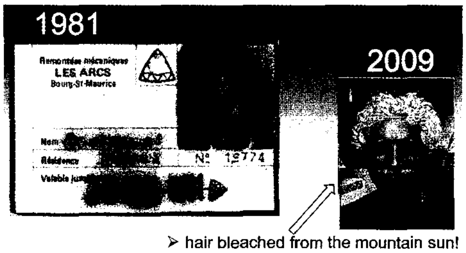

Figure 2 – My ski pass from Les Arcs in 1981 (left) and my portrait from a Moriond talk in 2009 (right).

Physics. Moriond is known as a ski-conference, but physics comes first! Skiing provides a physical release for the participants from an intense program of presentations of new results by young and mature physicists and engineers. The conference is open to both experimentalists and theorists participating in a common session. It is this model that introduced me to theorists and inspired my interest in phenomenology, which helped me better understand my experimental results. With discussions at breakfast, lunch, and dinner, and often heated arguments on the ski lifts, it builds friendships that last for a lifetime.

2 Moriond 1976 in Flaine – My first Moriond

I was invited to Moriond 1976 by John Illiopoulos, who was then at Rockefeller to talk on the observation of $\nu p_\mu \to p_\mu$ in pp collisions in the CIR (Columbia, Illinois, Rockefeller) experiment at the Brookhaven AGS. To fulfill the skiing "requirement," he said, bring along your ice-skates.

Well, when I went to the outdoor skating rink the day I arrived in Flaine, I saw skiers coming down the mountain and was fascinated. The next day I arranged for a skiing lesson, and the instructor put me on two-foot-long skis. I did well on them, skiing on a baby slope. After the lesson, he told me that I could go on my own on a certain chair and come slowly down the slope.

I took the wrong chair by mistake and ended up on the very top of the mountain. Coming down was impossible, so I decided to descend by sliding on my butt. A friendly skier with a German accent stopped by me and asked if I needed help "to get up." No, I replied, I am doing OK sliding on my butt and using my skies as brakes. "Ah so!" he said and gave me a strange look!

Moriond 1976 was packed with physics results and proposals for the future, too many to list here. The Moriond experience committed me to be coming back, and I gladly accepted Tran's invitation to the 1997 Moriond as a summary speaker of the "Electromagnetic and Leptonic Interactions" session.

3 Moriond 1977 in Flaine – My ski-enhanced Moriond

Excited about skiing in Flaine again, this time I brought along a pair of two-meter-long purple Head skis with bindings preset to *expert* mode. My friends, Illiopoulos and the Baltays (Charlie and his wife Ginnie) among them, conspired to take me to Diamond Noir, the steepest slope in Flaine (Fig. 3). Ginnie goes first, falls, tumbles all the way down, breaks one ski and both poles, loses the other ski, and falls flat at the bottom of the slope. Oh, no! I cried, thinking of the worst. But then, to my great relief, she stands up and waves with her broken poles.

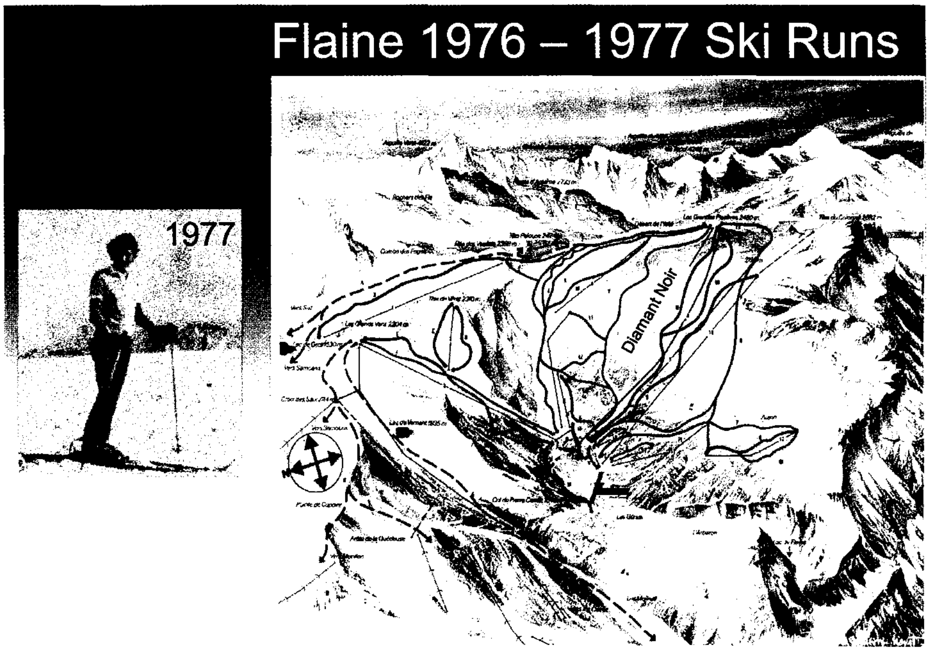

Figure 3 – Flaine 1976-77: my first time on long skis (left) and the ski-run plan (Diamond Noir story in text).

"Your turn is next," ordered the team with a smirk. "No problem," I said and threw myself down the slope, making a wide turn and getting stuck on the right side of the tube-like slope pondering what to do next. A skier stopped by and yelled, "What on earth are you doing on this slope?" Recognizing him as my last year's ski instructor, I replied, "I am practicing the tips you gave me last year." "Good luck," he said with shaking his head in disbelief, and disappeared skiing down into a passing cloud. Swinging from one side of the tube to the other, I came down after multiple falls to the delight of my friends for my entertaining performance.

Physics at Moriond 1977. Neutral currents, charm, and dileptons dominated the conference. Martin Perl's talk confirming the discovery of the τ-lepton brought down the house! In 1976 he show a preliminary result on the subject that raised a lot of interest, but also some doubts. If a third lepton were to exist, it would be probably paired with a neutrino, which would clash with the existing prejudice favoring the two-neutrino theory of the standard model. This would be revolutionary! Yet, Perl presented evidence for a third lepton in 1976 and, after more studies, he promoted his result to a discovery of the τ in 1977. I remember him telling me about it on the conference bus from CERN to Flaine. I will never forget that moment.

Figures 4, 5, and 6 present, respectively, the general categories of physics topics covered in Moriond 1977, Perl's contribution, and the concluding remarks of my summary talk.

FLAINE 1977: Summary of EM & Leptonic Interactions Session – slide 1

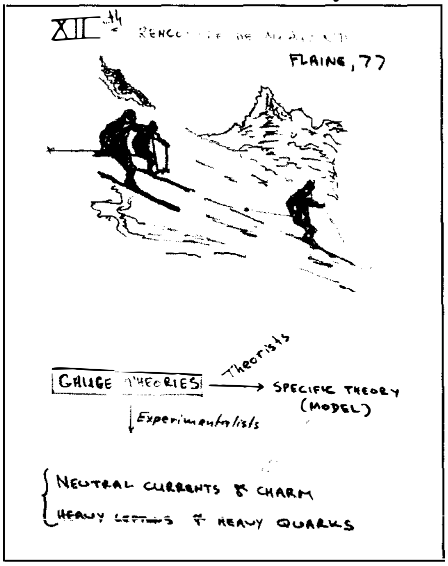

- Neutral currents
  - ν_μ+p → ν_μ+p observed
  - Columbia, Illinois, Rockefeller
- Charm
  - SPEAR (LBL-SLAC) → DD*
  - e^+e^- → KX vs $\sqrt{s}$ (SPRAR / DORIS)
- Dileptons
  - Dimuons, $e\mu$, ...
- Heavy leptons
  - τ → τριτον (Martin Perl)

Figure 4 – Original slide 1 of my Moriond 1977 summary talk (left) and reported discoveries (right).

The τ (τριτον) Lepton

EVIDENCE FOR, AND PROPERTIES OF, THE NEW CHARGED HEAVY LEPTON* †

Martin L. Perl
Stanford Linear Accelerator Center
Stanford, California 94305, USA

*Paper presented at the XII Rencontre de Moriond (Flaine, March 6-18, 1977; to be published in the Proceedings of the XII Recontre de Moriond, edited by Tran Thanh Van, R.M.I.E.M. Orsay.

Figure 5 – Nobel Laureate Martin Perl announcing the τ (triton) discovery at Moriond 1977.

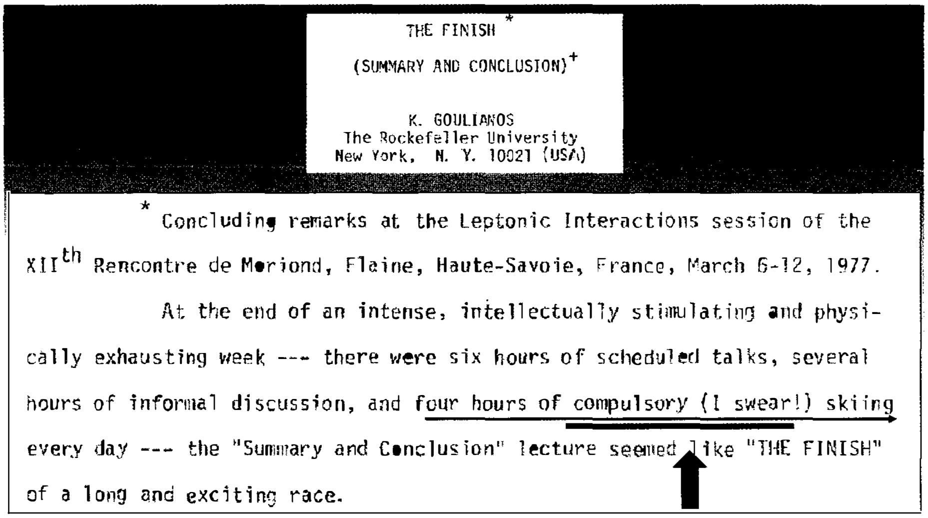

THE FINISH*

(SUMMARY AND CONCLUSION)+

K. GOULIANOS
The Rockefeller University
New York, N. Y. 10021 (USA)

* Concluding remarks at the Leptonic Interactions session of the XIIth Rencontre de Moriond, Flaine, Haute-Savoie, France, March 6-12, 1977.

At the end of an intense, intellectually stimulating and physically exhausting week --- there were six hours of scheduled talks, several hours of informal discussion, and four hours of compulsory (I swear!) skiing every day --- the "Summary and Conclusion" lecture seemed like "THE FINISH" of a long and exciting race.

Figure 6 – Concluding remarks of my summary talk "The Finish" at Moriond 1977.

4 Moriond 1978 in Les Arcs – what an experience!

After two years in Flaine, Tran moved the Moriond Conference to Les Arcs, another French resort. The physics experience was still dynamic, featuring, among others, Steve Ellis and Gordon Kane on gluons, Fig. 7; Leon Lederman (**Leon**) on the Upsilon observation, Fig. 8 (left); and myself (**the Peon**), Fig. 8 (right), on diffractive hadron dissociation.

Skiing in Les Arcs was, to say it kindly, more intense. Remembering my encounters with the rather unfriendly mountain slopes brings a mixed feeling of fear and accomplishment. There are many *cutting-edge* adventures to report – please query me the next time we meet.

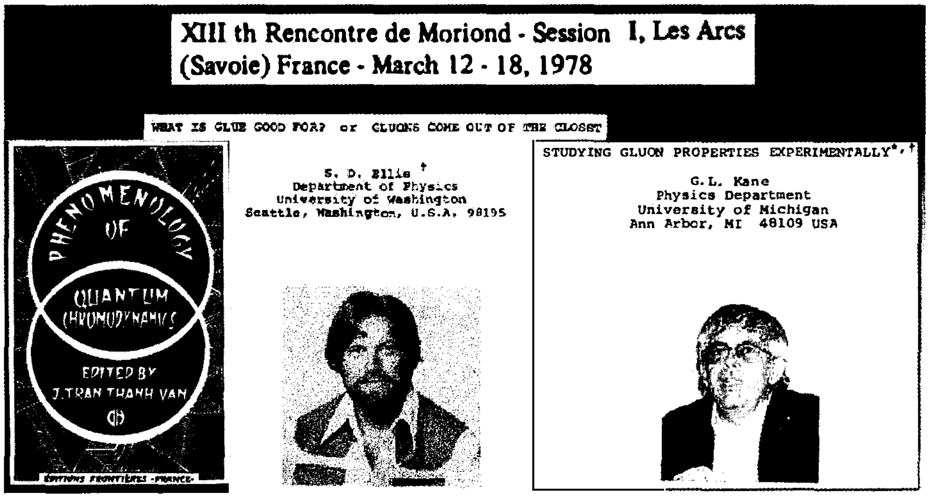

Figure 7 – The Moriond Proceedings 1978 cover page (left), Steve Ellis (middle), and Gorgon Kane (right).

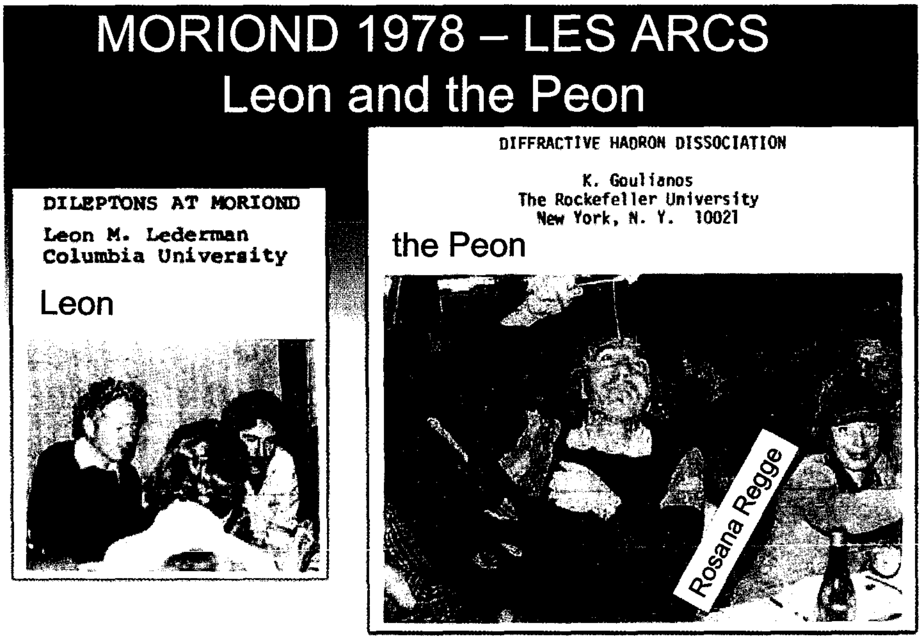

Figure 8 – Leon and the Peon: **Leon** Lederman with Steve Ellis and unidentified participant (left), and **the Peon** (myself) demonstrating a spaghetti-eating technique I invented, with **Rosana Regge** (right) ignoring me!

5 My Moriond

Moriond is the conference that shaped my life by its ingredients::

Figure 9 – Tran and Kim.

Participants: All welcome:
Professors, Students, Scientists, Engineers.
Prerequisites: A passion for science – and skiing!
⇒ Ancient Greece: **healthy mind in healthy body.**
Rewards: Meet other scientists, make life-long friends.
Meet Kim and Tran, and your hard work will be fun!

Acknowledgments

Warm thanks to The Rockefeller University and the U.S. Department of Energy Office of Science for their financial support to conduct the research on which the present paper is based, and to my colleagues at Rockefeller, CDF, and CMS for many useful discussions.

9.
Closing

Experimental Summary - Moriond QCD 2015

Thomas J. LeCompte
High Energy Physics Division
Argonne National Laboratory 9700 S. Cass Avenue Argonne, IL 60439, USA

A summary of the main experimental results presented at the 50^{th} edition of the Rencontres de Moriond - QCD held in La Thuile (Italy), March 21-29, 2015 is presented.

1 Introduction

For nearly fifty years, the Rencontres de Moriond and its spiritual godfather, Jean Tran Than Van, has served as a venue not just for the presentation of the newest results, but also for fitting these results into a larger framework. In my summary talk, and in the corresponding proceedings, I attempted to do just that. Inevitably some prejudice and personal opinion has leaked in; I hope both audiences will forgive me.

The discovery of a Higgs boson at the LHC was a major accomplishment of the field, but at the same time its mass of 125 GeV presents us with something of a puzzle. It is too light to be heavy, and too heavy to be light. By "too light to be heavy", I mean that it is not at the Planck scale, so some symmetry mechanism appears to be in place to keep the mass small, and by "too heavy to be light", I mean that something is keeping this symmetry from working too well and making the Higgs boson even lighter than it is. That something is generally thought to be new physics at the TeV scale. However, flavor physics is telling us that any deviations from the Standard Model that affect low-energy observables is at a higher scale: 10 TeV or higher. One of the key tasks is to reconcile this - a task that includes challenging this picture I have just painted.

The second challenge is that most of the matter in the universe is now known to be composed of a kind of matter not present in the Standard Model. At a minimum, this needs to be identified. Ideally we should be able to produce and study it in the laboratory.

Apart from this, this is the Moriond **QCD** conference. QCD plays an important role in answering the above questions - one needs it to understand background, initial conditions and in many cases the signal being searched for - but it is also a beautiful theory in its own right. QCD provides an opportunity to study - and marvel at - a non-Abelian gauge theory in its purest form.

2 Heavy Ion Physics [1–10]

The basic paradigm of heavy ion physics is the following:

- In A-A (nucleus-nucleus) collisions one expects to see new phenomena, such as production of quark-gluon plasma, or collective phenomena such as flow.
- *pp* (proton-proton) collisions serve as reference data.
- *p*A (proton-nucleus) collisions also serve as reference data, but in this case, nuclear size and structure effects are included, at least for one side of the collision. The recent p+Pb run at the LHC has provided a new source for this data.

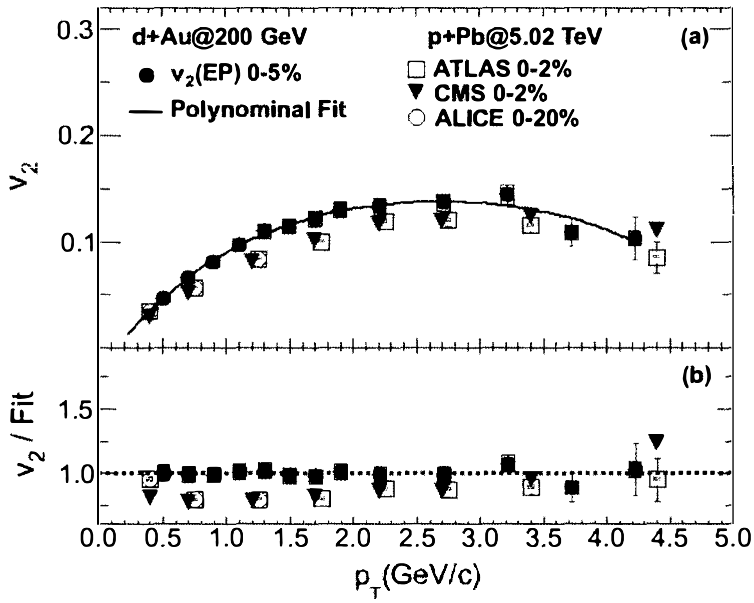

Figure 1 – Elliptic flow measurements in d+Au at RHIC and p+Pb at the LHC.

Limits to this paradigm are starting to show. Perhaps the best evidence for this is displayed in Figure 1, where it shows collective behavior, in this case elliptical flow, even in pA collisions. The same behavior is observed in multiple experiments at both RHIC (in d+Au collisions) and the LHC (in p+Pb collisions). The idea that these systems would be in some sense too small to produce any sort of collective behavior is shown not to be the case. Indeed, the degree of collective behavior seems to be universal.

Possibly related to that is the presence of a large same-side "ridge" in the $\eta - \phi$ plane in pA collisions. A similar structure is visible in AA, but is present only weakly (if at all) in *pp*. This is a second case of collective behavior observed in proton-nucleus collisions.

The idea that proton-nucleus collisions provide a reference dataset where nothing interesting happens seems not to be correct, as even small systems show collective behavior. This doesn't mean that this is useless as a reference dataset, but it does imply that detailed quantitative understanding may take some additional work to explain this more complex picture.

3 Light Quarks, Parton Densities and Electroweak [11–19]

QCD is now being probed at extreme scales - scales we wouldn't have even imagined in the not-too-distant-past. Figure 2 shows that at the LHC comparisons between theory and experiment in W+jets events can go out as far as 8 or more jets. Similarly, Figure 3 shows that in these W+jets events, the leading jet transverse momenta go out to a TeV. Overall, the agreement is rather good, although this program does expose some areas for improvement, for example the leading jet p_T distribution shows some tension with some of the Monte Carlo generators. Overall, events with many jets pose a challenge for these calculations.

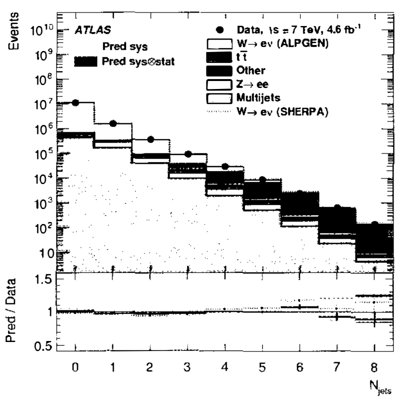

Figure 2 – Jet multiplicity distribution in W+jets events at the LHC

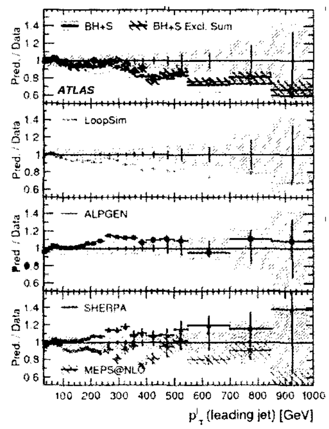

Figure 3 – Leading jet p_T distribution in W+jets events at the LHC

Another area where QCD is entering a more extreme arena is the forward physics program of LHCb. LHCb covers a complementary forward region relative to the ATLAS or CMS experiments, as shown in Figure 4. The center of mass energy of the LHC is sufficiently high to produce W and Z bosons visible in the LHCb detectors. These give precise measurements of the quark distributions at low x: a collision that produces a weak vector boson in the forward region involves one parton at high x and one at low x. The product of the two x's is such that typically one is in a region where the parton density is well-known and thus the rate probes the density of the other.

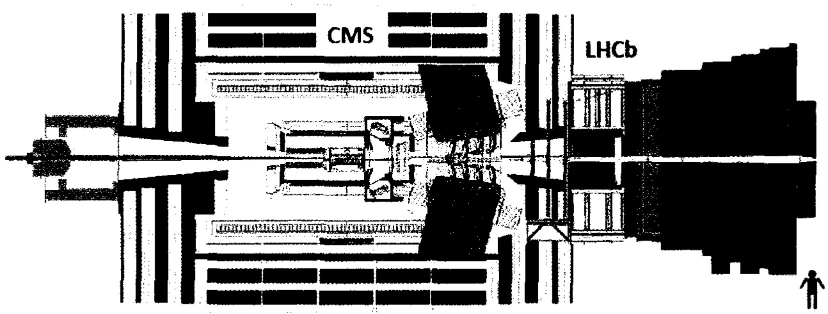

Figure 4 – Respective coverage of the CMS and LHCb Experiments

A puzzle emerged at this conference. The ratio of $Z+$ jets to $\gamma+$ jets as shown by CMS has a shape predicted by MadGraph. However, the measurement is a factor of approximately 20% below theory. This was - and remains - difficult to understand, as most of the theoretical and experimental uncertainties cancel in the ratio, leaving only the vector and axial charges of the participating quarks. This generated much discussion, but no real solution.

4 Quarkonia and Heavy Flavor [20–24]

Below open charm threshold, things are relatively well-understood. Hydrogen-like quantum numbers can be assigned to all the known particles, and indeed, we name them by their quantum numbers: the $\psi(2S)$ is called that because it is the first radial excitation of the $^3S_1$ $c\bar{c}$ state.

Above open charm threshold, things are more confusing: there are states like the $\psi(3770)$ which fit well into the $q\bar{q}$ framework, and states like the X, Y and Z's which do not. Under the working assumption that these are all aspects of the same new phenomenon, we know that these cannot be $q\bar{q}$ states, as the Z's contain hidden charm, electric charge, and as reported at this meeting, isospin.

Four explanations for these states were put forward:

- A four-quark $q\bar{q}q\bar{q}$ state
- Diaquonium, a $(Q\bar{q})(\overline{Q}q)$ state.
- Hydrocharmonium, a $(q(Q\overline{Q})\bar{q})$ state
- A meson molecule, a bound $D\overline{D}$ state, where here D represents a generic charm meson.

Additionally, the neutral members of this family might have an admixture of $c\bar{c}$.

It is not clear to me that these explanations are mutually exclusive. These ideas may be particular idealizations one might expand around, possibly even with different particles occupying different places in this model space. There probably is some $c\bar{c}$ admixture in the $X(3872)$, as the decays $X \to J/\psi+\gamma$ and $X\psi(2S)+\gamma$ have both been observed. It is easier to imagine this decay as an E1 transition than a single photon annihilation between a light quark and antiquark.

Beyond charm, results from ATLAS on the b-quark analogue of the $X(3872)$ were shown. No signal was observed. This may not be surprising: the $X(3872)$ is very near DD^* threshold, and decays via the isospin violating decay $X \to J\psi + \pi^+\pi^-$. So close to threshold, given the mass differences between The charged and neutral D and D^*, isospin is not expected to be a good symmetry. Going from charm to bottom, there is no guarantee that the numeric factors that made the $X(3872)$ easy to spot will still be in play.

Finally, as a historic footnote, there may be analogues In the strange sector, the $a_0(980)$ and $f_0(980)$ are candidates. They are strongly coupled to the $K\overline{K}$ system, and the right side of the resonance decays almost exclusively to $K\overline{K}$, while the left side, below threshold, decays to $\eta\pi$ or $\pi\pi$ respectively. Their quantum numbers are 0^{++}, which in the $q\bar{q}$ picture suggests a $^3P_0$ state. Such a state is difficult to incorporate into an $s\bar{s}$ picture: it is lighter than the S-wave $\phi(1020)$; it is nowhere near the $^3P_1$ and $^3P_2$ members of the same multiplet; and there is an additional 0^{++} state that *is* near the the $^3P_1$ and $^3P_2$. A strong case can be made that these particles, like the X, Y and Z's are some sort of $qq\overline{q}\overline{q}$ state.

5 Searches for BSM Particles [25–29]

Results from more than one hundred searches were shown; there is no evidence for any new particles or phenomena beyond those in the Standard Model. A comprehensive listing of what has *not* been found would make for a boring summary. Instead, I will discuss some of the ideas presented that can enhance the sensitivity for these searches.

Searches for long-lived or weakly interacting particles have been a niche interest for some time, but recently the popularity of these searches has soared. One possibly explanation is that 27% of the surviving p19MSSM models have these long-lived particles. Presumably these arise by having a near-degenerate LSP and NLSP, reducing the allowed decay modes and phase space. These searches are difficult to conduct at colliders, since the detectors were designed around different signatures; the triggering may have to be adapted (ATLAS, for example, has a trigger that selects events with particles decaying in the midst of the muon spectrometer); and even calculating the luminosity can become more complicated. Once the decay time exceeds one bunch crossing, corrections need to be made.

In the long gap between LHC Run 1 and Run 2, cleverness is the only method by which limits can be improved. One idea used by both experiments is to combine different channels, rather than simply taking the most sensitive channel. Limits are improved slightly: perhaps 50 GeV in a search with limits near 1.3 TeV. These improvements are largest when multiple channels have comparable sensitivity. These techniques, of course, can immediately be applied to the Run 2 data when it comes in, and this technique is at its best when it is planned for in the beginning, so the subsamples can be kept orthogonal for ease of combination.

Another idea to extend the reach involves using observables other than invariant masses, mass differences, or related quantities such as missing transverse energy. For example, if the stop squark is just slightly heavier than the top quark, it's signal can be buried under the top quark background. However, the stop squark is a scalar, so one can look for an angular distribution compatible with production of two scalars and inconsistent with pure QCD production. This permits sensitivity all the way down to the top quark mass.

Similarly, one can design searches around Higgs boson decays or vector boson fusion production of new particles. These tools were invented for the Higgs boson search, but can be applied in searches for colorless particles with weak charge.

6 Dark Matter and Gravity [30–32]

While there were only a relatively small number of talks devoted to Dark Matter, a very interesting and important point was brought up regarding collider limits on Dark Matter. Figure 5 (left) shows a collider limit for a process related to Dark Matter production, and Figure 5 (right) has translated this into a limit on the mass and cross-section of the Dark Matter particle.

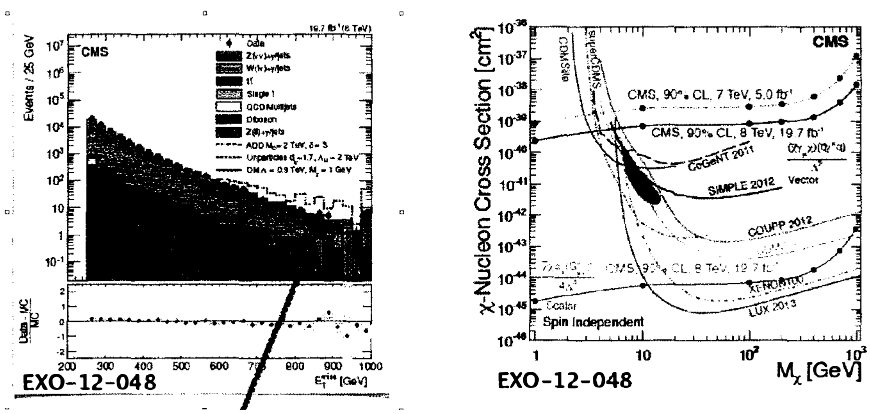

Figure 5 – Left: A CMS measurement with sensitivity to Dark Matter. Right: The same measurement cast as a Dark Matter limit.

The difficulty arises because the framework used to make the transformation has a limited range of validity. The fact that collider measurements are complementary to the direct searches tends to aggravate this problem: the fact that the measurements are far from the limits from direct searches and the fact that the collider measurements can be outside the valid region are two sides of the same coin.

The collider experiments are certain of their measurements. It is only the translation to the framework designed to compare direct detection experiments where the problem begins. Obviously, some changes need to be made. There were formal and informal proposals made at this conference, but no real consensus. I suspect that when the dust settles, we will not have a recipe for turning collider measurements into equivalent direct searches, but a recipe for turning results from searches with a wide variety of techniques into a single common plot.

This problem is not unique to Dark Matter searches. It is simply the case that this problem is most evident here. Fundamentally, so long as we do not see an excess, it doesn't really matter which model we use to describe the exclusion. However, once we see a signal, sorting it out will take some time. If we saw, for example, a peak in the $m(t\bar{t})$ distribution, would we conclude that we see evidence of extra dimensions, or would we conclude we see a topcolor Z'?

7 Top Quarks [33–38]

Many results were presented involving top quarks; I will describe only two of the general themes that appeared in multiple talks.

7.1 The $|V_{tb}|$ story

Very soon after the discovery of the top quark, the CDF experiment set the first direct constraints on the CKM parameter $|V_{tb}|$. [39, 40] Eq. 1 shows the relationship between the fraction of time the top quark decays to a bottom quark and $|V_{tb}|$.

$$R \equiv \frac{BF(t \to Wb)}{BF(t \to Wq)} = \frac{|V_{tb}|^2}{|V_{td}|^2 + |V_{ts}|^2 + |V_{tb}|^2} \tag{1}$$

This method measures $|V_{tb}|$ relative to the small elements $|V_{td}|$ and $|V_{ts}|$. At the time, the more direct measurement of $|V_{tb}|$, taking advantage of the fact that single top quark production is proportional to $|V_{tb}|^2$, was impossible because of the low rate of this process.

Today, this is no longer the case. Single top production is commonplace at hadron colliders, with nine separate measurements shown at this conference. The smallest uncertainties were 4% and 5%, comparable to the best measurement using R, CDF's 4.3%.

Given this information, plus the fact that the Higgs boson production rate tells us there are exactly three families of quarks, I believe that these measurements will be used differently in the future. The consistency of $|V_{tb}|$ in the new measurements will be assumed, which will turn this pair of measurements into a way of determining an experiment's b-tagging efficiency in data.

7.2 The A_{FB} Story

In 2008, the CDF experiment reported [41] a top quark forward-backward asymmetry more than two standard deviations above the then-current Standard Model prediction, a discrepancy that grew to almost 3σ with additional data and more refined analyses. This led to some interesting speculation about the possible cause: Z' bosons, axigluons, and so forth.

Since then, two things have happened. One is that the theoretical prediction has moved up, and the other is that D0 and the LHC experiments have weighed in. Because the LHC is a pp collider, the forward-backward asymmetry manifests as a narrow-wide asymmetry, and because LHC top quark production is dominated by gluons, the effect is diluted. Nonetheless, the large rate of top quark production compensates, and the LHC and Tevatron sensitivities are similar.

The original measurement is now much less improbable, and today is on the high side of a consistent ensemble of measurements, an ensemble which is also consistent with QCD. Additionally, no effect is seen with bottom quarks, although in this case the physics is only similar, not identical. Nevertheless, in my opinion we can close the book on this anomaly.

8 Bottom Quarks and Weak Interactions [42–49]

As discussed earlier, the fact that the flavor sector agrees so well with the Standard Model, as demonstrated in Figure 6, suggests that the scale of new physics influencing flavor is at or above 10 TeV.

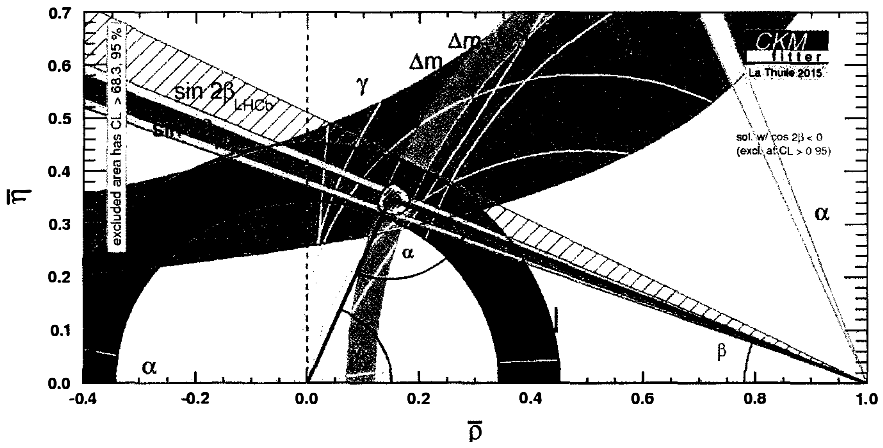

Figure 6 – Despite a few $\sim 2\sigma$ anomalies, the CKM picture holds up over many measurements.

A few discrepant results were reported:

- The decay $B \to K^{*}\mu\mu$ has a 2-3 σ discrepancy with respect to the Standard Model, mostly in the $C5'$ parameter.
- A 2.6σ discrepancy in the rates of $B \to K\mu\mu$ and $B \to Kee$.
- A 3.1σ discrepancy in the decay $B_s \to \phi\mu\mu$.
- A tension in extracting $|V_{ub}|$ from different datasets.

There was much theoretical discussion about possible explanations [50], although given the sheer number of measurements, a few anomalies of this magnitude would be expected.

Perhaps more surprising was the combined LHCb and CMS measurement of the branching fraction $B_s \to \mu\mu$, which is almost exactly at the Standard Model prediction. If anything, it's a bit low. New physics can interfere destructively, but the measurement tells us it cannot be very large.

9 The Higgs Boson [51–56]

At this conference the Higgs boson mass of $125.09 \pm 0.21 \pm 0.11$ GeV, from the combined measurements of both LHC experiments was shown. The individual measurements can be seen in Figure 7. At one time, this measurement hinted that there could be two particles of

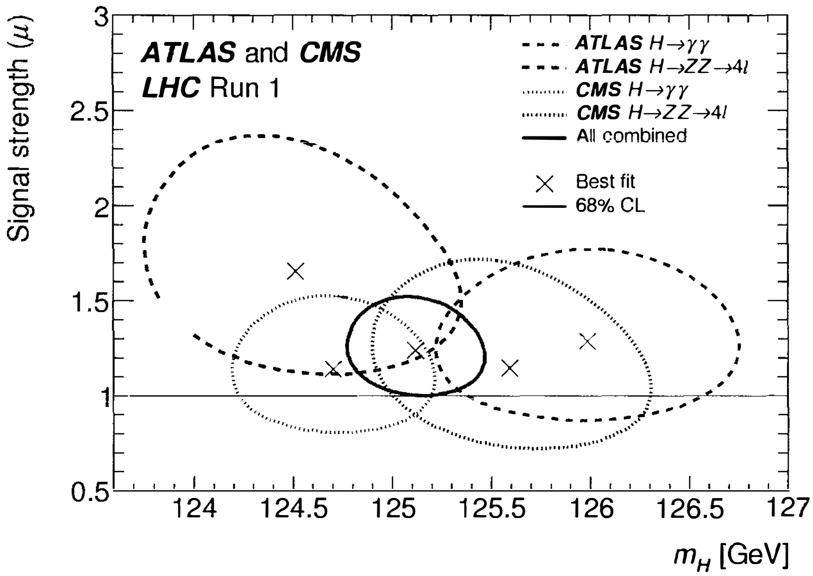

Figure 7 – Higgs boson mass measurements from the LHC.

similar, but not identical, masses, one decaying to ZZ^* and the other decaying to $\gamma\gamma$. There is no longer any reason to believe this, as the mass measurements are now completely consistent with a single particle.

Table 1: Experimental Data bearing on Higgs decays to Fermions

	VH, $H \to b\bar{b}$ Obs. (Exp.)	$H \to \tau\tau$ Obs. (Exp.)	$H \to$ fermions Obs. (Exp.)
ATLAS	1.4 (2.6) σ	4.5 (3.4) σ	4.5 σ
CMS	2.0 (2.5) σ	3.2 (3.7) σ	3.8 (4.4) σ
Combined	2.2 σ	5.3 σ	5.7 σ

Table 1 shows the ATLAS and CMS measurements of Higgs boson decays to fermions, plus my own unofficial combination using Fisher's method. The combination is significant, and the $H \to \tau\tau$ signal is significant on its own. The best evidence for $H \to b\bar{b}$ is still from the Tevatron.

All evidence suggests that the Higgs boson discovered is indeed a scalar with even parity. It is perhaps worth mentioning that while the fits to determine this are very complicated, the ideas behind them are actually quite simple. For example, in the decay $H \to ZZ^*$, conservation of energy implies

$$m(H) = m(Z) + m(Z^*) + \frac{L^2}{2I} \tag{2}$$

which in turn implies

$$\frac{L^2}{2I} = 34 \text{ GeV} - m(Z^*). \tag{3}$$

The mass distribution of the off-shell Z therefore traces out the orbital angular momentum between the on- and off- shell Z. If the observed Higgs boson were a pseudoscalar instead of a scalar, it would have a P-wave decay instead of an S-wave decay. This, in turn, would shift the $m(Z^*)$ distribution lower.

The evidence that the Higgs boson couples to bosons is unequivocal. The evidence that it couples to the third fermion family is very strong, but there is absolutely no evidence yet that it couples to the other two. The production rate tells us that there are only three sequential families of quarks and leptons; additional fermion fields must either be vector-like or get their masses from a different Higgs boson. Searches for a second Higgs boson or deviations from the Standard Model copling predictions all came up negative.

10 Conclusions

The tension that I opened with still remains, and there are no credible hints that the Standard Model is beginning to yield. The Higgs boson mass is pointing us towards new particles or phenomena at the TeV scale and flavor physics is pointing at a scale at least an order of magnitude higher. The nature of Dark Matter is still elusive. It is my sincere hope that the next round of experiments, including the 13 TeV LHC Run 2 and the KEK and Fermilab intensity programs will shed some light on this situation.

Acknowledgments

I thank the organizers for their kind invitation, and for the environment and "Moriond Spirit" they were able to create, and my fellow attendees for the interesting and often spirited discussions we had. Even a non-skier like myself found the week extraordinary.

References

1. R. Bertens, these proceedings.
2. F. Bock, these proceedings.
3. B. Huang, these proceedings.
4. M. Lamont, these proceedings.
5. E. Leogrande, these proceedings.
6. V. Pozdnyakov, these proceedings.
7. C. Roland, these proceedings.
8. S. Tuo, these proceedings.
9. J. Velovska, these proceedings.
10. K. Wozniak, these proceedings.
11. S.Lammers, these proceedings.
12. D. Johnson, these proceedings.
13. D. Brizger, these proceedings.
14. S. Carmada, these proceedings.
15. A. Hafner, these proceedings.
16. M. Misheva, these proceedings.
17. P. Svoisky, these proceedings.
18. G. Mavromanolakis, these proceedings.
19. B. Lindquist, these proceedings.
20. R. Chistov, these proceedings.
21. M. Gagliardi, these proceedings.
22. T. Skwarnicki, these proceedings.
23. W. Yan, these proceedings.

24. K. Zhu, these proceedings.
25. Z. Marshall, these proceedings.
26. S. Folgueras, these proceedings.
27. H. W. Wulsin, these proceedings.
28. E. Kajomovitz, these proceedings.
29. O. Ruchayskiy, these proceedings.
30. Z. Demiragli, these proceedings.
31. G. Landsberg, these proceedings.
32. J. Hirschauer, these proceedings.
33. F. Balli, these proceedings.
34. G. Benelli, these proceedings.
35. O. Brandt, these proceedings.
36. Y. Chao, these proceedings.
37. M Cremonesi, these proceedings.
38. C. Escobar, these proceedings.
39. CDF Collaboration, Conf.Proc., C9510211, 581-583 (1995)
40. T. Affolder, (CDF Collaboration), Phys.Rev.Lett. **86** 3233 (2001)
41. T. Affolder, (CDF Collaboration), Phys.Rev.Lett. **101** 202001 (2008)
42. A. Carbone, these proceedings.
43. A. Crivellin, these proceedings.
44. F. Dettori, these proceedings.
45. L. Gladilin, these proceedings.
46. N. Hussain, these proceedings.
47. C.-D. Lu, these proceedings.
48. D. Lucchesi, these proceedings.
49. D. Strom, these proceedings.
50. G. Zanderighi, these proceedings.
51. C. Anastopoulos, these proceedings.
52. T. Masubuchi, these proceedings.
53. A. Mehta, these proceedings.
54. A. Nayak, these proceedings.
55. R. Plestina, these proceedings.
56. S. Xie, these proceedings.

QCD and High Energy Interactions: Moriond 2015 Theory Summary

G.ZANDERIGHI
CERN, PH-TH, CH-1211 Geneva 23, Switzerland
and
Department of Physics, Theoretical Physics, 1 Keble Road,Oxford OX1 3NP, England

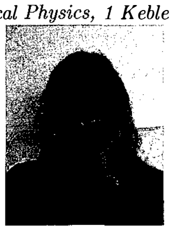

I will summarise the new theory developments that emerged during the 2015 QCD Moriond conference. I will give my perspective on some of the topics and emphasise what I consider most relevant.

1 Introduction

We had more than 30 theory talks covering a rather broad range of topics. The theory talks were allocated to different sessions: Higgs and top, Flavour, QCD, the latter divided into more perturbative/technical aspects and more non-perturbative/formal developments, New Phenomena and Heavy Ions. Sections in this summary reflect the sessions we had at the conference.

2 Higgs and top

Remarkably, we had only one theory talk in the Higgs and top section.[a] Bernhard Mistlberger presented first N^{3}LO results for the inclusive gluon-fusion Higgs cross section in the infinite top-mass effective theory.[1] This calculation is, in my opinion, the theory highlight of the meeting, hence I will spend few words on this topic.

In order to put this work into context, it is useful to examine the left panel of Fig. 1, which shows the slow perturbative convergence of the Higgs cross section. Furthermore, it is evident from the figure that the renormalisation (and factorisation) scale variation, that are commonly used to estimate theory uncertainties, underestimate the shift between different perturbative orders. Fig. 1 (right), presented at the general assembly meeting of the Higgs cross section working group in January,[3] shows results for the preferred total gluon-fusion cross section from different groups. Each group provided a prediction for the cross section obtained by using as a central renormalisation and factorisation scale choice $m_H/2$ (light blue) and m_H (dark blue). The bands illustrate the scale uncertainty, obtained by varying renormalisation and factorisation scales independently by a factor 2 (avoiding the variation where they differ by a factor 4), while

[a]Next-to-next-to-leading order results for top-pair production were presented in the QCD session.

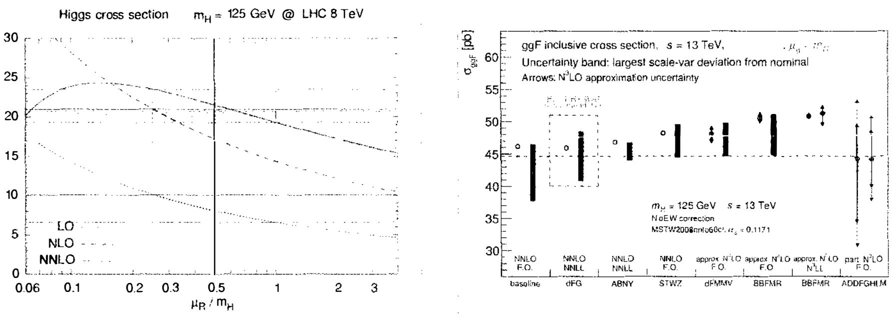

Figure 1 – Left plot: total gluon-fusion Higgs cross section at the LHC (8 TeV) as a function of the renormalisation scale at various orders in perturbation theory. The plot has been obtained using the code of ref. [2]. Right plot: a comparison of predictions for the total gluon-fusion Higgs cross section at the LHC (13 TeV) from various groups.

the red errors denote the total uncertainty on the numbers as estimated by the groups. It is clear from the plot that there was no consensus on the size of the uncertainty on this cross section. This becomes particularly evident from the uncertainties quoted by the last two groups. However, the amount of perturbative control on this cross section has a direct impact on a range of new physics searches in the Higgs sector, hence it was crucial to improve on these predictions by computing the cross section at N^{3}LO. This calculation is however extremely challenging. In fact, the computation involves $\mathcal{O}(10^5)$ interference diagrams (for comparison only 1000 at NNLO), about 60 millions of loop and phase space integrals (47000 at NNLO) and about 1000 master integrals (26 at NNLO). The calculation was performed as an expansion around the threshold, where up to 37 terms in the expansion could be computed. This result is shown in the left panel of Fig. 2, while the right panel shows the dependence of the cross section on the renormalisation

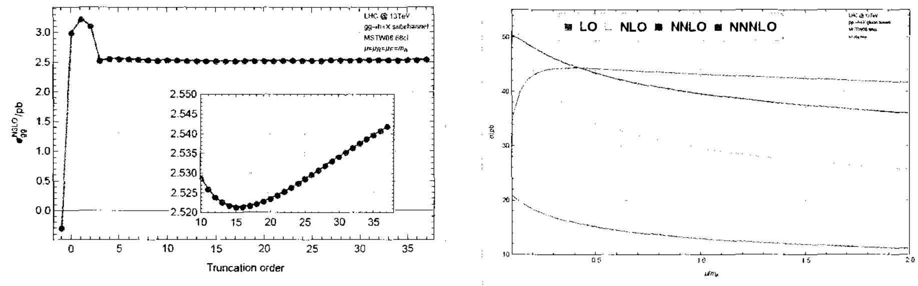

Figure 2 – Left plot: the N^{3}LO correction from the gg channel to the total gluon-fusion Higgs cross section as a function of the number of terms included in the threshold expansion. Right plot: scale variation for the gluon-fusion cross section at all perturbative orders through N^{3}LO.

and factorisation scales (varied together) at all perturbative orders through N^{3}LO. The numbers to take home are that the N^{3}LO corrections amount to about 2% at scale $M_H/2$ and the residual uncertainty as estimated from scale variation is also about 2-3%. At this level of precision, other uncertainties (errors on parton distribution functions, treatment of electroweak corrections, exact top-mass corrections beyond the heavy-top approximation, top-bottom interference in loops...) now become all important. Updated predictions, that will also include an independent scale variation, will provide a more robust estimate of the uncertainty due to missing higher orders.

Nonetheless, the very little experience that we have with scale variation at this order may suggest a conservative approach.

3 Flavour

The flavour day was possibly the most exciting day of the conference because of the flavour anomalies observed recently at the LHC. Nazila Mahmoudi presented a concise introduction to flavour physics, recalling in particular the reasons why the flavour physics is so rich and interesting. [4] First of all, flavour physics is sensitive to new physics (NP) energies scales that are much larger than the collider energy, hence through flavour physics one could probe NP before it is observed directly in collider experiments. Furthermore, CP violation is closely related to flavour physics: the only source of CP violation in the Standard Model (SM) comes from the Cabibbo-Kobayashi-Maskawa (CKM) matrix, but for baryogenesis we know that we need other sources of CP violation. On top of this, there is the "SM flavour puzzle", i.e. the origin of masses and mixing of quarks and leptons, and the "new physics flavour puzzle", i.e. the mechanism protecting TeV-scale NP from causing large deviations from the SM predictions in the flavour observables that we have measured so far. Recently, there has been a lot of new data in this sector mainly from LHCb, but also from ATLAS and CMS. One of the new LHCb measurements concerns the CKM element V_{ub}. There has been a longstanding tension in V_{ub} (but also in V_{cb}) from inclusive and exclusive decays. It was long believed that this measurement was not possible at LHCb, yet V_{ub} was recently measured there. This measurement, which was presented for the first time at the Electroweak Moriond meeting this year, seems to confirm the exclusive measurement.

Looking at other LHC data, almost all measurements are currently consistent with the SM. Yet, recently four hints for new physics in the flavour sector have been reported:

- the branching ratio $H \to \mu\tau$ was measured to be $(0.84 \pm 0.40)\%$ - rather than 0;
- in the decay $B \to K^*\mu^+\mu^-$ an anomaly was observed in an angular distribution called P_5';
- the SM branching ratio $B_s \to \phi\mu^+\mu^-$ at high invariant mass is above measurements;
- the ratio $R_K \equiv \mathrm{Br}(B^+ \to K^+\mu^+\mu^-)/\mathrm{Br}(B^+ \to K^+e^+e^-)$ was measured to be 0.75 ± 0.10, rather than 1.

Adolfo Guevara focused on the anomaly in $R(K)$ and showed that the discrepancy can not be attributed to long-distance, poorly-modelled effects. [5] While this is not an exciting finding, it is of course very important to have a solid estimate on long-distance effects. Ben Grinstein presented a very concise introduction to effective field theories (EFTs), and stressed that the reason for using EFTs is that they often have more predictive power. [6] This is due both, to the fact that they involve less free parameters and that you can often simplify (technically challenging) calculations. In particular, in terms of dimension 6 operators one can write the following contributions to the Lagrangian:

$$\mathcal{L}\mathrm{eff} = -\frac{G_F}{\sqrt{2}} \sum_{p=u,c} \lambda_{ps} \left(C_1 \mathcal{O}_1^p + C_2 \mathcal{O}_2^p + \sum_{i=3}^{10} C_i \mathcal{O}_i \right) . \tag{1}$$

For the above anomalies, of particular interest are the electromagnetic dipole, the vector and axial-vector operators $\mathcal{O}_7$, $\mathcal{O}_9$ and $\mathcal{O}_{10}$, respectively

$$\mathcal{O}_7 = \frac{e}{(4\pi)^2} m_b \left[\bar{s}\sigma^{\mu\nu} P_R b\right] F_{\mu\nu}, \quad \mathcal{O}_9 = \frac{e^2}{(4\pi)^2} \left[\bar{s}\gamma^\mu P_L b\right] \left[\bar{l}\gamma^\mu l\right], \quad \mathcal{O}_{10} = \frac{e^2}{(4\pi)^2} \left[\bar{s}\gamma^\mu P_L b\right] \left[\bar{l}\gamma^\mu \gamma_5 l\right] . \tag{2}$$

Grinstein pointed out that taking into account all bounds, and assuming that NP effects are only due to scalar and tensor semi-leptonic operators one can constraint $0.982 \le R_K \le 1.007$.

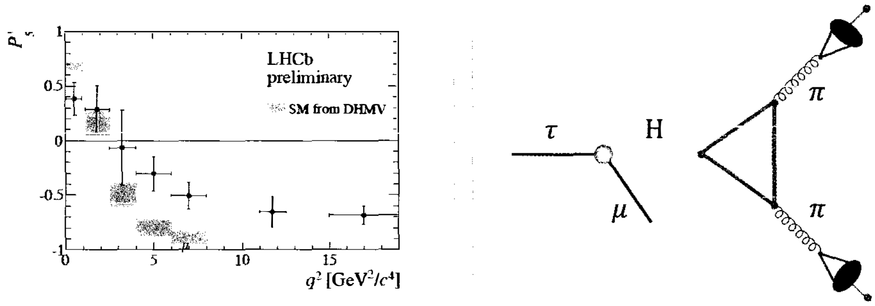

Figure 3 – Left plot: LHCb measurement of P_5' compared to SM predictions as a function of the momentum transfer. Plot taken from ref. [7]. Right plot: representation of the decay $\tau \to \mu H(\to \pi\pi)$.

On the other hand, the measured value of R_K can be explained with a correction to the Wilson coefficient of the vector operator, $C_9^{\rm NP} \approx -1$ (other explanations for the measured value of R_K could also come from a Z' or leptoquarks).

Sebastian Descotes-Genon focused on the $B \to K^*\mu^+\mu^-$ anomaly, shown in Fig. 3 (left panel). [8] He explained how different kinematic regimes at low or high momentum transfer q^2 imply a high or low recoil of K^* and hence NLO QCD factorisation or heavy quark effective theory become the appropriate tools to employ in the two regimes, respectively. He also explained how observables like P_5' are constructed in such a way as to cancel large uncertainties from soft form factors and that residual effects of power corrections are estimated to be about 10%. The conclusion of the study is that the LHCb measurement supports $C_9^{\rm NP} \sim -1$, but there is room for NP also in other Wilson coefficients. Discussions about the accuracy of the theory predictions and the interpretation of data in terms of new physics are still ongoing.

Andreas Crivellin pointed out that all four LHCb anomalies could be explained in two models with gauged $L_\mu - L_\tau$: either a two-Higgs doublet-model (2HDM) with vector-like quarks or a three-Higgs doublet-model (3HDM) with gauged flavour dependent B-L charges. [9] Such a model predicts also a non-vanishing $\tau \to 3\mu$ decay. Since the model has a point-like $H\mu\tau$ vertex, a question was raised whether this is consistent with current limits on $\tau \to \mu\pi\pi$, which involves a Higgs exchange and the decay of the Higgs to two gluons through a top loop, illustrated in the right panel of Fig. 3. After a quick calculation Crivellin and Grinstein established that the model is still allowed. [b] This example illustrated how difficult it is today to design new models that explain possible anomalies but are not yet excluded by precision data. Still looking at extended Higgs sectors, Eibun Senaha presented a scale-invariant 2HDM with Coleman-Weinberg (CW) symmetry breaking, rather than spontaneous symmetry breaking as in the SM Higgs mechanism. [10] The model predicts deviations, for instance in the $h \to \gamma\gamma$ decay and in the hhh coupling that are potentially detectable in future experiments. Another 2HDM, a Branco-Grimus-Lavoura (BGL) model, with naturally suppressed FCNC as a result of a symmetry of the Lagrangian was discussed by Gustavo Castelo-Branco. [11] In BGL models the entire flavour structure is controlled by the CKM matrix. 2HDM are an excellent framework to study NP in the scalar sector. For instance, it is not clear yet whether the discovered Higgs has small FCNCs. Hence, Branco pointed out that it is very important to search for flavour violation in the scalar sector. He stressed that theorists have been wrong many times, it is therefore important to look without prejudice, in particular to look also for interactions or deviations that are not predicted in more common NP scenarios.

[b] Greg Landsberg however pointed out that if you have four anomalies, and a model that explains all four of them, the model is wrong as at least one anomaly will surely go away.

A last theory talk in the flavour session was given by Cai-Dian Lu, who pointed out that when the final state consists of two vector particles, an angular study of the vector's decay products provides an insight into the spin structure of flavour-changing interactions. [12] He stressed that, in particular, the meson decays $B_{u,d,c,s} \to VV$ have a very rich phenomenology. Describing them is however difficult and many theoretical approaches exist, but most of them can not fully explain all measurements. He used a perturbative QCD approach, and stressed the important role of annihilation-type diagrams. Lu then presented many predictions and comparisons to data. Some looked very successful, others less so, however no theory uncertainties were given, so that it was difficult to draw conclusions.

4 QCD

Almost all talks in the QCD sessions were theoretical. The day was split into a more perturbative morning focusing on calculations of higher-order corrections, and a more non-perturbative afternoon, mostly involving new theoretical developments.

4.1 Perturbative QCD

First of all, it is important to remind ourselves why it is important to push the perturbative accuracy to higher orders. We have by now seen amazing results from Run I at the LHC, including competitive measurements of SM parameters (even of the strong coupling constant α_s), precision Higgs physics, jets spectra up to several TeVs, constraints on anomalous couplings, on NP models, on dark matter (DM) candidates and more, as summarised by Tom Le Compte. [13] Even better results are expected at Run II. An optimal use of the machine can be achieved when the experimental (statistical and systematic) and theoretical uncertainties are comparable. Currently, the use and interpretation of some cross sections is already limited by large theory uncertainties, mostly estimated via a variation of renormalisation and factorisation scales. Hence, it is mandatory to push the perturbative accuracy even further. Pier Paolo Mastrolia presented a beautiful review of modern methods for higher-order calculations. [14] He stressed the richness and power of factorisation, which is at the core of unitarity approaches and presented an interesting analogy between quantum mechanics and Feynman integrals. He then discussed a unitarity formalism, the Magnus Expansion, for multi-loop master integrals. Future directions include the treatment of multi-loop diagrams with internal masses and more legs and an automated analytic treatment of the one-loop case. Analytic results are in fact typically superior to numerical ones, since they are faster and numerically more stable.

Jonas Lindert showed novel one-loop methods at work: he presented the QCD and electroweak (EW) corrections to onshell W production in association with 1, 2, or 3 jets obtained using `OPENLOOPS`, `MUNICH` and `SHERPA`. [15] While NLO EW corrections might seem just a trivial extension of the QCD case, they are in fact technically much more complicated then just NLO QCD and involve a lot of subtleties. The phenomenological results for W plus multi-jet production that he presented are very rich, in particular one can observe a non-trivial dependence on the jet multiplicity. W plus multi-jet events play a key role for tests of the SM and for beyond SM (BSM) searches based on signatures with jets, a lepton and missing transverse energy (MET). One of the main outcomes of the results presented by Jonas is that EW corrections are important in the TeV region (where all order Sudakov effects should also be included). For the future, the plan is to include vector bosons decays, parton shower corrections and to extend multi-jet merging to NLO QCD+EW.

Beyond NLO corrections, Fabrizio Caola presented a brief review of the status of NNLO, including the motivation to push the perturbative accuracy to this order, the different methods used, the processes known or almost known (Higgs, Drell-Yan, $t\bar{t}$, single top, V+1 jet, dijets, dibosons, H+1 jet). [16] The main message from his talk is very positive, i.e. that the NNLO technology is now ready to cope with LHC demands. However, because the phenomenological

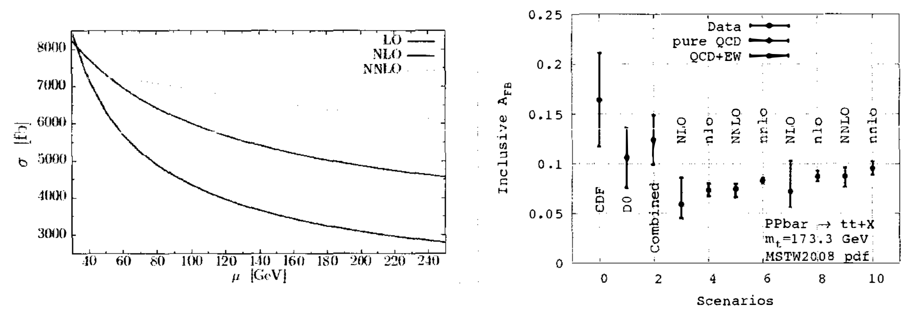

Figure 4 – Left plot: the Higgs plus one jet cross section at the 8 TeV LHC at various orders in perturbation theory as a function of the renormalisation and factorisation scale, both set to μ. Jets are defined using the anti-k_t algorithm with $R = 0.5$ and $p_{t,\mathrm{cut}} > 30$ GeV. Right plot: data for the the forward-backward asymmetry from D0 and CDF (blue) compared to various theory predictions including only QCD corrections (black) or including both QCD and EW corrections (red).

environment is so rich, it will not be enough here to provide numbers for cross sections or few distributions, and there will be a lot of pressure on the authors to release codes as soon as possible. He also showed results for Higgs plus one jet production at NNLO, which at the time of the conference were new and still unpublished. The NNLO corrections turn out to be sizable (of the order of 20% if the Higgs mass is taken as a central renormalisation and factorisation scale), and reduce the scale-dependence of the cross section, as can be seen from Fig. 4 (left). This was expected given the large corrections in the case of inclusive Higgs production, and emphasizes the importance of including NNLO corrections.

Another important NNLO calculation was presented by Michael Czakon, who discussed the long-standing tension between SM predictions and Tevatron measurements of the forward-backward (FB) asymmetry, for which plenty of tentative BSM explanations have been given in the past.[17] Recently, the SM theory prediction for the asymmetry has been upgraded to include full NNLO corrections. A limitation of the calculation is that the top quarks are stable, i.e. the result is fully inclusive in the top decay. One ambiguity that arises is due to the fact that the FB asymmetry is the ratio of the asymmetric over the symmetric cross section, hence one can choose to expand the ratio in powers of the coupling constant, or not. These two approximations are denoted by nnlo and NNLO in the right panel of Fig. 4, respectively. Furthermore, there is an ambiguity in how to combine EW and QCD corrections, either in an additive or in a multiplicative way. Fig. 4 (right) shows that there is now perfect agreement between the D0 result and NNLO theory, while the NNLO result is just $1.5\,\sigma$ below the CDF measurement. The fact that the discrepancy in the asymmetry is not present any longer is mostly due to the updated measurement of D0, however the NNLO calculation was very important to confirm the robustness of the SM prediction. The calculation of the NNLO top cross section was presented two years ago, it took then a long time to provide predictions for the Tevatron asymmetry. One might then wonder whether it is realistic to expect distributions for the LHC in a reasonable amount of time, especially given the tension in the transverse momentum spectrum of boosted tops between next-to-leading-order (or LO matrix element plus parton shower generators) and ATLAS data.[18] Michael Czakon is now working on a completely new software based on a four dimensional subtraction scheme, which will be several orders of magnitudes faster than the first NNLO code for top-pair production.

While fixed-order calculations are very valuable in general, they are known to fail in particular regions of phase space. In these regions, either parton showers or analytic resummations can be employed. In Higgs studies involving a jet-veto, it was suggested some time ago that there are

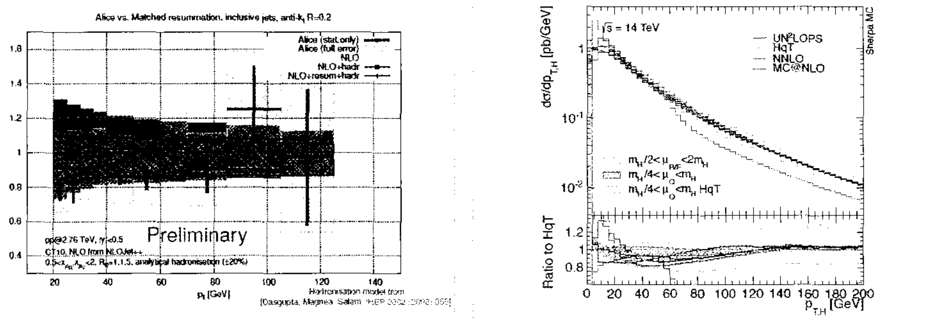

Figure 5 – Left plot: inclusive jet distribution measured at ALICE (red points and orange bands), compared to pure NLO with hadronisation corrections (green band) and a calculation that includes also $\ln(R)$ terms to all orders (blue band). Jets are defined using the anti-k_t algorithm with $R = 0.2$. A reduction of theoretical uncertainty can be observed. Right plot: the Higgs transverse momentum spectrum using the UN^{2}LOPS method, compared to other calculations.

potentially large logarithms related to the use of small jet radii. In fact, when the jet radius is small, the effect of emissions outside the jet, that reduce the energy, can become important. Because of the phase space constraints, this effect scales as $\ln(R)$. Frederic Dreyer explained that in a number recent jet-studies smaller jet-radii R are being used (e.g. $R = 0.2$ in heavy-ions to mitigate pile-up, or in jet-substructure studies).[19] Frederic showed that a resummation of leading $\ln(R)$ terms has been recently carried out using an evolution equation for the quark generating function. Fig. 5 (left) illustrates the reduced scale dependence that can be achieved once the $\ln(R)$ resummation is performed for inclusive jet production. The plot also shows a comparison with experimental measurements from ALICE. There is good agreement within the currently large experimental errors. It is clear that this work will be even more relevant for future analyses, when more precise data will be available and the use of smaller jet radii will become more widespread in order to reduce increasing pileup contamination and to study more highly collimated jets.

Still in the spirit of improving fixed-order calculations, Stefan Prestel discussed going beyond NNLO by merging NNLO and parton showers.[20] This is important to have the best possible perturbative prediction and the fully exclusive description (i.e. the best of both worlds). NNLO was recently merged to a parton shower in the UNNLOPS approach for Drell Yan and Higgs production. Results for the Higgs transverse momentum distribution are shown in Fig. 5 (right). Currently, within this approach, the zero-p_t bin is problematic, since the virtual correction is not spread by the parton shower, but it sits all at zero transverse momentum. In future, it would be desirable to extend the NNLOPS description to more complicated processes, however such a task is not trivial no matter which NNLOPS approach one considers.

While the calculation of higher-order terms in the perturbative expansion is obviously very useful to reduce the theoretical uncertainty, it is also important to have a solid procedure to estimate this residual uncertainty. This is obviously difficult, as the knowledge of the next term in the expansion would be required to provide a very reliable estimate of the theoretical uncertainty. A widely adopted procedure to estimate this uncertainty consists in varying the renormalisation and factorisation scales around a central value, which is chosen to reflect the hardness of the hard process. Emanuele Bagnaschi discussed how this scale-variation procedure has severe limitations in estimating the true theory uncertainty.[21] On top of this, the theory uncertainty has no statistical meaning, so it cannot be combined "properly" with experimental statistical uncertainties. In 2011 Cacciari-Houdeau (CH) proposed a Bayesian approach to estimate missing higher orders. Recently the CH method was modified to use a variable expansion parameter ($\overline{\text{CH}}$).

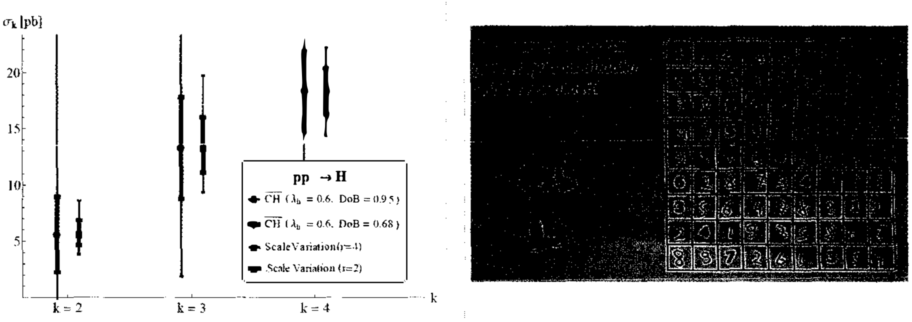

Figure 6 – Left plot: a comparison between two methods to estimate the theoretical uncertainties, scale variation (red) and the $\overline{\text{CH}}$ approach. Right plot: a (non-standard) application of random matrix theory.

Furthermore, a first comprehensive set of more then 30 observables was used to compare the $\overline{\text{CH}}$ method to standard scale variation, including, for the first time, hadronic observables. Fig. 6 (left) shows a comparison between the scale variation uncertainties and the $\overline{\text{CH}}$ uncertainties for Higgs production. k denotes the order at which the calculation is performed. The scales have been varied by a factor 2 or a factor 4, while for the $\overline{\text{CH}}$ approach, the 68% and 95% confidence intervals are shown. The general conclusion from this and other plots is that in many cases, scale variation appears to do a good job in estimating the size of the uncertainty. Furthermore, in most cases where the procedure fails, we believe we understand the reason. On the other hand there is value in having a quantitative, statistical meaning to any statement referring to theory uncertainties. In future, one can expect many valuable comparisons between the $\overline{\text{CH}}$ approach and standard scale variation using new NNLO calculations that are becoming available.

Another source of theoretical uncertainty, beyond missing higher orders comes from our limited knowledge of the strong coupling constant. David D'Enterria pointed out that in fact α_s is to date the least precise known of all couplings (known to about (0.5-1)%), and this impacts all LHC cross sections. [22] Furthermore, a very precise knowledge of the strong coupling is a key for SM precision fits and is relevant in BSM studies (e.g. for coupling unification at GUT). The current world average is $\alpha_s = 0.1185 \pm 0.0006$. David presented new fits of α_s using the jet fragmentation function in e^+e^- and DIS data using an approximate NNLO calculation matched to NNLL. These fits give a value of the coupling of $\alpha_s = 0.1205 \pm 0.0010$. In future the plan is to extend the calculation to full NNLO+NNLL. Still, these fits are by far not trivial, as they require a careful treatment of the correlation between data and of heavy-quark thresholds.

4.2 Less perturbative QCD

In-between fixed-order expansions and non-perturbative regions, there are regions of phase space where calculations are needed that resum large classes of corrections to all orders in the coupling constant, typically those accompanied by large logarithms. Many of these resummed calculations rely on the formulation of a factorisation theorem. Such a factorisation, while not necessary, turns out to be very useful in many cases, as it allows one to split the calculations into various elements that are simpler to calculate and that can be computed in one context and used in a different one. Mark Harley presented a clear introduction to some of these ingredients, i.e. Wilson lines, soft functions, (cusp) anomalous dimensions and webs. [23] The aim of his work is a better description of universal soft singularities. Webs in this respect are very useful: they organise diagrammatic contributions to the exponent of the soft function, and one can show that all such contributions appear with connected colour factors. Subtracted webs are what remains in the exponent after the removal of multiple UV poles. Finally, multiple gluon exchange webs

(MGEW) are subtracted webs with no gluon self-interaction (i.e. only dipole-like exchanges). It has been conjectured, and confirmed by explicit calculations in specific cases, that the integrand of MGEWs contains no polylogarithms, only logarithmic functions, each dependent on a single cusp angle. It is still an open question whether this always holds for MGEWs and it is not clear why does this happen. Furthermore, work is under way to extend current techniques to compute more general webs: in particular, results for completely connected diagrams at three loops were recently announced at the Radcor-Loopfest conference.[24]

Regarding the treatment of radiation from the initial state partons, all higher-order calculations mentioned so far rely now on collinear factorisation, which however does not work well when one incoming parton carries a very low momentum fraction. Sebastian Sapeta discussed an improved transverse momentum dependent factorisation for forward dijet production in dense (small x)-dilute (large x) hadronic collisions.[25] This is the only existing approach which is valid in all regions of the transverse momentum of the target, from very high transverse momenta, where high-energy factorisation is usually applied, to very low ones, where collinear factorisation holds. Hence, this approach provides a robust framework for studies of saturation domains with hard probes. The final aim is to gain a better understanding of factorisation breaking and the nucleon structure.

While perturbative corrections can be calculated, non-perturbative corrections are usually just modelled. Sharka Todorova-Nova pointed out that the Lund string fragmentation model has been very successful. It has been implemented in Pythia and, after tuning, it describes data well in general. Still, it has limitations and some data is not well described by it. Hence, she presented a study of quantum properties of three-dimensional helix-shaped QCD strings.[26] The model is predictive after fixing two parameters for the string. According to Sharka, in the near future it will be possible to compare predictions from the model with upcoming measurements. Shi-Yuan Li pointed out that colour connections are the bridge between parton and hadron systems.[27] Four-quark systems ($ccbb$, $bbbb$, etc.) have an intrinsic ambiguity in the colour wave-function, which leads to different meson production. Li encouraged phenomenological studies in e^+e^- collisions to look and interpret different meson production as evidence of certain colour connections.

Various approaches to non-perturbative dynamics use symmetries and dualities to obtain results at strong coupling. Miguel Costa presented an AdS/QCD phenomenological model that matches well the intercept and slope of Donnachie-Landshoff pomeron.[28] The model is predictive, since everything in the model is fixed from soft pomeron exchange. A careful analysis of data for deep inelastic scattering (DIS), deeply virtual Compton scattering (DVSC) and virtual meson production (VMP) is hence interesting. Andrew Koshelkin looked at multi-particle dynamics and pion production using a flux tube (a compactification to two dimensions) and showed a comparison to ALICE data for the transverse momentum distributions in high-energy proton-proton collisions.[29] Giancarlo D'Ambrosio pointed out that soft wall models in holographic QCD have correct Regge trajectories but a wrong operator product expansion (OPE).[30] Hence, he presented a modified version of the dilaton potential that allows one to comply OPE. OPE is recovered by adding a boundary term. Low energy chiral parameters, F_π and L_{10}, are well described analytically by the model in terms of Regge spacing and QCD condensates.

We had a single lattice talk at the meeting on random matrix theory. Chiral Random Matrix Theory is a powerful mathematical tool to calculate eigenvalue correlations in the IR limit of QCD. The way it works is simply to replace the Hamiltonian with a Random Matrix with the same global properties. Once this is done, one can compute observables by averaging over ensembles. Here it is critical to identify what are the universal quantities (i.e. those that are independent of the probability distribution). Savvas Zafeiropoulos considered explicitly the case of $N_c = 2$ QCD and presented a study of the discretisation for D_5 (i.e. the hermitian version of Wilson operator D_W) and D_W itself.[31] In the future he plans to study the case of adjoint QCD, which has a different chiral symmetry breaking mechanism.[c]

5 New Phenomena

Unfortunately, no evidence for new phenomena has been seen in Run I at the LHC. Possibly the strongest motivation for physics beyond the SM is the astrophysical evidence for DM in galaxies and in cosmological observations. Leszek Roszkowski pointed out that the measured value of the Higgs mass of 125 GeV allows for rather heavy SUSY states, too heavy to be produced at the LHC. DM searches provide then important complementary bounds to collider searches.[32] In particular he emphasised the possible future role of the Cherenkov Telescope Array (CTA) experiment, a next generation ground-based very high energy gamma-ray instrument. Beside exploring the origin of cosmic rays and their role in the Universe, the nature and variety of particle acceleration around black holes, the CTA aims at searching for the ultimate nature of matter and physics beyond the Standard Model. For instance within the CMSSM, it will allow one to explore mass ranges (for m_0 and $m_{1/2}$) that are out of reach at the LHC, as can be seen from Fig. 7 (left). On the other hand, the existing tension with $(g-2)_\mu$, if taken seriously, requires light-ish SUSY particles, which should be within LHC reach.

Another possible future experiment that is complementary to the LHC is SHIP (Search of Hidden Particles). Oleg Ruchayskiy pointed out that we might not have detected new particles at the LHC either because they are too heavy, or because they are light but very weakly coupled.[33] The first case, will be investigated by energy frontier experiments, currently the LHC Run II. The second option can be explored by going to the so-called intensity frontier. This is precisely what SHIP aims to do. The idea is just to take a highest energy/intensity proton beam, dump it into a target, followed by the closest, longest and widest possible and technically feasible decay tunnel. Oleg showed that for instance a Neutrino minimal SM, which addresses neutrino oscillations, DM, baryon asymmetry, and inflation, an be explored with SHIP. Similarly, SHIP can explore other models that involve very weakly interacting long lived particles including Heavy Neutral Leptons, right-handed partners of the active neutrinos, light supersymmetric particles (sgoldstinos, etc.), scalar, axion and vector portals to a hidden sector.

The complementarity between direct and indirect DM detection experiments and the LHC was also stressed by Greg Landsberg.[34] In fact, freeze-out, direct detection and collider production can be all represented using the same diagram and crossing the direction of time. DM is typically searched for at the LHC through so-called mono-X searches, i.e. the production of one (or more) SM particles or jets accompanied by a large MET that is attributed to DM particles escaping detection. Often DM searches use an EFT where the mediator has been integrated out. Greg pointed out that since the mediator is integrated out, the dynamics might not be properly described, and hence the interpretation of EFT results becomes problematic. Following the strategy used in SUSY searches, Greg suggested to use so-called simplified models. Here one identifies simple models and works out the signatures. The simplification limits the number of arbitrary parameters, still providing a robust benchmark.[d] The simplified model for DM searches used by Greg uses an s-channel spin-1 mediator, that interacts to DM and fermions. This is a four-parameter model. Extensions for instance to include the case of t-channel mediators, or spin-0 interactions are also possible. Fig. 7 (right) shows a comparison of EFT bounds (green) to the above simplified model assuming the spin-1 mediator to have pure axial-vector couplings. It is evident that in some regions of parameter space EFT results are too optimistic, in others they provide too loose bounds.

[c] An application of random matrix theory, in a different context, is illustrated in Fig. 6 (right panel).

[d] It is important to keep in mind that while simplified models are practical tools, they can exhaust their value as a benchmark at some point, as, I believe, is the case for the CMSSM now.

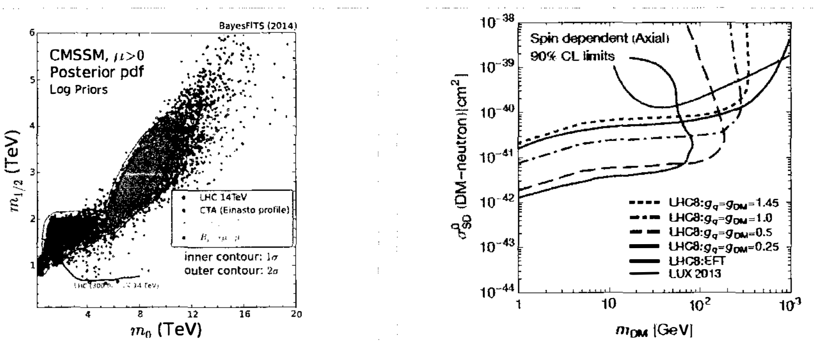

Figure 7 – Left plot: illustration of the range of the $m_{1/2}$ and m_0 plane that can be explored by various experiments. Right plot: bounds for the spin-dependent cross section that can be obtained within an EFT approach (green), or using a simplified model with different choices of the coupling of the mediator to quarks and DM (blue). Bounds from LUX (red) are also shown. Plot taken from ref. [35].

6 Heavy Ions

Our Friday started with a very comprehensive introductory talk on heavy ions (HI) by Carlos Salgado.[36] He pointed out that behind a simple QCD Lagrangian, there are very rich emerging phenomena, like asymptotic freedom, confinement, chiral symmetry breaking, mass generation, new phases of matter, and a very rich hadron spectrum. Some of the questions raised by observations can be further studied with heavy-ion collisions. For instance one can study the structure of the hadrons and nuclei at high energy, one can try to understand if the created medium is thermalised and what are the properties of the produced medium. In this context, for a long time proton-nucleon collisions (pA) were considered a benchmark point needed to subtract the background from nucleon-nucleon (AA) collisions. However pA collisions seems to have taken up an unexpected role since results for pA collisions turn out to have some features similar to those for AA collisions, in particular concerning the collective, hydro-dynamical behaviour. This raises the important question of whether such a small system can also thermalise. One of the standard probes of a hydro-dynamical behaviour is the so-called elliptic flow, i.e. the flow due to the fact that there is more momentum in the plane of the collision, compared to the transverse direction (a simple consequence of having a higher pressure gradient in the plane). Data are based on measuring two or more particle correlations. Recently, there has been a lot of theoretical work in trying to add fluctuations in initial conditions and in including viscosity corrections. Another standard tool is measuring jet quenching in medium. The idea here is simply that a medium suppresses the propagation of coloured particles, compared to the free propagation, hence this results in jet suppression. The simplest observable of jets in nuclear collisions is the measurement of the one-particle inclusive production at high transverse momentum. The effect of the surrounding matter can then be identified by the suppression of the signal, with respect to the proton-proton collisions, due to energy loss. A standard probe of medium effects uses the nuclear modification ratio, defined as

$$R_{AA} \equiv \frac{d\sigma^{AA}/dydp_T}{N_{Coll}d\sigma^{pp}/dydp_T}, \tag{3}$$

where N_{coll} is a normalization factor computed in the Glauber model to allow the comparison with the proton-proton cross section. The suppression of high-p_T hadrons was one of the first, and also one of the main, observations at RHIC. Fig. 8 (left) shows the effect of the suppression at the LHC, where the propagation of all particles interacting with the medium are suppressed. This can be seen from the fact that R_{AA} is smaller than one, while for isolated photons and EW bosons, that do not interact with the medium, R_{AA} is compatible with one. Carlos then

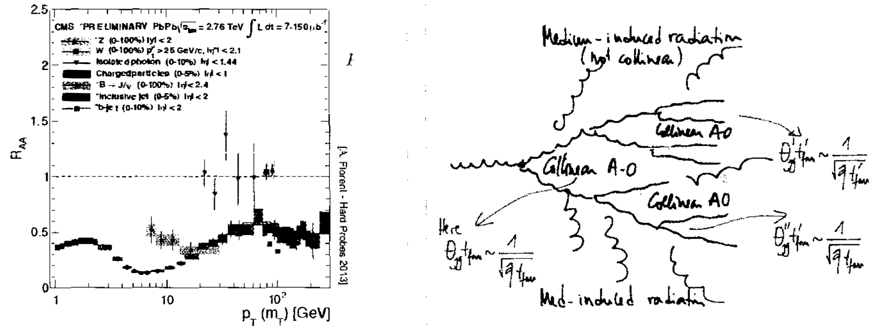

Figure 8 – Left plot: the nuclear modification ratio as a function of the transverse momentum. Right plot: a new picture of jet-quenching that involves two components, a vacuum-like, angular-ordered component (red) and a medium-induced, not collinear radiation (bluc).

presented a new picture of jet-quenching, illustrated in Fig. 8 (right), where the parton shower is composed of two overlapping components, which can be understood as a reorganisation of the jet into multi-jets, with vacuum-like collinear radiation, that effectively act as single emitters for the medium-induced radiation. It will be interesting to see how future measurements compare to this new picture.

When studying correlations, Matt Luzum pointed out that it is instructive to study two-particle correlation as a function of the transverse momentum vector of the particles.[37] In fact, the hydro-dynamic behavior imposes constraints on the momentum structure of two-particle correlation. One can define a full correlation matrix

$$V_{n\Delta}(p_T^a, p_T^b) = \left\langle \frac{1}{N_{\text{pairs}}^{a,b}} \sum_{\text{pairs}\{\text{a,b}\}} \cos n\Delta\Phi \right\rangle , \tag{4}$$

where $N_{a,b}$ is the number of particles with momenta p_T^a and p_T^b in a given event, $\sum_{\text{pairs}\{\text{a,b}\}}$ is the summation over all sets of these pairs, and $\Delta\Phi = \Phi^a - \Phi^b$ their relative azimuthal angle. This quantity can be used to define

$$r_n \equiv \frac{V_{n\Delta}(p_T^a, p_T^b)}{\sqrt{V_{n\Delta}(p_T^a, p_T^a) V_{n\Delta}(p_T^b, p_T^b)}} . \tag{5}$$

Values of $r_n = 1$ indicate no correlations, while $|r_n| > 1$ arc a sign of non-flow dynamics. CMS and ALICE data for r_2 and r_3 was also shown, however more data are needed, I believe, to draw solid conclusions.

Alexey Boyarsky discussed the chiral magnetic effect.[38] This is experimentally searched for at RHIC through a charge asymmetry of particles. It is usually widely discussed in the context of quark-gluon plasma and heavy ions. This effect is related to the fact that the SM plasma at finite densities of lepton and baryon numbers becomes unstable and tends to develop large-scale magnetic fields. The goal of Alexey's talk was to show that this effect is more general, and has to do with relativistic plasma of charged fermions (leptons and quarks). The conclusion is then that this effect can be important in other contexts whenever you have a relativistic magnetised plasma (such as in the early universe, in neutron stars, in astrophysical jets, and in quark-gluon plasma). Elena Petreska discussed magnetic Wilson loops in the classical field of high-energy HI collisions.[39] In the abelian case, the Wilson loop measures simply a flux, while in the non-abelian case the Wilson loop obey area law for uncorrelated magnetic vortices, which is found to hold for large enough areas.

Alexander Bylinkin discussed the origin of the thermal component in transverse momentum spectra in high-energy hadronic collisions. [40] It is well-known that black holes radiate thermal radiation with a temperature that is proportional to the acceleration of gravity at the surface. Similarly, an observer moving with acceleration a detects a thermal radiation proportional to his acceleration. This is usually referred to as Unruh radiation. In both cases, the effect is due to the presence of an event horizon, for instance, in the accelerated frame, part of the space-time is causally disconnected from the accelerating observer. In the case of high-energy collisions, confinement is proposed to produce the effective event horizon for coloured particles. This results then in thermal hadron production with temperature of about 160 MeV. Bylinkin used these observations to present a two-component model for hadro-production. The two components are attributed to two different mechanisms: hard radiation with a saturation scale, and a thermal Unruh-like radiation. Bylinkin showed that there is good agreement between the available experimental data and the predictions of the model for rapidity distributions, average transverse momentum as a fnction of multiplicity, and transverse momentum spectra, which have been notoriously difficult to describe with standard approaches.

7 Looking ahead

I am very much looking forward to coming Moriond meetings with lots of exciting new experimental data. While we all have high hopes, we also wonder what will happen if, despite the tremendous experimental and theoretical efforts, we do find any sign of new physics in Run II at the LHC. It is important to remember that exploring the unknown is valuable in it's own right. Surely it will not be wise to draw too quick conclusions, but whatever happens, we will learn something by going to a new frontier (Run II, HL-LHC, FCC, ...).

Acknowledgments

I would like to thank the organisers for the invitation to participate to this splendid meeting and all participants for many stimulating discussions and new insights. My work is supported by the ERC consolidator grant HICCUP (614577). I would also like to express a special thanks to the Mainz Institute for Theoretical Physics (MITP) for its hospitality while completing this writeup.

References

1. B. Mistlberger, these proceedings; C. Anastasiou, C. Duhr, F. Dulat, F. Herzog and B. Mistlberger, Phys. Rev. Lett. **114** (2015) 21, 212001 [arXiv:1503.06056 [hep-ph]].
2. R. D. Ball, M. Bonvini, S. Forte, S. Marzani and G. Ridolfi, Nucl. Phys. B **874** (2013) 746 [arXiv:1303.3590 [hep-ph]].
3. https://indico.cern.ch/event/331452/
4. F. Mahmoudi, arXiv:1506.07843 [hep-ph].
5. A. Guevara, these proceedings;A. Guevara, G. L. Castro, P. Roig and S. L. Tostado, arXiv:1505.01053 [hep-ph].
6. B. Grinstein, these proceedings; R. Alonso, B. Grinstein and J. Martin Camalich, Phys. Rev. Lett. **113** (2014) 241802 [arXiv:1407.7044 [hep-ph]].
7. R. Aaij *et al.* [LHCb Collaboration], Phys. Rev. Lett. **111** (2013) 18, 181801 [arXiv:1308.4544 [hep-ex]].
8. Sebastian Descotes-Genon, these proceedings; S. Descotes-Genon, L. Hofer, J. Matias and J. Virto, JHEP **1412** (2014) 125 [arXiv:1407.8526 [hep-ph]]; S. Descotes-Genon, L. Hofer, J. Matias and J. Virto, arXiv:1503.03328 [hep-ph].
9. Andreas Crivellin, these proceedings; A. Crivellin, G. DAmbrosio and J. Heeck, Phys. Rev. Lett. **114** (2015) 151801 [arXiv:1501.00993 [hep-ph]]; A. Crivellin, G. DAmbrosio and J. Heeck, Phys. Rev. D **91** (2015) 7, 075006 [arXiv:1503.03477 [hep-ph]].
10. Eibun Senaha, these proceedings; K. Fuyuto and E. Senaha, Phys. Lett. B **747** (2015) 152.
11. Gustavo Castelo-Branco, these proceedings.

12. Cai-Dian Lu, these proceedings; Z. T. Zou, A. Ali, C. D. Lu, X. Liu and Y. Li, Phys. Rev. D **91** (2015) 054033 [arXiv:1501.00784 [hep-ph]].
13. T. Le Compte, these proceedings.
14. P. Mastrolia, these proceedings; M. Argeri, S. Di Vita, P. Mastrolia, E. Mirabella, J. Schlenk, U. Schubert and L. Tancredi, JHEP **1403** (2014) 082 [arXiv:1401.2979 [hep-ph]].
15. J. Lindert, these proceedings; S. Kallweit, J. M. Lindert, P. Maierhfer, S. Pozzorini and M. Schnherr, JHEP **1504** (2015) 012 [arXiv:1412.5157 [hep-ph]].
16. F. Caola, these proceedings; R. Boughezal, F. Caola, K. Melnikov, F. Petriello and M. Schulze, arXiv:1504.07922 [hep-ph]. HEP :: Search :: Help :: Terms of use :: Privacy policy Powered by Invenio v1.1.2+ Problems/Questions to feedback@inspirehep.net
17. M. Czakon, these proceedings; M. Czakon, P. Fiedler and A. Mitov, arXiv:1411.3007 [hep-ph].
18. The ATLAS collaboration [ATLAS Collaboration], ATLAS-CONF-2014-057, ATLAS-COM-CONF-2013-113.
19. F. Dreyer, these proceedings; M. Dasgupta, F. Dreyer, G. P. Salam and G. Soyez, JHEP **1504** (2015) 039 [arXiv:1411.5182 [hep-ph]].
20. S. Prestel, these proceedings; S. Hoeche, Y. Li and S. Prestel, Phys. Rev. D **90** (2014) 5, 054011 [arXiv:1407.3773 [hep-ph]].
21. E. Bagnaschi, these proceedings; E. Bagnaschi, M. Cacciari, A. Guffanti and L. Jenniches, JHEP **1502** (2015) 133 [arXiv:1409.5036 [hep-ph]].
22. D. d'Enterria and a. R. Prez-Ramos, arXiv:1505.02624 [hep-ph]; R. Prez-Ramos and D. d'Enterria, EPJ Web Conf. **90** (2015) 04001 [arXiv:1412.2102 [hep-ph]].
23. M. Harley, arXiv:1505.05799 [hep-ph]; G. Falcioni, E. Gardi, M. Harley, L. Magnea and C. D. White, JHEP **1410** (2014) 10 [arXiv:1407.3477 [hep-ph]].
24. https://hepconf.physics.ucla.edu/radcor-loopfest/talks/gardi.pdf
25. S. Sapeta, these proceedings; P. Kotko, K. Kutak, C. Marquet, E. Petreska, S. Sapeta and A. van Hameren, arXiv:1503.03421 [hep-ph].
26. Sarka Todorova-Nova, these proceedings; S. Todorova-Nova, Phys. Rev. D **89** (2014) 1, 015002 [arXiv:1309.6761 [hep-ph]].
27. Shi-Yuan Li, these proceedings; Y. Jin, S. Y. Li, Z. G. Si, Z. J. Yang and T. Yao, Phys. Lett. B **727** (2013) 468 [arXiv:1309.5849 [hep-ph]].
28. Miguel Costa, these proceedings; R. C. Brower, M. S. Costa, M. Djuri?, T. Raben and C. I. Tan, JHEP **1502** (2015) 104 [arXiv:1409.2730 [hep-th]].
29. A. V. Koshelkin and C. Y. Wong, EPJ Web Conf. **90** (2015) 01004;
30. Giancarlo DAmbrosio, these proceedings; L. Cappiello, G. D'Ambrosio and D. Greynat, arXiv:1505.01000 [hep-ph].
31. M. Kieburg, J. Verbaarschot and S. Zafeiropoulos, arXiv:1505.03911 [hep-lat]; M. Kieburg, J. J. M. Verbaarschot and S. Zafeiropoulos, Phys. Rev. D **88** (2013) 094502 [arXiv:1307.7251 [hep-lat]].
32. Lezsek Roszkowski, these proceedings; K. Kowalska, L. Roszkowski, E. M. Sessolo and A. J. Williams, JHEP **1506** (2015) 020 [arXiv:1503.08219 [hep-ph]].
33. Oleg Ruchayskiy, these proceedings; S. Alekhin, W. Altmannshofer, T. Asaka, B. Batell, F. Bezrukov, K. Bondarenko, A. Boyarsky and N. Craig *et al.*, arXiv:1504.04855 [hep-ph];
34. G. Landsberg, arXiv:1506.00660 [hep-ph]; J. Abdallah, H. Araujo, A. Arbey, A. Ashkenazi, A. Belyaev, J. Berger, C. Boehm and A. Boveia *et al.*, arXiv:1506.03116 [hep-ph].
35. S. Malik, C. McCabe, H. Araujo, A. Belyaev, C. Boehm, J. Brooke, O. Buchmueller and G. Davies *et al.*, arXiv:1409.4075 [hep-ex].
36. Carlos Salgado, these proceedings; L. Apolinrio, G. Milhano, N. Armesto and C. A. Salgado, arXiv:1505.06593 [hep-ph].
37. Matt Luzum, these proceedings; I. Kozlov, M. Luzum, G. Denicol, S. Jeon and C. Gale, arXiv:1405.3976 [nucl-th].
38. Alexey Boyarsky, these proceedings; A. Boyarsky, O. Ruchayskiy and M. Shaposhnikov, Phys. Rev. Lett. **109** (2012) 111602 [arXiv:1204.3604 [hep-ph]].
39. Elena Petreska, these proceedings; A. Dumitru, Y. Nara and E. Petreska, Phys. Rev. D **88** (2013) 5, 054016 [arXiv:1302.2064 [hep-ph]].
40. Alexander Bylinkin, these proceedings; A. A. Bylinkin, N. S. Chernyavskaya and A. A. Rostovtsev, arXiv:1506.04285 [hep-ph].

Authors index

Landsberg, G.	Moving beyond effective field theory in dark matter searches at colliders
LeCompte, T.	Experimental summary
Leogrande, E.	Soft physics and collective phenomena in p–Pb collisions from ALICE
Li, S-Y	Colour connection and the doubly-heavy hadron production in e^+e^- annihilations
Li, Y.	Combining parton showers and NNLO matrix elements
Lindert, J.	NLO QCD+EW automation and precise predictions for V+multijet production
Lópes Castro, G.	A new long distance contribution to $B^\pm \to K^\pm/\pi^\pm\ell^+\ell^-$ DECAYS
Lucchesi, D.	Recent Heavy Flavor Physics Results from the Tevatron
Mahmoudi, N.	Introduction to Heavy Flavours
Maierhöfer, P.	NLO QCD+EW automation and precise predictions for V+multijet production
Makek, M.	Heavy Quarks and Quarkonia from Phenix
Marshall, Z.	Strong Production SUSY Searches at ATLAS and CMS
Mastrolia, P.	QCD Amplitudes: new perspectives on Feynman integral calculus
Masubuchi, T.	Measurement of other Higgs boson properties
Matias, J.	$B \to K^*\mu\mu$: theory interpretation or *A hitchiker's guide to* $B \to K^*\mu\mu$ *optimised observables*
Misheva, M.	Fisrt observation and study of $K^\pm \to \pi^\pm\pi^0e^+e^-$ decay at the NA48/2 experiment
Nayak, A.	Study of Higgs production in fermionic decay channels at the LHC
Pérez-Ramos, R.	α_s determination at NNLO*+NNLL accuracy from the energy evolution of jet fragmentation functions at low z
Petreska, E.	Magnetic Wilson loop in the classical field of high-energy heavy-ion collisions
Plestina, R.	Combination of Higgs Boson Coupling Measurements from ATLAS and CMS
Pozdnyakov, V.	Hard Probes at ATLAS
Pozzorini, S.	NLO QCD+EW automation and precise predictions for V+multijet production
Prestel, S.	Combining parton showers and NNLO matrix elements
Roig, P.	A new long distance contribution to $B^\pm \to K^\pm/\pi^\pm\ell^+\ell^-$ DECAYS
Roszkowski, L.	Looking for supersymmetry: $\sim$ 1TeV WIMP and the power of complementarity in LHC and dark matter searches
Salam, G.	Small-radius jets to all orders
Sapeta, S.	Forward dijet production and improved TMD factorization in dilute-dense hadronic collisions
Schönherr, M.	NLO QCD+EW automation and precise predictions for V+multijet production
Senaha, E.	Electroweak baryogenesis in a scale invariant model and Higgs phenomenology
Sessolo, S.	Looking for supersymmetry: $\sim$ 1TeV WIMP and the power of complementarity in LHC and dark matter searches
Skwarnicki, T.	Heavy quark spectroscopy at LHCb
Soyez, G.	Small-radius jets to all orders
Svoisky, P.	Recent QCD Results from the Tevatron
Todorova-Nová , Š.	Quantization of the QCD string with a helical structure
Tostado, S; L.	A new long distance contribution to $B^\pm \to K^\pm/\pi^\pm\ell^+\ell^-$ DECAYS
Trojanowski, S.	Looking for supersymmetry: $\sim$ 1TeV WIMP and the power of complementarity in LHC and dark matter searches
Velkovska, J.	Geometry and Collective Behavior in Small Systems from PHENIX
Verbaarschot, J.	Discretization effects in $N_c = 2$ QCD and Random Matrix Theory
Virto, J.	$B \to K^*\mu\mu$: theory interpretation or *A hitchiker's guide to* $B \to K^*\mu\mu$ *optimised observables*
Williams, A. J.	Looking for supersymmetry: $\sim$ 1TeV WIMP and the power of complementarity in LHC and dark matter searches
Wong, C-Y.	Multiparticle Dynamics and Pion Production in a Flux Tube
Wozniak, K.	Flow measurements in p+Pb and their comparison with Pb+Pb at ATLAS
Wulsin, H. W.	Thinking outside the beamspot: Other SUSY searches at the LHC (long-lived particles and R-parity violation)
Xie, S.	Studies of Higgs Boson Properties in Future LHC Runs
Yan, W.	Studies of charmonium at BESIII
Zafeiropoulos, S.	Discretization effects in $N_c = 2$ QCD and Random Matrix Theory
Zanderighi, G.	Theoretical summary
Zhu, K.	Exotic charmonium-like at BES III
Zou, Z-T.	Polarization study in B decays to vector meson final states

List of Participants

Family name	First name	Institution logo	Country	Email address
Anastopoulos	Christos	Dpt. Physics and Astronomy	UK	Christos.Anastopoulos@cern.ch
Augé	Étienne	LAL	France	auge@lal.in2p3.fr
Augustin	Jean-Eudes	LPNHE	France	augustin@in2p3.fr
Bagnaschi	Emanuele	DESY	Germany	emanuele.bagnaschi@desy.de
Balli	Fabrice	University of Manchester	UK	fabrice.balli@cern.ch
Benelli	Gabriele	University of Kansas / CERN	Switzerland	Gabriele.Benelli@cern.ch
Bertens	Redmer	Utrecht University	The Netherlands	rbertens@cern.ch
Blekman	Freya	VUB	Belgium	freya.blekman@vub.ac.be
Bock	Friederike	LBNL	USA	friederike.bock@cern.ch
Boyarsky	Alexey	Leiden University	The Netherlands	boyarsky@mail.cern.ch
Brandt	Oleg	Kirchhoff-Institüt für Physik	Germany	oleg.brandt@kip.uni-heidelberg.de
Britzger	Daniel	DESY	Germany	daniel.britzger@desy.de
Bylinkin	Alexander	Moscow Institute of Physics & Technology	Russia	alexander.bylinkin@gmail.com
Camarda	Stefano	DESY	Germany	stefano.camarda@desy.de
Caola	Fabrizio	CERN	Switzerland	fabrizio.caola@cern.ch
Carbone	Angelo	Università di Biologna	Italy	carbone@bo.infn.it
:astelo Branco	Gustavo	Instituto Superior Técnico	Portugal	gbranco@tecnico.ulisboa.pt
Chao	Yuan	National Taiwan University	Taiwan	yuanchao@cern.ch
Chistov	Ruslan	ITEP	Russia	chistov@itep.ru
Costa	Miguel	Universidade do Porto	Portugal	miguelc@fc.up.pt
Cremonesi	Matteo	Fermilab	USA	matteoc@fnal.gov
Crivellin	Andreas	CERN	Switzerland	andreas.crivellin@cern.ch
Czakon	Michal	Inst. Th. Particle Physics & Cosmology	Germany	mczakon@physik.rwth-aachen.de
D'Ambrosio	Giancarlo	CERN - TH Division	Switzerland	gdambros@na.infn.it
d'Enterria	David	CERN	Switzerland	dde@cern.ch
Demiragli	Zeynep	MIT	USA	zeynep.demiragli@cern.ch
scotes-Genon	Sébastien	LPT	France	descotes@th.u-psud.fr
Dettori	Francesco	CERN	Switzerland	francesco.dettori@cern.ch
Djuric	Marko	Universidade do Porto	Portugal	djuric@fc.up.pt
Dreyer	Frédéric	LPTHE	France	frederic.dreyer@cern.ch
scobar Ibáñez	Carlos	University of Pittsburgh / CERN	Switzerland	cescobar@cern.ch
Folgueras	Santiago	Universidad de Oviedo	Spain	santiago.folgueras@cern.ch
Gagliardi	Martino	Università degli Studi	Italy	martino.gagliardi@cern.ch
Gladilin	Leonid	Lomonosov Moscow State Univ. - SINP	Russia	gladilin@mail.cern.ch
Goulianos	Konstantin	The Rockefeller University	USA	dino@rockefeller.edu
Grinstein	Benjamin	UC San Diego	USA	bgrinstein@ucsd.edu
Guevara	Adolfo	Cinvestav	Mexico	aguevara@fis.cinvestav.mx
imarães Costa	João	Harvard University	USA	guimaraes@physics.harvard.edu
Hafner	Andreas	Universität Mainz	Germany	hafner@slac.stanford.edu
Harley	Mark	The University of Edinburgh	UK	mark.harley@ed.ac.uk
Heintz	Ulrich	Brown University	USA	ulrich_heintz@brown.edu
Hirschauer	James	Fermilab	USA	jhirsch@fnal.gov
Huang	Bingchu	University of Illinois	USA	bingchu@uic.edu
Hussain	Nazim	University of Oxford	UK	nazim.hussain@physics.ox.ac.uk
Johnson	Daniel	CERN	Switzerland	daniel.johnson@cern.ch
Kado	Marumi	LAL / CERN	France	kado@lal.in2p3.fr
Kajomovitz	Enrique	Duke University	USA	enrique.kajomovitz@gmail.com
Kepka	Oldrich	Academy of Sciences	Czech Republic	oldrich.kepka@cern.ch
Klima	Boaz	Fermilab	USA	klima@fnal.gov
Koshelkin	Andrei	National Nuclear Research Univ. - MEPHI	Russia	a_kosh@internets.ru
Krawczyk	Maria	University of Warsaw	Poland	krawczyk@fuw.edu.pl

Lammers Sabine	Indiana University	USA	slammers@indiana.edu
Lamont Matthew	Brookhaven National Lab.	USA	macl@bnl.gov
Landsberg Greg	Brown University	USA	landsberg@hep.brown.edu
LeCompte Thomas	Argonne National Lab.	USA	lecompte@anl.gov
Leogrande Emilia	Utrecht University	The Netherlands	emilia.leogrande@cern.ch
Li Shi-Yuan	Shandong University	China	lishy@sdu.edu.cn
Lindert Jonas	Universität Zürich	Switzerland	lindert@physik.uzh.ch
Lindquist Brian	Stony Brook University	USA	blindqui@cern.ch
Lu Cai-Dian	IHEP	China	lucd@ihep.ac.cn
Lucchesi Donatella	Università di Padova - INFN	Italy	donatella.lucchesi@pd.infn.it
Luzum Matthew	Universidade de Santiago de Compostela	Spain	matthew.luzum@usc.es
Mahmoudi Farvah Nazila	Université de Lyon	France	nazila@cern.ch
Makek Mihael	University of Zagreb	Croatia	mihaelmakek@gmail.com
Marquet Cyrille	École Polytechnique - CPhT	France	marquet@cpht.polytechnique.fr
Marshall Zachary	LBNL	USA	ZLMarshall@lbl.gov
Mastrolia Pierpaolo	Università di Padova	Italy	pierpaolo.mastrolia@cern.ch
Masubuchi Tatsuya	ICEPP	Japan	tatsuya.masubuchi@cern.ch
Mavromanolakis Georgios	University of Cyprus	Cyprus	gmavroma@gmail.com
Mehta Andrew	Liverpool University	UK	mehtaandrew@gmail.com
Misheva Milena	JINR	Russia	dyulendarova.milena@gmail.con
Mistlberger Bernhard	ETH	Switzerland	bernhard.mistlberger@gmail.cor
Narain Meenakshi	Brown University	USA	Meenakshi_Narain@brown.edu
Nayak Aruna Kumar	DESY	Germany	Aruna.Nayak@cern.ch
Olsen Jim	Princeton University	USA	jolsen@princeton.edu
Petreska Elena	École Polytechnique - CPhT	France	elena.petreska@polytechnique.e
Pietrzyk Bolek	LAPP	France	pietrzyk@lapp.in2p3.fr
Plestina Roko	IHEP	China	roko.plestina@cern.ch
Pozdnyakov Valery	JINR	Russia	Valery.Pozdnyakov@cern.ch
Prestel Stefan	SLAC	USA	prestel@slac.stanford.edu
Roland Christof	MIT	USA	christof.roland@cern.ch
Roszkowski Leszek	NCBR	Poland	leszek@fuw.edu.pl
Ruchayskiy Oleg	EPFL	Switzerland	oleg.ruchayskiy@epfl.ch
Salgado Carlos A.	Universidade de Santiago de Compostela	Spain	carlos.salgado@usc.es
Sapeta Sebastian	CERN - TH Division	Switzerland	sebastian.sapeta@cern.ch
Savard Pierre	TRIUMF - University of Toronto	Canada	savard@physics.utoronto.ca
Senaha Eibun	Nagoya University	Japan	senaha@eken.phys.nagoya-u.ac.
Skwarnicki Tomasz	Syracuse University	USA	tskwarni@syr.edu
Strom Derek	VUB	Belgium	derek.axel.strom@cern.ch
Svoisky Peter	University of Oklahoma	USA	psvoisky@gmail.com
Tan Chung-I	Brown University	USA	chung-i_tan@brown.edu
Todorova Sarka	Charles University	Czech Republic	sarka.todorova@cern.ch
Tran Thanh Van Jean	Rencontres du Vietnam	France	jtrantv@gmail.com
Tuo Shengquan	Vanderbilt University	USA	Shengquan.Tuo@Vanderbilt.Edu
Velkovska Julia	Vanderlbilt University	USA	julia.velkovska@vanderbilt.edu
Wozniak Krzysztof	Institute for Nuclear Physics	Poland	krzysztof.wozniak@ifj.edu.pl
Wulsin Wells	Ohio State University	USA	wulsin.1@osu.edu
Xie Si	Caltech	USA	sixie@hep.caltech.edu
Yan Wenbiao	University of Science and Technology	China	wenbiao@ustc.edu.cn
Zafeiropoulos Savvas	Goethe Universität	Germany	zafeiro@th.physik.uni-frankfurt.c
Zanderighi Giulia	CERN	Switzerland	g.zanderighi1@physics.ox.ac.uk
Zhu Kai	IHEP	China	zhuk@ihep.ac.cn